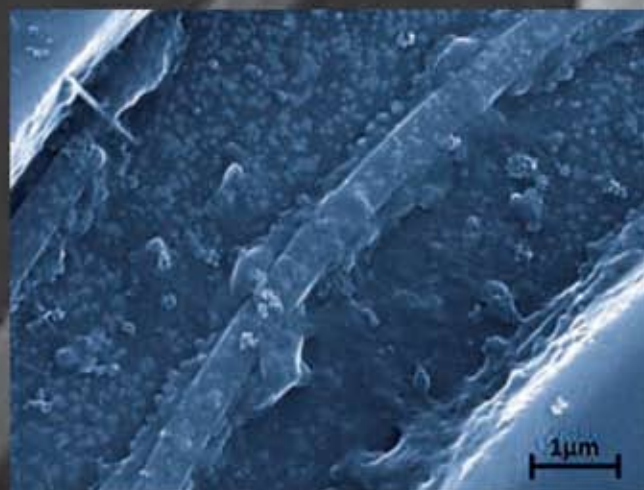
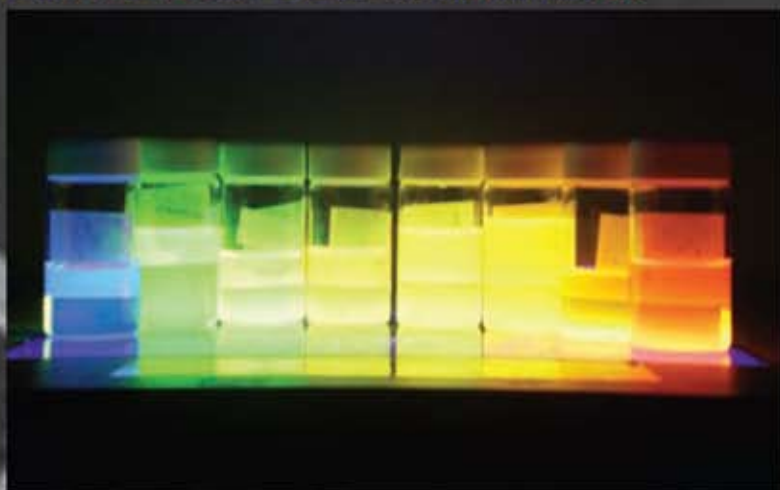




**NATIONAL NANOTECHNOLOGY INFRASTRUCTURE NETWORK  
RESEARCH EXPERIENCE FOR UNDERGRADUATES  
(NNIN REU) PROGRAM**



# **2012 Research Accomplishments**



# The National Nanotechnology Infrastructure Network Research Experience for Undergraduates Program

## 2012 Research Accomplishments

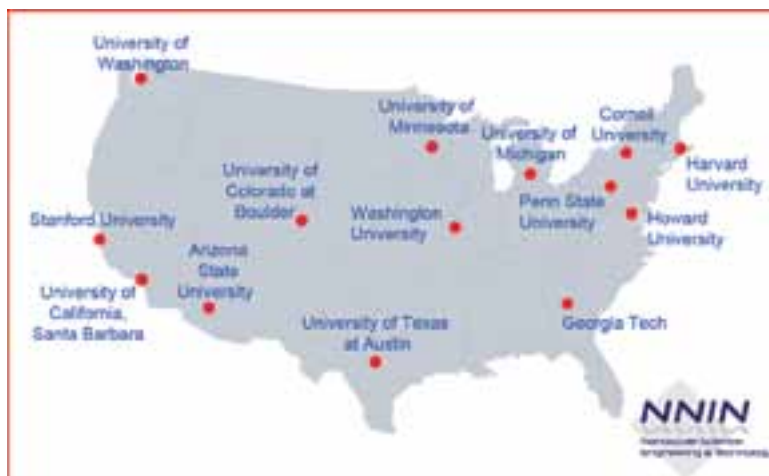
**2012 NNIN REU Reports by Research Focus; i-xi**

**The NNIN Sites & Corporate Sponsors; xii**

**Welcome, Prof. Roger Howe, NNIN Director; xiii**

**2012 NNIN Interns, by Site:**

<i>Arizona State, page xiv</i>	<i>University of Colorado, page xxii</i>
<i>Cornell, page xv</i>	<i>University of Michigan, page xxiii</i>
<i>Georgia Tech, page xvi</i>	<i>University of Minnesota, page xxiv</i>
<i>Harvard, page xvii</i>	<i>University of Texas, page xxv</i>
<i>Howard, page xviii</i>	<i>University of Washington, page xxvi</i>
<i>Penn State, page xix</i>	<i>Washington University, page xxvii</i>
<i>Stanford, page xx</i>	<i>NNIN iREU Program, page xxviii</i>
<i>UCSB, page xxi</i>	



**Commonly Used Abbreviations & Their Meanings; xxix-xxxviii**

### Biological Applications, pages 2-41

**Patterning of Biomolecules  
Using Dip Pen Nanolithography . . . . . 2**

*Ali Abdallah*                      *NNIN REU Site: Michigan*

**Towards Electro-Chemical Gating by CMOS . . . . . 4**

*Sharlin Anwar*                      *NNIN REU Site: Cornell*

**Cellular Binding of Quantum Dots . . . . . 6**

*Quachel Bazile*                      *NNIN REU Site: Georgia Tech*

**Optimization of Protocol for Fabrication  
of a Polymer Filter from a PDMS Mold . . . . . 8**

*Colin Burns-Heffner*                      *NNIN REU Site: Penn State*

**Towards Ink-Jet Fabricated PEDOT:PSS Organic  
Electrochemical Transistors with Embedded Enzymes . 10**

*Audrey Dang*                      *NNIN iREU Site: France*

**DNA Extension in Nanochannels . . . . . 12**

*Leon Dean*                      *NNIN REU Site: Minnesota*

**Biocompatible Dry Adhesives Mimicking  
Gecko Spatulae for EEG Electrodes . . . . . 14**

*Jennifer Gilbertson*                      *NNIN iREU Site: France*

**Optimizing Liposomal Uptake and Content Release  
Using Glioblastoma Multiforme as a Model System . . . 16**

*Sonali Gupta*                      *NNIN REU Site: Georgia Tech*





**Development of an *in vitro* Muscle Regeneration Model using a Combination of Microfluidics and Micropatterning . . . . . 18**  
*Camryn Johnson NNIN REU Site: Cornell*

**A Novel, Photoswitchable Poly(ethylene glycol) Biosurface with Applications for High-Throughput Cell Migration Assays . . . . . 20**  
*Olivia Lambdin NNIN iREU Site: Japan*

**The Effectiveness of Physical Sunscreens in Preventing UVB-Induced Mechanical Damage to the Stratum Corneum . . . . . 22**  
*Corinne Lampe NNIN REU Site: Stanford*

**Monitoring and Imaging Hypoxic Cells using Perfluorinated Near-Infrared Fluorescent Micelles . . . . . 24**  
*Kaleigh Margita NNIN REU Site: WUSTL*

**Measuring the Effects of RAD51 Assembly on dsDNA with Magnetic Tweezers. . . . . 26**  
*Morgan McGuinness NNIN iREU Site: Netherlands*

**Fabrication of a Selective Ion Pump: Anodization of an Aluminum Oxide Membrane . . . . . 28**  
*Christopher Nakamoto NNIN REU Site: UCSB*

**Silicone Nanoparticles for DNA Drug Delivery . . . . . 30**  
*Kendall Pletcher NNIN iREU Site: Japan*

**A Microfluidic Gradient Generating Device Integrated with Nanopatterned Matrices for Studying Guided Cell Migration . . . . . 32**  
*Radu Reit NNIN REU Site: UW*

**Uptake of Nanoparticles in the Olfactory System and Transport to the Brain in Locust. . . . . 34**  
*Jonathan Schoening NNIN REU Site: WUSTL*

**Progress Towards Electrical Interface Chips for BioMEMS. . . . . 36**  
*Stephanie Swartz NNIN REU Site: Colorado*

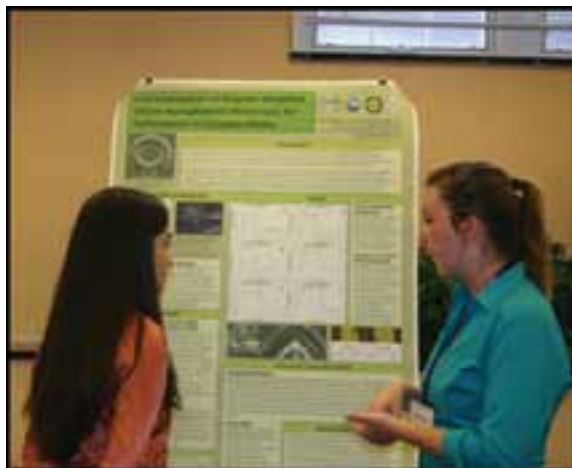


**Nanocharacterization of Polymer-Modified Microring Resonators for Performance in Complex Media . . . . . 38**

*Brianna Thielen NNIN REU Site: UW*

**High Fidelity Method for Microfabricating *in vitro* Neural Networks . . . . . 40**

*Geoffrey Vrla NNIN REU Site: Minnesota*



**Chemistry, pages 42-55**

**Interaction of Engineered Nanoparticles with Artificial Cell Membranes . . . . . 42**

*Rachel Benton NNIN REU Site: UW*

**Fabricating Parylene-C Shadow Masks for Applications in Short-Channel Top-Contact Carbon Nanotube Flexible Transistors . . . . . 44**

*Kelsey Hirotsu NNIN REU Site: Stanford*

**The Electrochemistry of Catalyzed Metal Multilayers . . 46**

*Briana James NNIN REU Site: Howard*

**Implementing Gaussian Quadrature in Molecular Plasmonics . . . . . 48**

*Alexander B. Lee NNIN REU Site: UW*

**Identification of Carbon Nanostructures (Fullerenes) in Cigarette Ash . . . . . 50**

*Ian MacKenzie NNIN REU Site: WUSTL*

**Investigation of Molecular Structures for Soft Matters with Mechanoresponsive Colors . . . . . 52**

*Kelly Suralik NNIN iREU Site: Japan*

**Effects of Membrane Surface Modification on Calcium Carbonate Fouling and Membrane Efficiency for Desalination . . . . . 54**

*Whitney Wong NNIN REU Site: WUSTL*





**Electronics, pages 56-75**

**Transparent and Stretchable Metal Electrodes . . . . .56**  
*Soichi Hirokawa* *NNIN REU Site: Colorado*

**Silicon Carbide Device Simulation and Measurement .58**  
*Keevin Hood* *NNIN REU Site: Arizona*

**Monolithic Integration of HEMT-Based Common Gate Oscillator with Active Integrated Antenna in the GaN Material System . . . . .60**  
*Kevin Huang* *NNIN iREU Site: Germany*

**Characterization of Phase Change Materials for Radio Frequency Applications . . . . .62**  
*Gwendolyn Hummel* *NNIN REU Site: Michigan*

**Fabrication and Characterization of Vertical Silicon Nanopillar Schottky Diodes . . . . .64**  
*Adam Overvig* *NNIN REU Site: Arizona*

**Electrochemical Deposition of Polythiophene onto Carbon Nanotube Arrays.. . . .66**  
*Ryan Parry* *NNIN REU Site: Georgia Tech*

**Understanding Performance Limitations in Organic Transistors . . . . .68**  
*William Scheideler* *NNIN iREU Site: Japan*

**Spin Torque Ferromagnetic Resonance with the Spin Hall Effect . . . . .70**  
*Oliver Switzer* *NNIN REU Site: Cornell*

**Self Assembled Monolayers on Inkjet-Printed ITO . . . .72**  
*Ashley Truxal* *NNIN REU Site: Michigan*

**Fabrication of GaAs-Based Integrated Circuits by Advanced Nanofabrication Techniques. . . . .74**  
*Daryl Vulis* *NNIN iREU Site: Japan*



**Materials, pages 76-127**

**Water-in-Ferrofluid Digital Microfluidic System for Single Cell Isolation and Transport . . . . . 76**  
*Elsie V. Bjarnason NNIN REU Site: Stanford*

**Hydrogen Impurities in Tin Dioxide Films Deposited by Pulsed Laser Deposition.. . . . . 78**  
*Alex Bryant NNIN iREU Site: Japan*

**Correlation between Surface Morphology and Hall Mobility between AlGaAs/GaAs <111> Heterojunctions . . . . . 80**  
*Isidro Calderon, Jr. NNIN REU Site: UCSB*

**Electrical Characterization of Heat-Treated Tin Monosulfide Thin Films. . . . . 82**  
*Annabel Chew NNIN REU Site: Harvard*

**Ionic Transport Across Atomically Thin Graphene Membranes . . . . . 84**  
*Lauren Cosgriff NNIN REU Site: Colorado*

**Synthesis and Characterization of Potassium Sodium Niobate, a Lead-Free Ferroelectric . . . . . 86**  
*Dmitriy Davydovich NNIN REU Site: Penn State*

**Phase Transformations in Metal Contacts to  $In_{0.53}Ga_{0.47}As$  Nanowires . . . . . 88**  
*Donna Deng NNIN REU Site: Penn State*

**Growth of Boron Nitride Nanowires.. . . . . 90**  
*Anderson Hayes NNIN REU Site: Howard*

**Controlling and Understanding the Effects of Reactive Colloids' Packing on Silicon Etching Patterns . . . . . 92**  
*Codey Henderson NNIN REU Site: Penn State*

**Assembly of Thermo-Responsive Microcapsules . . . . . 94**  
*Ian Holmes NNIN REU Site: Harvard*

**Effect of Inert Nanoparticles on Cement Hydration. . . . . 96**  
*Melinda Jue NNIN REU Site: Georgia Tech*





**Materials, continued**

**Influence of Optical Stress on Mixed Oxide Transistors . . . . . 98**  
*Andrew Knight* *NNIN REU Site: Arizona*

**Giant Magnetoresistive Sensors for Biological Applications . . . . . 100**  
*Jonathan Lee* *NNIN REU Site: Minnesota*

**Selective Atomic Layer Deposition . . . . . 102**  
*Clay Long* *NNIN REU Site: Cornell*

**Optimizing the Electrochemical Performance of Cathode Materials for Lithium Ion Rechargeable Batteries . . . . . 104**  
*Peter Luo* *NNIN REU Site: WUSTL*

**Growth and Characterization of GaAs/InAs Quantum Dots By Molecular Beam Epitaxy . . . . . 106**  
*Donnita M. McArthur* *NNIN REU Site: Howard*

**Transport in Near-Surface Two-Dimensional Electron Systems . . . . . 108**  
*Ryan McMorris* *NNIN REU Site: UCSB*

**Controlling the Composition and Morphology of Si<sub>1-x</sub>Ge<sub>x</sub> Nanowires . . . . . 110**  
*Ryan Murphy* *NNIN REU Site: Georgia Tech*

**Indium Arsenide Quantum Dot Lasers . . . . . 112**  
*Justin Norman* *NNIN REU Site: UCSB*

**Work Function Tuning in Amorphous TaWSiC Metal Gates for Integrated Circuits . . . . . 114**  
*Jordan Occeña* *NNIN REU Site: Stanford*

**Formation of Quantum Dots by Aerosol Reactor . . . . . 116**  
*Adam Roberge* *NNIN REU Site: WUSTL*

**Etch Study of Zirconium Oxide Nanoparticle Photoresist . . . . . 118**  
*Andrew Sanville* *NNIN REU Site: Cornell*

**Investigation of TiO<sub>2</sub> Films Deposited by Low-Temperature ALD Process for Future CMOS . . . . . 120**  
*Karl Schliep* *NNIN iREU Site: Japan*

**Engineering Carbon Nanotube Microdrops Using Microfluidic Devices . . . . . 122**  
*YooSun Shim* *NNIN REU Site: Harvard*

**Heteroepitaxial Growth of Diamond on SiC Substrates . . . . . 124**  
*Andrew Tam* *NNIN REU Site: Howard*

**Carbon Doping of <10-11> GaN by Plasma-Assisted Molecular Beam Epitaxy . . . . . 126**  
*Caroline Yu* *NNIN REU Site: UCSB*



**Mechanical Devices, pages 128-139**

**Characterization of XeF<sub>2</sub> Etching for Release of Piezoelectric Micro-Robots . . . . . 128**

*Ramon Alonso NNIN REU Site: Michigan*

**Two-Dimensional Buckled Nanoscale Nanomembrane as Tunable Grating .. . . . 130**

*Adel Azghadi NNIN REU Site: Arizona*

**Nanoparticle Sorting in Microfluidic Channels .. . . . 132**

*Rachel Baarda NNIN REU Site: UCSB*

**Carbon Nanotube Microfluidic Channels for Cell Manipulation .. . . . 134**

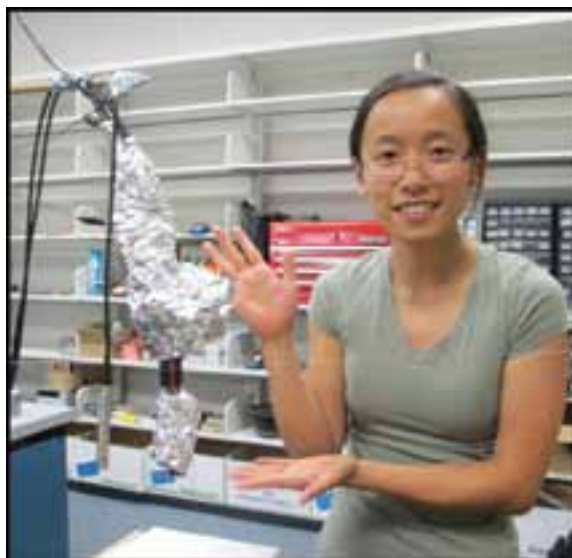
*Michael Bellavia NNIN REU Site: Michigan*

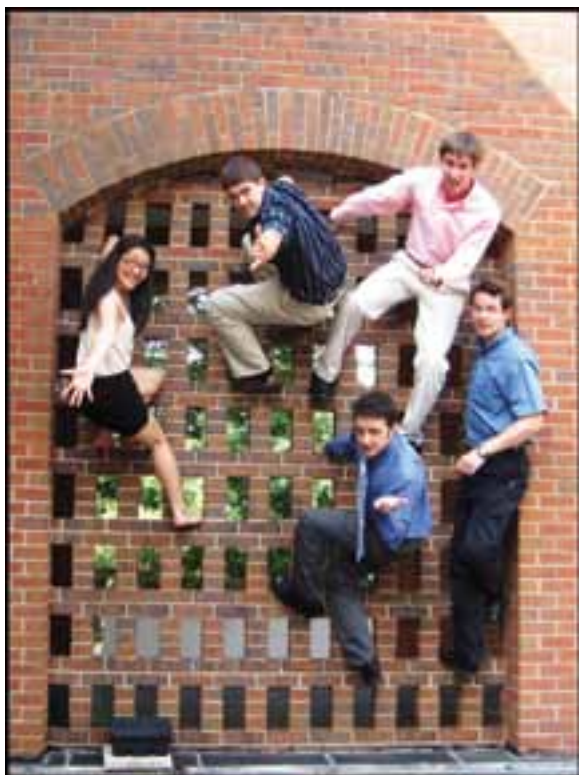
**Fabrication of MEMS Using Cheap Substrates.. . . . 136**

*Ryan Gaudreau NNIN REU Site: Howard*

**Fabrication and Characterization of a Micromachined In-Plane Directional Piezoelectronic Microphone .. . . . 138**

*Jia Gloria Lee NNIN REU Site: Texas at Austin*





**Optics & Opto-Electronics, pages 140-171**

**Optimizing the Delivery of Toxins and Glycans to Photonic Biosensor Surfaces. . . . . 140**  
*Abubakar Abid* *NNIN REU Site: Georgia Tech*

**Silicon Heterojunction Photovoltaic Cells.. . . . . 142**  
*Hans Banerjee* *NNIN REU Site: Texas at Austin*

**Anti-Reflective Coatings for Room Temperature Terahertz Quantum Cascade Laser Sources .. . . . 144**  
*Alexander Buck* *NNIN REU Site: Texas at Austin*

**Fabrication of Metallic and Dielectric NWs for Realizing Optical Filters . . . . . 146**  
*Amanda Ellison* *NNIN REU Site: WUSTL*

**Integration of Embedded CMOS Chips for On-Chip Optical Communication. . . . . 148**  
*Kyle Guess* *NNIN REU Site: UCSB*

**Microring Resonators in Silicon Photonic Circuits .. 150**  
*Daniel Klemme* *NNIN REU Site: Colorado*

**Microheaters for Thermo-Optic Tuning of Silicon Photonic Devices. . . . . 152**  
*Juan Pablo Llinás* *NNIN REU Site: Colorado*

**Metasurface Dichroic Mirrors and Applications to Solar Energy via Spectral Splitting.. 154**  
*Adam J. McMullen* *NNIN REU Site: Texas at Austin*

**Strain Color Coding Using Localized Surface Plasmon Resonance of Gold Nanoparticles .. . . . 156**  
*Jared Newton* *NNIN REU Site: WUSTL*

**Sub-Wavelength Gratings for Multi-Spectral Infrared Detection and Imaging. . 158**  
*Katherine Nygren* *NNIN REU Site: Michigan*

**Top-Gated Graphene-Based Ultrafast Electro-Optic Modulators .. . . . 160**  
*Jacob M. Rothenberg* *NNIN REU Site: Colorado*

**Volume Nano-Structured Optics for 3D Superresolution Imaging.. . . . . 162**  
*Aubrey Shapero* *NNIN REU Site: Colorado*

**CIS Nanocrystals with Inorganic Ligands for Photovoltaics Devices .. . . . 164**  
*Cherelle Thomas* *NNIN REU Site: Texas at Austin*

**Development of AirSpaced VIPA's for Use in Optical Coherence Tomography .. . . . 166**  
*Timothy Welsh* *NNIN REU Site: Stanford*

**Enhancing the Luminescence Efficiency of GaSb-Based Dilute-Nitrides by Rapid Thermal Annealing .. . . . 168**  
*Nathaniel Wendt* *NNIN REU Site: Texas at Austin*

**Electrically and Optically Obtaining Q of High Stress SiN Devices .. . . . 170**  
*Patrick Yu* *NNIN REU Site: Cornell*

**Physics & Nanostructure Physics, pages 172-197**

**Characterization of Si-Nanowires for Biosensor Applications** . . . . . 172  
*Andrew Acevedo*                      *NNIN iREU Site: Germany*

**Production of Solid State Spin Qubits** . . . . . 174  
*Dashiell R. Bodington*                      *NNIN REU Site: UCSB*

**Fractal Electrodes** . . . . . 176  
*Patrick Butera*                      *NNIN REU Site: Arizona*

**Improving Superconducting Resonators for use in Quantum Computing** . . . . . 178  
*Marcos Echeverria*                      *NNIN REU Site: UCSB*

**The Effects of Surface Passivation on Trap Levels in Silicon Nanocrystals** . . . . . 180  
*William Andres Gaviria Rojas* *NNIN REU Site: Minnesota*

**Self-Organized Nanostructural Pattern Formation under Ion Beam Irradiation** . . . . . 182  
*Michael Hovish*                      *NNIN REU Site: Harvard*

**Cryoelectronic Characterization of Organic Molecules** . . . . . 184  
*Matthew Kiok*                      *NNIN iREU Site: Germany*

**Construction of a Modulated Potential Superlattice** . 186  
*Phillip Meyerhofer*                      *NNIN REU Site: Penn State*

**Optical Characterization and Solar Cell Application of GaAs/Al<sub>0.8</sub>Ga<sub>0.2</sub>As Quantum Wells** . . 188  
*Lauren M. Otto*                      *NNIN iREU Site: Japan*

**Oxidation of CVD Grown Carbon Nanotubes for Applying Magnetic Complexes for Spin Transport Measurements** . . . . . 190  
*Francisco Pelaez, III*                      *NNIN iREU Site: Germany*

**Monolayer Molybdenum Diselenide** . . . . . 192  
*Elisa M. Russo*                      *NNIN REU Site: Cornell*





**Physics & Nanostructure, continued**

**Oxidation Effect in Single Dot Quantum Junctions . . . 194**  
*Reyu Sakakibara* *NNIN iREU Site: Netherlands*

**A 3D Circuit QED Architecture with Separate Readout and Coupling Cavities . . . . . 196**  
*Kevin Tien* *NNIN iREU Site: Netherlands*

**Process & Characterization, pages 198-221**

**Production and Characterization of Topological Insulators. . . . . 198**  
*Adam Blonsky* *NNIN REU Site: UW*

**AFM-Assisted Etching and Electrical Characterization of Graphene. . . . . 200**  
*Camille L.M. Everhart* *NNIN REU Site: Cornell*

**Engineering the Charge Occupancy of Nitrogen Vacancies in Diamond . . . . . 202**  
*William Gilpin* *NNIN REU Site: Harvard*

**Sacrificial Polymers and Their use in Patternable Air-Gap Fabrication . . . . . 204**  
*David Goldfeld* *NNIN REU Site: Georgia Tech*

**Biomaterialized Nanopore Membranes on Silicon for Nanoparticle Translocation . . . . . 206**  
*Melissa Gosse* *NNIN REU Site: Arizona*

**Fabrication of Graphene Field Effect Transistors . . . . 208**  
*Lee Hamstra* *NNIN REU Site: Colorado*

**Testing the Properties and Characteristics of Chitin Thin Films . . . . . 210**  
*Kamil Makhneja* *NNIN REU Site: UW*



**Process & Characterization, continued**

**Temperature Dependent  
Electrical Resistivity of  $\text{La}_x\text{Lu}_{1-x}\text{As}$  . . . . . 212**  
*Maria Michael NNIN REU Site: Texas at Austin*

**Photovoltaic Devices  
Fabricated with CIGS Nanocrystal Inks. . . . . 214**  
*Isao Mori NNIN iREG Site: Texas at Austin*

**Substrate Conformal Imprint Lithography . . . . . 216**  
*Frazier Mork NNIN REU Site: Cornell*

**Engineered Metallic Structures and Nanofabrication  
Techniques for Plasmonic Biosensors . . . . . 218**  
*Stephen Olson NNIN REU Site: Minnesota*

**Atomic Layer Deposition Process Optimization and  
Characterization of Amorphous Metal-Oxide Films . . 220**  
*Emily Ross NNIN REU Site: Stanford*

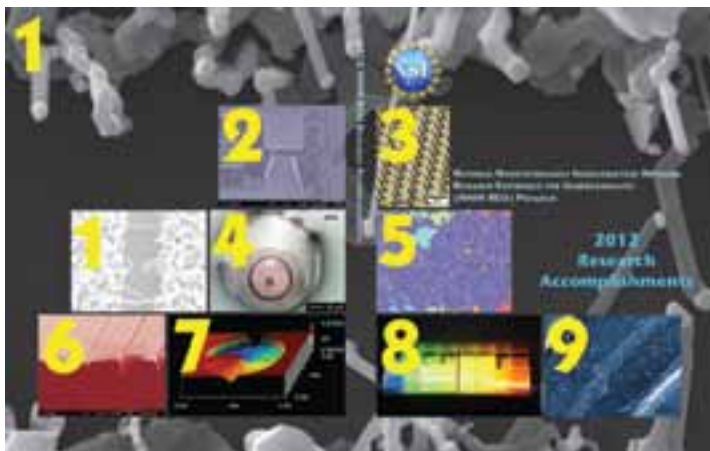


**Societal & Ethical Issues of Nanotechnology,  
pages 222-225**

**A Study of Integrating Societal  
and Ethical Issues into NNIN REU . . . . . 222**  
*Merrill Brady NNIN REU Site: Cornell*

**Nanotechnology Companies in the U.S.A:  
A Web-Based Analysis of  
Companies and Poverty Alleviation . . . . . 224**  
*Duy Do NNIN REU Site: Georgia Tech*

**Index, pages 227-230**



**COVER LEGEND**

- 1. Blonsky, University of Washington, Figure 3 page 198
- 2. Hamstra, University of Colorado, Figure 4 page 208
- 3. Gilpin, Harvard University, Figure 2 page 202
- 4. Gosse, Arizona State University, Figure 4 page 206
- 5. Hirokawa, University of Colorado, Figure 1 page 56
- 6. Olson, University of Minnesota, Figure 2 page 218
- 7. Shapero, University of Colorado, Figure 1 page 162
- 8. Roberge, WUSTL, Figure 2 page 116
- 9. Thielen, University of Washington, Figure 3 page 38

*The photographs in the table of contents were provided by the NNIN REU and iREU interns, and NNIN staff.  
The convocation photographs in the table of contents and introduction were taken by Melanie-Claire Mallison.  
This book is printed on 10% post-consumer paper, using soy-based inks. Please do your part to reduce, reuse, and recycle.*

# The National Nanotechnology Infrastructure Network

<http://www.nnin.org/>

is comprised of the following fourteen sites, and is supported by  
The National Science Foundation, the NNIN sites, our corporate sponsors, and research users.

**ASU NanoFab, Arizona State University**

Ira A. Fulton Schools of Engineering  
PO Box 876206  
Tempe, AZ 85287-6206  
(480) 965-3808 • <http://www.fulton.asu.edu/nanofab/>

**Cornell NanoScale Science & Technology Facility, Cornell University**

250 Duffield Hall, 343 Campus Rd  
Ithaca, NY 14853-2700  
(607) 255-2329 • <http://www.cnf.cornell.edu>

**Nanotechnology Research Center, Georgia Institute of Technology**

791 Atlantic Dr NW  
Atlanta, GA 30332-0269  
(404) 385-4307 • <http://www.nrc.gatech.edu>

**Center for Nanoscale Systems, Harvard University**

11 Oxford Street, LISE 306  
Cambridge, MA 02138-2901  
(617) 384-7411 • <http://www.cns.fas.harvard.edu>

**Howard Nanoscale Science & Engineering Facility, Howard University**

Downing Hall Room 1124  
2300 Sixth St NW  
Washington, DC 20059-1015  
(202) 806-6618 • <http://www.msrece.howard.edu/>

**Penn State Nanofabrication Laboratory, The Pennsylvania State University**

Millennium Science Complex Building  
University Park, PA 16802  
(814) 865-7443 • <http://www.mri.psu.edu/facilities/nnin>

**Stanford Nanofabrication Facility, Stanford University**

P.G. Allen Bldg, 420 Via Palou  
Stanford, CA 94305-4070  
(650) 725-3607 • <http://snf.stanford.edu/>

**Nanotech, University of California, Santa Barbara**

ECE Dept, Engineering Science Bldg 1109F  
Santa Barbara, CA 93106-9560  
(805) 893-5999 • <http://www.nanotech.ucsb.edu/>

**Colorado Nanofabrication Laboratory, University of Colorado at Boulder**

ECEE Campus Box 425  
Boulder, CO 80309-0425  
(303) 492-5324 • <http://cnl.colorado.edu/>

**Lurie Nanofabrication Facility, The University of Michigan, Ann Arbor**

1301 Beal Ave 1241 EECS  
Ann Arbor, MI 48109-2122  
(734) 763-0231 • <http://www.lnf.umich.edu>

**Nanofabrication Center, University of Minnesota-Twin Cities**

200 Union St SE  
1-165 Keller Hall  
Minneapolis, MN 55455-0171  
(612) 625-3069 • <http://www.nfc.umn.edu/>

**Microelectronics Research Center, The University of Texas at Austin**

J.J. Pickle Research Campus  
10100 Burnet Rd, Bldg 160  
Austin, TX 78758-4445  
(512) 471-4493 • <http://www.mrc.utexas.edu/>

**NanoTech User Facility, University of Washington**

Molecular Engineering & Sciences Building  
Box 352143, Rm G43E  
Seattle, WA 98195  
(206) 616-2169 • <https://depts.washington.edu/ntuf/facility/>

**Nano Research Facility, Washington University in St. Louis**

Brauer Hall, Room 010  
Campus Box 1180, One Brookings Drive  
St. Louis, MO 63130-4899  
(314) 935-7264 • <http://www.nano.wustl.edu/>

**NNIN REU Corporate Sponsors:**

Agilent Technologies  
Analog Devices  
Applied Materials  
Cambridge Nanotech  
Canon  
Daihen Corporation  
Ericsson  
IBM Corporation  
Infineon  
Intel Corporation  
Invensense  
National Semiconductor Corporation  
NEC Corporation  
NXP Semiconductors  
OCI Company  
Qualcomm  
Renesas Electronics Corporation  
Robert Bosch Corp.  
STMicroelectronics  
Texas Instruments, Incorporated  
Toshiba



*The 2012 NNIN REU Interns at the network convocation, held August 12-15, in Washington, DC. Photograph by Melanie-Claire Mallison.*

## Welcome to the 2012 edition of NNIN REU Research Accomplishments!

This publication reflects the hard work of the undergraduate researchers, as well as the dedication and commitment of their mentors, the NNIN site staff, REU coordinators, and the principal investigators.

Our summer program brings undergraduates from colleges and universities across the U.S. into some of the nation's leading academic nanofabrication laboratories for an intensive ten-week research experience. The participants are trained in safe laboratory practices, learn the essential scientific background for their project, and then perform independent research in nanotechnology, under the guidance of their mentor. For many of the students, the NNIN REU is their first experience when the answer, or even the existence of an answer, is not yet known. The summer experience provides the students with a sample of what life for them could be like as a graduate student in applied science and engineering, both in and outside the clean room. For many, the NNIN REU helps them to decide to pursue a career in research and development.

During the summer of 2012; 94 students participated in our Research Experience for Undergraduates (REU) Program. Returning from the previous summer's NNIN REU Program, 17 students were selected to participate in NNIN's International Research Experience for Undergraduates (iREU) Program in France, Germany, Japan, and the Netherlands. In addition, one graduate student from Japan participated in our research exchange (iREG) program.

NNIN is committed to making all three of these programs a significant experience for the participants, by focusing on advanced research and knowledge, seeking strong mentors and staff support, exposing the students to a professional research environment, and having high expectations for the summer research projects, as well as for the presentations at the final convocation. The students' exposure to a wider variety of research conducted by their peers and the other nanofab users across diverse disciplines of science and engineering provides a significant complementary experience.

I would like to thank the NNIN REU staff, graduate student mentors, and faculty for their contributions to the success of this year's programs. Particular thanks are due to Ms. Melanie-Claire Mallison and Dr. Lynn Rathbun for their contributions to organizing the logistics of these programs. In addition, I am grateful to them for organizing the network-wide convocation in Chevy Chase, Maryland.

I wish all our program participants the best for their future careers, whether in science, engineering, or other disciplines. I hope you will build on this summer's experience and I look forward to hearing from you on your future successes!

Roger T. Howe  
 Director, NNIN  
 rthowe@stanford.edu





**The 2012 NNIN REU Program @  
Cornell NanoScale Science & Technology Facility, Cornell University**

**Ms. Sharlin Anwar** ... .. **page 4**  
**Ms. Merrill Brady** .. ... **page 222**  
**Ms. Camille Everhart** ... .. **page 200**  
**Ms. Camryn Johnson** . ... . **page 18**  
**Mr. Clay Long** ... .. **page 102**  
**Mr. Frazier Mork**... .. **page 216**  
**Ms. Elisa Russo** .. ... **page 192**  
**Mr. Andrew Sanville** . ... . **page 118**  
**Mr. Oliver Switzer** . ... . **page 70**  
**Mr. Patrick Yu**... .. **page 170**



**The 2012 NNIN REU Program @  
Nanotechnology Research Center, Georgia Institute of Technology**

**Mr. Abubakar Abid... ..page 140**  
**Ms. Quachel Bazile ... .. page 6**  
**Mr. Duy Do ... ..page 224**  
**Mr. David Goldfeld ... ..page 204**  
**Ms. Sonali Gupta... .. page 16**  
**Ms. Melinda Jue. .... page 96**  
**Mr. Ryan Murphy.. ....page 110**  
**Mr. Ryan Parry.. .... page 66**



**The 2012 NNIN REU Program @ Center for Nanoscale Systems, Harvard University**

**Ms. Annabel Chew** ... .. page 82  
**Mr. William Gilpin** ... ..page 202  
**Mr. Ian Holmes.** ... .. page 94  
**Mr. Michael Hovish**... ..page 182  
**Ms. YooSun Shim** .. ...page 122



**The 2012 NNIN REU Program @  
Howard Nanoscale Science & Engineering Facility, Howard University**

**Mr. Ryan Gaudreau... ..page 136**

**Mr. Anderson Hayes.. ..page 90**

**Ms. Briana James .. ..page 46**

**Ms. Donnita McArthur.. ..page 106**

**Mr. Andrew Tam... ..page 124**



**The 2012 NNIN REU Program @  
Penn State Nanofabrication Laboratory, The Pennsylvania State University**

**Mr. Colin Burns-Heffner ... .. page 8**

**Mr. Dmitriy Davydovich ... .. page 86**

**Ms. Donna Deng ... .. page 88**

**Mr. Codey Henderson ... .. page 92**

**Mr. Phillip Meyerhofer . ... ..page 186**



**The 2012 NNIN REU Program @  
Stanford Nanofabrication Facility, Stanford University**

**Ms. Elsie Bjarnason ... .. page 76**

**Ms. Kelsey Hirotsu. ... .. page 44**

**Ms. Corinne Lampe ... .. page 22**

**Mr. Jordan Occena ... .. page 114**

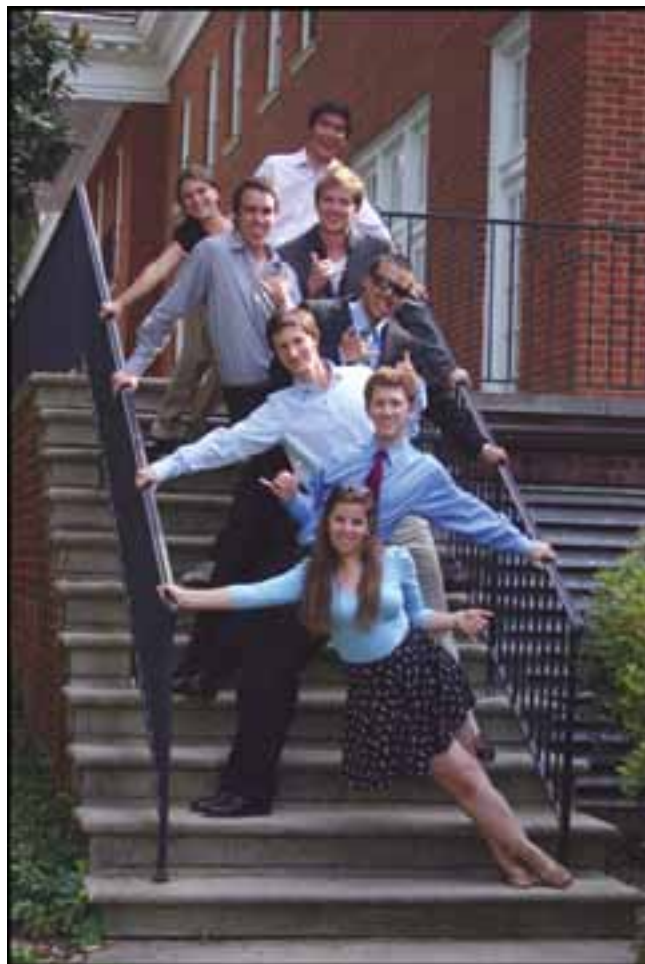
**Ms. Emily Ross ... .. page 220**

**Mr. Timothy Welsh ... .. page 166**



**The 2012 NNIN REU Program @ Nanotech, University of California, Santa Barbara**

**Ms. Rachel Baarda ... ..page 132**  
**Mr. Dashiell Bodington ... ..page 174**  
**Mr. Isidro Calderon, Jr. ... ..page 80**  
**Mr. Marcos Echeverria... ..page 178**  
**Mr. Kyle Guess... ..page 148**  
**Mr. Ryan McMorris ... ..page 108**  
**Mr. Christopher Nakamoto .. ..page 28**  
**Mr. Justin Norman ... ..page 112**  
**Ms. Caroline Yu . ... ..page 126**



**The 2012 NNIN REU Program @  
Colorado Nanofabrication Laboratory, University of Colorado at Boulder**

**Ms. Lauren Cosgriff... .. page 84**  
**Mr. Lee Hamstra ... .. page 208**  
**Mr. Soichi Hirokawa . . . . . page 56**  
**Mr. Daniel Klemme... .. page 150**  
**Mr. Juan Llinas .. . . . page 152**  
**Mr. Jacob Rothenberg .. . . . page 160**  
**Mr. Aubrey Michael Shapero ... .. page 162**  
**Ms. Stephanie Swartz ... .. page 36**



**The 2012 NNIN REU Program @  
Lurie Nanofabrication Facility, The University of Michigan, Ann Arbor**

**Mr. Ali Abdallah ... .. page 2**  
**Mr. Ramon Alonso ... ..page 128**  
**Mr. Michael Bellavia . ... ..page 134**  
**Ms. Gwendolyn Hummel .. ... . page 62**  
**Ms. Katherine Nygren... ..page 158**  
**Ms. Ashley Truxal.. ... . page 72**



**The 2012 NNIN REU Program @  
Nanofabrication Center, University of Minnesota-Twin Cities**

**Mr. Leon Dean... .. page 12**

**Mr. William Gaviria .. .. page 180**

**Mr. Jonathan Lee .. .. page 100**

**Mr. Stephen Olson ... .. page 218**

**Mr. Geoffrey Vrla .. .. page 40**



**The 2012 NNIN REU & iREG Programs @  
Microelectronics Research Center, The University of Texas at Austin**

**Mr. Hans Banerjee** ... ..page 142  
**Mr. Alexander Buck**.. ... ..page 144  
**Ms. Jia Gloria Lee** .. ... ..page 138  
**Mr. Adam McMullen** . ... ..page 154  
**Ms. Maria Michael.** ... ..page 212  
**Mr Isao Mori**.. ... ..page 214  
**Ms. Cherrelle Thomas**... ..page 164  
**Mr. Nathaniel Wendt** ... ..page 168



**The 2012 NNIN REU Program @  
Center for Nanotechnology, University of Washington**

**Ms. Rachel Benton ... .. page 42**

**Mr. Adam Blonsky. ... .. page 198**

**Mr. Alexander Lee. ... .. page 48**

**Mr. Kamil Makhnejia ... .. page 210**

**Mr. Radu Reit ... .. page 32**

**Ms. Brianna Thielen.. ... .. page 38**



**The 2012 NNIN REU Program @  
Nano Research Facility, Washington University in St. Louis**

**Ms. Amanda Ellison** . . . . . page 146

**Mr. Peter Luo** . . . . . page 104

**Mr. Ian MacKenzie** . . . . . page 50

**Ms. Kaleigh Margita** . . . . . page 24

**Mr. Jared Newton** . . . . . page 156

**Mr. Adam Roberge** . . . . . page 116

**Mr. Jonathan Schoening**... . . . . page 34

**Ms. Whitney Wong** . . . . . page 54



### The 2012 NNIN iREU Program



**Mr. Andrew Acevedo** ... .. page 172

**Mr. Alex Bryant** . . . . . page 78

**Ms. Audrey Dang** .. . . . page 10

**Ms. Jennifer Gilbertson** . . . . . page 14

**Mr. Kevin Huang**... . . . . page 60

**Mr. Matthew Kiok** . . . . . page 184

**Ms. Olivia Lambdin** ... . . . . page 20

**Ms. Morgan McGuinness**... . . . . page 26

**Ms. Lauren Otto** ... . . . . page 188

**Mr. Francisco Pelaez, III** ... . . . . page 190

**Ms. Kendall Pletcher** . . . . . page 30

**Ms. Reyu Sakakibara** . . . . . page 194

**Mr. William Scheideler** . . . . . page 68

**Mr. Karl Schliep** ... . . . . page 120

**Ms. Kelly Suralik** ... . . . . page 52

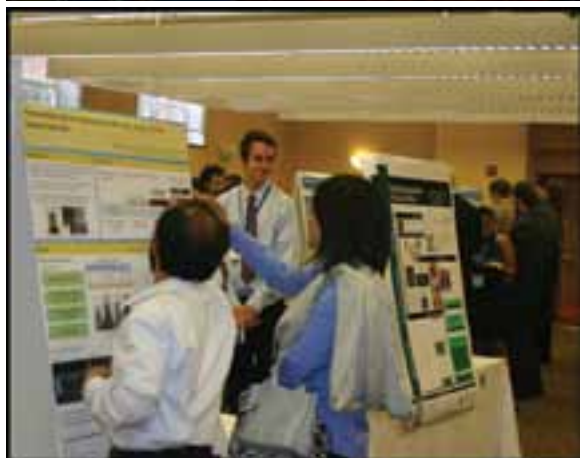
**Mr. Kevin Tien**... . . . . page 196

**Ms. Daryl Vulis** .. . . . page 74

## Commonly Used Abbreviations & Their Meanings

$\mu$ l.....	microliter
$\mu$ m.....	micron, micrometer
$\mu$ N.....	micro-Newtons
<.....	is less than
>.....	is greater than
~.....	approximately
1D.....	one dimensional
2D.....	two dimensional
2DEG.....	two dimensional electron gas
3D.....	three dimensional
3DOM carbon.....	three-dimensionally ordered macroporous carbon
$^4$ He.....	helium-4
a-Si.....	amorphous silicon
A&M.....	Agricultural & Mechanical
AC.....	alternating current
AFM.....	atomic force microscopy/microscope
Ag.....	silver
agLDL.....	aggregated low-density lipoproteins
AgNO <sub>3</sub> .....	silver nitrate
AgSR.....	silver-alkanethiolate
AIC.....	aluminum-induced crystallization
Al.....	aluminum
Al <sub>2</sub> O <sub>3</sub> .....	aluminum oxide
ALD.....	atomic layer deposition
AlGaN.....	aluminum gallium nitride
AM.....	amplitude modulation
APD.....	avalanche photodiode
APS.....	advanced photon source
Ar.....	argon
ARC.....	anti-reflective coating
ArF.....	argon fluoride
As.....	arsenide
AST.....	aspartate transaminase
atm.....	standard atmosphere (as a unit of pressure)
ATRP.....	atom transfer radical polymerization
Au.....	gold
AuNPs.....	gold nanoparticles
BAM.....	bisphenol aminomethyl
BCL <sub>3</sub> .....	boron trichloride
BDM.....	2,3-butanedione monoxime
BES.....	bioelectrochemical system
BHJ.....	bulk heterojunction
Bi.....	bismuth
BioSAXS.....	biological small angle x-ray scattering
BN.....	boron nitride
BOE.....	buffered oxide etch
BOX.....	buried oxide layer
BPB.....	bisphenol base
BPF.....	bisphenol F
BSA.....	bovine serum albumin
BST.....	barium strontium titanate
BTO.....	barium titanate
C.....	carbon
C.....	centigrade





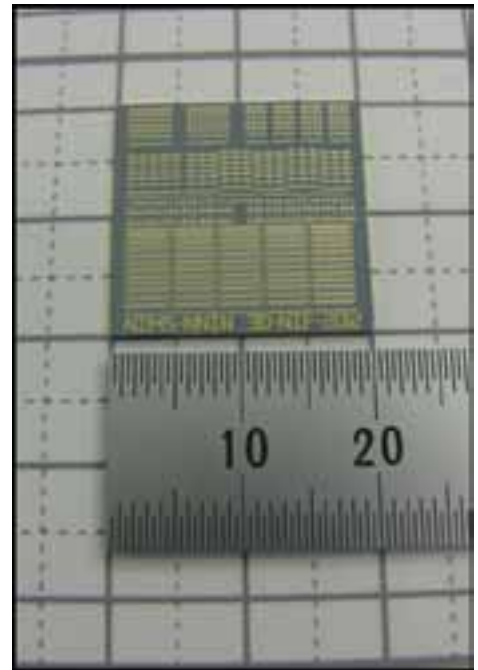
C-V	capacitance-voltage
$C_3N_4$	carbon nitride
$C_4F_8$	octafluorocyclobutane, or perfluorocyclobutane
CAD	computer-aided design
CCS	continuous compositional spreads
Cd	cadmium
CdS	cadmium sulfide
CdSe	cadmium selenide
CDW	charge-density-wave
Ce	cerium
$CF_4$	carbon tetrafluoride or tetrafluoromethane
CFD	computational fluid dynamics
CFMA	carbon-fiber microelectrode amperometry
$CH_4$	methane
$CHF_3$	trifluoromethane
CIGS	copper indium gallium diselenide
CION	colloidal iron oxide nanoparticles
Cl	chlorine
$Cl_2$	chlorine gas
$Cl_2/SF_6$	chlorine sulfur hexafluoride
cm	centimeter
CMOS	complementary metal oxide semiconductor
CMOSFET	complimentary metal oxide field effect transistor
CMP	chemical mechanical polishing
CNL	charge neutrality level
CNTFET	carbon nanotube field-effect transistor
Co	cobalt
$CO_2$	carbon dioxide
COF	covalent organic framework
CoFeAl	cobalt iron aluminum
CoP	cobalt porphyrin
CPC	colloidal photonic crystal
CPD	contact potential difference
Cr	chromium
CRDS	cavity ring-down spectrometer
CTC	circulating tumor cell
CTC	composite thermal capacitors
CTL	confinement tuning layer
Cu	copper
$Cu_2ZnSnS_4$	copper zinc tin sulfide
CVD	cardiovascular disease
CVD	chemical vapor deposition
CW	continuous wave
CXRF	confocal x-ray fluorescence microscopy
DC	direct current
DCB	double cantilever beam
DCE	1,2-dichloroethane
DCM	dichloromethane
DEP	dielectrophoresis
DFT	density functional theory
DFT	discrete Fourier transform
DH-PSF	double helix point-spread function
DI	de-ionized
DIC	differential interference contrast
DMF	dimethyl formamide
DNA	deoxyribonucleic acid
DNP	dynamic nuclear polarization





GaNAs .....	gallium indium nitride arsenide
GaN .....	gallium nitride
GaP .....	gallium phosphide
GaSb .....	gallium antimonide
GASP .....	growth advantage in stationary phase
GB .....	glass bead
GBLMA .....	$\alpha$ -gamma butyrolactone methacrylate
GC .....	gas chromatograph
GC-C-IRMS .....	gas chromatography combustion isotope ratio mass spectrometry
Ge .....	germanium
GEDI $\mu$ devices .....	geometrically enhanced differential immunocapture microdevices
GFET .....	graphene field effect transistor
GHz .....	gigahertz
GI .....	gastrointestinal
GMFI .....	gross mean fluorescence intensity
GMR .....	giant magnetoresistance
GNR .....	gold nanorod
GNR .....	graphene nanoribbons
GPa .....	gigapascal
GPC .....	gel permeation chromatography
GPS .....	global positioning system
GRIN .....	gradient refractive index
GUI .....	graphical user interface
GVD .....	group-velocity dispersion
h .....	hours
H .....	hydrogen
H-NMR .....	hydrogen-1 nuclear magnetic resonance spectroscopy
H <sub>2</sub> O <sub>2</sub> .....	hydrogen peroxide
HAMA .....	hydroxyl adamantyl methacrylate
HAuCl <sub>4</sub> .....	chloroauric acid
hBN .....	hexagonal boron nitride
hcp .....	hexagonal close packing
HCPI .....	Heme Carrier Protein 1
He .....	helium
HEMTs .....	high electron mobility transistors
HF .....	hydrofluoric acid
HFES .....	hydrofluoroethers
HfO <sub>2</sub> .....	hafnium dioxide
Hg .....	mercury
high- $\kappa$ .....	high dielectric constant
HMDS .....	hexamethyldisilazane
HMGB .....	high-mobility group box protein
HOMO-LUMO .....	highest occupied molecular orbital & lowest unoccupied molecular orbital
HOPG .....	highly oriented pyrolytic graphite
HRS .....	high resistance state
HRTEM .....	high-resolution transmission electron microscopy
HS-ssDNA .....	thiol terminated single stranded deoxyribonucleic acid
HSQ .....	hydrogen silsesquioxane
HSQ/FOx .....	negative electron beam resist hydrogen silsesquioxane
Hz .....	hertz
I-V .....	current-voltage
I/O .....	input/output
IC .....	integrated circuit
ICP .....	inductively coupled plasma
ICP-MS .....	inductively coupled plasma mass

ICP-RIE.....inductively coupled plasma reactive ion etcher  
 IFVD .....impurity free vacancy diffusion  
 IID .....impurity induced disordering  
 IIEI .....ion implant enhanced interdiffusion  
 In .....indium  
*in situ*.....Latin phrase which translated literally as ‘in position’ -- to examine the phenomenon exactly in place where it occurs  
*in vitro* .....Latin for “within glass” -- refers to studies in experimental biology that are conducted using components of an organism that have been isolated from their usual biological context in order to permit a more detailed or more convenient analysis than can be done with whole organisms.  
*in vivo*.....Latin for “within the living” -- experimentation using a whole, living organism  
 InAlN .....indium aluminum nitride  
 InAs.....indium arsenide  
 InAs NWs.....indium arsenide nanowires  
 InGaAsN .....indium gallium arsenide nitride  
 InP .....indium phosphide  
 IPA.....isopropyl alcohol  
 IPE.....ion & plasma equipment  
 IPT.....in-plane torque  
 IR.....infrared  
 IRMS.....isotope ratio mass spectrometry  
 IrO<sub>2</sub> or IrO<sub>x</sub>.....iridium oxide  
 ISFET .....ion-sensitive field effect transistor  
 ITO .....indium tin oxide  
 κ .....dielectric constant  
 K.....Kelvin (a unit of measurement for temperature)  
 kDa.....kilodaltons  
 KFM.....Kelvin force microscopy  
 kg.....kilogram  
 kHz.....kilohertz  
 KOH.....potassium hydroxide  
 KPFM.....Kelvin probe force microscopy  
 L/D .....length-to-diameter  
 La .....lanthanum  
 LAO .....lanthanum aluminum oxide  
 LED.....light-emitting diode  
 LER.....line edge roughness  
 LO .....local oscillator  
 low-κ.....low dielectric constant  
 LPCVD .....low pressure chemical vapor deposition  
 lpm .....liter per minute  
 LRS .....low resistance state  
 LSPR.....localized surface plasmon resonance  
 Lu .....lutetium  
 LWGs .....liquid-core/liquid-cladding waveguides  
 LWR.....line width roughness  
 M-OPTG .....microring-based optical pulse-train generator  
 MACE.....metal-assisted chemical etching  
 MAMA.....methyl adamantyl methacrylate  
 MBE.....molecular beam epitaxy  
 MCBJ .....mechanically controllable break junction  
 MD .....molecular dynamics  
 ME.....magnetoelectric  
 MEG.....maleimide-ethylene glycol disulfide





MEMs .....	microelectromechanical systems
MFC .....	microbial fuel
MFMR.....	microfabricated micro-reactors
MgO .....	magnesium oxide
MGs.....	molecular glasses
MHz .....	megahertz
micron .....	micrometer, aka $\mu\text{m}$
MIFIS .....	metal-insulator-ferroelectric-insulator-semiconductor
min .....	minutes
ml .....	milliliter
mm .....	millimeter
mM.....	millimolar
MMA-MAA.....	methyl-methacrylate-co-methacrylic acid
mmHg .....	millimeters of mercury; unit of pressure measurement
MnO <sub>2</sub> NPs .....	manganese oxide nanoparticles
Mo .....	molybdenum
MOCVD.....	metal oxide chemical vapor deposition
MONOS .....	metal/oxide/nitride/oxide/semiconductor
MOS .....	metal oxide semiconductor
MOSFET.....	metal oxide semiconductor field effect transistor
MOVPE.....	metal organic vapor phase epitaxy
MPM .....	multiphoton microscopy
MQCA.....	magnetic quantum-dot cellular automata
MQW .....	multiple quantum well
MRA.....	multifunction reconfigurable antenna
MRAM.....	magnetic random access memory
MRFM.....	magnetic resonance force microscopy
MRI.....	magnetic resonance imaging
ms.....	microsecond
MSM .....	metal-semiconductor-metal
MTJ .....	magnetic tunneling junction
mTorr.....	millitorr
mV.....	millivolt
MVD .....	molecular vapor deposition
MWNT.....	multiwalled carbon nanotube
M $\Omega$ .....	megohms
N.....	nitrogen
n-type .....	negative semiconductor
N <sub>2</sub> .....	nitrous oxide
nA.....	nanoAmperes
NaCl.....	sodium chloride
Nb.....	niobium
NEMs .....	nanoelectromechanical systems
NEXAFS.....	near edge x-ray absorption fine structure
NH <sub>4</sub> F .....	ammonium fluoride
Ni.....	nickel
NIR.....	near-infrared
nL .....	nanoliter
nm .....	nanometer
NMP .....	n-methyl-2-pyrrolidone
NMR .....	nuclear magnetic resonance microscopy / spectroscopy
NORIS.....	nanometrology optical ruler imaging system
NPR.....	nonlinear polarization rotation
NPs.....	nanoparticles
NPs.....	nanopores
ns .....	nanosecond
NSF .....	National Science Foundation





PPM.....	photolithographic phase masks
PS .....	polystyrene
PSL.....	polystyrene latex
PSMO.....	praseodymium strontium manganite
PS $\mu$ M .....	phase separation micro-molding
Pt .....	platinum
Pt/Ir .....	platinum/iridium
PTX.....	paclitaxel
PV.....	photovoltaic
PVA.....	poly-vinyl alcohol
PVC.....	polyvinyl chloride
PVDF .....	polyvinylidene fluoride
PVP .....	polyvinylpyrrolidone
Py .....	Ni <sub>81</sub> Fe <sub>19</sub>
PZT.....	lead zirconate titanate (PbZr <sub>0.52</sub> Ti <sub>0.48</sub> O <sub>3</sub> )
Q.....	high quality factor
QD.....	quantum dots
QW .....	quantum well
QWL.....	quantum well intermixing
RF.....	radio frequency
RF MEMS .....	radio frequency microelectromechanical systems
RFID .....	radio frequency identification
RIE .....	reactive ion etch
RMS or rms.....	root mean square
RNA .....	ribonucleic acid
ROS.....	reactive oxygen species
RPEVCD.....	remote plasma-enhanced chemical vapor deposition
RRAM.....	resistive random access memory
RTA .....	rapid thermal anneal
RTD.....	resistance temperature device
s .....	seconds
S .....	sulfur
SA-MOVPE.....	selective area metal organic vapor phase epitaxy
SABC .....	surface active block copolymers
SAED.....	selected area electron diffraction
SAMs .....	self-assembled monolayers
Sb .....	antimony
SBH.....	Schottky barrier height
Sc.....	scandium
SCAN.....	single-chromatin analysis at the nanoscale
scm .....	standard cubic centimeters per minute
scCO <sub>2</sub> .....	supercritical carbon dioxide
SCOFET.....	single crystal organic field effect transistor
SCORE.....	SNARE Complex Reporter
SDS .....	sodium dodecyl sulfate
Se.....	selenium
sec .....	seconds
SECM.....	scanning electrochemical microscopy
SEM .....	scanning electron microscopy/microscope
SERS .....	surface enhanced Raman spectroscopy
SF <sub>6</sub> .....	sulfur hexafluoride
SFLS .....	supercritical fluid-liquid-solid
SH .....	second harmonic
Si .....	silicon
Si <sub>3</sub> N <sub>4</sub> .....	silicon nitride
SiAlON .....	silicon aluminum oxynitride
SiC.....	silicon carbide

SiH <sub>4</sub> .....	silane
SiN.....	silicon nitride
SiNWs.....	silicon nanowires
SiO <sub>2</sub> .....	silicon dioxide
SIROF.....	sputtered iridium oxide film
SLBs.....	supported lipid bilayers
SLG.....	single-layer graphene
SLM.....	spatial light modulator
SLUG.....	superconducting low-inductance undulatory galvanometer
SMS.....	single molecule spectroscopy
Sn.....	tin
SnO <sub>2</sub> .....	tin oxide
SNPs.....	silver nanoparticles
SNR.....	signal-to-noise ratio
SOFC.....	solid oxide fuel cells
SOI.....	silicon-on-insulator
SPCM.....	scanning photocurrent microscopy
SPD.....	switching phase diagram
SPR.....	surface plasmon resonance
Sr <sub>2</sub> RuO <sub>4</sub> .....	strontium ruthenate
SrTiO <sub>3</sub> .....	strontium titanate
ssDNA.....	single-stranded deoxyribonucleic acid
STEM.....	scanning transmission electron microscopy/microscope
STJ.....	superconducting tunnel junction
STM.....	scanning tunneling microscopy/microscope
STO.....	strontium titanate
STT.....	spin-transfer torques
STT-MRAM.....	spin-transfer torque random access memory
SVA.....	solvent vapor annealing
<i>t</i> -BOC.....	<i>tert</i> -butoxycarbonyl
Ta.....	tantalum
Ta <sub>2</sub> O <sub>5</sub> .....	tantalum pentoxide
TaN.....	tantalum nitride
TCO.....	transparent conducting oxide
Te.....	crystalline tellurium
TE.....	transverse electric
TEC.....	thermionic energy converter
TEM.....	tunneling electron microscopy/microscope
TER.....	transepithelial resistance
TFM.....	traction force microscopy
TFT.....	thin-film transistor
Tg.....	glass transition temperature
TH.....	third harmonic
THz.....	terahertz
Ti.....	titanium
TiN.....	titanium nitride
TiO <sub>2</sub> .....	titanium dioxide
TLM.....	transfer length measurement
TM.....	transverse magnetic
TMAH.....	tetramethylammonium hydroxide
TMOS.....	tetramethyl orthosilicate
TMR.....	tunneling magnetoresistance
TO.....	thermo-optic
TO.....	torsional oscillator
TO.....	transformation optics
TPoS.....	thin-film piezoelectric-on-substrate
TRT.....	thermal release tape





- TSVs .....through silicon vias
- TTD.....transverse translational diversity
- TTV.....total thickness variation
- TXM.....transmission x-ray microscopy
- UHV .....ultra-high vacuum
- UV .....ultraviolet
- UV-Vis .....ultraviolet-visible
- V .....vanadium
- V .....voltage
- VA-CNT .....vertically aligned carbon nanotube
- vdW.....van der Waals
- VLS .....vapor-liquid-solid
- VRMs.....voltage regulator modules
- VSM.....vibrating sample magnetometry
- W .....tungsten
- WDM .....wavelength-division multiplexing
- We number .....Weber number
- WGM .....whispering gallery mode
- XeF<sub>2</sub> .....xenon difluoride
- XMCD.....x-ray magnetic circular dichroism
- XPM.....cross-phase modulation
- XPS .....x-ray photoelectron spectroscopy
- XRD .....x-ray diffraction
- XRR .....x-ray reflectivity
- YBCO .....yttrium-barium-copper-oxide
- YBS.....y-branch switch
- ZMW .....zero-mode waveguide
- ZnO .....zinc oxide
- ZnO:Al .....zinc aluminum oxide
- ZnS.....zinc sulfide or zinc-blende
- Zr.....zirconium
- ZrO<sub>2</sub>.....zirconium dioxide
- ZTO.....zinc tin oxide







---

**The National Nanotechnology Infrastructure Network  
Research Experience for Undergraduates Program**

**2012 Research Accomplishments**

---

## Patterning of Biomolecules Using Dip Pen Nanolithography

**Ali Abdallah**

**Biomedical Engineering, Wayne State University**

*NNIN REU Site: Lurie Nanofabrication Facility, University of Michigan, Ann Arbor, MI*

*NNIN REU Principal Investigator: Dr. Edgar Meyhofer, Mechanical Engineering, University of Michigan*

*NNIN REU Mentor: Dr. Pilar Herrera-Fierro, Electrical Engineering and Computer Science, University of Michigan*

*Contact: ahabdallah27@gmail.com, meyhofe@umich.edu, pilarhf@umich.edu*

### Introduction:

Kinesin and dynein are biomolecular motors in eukaryotic cells that transport intracellular cargoes along the cytoskeletal networks of microtubules in opposite directions. Interestingly, these proteins bind to the same cargo and are widely believed to be responsible for the bidirectional transport of cargoes [1, 2]. While the basic working principles of individual bimolecular motors are now understood in some detail, how multiple motors interact in the cells remains entirely unclear.

This work's goal was to precisely pattern motors using Dip Pen Nanolithography (DPN) such that their interactions can be studied *in vitro*. NanoInk's DPN 5000 was used to carry out the patterning process. First, however, another protein, bovine serum albumin (BSA), a less costly and readily available protein, was patterned to develop the proper methodology of patterning. Subsequently, the approach developed for BSA will be translated to patterning the motors. Patterned motors will be examined for ATPase activity and microtubule gliding to ensure functionality in *in vitro* motility assays.

### Experimental Procedure:

First, fluorescently labeled bovine serum albumin (BSA), a less costly and readily available protein, was patterned to develop the proper methodology of patterning. Subsequently, the approach developed for BSA will be translated to patterning the motors. BSA is in solution of concentration 2.62 g/L. A 1:10 mixture was composed of it and a mixture of 40% glycerol and 60% Brinkley reassociation buffer (BRB 80). We used an A-tip type probe from Nanoink, a probe with a single cantilever tip, and made a ten-dot, five-second dwell time per dot pattern. Using the fluorescing of the fluorescently-labeled BSA, these patterns were viewed using an Olympus BX-51 fluorescence microscope.

To properly examine the proper protocol for patterning, tip loading, bleeding, and the use of different substrates were examined. We experimented with loading the tip by using ink wells provided by NanoInk, pipetting the ink directly atop the tip, and manually guiding the tip into a pipetted droplet. After we determined which loading method to use, we examined whether the tip must be pre-bled by patterning multiple patterns under known working conditions established from ink that NanoInk provided and examined results under

the microscope. Finally, we prepared clean cover glasses differently ensuring the substrate was solely glass. The substrates were prepared as follows: O<sub>2</sub> plasma treated surface, 30 second hydrofluoric acid (HF) bathed surface, supercritical CO<sub>2</sub> sprayed surface, and a surface with the following recipe: 30 second HF bath, eight-minute de-ionized rocker bath, two-minute annealing at 300°C, Omniccoat<sup>®</sup> spun on surface for 10 seconds at 500 rpm and 20 seconds at 3000 rpm, one-minute annealing at 300°C, SU-8 5 spun under same conditions with a three-minute annealing time at 65°C, two-minute SU-8 developer bath, and finally an isopropanol rinse of the substrate.

We examined the preferred surface by patterning on the substrates and examining the surface hydrophobicity using a goniometer from Ramé Hart Instruments Co.

### Results and Conclusions:

When placed under the fluorescence microscope, ink was not visible from either the ink well or pipetting method. We then tried manually guiding the tip into the ink and found an abundant amount of ink on the tip (shown in Figure 1). We also found that sonicating the tip in acetone helped the



*Figure 1: Microscopic image of fluorescent ink atop tip when tip is manually guided.*

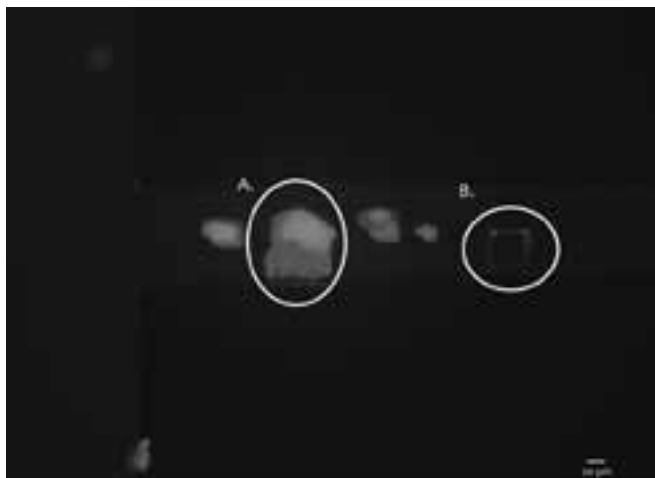


Figure 2: Microscopic image of resulting pattern when tip is not pre-bleed.

tip maintain ink. To further conclude the better method, patterning was conducted under each loading method and we found that the inkwell and pipetting method produced no consistent pattern while the other method did.

Using the guided tip technique, we next examined whether the tip had to be pre-bleed. The tip not pre-bleed (Figure 2A) resulted in a blob of ink as opposed to a proper pattern (Figure 2B); indicating that the tip must be pre-bleed so that the excess ink can be exhausted.

The most effective way to bleed the tip is to use the laser feedback on the DPN while the tip is on the substrate. If the laser feedback is not steady then there is excess ink. Also, approaching and withdrawing the tip from the surface until the laser feedback is steady is necessary to provide the most accurate patterns.



Figure 3: Microscopic image of pattern produced on SU-8 developed substrate.

Quantitative Analysis of Substrate				
Substrate	Average	Standard Deviation	Streaking	Advancing Angle (°)
O <sub>2</sub> Plasma Etch	7.822	1.008	Yes	0
HF Etch	3.352	0.9103	Yes	0
CO <sub>2</sub> Etch	2.212	1.332	No	30
SU8 Developed	1.032	0.213	No	130

Figure 4: Table depicting quantitative comparison of different substrates.

Figure 4 shows an indirect correlation between surface hydrophobicity and dot size and also shows that streaking occurs on the really hydrophilic surfaces and not on the less hydrophilic surfaces. It also shows that the SU-8 developer treated substrate produces the most consistent dot size.

It was also noticed that the constant height mode was more efficient than constant force mode of the DPN 5000 since the tip withdrew after each dwell time, thereby further preventing streaking. It was important to prevent streaking in order to ensure molecules were only present in desired locations to properly analyze the motors.

**Future Work:**

The method established must now be translated to the patterning of motor proteins. If patterning is successful under the same protocol, the (motor) proteins must be examined for functionality when patterned. If the motors are functional, we must develop an *in vitro* motility assays to examine the interaction between motor proteins.

**Acknowledgements:**

I would like to thank the National Nanotechnology Infrastructure Network Research Experience for Undergraduates Program, the National Science Foundation, the Lurie Nanofabrication Facility and staff, Dr. Edgar Meyhofer, and Dr. Pilar Herrera-fierro and her lab group, especially Anthony Nguyen and Tae-Hyung Kang, for their support in my endeavor; without them my success would have been much more limited.

**References:**

[1] Hollenbeck, P. Saxton, W. The Axonal Transport of Mitochondria. *Journal of Cell Science*. 118. 5411-5419. 2005.  
 [2] Holzbaur, E et. Goldman, Y. Coordination of Molecular Motors: From *in vitro* Assays of intracellular Dynamics. *Current Opinion in Cell Biology*. 22. 4-13.

## Towards Electro-Chemical Gating by CMOS

**Sharlin Anwar**

**Biomedical Engineering, The City College of New York**

*NNIN REU Site: Cornell NanoScale Science and Technology Facility, Cornell University, Ithaca, NY*

*NNIN REU Principal Investigator: Edwin C. Kan, School of Electrical and Computer Engineering, Cornell University*

*NNIN REU Mentor: Krishna Jayant, School of Electrical and Computer Engineering, Cornell University*

*Contact: sa778@cornell.edu, kan@ece.cornell.edu, kj75@cornell.edu*

### Abstract:

Electrolyte-oxide-semiconductor (EOS) capacitors were fabricated to elucidate; (a) the dynamics of the ionic double layer under field-effect modulation, (b) the effect of electrolyte composition on the zero-field voltage, and (c) the role of insulator surface groups on the differential capacitance of the fluidic double layer. Surface groups, owing to their amphoteric nature, are known to regulate charge when a potential is applied, which in turn sets up the double layer at the solid-electrolyte surface [1]. Through this study, we show a complex interplay between double layer dynamics, ionic composition and surface groups through capacitance-voltage measurements. Valency of the cationic species was shown to result in a strong hysteretic effect dependent on surface charge density. Varying time intervals during the cyclic sweep indicated the dynamics of ionic adsorption/desorption effects. The potential of hydrogen (pH) dependence was shown to exhibit near-Nernstian sensitivity. The pH response increased for increase in surface charge density, indicating that ionic adsorption might play the additional role in determining the zero-field potential.

### Introduction:

Electro-fluidic gating is an effect where an applied field imparts control over the ionic layer on an electrolyte/solid interface, called the electric double layer [1]. Fields emanating

from buried electrodes in solution are usually screened by counterions over a characteristic length, termed the Debye length. Beyond this length scale, Coulomb forces exerted on molecules are negligible. Recently the chemical nature of the interface was found to play a profound effect on charge modulation.

Through this study, we aimed to understand how the electrofluidic gating effect changed with different interface chemistries. We performed the study using simple EOS capacitors (Figure 1) with different dielectric layers.

### Experimental Procedure:

The fabrication process consisted of three splits. The first split had 30 nm of thermally grown silicon dioxide ( $\text{SiO}_2$ ) deposited on a clean Si wafer followed by a patterning to open up the capacitor areas. Positive photoresist SPR 220 3.0 was used and exposure was done by ABM contact aligner. A descum was carried out for 10s in the Oxford 82 etcher. The second process split included various oxide layers deposited on the Si wafers by the atomic layer deposition (ALD) tool, including hafnium oxide ( $\text{HfO}_2$ ), tantalum oxide ( $\text{Ta}_2\text{O}_5$ ), aluminum oxide ( $\text{Al}_2\text{O}_3$ ) and  $\text{SiO}_2$  interfaces. The third process split included 20 nm of thermally grown  $\text{SiO}_2$  on a metal-oxide-semiconducting (MOS) cleaned Si wafer, followed by 70 nm of  $n^+$  polysilicon.

The wafers were then spun with SPR 220 (3.0) and exposed through the ABM contact aligner. The YES Image Reversal oven was employed to change the tone of the photoresist from positive to negative. After development, the wafers were  $\text{CHF}_3/\text{O}_2$  etched in the Oxford 82 etcher, leaving blocks of polysilicon on the wafer. After stripping off the photoresist, 200 nm layer of silicon nitride ( $\text{Si}_3\text{N}_4$ ) was deposited on the wafer to serve as the passivation layer. A subsequent photolithography step was performed to open up the capacitor active area. An RIE etch was performed to remove any residual resist. The wafers consisted of capacitors of three different sizes ranging from  $300 \mu\text{m} \times 300 \mu\text{m}$  to  $1000 \mu\text{m} \times 1000 \mu\text{m}$ . Capacitance versus voltage (CV) measurements were made on the devices with the Keithley 4200 semiconductor characterization system.

Here we report measurements with the largest capacitor.

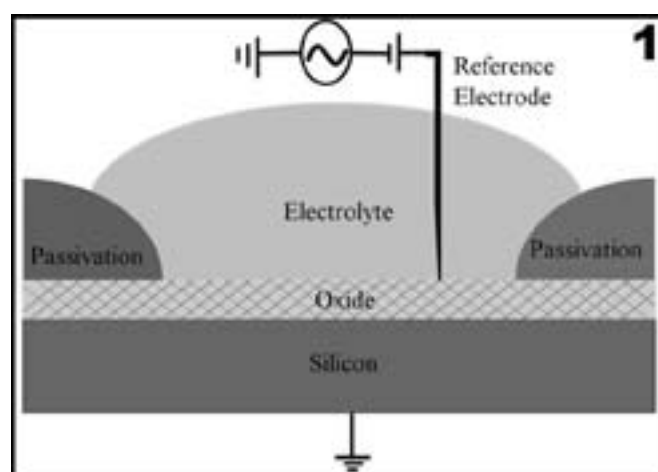


Figure 1: The EOS capacitor device.

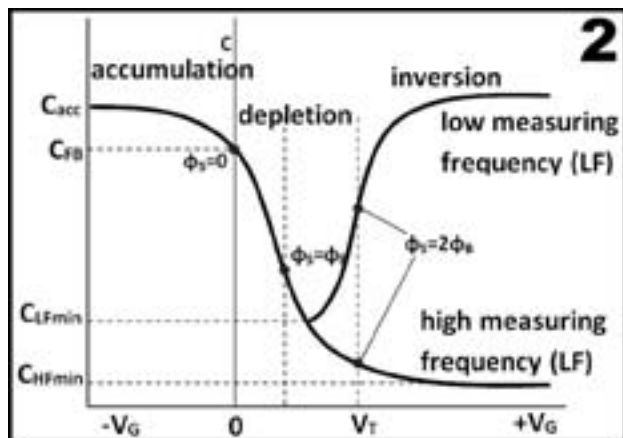


Figure 2: Typical MOS capacitor CV behavior.

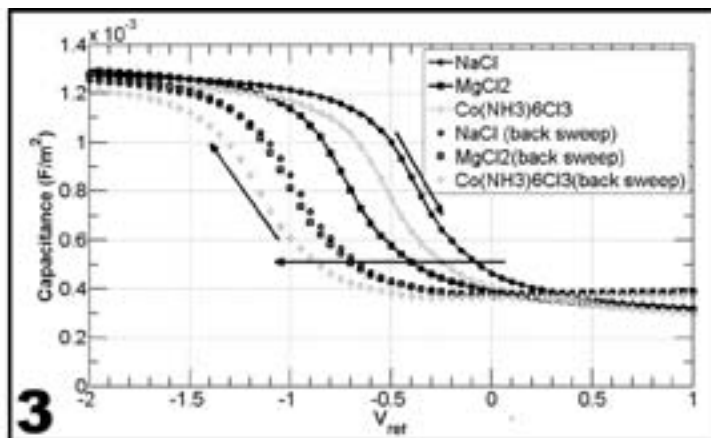


Figure 3: Cation valency comparison on polysilicon capacitors performed at pH 7.

## Results and Conclusions:

CV measurements reported here were carried out on three different surfaces consisting of; (a) polysilicon, (b)  $\text{Al}_2\text{O}_3$ , and (c) thermal  $\text{SiO}_2$ . Behavior of a typical MOS capacitor is shown in Figure 2. The inversion characteristic of a MOS capacitor is a strong function of applied frequency. Exceeding a cutoff frequency, originally mobile charges (either electrons at the silicon interface or ions at the electrolyte-solid interface) will stop responding to the AC excitation and behave like a simple dielectric layer, which decreases the overall capacitance. We chose a frequency where ions continued to respond while electrons at the silicon interface did not. A frequency of 5 kHz was used to perform our measurements.

**Comparison of pH.** The capacitors were tested with 20 mmol sodium chloride (NaCl) electrolyte of pH 3, pH 5, pH 7, pH 9 and pH 11. With decreasing pH, the zero-field voltage shift reduced, indicating a larger positive charge adsorption to the interface. As the pH reduced, the number of  $\text{H}^+$  ions increased, modulating the charge in silicon. For polysilicon,  $\text{Al}_2\text{O}_3$  and thermal  $\text{SiO}_2$ , the flat-band voltage, as a function of pH, showed a clear 50 mV/pH response, which was in line with Nernstian theory. The pH response was found to be higher however as the surface charge density increased.

**Concentration Comparison.** We tested four different concentrations of NaCl (0.1 mmol, 1 mmol, 20 mmol and 100 mmol) to evaluate how the zero-field voltage changed as a function of electrolyte concentration. It was observed that with increasing concentration, the capacitance in the accumulation region increased primarily due the double layer capacitance, but the zero-field voltage remained more or less constant within  $\pm 50$  mV. We attribute this to screening-limited response where the interface acted like a buffer.

**Cation Valency Comparison.** We tested EOS capacitors using 20 mmol NaCl,  $\text{MgCl}_2$  and  $\text{Co}(\text{NH}_3)_6\text{Cl}_3$  to assess the effect of cation valency on the behavior of the double layer. It was observed that with increasing valency both the accumulation capacitance and the zero-field voltage lowered.

The decrease in zero-field voltage was also different for higher valency ions.

A large hysteric effect was observed on both polysilicon and  $\text{Al}_2\text{O}_3$  capacitors. We attributed this to ion-specific effects, which were caused by large density of surface sites and roughness. The positive sweep (-2V to 2V) implied a large density of negative charge accumulation at the oxide interface, while on the return it indicated the opposite (cation adsorption). This excess positive charge led to a memory effect at the interface due to differential desorption rates.

## Future Work:

Various effects such as ion size and ion-ion correlations need to be included to understand the interface behavior further with complex electrolytes.

## Acknowledgments:

I would like to acknowledge the NNIN REU Program and the NSF for granting me the summer research opportunity. I would like to thank Cornell NanoScale Science and Technology Facility (CNF) Research Experience for Undergraduates Program coordinators Melanie-Claire Mallison and Rob Ilic for their support. I would like to thank all CNF staff especially Noah Clay and Garry J. Bordonaro, my research group members Joshua B. Phelps and Shantanu Rajwade, for useful discussions. Last but not the least; I would like to thank my Principal Investigator Prof. Edwin C. Kan for accepting me into his research group and my mentor Krishna Jayant for being the perfect guide and teacher.

## References:

- [1] Jiang, Z.; Stein, D. Electrofluidic Gating of a Chemically Reactive Surface. *Langmuir* 2010, 26, (11), 8161-8173.

## Cellular Binding of Quantum Dots

**Quachel Bazile**

**Chemistry, Elizabeth City State University**

*NNIN REU Site: Nanotechnology Research Center, Georgia Institute of Technology, Atlanta, GA*

*NNIN REU Principal Investigator: Professor Christine K. Payne, Chemistry, Georgia Institute of Technology*

*NNIN REU Mentor: Candace C. Fleischer, Chemistry, Georgia Institute of Technology*

*Contact: qbazile@gmail.com, christine.payne@chemistry.gatech.edu, ccthompson@gatech.edu*

### Introduction:

The need for new innovative treatments has led to the increase in nanoparticle (NP) research. NPs can improve treatment through drug delivery, cellular imaging and gene therapy. To properly use NPs for treatment, it is important to understand how NPs interact with the cellular environment. Recent research was done that compared cellular binding on cationic and anionic polystyrene NPs [1]. The results concluded that the cellular binding of cationic polystyrene NPs was enhanced in the presence of serum proteins and inhibited in the absence of serum proteins. The results also entailed that anionic polystyrene NPs cellular binding was inhibited in the presence of serum proteins and enhanced in the absence of serum proteins [1]. Serum proteins are a mixture of multiple proteins that are isolated from whole blood. Serum proteins may influence how NPs bind to cells because they have select sites on the cell where they bind [2]. The purpose of this research was to measure quantum dot (QD) binding to cells in the presence and absence of serum proteins and compare to prior work done with polystyrene NPs and cellular binding.

QDs are semiconductor nanocrystals that are fluorescent. QDs are fluorescent because they have a large band gap and when excited, energy is given off. QDs are used for variety of applications including imaging, solar cells, and LEDs [3]. To compare the difference between cationic and anionic QDs a coupling reaction was done to change the anionic QDs to cationic QDs.

### Experimental Procedure:

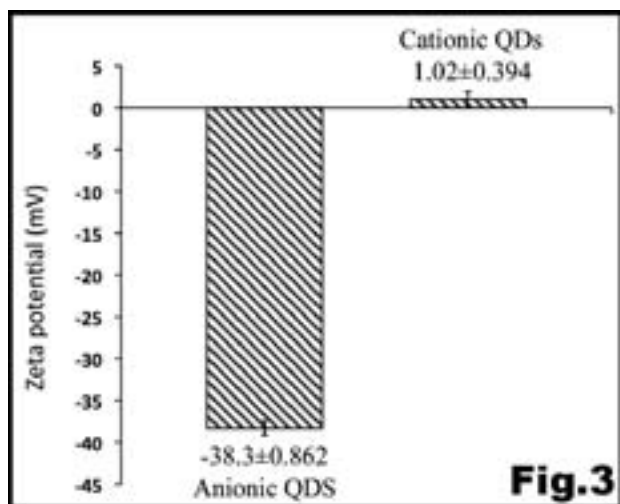
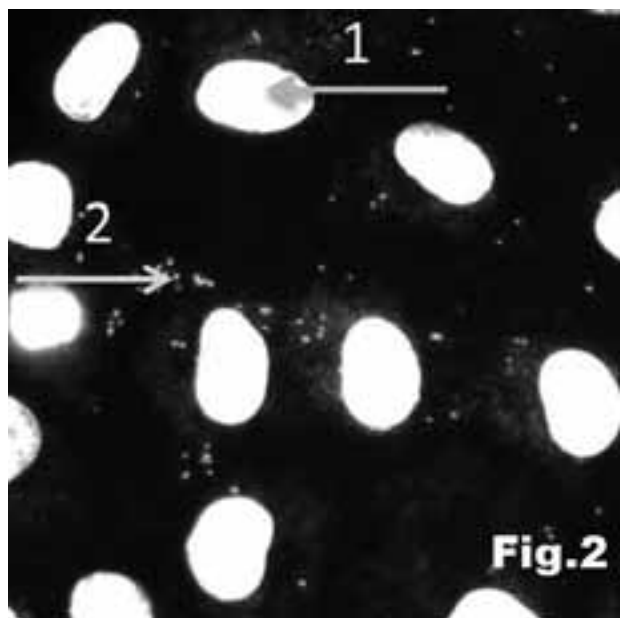
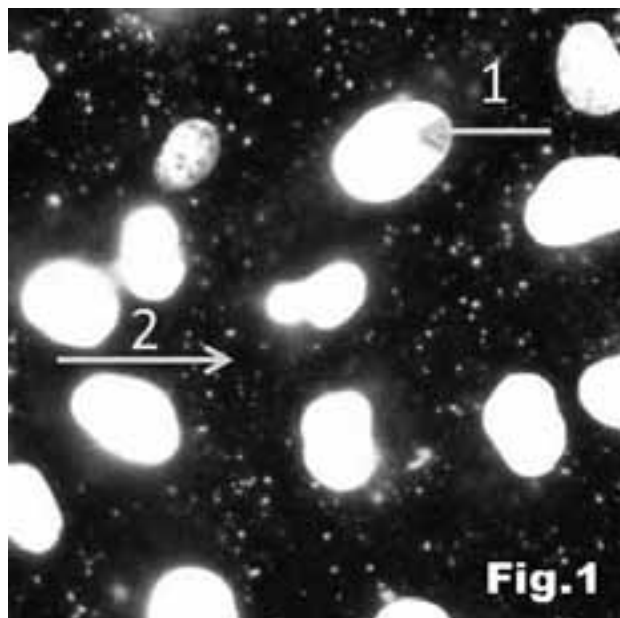
**Characterization.** The Nano-ZS Zetasizer (Malvern Instruments) was used to determine the hydrodynamic diameter and the zeta potential or effective surface charge of QDs. An 800 pM solution of QDs was used for both measurements, and all samples were measured in triplicate.

**Cellular Binding.** Carboxylate-modified QDs (Invitrogen, 525 nm emission) were used in cellular binding experiments in minimum essential medium (MEM), and MEM with 10% fetal bovine serum (FBS). Monkey kidney epithelial (BS-C-1) cells were cooled for 20 minutes at 4°C followed by a 20-minute incubation with QDs and 4',6-diamidino-2-phenylindole (DAPI). DAPI is a fluorescent stain that was used to see the cell nucleus while imaging. The cells were then rinsed twice with phosphate buffer saline (PBS) and imaged using epi-fluorescence microscopy.

**Cationic QD Formation.** To modify the anionic QDs to cationic QDs, a coupling reaction was done. The reaction was done in a borate buffer (10 mM, pH 7.4). Amine groups were coupled to the carboxyl groups on the QDs using ethylene diamine (ED, Sigma Aldrich) as the coupling group. 1[3-(dimethylamino)propyl]-3-ethylcarbodiimide (EDC, Thermo Scientific) was used as the coupling reagent. In a glass vial, QDs (80 nM), ED (135 mM), and EDC (1 M) were combined and incubated under stirring for five hours. After incubation, the solution was filtered using ultrafiltration (Millipore, 100K MWCO). To determine the final surface charge of the product, the zeta potential was measured.

### Results and Conclusions:

We found that cellular binding is enhanced significantly in the absence of serum proteins (Figure 1). In comparison, cellular binding of anionic QDs in the presence of serum protein is inhibited (Figure 2). The results of cellular binding of the anionic QDs were similar to the results of anionic polystyrene NPs. For both types of NPs, cellular binding was inhibited in the presence of serum proteins and enhanced in the absence of serum protein. This suggests that the charge of the NP not the composition of the NP dictates cellular binding.



When amine groups were coupled to the carboxylate groups the QDs became more positive (Figure 3). The cellular binding of these cationic QDs were measured on BS-C-1 cells. No binding was observed. This may be due to the fact that the amine modified QDs were not as positive as expected.

#### Future Work:

In the future, the QD coupling reaction will be optimized to yield more positive QDs. Cellular binding studies with cationic QDs will also be completed. A comparison between the cationic QDs results and polystyrene NP results will also be done.

#### Acknowledgments:

This project was funded by NSF and by the NNIN REU Program. Thanks to Candace Fleischer for the help and support on the project, as well as Professor Christine Payne and the Payne lab. Thank you also to the Georgia Institute of Technology NNIN staff.

#### References:

- [1] Fleischer, C. and Payne, C. J. Phys. Chem. B. 2012, 116,8901-8907.
- [2] Anderson, N., Anderson, A., Mol. Cell. Proteomics 2002, 1845-867.
- [3] Linda, S. Anal. Chem. 2004, 76 (23), 453A.

*Figure 1, top: Cellular binding of anionic QDs to live BS-C-1 cells in minimum essential medium (MEM). Epifluorescence microscopy was used to acquire images. Arrow 1 in the image is the nuclei, stained with DAPI, and Arrow 2 indicates the QDs. QDs bind to cells in the absence of serum proteins.*

*Figure 2, middle: Cellular binding of anionic QDs to live BS-C-1 cells in MEM + 10% fetal bovine serum (FBS). FBS is a mixture of serum proteins. Epifluorescence microscopy was used to acquire images. Arrow 1 in the image is the nuclei, stained with DAPI, and Arrow 2 is the QDs. In the presence of serum proteins, QD cellular binding is inhibited.*

*Figure 3, bottom: The graph shows the surface charge or zeta potential of the QDs before and after the coupling reaction. The anionic QDs were measured in water. The cationic QDs were measured in a borate buffer solution (10 mM, pH 7.4). These samples were measured on the Zetasizer (Nano-ZS, Malvern Instruments). Each sample was measured in triplicate.*

## Optimization of Protocol for Fabrication of a Polymer Filter from a PDMS Mold

**Colin Burns-Heffner**

**Bioengineering, Clemson University**

*NNIN REU Site: Penn State Nanofabrication Laboratory, The Pennsylvania State University, University Park, PA*

*NNIN REU Principal Investigator: Dr. Siyang Zheng, Bioengineering, The Pennsylvania State University*

*NNIN REU Mentors: Ramdane Harouaka and Yin-Ting Yeh, Bioengineering, The Pennsylvania State University*

*Contact: cburnsh@clemson.edu, siyang@psu.edu, rah251@psu.edu*

### Abstract:

Microfabricated structures have been demonstrated to filter specific types of cells out of blood samples when incorporated into a parylene filter. However, the process for creating these parylene filters can be time consuming, and requires expensive equipment. Also, the fabrication process utilizes harsh temperatures and specific techniques that are incompatible with softer polymers such as polydimethylsiloxane (PDMS), biodegradable polymers, or other implantable biomaterials [1]. The focus of this project was to optimize a protocol for an alternative micromolding fabrication process. We found the optimal combination of surfactant-based release agents to consistently create high quality molds with a high aspect ratio and features as small as 1  $\mu\text{m}$ . We also successfully fabricated a PDMS filter using this micromolding process.

### Introduction:

This project tested different methods of creating a polymer filter from a PDMS mold. The original filter, consisting of parylene, was used to create the polymer mold. This mold then served to fabricate more filters consisting of different polymers.

First, the mold material was optimized. Several types of PDMS as well as polyurethane were employed. The optimal protocol was found to be PDMS at a 5:1 base to crosslinking agent ratio, using a release agent of either a 0.1% SDS solution or 1% Triton X-100 solution with 95% ethanol as the solvent. Once the mold process was optimized, the next step was to then optimize a process of using the molds to stamp out filters out of PDMS which have been spun onto a silicon wafer. This project demonstrated in one instance that this process is feasible, but further optimization is necessary in order to make it more consistent and repeatable.

### Experimental Procedure:

The first step was to determine which polymer would be most suitable for the mold. Polyurethane and a 1:1 ratio of 10:1 PDMS and Blue PDMS were tested against the standard, 5:1

PDMS. To fabricate the mold, the parylene filter was dipped in isopropyl alcohol (IPA) and laid flat on the bottom of a polystyrene container. This was then placed in a vacuum hood 15-20 minutes. Next, a pipette was used to place two drops of release agent onto the filter, making sure to completely cover the filter. The container with the filter was then placed back inside the vacuum hood for 30 minutes. Then, the mold polymer (either polyurethane, a 1:1 ratio of 10:1 PDMS and Blue PDMS, or 5:1 PDMS) was then poured over another container with a parylene filter in it. This was then left to cure overnight.

PDMS 5:1 was proven to be the best option in terms of feature resolution. Once this was determined, different release agents were tested at different concentrations to find the optimal combination: a 0.3 g Fairy dish soap solution, Triton X-100 at 0.1% and 1.0% concentrations by volume, and SDS solutions at 0.1% and 1.0% concentrations by mass were tested, utilizing 95% ethanol as the solvent. To test these release agents, the same process described above was used, and the 5:1 clear PDMS was used as the polymer for the mold. To cure, the container was placed on a hot plate at 80°C for one hour, and then cut out of the container with a size 22 mm circular punch tool. Tweezers were used to peel off the filter.

In order to fabricate filters from the molds, the general procedure that was followed was to take the molds that were fabricated in stage 1, and first apply release agent to them. Using a pipette, 50  $\mu\text{l}$  of either Triton X-100 (1.0%) solution or SDS (0.1%) solution were applied to each mold. These molds were then placed in a vacuum hood for 30 minutes to dry the release agent. 10:1 PDMS was prepared, and 10 ml of the PDMS was used to spin a 10  $\mu\text{m}$  layer of PDMS onto a silicon wafer (Single Polished 325  $\mu\text{m}$  N-type 10-20). The recipe for spinning was 10 seconds at 500 rpm, and 5 minutes at 4000 rpm. The wafer was then removed from the spinner, the molds were placed on the PDMS-coated wafer and placed in a vacuum oven to be vacuum baked at 80°C overnight. The molds were then removed from the wafer using tweezers. The wafer then contained the filters stamped out on its surface.

**Results and Conclusions:**

Out of the three polymers tested, the 5:1 PDMS produced the best quality result, as shown in Figure 1. The 0.1% SDS solution and the 1% Triton X-100 solution proved to be the best release agents in terms of feature quality and amount of residue left, as seen in Table 2. In the second stage of the experiment, the only successful filter fabricated was in the first trial, with a single polished 325  $\mu\text{m}$  N-type 10-20 wafer, a mold that was made using 1.0% Triton-X, and then treated with 0.1% SDS. This one filter was the only successful filter — even when the same conditions were repeated — and the reasons why are currently unknown. It is believed that there is an affinity issue between the PDMS and the release agent-treated mold. It could also be a cleanliness issue; there may

have been small contaminations. HMDS treatment did clearly seem to be detrimental, and the application of pressure didn't help either. The affinity issue needs to be resolved in order to optimize this process. However, since it did work once, the process has been proven to be successful under the right conditions.

**References:**

[1] S. Y. Zheng, H. K. Lin, B. Lu, A. Williams, R. Datar, R. J. Cote and Y. C. Tai, 3D microfilter device for viable CTC enrichment from blood, Biomed. Microdevices, 2011, 13, 203–213.

Polymer	Release Agent	Results
5:1 Clear PDMS	Fairy 0.3g	Worked well, small and large features visible. Clean, except for a little residue. The filter came off of the mold easily
Polyurethane	Fairy 0.3g	Some features visible. Not the small ones. Not very clean, poor quality, many bubbles, although not on area of filter mold.
1:1 Blue and Clear PDMS	Fairy 0.3g	Not as clean or uniform as the 5:1 clear PDMS

Figure 1: Results of mold material optimization.

Release Agent	Mold Polymer	Results
Fairy 0.3g	5:1 PDMS	Worked well, small and large features visible. Still showing a little residue, consistently throughout. The filter came off of the mold easily
0.1% TritonX (70% Et)	5:1 PDMS	Filter completely stuck to PDMS, small part did come off, and mold underneath was not clean, bad resolution, features not complete
0.1% TritonX (95% Et)	5:1 PDMS	Filter was slightly difficult to remove, but it did come off, in pieces. Features, however, came out very clean with good resolution. Small and large features visible.
1.0% TritonX (95% Et)	5:1 PDMS	Filter came off easily, slight residue but not much. Features very clean, almost perfect.
0.1% SDS (95% Et)	5:1 PDMS	Filter came off easily. Some spots of residue, but features were almost perfect, large and small.
1.0% SDS (95% Et)	5:1 PDMS	Filter came off easily, but there was substantial residue. Features came out well but very high amount of residue left from the release agent.

Figure 2: Results of mold release agent optimization.

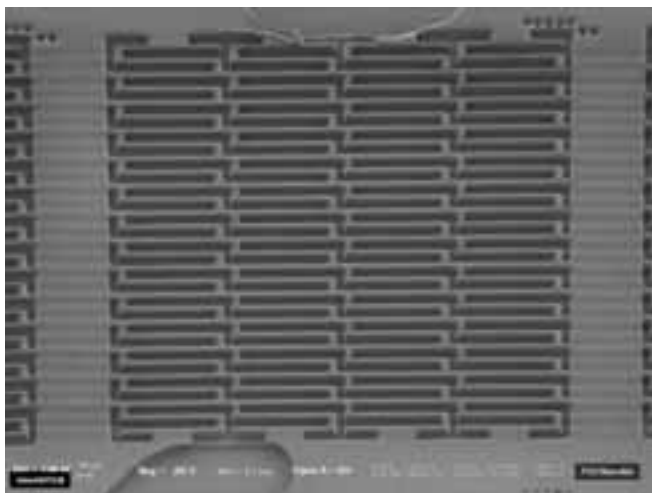


Figure 3: PDMS filter fabricated using molding process.

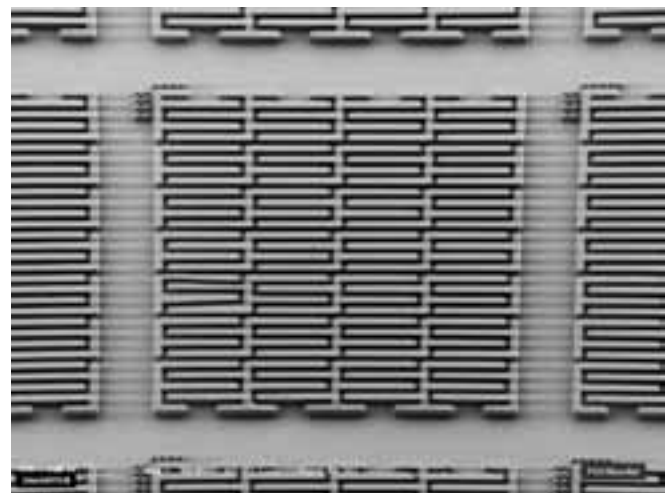


Figure 4: PDMS molds fabricated using molding process.

## Towards Ink-Jet Fabricated PEDOT:PSS Organic Electrochemical Transistors with Embedded Enzymes

**Audrey Dang**

**Chemical Engineering, Vanderbilt University**

*NNIN iREU Site: Centre Microélectronique de Provence, Ecole Nationale Supérieure des Mines de Saint Etienne, France*

*NNIN iREU Principal Investigator: Professor George Malliaras, Department of Bioelectronics,  
Centre Microélectronique de Provence, Ecole Nationale Supérieure des Mines de Saint Etienne, France*

*NNIN iREU Mentor: Associate Professor Sébastien Sanaur, Department of Bioelectronics,  
Centre Microélectronique de Provence, Ecole Nationale Supérieure des Mines de Saint Etienne, France*

*Contact: audrey.j.dang@vanderbilt.edu, malliaras@emse.fr, sanaur@emse.fr*

### Abstract and Introduction:

Ink-jet printing is a promising method for the low cost fabrication of electronics and sensing devices. Indeed, its ease of processing includes additive patterning, simple modification of device geometry, non-contact processing, and diverse substrate possibilities.

Commercially available as an ink for printing, poly(3,4-ethylene dioxythiophene)-poly(4-styrenesulfonate) (PEDOT:PSS) is a degenerately-doped *p*-type organic semiconductor polymer which has been investigated extensively for the fabrication of organic electrochemical transistors (OECTs). Like other transistors, OECTs benefit from inherent signal amplification [1]. In contrast to traditional transistors, OECTs operate at biocompatible working voltages in electrolyte. OECTs are thus excellent candidates for biosensing and integration into *in vitro* and *in vivo* applications. In addition, a planar monolayer geometry is possible allowing simple fabrication by inkjet printing.

In the operation of an OECT, application of positive gate voltage increases cation concentration in the channel, which results in dedoping of the conducting polymer. The dedoped channel is less conductive resulting in a lower drain current. Thus, the change in gate voltage results in an amplified change in drain current.

Glucose sensing with an all-PEDOT:PSS OECT has been previously demonstrated with glucose oxidase (GOx) located in the electrolyte [2]. In this device design, electrons were shuttled by a mediator from the enzyme in solution to the PEDOT:PSS gate. Thus, the effective gate voltage and in result the drain current were modulated in response to changes in glucose concentration. Limitations of this device include the presence of reagents in the electrolyte. In contrast, Yun, et al., embedded GOx and horseradish peroxidase enzyme in a PEDOT:PSS electrode by inkjet printing a single bioelectronic ink consisting of the enzymes in an aqueous dispersion of PEDOT:PSS [3]. The aim of this project was to ink-jet print an OECT with GOx embedded in its PEDOT:PSS electrodes for glucose sensing. We report progress in the development of the fabrication of such devices.

### Methods and Results:

Devices were printed with a Dimatix Materials Printer 2800 (DMP 2800). The DMP 2800 is a piezoelectric printer with a disposable cartridge that dispenses 10 pL drops of ink from 16 nozzles. Four layers were printed on glass slides coated in a vapor-deposited layer of Parylene-C that was treated with oxygen plasma just prior to printing (Figure 1).

The ink used in this project was a 1.8 wt.% dispersion of PEDOT:PSS in water with ethylene glycol and ethanol (Agfa Orgacon II-1005). Normal processing of this commercial ink entailed steps such as sonication and high-temperature annealing which would denature enzymes. Thus, modifications were necessary to preserve the activity of the enzyme while maintaining the desired electrical and mechanical properties of the conducting polymer.

PEDOT:PSS is normally annealed at temperatures exceeding 100°C for over 60 minutes, but native GOx is significantly denatured after 60 minutes at 60°C [4]. An alternative annealing process was therefore required to minimize enzyme denaturation. Drying the printed devices under vacuum at 25°C for 48 hours resulted in electrical properties very similar to those of devices baked at 150°C for one hour (Figure 2). While less mechanically robust than the devices baked at higher temperatures, the vacuum dried devices were sufficiently robust for characterization and testing.

Enzymes are also sensitive to salt concentration and pH. To achieve physiological salt concentration and to mitigate the ink pH of 1.5, the ink was mixed with 10X phosphate buffered saline (PBS) in a 10:1 volume ratio and then stirred overnight. In addition, extended sonication can damage the structure of the enzyme. The PEDOT:PSS-PBS ink was sonicated for one minute periods alternated with cooling at 4°C in a refrigerator. When prepared in this way the PEDOT:PSS-PBS ink was successfully jetted. While resistance of the final devices increased with addition of PBS, the modulation of the transistors was maintained (Figure 3).

In the next step of the project, GOx was added to the PEDOT:PSS-PBS ink. The enzyme was dissolved in 10X PBS before mixing with the PEDOT:PSS ink to result in a final

concentration of 400 U GOx/mL. The ink was mixed overnight and sonicated as previously described. Jetting with the bioelectronic ink was poor or nonexistent even if the ink was filtered. Aggregates most likely blocked the cartridge nozzles or otherwise interfered with jetting. Such aggregates could be observed by optical microscope in a spuncoat film of the ink with enzyme (Figure 4).

**Conclusions and Future Work:**

A suitable annealing condition for printing PEDOT:PSS ink with enzyme was found. Mixing PEDOT:PSS ink with PBS resulted in a jettable ink that produced devices with lower current magnitude but modulation similar to that of devices printed with the original ink. Addition of GOx to PEDOT:PSS-PBS ink resulted in aggregation that prevented jetting.

Future work includes assessing the activity of the enzyme after ink preparation and reducing enzyme aggregation.

**Acknowledgments:**

I am very grateful to the entire Bioelectronics Department especially Professor George Malliaras and Associate Professor Sébastien Sanaur for their gracious welcome and support. Many thanks to Dr. Lynn Rathbun for making this experience possible, and the NNIN iREU Program and the NSF for funding.

**References:**

- [1] Bernards, D.A., et al., "Enzymatic sensing with organic electrochemical transistors." *Journal of Materials chemistry*. Vol.18, 116-120 (2007).
- [2] Shim, N.Y., et al., "All-Plastic Electrochemical Transistor for Glucose Sensing Using a Ferrocene Mediator." *Sensors*. V.9, 9896-9902 (2009).
- [3] Yun, Y.H., et al., "A Glucose Sensor Fabricated by Piezoelectric Inkjet Printing of Conducting Polymers and Bionzymes." *Anal.Sci*. V.27, 375-379 (2011).
- [4] Gouda, M.D., et al., "Thermal Inactivation of Glucose Oxidase: Mechanism and Stabilization Using Additives." *The Journal of Biological Chemistry*. Vol 278, 24324-24333 (2003).

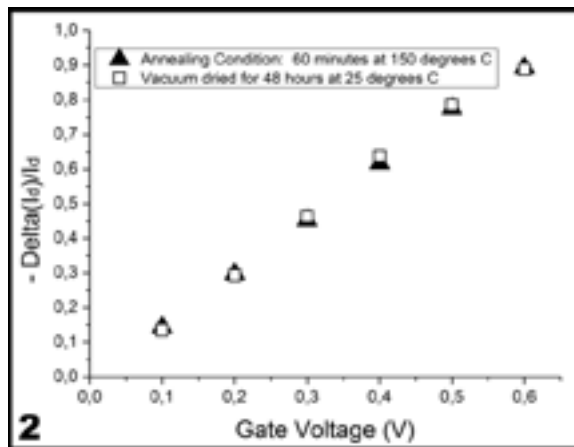


Figure 2: Normalized response for ink-jet printed OECTs fabricated with different annealing conditions.

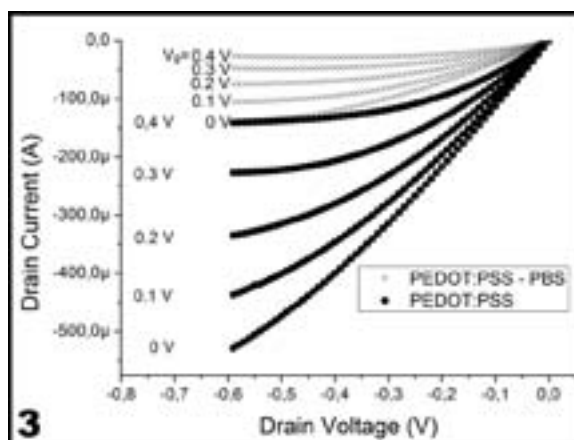


Figure 3: Output curves for OECTs printed with PEDOT:PSS and PEDOT:PSS-PBS inks.

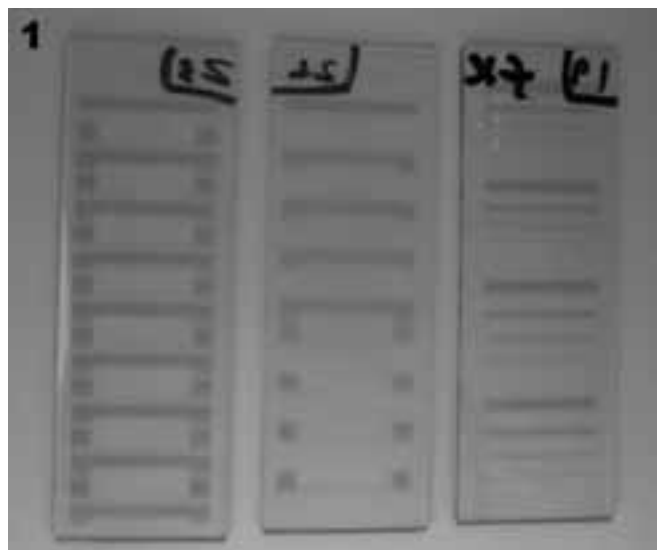


Figure 1: Inkjet-printed PEDOT:PSS OECTs on standard glass slide (26 mm by 76 mm).

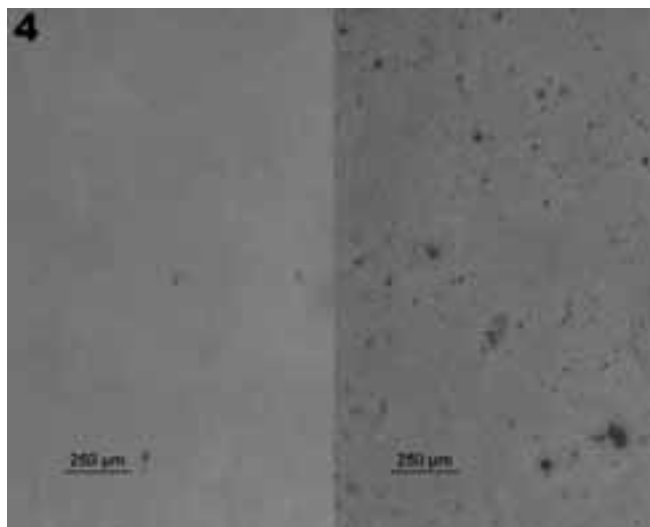


Figure 4: Left SEM, spincoat film of PEDOT:PSS-PBS ink. Right SEM, spincoat film of PEDOT:PSS-PBS-GOx ink.

## DNA Extension in Nanochannels

Leon Dean

Chemical Engineering, University of Texas at Austin

NNIN REU Site: Nanofabrication Center, University of Minnesota-Twin Cities, Minneapolis, MN

NNIN REU Principal Investigator: Kevin Dorfman, Chemical Engr. and Materials Science, University of Minnesota-Twin Cities

NNIN REU Mentor: Julian Sheats, Chemical Engineering and Materials Science, University of Minnesota-Twin Cities

Contact: leondean@utexas.edu, jtsheat@umn.edu, dorfman@umn.edu

### Abstract:

Confining deoxyribonucleic acid (DNA) in nanochannels is an effective method for achieving the elongation necessary for DNA barcoding. Recent simulations have shown that semiflexible polymers like DNA exhibit different confinement behavior than flexible polymers in intermediate channel sizes. The purpose of this study is to measure the fractional extension of lambda DNA ( $\lambda$ -DNA) as a function of nanochannel width in a range of channel sizes and to compare the experimental results to the aforementioned simulation results. Several nanofluidic devices containing arrays of nanochannels were fabricated, and preliminary extension measurements were made. The results should improve theoretical understanding of the dynamics of single DNA molecules confined in nanochannels.

### Introduction:

DNA barcoding has emerged as a useful technology for high-throughput genome mapping, but requires a method for elongating individual DNA molecules. The two most common elongation methods are molecular combing [1] and channel confinement [2]. Understanding DNA confinement behavior is critical for the accurate assessment of the locations of fluorescently-labeled probes along confined DNA molecules.

All polymers can be characterized by contour length ( $L$ ), the length of a fully extended chain, persistence length ( $l_p$ ), a measure of backbone stiffness, and effective width ( $w$ ). For a confined polymer, the channel width ( $D$ ) is also an important parameter. Channel width has a profound effect on extension ( $X$ ), which is the observed length of the confined polymer chain. For the dyed  $\lambda$ -phage DNA used in this experiment,  $L \approx 21 \mu\text{m}$ ,  $l_p \approx 53 \text{ nm}$ , and  $w \approx 4.6 \text{ nm}$  [3].  $D$  can be replaced by the geometric mean of the channel depth and width [4].

The theory explaining mean fractional extension ( $\langle X \rangle / L$ ) as a function of  $D$  is well-defined for flexible polymers.

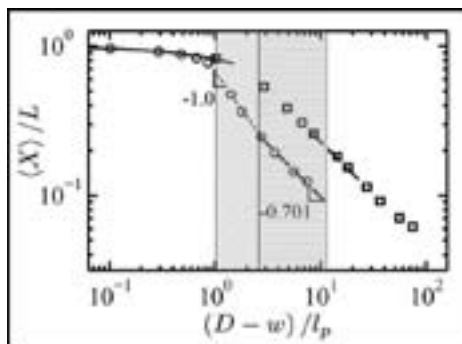


Figure 1: Log-log plot of fractional extension versus effective nanochannel width from simulation for a semiflexible polymer (circles) and a flexible polymer (squares). Adapted with permission from [5].

In the weak confinement regime, corresponding to larger values of  $D$ , the scaling law is derived from de Gennes blob theory. In the strong confinement regime, corresponding to smaller values of  $D$ , the scaling law is derived from Odijk deflection theory [3]. However, recent Monte Carlo simulations have shown that additional confinement regimes exist between the de Gennes and the Odijk regimes for semiflexible polymers like DNA [3, 5]. Figure 1 illustrates how semiflexible polymers exhibit behavior different from flexible polymers in the shaded transition regimes. The given

slopes correspond to the exponents for the scaling laws in the respective regimes.

### Experimental Procedure:

Experimental measurements within the additional regimes were performed in nanofluidic devices fabricated on silicon substrates. Each device contained a nanochannel array between two parallel microchannels with reservoirs for loading. The nanochannel array was patterned by electron beam lithography, which controlled the widths of the channels, followed by reactive ion etching, which controlled the depth of the channels. The microchannels and reservoirs were patterned by contact photolithography and etched with a deep Bosch process. Access holes were cut into the reservoirs with a wet potassium hydroxide etch, while the rest of the device was protected by a film of silicon nitride. A silicon oxide layer of  $\sim 200 \text{ nm}$  was thermally grown to provide electrical insulation. All devices were anodic-bonded to fused silica in order to enclose the channels. Resulting devices contained nanochannels with  $D$  between 50 and 500 nm. Nanochannel lengths were either 1 mm or 100  $\mu\text{m}$ . Figure 2 shows a nanochannel before bonding.

The device was filled with 2.2X TBE (tris, borate, ethylenediaminetetraacetic acid) aqueous buffer containing  $\beta$ -mercaptoethanol (5% w/w) and ascorbic acid (0.07% w/w) to suppress bleaching, as well as polyvinylpyrrolidone

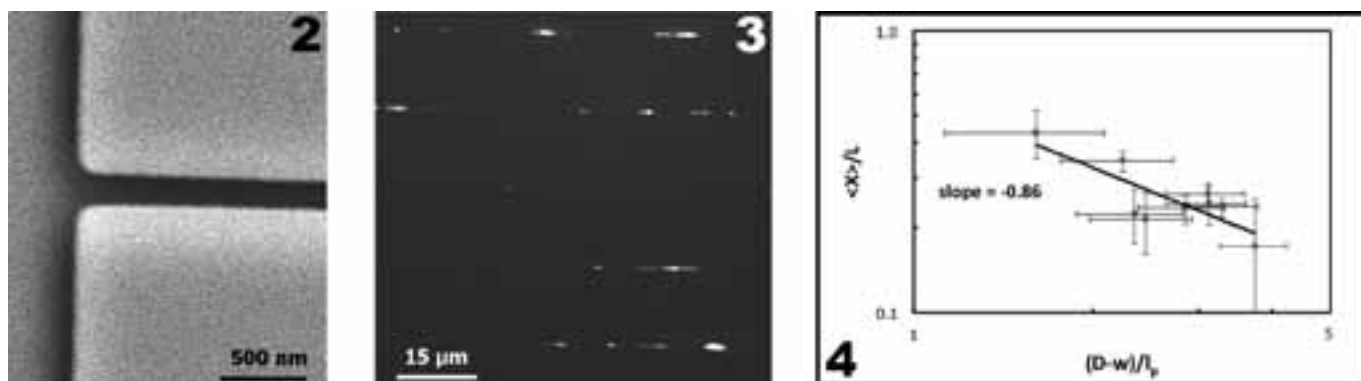


Figure 2, left: SEM of the entrance of a nanochannel with dimensions of 180 nm  $\times$  160 nm.

Figure 3, middle: Optical micrograph of fluorescently dyed  $\lambda$ -DNA molecules inserted into nanochannels.

Figure 4, right: Log-log plot of fractional extension versus effective nanochannel width from experiment for dyed  $\lambda$ -DNA. Horizontal error bars represent instrument uncertainty and vertical error bars represent the standard deviation of multiple measurements.

(0.07% w/w) to prevent sticking of the DNA. It was found that the nanochannels with shorter lengths filled spontaneously by capillary action, while the nanochannels with longer lengths typically required pre-filling with a lower surface tension fluid like ethanol [6].

The  $\lambda$ -DNA, dyed with YOYO-1, was inserted into a reservoir and pumped through a microchannel. Then electrophoresis was applied across the nanochannels to force some DNA molecules into nanochannels. Optical microscopy images were taken with a 100 $\times$  oil immersion objective under fluorescent light.

### Results and Conclusions:

Figure 3 shows a representative image of DNA successfully inserted into nanochannels. The figure includes fragmented molecules resulting from photocleavage or shear cleavage. Other regions contained agglomerations of stuck DNA molecules which did not respond to an electric field.

After the fragmented and stuck DNA molecules were removed as outliers, the rest of the elongated DNA molecules were analyzed. For each molecule, a threshold intensity value was established and the length of the intensity profile above that threshold was measured. Typically,  $\sim$  100 measurements were obtained for each molecule and averaged into a mean extension.

Figure 4 shows a plot of mean fractional extension versus effective channel width. The exponent of the power law regression is -0.86, which closely corresponds to previous research [4] and lies in between the simulation exponents of -1.0 and -0.701 for the two additional regimes.

The number of experimental data points is insufficient to make further conclusions.

### Future Work:

Additional extensions measurements will be gathered at many different channel sizes in order to fill more data points into Figure 4. In conjunction with reduced uncertainty, this will allow the determination of experimental scaling laws for fractional extension as a function of channel width as well as any transition points within the additional confinement regimes.

### Acknowledgments:

The author thanks Dr. Julian Sheats and Prof. Kevin Dorfman, along with the University of Minnesota Nanofabrication Center staff, for help throughout the project. The author also thanks the NNIN REU Program and the NSF for financial support.

### References:

- [1] Michalet, X. et al. *Science*, 277, 5331, 1518-1523 (1997).
- [2] Lam, E.T. et al. *Nature Biotechnology*, 30, 771-776 (2012).
- [3] Wang, Y., Tree, D.R., and Dorfman, K.D. *Macromolecules*, 44, 6594-6604 (2011).
- [4] Reisner, W. et al. *Physical Review Letters*, 94, 196101 (2005).
- [5] Tree, D.R., Wang, Y., and Dorfman, K.D. *Physical Review Letters*, 108, 228105 (2012).
- [6] Han, A., et al., *J. of Colloid and Interface Science*, 293, 151-157 (2006).

## Biocompatible Dry Adhesives Mimicking Gecko Spatulae for EEG Electrodes

Jennifer Gilbertson

Chemistry, Beloit College

NNIN iREU Site: Centre Microélectronique de Provence, Ecole Nationale Supérieure des Mines de Saint Etienne, France

NNIN iREU Principal Investigator: Professor George G. Malliaras, Department of Bioelectronics,  
Centre Microélectronique de Provence, Ecole Nationale Supérieure des Mines de Saint Etienne, France

NNIN iREU Mentor: Pierre Leleux, Department of Bioelectronics, Centre Microélectronique de Provence,  
Ecole Nationale Supérieure des Mines de Saint Etienne, France

Contact: gilbert@beloit.edu, malliaras@emse.fr, leleux@emse.fr

### Introduction:

Electroencephalography (EEG) electrodes record the electrical activity along the scalp, rendering them important tools in diagnosing the cerebral origins of neurological disorders such as epilepsy. Compared to other methods of monitoring neural activity, EEG is noninvasive and inexpensive, but suffers from a low signal-to-noise ratio and poor long-term skin adherence.

This project developed a polydimethylsiloxane (PDMS) dry adhesive which was coated in a conducting polymer, poly(3,4-ethylenedioxythiophene) doped with poly(styrene sulfonate) (PEDOT:PSS) to increase the accuracy and durability of the electrodes. The PDMS polymer was cast onto a patterned photoresist mold.

Modeled after naturally occurring adhesives such as gecko foot pads, the synthetic micro-pillars are reusable, less irritating than current adhesive pads, and can stay on the skin for longer periods of time. The presence of microstructures on the surface of the electrodes increases the effective area of the electrodes, increasing the conductivity and lowering the electrode impedance.

### Methods:

A silicon wafer was cleaned by oxygen plasma using a reactive ion etcher (RIE) (Oxford Instruments PlasmaLab 80+) followed by UV-light treatment (Nanonex) and acetone wash. A layer of chrome followed by a layer of gold was evaporated onto the wafer using a metal evaporator (Alliance Concept EVA450) (Figure 1). A 1.5  $\mu\text{m}$  layer of LOR 5A photoresist was spin-coated onto the wafer (1000 rpm/45 seconds). The wafer was soft-baked at 150°C for five minutes and exposed with UV light for 30 seconds. A layer of AZ 9260 photoresist was spin-coated onto the substrate (1000 rpm/30 seconds) resulting in a thickness of 15 to 20  $\mu\text{m}$ , followed by a two minute soft bake at 100°C. The samples were exposed to UV light again for 30 seconds using a mask.

The wafers were developed in 1:1 diluted AZ developer, rinsed, and underwent a second development for 40 seconds in MF-26A developer. An optical microscope (Nikon) was used to image the molds. The depth of the molds was quantified using an optical profilometer (Veeco-WYKO NT1100).

PDMS was mixed at a 10:1 elastome to curing agent ratio. After degassing, the PDMS was spin-coated onto the mold at 250 rpm for 30 seconds and cured in an oven at 70°C. When cool, the PDMS was peeled off of the mold by hand and placed onto a glass slide with the microstructures facing up. The PDMS surface was activated with a 100 W, 30 seconds oxygen plasma etching. Conducting polymer PEDOT:PSS (Clevios PH 1000, HC Starck) was spin-coated onto the PDMS, soft-baked at 110°C for one minute, and hard-baked for 45 minutes at 145°C.

Following fabrication, the microstructures were imaged with a scanning electron microscope (SEM, Carlos Zeiss 55). A voltmeter was used to examine the resistivity of sections of PEDOT:PSS coated PDMS (0.5  $\times$  1.5 cm). A potentiostat (Metrohm Autolab) was used to measure the impedance.

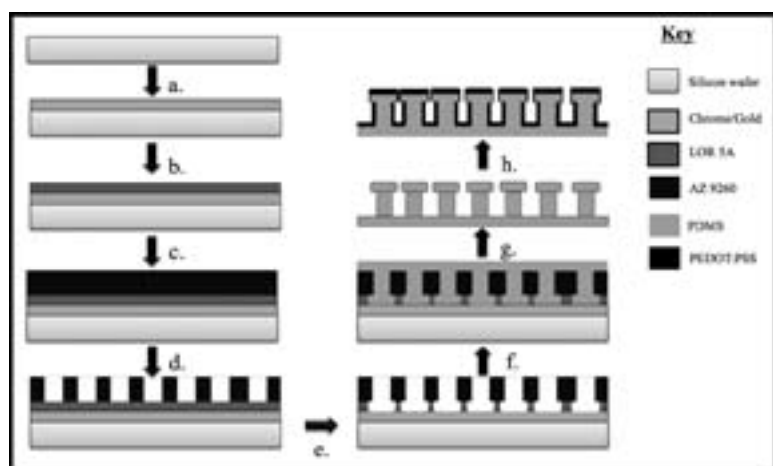


Figure 1: Schematic of mold fabrication and polymer casting. a) Metal evaporation. b) LOR 5A photoresist deposition. c) AZ 9260 photoresist deposition. d) UV exposure and AZ development. e) MF-26A development. f) PDMS casting. g) Cast removal. h) PEDOT:PSS spin-coating.

A goniometer (Apollo OCA 200) was used to calculate the contact angle for structured and flat PDMS with four different substances (water, ethylene glycol, 40% ethylene glycol by volume, and diiodomethane).

### Results:

An adhesive comprised of 40  $\mu\text{m}$  pillars with a spacing of 20  $\mu\text{m}$  was successfully fabricated. An optical surface profiler /profilometer was used to determine that the depth of the molds was 14  $\mu\text{m}$  on average. The mold and resulting PDMS cast had identical topography.

SEM was used to image the PDMS cast before and following the deposition of PEDOT:PSS. Figure 2 demonstrates that a thin spin-coated layer of PEDOT:PSS does not obscure the form of the structures.

Surface activation by oxygen plasma rendered the PDMS temporarily hydrophilic due to the SiOH groups on its surface, allowing for the deposition of PEDOT:PSS. Following PEDOT:PSS deposition, electrical characterization revealed that the surface conductivity of the PDMS/PEDOT:PSS structures was higher than the flat PDMS/PEDOT:PSS samples.

Impedance tests demonstrated a marked difference between flat and structured PDMS coated with PEDOT:PSS. This effect lessened as the PEDOT:PSS layer thickness decreased (Figure 3).

The contact angle data was used to calculate the surface energy of structured (14.95 mN/m) and flat PDMS (19.41 mN/m). A lower surface energy corresponds to a higher contact angle, indicating that the surface with the micropillars is more hydrophobic than the flat PDMS. The hydrophobic surface of PDMS allows for the adhesive to be rinsed with water to remove any dead skin or dust without damaging the microstructures. These adhesives are therefore reusable as well as nontoxic.

### Conclusions and Future Work:

We successfully fabricated photoresist molds and PDMS casts with 40  $\mu\text{m}$  features. The photoresist mold fabrication is less expensive than other methods [1] and easily adaptable to different feature sizes. This research has demonstrated that the increased surface area of the microstructures lowers the impedance compared with flat PDMS, and initial tests have also demonstrated lower electrical resistance.

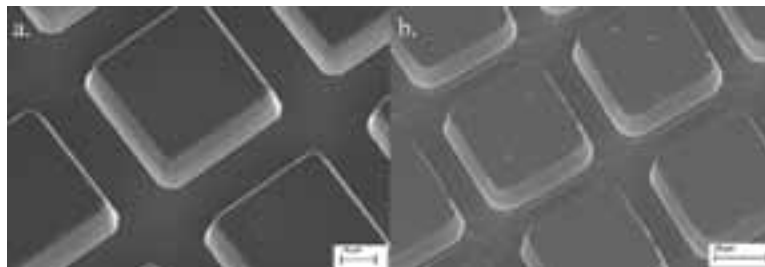


Figure 2: SEM images of (a) PDMS microstructures and (b) PDMS microstructures coated with PEDOT:PSS.

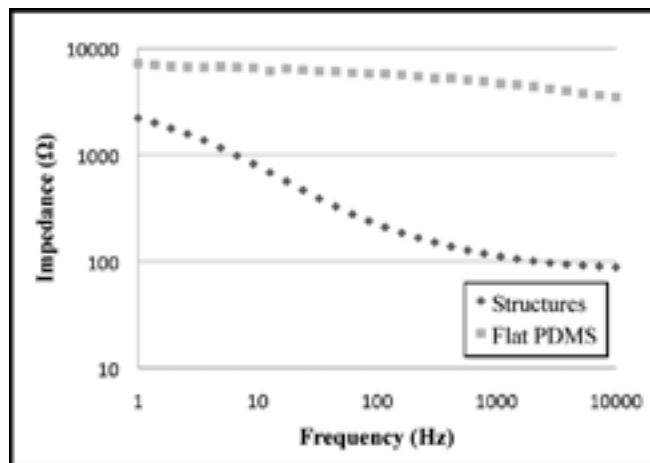


Figure 3: Impedance measurements for flat PDMS and microstructures coated in PEDOT:PSS.

Future work will focus on decreasing the size of the structures and increasing the aspect ratio. Previous research has demonstrated that increased aspect ratio will increase the adhesiveness of the microstructures [1]. Smaller micropillars would also increase the micropillars per unit area, further increasing adhesiveness and surface area.

### References:

- [1] Kwak, M.K.; "Rational Design and Enhanced Biocompatibility of a Dry Adhesive Medical Skin Patch"; *Advanced Materials*, 23, 3949-53 (2011).

## Optimizing Liposomal Uptake and Content Release Using Glioblastoma Multiforme as a Model System

**Sonali Gupta**

**Biophysics, New College of Florida**

*NNIN REU Site: Nanotechnology Research Center, Georgia Institute of Technology, Atlanta, GA*

*NNIN REU Principal Investigator: Dr. Ravi V. Bellamkonda, Neurological Biomaterials and Cancer Therapeutics Lab, Department of Biomedical Engineering, Georgia Institute of Technology*

*NNIN REU Mentor: Dr. S. Balakrishna Pai, Neurological Biomaterials and Cancer Therapeutics Lab, Department of Biomedical Engineering, Georgia Institute of Technology*

*Contact: sonali.gupta@ncf.edu, ravi@gatech.edu, balakrishna.pai@bme.gatech.edu*

### Optimizing Liposomal Drug Delivery:

Liposomes are hollow vesicles of various sizes and morphologies composed of a phospholipid bilayer membrane. They can be used to encapsulate agents in targeted drug delivery systems where the drug only reaches the specific cellular pathway or type of cell it is intended to target. The liposome thus acts as a protective bubble, minimizing drug loss and reducing side effects, which can be especially valuable when using cytotoxic or immunosuppressive drugs.

The model system used to study optimization of targeted drug delivery is glioblastoma multiforme (GBM), a highly malignant cancer that metastasizes easily through soft brain tissue. A compound called imipramine blue (IB), which prevents actin polymerization, effectively localized tumor growth in GBM cells [1]. This greatly aids surgical removal and creates a more defined target for chemotherapy drugs. However, the half life of free IB in circulation is only 11 minutes, compared to 18 hours when packaged within liposomes. When treated with 160 nm liposomal IB followed by liposomal doxorubicin, a chemotherapy drug, rats with GBM had a survival rate of 100% and demonstrated no signs of regrowth [1]. The delivery of drugs to GBM cells is dependent on rapid vascularization around tumor growth which results in nonuniform vascular walls with pores measuring about 200 nm in radius. Since healthy vasculature only allows passive diffusion of particles about 10 nm in size, liposomes in circulation are only absorbed into tumorous regions.

Adjustments to the intrinsic properties of liposomes — size, phospholipids composing the membrane, the method of formation, and the thermodynamics of the structure — can significantly impact the overall drug delivery process. This study aims to find relationships between these variables and the rate of diffusion of liposomes, the rate at which they leak their contents, and their overall stability. This strategy preserves the low circulation time and diffusive potential characteristic of spherical liposomes without surface ornamentation, and doesn't require exogenous factors, like radiation, to induce drug release.

### Methodology:

In past studies it was observed that the 160 nm liposomes were accumulating around the GBM vasculature [1]. Reducing the size should address this by allowing the drug to diffuse to the periphery of the tumor thereby increasing overall uptake. Liposomes less than 100 nm, or small unilamellar vesicles (SULVs), are generally unstable due to membranous stress from a high surface curvature [2]. To relieve this tension, a short chain phospholipid, dihexanoyl phosphatidylcholine (DHPC) was used to attenuate the longer chain phospholipids, dimyristoyl phosphatidylcholine (DMPC) and dimyristoyl phosphatidylglycerol (DMPG). Temperature and concentration of phospholipids primarily dictated the structure, size, and stability of the liposomes [2].

Figure 1 shows how SULV formation pathways rely on structural (disklike and ellipsoidal) precursors in solution, and the parametric ranges they require. The critical temperature is  $T_c \approx 23^\circ\text{C}$ , the point at which the phospholipid chain melts. Lamellar sheets were formed at  $45^\circ\text{C}$  with 25% lipid wt., and diluted in one step to concentrations between 2.5% and 0.1% lipid wt. Initial dynamic light scattering (DLS) experiments indicated high polydispersity in size suggesting the formation of large liposomes with high thermodynamic stability. Extrusion through a 50 nm nuclepore membrane was predicted to significantly lower the yield, so this pathway was abandoned altogether.

The process was repeated at  $4^\circ\text{C}$  forming disklike bicelles at 1.5% to 0.75% lipid wt., and ellipsoids between 0.09% and 0.03% lipid wt. These solutions were heated to  $45^\circ\text{C}$ , extruded, and tested using DLS at  $37.5^\circ\text{C}$ . The intensity was measured at different angles, and cumulant analysis was used to determine the average decay rate,  $\Gamma$ , shown in Figure 2a, right, where  $q$  is the scattering vector and  $D$  is the diffusion coefficient. The Einstein-Stokes equation, Figure 2b is used to determine the average hydrodynamic radius,  $R$ .

$$(2a) \quad \Gamma = -Dq^2$$

$$(2b) \quad D = \frac{kT}{6\pi\eta R}$$

Figure 2

**Radii of SULVs with Disklike and Ellipsoidal Precursors:**

SULVs were successfully created ranging from 30-70 nm. Figure 3 shows that the average hydrodynamic radii of SULVs formed from ellipsoidal precursors range from 58.2 to 66.4 nm. Significant variation from the trendline indicates greater polydispersity, both in size and structure. The average radius was greater than 50 nm, even after extrusion, suggesting that these liposomes may have collapsed or aggregated. Of the disklike precursors, only the 0.75% lipid wt. solution yielded data as more concentrated solutions exhibited multiple scattering effects. This solution had an average hydrodynamic radius of 34.3 nm, as shown in Figure 4. Additional solutions of this precursor with varying concentrations will have to be tested to conclusively demonstrate that disklike bicelles consistently yield stable SULVs with radii less than 50 nm.

**Future Work:**

Future experiments will use rhodamine conjugated to liposome membranes to image their diffusion through cellular media. Liposomes packaged with rhodamine will also be used to test whether leakage rate is dependent upon vesicle size. Differential scanning calorimetry will show how phase-transition effects change with liposome size, phospholipids used, and on formation pathway. Cancer cells have greater cellular entropy due to a higher glycolytic rate. Lowering the liposomes' phase transition entropy by varying these intrinsic variables could cause significant pre-transition effects in liposome membranes and thus increase the rate of drug leakage within cancer cells.

**Acknowledgements:**

I am grateful for my mentor, Dr. S. Balakrishna Pai, for all his guidance and who made this research a very positive experience. I also thank Dr. Ravi Bellamkonda for his counsel during the course of my studies, and Dr. Alberto Fernandez-Nieves for use of the Soft Condensed Matter Lab at Georgia Tech. I especially want to thank John S. Hyatt and Andrea Scotti for their invaluable help with DLS. I thank Yossi Ovadia for his good cheer, and Nassir Mokarram for his

advice. Finally I thank the NNIN REU Program — and its Georgia Tech coordinators, Dr. Nancy Healy, Leslie O'Neill, Joyce Palmer — and the NSF for funding this research.

**References:**

- [1] Munson, J. M., et al., *Sci,Trans,Med.*, 4(127), 127ra36-127ra36 (2012).
- [2] Nieh, M.-P., et al. *Langmuir*, 21(15), 6656-61 (2005).

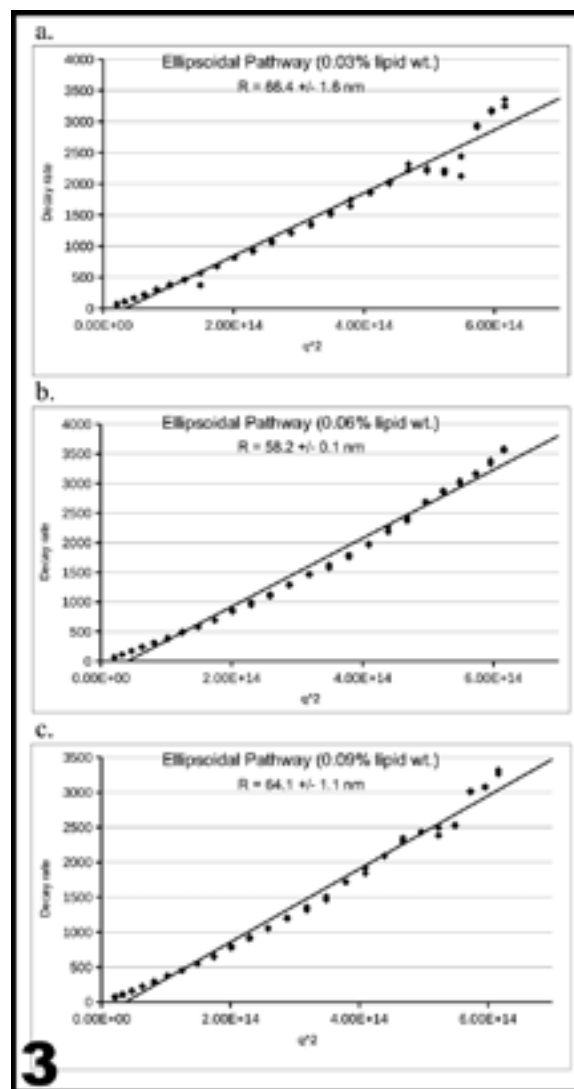


Figure 3: Average hydrodynamic radii of SULVs.

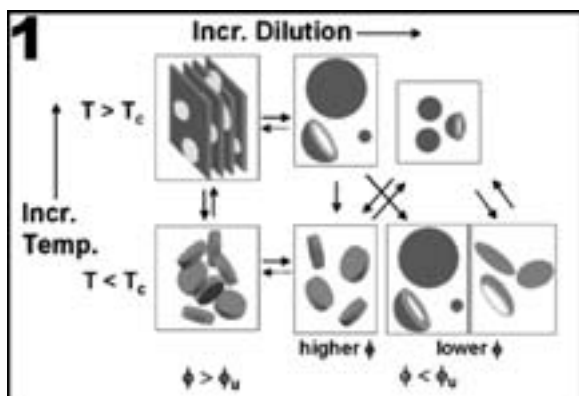


Figure 1: SULV formation pathways rely on structural (disklike and ellipsoidal) precursors in solution.

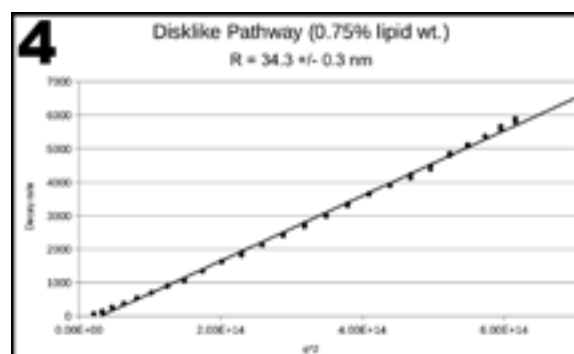


Figure 4: Solution with an average hydrodynamic radius of 34.3 nm.

## Development of an *in vitro* Muscle Regeneration Model using a Combination of Microfluidics and Micropatterning

**Camryn Johnson**

**Biological Engineering, Louisiana State University at Baton Rouge**

*NNIN REU Site: Cornell NanoScale Science and Technology Facility, Cornell University, Ithaca, NY*

*NNIN REU Principal Investigator: Dr. Jan Lammerding, Department of Biomedical Engineering and the Weill Institute for Cell and Molecular Biology, Cornell University*

*NNIN REU Mentor: Dr. Patricia Davidson, Department of Biomedical Engineering and the Weill Institute for Cell and Molecular Biology, Cornell University*

*Contact: cjoh197@lsu.edu, jan.lammerding@cornell.edu, patricia.davidson@cornell.edu*

### Abstract:

Mutations in nuclear envelope proteins that connect the cell nucleus to the cytoskeleton cause muscular diseases [1]. While the exact disease mechanism remains unknown, it is thought that incorrect positioning of nuclei inside the muscle cell may play a critical role. The goal of this project was to develop a microfluidic device that enables imaging nuclear position during muscle development in cultured muscle cells under physiological conditions. Our device consisted of channels to provide culture media to the cells, channels for localized perfusion of agrin, and a micropatterned substrate to induce aligned muscle fibers. We designed several variations of the device based off of a recently published design [2]. We fabricated and tested these devices, which included designing systems of delivering medium and agrin to the cells. We conducted several pilot studies in order to validate the final device. The device will now be used in the Principal Investigator's laboratory to observe the maturation of mutant and normal muscle cells.

### Introduction:

Muscle biopsies of dystrophy patients show abnormal nuclear positioning, but the exact relevance and mechanism of abnormal nuclear location remains unknown. In normal muscle development, single-nucleated myoblasts fuse to form a multi-nucleated myotube. Subsequently, these nuclei migrate to the periphery of the cell. Biopsies provide only a single image of this process. The goal of our project was to use microfluidics and micropatterning to create a device for time-lapse imaging of nuclear positions during maturation of mutant and normal muscle cells.

The main design considerations for our microfluidic device were to continually provide medium to the cells and to deliver agrin to a sub-region of the cells. Agrin stimulates a subset of nuclei, known as synaptic nuclei, to migrate to the neuromuscular junction, where the muscle cells interact with the nerve cell. In the final version of the design, cells will be plated on a micropatterned substrate to induce formation of linear muscle fibers. Figure 1 shows a schematic overview of the device.

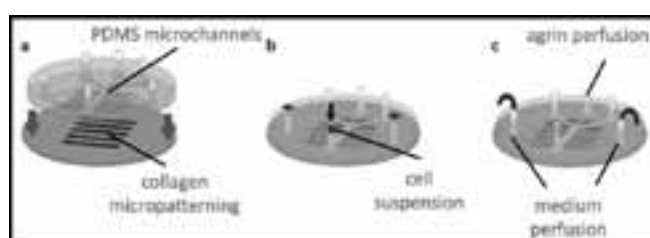


Figure 1: A schematic of the components of the device [2].

### Experimental Procedure:

To create microfluidic features with different heights, we used a two-layer fabrication approach. The first layer was 25  $\mu\text{m}$  thick; the second layer 250  $\mu\text{m}$  thick. Figure 2 shows the design of each layer. The two-layer design allowed us to create channels of different heights for different flow rates within the same device. We created separate masks for each wafer using the Heidelberg.

We spin-coated the first layer of SU-8 2015 onto our wafer and baked it. We exposed our wafer to ultraviolet light through the first mask using the ABM contact aligner, followed by another bake. We developed only the alignment marks with SU-8 developer and then placed a piece of tape over each mark. Next, we added a layer of SU-8 2075 by spin-coating. We removed the tape, pulling the SU-8 off the alignment marks. We then baked and exposed the wafer using the second mask, this time fully developing the entire wafer. Subsequently, we deposited a layer of fluorooctatrchlorosilane (FOTS) on the wafer using molecular vapor deposition to prevent stiction of polydimethylsiloxane (PDMS). We then created our devices by casting PDMS over the wafer. After curing, the PDMS devices were removed from the wafer and bonded to glass slides by activating both the PDMS and the glass slide with oxygen plasma and placing them together.

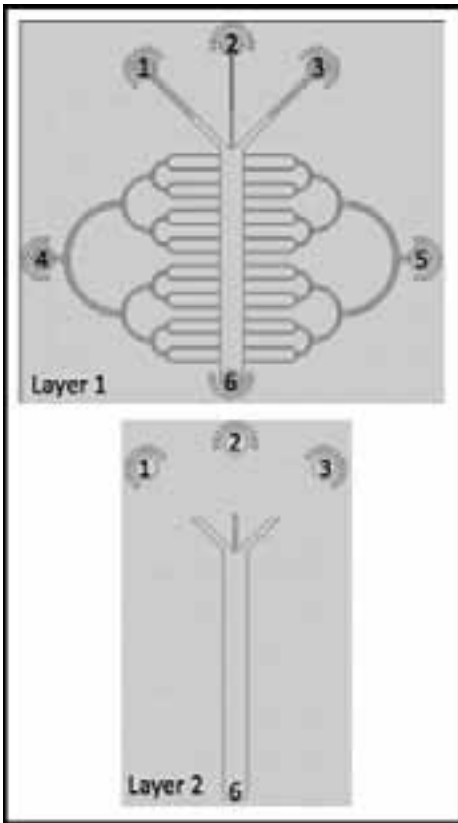


Figure 2: The design for each layer of the device.

### Results and Conclusions:

We fabricated devices using a few variations of our design with different widths and heights of the channels. We successfully created the two-layer wafers and produced PDMS replicas. We tested the complete connection of the channels on the devices by perfusing fluorescently-labeled dextran through the channels. Figure 3 shows a 3D rendering of this test.

We also evaluated different approaches of providing medium to the cells and locally delivering agrin. During our tests, a reservoir of food coloring (simulating medium) was placed approximately one foot above the device and connected to inlet 5 (refer to Figure 2). Hydrostatic pressure alone pushed medium through the device and out inlet 4. For our agrin system, inlet 2 was connected to a reservoir of fluorescently-labeled dextran (simulating an agrin suspension).



Figure 3: 3D reconstruction from confocal image stack of microfluidic device filled with fluorescently-labeled dextran to visualize the microfluidic system.

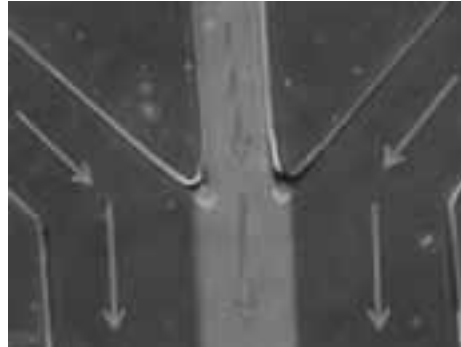


Figure 4: Dextran and sheath fluid are perfused through the device using a syringe pump.

Inlets 1 and 3 were connected to reservoirs of sheath fluid, which helped control the confined delivery of dextran. Inlet 6 was connected to a syringe pump, which aspirated the dextran and sheath fluid from the device. Both systems were validated using food coloring and dextran (Figure 4).

The technique for providing medium to the cells successfully supplied a sufficiently slow rate to prevent applying excess shear stress to the cells. We had the most success with the devices in which the second layer also contained the channel connected to the agrin outlet. This design cut down significantly on air bubbles. In conclusion, the devices performed as desired and are now ready for the seeding muscle cells.

### Future Work:

After our successful pilot studies and validation, the microfluidic device will now be used in the Lammerding laboratory to study the effect of disease-causing mutation on nuclear positioning in muscle cells. The micropatterning technique will be optimized and then combined with the microfluidics device.

### Acknowledgments:

This work was supported by funding from the National Nanotechnology Infrastructure Network Research Experience for Undergraduates (NNIN REU) Program, the National Science Foundation, Cornell NanoScale Science and Technology Facility, and Cornell University, as well as a grant from the Department of Defense Breast Cancer Research Program (BC102152) to J. Lammerding. Special thanks to my PI Dr. Jan Lammerding, my mentor Dr. Patricia Davidson, the CNF REU program coordinators Melanie-Claire Mallison and Rob Ilic, and all the staff at CNF.

### References:

- [1] Ho, CY, Lammerding, J. *Journal of Cell Science* (2012): 2087-93.
- [2] Tourovskaja, A., X. Figueroa-Masot, and A. Folch. *Nature Protocols* 1.3 (2006): 1092-104.

## A Novel, Photoswitchable Poly(ethylene glycol) Biosurface with Applications for High-Throughput Cell Migration Assays

**Olivia Lambdin**

**Biological Systems Engineering, University of Nebraska - Lincoln**

*NNIN iREU Site: National Institute for Materials Science (NIMS), Tsukuba, Ibaraki, Japan*

*NNIN iREU Principal Investigator: Dr. Yukio Nagasaki, International Center for Materials Nanoarchitectonics, National Institute for Material Science*

*NNIN iREU Mentor: Dr. Jun Nakanishi, International Center for Materials Nanoarchitectonics, National Institute for Material Science*

*Contact: olambdin@gmail.com, nagasaki@nagalabo.jp, nakanishi.jun@nims.go.jp*

### Introduction:

Mimicking *in vivo* conditions *in vitro* is of great importance to a wide range of disciplines. Biologists who wish to conduct more accurate studies of biological processes, tissue engineers who aspire to reconstruct organs, and pharmacologists who aim to better understand the effect of drugs on biological systems all depend on model systems that replicate the native microstructure of the human body. Various approaches have been developed to achieve this, including soft lithography and microfluidic devices. Novel biosurfaces that change cell adhesiveness via external stimuli (heat, voltage, light, etc.) – labeled “dynamic substrates” – have also attracted much attention as a viable option [1]. This summer, we investigated the latter, a novel photoswitchable poly(ethylene glycol) (PEG) biosurface that is responsive to UV light, which has also been tailored towards glass-bottom, 96-well plates. The surface shows promise for cell migration studies and other biological applications.

### Material and Methods:

**Surface Functionalization.** Three types of photocleavable PEG polymers were synthesized as previously described [2]. In short, PEG-azides with molecular weights of 2000 Da, 5000 Da, and 11,000 Da were each combined with a photocleavable linker, 1-(5-methoxy-2-nitro-4-prop-2-ynyloxyphenyl)ethyl N-succinimidyl carbonate, in a 1 to 1.1 molar ratio under a copper catalyst and acetonitrile solvent. Compounds were purified by recrystallization and then analyzed with NMR.

**Surface Functionalization.** The functionalization of glass-bottom wells in 96-well plates required three steps. After washing with methanol, 50  $\mu\text{L}$  of a 1 mg/mL poly-d-lysine (PDL) solution in 0.15 M NaCl was allowed to adsorb onto the glass surface. Following washing with  $\text{H}_2\text{O}$ , 50  $\mu\text{L}$  of 1 mg/mL photocleavable PEG in 0.1 M sodium phosphate (pH = 7) and 0.6 M potassium sulfate was added to induce overnight PEGylation of the PDL surface. For mixed-chain tethered surfaces, PEGylation was repeated with a photocleavable PEG of lower molecular weight.

**Photopatterning.** A photomask was placed in the field diaphragm of an inverted microscope, and a mercury arc lamp exposed individual wells to a 10 J/cm<sup>2</sup> dose of UV light ( $\lambda = 365$  nm) through a 10X objective.

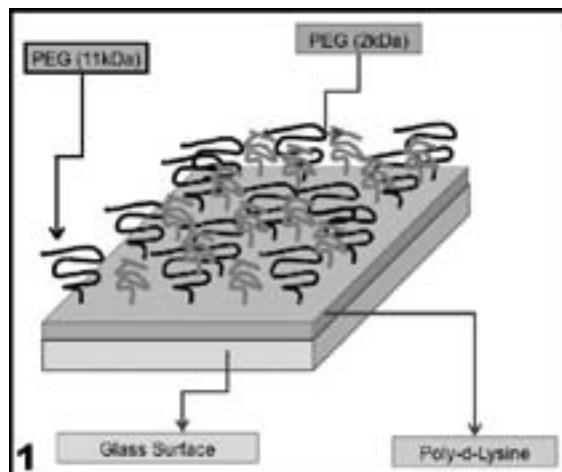
**Cell Deposition.** Madin-Darby canine kidney cells (MDCK) were deposited onto the photopatterned surfaces at 15,000 cells per well. One hour later, the surfaces were washed with medium three times. Cells were incubated overnight before further studies were conducted.

**Cell Migration Studies.** Various concentrations of cytochalasin d were added to cell-patterned wells. A flood exposure of 10 J/cm<sup>2</sup> initiated cell migration to previously uninhabited areas. Cell migration was monitored at approximately two-hour intervals and MetaMorph software was used to calculate change in cell-pattern area.

### Results and Discussion:

Our project focused on the functionalization, characterization, and application of a novel, photoswitchable surface to glass-bottom, 96-well plates, an inexpensive platform for high-throughput bioassays. The platform we investigated was a photocleavable, mixed-chain-tethered PEG surface grafted to PDL (PDL-g-PEG).

Both PEG and PDL have attracted much attention in literature. Because PDL is a cationic polyelectrolyte, it can easily adsorb onto negatively charged surfaces and is commonly used to enhance cell adhesion. On the other hand, PEG-tethered surfaces are anti-biofouling, where the effectiveness of repelling cells and proteins depends on the chain length and density of the PEG brush. However, a tradeoff exists between PEG length and brush density. In order to achieve both, a shorter PEG brush was introduced to a longer PEG-tethered surface. This mixed-chain-tethered PEG surface retained the long chain length while having increased density [3].



To transform this surface into a dynamic platform that switched from cell repelling to cell adhesive, the PEG chains were grafted to the PDL via the photocleavable linker molecule with a 2-nitrobenzyl group. Upon UV exposure, the 2-nitrobenzyl linker group was cleaved, releasing the mixed PEG brush and exposing the underlying PDL. Thus, irradiated areas switched from cell repelling to cell adhesive. This biosurface is visualized in Figure 1.

Three types of mixed-chain-tethered PEG surfaces grafted onto PDL were investigated: PDL-g-PEG (5kDa+2kDa), PDL-g-PEG (11kDa+2kDa), and PDL-g-PEG (11kDa+5kDa). Surface zeta potential measurements demonstrated the progressive functionalization of the glass surfaces. As shown in Figure 2, the inherently negative charge of the glass surface was altered to a largely positive charge upon adsorption of PDL. Grafting of the first PEG layer reduced the positive zeta potential from 66.86 mV to 2.4 mV. And the second PEGylation of the smaller chain brush reduced the potential further. These changes in zeta potential measurements suggest successful grafting of the PEG polymers to PDL.

The functionalized wells were then irradiated with UV using a photomask with a circular pattern. MDCK cells were seeded into these wells and allowed to populate on the photopatterned surface. Once cellular patterns were grown to confluence, cell migration tests were conducted. High-throughput screening of cytochalasin d, a cell migration inhibitor, was carried out. By testing a range of concentrations, a window of the dose-response curve was obtained, from which the half maximal inhibitory concentration ( $IC_{50}$ ) could be derived. Figures 3 and 4 illustrate our preliminary findings.

In conclusion, we believe we have transformed a common piece of lab equipment into a novel, dynamic platform. While high-throughput drug screening of cell migration inhibitors has been demonstrated, we believe this easily functionalized surface has an extensive range of biological applications.

#### Acknowledgements:

I thank Nakanishi-sensei and Nagasaki-sensei for their continuous support and inspiration. I also thank the following organizations for making my work possible: National Science Foundation, National Nanotechnology Infrastructure Network International Research Experience for Undergraduates (NNIN iREU) Program, and National Institute for Material Science.

#### References:

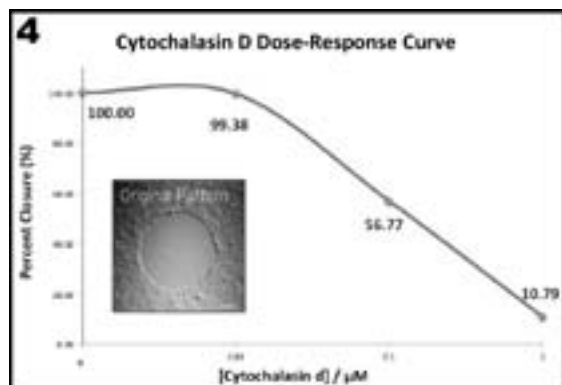
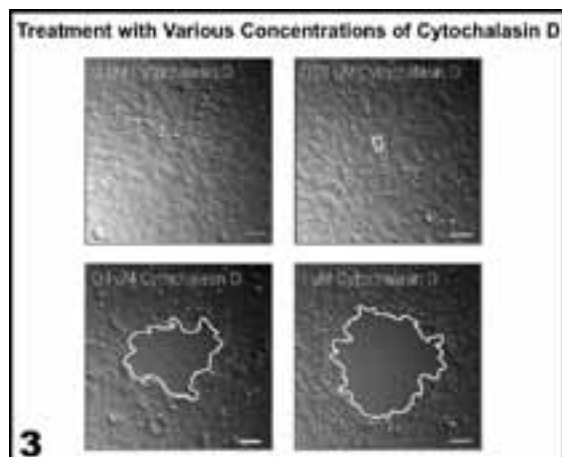
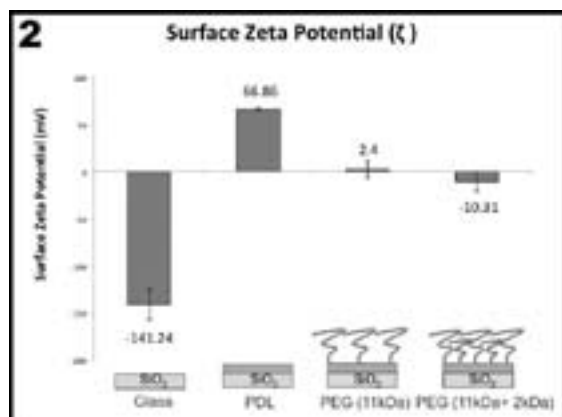
- [1] Nakanishi et al., Analytical Sciences 24, 67-72 (2008).
- [2] Kaneko et al. Phys. Chem. Chem. Phys 13, 4051-4059 (2011).
- [3] Nagasaki, Y. Polymer Journal 1-10 (2011).

Figure 1: Visualization of PDL-g-PEG (11kDa+2kDa) biosurface.

Figure 2: Zeta potential shown for each step of PDL-g-PEG (11kDa+2kDa) functionalization.

Figure 3: Effect of cytochalasin d on MDCK circular-patterned areas on PDL-g-PEG (11kDa+2kDa) surfaces, observed 22 hours after flood exposure.

Figure 4: Cytochalasin d dose-response shown 22 hours after flood exposure of PDL-g-PEG (11kDa+2kDa) surfaces.



## The Effectiveness of Physical Sunscreens in Preventing UVB-Induced Mechanical Damage to the Stratum Corneum

Corinne Lampe

Biomedical Engineering, University of Rochester

NNIN REU Site: Stanford Nanofabrication Facility, Stanford University, Stanford, CA

NNIN REU Principal Investigator: Prof. Reinhold Dauskardt, Materials Science, Stanford University

NNIN REU Mentor: Krysta Biniek, Materials Science, Stanford University

Contact: clampe@u.rochester.edu, dauskardt@stanford.edu, kbiniek@stanford.edu

### Introduction:

The stratum corneum (SC) is the outermost layer of skin and the body's first line of defense against environmental exposures such as ultraviolet (UV) radiation [1]. The SC consists of cells, called corneocytes, held together by corneodesmosomes and intercellular lipids [1]. Previous research in the Dauskardt lab has shown that medium wave UV (UVB) decreases the cohesion of corneocytes, quantified by a decrease in delamination energy, by affecting the properties of intercellular lipids and corneodesmosomes. The focus of this project was to investigate whether physical sunscreens, whose active ingredients are zinc oxide (ZnO) and titanium dioxide (TiO<sub>2</sub>), prevent UVB-induced damage to the mechanical properties of the SC.

### Experimental Procedure:

Experiments were conducted using cadaver SC. Each experiment had a control group, which consisted of SC samples coated with sunscreen, and an experimental group, which consisted of SC samples coated with an equal amount of sunscreen but exposed to UVB radiation. Experiments were performed with broadband (BB) UVB, having a wavelength of 280-315 nm, as well as narrowband (NB) UVB, having a wavelength of 311 nm [2]. Double cantilever beam (DCB) testing was done to determine the delamination energy,  $G_c$ , of the samples. The DCB sample configuration is shown in Figure 1. For all experiments,  $G_c$  is the amount of energy required to remove the top layer of the SC.

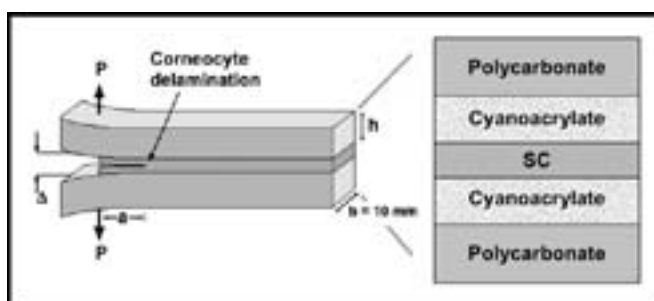


Figure 1: DCB apparatus. The SC (sunscreen removed) was adhered between two pieces of polycarbonate using Krazy® glue. The sample was placed in tension at a rate of 2  $\mu\text{m}$  per second, allowing the sample to slowly fracture over time.

### Results:

The size of the ZnO and TiO<sub>2</sub> particles may have had an effect on the mechanical properties of the SC. Currently, many physical sunscreens are produced with nanoparticles (< 100 nm in diameter) of ZnO and TiO<sub>2</sub> [3,4]. These small particles do not scatter visible light and therefore, appear clear on the skin [3]. Little research has been done regarding the mechanical effects of these particles on the SC, and since sunscreen companies are not required to label the presence of nanoparticles in their products, particle size within the two sunscreens used was initially unknown [4]. Dynamic light scattering (DLS) and scanning electron microscopy (SEM) were performed to characterize particle size.

The results of DLS testing showed that the TiO<sub>2</sub> had an average diameter of 3  $\mu\text{m}$ . SEM images showed that both sunscreens contained particles less than 200 nm, as well as larger agglomerations. However, there are limitations with DLS that should be taken into consideration, such as the risk of contamination from environmental particles, such as dust. Furthermore, SEM images would ideally be taken of the active ingredient alone, without the inactive ingredients present.

UV visible spectroscopy testing was done to determine any wavelengths of light passing through the sunscreens. In both cases, very little UVB penetrated the sunscreen. However, slightly more UVB penetrated the ZnO sunscreen.

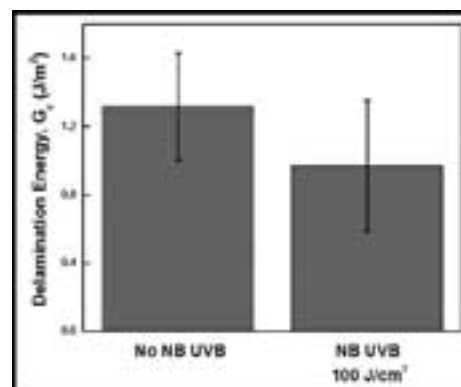


Figure 2: Delamination energy of SC with 21% ZnO sunscreen exposed to NB UVB.

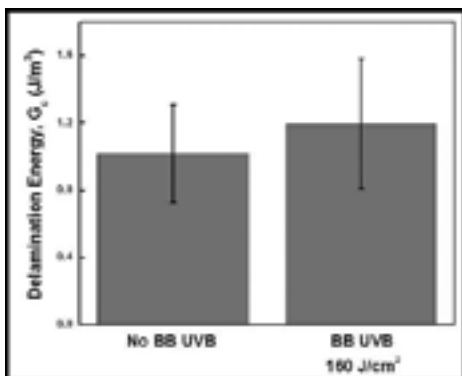
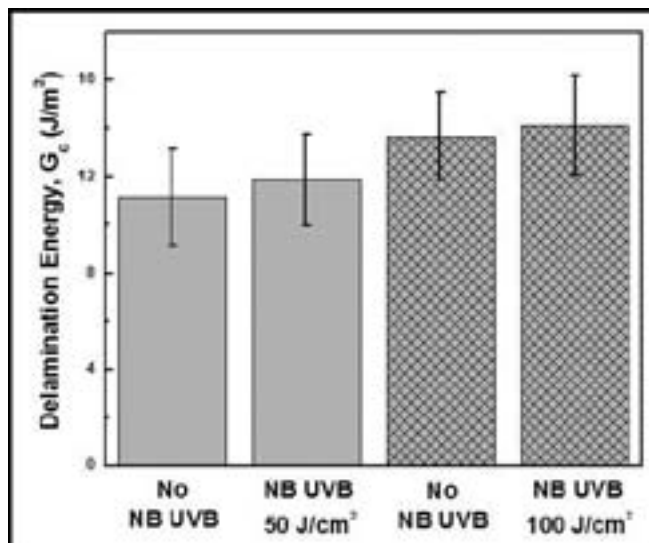


Figure 3, above: Delamination energy of SC with 9.1% TiO<sub>2</sub> sunscreen exposed to BB UVB.

Figure 4, right: Delamination energy of SC with 9.1% TiO<sub>2</sub> sunscreen exposed to NB UVB.



When samples with a sunscreen of SPF 30 and an active ingredient of 21% ZnO were exposed to UVB,  $G_c$  slightly decreased, although it was within statistical error (Figure 2). Based on previous data revealing a significant decrease in  $G_c$  with increased UVB exposure, the slight difference in  $G_c$  between the radiated and non-radiated samples suggests that the sunscreen was effective in maintaining the mechanical structure of the SC.

Like the zinc oxide sunscreen, the TiO<sub>2</sub> sunscreen (SPF 30, 9.1% TiO<sub>2</sub>) was relatively effective in maintaining the mechanical structure of the SC. The sunscreen appeared to be effective regardless of the dosage and type of radiation (BB versus NB).

### Conclusions:

DLS and SEM testing showed that the TiO<sub>2</sub> and ZnO sunscreens contained micron- and nano-sized particles. The micron-sized particles may have resulted from agglomerations of nanoparticles.

The two sunscreens were effective in preventing mechanical damage to the SC when exposed to UVB. However, the  $G_c$  of the control group was not identical to the  $G_c$  of the radiated samples. Radiated samples coated with ZnO had a slightly lower  $G_c$  when compared to the control, suggesting that slightly more UVB was penetrating the sunscreen than was ideal. In contrast, radiated samples coated with TiO<sub>2</sub> had a slightly higher  $G_c$  when compared to the control, suggesting that there is a unique interaction between UVB and TiO<sub>2</sub> that may slightly increase the cohesion of corneocytes.

### Future Work:

We would like to perform further experiments to verify the slight increase in  $G_c$  observed with the radiated samples

coated with TiO<sub>2</sub>. Additionally, particle size within more sunscreens should be characterized, and the UV exposure experiments should be repeated using sunscreens found to have nanoparticles to determine any mechanical effects on the SC caused by nanoparticles in combination with UV. Finally, we would like to look at the effects of UVA on the  $G_c$  of the SC. It is important to understand what affects the mechanical structure of the SC because with a loss of structure comes a loss of barrier function.

### Acknowledgements:

I would like to thank Prof. Reinhold Dauskardt, Krysta Biniek, the Dauskardt lab, Dr. Michael Deal, Maureen Baran, James Conway, Stanford Nanofabrication Facility, Stanford's Center for Integrated Systems, National Science Foundation and National Nanotechnology Infrastructure Network Research Experience for Undergraduates Program.

### References:

- [1] Harding, Clive R. "The Stratum Corneum: Structure and Function in Health and Disease." *Dermatologic Therapy* 17 (2004): 6-15. Blackwell Publishing, Inc.
- [2] Svobodova, Alena, Daniela Walterova, and Jitka Vostalova. "Ultraviolet Light Induced Alteration to the Skin." *Biomed Pap Med Fac Univ Palacky Olomouc Czech Repub.* 150.1 (2006): 25-38.
- [3] "Clear Sunscreen: How Light Interacts with Matter." *NanoSense Activities*. SRI International, 2008. <<http://nanosense.org/activities/clearsunscreen/index.html>>.
- [4] Burnett, M.E., and S.Q. Wang. "Current Sunscreen Controversies: a Critical Review." *Photodermatology, Photoimmunology and Photomedicine* 27 (2011): 58-67. John Wiley & Sons A/S.

## Monitoring and Imaging Hypoxic Cells using Perfluorinated Near-Infrared Fluorescent Micelles

**Kaleigh Margita**

**Chemistry, Newberry College**

*NNIN REU Site: Nano Research Facility, Washington University in St. Louis, St. Louis, MO*

*NNIN REU Principal Investigator: Prof. Samuel Achilefu, Optical Radiology Laboratory, Mallinckrodt Institute of Radiology, Washington University in St. Louis School of Medicine*

*NNIN REU Mentor: Dr. Rui Tang, Optical Radiology Laboratory, Mallinckrodt Institute of Radiology, Washington University in St. Louis School of Medicine*

*Contact: kaleigh.margita@newberry.edu, achilefus@mir.wustl.edu, tangr.mir@wustl.edu*

### Introduction:

In the poorly formed blood vessel networks of solid tumors, hypoxic regions, or areas of low oxygen concentration, develop due to the ineffective delivery of oxygen by the cells. These hypoxic tumors are often resistant to conventional treatment methods [1]. Therefore, the development of a complementary strategy to detect and deliver oxygen to hypoxic tumors would improve treatment response. This could be achieved with multifunctional nanoparticles that are designed to report hypoxia and deliver oxygen to the target tissue. Specifically, quantum dots (Qdots), nanometer semiconductor particles, are used in optical imaging because of their near infrared fluorescence properties, brightness, photostability and potential for multivalent functionalization. In this study, we functionalized Qdots with perfluorocarbons to form novel micelles. We chose perfluorocarbons because of their oxygen carrying abilities [2]. To solubilize the nanoparticle in aqueous solution, an amphiphilic molecule was also prepared and used to formulate the micelle construct [3]. Thus, we developed new perfluorocarbon-coated quantum dots that are capable of monitoring and imaging hypoxic cells. In addition, the materials can effectively deliver oxygen to hypoxic tissues, which will improve the treatment of these difficult tumors.

### Materials:

PbS Quantum Evidot was acquired from Evident Technology (Troy, NY). Perfluorodecane-thiol, perfluorocetyl bromide, toluene, and hexane were purchased from Sigma Aldrich (St. Louis, MO). Oxygen UHP was obtained from Airgas (St. Louis, MO) and deionized water was obtained from MillQ System (Billerica, MA).

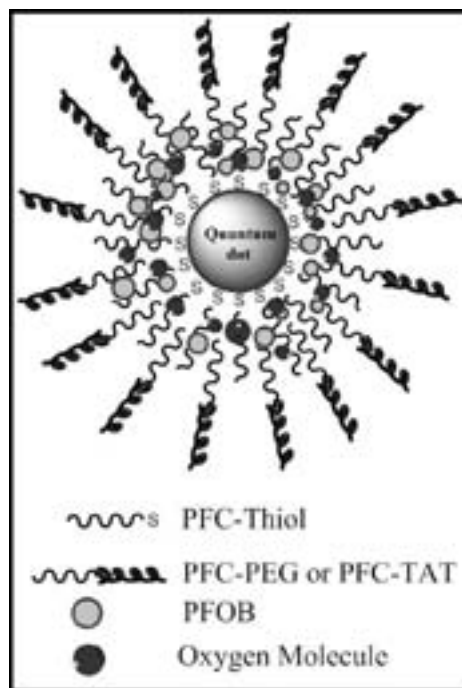


Figure 1: Micelle construct.

### Synthesis of the Micelle:

Lead sulfide quantum dots (Qdots, 10 mg/mL) were functionalized with multiple perfluorocarbon surfactants. First, perfluorodecane (PFC) thiol was added to Qdots based on a previous research patent, resulting in a 0.05 volume ratio of Qdots in PFC-thiol [4]. The trioctylphosphine oxide (TOPO) ligands originally coating the Qdots were replaced by the PFC-thiol surfactant. Second, polyethylene glycol-perfluorocarbon (PFC-PEG, 16 mg) was synthesized and added to 20  $\mu$ l of the 0.05 concentrated sample PFC-thiol Qdot solution, based on concentration calculations ensuring that each individual quantum dot would be completely coated with PFC-PEG instead of forming large aggregates.

After centrifugation, the suspension of the micelle in deionized water (200  $\mu$ L) illustrated that the PFC-PEG

efficiently made the Qdots hydrophilic. To a new solution, with a similar approach, 20  $\mu$ l of PFOB saturated the solution according to surface area calculations. The final Qdot construct formed is shown in Figure 1.

The novel micelle construct was then saturated in an oxygenated environment for two hours. Fluorescent quenching was observed, due to PFOB's ligand structure, which effectively holds oxygen molecules. An attempt at restoring the fluorescence was completed by displacing the oxygen molecules with nitrogen, but to prove the PFOB containing the oxygen was the cause of the quenching, the Qdots and samples functionalized with each surfactant addition were also submitted to the oxygenated environment for comparison of fluorescent emission.

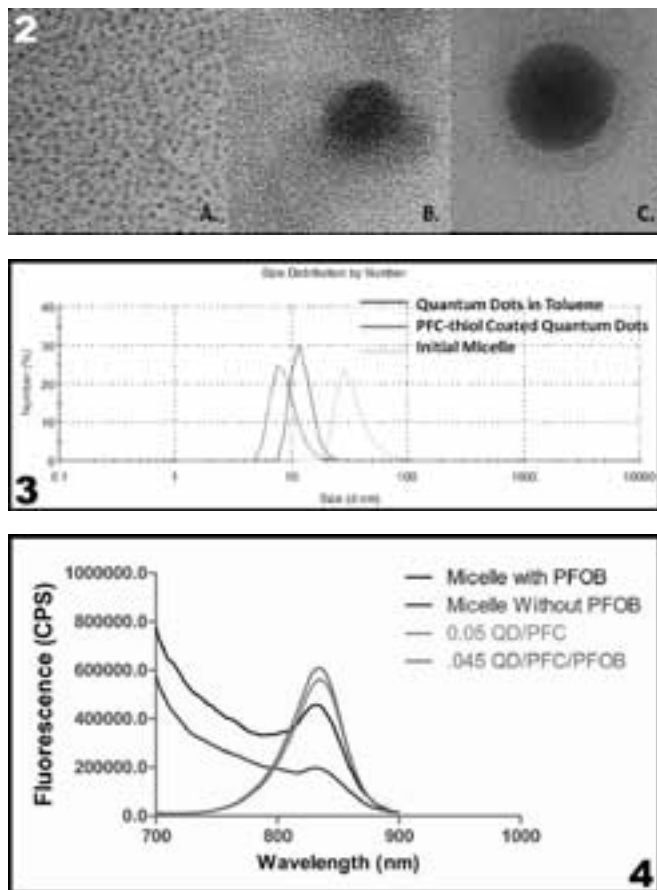


Figure 2, top: TEM images; A) Qdot in toluene, B) Micelle without PFOB, and C) Micelle with PFOB.

Figure 3, middle: DLS for each surfactant addition.

Figure 4, bottom: Fluorescence of micelles compared to surfactant additions.

### Characterization:

The size of the initial PbS Qdots and Qdots with each surfactant coating addition was confirmed by transmission electron microscopy (TEM) images taken on the FEI Tecnai Spirit 120KV, and the hydrodynamic diameter measurements from the dynamic light scattering (DLS) information obtained from the Malvern Zetasizer Nano ZS. The change in size after each surfactant layer addition and of the final micelle (with and without PFOB) was compared. Fluorescence emission data was recorded from the Fluorolog-3 spectrophotometer (Horiba Jobin Yvon). An optimized concentration was determined via the emission efficiency comparison. The quenching effect was also observed via the emission measurement of the micelle construct.

### Results and Conclusions:

The TEM images (Figure 2-A) for the PbS Qdots in toluene collaborated with the DLS (Figure 3) measurement of the

hydrodynamic diameter including the TOPO ligands, proving the 2 nm size. As hypothesized, the replacement of the Qdot TOPO ligands in the addition of the relatively smaller PFC-thiol ligand was shown by the slight decrease in the DLS size. The production of varying concentrations of PFC-thiol and Qdots showed that low amounts of PFC-thiol or high amounts of Qdots can cause the unsuccessful coating and Qdot precipitation. A temporal evolution of the fluorescence of the remaining concentrations of 0.05 and 0.2 volumes of Qdots in PFC-thiol proved that emission was not concentration dependent after 10  $\mu$ l of Qdot. The 0.05 and 0.1 concentrated samples were observed over five days and the 0.05 sample had a fairly high fluorescence, for a less concentrated sample, making it the feasible choice.

With the next surfactant addition, DLS data (Figure 3) showed an increase in size indicating the PFC-PEG surfactant successfully coated the Qdots. After centrifugation, the brown pellets formed were suspended in water demonstrating that the successful formation of hydrophilic micelle. TEM images of the micelle are shown in Figure 2-B. Micelles containing PFOB were successfully created via similar procedure and DLS (Figure 3) and TEM (Figure 2-C) information obtained showed no size increase compared to the micelle without PFOB. The fluorescence of the micelle containing PFOB showed improved emission efficiency due to the better coating of Qdots in this construct.

Oxygenation of the micelle construct was successful and quenched fluorescence was observed. De-oxygenation with nitrogen and restoring the fluorescence of this construct need to be further investigated.

### Conclusions:

Qdots were successfully functionalized with perfluorocarbons compounds and solubilized in an aqueous solution for the monitoring and imaging of hypoxic cells. The micelle construct was also proven capable of containing oxygen to be delivered to hypoxic cell regions.

### Acknowledgements:

Thank you to Professor Samuel Achilefu, Dr. Rui Tang, and the National Nanotechnology Infrastructure Network REU Program for this opportunity.

### References:

- [1] Brown, J.M. Bruce F. Cain Memorial Award Lecture. Cancer Res. 1999, 59 pp 5863-5870.
- [2] Caruthers, S; etc. Proceedings of the IEEE. 2008, 96, (3), pp 397-415.
- [3] Maibaum, L.; etc. J. Phys. Chem, 2004, 108, 6778-6781.
- [4] Chung, B.H.; etc. U.S. Patent 20100233094, Sep. 16, 2010.

## Measuring the Effects of RAD51 Assembly on dsDNA with Magnetic Tweezers

**Morgan McGuinness**

**Physics and Mathematics, Lafayette College**

*NNIN iREU Site: Delft University of Technology (TU Delft), Netherlands*

*NNIN iREU Principal Investigator: Nynke Dekker, Bionanoscience, Delft University of Technology*

*NNIN iREU Mentor: Mina Lee, Bionanoscience, Delft University of Technology*

*Contact: mcguinnm@lafayette.edu, n.h.dekker@tudelft.nl, m.lee@tudelft.nl*

### Introduction:

RAD51 is a protein in eukaryotic cells that is involved in the repair of double-strand breaks in deoxyribonucleic acid (DNA) by homologous recombination. RAD51 assembles on the resected single strands of the damaged region of the DNA, finds a homologous sequence of an intact double-stranded DNA (dsDNA) molecule, and promotes single-stranded DNA (ssDNA) invasion into this sequence [1]. Studying this protein can help us to understand the activity of RAD51 within the nucleus and properties of RAD51-dsDNA filaments during crucial repair processes. Magnetic tweezers provides a means to conduct experiments with RAD51 and dsDNA.

Magnetic tweezers are a single-molecule technique that allows us to apply a torque and an upward force to DNA molecules. The conventional magnetic tweezers setup consists of two cubic magnets above a flow cell, inside which paramagnetic beads are tethered to the bottom via a DNA molecule. As the magnets are rotated, raised, or lowered, the paramagnetic bead will rotate or experience a lesser or greater magnetic force, respectively. The magnetic torquetweezers (MTT) setup is similar to conventional magnetic tweezers, however it consists of a cylindrical magnet that applies an upward force to the tethered bead and a small side magnet that applies a torque. The torsional trap stiffness of MTT is much weaker than that of conventional magnetic tweezers, allowing for greater angular fluctuations of the tethered bead and the measurement of torque [2]. In our experiment, we use MTT to calculate the torsional modulus of RAD51-DNA filaments under torsional stress.

### Methods:

Anti-digoxigenin (100  $\mu\text{g/ml}$ , Roche) and bovine serum albumin (BSA; Sigma) were incubated to allow for DNA tethering and to passivate

the surface, respectively. The 8 kB dsDNA, functionalized with digoxigenin on one end and with biotin on the other, was first bound to 1.4  $\mu\text{m}$  radius paramagnetic M-270 beads (Invitrogen). The tethered beads were then incubated inside the flow cell to allow attachment of DNA to the bottom surface. Most tethered beads were bound to 0.5  $\mu\text{m}$  radius biotinylated latex Fluosphere fiducial beads (Invitrogen). We used 1.5  $\mu\text{m}$  radius nonmagnetic latex beads (Life Sciences) that were bound nonspecifically to the bottom surface of the flow cell as reference beads to correct for drift in the magnetic tweezers microscope.

The flow cell was placed over an oil-immersion objective (Olympus ACH 100X, numerical aperture = 1.25) connected to a CCD camera (Pulnix TM-6710CL), and illuminated with collimated LED. Preliminary measurements were taken with conventional magnetic tweezers to ensure that both strands of the molecule of interest were intact and that the paramagnetic bead was tethered by only one molecule. The

flow cell surface was passivated with BSA again, and MTT were then used. RAD51 was incubated in the flow cell while the magnet was incrementally rotated to -300 turns to prevent loops, or supercoils, from forming in the DNA molecule while the RAD51 assembled. To track the z-height of the paramagnetic bead, the diffraction pattern calibration profiles of one paramagnetic and one reference bead were used [3]. Angular tracking was made possible by the attachment of a small marker bead to the tethered bead [2] (Figure 1).

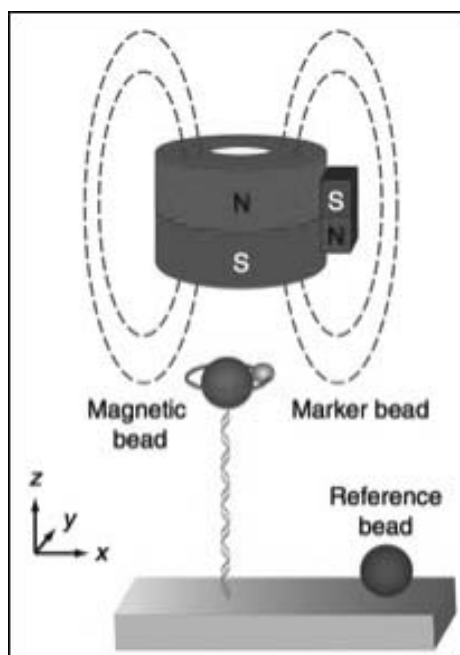


*Figure 1: The MTT setup is shown with the dashed lines representing magnetic field lines.*

### Buffer Conditions:

A TE tethering buffer (200 mM NaCl, 10 mM Tris-HCl (pH 7.5), 1 mM EDTA, and 10 mM  $\text{NaN}_3$  supplemented with 0.01-0.02% Triton-X during and after the bead-DNA binding process) was used

during flow cell preparation. Preliminary measurements were carried out in 100 mM NaCl buffer (100 mM NaCl, 10 mM Tris-HCl (pH 7.5), 1 mM EDTA, 10 mM  $\text{NaN}_3$  supplemented with 0.01-0.02% Triton-X). The binding of RAD51 to DNA and measurements with MTT were carried out in  $\text{Ca}^{2+}$  Assembly buffer (25 mM Tris-HCl (pH 7.5), 25 mM KCl, 2 mM  $\text{CaCl}_2$ , 1 mM DTT, 1 mM ATP, 0.5 mg/ml BSA, and 0.02-0.05% Triton-X).

### Results:

We derived the torsional modulus from the torque build-up of the RAD51-dsDNA filament after  $N$  turns, which was equal to  $2\pi Nk_B TC/L_C$  [2]. Here,  $k_B$  was the Boltzmann constant,  $T$  was temperature, and  $C$  and  $L_C$  were the torsional modulus and contour lengths of the RAD51-dsDNA molecule, respectively, which were derived from a force-extension curve.

Figure 2 shows the force-extension curve for bare dsDNA, and Figure 3 shows the force-extension curve for a RAD51-dsDNA filament.  $L_C$  is a function of force, and from these figures we see that  $L_C$  of the bare dsDNA was  $2.88 \mu\text{m}$  and  $L_C$  of the RAD51-dsDNA filament was  $4.09 \mu\text{m}$ . Figure 4 shows the mean angle of the filament versus  $N$ , determined by angular tracking of the paramagnetic bead. The torsional modulus was  $553 \pm 80.2 \text{ nm}$  at  $3.5 \text{ pN}$ .

### Discussion:

Previous studies have found that RAD51 assembly results in a  $\sim 50\%$  increase in  $L_C$  of the dsDNA filament [1]. This is consistent with our measurements, which showed a 42.01% increase in  $L_C$ . Lipfert, et al. [2], measured the torsional modulus of bare 8 kB dsDNA and RecA-dsDNA (RecA is a protein in bacteria homologous to RAD51) to be  $\sim 95 \text{ nm}$  and  $173 \pm 5 \text{ nm}$  at  $3.5 \text{ pN}$ , respectfully. Comparing this with our results, we see that RAD51 assembly increased the torsional modulus of bare dsDNA by  $\sim 580\%$ , in contrast to a 180% increase caused by RecA assembly.

### Acknowledgements:

This research was supported by the National Nanotechnology Infrastructure Network International Research Experience for Undergraduates (NNIN iREU) Program and the National Science Foundation. I would also like to thank the Nynke Dekker Lab at the Delft University of Technology for their valuable guidance and support.

### References:

- [1] Hilario, J., Amitani, I., et al. Dutch PNAS. 2009, 106, 361-368.
- [2] Lipfert, J., Kerssemakers, J., et al. Nat. Methods. 2010, 7, 977-980.
- [3] Vilfan, I. D., Lipfert, J., et al. Handbook of Single-Molecule Biophysics. 2009, 371-395.

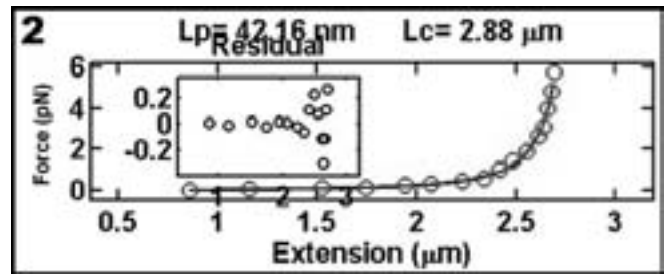


Figure 2: The force-extension curve of the bare dsDNA filament gives  $L_C$  of that filament.

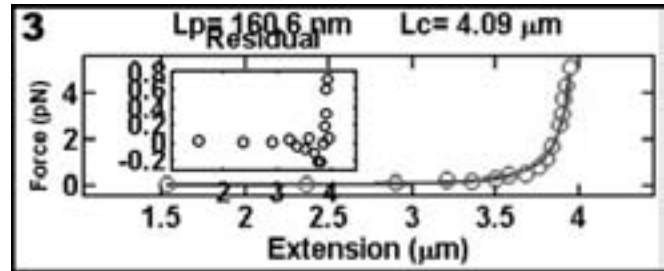


Figure 3: The force-extension curve of the RAD51-dsDNA filament gives  $L_C$  of that filament.

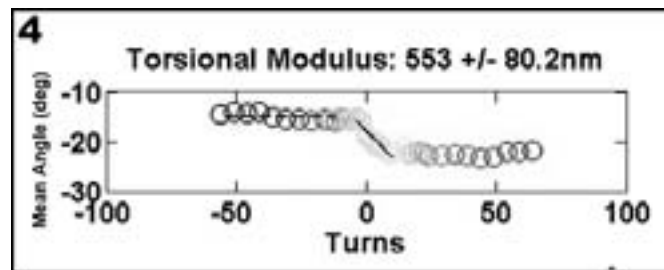


Figure 4: The torsional modulus is derived from the mean angle of the filament versus  $N$ .

## Fabrication of a Selective Ion Pump: Anodization of an Aluminum Oxide Membrane

**Christopher Nakamoto**  
Chemistry, Beloit College

NNIN REU Site: Nanotech, University of California, Santa Barbara, CA

NNIN REU Principal Investigator: Dr. Luke Theogarajan, Electrical and Computer Engr., University of California, Santa Barbara

NNIN REU Mentor: Samuel Beach, Electrical and Computer Engineering, University of California, Santa Barbara

Contact: nakamotoc@beloit.edu, ltheogar@ece.ucsb.edu, beach@umail.ucsb.edu

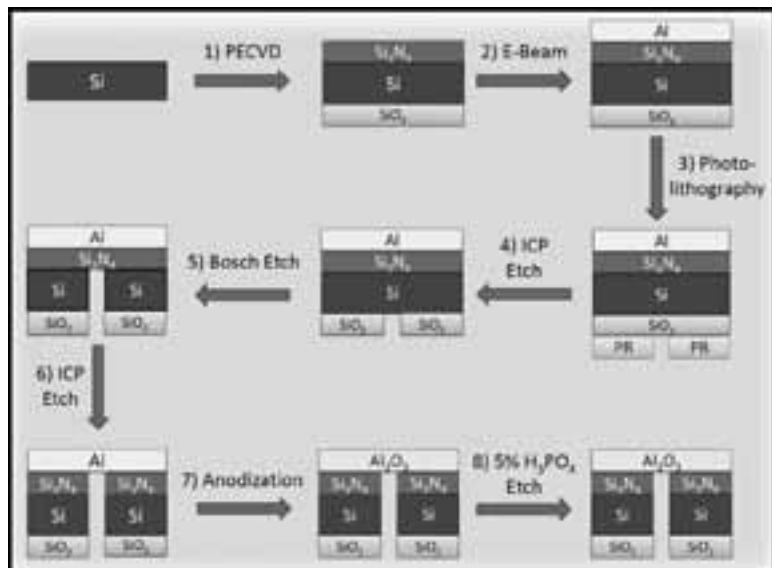


Figure 1: An outline of the fabrication process.

### Abstract:

Anodized aluminum oxide nanoporous membranes show great potential for biological interfaces due to their controllable pore size, pore regularity, and biological stability. In this study, anodized aluminum oxide was investigated for use in a through silicon selective neural ion pump. A thin layer of aluminum and silicon nitride was suspended over a  $120\ \mu\text{m}$  by  $120\ \mu\text{m}$  window in a silicon wafer. The anodization of the aluminum layer was achieved using sulfuric or oxalic acid at voltages between 12.5 and 40 V at  $1^\circ\text{C}$ , to form pores between 12.5 and 27.5 nm. The silicon nitride and alumina barrier layer formed were then etched using reactive ion etching and phosphoric acid etching to form a suspended aluminum oxide nanopore membrane.

### Introduction:

Electronically interfacing with nervous systems holds immense potential for restoring function to damaged sensory organs [1]. Neural network interfacing, however, has thus

far been limited by dangers and inefficiencies in electrode stimulation of neurons [2]. Implementing a selective neural ion pump to stimulate a neural response instead can stimulate neurons more safely and efficiently, but for this method to be practical, pumps would have to be small enough to reference individual or small groups of neurons and quickly deliver sufficient amounts of  $\text{K}^+$  [3]. This can be achieved by decreasing the path length the  $\text{K}^+$  would have to travel by fabricating a three dimensional stack device with a thin rigid membrane, in contrast to planar ion pumps demonstrated by Richter-Dahlform et al. [4].

In this study, nanoporous anodized aluminum oxide (AAO) was tested as a membrane material, because it demonstrates controllable pore size, pore regularity, and biocompatibility [5]. Anodization is also a scalable process making the move from single pumps to an array of pumps relatively easy. For these reasons, AAO membranes were fabricated and suspended over through silicon (Si) windows in preparation for use in a selective neural ion pump.

### Experimental Procedure:

Using plasma enhanced chemical vapor deposition, 100 nm of silicon nitride ( $\text{Si}_x\text{N}_y$ ) and  $1.5\ \mu\text{m}$  of silicon oxide ( $\text{SiO}_2$ ) were deposited on opposite sides of a 0.5 mm thick double-side polished Si wafer. Then 100 to 1000 nm of aluminum (Al) was deposited onto the  $\text{Si}_x\text{N}_y$  layer using electron beam evaporation. Using photolithography, a hard mask was etched into the  $\text{SiO}_2$  layer for Bosch etching. Four hours and thirty-seven minutes of Bosch

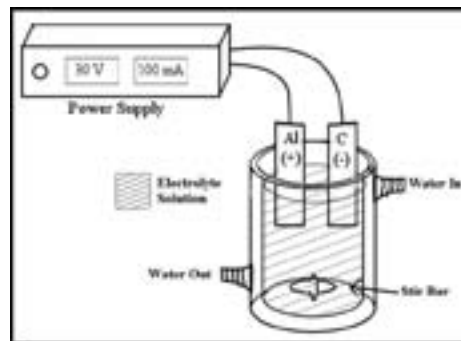


Figure 2: A diagram of the anodization setup.

etching separated the wafer into 15 by 15 mm squares with 120 by 120  $\mu\text{m}$  windows through the Si in the center. Across the windows a thin layer of  $\text{Si}_x\text{N}_y$  and Al was left suspended. The  $\text{Si}_x\text{N}_y$  layer was then removed using ICP etching leaving the Al layer. This was then anodized using the setup shown in Figure 2. 3M insulating tape was used to protect the  $\text{SiO}_2$  side so that pore formation occurred only on the side exposed to solution.

Anodizations took place at  $1^\circ\text{C}$  in 0.3 M oxalic acid or 5% (w) sulfuric acid using a graphite counter electrode. A constant voltage set between 12.5 and 40 V with a maximum current of 100 mA was applied for 2 to 60 minutes producing AAO nanopores with a thin barrier layer of alumina at the bottom of each pore. The 3M tape was removed and SPR220-3.0 photoresist was applied to the opposite side protecting the AAO except where exposed by the Si window. This allowed the barrier layer to then be etched using 5% (w) o-phosphoric acid, keeping pores intact. The nanoporous membranes were then characterized by field emission scanning electron microscopy (FESEM) to determine pore diameter, uniformity, and depth.

### Results:

FESEM images of the resulting pores showed a linear relationship between average pore diameter and applied anodization voltage. Pores formed at a ratio of 0.59 nm/V and 0.68 nm/V for oxalic acid and sulfuric acid respectively, as shown in Figure 3. Irregularities in the Al surface during pore nucleation and an insufficient anodization length resulted in pores with lower regularity than those formed in other two-step processes as described by Wood and O'Sullivan [6]. The pores did, however, form completely through the Al as seen in the cross sectional image in Figure 4.

Backlit optical microscopy was used to evaluate the completed suspended membrane and the successful anodization of the Al. Unanodized Al or unremoved Si and  $\text{Si}_x\text{N}_y$  would show up as shadows on the optical microscope image. The absence of these shadows confirmed the suspension of a thin AAO membrane.

### Future Work:

The next step in this project is to use these membranes in fabricating a selective ion pump similar to the pumps fabricated by Richter-Dahlfors, et al., and test the ion pump's ability to deliver  $\text{K}^+$ .

### Acknowledgements:

I would like to thank Dr. Theogarajan, Samuel Beach, Steven Wienecke, Samantha Cruz, the UCSB Nanofab staff, and the Theogarajan group for their help. And the National Nanotechnology Infrastructure Network Research Experience for Undergraduates (NNIN REU) Program and National Science Foundation for this research experience.

### References:

- [1] Wolfrum, B.; Mourzina, Y.; Sommerhage, F.; Offenhäusser, A. *Nano Lett.* 2006, 6, 453.
- [2] Cogan, S.F.; Guzelian, A.A.; Agnew, W.F.; Yuen, T.G.H.; McCreery, D.B. *J. Neuroscience Methods* 2004, 2, 141.
- [3] Theogarajan, L.S.; Jensen, R.J.; Rizzo, J.F. *Investigative Ophthalmology and Visual Science* 2004, 45, 4215.
- [4] Isaksson, J.; Kjåkk, P.; Nilsson, D.; Robinson, N.D.; Berggren, M.; Richter-Dahlfors, A. *Nature Mater.* 2007, 6, 673.
- [5] Lee, W.; Ji, R.; Gösele, U.; Nielsch, K. *Nature Mater.* 2006, 5, 741.
- [6] O'Sullivan, J. P.; Wood, G. C. *Proc. R. Soc. London* 1970, A317, 511.

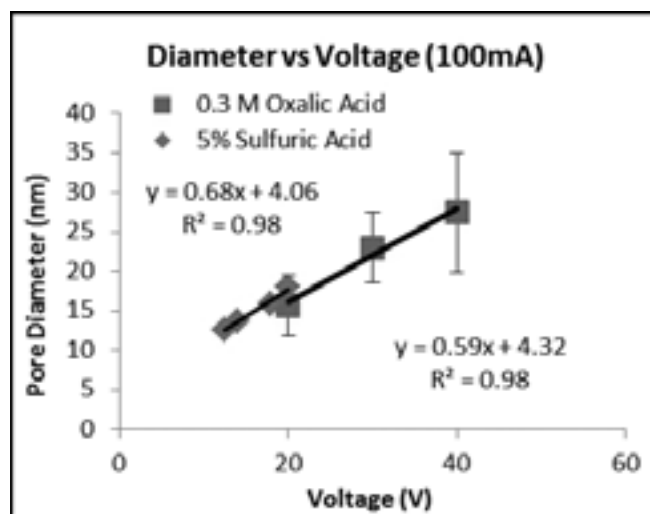


Figure 3: A plot of the average pore diameter against anodization voltage base on FESEM images.

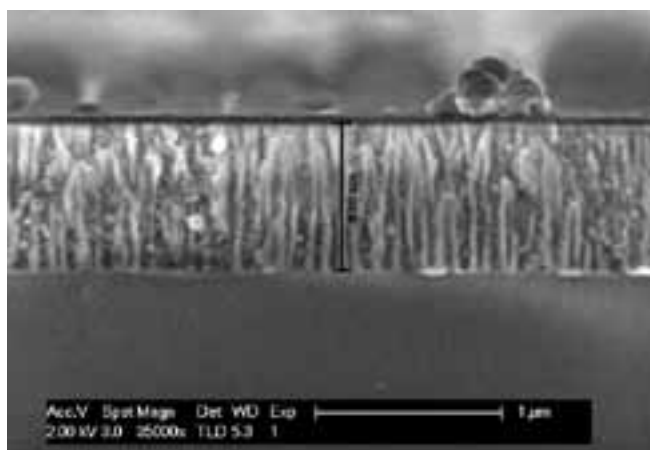


Figure 4: FESEM images of a cross section of AAO nanopores.

## Silicone Nanoparticles for DNA Drug Delivery

**Kendall Pletcher**

**Bioengineering, Franklin W. Olin College of Engineering**

*NNIN iREU Site: National Institute for Materials Science (NIMS), Tsukuba, Ibaraki, Japan*

*NNIN iREU Principal Investigator: Dr. Nobutaka Hanagata, Biosystem Control Group, National Institute of Materials Science*

*NNIN iREU Mentor: Dr. Svetlana Chechetka, Biosystem Control Group, National Institute of Materials Science*

*Contact: kendall.pletcher@students.olin.edu, hanagata.nobutaka@nims.go.jp, chechetka.svetlana@nims.go.jp*

### Abstract:

Because of its role in immune-system activation, high-mobility group box protein (HMGB) has been targeted for treatment of auto-immune diseases. It has been found that single-stranded deoxyribonucleic acid (DNA) fragments, oligodeoxynucleotides (ODN), can competitively bind to HMGB, blocking apoptotic DNA responsible for prompting improper immune responses leading to autoimmune diseases. This study examined the immune response of cells that were stimulated with five ODN of different backbones, sequences, and lengths, either free or in a NP-ODN complex to examine the effect of nanoparticles (NP) on the efficacy of the DNA drug. The NP-ODN complex was found to enhance the suppressive effect of the ODN on interferon alpha (IFN- $\alpha$ ) production, but had no effect on the production of chemokine ligand 5 (CCL5). These findings suggest that ODN-HMGB binding mode can effect downstream signal transduction and, additionally, that there is promise in NP design for the purpose of affecting the function of DNA drugs.

### Introduction:

Pattern recognition receptors (PPRs) recognize conserved pathogen-associated molecular patterns and activate cells of the innate immune system, playing an integral role in protecting against microbial pathogens. However, the activation of PPRs can also result in harmful immune responses such as in the case of life-threatening inflammation and autoimmunity. One approach to curb such inappropriate immune responses has shown promise: HMGB targeted therapies may suppress innate immune responses due to the role of HMGB in triggering all nucleic acid receptor-mediated innate immune responses [1]. Consequently, it has been suggested that nucleic acids with high binding affinity for HMGB may function as suppressing agents for HMGB-mediated diseases. Thus, competitive binding of ODN to HMGB may have clinical applications for treatment of autoimmune diseases.

This study looks at the immune response-inhibiting effects of six different ODN, examining the effect of backbone, length, and sequence of the ODN on the inhibitory effect observed.

Additionally, silicon nanoparticles (Si-NPs) are introduced as delivery agents for the ODN and examined to determine therapeutic effects. The inhibitory effects of each ODN in complexes with NPs and alone are shown and the significance of the findings are discussed.

### Methods:

Six single-stranded ODN were used in this study:

1. CG PT (CG sequence, phosphorothioate backbone, 24 base length),
2. GC PT (GC sequence, phosphorothioate backbone, 24 base length),
3. x1GC PD (GC sequence, phosphodiester backbone, 24 base length),
4. x2GC PD (GC sequence, phosphodiester backbone, 48 base length),
5. x3GC PD (GC sequence, phosphodiester backbone, 72 base length), and
6. x3CG PD (CG sequence, phosphodiester backbone, 72 base length).

These ODNs were electrostatically bound onto allylamine-modified Si-NPs with average diameter of 3.4 nm.

Mouse fibroblast cells were treated with free ODNs or NP-ODN conjugates for 1 h, and then B-DNA was added into

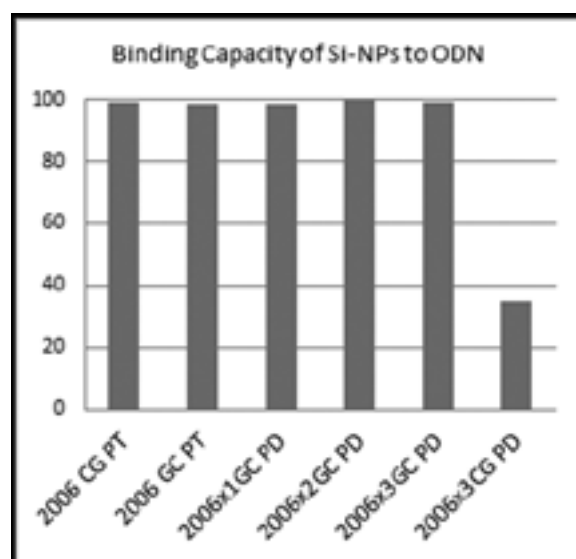


Figure 1: Binding Capacity. 2006x3 CG PD was found to have a much lower binding capacity (35%) than the other five ODNs, of which each sported nearly 100%.

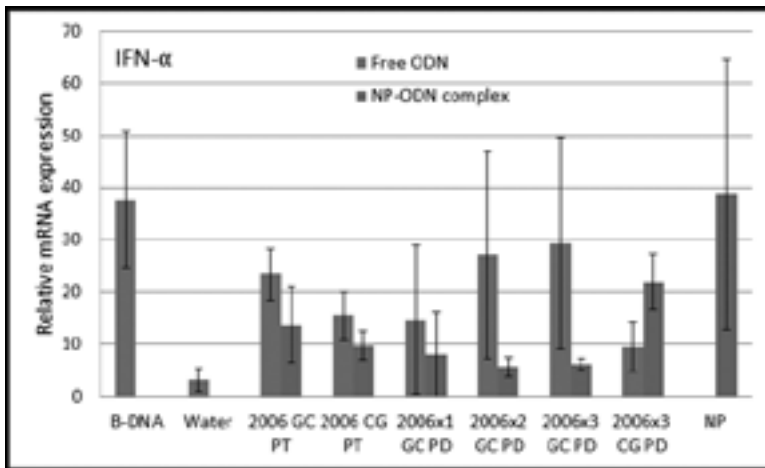


Figure 2: IFN- $\alpha$  Results. NP-ODN complexes were found to express lower levels of IFN- $\alpha$  with the exception of 2006x3 CG PD. No significant differences due to backbone, sequence, or length of ODN were found.

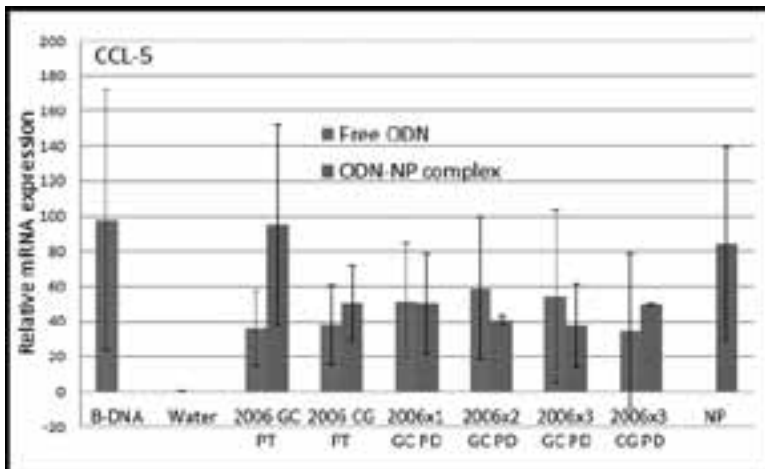


Figure 3: CCL5 Results. NP-ODN complexes were not found to significantly affect the results, as were differences due to backbone, sequence, and length of ODN.

culture medium to stimulate HMGB. After 24 h, total RNA was extracted to examine the expression level of IFN- $\alpha$  and CCL5 genes by using quantitative real time PCR (qRT-PCR).

### Results and Discussion:

Binding capacity results showed that four of the ODN used featured nearly 100% binding capacity. However, 2006x3 CG PD that consisted of the 72 base phosphodiester backbone CG sequence featured a much lower binding capacity of 35% (Figure 1).

Results of IFN- $\alpha$  qRT-PCR showed that the cells stimulated with NP-ODN complexes produced less IFN- $\alpha$  relative mRNA expression than those stimulated with free ODN alone (Figure 2). The only exception to this trend was found to be 2006x3 CG PD. The solitary nature of this result implies

that the significantly lower binding capacity of the 2006x3 CG PD ODN to Si-NPs affected the results.

Results of CCL5 qRT-PCR showed no significant differences between cells stimulated with NP-ODN complexes compared to those stimulated with free ODN (Figure 3). No significant differences in relative IFN- $\alpha$  or CCL5 mRNA expression were observed due to changes in backbone, sequence, or length of ODN in stimulation.

The effect of the NP-ODN complexes on IFN- $\alpha$  and CCL5 production is significant in its implication of the importance of interaction mode. Due to the difference in responses triggered by free ODN and NP-ODN complexes, there is evidence that the interaction mode between HMGB and ODN can affect the resulting downstream signal transduction. Thus, altering NP conformation and NP-ODN binding mode can be used to alter the production of a single cytokine. Additionally, because the complexes in this study affected production of only one of the cytokines of interest, there is evidence that a single stimulation method can be designed such that it affects the production of several different cytokines in predictable but dissimilar ways.

### Conclusions:

Backbone, sequence, and length of the ODN used in stimulation were not found to affect the relative mRNA expression for either IFN- $\alpha$  or CCL5. However, the use of NP-ODN complexes in stimulation were found to increase the inhibitory effect of the ODN on IFN- $\alpha$  production while not clearly affecting the production of CCL5, signifying the importance on binding mode on downstream signal transduction in the HMGB-mediated mechanism of auto-immune disease.

### Acknowledgements:

I would like to acknowledge the work of Chinnathambi Shanmugavel and Svetlana Chechetka, who aided the author throughout, and Dr. Nobutaka Hanagata, for his invaluable guidance. This work would not have been possible without funding and support from the National Science Foundation, the NNIN iREU Program, and the National Institute of Materials Science.

### References:

- [1] Yanai, Hideyuki et al. "Suppression of immune responses by nonimmunogenic oligodeoxynucleotides with high affinity for high-mobility group box proteins (HMGBs)"; Proc Natl Acad Sci USA. 2011 July 12; 108(28):11542-7.

## A Microfluidic Gradient Generating Device Integrated with Nanopatterned Matrices for Studying Guided Cell Migration

**Radu Reit**

**Biomedical Engineering, Georgia Institute of Technology**

*NNIN REU Site: NanoTech User Facility, University of Washington, Seattle, WA*

*NNIN REU Principal Investigator: Deok-Ho Kim, Bioengineering, University of Washington*

*NNIN REU Mentor: Nirveek Bhattacharjee, Bioengineering, University of Washington*

*Contact: rreit3@gatech.edu, deokho@uw.edu, nirveek@u.washington.edu*

### Abstract:

Migrating cells are inherently sensitive to a plethora of diffusible and immobilized cues, which are integrated to coordinate their directional migration in various contexts of organizational development, physiology and disease *in vivo*. However, the combined effects of these complex guidance cues on directional cell migration remains poorly understood, partly due to complete neglect of these combinational factors in most *in vitro* experimentation. Here, we developed a novel microfluidic platform with a nanostructured surface interface, allowing integrative stimulus delivery of chemoattractant factors and topographical cues to migrating cells. We combined nano-grooved substrates with open well microfluidic chambers to study the effects of chemoattractant factors and matrix topography on directional cell migration. Co-current and countercurrent flows of stromal derived factor-1 alpha (SDF-1 $\alpha$ ) alongside bovine serum albumin (BSA)-labeled with fluorescent Rhodamine were used to study microfluidic gradient generation and the subsequent cell homing response. Using this platform, in a single experiment, we could simultaneously characterize cell migration and associated cell shape changes under well-defined variations in chemoattractant factors and matrix topography.

### Introduction:

Migrating cells are inherently sensitive to a plethora of diffusible and immobilized cues that are present in a combinatorial fashion, and are integrated by intracellular signal transduction machinery to coordinate their directional migration in various physiological and pathological contexts *in vivo*. A significant challenge faced by biomedical researchers is to study these factors combinatorially *in vitro* and understand their roles in determining cellular motility and directionality. Microfluidic chambers allow for a robust, high-throughput measurement technique for the study of chemotaxis and polarized cell movement [1]. Additionally, topographically amended substrates enhance sensitivity of migration, and allow integration of mechanical cues in experimental design [2]. However, the effect of combining

these various extracellular cues and their subsequent effects on directed cellular homing remains vastly unexplored. Here we developed a novel microfluidic platform with a nanostructured surface interface, allowing integrative stimulus delivery of chemoattractant factors and topographical cues to migrating cells.

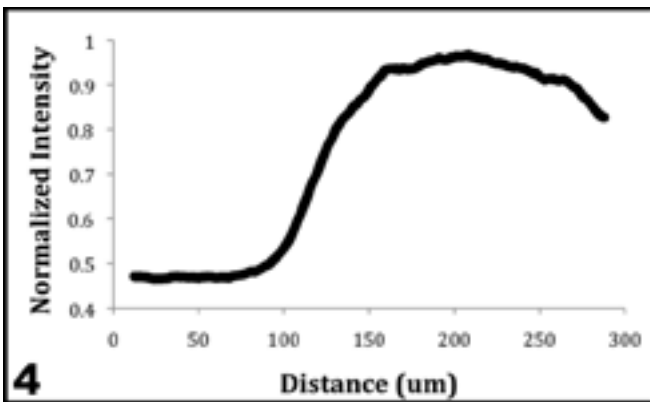
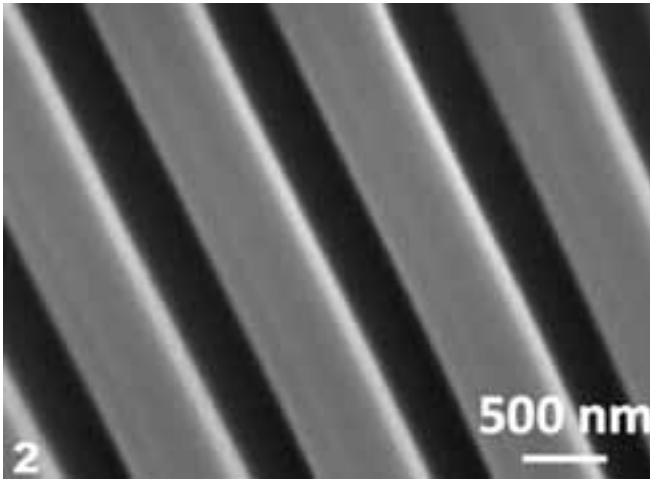
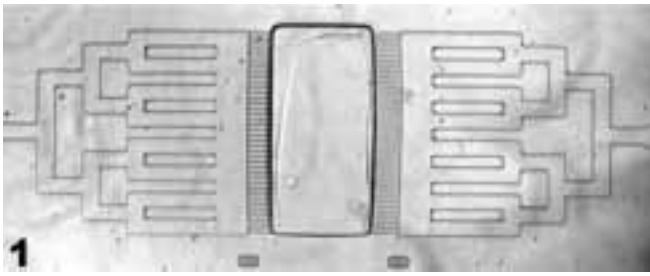
### Experimental Procedure:

Nano-patterned polydimethylsiloxane (PDMS) was fabricated using soft lithography nanofabrication techniques to form patterns with 550 nm wide and 500 nm tall grooves, with a groove-to-ridge ratio of 1:1. Both flat and nano-grooved substrates were plasma-treated for 60 seconds at 650 mTorr and 60W, and then surface bound to a PDMS 4-well open-chamber microfluidic device. Co-current and countercurrent gradients were characterized using fluorescently labeled bovine serum albumin (BSA) flowed in at 1.6  $\mu$ L/min.

### Results and Conclusions:

Microfluidic chambers and nanogrooved substrates were combined to create a device to test the effects of multiple extracellular factors synergistically *in vitro*. Figure 1 shows a well of the completed integrated device with the nanogrooved substrates along the bottom of the main cell-culture area shown in Figure 2. Microfluidic gradients were established, as shown in Figure 3, and later characterized for shape and linearity in Figure 4 at steady state.

In this study, we fabricated a high throughput microfluidic device using a nanopatterned PDMS substrate and an open-well microfluidic chamber. Protein flow gradients were characterized for linearity and used to optimize the flow rate for a biologically relevant chemotactic gradient. Overall, an easy-to-use, topographically mimetic microfluidic device was constructed for the combined study of chemotactic gradients and topography on directed cell migration.



### Future Work:

Upcoming experiments utilizing the microfluidic will focus on the role of cooperative and competing soluble factor gradients on the effects of directed cellular homing atop nanopatterned substrates. Co-current gradients will be established for the study of the synergistic effects of multiple soluble factors on cellular migration in the presence of multiple chemotactic gradients and compared with the observed individual soluble factor effects. Similarly, countercurrent gradients will be established for the study of the competing effect of chemotactic gradients and used to better understand the cellular sensitivity to specific chemoattractants. Both these experiments will serve to better understand the cell migration response to soluble factor gradients on a much more physiologically relevant substrate and will allow for the understanding of basic cellular migration in a more complex and relevant environment of microfluidic gradients.

### Acknowledgments:

The author would like to thank the National Science Foundation, and National Nanotechnology Infrastructure Network Research Experience for Undergraduates (NNIN REU) Program, as well as the University of Washington Bioengineering Department and the University of Washington Nanotechnology User Facility (UW NTUF) for research support and funding.

### References:

- [1] Keenan, T. M., Frevert, C. W., Wu, A., Wong, V., and Folch, A. (2010). A new method for studying gradient-induced neutrophil desensitization based on an open microfluidic chamber. *Lab on a chip*, 10(1), 116-22.
- [2] Park, J., Kim, H.-N., Kim, D.-H., Levchenko, A., and Suh, K.-Y. (2012). Quantitative analysis of the combined effect of substrate rigidity and topographic guidance on cell morphology. *IEEE transactions on nanobioscience*, 11(1), 28-36.

*Figure 1: Phase 4x objective image of PDMS microfluidic chamber.*

*Figure 2: SEM image of 550 nm PDMS patterns within the exposed cell culture well.*

*Figure 3: Fluorescently labeled protein flow through the right hand channel.*

*Figure 4: Intensity profile of fluorescently labeled protein along the width of the microfluidic chamber.*

## Uptake of Nanoparticles in the Olfactory System and Transport to the Brain in Locust

**Jonathan Schoening**

**Biochemistry, Clarke University**

NNIN REU Site: Nano Research Facility, Washington University in St. Louis, St. Louis, MO

NNIN REU Principal Investigator: Dr. Pratim Biswas,

Energy, Environmental and Chemical Engineering, Washington University in St. Louis

NNIN REU Mentor: Tandeep Chadha, Energy, Environmental and Chemical Engineering, Washington University in St. Louis

Contact: jonathan.schoening@clarke.edu, pbiswas@wustl.edu, chadha@wustl.edu

### Abstract and Introduction:

The olfactory nerve, which projects directly from the nasal epithelium to the brain, is the shortest and most direct route to the brain. It has been suggested that nanoparticles deposited in the nasal epithelium are capable of being uptaken into the neurons and transported to the central nervous system [1]. This olfactory route is of particular concern as it completely bypasses the blood-brain barrier, responsible for protecting the brain from foreign materials. The growing use of nanoparticles in consumer and industrial products also underscores the importance of understanding how nanoparticles may gain access to the central nervous system.

We expect nanoparticle transport to the brain to begin with the uptake of nanoparticles by either receptor mediated or non-receptor mediated endocytosis. While the former requires interaction with surface proteins, the latter occurs randomly as the cell samples material from its extracellular environment. Once inside the cell, nanoparticles bind to “motor” proteins, which move along a microtubule system spanning the entire neuron [2]. While this is normally responsible for transporting important cellular proteins and organelles, it could also be used by nanoparticles to quickly travel to the brain.

It is unknown what impact nanoparticles may have on neuron activity once they reach the brain. To characterize this, we used

electrophysiology tests to measure what effect a nanoparticle injection in a sample’s brain had on its ability to perceive odors. We also used transmission electron microscopy (TEM) to determine the cellular localization of nanoparticles.

### Experimental Procedure:

Due to its relatively simple nervous system and established role in olfaction studies [3], locust (*Schistocerca americana*) was chosen as the experimental organism. It was prepared for a nanoparticle injection by exposing the brain and carefully removing excess tissue. A controlled air/hexanol mixture was passed over one of the locust’s antennae and its nervous response was measured by a gold-plated recording electrode placed in its antenna lobe as shown in Figure 1.

A gold nanoparticle (5 nm) suspension previously produced by the reduction of  $\text{HAuCl}_4$  with  $\text{NaBH}_4$  (Figure 2) was injected into the antenna lobe by a glass injection pipette. This was controlled by a pneumatic picopump to ensure consistent delivery of the odorant and injection of the nanoparticle suspension. A total of five trials were run before the nanoparticle injection, two were taken during the injection and five more were taken after the injection.

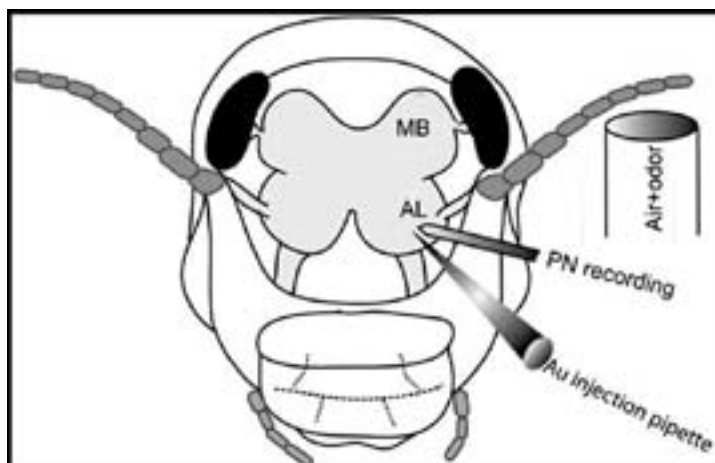


Figure 1: Experimental setup.

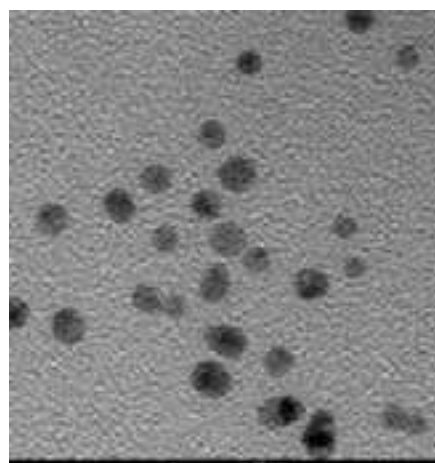


Figure 2: TEM of gold nanoparticles.

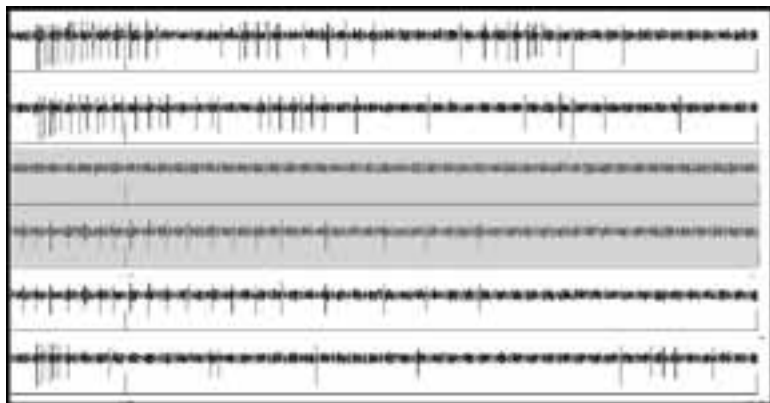


Figure 3, above: Electrophysiology results.

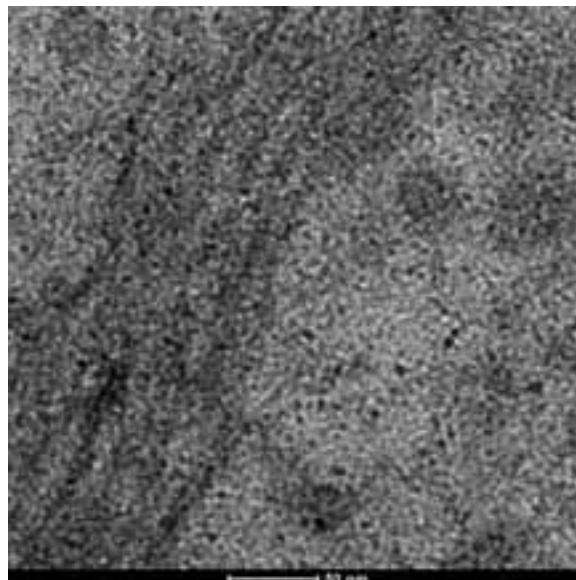


Figure 4, right: TEM of locust brain.

At the conclusion of the electrophysiology experiment, the brain was recovered and immediately fixed using glutaraldehyde to preserve the sample. A secondary fixative of osmium tetroxide was used to prevent lipid degradation as well as to add contrast to TEM images. After drying with ethanol and propylene oxide, the sample was embedded using Eponate 12. Thin (75 nm) sections were then cut using a diamond knife to prepare the sample for TEM.

### Results and Conclusions:

Simplified results for the electrophysiology experiment are presented in Figure 3. Two pre-exposure trials, two injection trials (highlighted) and two post-exposure trials are shown after the odorant was discontinued. Each is a function of voltage versus time, with spikes corresponding to neurons firing. Interestingly, some gold nanoparticles themselves appeared to cause a nervous response as spikes can be seen after their injection. There was also a clear drop in neuron activity after these injections, as the frequency of neuron firing was diminished. Pending a control experiment with a saline injection, this supports our claim that nanoparticles can affect neuron activity.

Figure 4 shows highly contrasted, spherical particles of diameter  $\sim 5$  nm, which is consistent with the characteristics of our gold nanoparticles. TEM appears to have verified the presence of gold nanoparticles inside brain cells and suggests that they are capable of crossing the synapse, shown running from the bottom left to the middle top of the image. Since this is where electrical signals are converted to chemical signals, this may be where interference is produced.

### Future Work:

Our results suggest that nanoparticles are able to interfere with normal neuron firing when injected into the brain. However,

this is an unlikely exposure route. To better model realistic exposure methods, this experiment should be repeated with nanoparticles delivered via an aerosol route. This could be accomplished by using an electrospray system to deliver nanoparticles to the locust's antennae.

Since surface charge is primarily responsible for nanoparticle interaction with proteins, repeating these trials with varying charged nanoparticles would allow for better characterization of relevant factors for nanoparticle interference with neuron activity. Other relevant properties worth studying include size and crystal phase.

### Acknowledgments:

I would like to thank Dr. Pratim Biswas, Tandeep Chadha, Dr. Debajit Saha, Howard Wynder, and members of the Nano Research Facility for their guidance and support during this project. Additionally, I would like to thank the National Nanotechnology Infrastructure Network Research Experience for Undergraduates Program and the National Science Foundation for providing funding.

### References:

- [1] Oberdörster, G., Oberdörster, E. and Oberdörster, J.; "Nanotoxicology: An Emerging Discipline Evolving from Studies of Ultrafine Particles"; *Environmental Health Perspectives*, Vol. 113 (7); pp. 823-839 (2005).
- [2] Brown, A.; "Axonal Transport of Membranous and Nonmembranous Cargoes: A Unified Perspective"; *The Journal of Cell Biology*, Vol. 160 (6); pp. 817-821 (2003).
- [3] Hildebrand, J. and Shepherd, G.; "Mechanisms of Olfactory Discrimination: Converging Evidence for Common Principles Across Phyla"; *The Annual Review of Neuroscience*; Vol. 20; pp. 595-631 (1997).

## Progress Towards Electrical Interface Chips for BioMEMS

**Stephanie Swartz**

**Physics, University of Rochester**

*NNIN REU Site: Colorado Nanofabrication Laboratory, University of Colorado, Boulder, CO*

*NNIN REU Principal Investigator: Professor Robert McLeod, Electrical Computer and Energy Engineering, University of Colorado at Boulder*

*NNIN REU Mentors: Martha Bodine and Callie Fiedler, Electrical Computer and Energy Eng., University of Colorado at Boulder (Fiedler; 2010 NNIN REU at the University of Colorado, Boulder)*

*Contact: sswartz3@u.rochester.edu, robert.mcleod@colorado.edu, martha.bodine@colorado.edu, callie.fiedler@gmail.com*

### Abstract and Introduction:

The conjunction of biology and nanolithography has allowed for the development of many unusual devices—unique hybrids of biological cells and man-made structures. Here, we describe the development of one such device, designed to characterize the contraction force of a skeletal muscle cell. Shimizu, et al. [1] measured the force of a single C2C12 myotube by anchoring it to a silicon cantilever and base, electrically stimulating the cell, observing the cantilever movement using an optical microscope, and calculating the resulting force of contraction. Building upon their work, we fabricated micron-scale cantilevers made of the non-cytotoxic photoresist SU-8 3050. In addition to developing the fabrication process for the SU-8 cantilevers, we characterized them using optical microscopy and profilometry. Currently, we are investigating optical frequency domain reflectometry (OFDR) as a method for more accurately measuring the movement of the cantilevers. Accurate characterization of cantilever movement as the cell contracts will allow for a more precise measurement of the force exerted by an individual skeletal muscle cell.

### Fabrication:

We used photolithography to fabricate SU-8 cantilevers onto glass slides. Following several cleaning steps, we spun on OmniCoat™ first for five seconds at a speed of 500 rpm and an acceleration of 100 rpm/s, and then 30 seconds at 3000 rpm and 255 rpm/s. We baked the OmniCoat™ for one minute at 200°C. Next, we spun on SU-8 3050 using the same spin parameters at the OmniCoat. Subsequently, we soft-baked the SU-8 on a hotplate at 95°C for 25 minutes. Using the MJB-4 mask aligner, we exposed the SU-8 through a chrome-coated glass mask for 31-34 seconds. We did a post-exposure bake (PEB) on the hotplate at 95°C for 3-5 minutes. Then, we developed the SU-8 while agitating the developer by hand for ~ 6 minutes. We cured the SU-8 on a hotplate at 200°C for five minutes and consequently developed the OmniCoat for ~ 30 seconds. We descumed for 600 seconds before etching the slides in agitated buffered oxide etchant (BOE). This step released the cantilevers. After each step requiring rinsing, we rinsed the glass slides in a water bath and dried them on a hotplate at 100°C.

### Characterization:

**Profilometry.** Although the data is not shown here, we determined the height of the cantilevers to be 40-50  $\mu\text{m}$  prior to etching using profilometry. Additionally, we measured the etch rate of the BOE to be ~ 0.46  $\mu\text{m}/\text{min}$ .

**Optical Microscopy.** We used optical microscopy to examine the quality of the cantilevers. After development, the cantilevers, shown in the bright field image in Figure 1, Panel A, were straight and totally developed. The dark field image in Panel B reveals that the cantilevers were adhered to the glass slide and the sidewalls were vertical. Conversely, the dark field image in Panel C reveals that the cantilever was no longer adhered to the slide after development. After etching, there was an unknown residue on the cantilever as shown in Panel D, which we were able to remove using a combination of solvents.

### Optical Frequency Domain Reflectometry (OFDR).

OFDR works on the following principle: a tunable laser couples light into SMF-28 optical fibers set up as a Mach-Zehnder interferometer, where at one end the fiber points at structures on the sample. Due to the Fresnel reflections off these structures, a frequency is detected and then Fourier transformed so that it corresponds to the round trip times of the light from the fiber tip to structures on the sample.

In order to detect a 15  $\mu\text{m}$  wide cantilever, we etched channels into the glass using a commercial glass-etching cream so that the center of the fiber tip points at the cantilever, as shown in Figure 2. Figure 3 shows what we believe to be peaks from the fiber tip and the cantilever. The black curve is the raw data. Using Igor Pro for data analysis, we mirrored the data to the left of the fiber peak and plotted it to the right of the fiber peak. We then subtracted the light-grey “mirrored data” from the black raw data to obtain the dark-grey curve for the cantilever peak only. Data analysis revealed that the cantilever was located ~ 0.885 mm away from the fiber, which is plausible given that the fiber was attached to the glass slide by hand using a stereoscope.

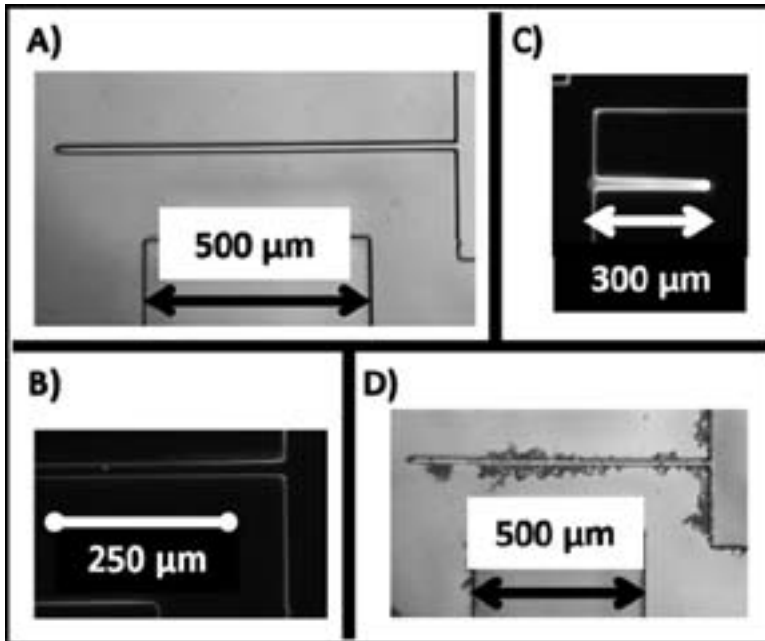


Figure 1: A) Bright field image of a good cantilever after development. B) Dark field image of a good cantilever after development. C) Dark field image of a bad cantilever after development. D) Bright field image of a good cantilever after etching with BOE.

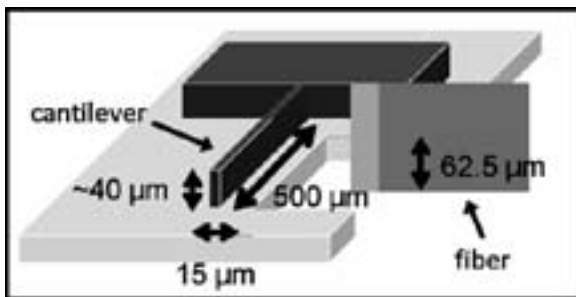


Figure 2: An optical fiber to be used with the OFDR system is glued to the glass slide so that it points at the cantilever.

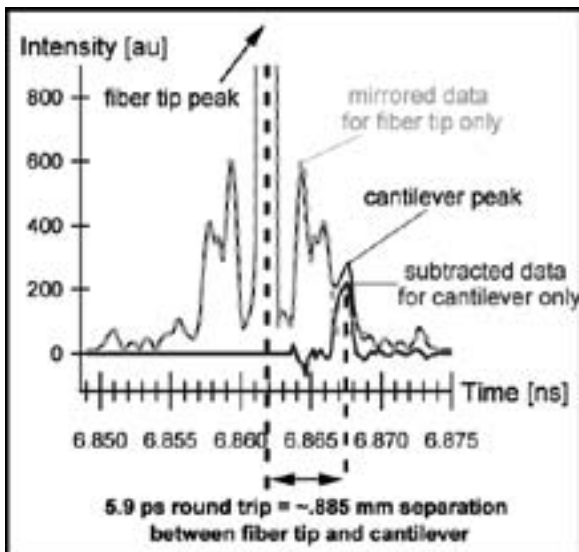


Figure 3: OFDR determined that the stationary 15 μm wide cantilever is located ~ 0.885 mm away from the fiber tip.

**Conclusions:**

As a result of optical microscopy, we were able to determine which cantilever dimensions allowed for better adhesion to the glass before etching, and the proper exposure and development times. In general, wider cantilevers (~ 15 μm) with lengths of 500 to 900 μm adhered better to the glass. OFDR has been successful so far at detecting a stationary cantilever, although a more precise setup will be required in order to test a moving cantilever. Particular attention should be paid to the noise, which affects OFDR measurements.

**Acknowledgements:**

The author would like to thank her mentors, Martha Bodine and Callie Fiedler, and her Principal Investigator, Robert McLeod. Additionally, the author would like to thank Christopher Roath, Ben Kowalski, Eric Moore, Bart van Zeghbroeck, Jan van Zeghbroeck, Tomoko Borsa, Zefram Marks, Tzu-Min Ou, Ian Haygood, Bounkeanha Chhun, Carol Higgins, Julie Robinson, Melanie-Claire Mallison, the National Science Foundation and the NNIN REU Program for making this research possible.

**References:**

[1] K. Shimizu et al., Biomedical Microdevices, Volume 12, Number 2 (2010), 247-252.

## Nanocharacterization of Polymer-Modified Microring Resonators for Performance in Complex Media

**Brianna Thielen**

**Engineering, Harvey Mudd College**

*NNIN REU Site: NanoTech User Facility, University of Washington, Seattle, WA*

*NNIN REU Principal Investigator: Prof. Daniel Ratner, Department of Bioengineering, University of Washington*

*NNIN REU Mentor: James T. Kirk, Department of Bioengineering, University of Washington*

*Contact: bthielen@hmc.edu, dratner@uw.edu, jtk8@u.washington.edu*

### Introduction:

Silicon photonic microring resonators are label-free biosensors that are able to detect very small changes in bound mass on the surface of a nanophotonic waveguide in real-time, while requiring only a few microliters of sample. However, to realize the full potential of this biosensing technology, it's necessary to address the challenge of surface fouling and biocompatibility when performing diagnostic assays in complex biological matrices (e.g. blood, plasma, serum). Due to high interfacial energy at the surface, proteins irreversibly adsorb to the microrings upon contact. This non-specific fouling of the sensor surface leads to false positives and reduces the device's ability to detect specific binding interactions.

One strategy used to reduce non-specific adsorption is to grow a thin zwitterionic polymer layer from the silicon substrate of the sensor, producing a hydrophilic, non-fouling coating. In this study, carboxybetaine acrylamide (CBAA) was polymerized from microring resonators using atom transfer radical polymerization (ATRP). Sensors were then exposed to undiluted human blood plasma to determine the extent of

fouling. The polymer film was characterized using atomic force microscopy (AFM) and scanning electron microscopy (SEM).

AFM, SEM, and plasma fouling data were used to refine the ATRP process in order to establish a polymerization procedure that enables a microring resonator biosensor to be used in real-world diagnostic applications.

### Methods:

**Polymerization.** First, trichlorosilane initiators were covalently bound to a surface by soaking in a toluene solution or by vapor deposition. Next, a CBAA polymer layer was grown via ATRP using a monomer/catalyst solution. After the reaction completed, the polymerized surface was tested for non-fouling properties. The initiator deposition procedure (liquid and vapor) and the reaction time (17- and 24-hour) were varied in order to determine optimal ATRP conditions.

**Non-Fouling Test on Silicon Microring Resonators.** Each silicon microring resonator biosensor chip contained 272 microring resonators (see Figure 1). An increase in resonance wavelength of a microring indicated an increase in mass density of the regions surrounding the ring.

Polymer-coated chips were tested for non-fouling properties by flowing undiluted human blood plasma over the chips for 15 minutes at a rate of 20  $\mu\text{L}/\text{minute}$ . Prior to and after being exposed to plasma, the chips were washed with phosphate buffered saline (PBS) at the same flow rate for 20 minutes.

### Results and Conclusions:

The first attribute of ATRP optimized in this study was the method of initiator deposition (liquid or vapor). For chips using liquid initiator deposition, high variance in signal attenuation indicated that the polymer growth was non-uniform (see Figures 2 and 3). The "liquid deposited" chip showed a fouling level of  $92 \pm 123 \text{ ng}/\text{cm}^2$ . Although this chip achieved a lower fouling level than many others, the high standard deviation indicated non-uniform polymer growth.

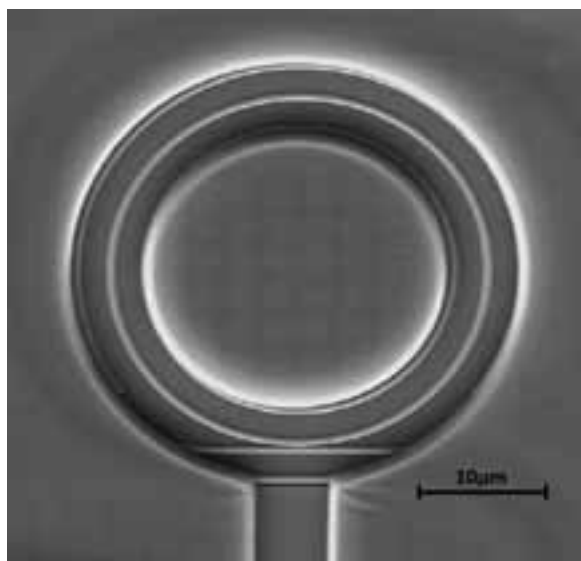


*Figure 1: An SEM image of a microring resonator. Light is directed down a waveguide that runs adjacent to each microring (bottom). Resonance wavelengths are coupled into the microring, causing a decrease in output power.*

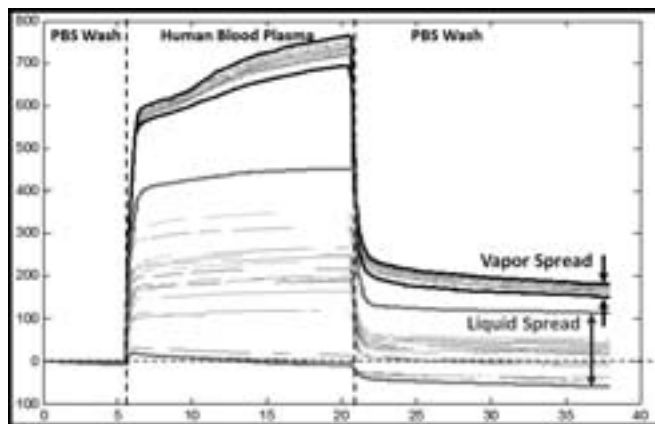


Figure 2: Microring resonator sensorgrams for vapor deposited (black) and liquid deposited (gray) chips. The liquid deposited chip is less uniform (as is apparent by examining the spread in each chip). The standard deviations are  $13 \text{ ng/cm}^2$  and  $123 \text{ ng/cm}^2$  respectively.

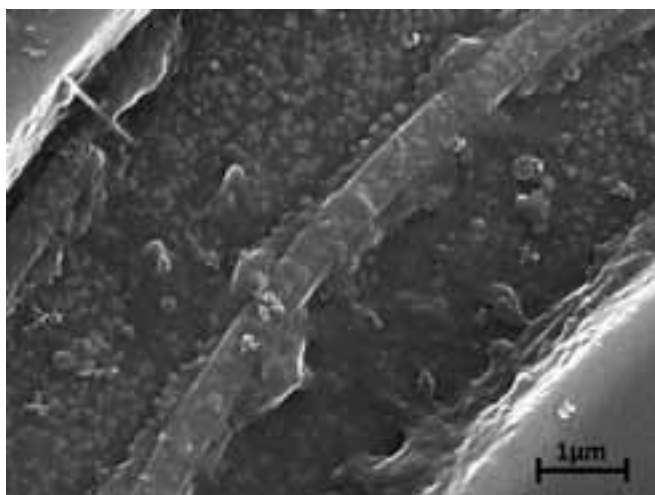


Figure 3: An SEM image of a microring resonator polymerized using liquid initiator deposition. Non-uniform polymer growth was confirmed using this (and other) SEM images.

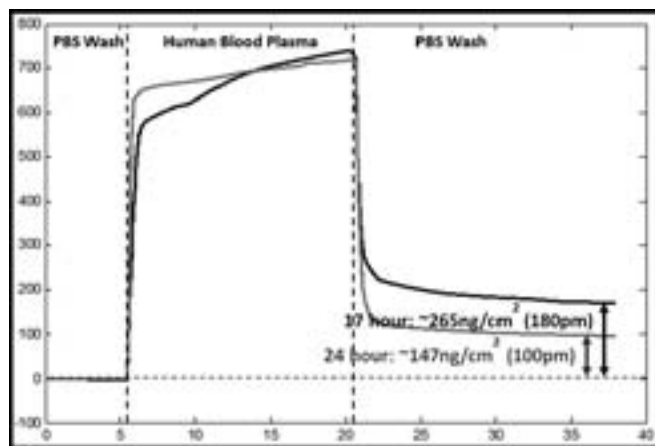


Figure 4: Microring resonator sensorgrams for 17-hour (black) and 24-hour (gray) ATRP reacted chips. These data showed fouling levels of  $265$  and  $147 \text{ ng/cm}^2$  respectively.

The “vapor deposited” chip showed a fouling level of  $265 \pm 13 \text{ ng/cm}^2$ . Although this is much higher than the ultra-low fouling goal of  $5 \text{ ng/cm}^2$  [2], the small standard deviation showed that vapor deposition created a much more uniform polymer layer and a more robust biosensor.

The ATRP reaction time was also optimized in this study. Average fouling levels were compared for 17- and 24-hour vapor deposited chips. The 17- and 24-hour chips showed fouling levels of approximately  $265 \text{ ng/cm}^2$  and  $147 \text{ ng/cm}^2$  respectively (see Figure 4). Lower fouling levels on the 24-hour chips indicated that longer reaction time produced a denser polymer film, yielding a lower fouling surface.

Although the “ultra-low fouling” levels described previously [2] have not yet been reached, the results of this study support using a 24-hour ATRP reaction using vapor deposition of initiators. The 24-hour fouling levels were consistently lower than 17-hour levels. Liquid deposition of initiators showed greatly varied levels of polymerization, indicating varied thicknesses on sensor arrays. SEM and AFM images confirmed that polymer coatings had varied thicknesses among microring arrays and that each ring layer was non-uniform.

These data suggest that initiators should be bound using vapor deposition and that a 24-hour ATRP reaction should be used in future experiments.

### Future Work:

Literature suggests that higher methanol percentage creates a denser film and a lower-fouling surface [1]. More manipulation of the solvent ratio could be experimented with to further decrease protein fouling levels. In addition, functionalization procedures (binding a capture element to the surface) will be tested for the non-fouling surface to enable specific analyte detection.

### Acknowledgments:

This work was sponsored by the National Science Foundation and the NNIN REU Program. The Nanotechnology User Facility at the University of Washington (UW) and its staff provided training for and access to the AFM and SEM. The Jiang lab in the Chemical Engineering Department at the UW provided training and materials necessary for the ATRP process. Finally, the Ratner lab in the Bioengineering Department at the UW provided equipment, materials, training, and all other resources necessary for this study.

### References:

- [1] C. Huang, 2012. *Macromolecular Journals* 33.11, 1003-1007.
- [2] H. Vaisocherová, 2009. *Biosensors and Bioelect.* 24.7, 1924-1930.
- [3] M. Iqbal, 2010. *IEEE J. Selected Top. in Quantum Elect.* 16.3, 654-661.
- [4] W. Norde, 2008. *Colloids and Surfaces B* 61.1, 1-9.

## High Fidelity Method for Microfabricating *in vitro* Neural Networks

**Geoffrey Vrla**

**Chemistry, Middlebury College**

*NNIN REU Site: Nanofabrication Center, University of Minnesota-Twin Cities, Minneapolis, MN*

*NNIN REU Principal Investigator: Dr. Patrick Alford, Biomedical Engineering, University of Minnesota-Twin Cities*

*NNIN REU Mentor: Eric Hald, Biomedical Engineering, University of Minnesota-Twin Cities*

*Contact: gvrla@middlebury.edu, pwalford@umn.edu, haldx002@umn.edu*

### Abstract:

Functional *in vitro* models of neural networks are essential for uncovering the underlying cellular mechanisms by which mechanical stress induces traumatic brain injury. However, current models do not capture the connectivity and organization of the brain's axonal tracts, limiting our ability to study how cellular dysfunction may be transmitted between distant regions of the brain. These models are inadequate due to insufficient fabrication techniques for consistently and accurately placing neurons in a network. Here, we propose a novel method for neural network fabrication that incorporates microfluidic cell placement onto micropatterned substrates. We fabricated a microfluidic device featuring cell traps that capture cells in an organized array, placing them in contact with a fibronectin-coated surface that provides guidance cues for network self-organization. As proof of concept, we used 3T3 fibroblasts to assess the efficiency of this technique. Compared to standard microcontact printing, microfluidic delivery of cells resulted in more consistent, uniform adherence of cells to patterned substrates. Development of this technique may allow fabrication of more authentic neural networks and provide a platform by which we may further investigate the role of diffuse axonal injury in the pathophysiological response to traumatic brain injury.

### Introduction:

Blast-induced traumatic brain injury (bTBI) is the most frequent injury suffered by American soldiers in Iraq and Afghanistan; however, the mechanism by which blast waves transduce brain injury remains poorly understood [1]. Although *in vivo* studies are the current focus of research, *in vitro* TBI models display the capability of providing unique insight into the cellular mechanisms that underlie bTBI [2].

These studies often involve synthetic biological tissues fabricated via microcontact printing, a technique used to pattern a substrate with extracellular-matrix guidance cues that promote cell and tissue self-organization. However, standard micropatterning techniques cannot consistently fabricate high fidelity neural networks due to lack of control over cell placement on extracellular-matrix features.

Here, we present a method for precise alignment of cells on a micropatterned substrate using a microfluidic device. Our

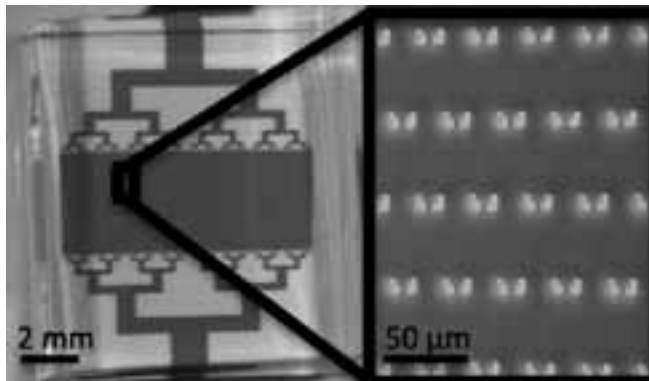


Figure 1: Microfluidic device featuring cell traps to immobilize cells.

device isolates and immobilizes cells in a uniform array, allowing for the adhesion of single cells to a micropatterned substrate with precise control over their relative positions. We utilized this technique to seed 3T3 fibroblasts on a network pattern of fibronectin, resulting in consistent cell connections resembling that of neural circuits.

### Experimental Procedure:

A polydimethylsiloxane (PDMS) microfluidic device (Figure 1) was designed in reference to a device used in [3]. Masters were fabricated from SU-8 3025 photoresist spun on silicon wafers using standard photolithography techniques. Masters were coated with Sylgard 184 PDMS (10:1 base:curing agent), degassed, and baked at 90°C for four hours.

A neural network pattern shown to most effectively promote polarized neural connections was adapted from [4]. PDMS stamps for this pattern were fabricated similarly to the microfluidic device. Stamps were coated with fibronectin (50 mg/mL in H<sub>2</sub>O) and incubated for one hour. Fibronectin was transferred to PDMS-coated glass coverslips following the procedure in [5].

A microfluidic device was aligned and temporarily sealed to a micropatterned coverslip using visual cues added to stamping patterns. Channels were rinsed with phosphate-buffered saline (PBS). A 3T3 fibroblast suspension (100 μL; 120,000 cells/mL) was drawn through the device using a house vacuum.

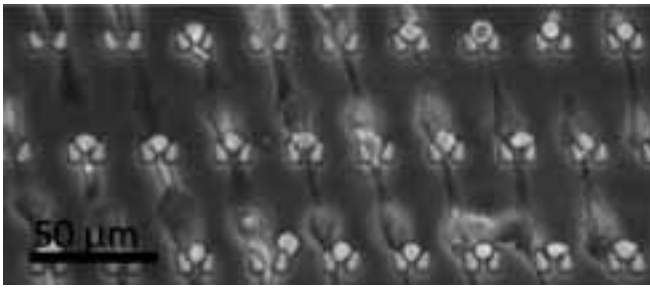


Figure 2: Cells seeded on a network pattern after two hours of incubation.

Immobilized cells were rinsed with culture media and incubated for two hours at 37°C and 5% CO<sub>2</sub> to allow network formation (Figure 2), followed by device removal.

Cells were fixed and permeabilized with 4% paraformaldehyde and 0.05% Triton-100 respectively (in PBS at 37°C). Cells were stained with AlexaFluor 488 Phalloidin and 4',6-diamidino-2-phenylindole (DAPI) in PBS, and imaged using an Olympus IX81ZDC inverted confocal microscope.

### Results and Discussion:

To assess the accuracy of cell transfer, fibroblasts were seeded on uniform fibronectin using microfluidic delivery. Adhered cells retained their orientation while immobilized in the capture cups, resulting in a highly organized array of cells compared to that obtained using standard techniques. The radial distribution function of fluorescently labeled nuclei displays areas of high cell density corresponding to known distances between capture cups (Figure 3), confirming the ability of this technique to influence the relative position of cells adhered to a substrate.

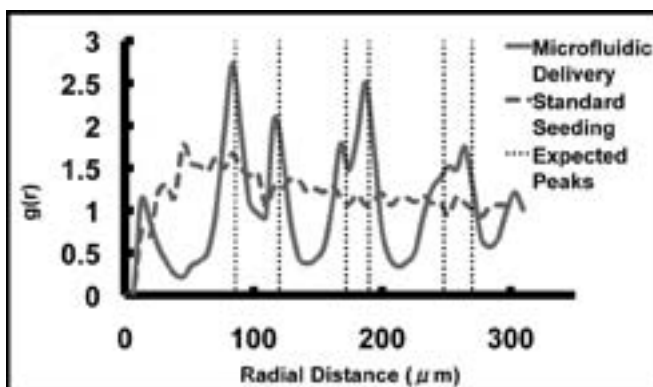


Figure 3: A radial distribution function of fluorescently labeled nuclei.

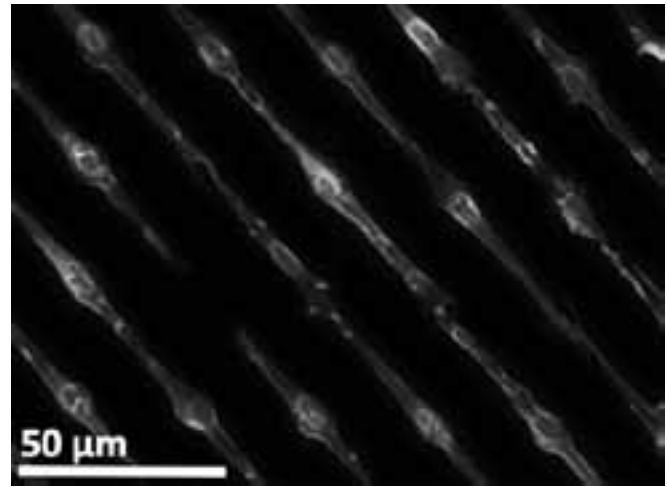


Figure 4: Fibroblasts seeded on a network pattern of fibronectin.

To investigate a potential application of this technique, fibroblasts were seeded on a fibronectin pattern resembling a neural network. Cells were accurately delivered to circular features, and extended radially to form physical contacts with neighboring cells (Figure 4). The linear nature of fibroblast nuclei affirms the success of this technique. When we extend this technique to primary neuronal cell lines, accurate soma placement may promote polarized neural connections and therefore a functional network.

Improved alignment of cells on a substrate as shown here can benefit tissue fabrication beyond neural systems. Countless distributions of cells, and therefore tissue models, can be obtained from adjusting the array of cell traps. For example, endothelial and smooth muscle cells captured in an array of concentric circles could be transferred to ring of extracellular-matrix to form structures resembling arterial cross sections. Models such as these could be employed in studies of vasospasm and other diseases characterized by blood-vessel hypercontractility such as bTBI.

### Acknowledgments:

I would like to thank the National Science Foundation and National Nanotechnology Infrastructure Network Research Experience for Undergraduates (NNIN REU) Program for funding this research, as well as Eric Hald, Patrick Alford, and the University of Minnesota.

## Interaction of Engineered Nanoparticles with Artificial Cell Membranes

**Rachel Benton**

**Chemical Engineering, North Carolina State University**

*NNIN REU Site: NanoTech User Facility, University of Washington, Seattle, WA*

*NNIN REU Principal Investigator: Jonathan D. Posner, Mechanical and Chemical Engineering, University of Washington*

*NNIN REU Mentor: Charles Corredor, Chemical Engineering, University of Washington*

*Contact: rabento2@ncsu.edu, jposner@uw.edu, corredor@uw.edu*

### Abstract:

Understanding the potential toxicity of engineered nanoparticles (ENPs) is vital due to their presence in over 1300 commercial products (e.g. toothpaste, sunscreen, and anti-bacterial coating on blankets). To further evaluate the potential consequences of ENPs, research must be performed to examine the interaction and mechanistic behavior between these particles and biological systems. This study seeks to understand these interactions by characterizing the effects of ENPs on artificial cell membranes. Understanding the interaction of engineered nanoparticles with lipid bilayers is an important step toward predicting subsequent biological effects and facilitates the design of safe nanoproducts. We believe that under some conditions ENPs can passively translocate across, and cause nanoscale defects in, lipid membranes. In this work, we quantify the disruption of liposomes induced by ENPs using a dye leakage assay. We measure dye leakage from lipid vesicles loaded with carboxy-fluorescein dye that are exposed to a diverse selection of ENPs. The amount of dye released correlated directly to the level of interaction between nanoparticles and the lipid vesicles.

### Introduction:

Engineered nanoparticles (ENPs) are being utilized in various commercial ventures and research studies. Because of the rapid growth in the field of nanotechnology, there is a high potential that at some point in these particles' lifespan, they will come in to contact with the environment and humans [1, 2]. As of yet, the effects of these particles on health and the environment are not sufficiently well known. While ENPs hold a great deal of promise, before reaping the benefits of nanotechnology, more extensive research must be done in the field of nanotoxicity to understand their potential risks.

Membrane permeability is a vital component of toxicity studies as the membrane controls what enters and exits a cell. Lipid bilayers serve as viable artificial cell membranes in that natural cell membranes are comprised of over 80% lipids [3]. These same lipids, due to their hydrophilic head and hydrophobic tail, will self-assemble into spherical liposomes.

This study seeks to understand the interaction of nanoparticles with artificial cell membranes by characterizing the effects of ENPs on liposome permeability using a dye leakage assay of liposomes exposed to ENPs.

### Preparation:

Phospholipids were suspended in carboxyfluorescein (fluorescent dye), forming lipid bilayers, then passed through a 100 nm polycarbonate membrane in the process of extrusion. This caused a homogenous population of liposomes to form. As the liposomes formed, they encapsulated carboxyfluorescein inside them. The resulting solution was washed using ultracentrifugation by forcing it through a 3kDa membrane to remove the excess dye from outside the liposomes. This left just the liposomes (diameter approximately 100 nm) loaded with carboxyfluorescein.

This liposome, with the entrapped fluorescent dye, was then exposed to target ENPs. These experiments focused on two types of silver (Ag) ENPs, each with a 20 nm core diameter; one coated with polyvinylpyrrolidone (PVP), and the other with sodium citrate (NaCT). If the nanoparticles caused a disruption in the lipid bilayer, then the dye encapsulated inside the liposome would leak out. This amount of leakage was measured using fluorescent spectroscopy.

The carboxyfluorescein was excited at 480 nm and emitted at 520 nm. Because of this, the intensity measurements from the spectrometer were taken at 517.5 nm. The percent of leaked dye was found using the following formula:

$$\text{Percent Leakage} = \frac{I - I_{min}}{I_{max} - I_{min}} \times 100$$

where  $I$  is the intensity after liposomes are exposed to ENPs,  $I_{min}$  is the intensity of the liposomes without any ENP exposure, and  $I_{max}$  is the intensity after the liposomes are treated with Triton-X, which is known to cause total leakage from the nanoparticles.

The percent leakage was measured for three different conditions: liposomes without nanoparticle exposure, liposomes exposed to Ag NPs coated with PVP, and liposomes exposed to Ag NPs coated with NaCT.

### Results:

Figure 1 and 2 show the percent leakage induced by Ag NPs as a function of time for 112 and 5600 PPB, respectively. The average percent leakage of fluorescent dye from the liposomes exposed to Ag NPs for both coatings was consistently higher than the liposomes without exposure for all tests. This showed a clear interaction between the ENPs and liposomes. In Figure 2, at approximately 1500 minutes, a greater percent leakage for liposomes exposed to sodium citrate coated Ag NPs was evident. The leakage also increased with increasing concentration. These results suggest that the surface functionality is a critical parameter in governing the disruption of bilayers induced by ENPs.

### Summary:

These results show that ENPs disrupt bilayers and induce leakage of their internal contents. However, it cannot be inferred from this experiment whether or not these ENPs are toxic. Showing an interaction between ENPs and liposomes is an evidence that these ENPs are causing a disruption in the lipid bilayer and thus potentially in cell membranes, but the biomechanics of this interaction remain unknown. Understanding the interaction of ENPs with lipid bilayers is an important step toward predicting subsequent biological effects and facilitates the design of safe nanoproducts.

### Acknowledgements:

I thank my Principal Investigator, Dr. Posner, and my mentor, Charles Corredor, as well as the rest of the Posner Research Group. I also acknowledge the National Science Foundation and the National Nanotechnology Infrastructure Network Research Experience for Undergraduates Program for the funding of my research. Thank you to University of Washington's Nanotech User Facility and to my program coordinator, Mack Carter. Finally, I would like to acknowledge Dr. Smith and Dr. Kavanagh from the Nanotoxicology Center at University of Washington with whom we collaborated with on this project.

### References:

- [1] Dean, L. Measurement helps solve nanoparticle toxicity challenges. *Chemistry International*, 34(4) (2012, July).
- [2] Nel, A. E., Madler, L., and Velegol, D. Understanding the biophysico-chemical interactions at the nano-bio interface. *Nature*. (2009).
- [3] Roiter, Y., Ornatska, M., and Aravind, R. R. Interaction of nanoparticles with lipid membrane. *Nano Letters*, 8(3), 941-944. (2008).

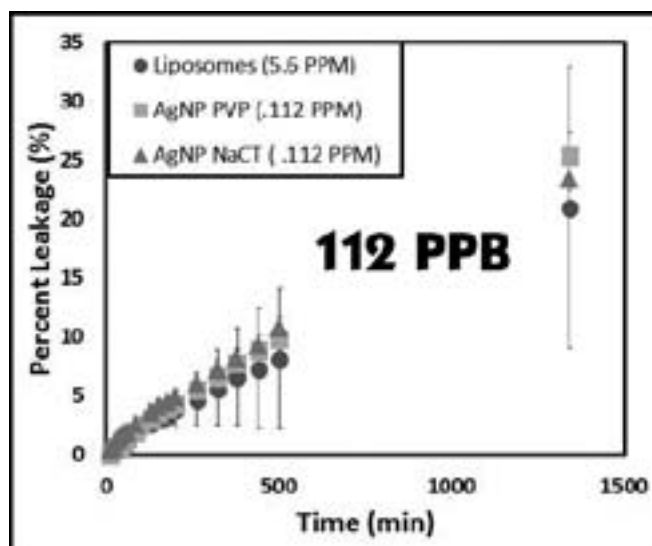


Figure 1: Kinetic measurements of liposomes after exposure to Ag NPs.

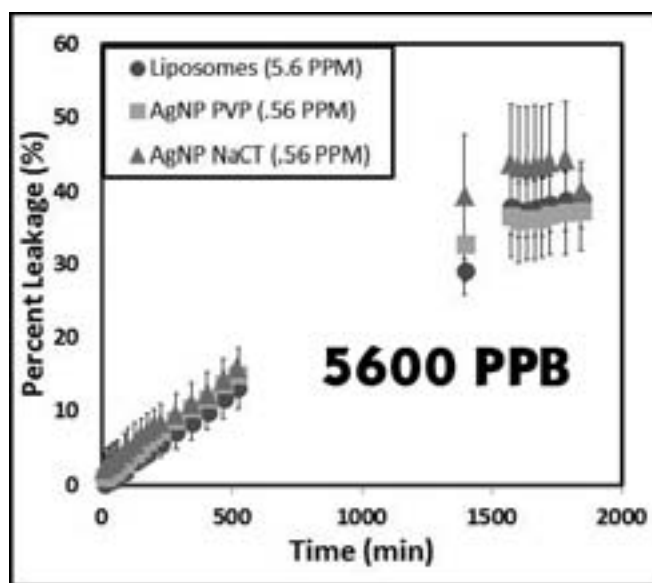


Figure 2: Kinetic measurements of liposomes after exposure to Ag NPs.

# Fabricating Parylene-C Shadow Masks for Applications in Short-Channel Top-Contact Carbon Nanotube Flexible Transistors

**Kelsey Hirotsu**

**Chemical and Biomolecular Engineering, Johns Hopkins University**

*NNIN REU Site: Stanford Nanofabrication Facility, Stanford University, Stanford, CA*

*NNIN REU Principal Investigator: Professor Zhenan Bao, Chemical Engineering, Stanford University*

*NNIN REU Mentor: Evan Wang, Materials Science and Engineering, Stanford University*

*Contact: khirotsu@jhu.edu, zbao@stanford.edu, whl0903@stanford.edu*

## Abstract:

Flexible transistors with semiconducting carbon nanotubes offer better mobility and stability than current organic material transistors for applications in flexible display and sensor devices. With carbon nanotubes as the semiconducting material, the transistors offer a higher performance due to the extraordinary electrical properties of single-walled carbon nanotubes (SWNTs). However, conventional metal shadow masks can only create flexible device transistors with a channel length of 50  $\mu\text{m}$  or greater. Parylene-C shadow masks can be used instead of metal masks because of their flexibility, adaptability for patterning, and their ability to fabricate transistors with much smaller channel lengths. Previously it has been shown that Parylene-C masks allow for a fine resolution with a smallest feature size of 4  $\mu\text{m}$ . We fabricated masks with features as small as 2  $\mu\text{m}$  wide, and additionally used our masks to create short-channel transistors. We successfully constructed short-channel top-contact SWNT network inflexible and flexible transistors on silicon (Si) and polyamide substrates with a mobility of 0.1 to 2  $\text{cm}^2/\text{V}\cdot\text{s}$  and on/off ratios on the magnitude of  $10^2$  to  $10^3$ .

## Introduction:

Parylene-C is a polymer that is flexible, transparent, biocompatible, and relatively inexpensive. Its characteristics allow for Parylene-C shadow masks to have the potential for various micropatterning applications [1]. Unlike conventional hard masks, parylene masks adhere to the surface of the substrate for better contact between the substrate and the stencil. While conventional hard masks can create features as small as 50  $\mu\text{m}$  wide, parylene masks have been used to make features as small as 4  $\mu\text{m}$  wide. Previously, flexible

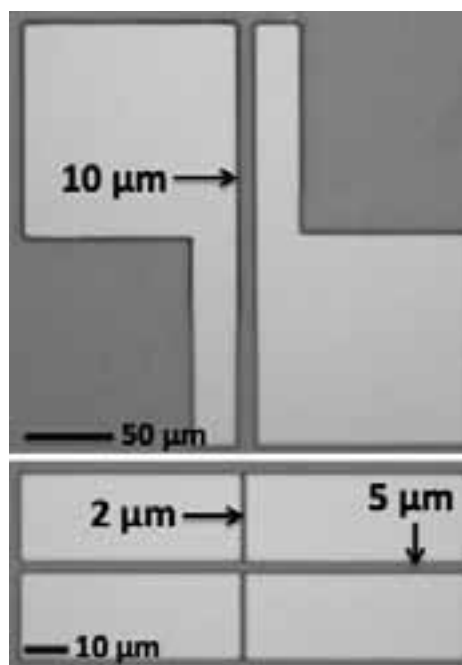


*Figure 1: 2, 5, and 10  $\mu\text{m}$  features etched into parylene on Si substrate.*

transistors have been fabricated with semiconducting carbon nanotube networks [2]. Short-channel inflexible transistors have also been fabricated, using Parylene-C shadow masks [3]. To optimize the performance of our flexible transistors, we combined features of both previously fabricated devices. We aimed to make Parylene-C shadow masks for use in the fabrication of short-channel flexible transistors with solution-sorted semiconducting carbon nanotube networks.

## Experimental Procedure:

To fabricate the parylene masks, we adopted a previously developed procedure to fit the capabilities of the Stanford Nanofabrication Facility and Bao lab equipment [1]. We exposed 4-inch silicon wafers coated with 15  $\mu\text{m}$  of parylene to oxygen plasma at 150 W RF power and at 150 mTorr to roughen the parylene to enhance aluminum adhesion. Then we evaporated 200 nm of aluminum onto the parylene and created a hard mask through conventional optical lithography. We patterned the aluminum through a wet etch (72% phosphoric acid, 3% nitric acid, 3% acetic acid, 22% water). Then we etched the parylene with oxygen plasma for one hour at the same parameters previously used to roughen the parylene, and finally, we etched away the aluminum hard mask with the same wet etchant (Figure 1).

To fabricate transistors with the parylene mask, we prepared substrate samples by soaking them in purified semiconducting SWNT solutions. To purify semiconducting SWNTs from metallic SWNTs, we used the Bao group's previously developed sorting process [4]. We peeled the mask off of the silicon wafer and placed it on the new substrate with carbon nanotubes, and then evaporated 40 nm of gold over the mask to fabricate the transistors (Figure 2 and 3).

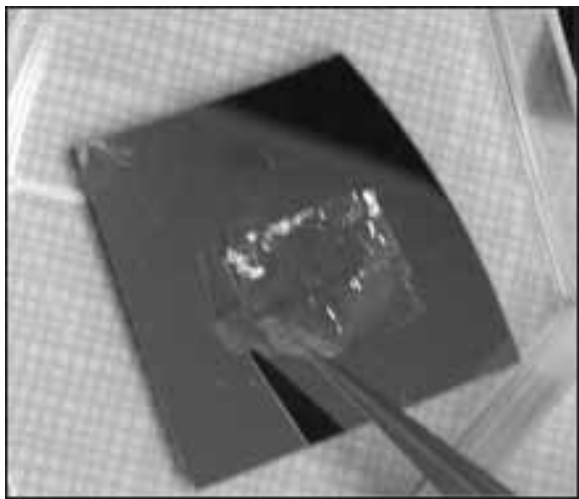


Figure 2: Parylene mask peeled off of Si substrate.

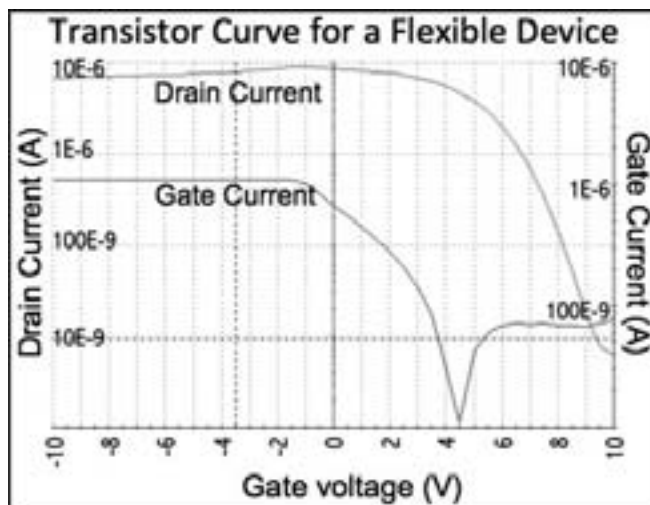


Figure 4: Keithley-generated flexible transistor curve.

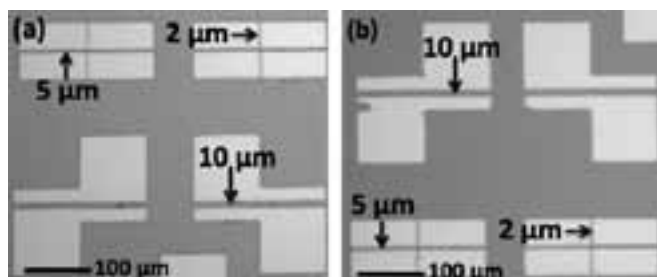


Figure 3: (a) Parylene mask placed onto SWNT-soaked substrate; (b) Gold on SWNT-soaked substrate after mask removal.

After the gold evaporation, we peeled the mask off and tested the transistors for their performance.

### Results and Discussion:

We consistently fabricated Parylene-C shadow masks with etched features ranging from  $2\ \mu\text{m}$  to  $50\ \mu\text{m}$  wide. The process was optimized and scaled-up to full wafer scale production of shadow masks. We fabricated inflexible and flexible transistors with the parylene masks and then tested the performance by measuring the current flow across transistors at various applied gate voltages. Both types of devices had a mobility of  $0.1$  to  $2\ \text{cm}^2/\text{V}\cdot\text{s}$  and on/off ratios on the magnitude of  $10^2$  to  $10^3$  for channel widths of  $20\ \mu\text{m}$  (Figure 4).

Although we fabricated transistors as small as  $2\ \mu\text{m}$  wide, it was difficult to test these transistors with the equipment we had. Therefore we only tested features  $5$ ,  $10$ ,  $20$  and  $30\ \mu\text{m}$  wide. From testing the inflexible and flexible transistors, the data indicated that we had fabricated functioning devices with good on/off ratios and mobilities. Furthermore, the parylene masks allowed for consistent transistor fabrication within a sample and between samples as well. The on/off ratios and mobility results for flexible transistors were similar to that of

inflexible transistors, indicating that the flexible substrate did not hinder the performance of the device.

### Future Work:

We aim to continue fabricating short-channel top-contact carbon nanotube flexible transistors to optimize their performance. Furthermore, bending tests will be conducted on the flexible transistors to assess their performance during and after strain. We also aim to optimize the purification process of the semiconducting carbon nanotubes using various solvents and polymers.

### Acknowledgements:

I would like to thank Professor Zhenan Bao, my mentor Evan Wang, the Bao Group at Stanford, Site Coordinator Michael Deal, Maureen Baran, the Stanford Nanofabrication Facility staff, the NNIN REU Program Coordinators, and lastly the NNIN, NSF, and CIS for financial support.

### References:

- [1] S. Selvarasah; "A reusable high aspect ratio Parylene-C shadow mask technology for diverse micropatterning applications"; ScienceDirect, vol 145-146, pp 306-315 (2008).
- [2] C. Wang; "Extremely bendable, high-performance integrated circuits using semiconducting carbon nanotube networks for digital, analog, and radio-frequency applications"; Nano Letters, vol 12, pp 1527-1533. (2012).
- [3] Y. Chung; "Low-voltage and short-channel pentacene field-effect transistors with top-contact geometry using Parylene-C shadow masks". Applied Physics Letters, vol 96 (2010).
- [4] H.W. Lee; "Selective dispersion of high purity semiconducting single-walled carbon nanotubes with regioregular poly(3-alkylthiophene)s"; Nature Communications, vol 2 (2011).

## The Electrochemistry of Catalyzed Metal Multilayers

**Briana James**

**Engineering Science, University of Virginia**

*NNIN REU Site: Howard Nanoscale Science and Engineering Facility, Howard University, Washington, DC*

*NNIN REU Principal Investigator and Mentor: Dr. Tina Brower-Thomas, Chemical Engineering, Howard University*

*Contacts: bnj3dw@virginia.edu, tina.browerthomas@howard.edu*



Figure 1: Research setup.

### Abstract:

Self-assembled multilayers (SAM) are a product of the bottom-up fabrication method, a technique in which substances are built from the molecular level through chemical reactions. With thoughtful manipulation, such fabrications could perform as numerous components in molecular devices. This project utilized the bottom-up method to produce multilayers of the 4,4' dimercaptobiphenyl (DMBP) attached to the group (II) B metal mercury (Hg). The focus was to analyze its electrochemical properties by cyclic voltammetry to determine if the structure could successfully conduct electrons. A current of potential energy was ramped up and inverted through the sample and the oxidation state of the mercury was analyzed. This reading concluded if mercury was being reduced. Currently a peak occurred around the potential 0.4 V when a monolayer of DMBP was capped with mercury, but the peak did not occur when bonded with a second DMBP. Trials are being conducted for confirmation of current data, to determine if multiple oxidation states of mercury are present, and provide understanding of other chemical properties of the substance.

### Preparation of Multilayers:

The initial monolayer was prepared by introducing a gold working electrode to a 1  $\mu$ M DMBP solution with 200 proof ethanol. The gold working electrode, with a disk diameter of 1.6 mm, was placed into the monolayer solution in a nitrogen atmosphere for three hours, as seen in the setup in Figure 1. The electrode was then rinsed off with ethanol and dried with a nitrogen jet gun. Mercury was introduced to the monolayer via a dilute solution of 0.008M mercury perchlorate ( $\text{Hg}(\text{ClO}_4)_2 \cdot (6\text{H}_2\text{O})$ ) and 200 proof ethanol. The electrode was again positioned in the solution for three hours with nitrogen, thoroughly washed with distilled water and ethanol, and then dried off with nitrogen. The gold electrode was alternatively introduced to the monolayer and mercury solution, creating DMBP and mercury multilayer. A cartoon of the assembled structure is shown in Figure 2. After every layer, cyclic voltammetry was performed to measure the sample's electrochemistry.

### Cyclic Voltammetry:

Cyclic voltammetry determines the electrochemical properties of a sample through a series of cathodic and anodic measurements. For this experiment, our general setup included three electrodes enclosed in a glass cell partially filled with a 0.1 M sodium perchlorate electrolyte solution. The gold electrode served as the substrate for the various monolayers formed. Its potential energy was ramped up to a maximum current of 600 mV, then inverted to a set minimum of -600 mV, scanning the sample for two sweeps and six sweeps. The known electrochemical behavior of the silver/silver chloride electrode was used as a reference to measure the potential energy of the working electrode. A platinum counter electrode maintained a stable environment for oxidation and reduction.

### Results:

Two attempts were completed. In the first attempt, five layers were made, three being the DMBP monolayer and two being Hg. Cyclic voltammetry of the first layer showed few peaks,

however as we continued building layers, a gradual increase in cathodic and anodic peaks occurred. Unfortunately, in the first attempt, we failed to eliminate oxygen as a factor in the experiment. We noticed this because of some peaks that were present that we could not attribute solely to the expected chemical reaction. We alleviated this problem in our second attempt by degassing the entire cell for 10 minutes prior to measuring the electrochemistry of the sample. During the second trial, we grew a total of three layers, two DMBP monolayers amid one layer of Hg. The sample with just the DMBP layer had very little peaks, similar to the results in the previous trial. The trial pertaining to the DMBP monolayer capped with a layer of Hg had two cathodic peaks, appearing around potential values of 500 mV and -200 mV. The same sample also had one anodic peak at an approximate potential value of -130 mV. Once another layer of DMBP was assembled on top of the DMBP and Hg layers, the cyclic voltammety showed similar occurrences of very little peaks. Graphs of both attempts are depicted in Figure 1 and Figure 3.

### Conclusions:

The occurrence of the anodic and cathodic peaks discussed previously indicates a significant change in the chemical behavior of the sample, suggesting successful formations of the DMBP and Hg multilayers. The sample capped with DMBP showed very few peaks, correlating with our expectations. At this state, Hg is not exposed to the electrolyte solution and there is no free electron available to react with the Hg. Future works would include continuing further trials on DMBP and Hg multilayers, and replacing DMBP with other organic molecules.

### Acknowledgements

I would like to offer my deepest gratitude to: Dr. Tina Brower-Thomas, Dr. Charles Hosten, Dr. Yilma Gultneh, Mr. Maraizu Ukaegletgobu, Ms. Heather Battiste-Alleyne, Mr. James Griffin, and the staff of HNF, the National Nanotechnology Infrastructure Network Research Experience for Undergraduates (NNIN REU) Program, and the National Science Foundation (NSF).

### References:

- [1] Brower, T. "Self-Assembled Multilayers of 4,4'-Dimercaptobiphenyl Formed by Cu(II)-Catalyzed Oxidation"; *Langmuir*, 18, 6207-6216, (2002).
- [2] Brower, T. "Growth of 4,4'-Dimercaptobiphenyl Using Group (II) B Elements"; Howard University Department of Chemical Engineering.

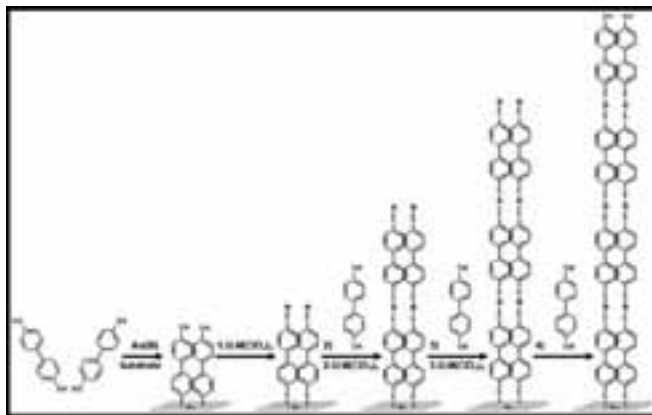


Figure 2: Multilayers of DMBP and Hg on gold substrate.

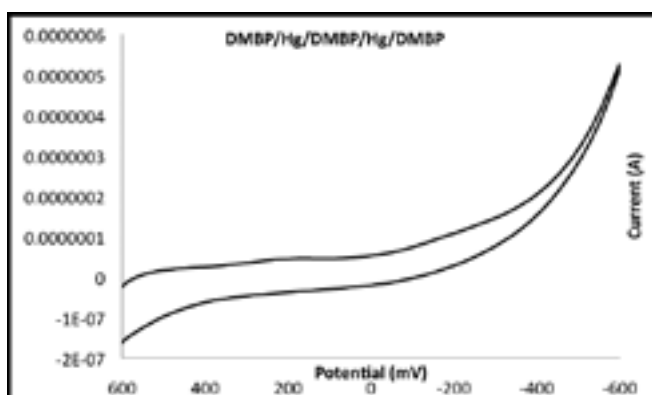


Figure 3: Cyclic voltammety of first attempt with three DMBP monolayers and two layers of Hg.

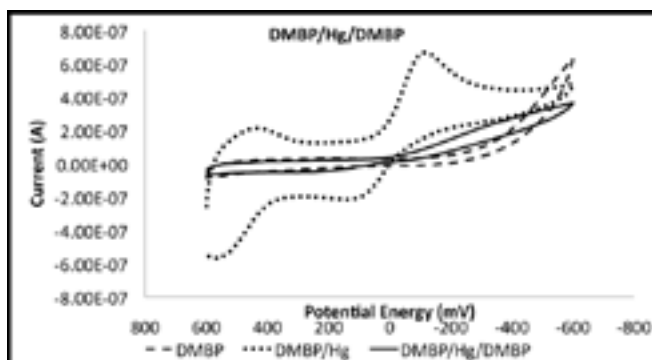


Figure 4: Cyclic voltammety of second attempt with two DMBP monolayers amid a layer of Hg.

## Implementing Gaussian Quadrature in Molecular Plasmonics

**Alexander B. Lee**

**Mathematical and Computational Biology, Harvey Mudd College**

*NNIN REU Site: NanoTech User Facility, University of Washington, Seattle, WA*

*NNIN REU Principal Investigator: Professor David J. Masiello, Department of Chemistry, University of Washington*

*NNIN REU Mentor: Jonathan P. Litz, Department of Chemistry, University of Washington*

*Contact: ablee@hmc.edu, masiello@uw.edu, jlitz@gmail.com*

### Abstract:

For certain metals that support localized surface plasmon resonances, the resonant frequency of the material's electrons falls within the realm of visible light. We can use light to collectively and coherently oscillate the surface electrons in nanoparticles made up of these metals, magnifying the light in intensity. Such an environment could potentially be used to catalyze reactions occurring near these particles. Interactions between the molecules and the nanoparticle may alter the molecular electronic landscape into a configuration that is favorable to the reaction. This interaction occurs in part through the image effect. The goal of this project was to develop a computationally feasible process in which to determine the molecule's electronic structure after it has been image-dressed by a nanoparticle of arbitrary shape. In order to make larger molecules more tractable, we implemented Gaussian quadrature instead of the trapezoidal rule to calculate the contour integral describing the electron density of the molecule. This change resulted in the code running approximately 100 times faster than before.

### Introduction:

When a localized surface plasmon resonance (LSPR)-supporting metal nanoparticle is excited with light, its surface electrons oscillate collectively and coherently. When multiple LSPR nanoparticles are brought together, hot spots form, localized regions of high electric field intensity. These hot spots could be used in catalytic applications [1, 2]. Subjecting the molecules to these electric fields will alter the electronic landscape of the molecules into something that is hopefully more favorable for the desired reaction.

The nanoparticle and the molecule interact through the image effect [3, 4]. The electric field from the plasmon pushes the electrons in the molecule, inducing a dipole moment. This dipole gives off its own electric field, pushing the electrons in the nanoparticle into an "image" dipole, thus reducing the net electric field inside the metal to zero. However, rearranging the electrons affects the plasmon, altering the resulting electric field. This altered electric field induces a new dipole in the molecule (see Figure 1). In this way, the nanoparticle and the molecule interact with each other an infinite number of times until the system converges to some configuration.

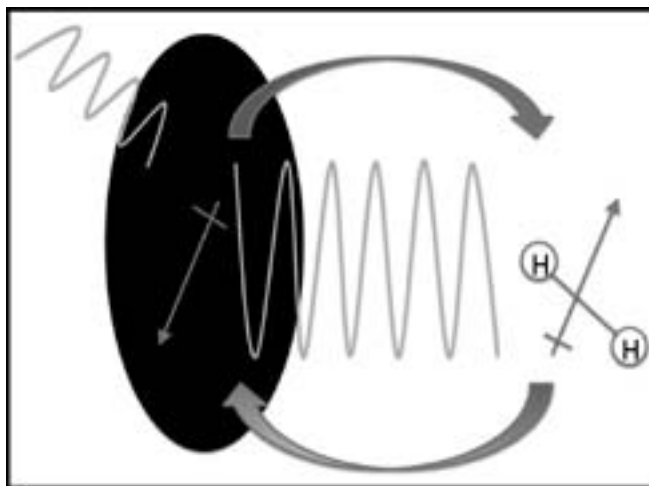


Figure 1: The molecule and nanoparticle repeatedly perturb each other through the image effect.

It was the goal of this project to develop a computationally feasible process to determine the electronic structure of this image-dressed molecule.

### Methodology:

We started by calculating the interacting Green's function,  $\mathcal{G}$ , for a molecule interacting with a nanoparticle [4]. We can use the Dyson expansion to write  $\mathcal{G}$  as an infinite geometric series as shown in Figure 2, where  $G$  is the noninteracting Green's function for the molecule in vacuum and  $\Sigma$  is the self-energy [5].  $\Sigma$  takes into account a single perturbation experienced by the molecule. Thus by calculating this infinite series, we took into account the infinite number of perturbations experienced by the molecule.

$$\mathcal{G} = G + (\Sigma G)G + (\Sigma G)^2G + (\Sigma G)^3G + \dots$$

Figure 2: The Dyson expansion of the interacting Green's function.

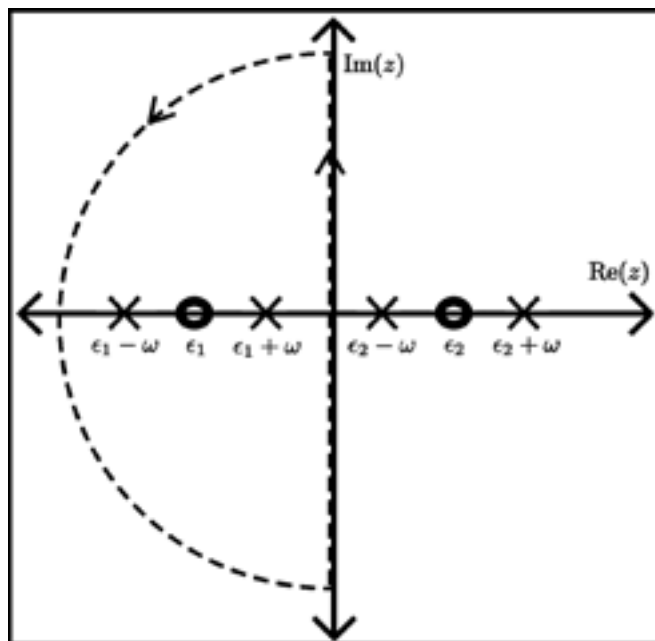


Figure 3:  $\mathcal{G}$  is integrated around singularities associated with occupied orbitals to obtain the interacting one-matrix.

We then took the integral of  $\mathcal{G}$  with respect to  $z$ , the frequency of interaction between the nanoparticle and the molecule. We integrated along a contour that encapsulated all singularities associated with occupied orbitals (see Figure 3). By computing this contour integral, we obtained the interacting one-matrix [6, 7]. Thus we were able to gain information on the electronic structure of the molecule in the form of an electron density.

To increase the speed of the code, Gaussian quadrature was implemented to numerically calculate the contour integral. Gaussian quadrature approximates the function as a  $2n-1$  degree Taylor polynomial, where  $n$  is the number of points taken. It does this by intelligently sampling the function as seen in Figure 4, where the  $x_i$ 's are the locations at which the function is sampled, and the  $w_i$ 's are the corresponding weights. These values are calculated independently from the function by a nonlinear system of  $2n$  equations.

By switching from the trapezoidal rule to Gaussian quadrature, we reduced the number of times we needed to sample the function from 100,000 to 1000. Thus, this change made the

$$\int_{-1}^1 f(x) dx \approx \sum_{i=1}^n w_i f(x_i)$$

Figure 4: Gaussian quadrature intelligently samples the function in order to approximate the integral.

code approximately 100 times faster than before. This made larger molecules, such as azulene, become more tractable as input molecules.

#### Future Work:

In its current state, the code only performs calculations for the alteration of one electron. We hope to further develop this process to consider the configuration of all electrons at the same time. This will allow us to make predictions in experimental spectroscopies as well as begin to model catalytic applications of plasmonics.

#### Acknowledgements:

I would like to thank the National Nanotechnology Infrastructure Network Research Experience for Undergraduates (NNIN REU) Program, the National Science Foundation and the University of Washington, with special thanks to my principal investigator, Professor David J. Masiello, my mentor, Jonathan P. Litz, and my site coordinator, Mack Carter.

#### References:

- [1] Christopher, P., H. Xin, and S. Linic, Nat. Chem. 3, 467 (2011).
- [2] Liu, Z., W. Hou, P. Pavaskar, M. Aykol, and S. B. Cronin, Nano Lett. 11, 1111 (2011).
- [3] Masiello, J. D. and G. C. Schatz, Phys. Rev. A 78, 064102 (2008).
- [4] Masiello, J. D. and G. C. Schatz, J. Chem. Phys. 132, 064102 (2010).
- [5] Fetter, A. L. and J. D. Walecka, "Quantum theory of many-particle systems," Chap. 3, (Dover ed, 2003).
- [6] Holleboom, L., and J. Snijders, Int. J. Quantum Chem. 34 289 (1988).
- [7] Holleboom, L., and J. Snijders, Int. J. Quantum Chem. 43, 259 (1992).
- [8] Litz, J., R. Brewster, A. Lee, and D. Masiello, in preparation (2012).

## Identification of Carbon Nanostructures (Fullerenes) in Cigarette Ash

Ian MacKenzie

Chemistry, Geneva College

NNIN REU Site: Nano Research Facility, Washington University in St. Louis, St. Louis, MO

NNIN REU Principal Investigator and Mentor: Dr. John Fortner, Department of Energy,  
Environmental and Chemical Engineering, Washington University in St. Louis

Contact: [ian.mackenzie@geneva.edu](mailto:ian.mackenzie@geneva.edu), [jfortner@seas.wustl.edu](mailto:jfortner@seas.wustl.edu)

### Abstract:

The production of fullerene materials ( $C_{60}$ ,  $C_{70}$ , etc.) has recently become a matter of increasing commercial interest and environmental concern. Although fullerene toxicity remains poorly defined, some forms have been shown to have cytotoxic effects, particularly when exposed to microbial communities. Therefore, the identification of (potential) fullerene sources is an important first step towards an accurate environmental exposure assessment. In this work, we tested the hypothesis that fullerenes (as  $C_{60}$  and  $C_{70}$ ) are formed in burning cigarettes by analyzing ash from several scenarios, including mimicked smoking events.

### Introduction:

Since the discovery of fullerene in 1985 by Kroto, et al., many synthetic methods have been proposed. Of particular interest is the synthesis of fullerene via pyrolysis of naphthalene [1]. This low molecular weight polycyclic aromatic hydrocarbon (PAH) can be found in environmentally significant quantities in coal tar, hydrocarbon fuels, and cigarette smoke [2, 3]. Pyrolysis has often been shown to occur in oxygen deficient environments inside a burning cigarette. Temperatures typically range between 700 and 920°C, but occasional microenvironments can reach up to 1200°C [4]. Previous studies have found the formation of fullerene via pyrolysis of PAHs to occur in the 1000-1100°C range [1, 5]. In this work, we demonstrate fullerene production via pyrolysis of high-tar cigarette tobacco.

Concern over the potential environmental impact of fullerenes has risen sharply in recent years. Although pristine  $C_{60}$  has been considered to show minimal cytotoxicity to rat lungs and microbial communities, functionalized  $C_{60}$  has been found to show some level of cytotoxic effects [6, 7]. Fullerene water suspensions have been demonstrated to show pronounced cytotoxic effects when exposed to *E. coli*, *P. aeruginosa*, and *B. subtilis* [8, 9]. Additionally, fullerene exposure to ozone can also result in increased levels of toxicity. Ozone will add to a fullerene 6,6-double bond to form a 1,2,3-trioxolane which spontaneously converts to the fullerene epoxide,  $C_{60}O$ , producing singlet oxygen, a reactive oxygen species known for lipid peroxidation and membrane degradation [10]. Thus,

inhalation of fullerene and exposure to even minimal amounts of ozone could lead to compromised membrane integrity in human lungs.

Therefore, considering the potential environmental impacts of  $C_{60}$ , our study sought to shed light on a (potentially) prevalent but previously unknown source of fullerenes.

### Experimental Procedure:

Six samples of domestic cigarette tobacco and a control of untreated whole leaf Burley tobacco were pyrolyzed at various temperature maximums over a range of pressure profiles using a Thermcraft Protégé split tube furnace. Trials were performed under 100% argon flow with linear flow rates between 0.242 and 2.55 liters per minute. Smoke particulates were collected using PTFE 0.2  $\mu\text{m}$  particulate filters and soluble ash and particulates were extracted into toluene using a Soxhlet apparatus. Two ash samples were also produced using custom-made smoking machines and extracted using the Soxhlet apparatus. Analysis on all samples was performed using a MALDI-TOF mass spectrometer.

### Results and Conclusions:

MALDI-TOF analysis is believed to indicate fullerene content in the majority of ash samples. Seven of the nine samples displayed a possible  $C_{60}$  m/z (mass-to-charge ratio) peak of 720 and/or  $C_{70}$  m/z peak of 840. The remaining two samples displayed peaks that could correspond to hydroxyl and epoxy group additions to  $C_{60}$  or  $C_{70}$ . Of particular interest was evidence of  $C_{70}$ , but no clear amount of  $C_{60}$ , in M1, a sample run under high pressure and temperature. The most abundant amount of  $C_{60}$  appeared in M100-8, a sample run at lower temperature under near atmospheric pressure. Sample conditions are shown in Table 1. Overall, the spectral data provided compelling evidence for the formation of the  $C_{60}$  and  $C_{70}$  fullerenes during cigarette smoking events.

Based upon these results, we make the following recommendations to the scientific community: 1) Cigarettes should be viewed as potential sources of fullerene

environmental exposure, 2) Increased effort should be given to proper cigarette containment and ash disposal until the environmental effects of fullerenes are more fully understood, 3) Further research should be conducted in this area. Ultimately, the evidence shown in this work should be used to promote healthier and safer environmental conditions.

### Future Work:

Further analysis is needed to confirm the presence of  $C_{60}$  and  $C_{70}$  in current samples. High performance liquid chromatography (HPLC) could be used to verify molecular UV-Vis spectra and retention times. In the future, additional high-carbon pyrolysis events should be investigated as potential fullerene sources. Cigar smoking is a natural candidate for such studies, as are forest fires and lean hydrocarbon fuel combustion.

### Acknowledgements:

I would like to thank my Principal Investigator, Dr. John Fortner, for all his help, LeafOnly, LLC., for their generous donation of whole leaf tobacco, and the Pulmonary Mouse Genetic and Smoking Core for the use of their smoking machines. Credit and thanks to Dr. Fong-Fu Hsu for the use of the MALDI-TOF mass spectrometer, and particular thanks to Michael Pride for his ever-willing assistance. This work was sponsored by the National Science Foundation and the National Nanotechnology Infrastructure Network Research Experience for Undergraduates Program. Especial thanks to program coordinators Dee Stewart and Nathan Reed, and to all the NNIN staff who made this wonderful opportunity possible.

### References:

- [1] Taylor, Roger. Nature 366.6457 (1993): p.728-31.
- [2] Alexeeff, G. Chronic Toxicity Summary Naphthalene. Environmental Health Hazard Assessment, [http://oehha.ca.gov/air/chronic\\_rels/pdf/91203.pdf](http://oehha.ca.gov/air/chronic_rels/pdf/91203.pdf)
- [3] Ding, Yan S. Environmental Science and Technology 39.2: 471-78. (2005).
- [4] Egerton, Alfred, K. Guban, and F.j. Weinberg. Combustion and Flame 7: 63-78. (1963)
- [5] Scott, Lawrence T. Science 295.5559: 1500-503. (2002).
- [6] Baker, G. Toxicological Sciences 101.1: 122-31. (2007).
- [7] Nyberg, Leila. Environmental Science and Technology 42.6: 1938-943. (2008).
- [8] Kang, Seoktae. Environmental Science and Technology 43.7: 2648-653. (2009).
- [9] Lyon, Delina Y. Environmental Science and Technology 40.14: 4360-366. (2006).
- [10] Anachkov, Metodi P. Fullerenes, Nanotubes and Carbon Nanostructures 11.2: 95-103. (2003).

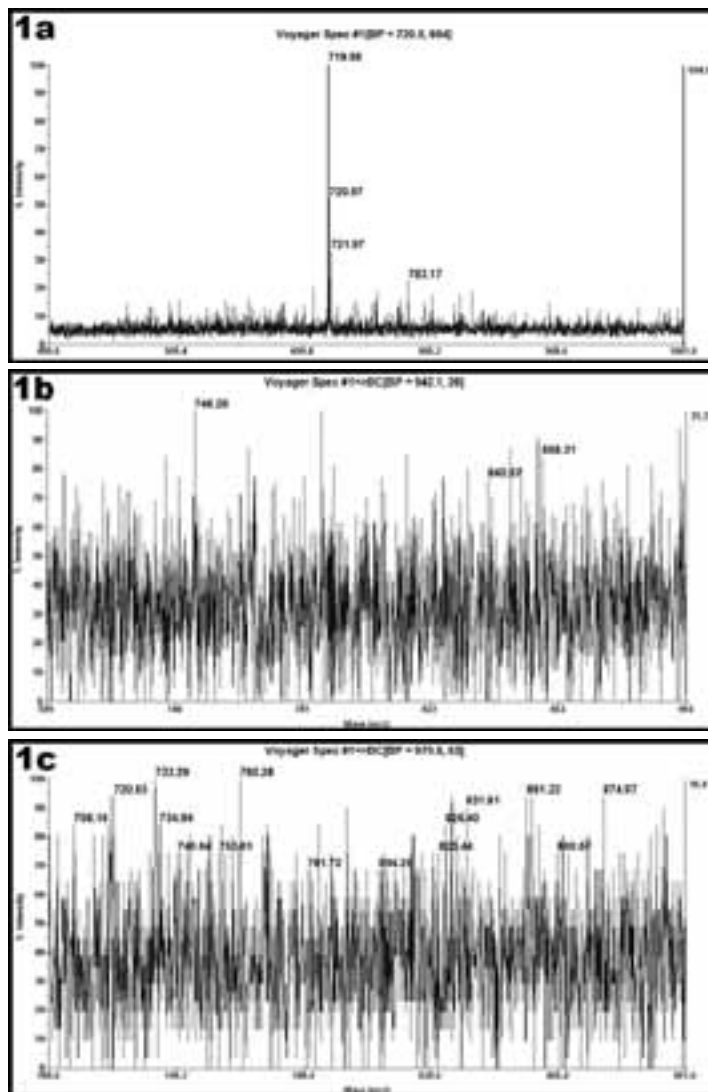


Figure 1: MALDI-TOF mass spectrum of samples a) M100-8, b) M1, and c) SM.

Sample ID	Temperature Set-point (°C)	Initial Tube Pressure (torr)	Result
M1	1200	~2100 (~40psi)	Possible C70
M5	1200	608	C60
C6	1200	622	C60
M7	1200	747	Possible C70
M100-8	800	735	Large C60
C9	800	684	C60
Control	800	487	No Fullerene
SM*	Natural	Natural	No Fullerene
SC*	Natural	Natural	C60

Table 1: Summary of sample conditions and results.

## Investigation of Molecular Structures for Soft Matters with Mechanoresponsive Colors

Kelly Suralik

Chemistry, Middlebury College

NNIN iREU Site: National Institute for Materials Science (NIMS), Tsukuba, Ibaraki, Japan

NNIN iREU Principal Investigator and Mentor: Dr. Kentaro Tashiro, Reticular Materials Group,  
International Center for Materials Nanoarchitectonics, National Institute for Materials Science

Contact: ksuralik@middlebury.edu, tashiro.kentaro@nims.go.jp

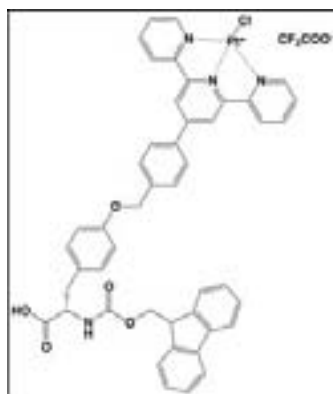
### Abstract:

Materials with mechanoresponses are a new discipline in organic soft matter synthesis. One mechanoresponse, thixotropy, is the tendency of a material to become less viscous upon the addition of mechanical stress such as shaking. Separately in other gels, a visible color change during the gel-to-solution transition has been observed. While gels with either thixotropic or color-change qualities have been reported, the molecular structure of a thixotropic gel with mechanoresponsive colors has not yet been confirmed. In this work, we investigate molecular structures of gels. Synthesized platinum-terpyridine (Pt-terpy) complexes bearing an amino acid moiety were manipulated by changing solvent, counter anion and molecular structure. Pt-terpy gels and corresponding solution samples were analyzed through stable-by-inversion tests and emission spectroscopy. A thixotropic Pt-terpy gel without (fluoro-9-yl)methoxycarbonyl (Fmoc) moiety exhibited a 648 nm emission peak, which indicated the presence of Pt-Pt interactions. Thixotropic gels that display mechanoresponsive colors may be applicable as oscillation sensors for buildings and earthquakes.

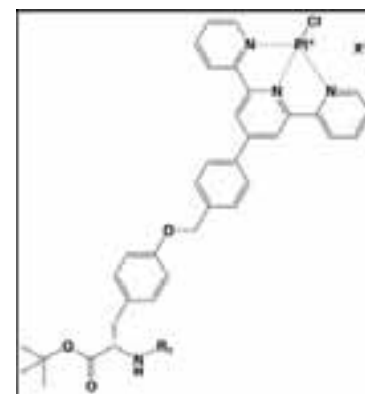
### Introduction:

Polymers with mechanoresponsive colors display a change in color when stretched due to the presence of mechanically sensitive chemical groups in the polymer linkages [1]. However, other soft matters may be able to exhibit responses to mechanical stimuli. Thixotropy is the property of a material to become less viscous upon added shear stress. By shaking a thixotropic gel, the inherent network structure will break down, and the gel will undergo a phase change from gel to solution [2]. After standing, the material will return to its original state as the gel network reforms. In a separate phenomenon, some gels visibly change color during the gel-to-solution transition [3]. The color modification is related to the different metal interactions of the metal centers in the gel phase relative to the solution phase.

The National Institute for Materials Science International Center for Materials Nanoarchitectonics (NIMS MANA)



Scheme 1:  
Molecular structure  
of Pt-terpy thixotropic gel.



Scheme 2: Basic molecular structure  
for synthesized Pt-terpy  
complex analogs.

Reticular Materials Group has previously synthesized a Pt-terpy thixotropic gel. The monomer for the thixotropic gel incorporates the Pt-terpy moiety and a functionalized tyrosine, shown in Scheme 1. The hydrogen bonding between the amino acid units are thought to cause the gelation capabilities of this complex. In addition, Pt-terpy possesses many spectral properties; specifically, emission at approximately 650 nm indicates Pt-Pt interactions [4]. However, the previously synthesized Pt-terpy thixotropic gel showed no absorption or emission that indicated the presence of Pt-Pt interactions.

A gel that exhibits both properties of thixotropy and color change upon phase transition has yet to be reported. In this study, we employed traditional organic synthesis procedures to manipulate the Pt-terpy complex structure in order to create a thixotropic gel with mechanoresponsive colors.

### Experimental Procedure:

A series of Pt-terpy complexes of analogous forms were synthesized and tested for their gelation potential and color change ability. The basic structure is shown in Scheme 2. Counter anion salts in 10x molar excess were dissolved in Pt-terpy solutions for anion exchange. Alteration to the

original Pt-terpy complex was accomplished primarily through the metalation of Pt to a functionalized multidentate ligand followed by deprotection of Fmoc. Matrix-assisted laser desorption/ionization time-of-flight mass spectrometry (MALDI-TOF MS) was completed to ensure successful synthesis.

For gelation, the Pt-terpy complex was completely dissolved in solvent. Water was added to the solution to trigger gelation, followed by mixing of the reaction vial and standing. The presence of gel qualities was analyzed through the stable-by-inversion test.

Emission spectroscopy was employed on gel and solution samples of the synthesized Pt-terpy forms. Absorption spectroscopy was used to determine the necessary wavelength of excitation for emission measurements. Emission peaks were examined to determine the presence of Pt-Pt interactions.

### Results and Conclusions:

The Pt-terpy complexes showed limited solubility in the water-miscible solvents (i.e. MeOH, CH<sub>3</sub>CN), and dimethyl sulfoxide was selected as the best solvent for the water-triggered gelation protocol. Pt-terpy complexes with a trifluoroacetate (CF<sub>3</sub>COO<sup>-</sup>) counter anion increased the solubility of the complexes and formed gels. The Pt-terpy complex must be reasonably soluble in the solvent in order for the gelation test to be valid. The Pt-terpy complex with X = CF<sub>3</sub>COO<sup>-</sup> and R<sub>1</sub> = H was successfully synthesized (Scheme 2), and a thixotropic gel formed. Comparison of emission spectra between gel and solution samples of Pt-terpy complex (X = CF<sub>3</sub>COO<sup>-</sup>, R<sub>1</sub> = H) showed that only the gel state emitted at 648 nm, as seen in Figure 1. Comparison of emission spectra between complexes where R<sub>1</sub> = H or Fmoc demonstrated that only Fmoc deprotected Pt-terpy complexes emitted at 650 nm, as seen in Figure 2. It is hypothesized that deprotection of Fmoc reduced  $\pi$ -stacking and emphasized interaction between metal centers. Therefore, we synthesized a Pt-terpy thixotropic gel that contained Pt-Pt interactions.

### Future Work:

Future work will analyze the gel characteristics and emission spectral properties of a Pt-terpy complex capped with a phenylacetylene ligand. It is thought that the presence of the phenylacetylene ligand will emphasize Pt-Pt interactions through  $\pi$ -orbital stacking of the ligand near the metal center. Later studies will synthetically alter the Pt-terpy structure further in order to achieve mechanoresponsive colors.

### Acknowledgements:

I extend sincere gratitude to Dr. Kentaro Tashiro and the Reticular Materials Group for their constant support. I thank NIMS, MANA, the NNIN Japan iREU interns,

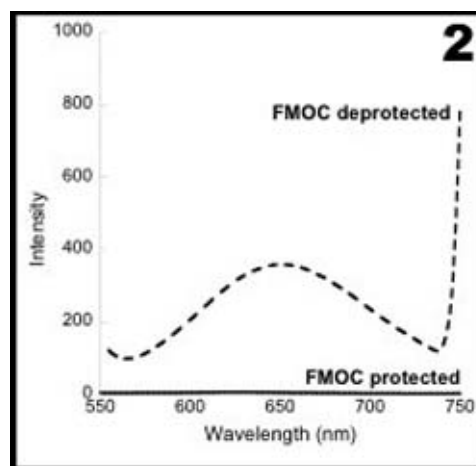
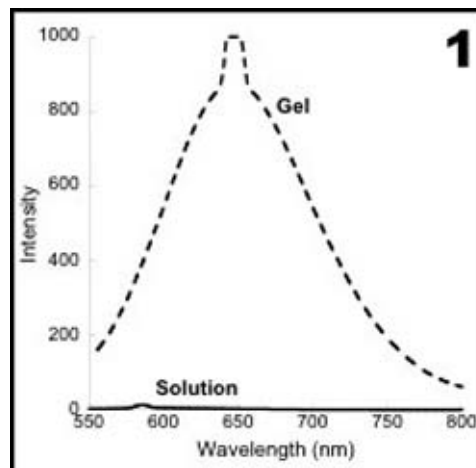


Figure 1, top: Emission spectra of [tBuO<sub>2</sub>C-Pt-NH<sub>2</sub>][Cl][CF<sub>3</sub>COO] gel and solution in DMSO/H<sub>2</sub>O.

Figure 2, bottom: Emission spectra of [tBuO<sub>2</sub>C-Pt-NH<sub>2</sub>][Cl][CF<sub>3</sub>COO] and [tBuO<sub>2</sub>C-Pt-NHFmoc][Cl][CF<sub>3</sub>COO] gels in DMSO/H<sub>2</sub>O.

Dr. Lynn Rathbun, Dr. Nancy Healy, and Dr. James Marti. I would also like to thank Dr. Michael Deal for all of his encouragement. I acknowledge the National Nanotechnology Infrastructure Network International Research Experience for Undergraduates (NNIN iREU) Program and the National Science Foundation for financial support.

### References:

- [1] Davies, et al., Nature.2009,459, 68-72.
- [2] Hoshizawa, et al., Chem. Lett. 2011,40, 1143-1145.
- [3] Yuen, et al., Angew. Chem. Int. Ed. 2008,47, 9895-9899.
- [4] Wong and Yam, Acc. Chem. Res. 2011,44, 424-434.

# Effects of Membrane Surface Modification on Calcium Carbonate Fouling and Membrane Efficiency for Desalination

**Whitney Wong**

**Biomedical Engineering, University of Texas at Austin**

*NNIN REU Site: Nano Research Facility, Washington University in St. Louis, St. Louis, MO*

*NNIN REU Principal Investigator: Dr. Young-Shin Jun, Department of Energy, Environmental and Chemical Engineering (EECE), Washington University in St. Louis*

*NNIN REU Mentor: Jessica Ray, EECE, Washington University in St. Louis*

*Contact: whitney.wong@utexas.edu, ysjun@seas.wustl.edu, jessica.ray@go.wustl.edu*

## Introduction:

Desalination can be used as a means to replenish freshwater supplies of communities with growing population needs. Reverse osmosis (RO) is a pressure-driven process that requires a semi-permeable membrane to selectively remove salts and other particulate matter from brackish water or seawater. Common RO membranes are thin-film composites (TFCs), which are composed of a thin polyamide layer supported by a porous polysulfone layer. Although membrane desalination is an efficient method, a persistent problem is that the membrane is highly susceptible to fouling—accumulation of particles onto the membrane surface over time that can clog or otherwise compromise the efficiency or performance of the membrane [1]. The main cause of fouling appears to be a hydrophobic interaction between the membrane surface and the solutes in the water [2]. In our approach, we grafted polyethylene glycol (PEG), a hydrophilic monomer, to help disrupt hydrophobic interactions with calcium carbonate ( $\text{CaCO}_3$ ), a common hydrophobic fouling agent (Figure 1). After membrane characterization, we analyzed the interaction between  $\text{CaCO}_3$  and the membrane surface.

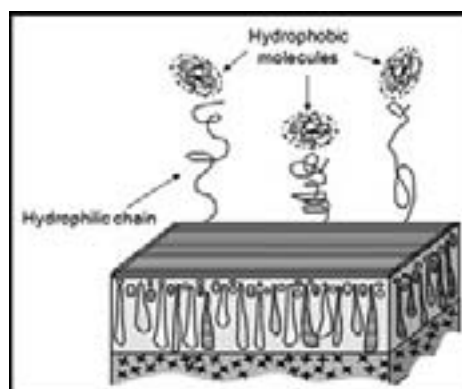


*Figure 1: Experimental approach. Graft PEG to membrane surface to help reduce fouling of hydrophobic solutes [3].*

## Experimental Procedures:

**Monomer Grafting.** Commercially available BW30 TFC membranes were purchased from Dow-Filmtec in flat sheet form. Grafting materials purchased from Sigma-Aldrich included potassium disulfite (PD) and potassium persulfate (PP) to initiate the reaction, polyethylene glycol (PEG) as the hydrophilic monomer, and ethyleneglycol dimethacrylate (EGDMA) as the crosslinker. Various concentrations and grafting times were tested. The final conditions chosen were a graft time of one hour with a solution that consisted of 0.1 M PEG, 0.01 M EGDMA, and a 0.025 M equimolar PP and PD solution.

**Contact Angle.** To determine the wettability of the membrane, we measured contact angles of samples with and without surface modification. Twenty microliters of de-ionized (DI) water was pipetted onto the membrane surface, where images were then captured using a Motic digital microscope and the Motic Image Plus 2.0 software.

**$\text{CaCO}_3$  Nucleation and Salinity Testing.** Various concentrations of sodium bicarbonate ( $\text{NaHCO}_3$ ) and calcium chloride dihydrate ( $\text{CaCl}_2$ ) were used to form  $\text{CaCO}_3$ , which could be deposited onto the membrane surface. To mimic brackish water

conditions, we replaced double-filtered water in the original solution with a background solution of sodium chloride ( $\text{NaCl}$ ). Concentrations of 0.1, 0.5, and 1 M  $\text{NaCl}$  were added to observe the effect of increasing  $\text{NaCl}$  on  $\text{CaCO}_3$  formation.

Because the  $\text{CaCO}_3$  saturation index (SI) changes with ionic strength, the Geochemist's Workbench software was used to calculate the adjusted  $\text{CaCl}_2$  and  $\text{NaHCO}_3$  concentrations to maintain an SI of 2.16 for calcite formation for all experiments.

Thus, a final solution with concentrations of 0.025 M  $\text{NaHCO}_3$  and 0.025 M  $\text{CaCl}_2$  was used.

## Results and Discussion:

Characterization of the membrane before and after grafting included scanning electron microscopy (SEM) and measuring contact angles. In order to see whether grafting was successful, contact angle measurements were determined to observe whether grafting made the membrane more hydrophilic. The best concentration, 0.1 M PEG for one hour, was chosen because it had a smaller contact angle than the unmodified membrane.

SEM proved to be a powerful tool for analyzing both the unmodified and grafted membranes after  $\text{CaCO}_3$  was deposited onto the surface. As the NaCl concentration increased, there was a definite increase in  $\text{CaCO}_3$  nucleation for both the unmodified and grafted membranes. An increase in nucleation as ionic strength increases has been reported in literature [4]. There was also a distinct decrease in the amount of nucleation between the unmodified and grafted membranes at each respective concentration of NaCl. For example, this can be seen in Figures 2 and 3.

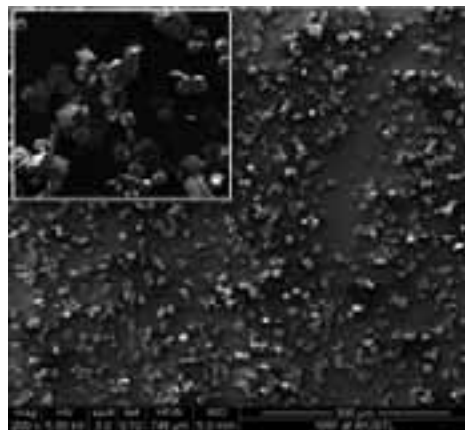


*Figure 2: Unmodified membrane with  $\text{CaCO}_3$  nucleation and a background solution of 0.5 M NaCl. Inset in the upper left corner is magnified with a scale of 40  $\mu\text{m}$ .*

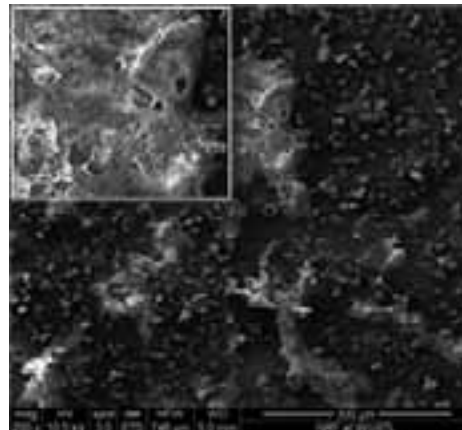


*Figure 3: PEG-grafted membrane with  $\text{CaCO}_3$  nucleation and a background solution of 0.5 M NaCl. There is less nucleation around and on dense areas of PEG. Inset in upper left corner is magnified with a scale of 50  $\mu\text{m}$ .*

A final observed trend was a difference in  $\text{CaCO}_3$  morphologies. In the unmodified membrane, amorphous  $\text{CaCO}_3$  (spherical), calcite (rhombohedral), and aragonite (fibrous-shaped) were identified. While in the grafted membrane, mostly calcite was observed. This could be due to the differences in binding sites after grafting with PEG.

### Conclusions and Future Work:

In this project, PEG was successfully grafted onto the TFC membrane surface. From the SEM images of both the unmodified and grafted membranes, there was clearly a decrease in the degree of  $\text{CaCO}_3$  nucleation as the surface became more hydrophilic. This was what was expected when a hydrophilic component was added to the membrane. After analyzing the interaction between the membranes and the  $\text{CaCO}_3$  particles, it was determined that hydrophilic/hydrophobic interactions govern nucleation.

In the future, a working laboratory-scale RO system is desired to test grafted membrane efficiency in salt rejection. There are implications for this grafting procedure to be a viable modification that could help to reduce water pretreatment costs, extend the lifetime of TFC membranes, and improve

the overall membrane desalination process. Thus, it is extremely important to test and compare the efficiency of the unmodified and grafted membranes.

### Acknowledgements:

Thank you to Dr. Young-Shin Jun, Jessica Ray, and everyone at the Environmental Nanochemistry Lab for their guidance and support. I would also like to give thanks to the Nano Research Facility, the National Nanotechnology Infrastructure Network Research Experience for Undergraduates (NNIN REU) Program, and the National Science Foundation for giving me this opportunity and an unforgettable experience.

### References:

- [1] Freger, et al.; *Membrane Science*, 209, 283-292 (2002).
- [2] Koo, et al.; "Fouling resistant reverse osmosis membranes"; 1-10 (2003).
- [3] Kang, et al.; *Polymer*, 48, 1165-1170 (2007).
- [4] Boerlage, S.; "Scaling and particulate fouling in membrane filtration systems"; Dissertation, Swets and Zeitlinger Publishers, 208 (2001).

## Transparent and Stretchable Metal Electrodes

**Soichi Hirokawa**

**Physics, Bowdoin College**

*NNIN REU Site: Colorado Nanofabrication Laboratory, University of Colorado, Boulder, CO*

*NNIN REU Principal Investigator: Prof. Mark Stoykovich, Chemical and Biological Engineering, University of Colorado, Boulder*

*NNIN REU Mentor: Ian Campbell, Chemical and Biological Engineering, University of Colorado, Boulder*

*Contact: shirokaw@bowdoin.edu, mark.stoykovich@colorado.edu, ian.p.campbell@colorado.edu*

### Abstract:

Thin layers of lamellar-forming polystyrene-*block*-poly (methyl-methacrylate) (PS-*b*-PMMA) provide the templates for fabricating nanowires with a “fingerprint” morphology. The electrical characteristics of the nanowires were measured, and largely deviated from simulated devices due to high defect density. Their highly curved conformation makes the nanowires strong candidates for electrical testing on flexible substrates under compression and elongation. The wires’ high transmittance on glass substrates reveals that they can function as transparent metal electrodes for use in electronic devices.

### Introduction:

Diblock copolymers are macromolecules composed of two chemically distinct blocks, each a linear repetition of a particular monomer, that self-assemble to create periodic microdomains, each of which exclusively contains one of the polymers that make up the copolymer [1]. Varying volume fractions of the blocks generates different morphologies. When the volume fractions of the two blocks are similar, block copolymers self-assemble into the lamellar morphology [1], where the block with the higher volume fraction shows greater connectivity [2].

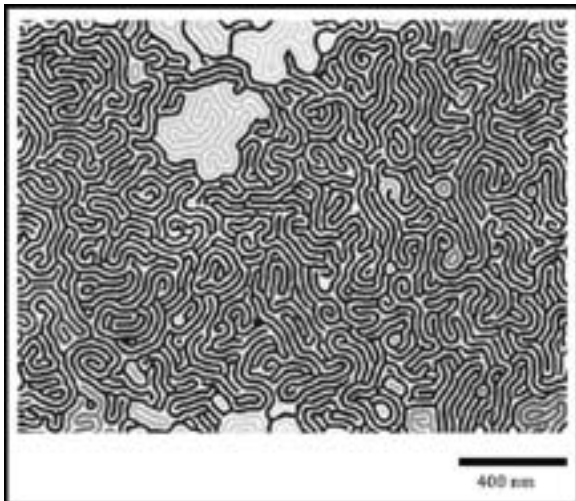


**Figure 1:** Color-coding for each PMMA backbone under a volume fraction  $f_{\text{PMMA}}$  of 0.55. (See cover for full color version.)

Figure 1 illustrates different continuous networks, each a different color, of PMMA, when the volume fraction of PMMA,  $f_{\text{PMMA}}$ , is 0.55 (see the cover of this publication for the full color rendition of this image). A single dominant network exists (blue) among small isolated networks. The high-connectivity, which offers redundant pathways from one point in the network to another, and the tortuous network conformation make block copolymers attractive for the fabrication of nanowires (NWs) [2-4]. Removing one block while preserving and using the other for patterning by thin-layer metal deposition allow for the formation of NWs. On transparent and stretchable substrates, these NWs should possess useful electrical properties, have high transmittance [5], and continue to perform well under mechanical strain.

### Experimental Procedure:

Neutral brush solution was spin-coated and annealed onto cleaned glass slides or silicon wafers, allowing the block copolymer to orient perpendicular to the substrate [3]. Block copolymer blends were spun onto the neutral substrates and annealed to produce self-assembled thin films. The samples were exposed to ultraviolet light to break down the PMMA and developed using acetic acid, creating a polystyrene template. After five seconds of oxygen plasma to remove the brush, 1 nm of chromium (Cr) and 5 nm of gold (Au) were evaporated into the vacancies left by PMMA. Sonication in toluene removed the polystyrene, leaving the NWs on the substrate.

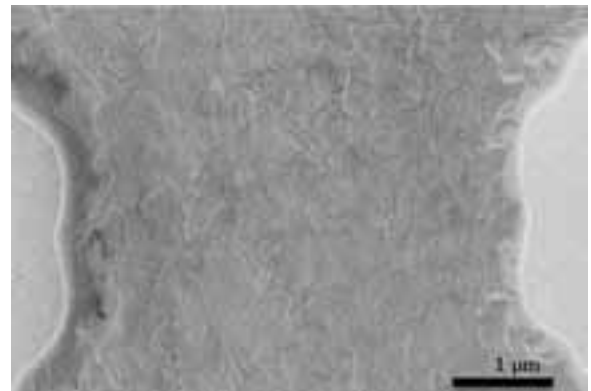


**Figure 2:** Nanowire network between micro-extensions from contact pads. Ideally, current must pass through these NWs.

Negative photoresist NR71 was spin-coated onto the nanowire samples for 40 seconds at 4000 RPM and exposed for 55 seconds using a mask-aligner and prepared mask containing contact pads with varying microwire features. The exposed samples were heated before development in RD6 for eight seconds, creating the pattern for the contact pads. After plasma treatment of 30 seconds, 10 nm of Cr followed by 100 nm of Au were evaporated, creating contact pads upon removing the remaining photoresist by sonication in acetone. Figure 2 illustrates the result of applying contact pads onto the nanowire samples, with a small gap between the microwire connectors to force current to pass through the NWs.

Current was measured using two probes from the probe station pressed onto the contact pads with potentials ranging from -10 millivolts to 10 millivolts applied across the samples.

Extinction coefficients for the NWs across the visible spectrum were measured on glass substrates using an Ocean Optics spectrometer and used to calculate transmittance.

### Results and Discussion:

Figure 3 demonstrates the electrical characteristics of the NWs with  $f_{\text{PMMA}} = 0.55$ . A linear relationship between current and voltage exists for systems with continuous nanowire pathways between contacts, indicating a constant resistance. Increasing contact width increases sheet resistance because out-of-plane transport constitutes a larger fraction of the current for thin contacts. Simulations predicted that increased contact width would cause decreased sheet resistance, but defects in the fabricated NWs led to comparatively large resistances.

Figure 4 is a graph of the transmittance of two NW samples with  $f_{\text{PMMA}} = 0.55$ . The similar spectra indicate consistency in the transparency of these devices. Approximately 90-95% of light across the visible spectrum passes through the glass samples, demonstrating high transparency in these thin films.

Block copolymers are a useful template for fabricating NWs. The electrical characteristics of these NWs show potential for electronic devices while the transmittance through these samples displays the possibility for these NWs to become incorporated into devices requiring high transparency. These block-copolymer templated NWs are competitive with state-of-the-art materials in many solid-state devices. The high curvature of these NWs predicts that they will continue to function under strain and compression.

### Future Work:

Improvements include producing defect-free samples for consistent device performance. A transfer process must be developed to test device performance under compression and strain. If the nanowires perform well under strain and compression, they can be incorporated into flexible solid-state devices.

### Acknowledgments:

The author thanks Professor Mark Stoykovich's research group, particularly PI Professor Stoykovich and mentor Ian Campbell, and the faculty and staff of the Colorado Nanofabrication Laboratory at the University of Colorado for their assistance on the project. The author acknowledges the support of the National Science Foundation for providing the funding for this research and of the NNIN REU Program.

### References:

- [1] Bates, F.S.; "Block Copolymers – Designer Soft Materials"; Physics Today; 52(2), 32(1999).
- [2] Campbell, I.P.; "Network Connectivity and Long-Range Continuity of Lamellar Morphologies in Block Copolymer Thin Films"; Macromolecules; 2012; 45; pg 1590.
- [3] Han, E.; "Effect of Composition of Substrate-Modifying Random Copolymers on the Orientation of Symmetric and Asymmetric Diblock Copolymer Domains"; Macromolecules; 2008; 41; pg. 9090.
- [4] Jeong, U.; "Enhancement in the Orientation of the Microdomain in Block Copolymer Thin Films Upon the Addition of Homopolymer"; Advanced Materials; 2004; Vol. 16, No. 6; pg. 533.
- [5] Lee, J.; "Solution-Processed Metal Nanowire Mesh Transport Electrodes"; 2008, Vol. 8 No. 2; pg. 689.

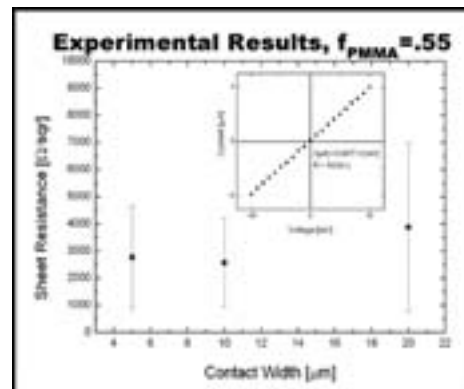


Figure 3: Sheet resistance and sample current-voltage curve with a nanowire network for  $f_{\text{PMMA}} = 0.55$ .

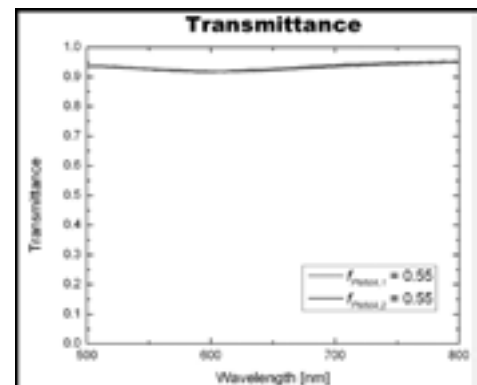


Figure 4: Transmittance across visible spectrum through two NW samples with  $f_{\text{PMMA}} = 0.55$ .

## Silicon Carbide Device Simulation and Measurement

**Keevin Hood**

**Electronics Engineering, Norfolk State University**

*NNIN REU Site: ASU NanoFab, Arizona State University, Tempe, AZ*

*NNIN REU Principal Investigator: Dr. Dieter Schroder, Electrical, Computer and Energy Engineering, Arizona State University*

*NNIN REU Mentor: Xuan Yang, School of Electrical, Computer and Energy Engineering, Arizona State University*

*Contact: k.j.hood@spartans.nsu.edu, schroder@asu.edu, xuan.yang@asu.edu*

### Abstract:

Fabricating semiconductor devices is very expensive and time consuming, but most importantly, can be wasted if there is no clear understanding of what to look for. Computer simulations can accurately predict the fabrication process and device behavior, and can show how a device can be improved for better performance. Metal-oxide-semiconductor (MOS) capacitors are the basic components of MOS transistors, which can store or amplify charges and are the building blocks of integrated circuits. Using the simulation of an MOS capacitor, we wanted to develop silicon carbide (SiC) as a profitable semiconductor so that production of higher quality SiC can become a common process. With the simulation software Silvaco, we simulated an MOS capacitor using molybdenum (Mo) for the metal or gate, silicon carbide (4H-SiC) for the semiconductor and silicon dioxide ( $\text{SiO}_2$ ) for the oxide. Then we measured different device parameters, including interface charge, oxide charge, and compared our results to a measured capacitance-voltage (C-V) curve of an MOS capacitor. Our purpose was to introduce SiC for more use in devices by: (a) simulating SiC MOS capacitors, (b) measure the C-V curve of the MOS capacitor with different characteristics, and (c) compare simulated with experimental data.

### Experimental Procedure:

We first set up two MOS capacitors for Silvaco. Each had different oxide thicknesses and were named n-SiC (Figure 1) and p-SiC (Figure 2). We ran different simulations on each capacitor to gather information on their C-V curves. Each simulation was developed using five groups. Structure specification contained the mesh, region, electrode, and doping sections. Material models specification contained material, models, contact, and interface sections. Numerical method selection contained the method section. Solution specification contained log, solve, load, and save sections. Results analysis contained extract and tonyplot sections.

We exported the data from Silvaco (see Table 1, at right) and then; imported the data into Excel, normalized the data, refitted plots using Origin, and finally, compared the shifts and degradation between cases and ideal curve.

### Results:

Our simulations of n-SiC and p-SiC devices showed a slight voltage shift and some degradation. In Figure 3, the ideal curve reaches depletion around 2 V. The interface state curve reaches depletion at 0 V, while oxide charges shift the depletion region to -2 V. In Figure 4, the ideal curve reaches depletion around 3.2 V. The interface state curve reaches depletion around 5 V and oxide charges shift the depletion region to 0 V.

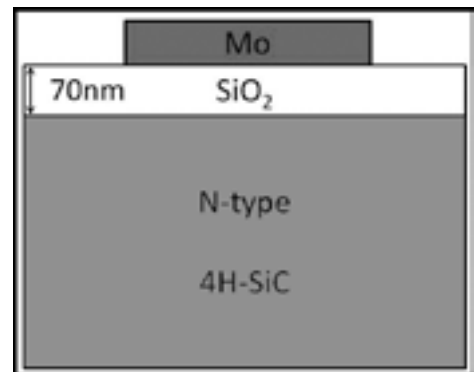


Figure 1: N-SiC MOS capacitor.

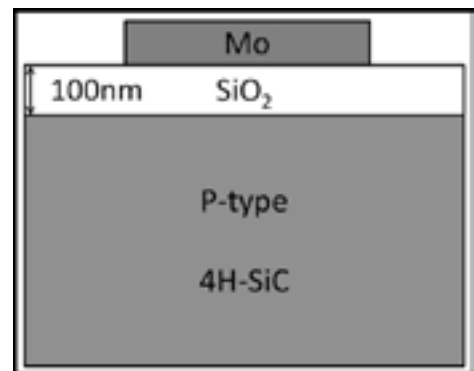


Figure 2: P-SiC MOS capacitor.

Silvaco
i. Run Time Environment
ii. Command File
iii. Structure Files
iv. ATLAS Device Simulator
v. Log Files and/or Solution Files
vi. Tonyplot

Our results show how the SiC MOS capacitor is stable and efficient even with oxide charges and interface states.

### Conclusions:

SiC is a potentially important high-temperature semiconductor for power device applications and it can operate at temperatures much higher than Si. Using Silvaco, we simulated the effect of SiC oxide charges and interface traps on the behavior of MOS capacitors. The simulation software uses Poisson's, Carrier Continuity, and many other equations in Atlas to solve and gather data to generate the C-V curves. P-type MOS capacitors were able to retain the shape of the ideal C-V curve with only slight inversion due to the oxide charge. N-type MOS capacitors were also able to retain the CV curve shape, but with degradation due to interface states and lateral curve shift due to the oxide charge.

### Future Work:

In the future, we hope to replace Si with SiC or take the technology to another level by building high-power devices using SiC. Even with defects, we have proven that SiC can still provide power and efficiency in devices. We will continue to research and simulate SiC and further prepare it for high-power use.

### Acknowledgments:

I would like to thank Dr. Dieter Schroder and Xuan (Charlie) Yang for helping and guiding me throughout my research period. Thank you, Wei-Chieh Kao, for helping me organize the information we gathered concerning our studies. I would also like to thank Dr. Trevor Thornton and the staff of the Center for Solid State Electronics Research for use of lab equipment and assistance throughout the program. I would also like to thank the National Nanotechnology Infrastructure Network Research Experience for Undergraduates Program and the National Science Foundation for their help in funding my research.

### References:

[1] Neamen, A. D. Semiconductor Physics and Devices, Tata McGraw-Hill, NY, 746 p., 2003.

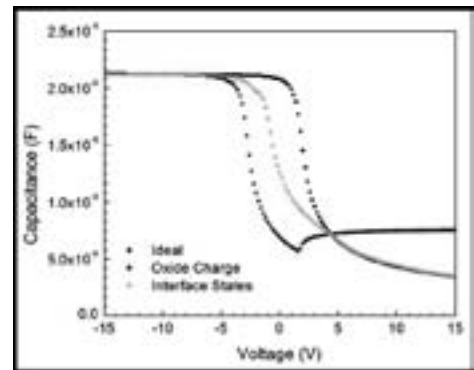


Figure 3: P-SiC results.

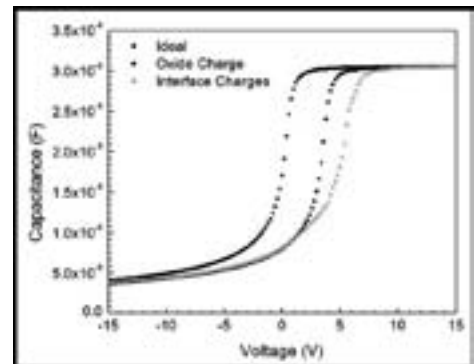


Figure 4: N-SiC results.

# Monolithic Integration of HEMT-Based Common Gate Oscillator with Active Integrated Antenna in the GaN Material System

**Kevin Huang**

**Engineering, Trinity College**

*NNIN iREU Site: Institut Für Bio- Und Nanosysteme (IBN), Forschungszentrum, Jülich, Germany*

*NNIN iREG Principal Investigator and Mentor: Dr. Martin Mikulics, Peter Grünberg Institut, Halbleiter-Nanoelektronik*

*Contact: kevin.huang.2012@trincoll.edu, m.mikulics@fz-juelich.de*

## Abstract and Introduction:

This project focused on the preparation of high electron mobility transistors (HEMTs) and the design of a HEMT-based, single-lithography-layer oscillator with active integrated antenna circuit with target oscillation frequencies up to 100 GHz. HEMT devices are well known for their suitability in high frequency microwave circuits, possibly for two reasons. Firstly, HEMTs offer high electron densities, high breakdown voltages and superior drain currents as well as transconductance, making the devices suitable for high power, high frequency application. Secondly, because of reduction in coulombic scattering and collisions, HEMT devices are known to display low-noise characteristics. These two factors combine make HEMTs amenable to nano-scale microwave oscillator design. Focus on reduction in device size is a growing demand and the prevalence of cellular phones, WiFi and other radio devices is increasing. Thus, the design of a low-cost, nano-scale microwave oscillating circuit is desirable. In this project, AlGaIn/GaN HEMTs were fabricated with recessed gates in order to enhance aspect ratio, transconductance, cutoff frequency and maximum frequency of oscillation [1].

## Methods:

This project can be divided into two main categories: HEMT fabrication and single-lithography-layer oscillator circuit design. In the former, AlGaIn/GaN HEMTs, consisting of undoped GaN buffer layer, AlN spacer layer and AlGaIn barrier layer, were grown on sapphire substrate. The device then underwent mesa isolation via argon sputtering techniques. Source/drain ohmic contacts were then patterned through a multilayered evaporation process in a Ti/Al/Ni/Au sequence [2]. After rapid thermal annealing, Schottky barrier Ni/Au gate contacts were placed using electron-beam lithography. Several series of HEMTs were fabricated with different gate lengths (100 nm, 300 nm, 500 nm) and source to drain spacings (3  $\mu\text{m}$ , 3.5  $\mu\text{m}$ , 4  $\mu\text{m}$ , 4.5  $\mu\text{m}$ , 5  $\mu\text{m}$ ). Argon dry etching was then used to create the recessed gate under the gate contact with recess depth of approximately 10 nm. For the oscillator design, the HEMT was the central device of interest. Thus, focus was given to HEMT fabrication and optimization regarding high frequency performance.

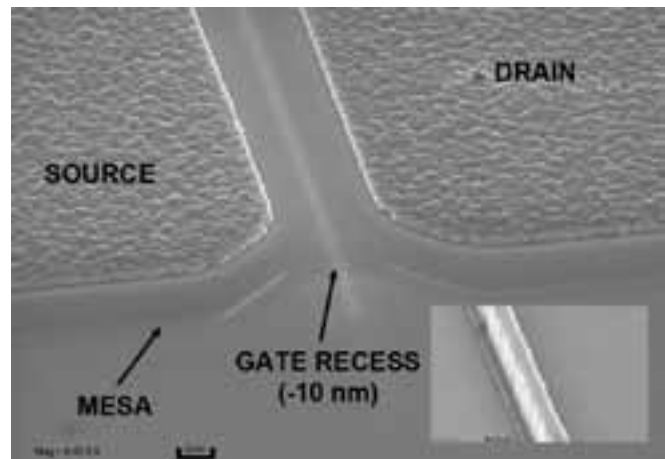


*Figure 1: SEM micrograph of HEMT structure with gate recess. Insert shows SEM micrograph of gate recess.*

Figure 1 shows a scanning electron microscope (SEM) image depicting an example of the HEMT structure without gate metallization: the mesa, patterned source/drain ohmic contacts, and the recessed gate structure. The inserted image shows an up-close SEM micrograph of the gate recess with gate metallization.

The second part of the project focused on the design of an oscillator and active integrated antenna with an oscillation frequency up to 100 GHz. A single-lithography-layer design is attractive because it can reduce manufacturing costs. To that end, a common gate oscillator circuit was selected for its simplicity and use of a voltage controlled transistor.

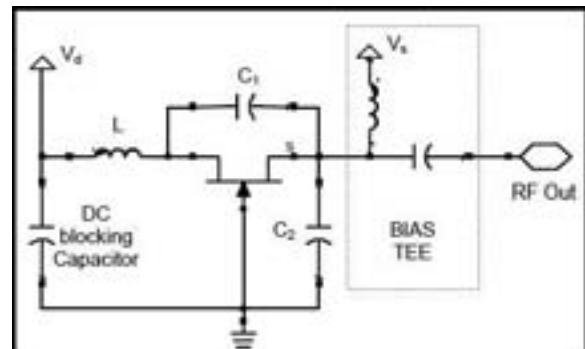


*Figure 2: Common-gate oscillator circuit schematic.*

Figure 2 shows the oscillator circuit schematic [3]. A circuit following this schematic was fabricated and tested successfully by Xu, et al., with gate-source bias of  $-5.3$  V and drain bias of  $20$  V [3]. The remaining discrete circuit elements in the oscillator schematic include inductors and capacitors that comprise the LC tank subcircuit, DC blocking and a bias tee. Meanderline and interdigital geometries were selected to achieve single-lithography-layer realization of inductors and capacitors respectively. First, the capacitors were designed based on previously obtained empirical results. C1 and C2 in Figure 2 were designed as interdigital capacitors with eight structural fingers, finger spacing of  $1$   $\mu\text{m}$ , finger width of  $200$  nm and overlap length of  $8$   $\mu\text{m}$ . This design yielded a capacitance of roughly  $2.7$  fF.

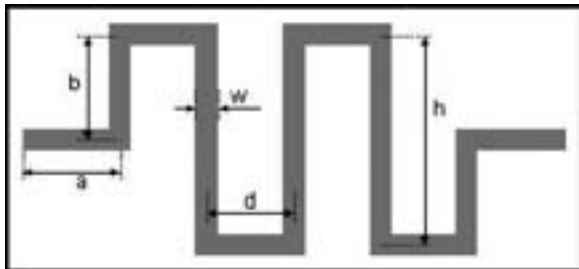


Figure 3: Meanderline inductor with characteristic dimensions.

Figure 3 shows a meanderline inductor with characteristic dimensions [4]. A five-turn meanderline inductor with  $a = 140$   $\mu\text{m}$ ,  $b = 160$   $\mu\text{m}$ ,  $d = 80$   $\mu\text{m}$ , and  $h = 320$   $\mu\text{m}$  and thickness of  $8$   $\mu\text{m}$  would yield an inductance of approximately  $1.5$  nH [5]. With these inductor and capacitor values, the tank circuit was calculated to oscillate at around  $111$  GHz.

The DC blocking capacitor was designed to achieve a capacitance approximately ten times that of C1, C2. To that end, the number of finger structures was increased to 24, and the overlap length was approximately  $24$   $\mu\text{m}$ , while maintaining the same finger spacing and finger width as C1 and C2, or  $1$   $\mu\text{m}$  and  $200$  nm respectively. The source bias tee structure was realized using a planar radial stub. More specifically, an oscillation frequency of  $111$  GHz of an electromagnetic wave yielded a wavelength,  $\lambda$ , of approximately  $2.68$  mm. A transmission stripline, orthogonal to the RF signal stripline, of length  $\lambda/4$  led to the radial stub. The stub angle was  $90^\circ$  with radius of  $\lambda/4$ .

Finally, for its wide-band characteristics, a simple bowtie antenna will be used as the integrated antenna element.

#### Future Work:

Future work includes arranging the described circuit elements for single-lithography-layer fabrication.

Furthermore, integration of coplanar waveguides for signal transmission is needed to improve signal quality and provide

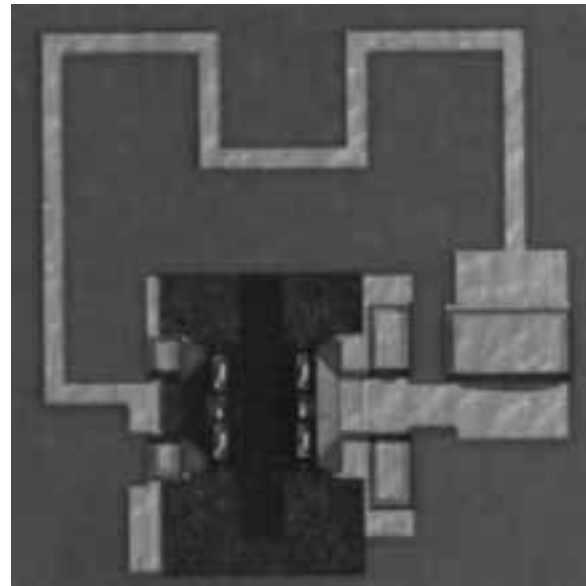


Figure 4: Example oscillator layout.

a better means to probe and inject signals. Figure 4 shows an example oscillator layout [3].

#### Acknowledgements:

This work was funded by the National Nanotechnology Infrastructure Network International Research Experience for Undergraduates (NNIN iREU) Program and was supported by the Forschungszentrum Jülich. All fabrication was performed in the Forschungszentrum Reinraum.

#### References:

- [1] M. Mikulics, A. Fox, M. Marso, D. Grützmacher, D. Donoval, and P. Kordos, "Electrical and Structural Characterization of AlGaIn/GaN FETs with Recessed Gate." *Vacuum* 86, 754-56 (2012).
- [2] M. Mikulics, et al., "Residual Strain in Recessed AlGaIn/GaN Heterostructure FETs Evaluated by Micro Photoluminescence Measurements." *Physica Status Solidi* 9, 911-14 (2012).
- [3] H. Xu, C. Sanabria, S. Heikman, S. Keller, U. K. Mishra, and R. A. York, "High Power GaN Oscillators Using Field-plated HEMT Structure." *Microwave Symp. Digest, 2005 IEEE MTT-S Int'l* (2005).
- [4] G. Stojanovic, L. Zivanov, and M. Damjanovic, "Compact Form of Expressions for Inductance Calculation of Meander Inductors." *Serbian Journal of Electrical Engineering* 1.3, 57-68 (2004).
- [5] G.W. Dahlmann, and E. M. Yeatman, "Microwave Characteristics of Meander Inductors Fabricated by 3D Self-assembly.: 8th IEEE International Symposium on High Performance Electron Devices for Microwave and Optoelectronic Applications, 128-33 (2000).

# Characterization of Phase Change Materials for Radio Frequency Applications

**Gwendolyn Hummel**

**Electrical Engineering, Illinois Institute of Technology**

*NNIN REU Site: Lurie Nanofabrication Facility, University of Michigan, Ann Arbor, MI*

*NNIN REU Principal Investigator: Professor Mina Rais-Zadeh, Electrical Engr. and Computer Science, University of Michigan*

*NNIN REU Mentor: Yonghyun Shim, Electrical Engineering and Computer Science, University of Michigan*

*Contact: gwendolyn.hummel@hotmail.com, minar@umich.edu, yhshim@umich.edu*

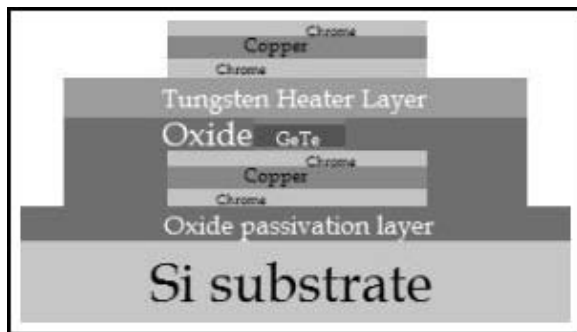


Figure 1: Cross-sectional schematic of device structure.

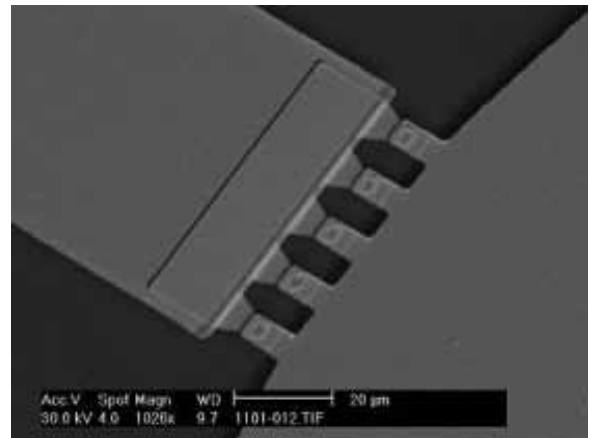


Figure 2: SEM image of a device with five  $2 \times 2 \mu\text{m}^2$  vias.

## Abstract:

Phase change materials are a class of compounds that can alter states between crystalline and amorphous when specific heating conditions are applied to them. Due to fast switching speed, long life cycles, and potential for high-density integration, these materials are currently being investigated for use in non-volatile memory applications [1, 2]. The focus of this project was to characterize a specific phase change material,  $\text{Ge}_{50}\text{Te}_{50}$ , to determine its possible capabilities for radio frequency (RF) applications. This material was chosen for use in RF switches due to its low crystalline state resistance and a high OFF/ON resistance ratio. The method of characterization was to fabricate simple ohmic switches and then apply voltages or currents with different pulse shapes and durations in order to obtain the phase transitions. The goals of this project were to optimize the switch design and fabrication method to achieve a low ON resistance and high OFF/ON resistance ratio, and to optimize the biasing conditions to obtain repeatable and reliable phase transitions. An extension of the project was investigating the effects of direct heating versus indirect heating. If the switches are successful, this material can be incorporated to design more advanced passive elements such as filters, phase shifters, and antennas.

## Introduction:

Previous work has been reported on the use of phase change materials from  $\text{GeSbTe}$  (GST) compounds in non-volatile memory applications. There has been a recent report on the application of  $\text{Ge}_{50}\text{Te}_{50}$  in switchable inductors [3].

The larger scope of this project included characterizing the  $\text{Ge}_{50}\text{Te}_{50}$  material using simple ohmic switches, then moving on to the characterization of more complicated designs, such as filters, to determine the overall use of the material in radio frequency applications.

The goals of this internship were to develop fabrication processes for implementing phase change switches (aka phase change vias). Materials in the stack were deliberately chosen, the specific thickness for the different layers was determined, and the etch times and recipes were optimized through fabrication of several test wafers and characterization steps. Once the optimal design was determined, the devices were fabricated and direct heating measurement techniques were employed to transition the vias.

### Experimental Procedure:

The switches were fabricated on silicon wafers. All liftoff molds and etch guides were created using photolithography. In order to isolate the devices from the silicon, wafers were passivated with a 2  $\mu\text{m}$  thick silicon dioxide layer deposited by plasma-enhanced chemical vapor deposition (PECVD). Then the bottom electrode was deposited in an evaporator. The bottom electrode consisted of three layers, 300  $\text{\AA}$  NiCr, 5000  $\text{\AA}$  Cu, and 300  $\text{\AA}$  NiCr. After liftoff, 3000  $\text{\AA}$  of oxide was deposited using PECVD, and then etched to form an insulation layer on top of the tips of the electrodes, with a via directly over the electrode. The 100 nm  $\text{Ge}_{50}\text{Te}_{50}$  layer, with 50  $\text{\AA}$  Ti adhesion layer and 100  $\text{\AA}$  Ti overcoat layer, was deposited on this via by sputtering.  $\text{Ge}_{50}\text{Te}_{50}$  liftoff was completed, and then a heater layer of 2500  $\text{\AA}$  of W was deposited using sputtering. Liftoff of the heater layer was completed, and then the top electrode was deposited. The top electrode also consisted of three layers, 200  $\text{\AA}$  NiCr, 3000  $\text{\AA}$  Cu, and 200  $\text{\AA}$  NiCr. After liftoff of the top electrode, the devices were complete.

Characterization results reported here were obtained using phase change vias with a tungsten layer in the stack, as discussed earlier. Repeatable phase transitions were obtained. The crystallization pulse was 200  $\mu\text{s}$  with a rise and fall time of 200  $\mu\text{s}$ , and amplitude of 1 V. The crystalline resistance was 100-300  $\Omega$ ; however, the resistance of the electrodes alone was measured to be around 75  $\Omega$ , yielding an ON resistance of  $\sim 30 \Omega$  for the phase change layer (see Figure 3). The pulse to amorphize was 2  $\mu\text{s}$  with a rise and fall time of 5 ns and amplitude of 2.5 V. However, the amorphization was easily obtained with several different pulses of different durations with amplitudes of 1.5 V or higher. The amorphous resistance was 800 k $\Omega$  -1 M $\Omega$  (see Figure 4).

While this OFF resistance is higher than previous work [1], and the OFF/ON resistance ratio is between  $10^4$  and  $10^5$ , the ON resistance could still be improved upon.

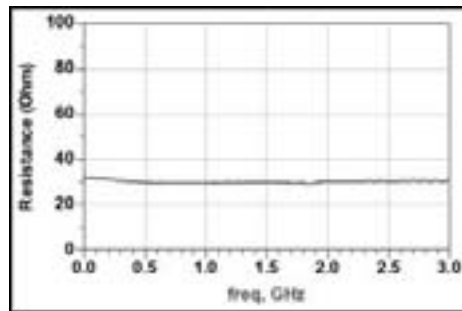


Figure 3: Crystalline resistance of the device shown in Figure 2.

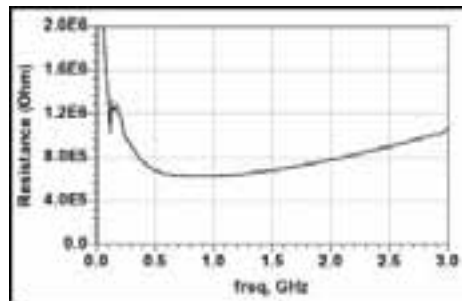


Figure 4: Amorphous resistance of the device shown in Figure 2.

Given these results,  $\text{Ge}_{50}\text{Te}_{50}$  has good potential for use in RF applications.

### Future Work:

While basic characterization of the material was completed during this internship, there remain many variations to be explored.

Further investigation could be conducted into the effect of various sputter pressures and powers on the  $\text{Ge}_{50}\text{Te}_{50}$  material. Different thicknesses of  $\text{Ge}_{50}\text{Te}_{50}$  for the via could have effects on the phase change conditions and should be further characterized. Also, the variations between direct and indirect heating should be examined.

This summer research has shown that  $\text{Ge}_{50}\text{Te}_{50}$  is a promising candidate for RF switching applications and can be used in tunable inductors, capacitors, and advanced devices such as antennas, phase shifters, and filters.

### Acknowledgements:

Thanks go to the National Nanotechnology Infrastructure Network Research Experience for Undergraduates Program and National Science Foundation for organization and funding; Professor Mina Rais-Zadeh and Yonghyun Shim for sponsoring this project; UMI coordinators for their work on the NNIN program; and the LNF staff for their training and guidance.

### References:

- [1] Lv, H., et al., "Electronic Properties of GST for non-volatile memory," *Microelectronics Journal* 37, (2006).
- [2] Ryu, Sang-ouk, "Characterization of  $\text{Ge}_{22}\text{Sb}_{22}\text{Te}_{56}$  and Sb-Excess  $\text{Ge}_{15}\text{Sb}_{47}\text{Te}_{38}$  Chalcogenide Thin Films for Phase-Change Memory Applications," *J. of Electronic Materials*, Volume 37, No. 4 (2008).
- [3] Wen, C., et al., "A Phase-change via-Reconfigurable On-Chip Inductor," *IEEE Electron Device Meeting*, 10.3.1 (2010).

## Fabrication and Characterization of Vertical Silicon Nanopillar Schottky Diodes

**Adam Overvig**

**Engineering Physics, Cornell University**

*NNIN REU Site: ASU NanoFab, Arizona State University, Tempe, AZ*

*NNIN REU Principal Investigators: Stephen Goodnick and Clarence Tracy, Electrical Engineering, Arizona State University*

*NNIN REU Mentor: Nishant Chandra, Electrical Engineering, Arizona State University*

*Contact: aovervig@comcast.net, stephen.goodnick@asu.edu, cjtracy@asu.edu, nchandr5@asu.edu*

### Introduction:

Schottky (rectifying metal-semiconductor) contacts have widespread use, particularly in high frequency [1] and high power electronic devices [2]. It is important that Schottky diodes be miniaturized to preserve their functionality as devices shrink to the nanoscale [3], for applications such as voltage clamping, rectification in switched-mode power supplies, and reverse current protection in photovoltaic systems [4]. Standing upright, nanopillars can access vertical dimension in device fabrication, which is recognized as an important step in maintaining and/or surpassing Moore's law [5]. Here, we present a low temperature (no thermal oxide required), top-down process for fabricating arrays of vertical n-type silicon nanopillar Schottky diodes that can be incorporated into planar complementary metal oxide semiconductor (CMOS)-integrated circuits. We also characterize our metal-semiconductor (nickel-silicon) contacts and note that they differ from planar diodes.

### Experimental Procedure:

A schematic representation of the fabrication process is shown in Figure 1. First, a hard mask of square-shaped  $\text{SiO}_2$  islands (side lengths of 40 to 100 nm) was formed in arrays with a 4  $\mu\text{m}$  pitch on an n-type ( $\sim 2 \times 10^{15} \text{ cm}^{-3}$ ) silicon (Si) substrate. This was done using electron beam lithography to expose arrays on a spin-coated 200 nm thick layer of 950K poly(methyl methacrylate) (PMMA). After developing the pattern at room temperature, roughly 50 nm of  $\text{SiO}_2$  was deposited with electron-beam evaporation. The excess resist was dissolved in acetone, lifting off the oxide layer except for the  $\text{SiO}_2$  islands.

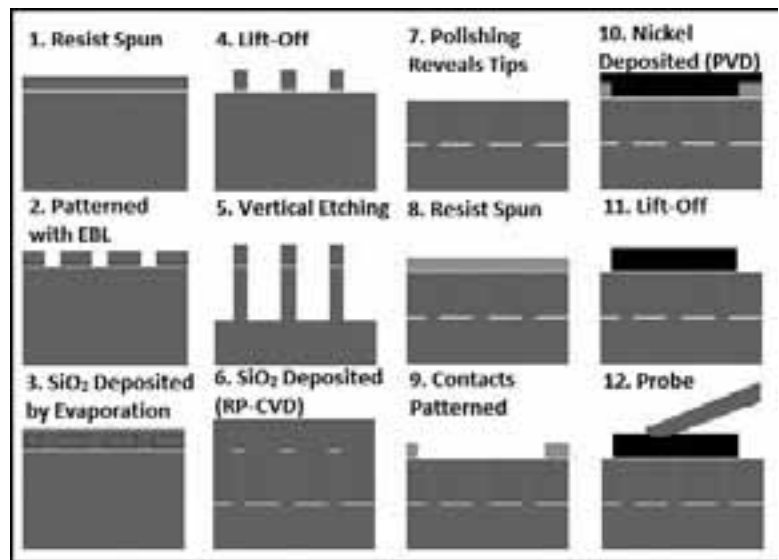


Figure 1: Schematic representation of fabrication process (not to scale).

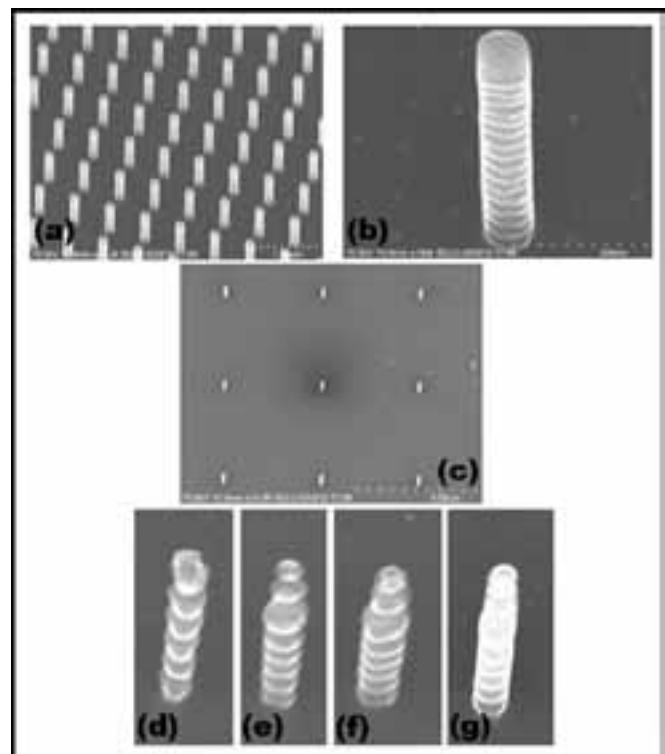


Figure 2: (a) SEM image of a 500 nm pitch array of 100 nm nanopillars after Bosch process using 4 sec etch, 2.5 sec deposition cycle. (b) Close-up of a 100 nm nanopillar in (a). (c) 4-micron pitch array of 100 nm diameter nanopillars obtained from using 8 sec etch, 5 sec deposition cycle. (d)-(g) Single nanopillars sized 40 nm, 60 nm, 80 nm, and 100 nm processed as in (c).

With this hard mask, nanopillars were formed with deep reactive-ion etching (RIE) making use of a Surface Technology Systems inductively coupled plasma (STS ICP) system. Employing what is known as the Bosch process, alternating modes of nearly anisotropic etching (using sulfur hexafluoride) and polymer deposition (using octafluorocyclobutane) produced vertical nanopillars approximately  $1\ \mu\text{m}$  tall.

Due to a small, unavoidable isotropic component in the etching mode, the nanopillar sidewalls were considerably scalloped. We were able to reduce the extent of scalloping by modifying the etching and deposition times during RIE. The resulting nanopillars are shown in Figure 2.

Finally, for support and electrical insulation, a conformal layer of  $\text{SiO}_2$  was deposited using remote plasma chemical vapor deposition (RP-CVD). Chemical-mechanical polishing (CMP) then partially removed this layer, revealing the Si tips. 100 nm of nickel was sputtered after another electron beam lithography step patterned the contact windows. Excess nickel was lifted-off by ultrasonic agitation in an acetone bath, and rapid thermal annealing (RTA) formed a nickel silicide-silicon contact, creating the Schottky effect.

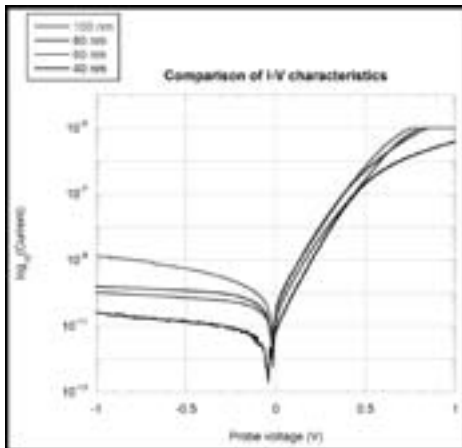


Figure 3: I-V characteristics of an array of 400 nanopillars of different diameters.

## Results and Conclusions:

The resulting diodes' current-voltage characteristics (Figure 3) were analyzed to extract the barrier height,  $\Phi_B$ ; the ideality factor,  $n$ ; and the series resistance,  $r_s$  in the thermionic current-voltage expressions (1) and (2):

$$I = I_s(\exp[q(V-Ir_s)/nkT]-1) \quad (1)$$

$$I_s = AA^*T^2\exp[-qV/kT] \quad (2)$$

Where  $q = 1.6 \times 10^{-19}\text{C}$ ,  $k = 1.381 \times 10^{-23}\text{J/K}$ ,  $T = 294\text{K}$ ,  $A$  is the diode contact area (assumed circular), and  $A^*$  is Richardson's constant,  $112\text{A/cm}^2\text{K}^2$  [6]. Typical values were 0.6 to 0.7eV for  $\Phi_B$ , 1.5 to 2.5 for  $n$ , and 10 to 100 k $\Omega$  for  $r_s$ . These results confirm Schottky behavior.

An unexpected outcome that differentiates these diodes from planar diodes was non-ideal current scaling with respect to both number of diodes and radius. For the former, a linear relation was expected since the diodes are probed in parallel, but not observed: current ratios between the 40, 160, 240 to the 400 pillar array were roughly 1%, 10%, and 15%, respectively, compared to the expected 10%, 40%, and 60%. For the latter, dependence on area (radius squared) was expected because the heights of the nanopillars are consistent, but the power was found to be about 1.2 instead of 2. This indicates a dependence on perimeter size, and hence the increased importance of surface states due to a higher surface area to volume ratio.

## Future Work:

Further research is needed to minimize scalloping to optimize nanopillar quality. The main parameter to be altered in this work should be the etch rate, in order to minimize the isotropy of the etching mode. Additionally, the non-ideal current scaling must be researched to be fully understood. One theory to account for this with respect to number of diodes is that a combination of inconsistent numbers of unintended "stray" nanopillars and faulty nanopillars are contacted with nickel, varying the actual amount probed from the assumed. Electron beam induced current (EBIC) is a method that could test this theory by illuminating the functioning diodes.

## Acknowledgements:

Thank you to my mentor, Nishant Chandra, and my PIs, Drs. Stephen Goodnick and Clarence Tracy, for their time and effort. Additionally, to the National Nanotechnology Infrastructure Network Research Experience for Undergraduates Program and the National Science Foundation for funding.

## References:

- [1] H.M. McGlothlin, D.T. Morissette, J.A. Cooper, and M.R. Melloch, "4 kV Silicon Carbide Schottky Diodes for High-Frequency Switching Applications," Device Research Conference Digest, 57th Annual, pp. 42-43, 1999.
- [2] S. Steinhoff, M. Reddig, and S. Knigge, "A New Generation of 600V GaAs Schottky Diodes for High Power Density PFC Applications," PCIM Conference, Nuremberg, Germany, 2005.
- [3] Q. Li, Y. Han, H. Min, and F. Zhou, "Fabrication and Modeling of Schottky Diode Integrated in Standard CMOS Process," White Papers Series, ed. 1, 2005.
- [4] B.L. Sharma, "Metal-Semiconductor Schottky Barrier Junctions and Their Applications," New York: Plenum, 1984.
- [5] G T. H. Lee, "A Vertical Leap for Microchips," Scientific American, vol. 286, pp. 52-59, 2002.
- [6] D.K. Schroder, "Semiconductor Material and Device Characterization," 2nd ed., John Wiley and Sons, Inc., 1998.

## Electrochemical Deposition of Polythiophene onto Carbon Nanotube Arrays

**Ryan Parry**

**Mechanical Engineering, North Carolina State University**

*NNIN REU Site: Nanotechnology Research Center, Georgia Institute of Technology, Atlanta, GA*

*NNIN REU Principal Investigator: Baratunde Cola, Mechanical Engineering, Georgia Institute of Technology*

*NNIN REU Mentor: Virendra Singh, Mechanical Engineering, Georgia Institute of Technology*

*Contact: rjparry@ncsu.edu, cola@gatech.edu, vsingh@gatech.edu*

### Introduction:

Each new generation of electronic products uses high-speed microchips that squeeze more transistors/power and performance into even smaller packages. This leads to excess heat generation within the semiconductor components, which causes the chip to fail over time. Heat sinks were added to help cool these chips. Heat sinks allow for the heat to dissipate from the chip to the heat sink to a cooler ambient, like air. When the heat sink and microchip were first put together, it was found that the two surfaces formed contact points and air gaps. Contact points are areas where the chip and the sink are connected together and heat can travel successfully from the chip to the sink. Air gaps are all the areas between the contact points where heat has trouble crossing from chip to sink. Since air is an insulator, the heat builds up on the chip at these air gaps and become hot spots, which lead to device failure.

Thermal interface materials (TIMs) were used to eliminate the air gaps within the component and consequently provide a path of heat removal from the component package surface through the heat sink and heat spreader. Therefore, TIMs are integral part of overall electronic product design. An ideal TIM will have both high thermal conductivity and the ability to conform to the surfaces well. These are two major characteristics that determine the total thermal interface resistance of different surfaces. In order to improve the life and performance of electronic devices, TIMs with improved thermal resistance are in urgent need.

Carbon nanotubes (CNTs) are being researched as a favorable TIM because of their high thermal conductivity. CNTs allow for vertically aligned columns to transfer the heat from the chip to the sink [1-4]. However, the poor adhesion of CNTs to the substrate limits their use as TIMs for high power devices. In order to improve the performance of CNT based TIMs, the problem of adhesion has to be addressed.

The goal of this current research was to develop a hybrid material that combined the high thermal conductivity of carbon nanotubes (CNTs) and exceptional mechanical compliance of polythiophene (Pth). We selected Pth as the polymer of choice as it is an electroactive polymer and can be deposited electrochemically. Additionally, Pth is thermally stable up to the device operating temperature.

### Experimental Procedure:

In a typical fabrication process, diced  $2 \times 3$  cm silicon wafers were cleaned extensively. Two different catalyst seed layers — 100 nm titanium (Ti) / 10 nm aluminum (Al) / 3 nm iron (Fe), and 40 nm silicon oxide ( $\text{SiO}_2$ ) / 10 nm nickel (Ni) — were deposited using a Denton Explorer e-beam evaporator. We used three minutes of low pressure chemical vapor deposition on the Ti/Al/Fe samples and 15 minutes of plasma-enhanced chemical vapor deposition on the  $\text{SiO}_2$ /Ni samples to induce CNT growth on the wafers using acetylene as precursor gas in a Black Magic PECVD reactor.

Finally, the CNT arrays were coated with Pth using three electrodes electrochemical deposition. The current was sent from the working electrode, the silicon wafer, to the

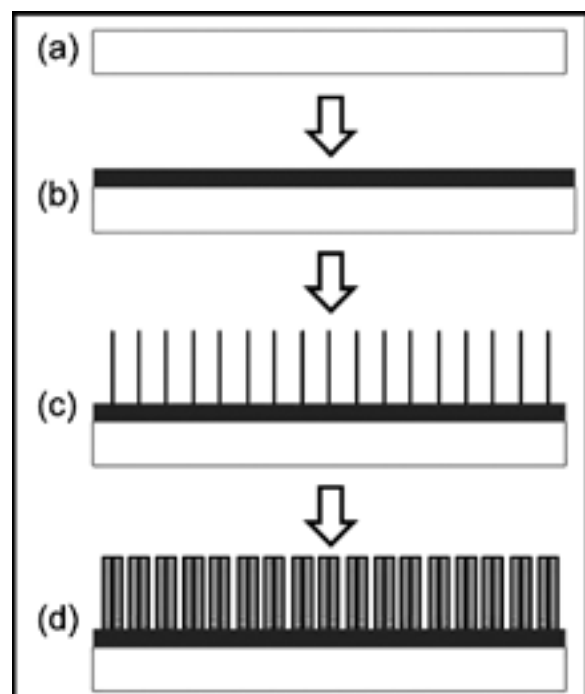


**Figure 1: Fabrication process. (a) Silicon wafers. (b) Deposition of catalyst layer. (c) CVD for CNT growth. (d) Pth electrodeposition.**

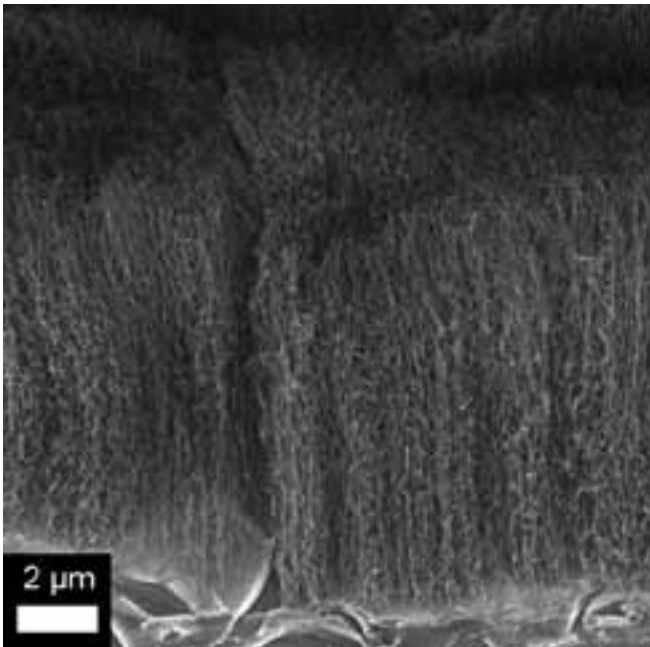


Figure 2: SEM image of Ti/Al/Fe CNT growth.

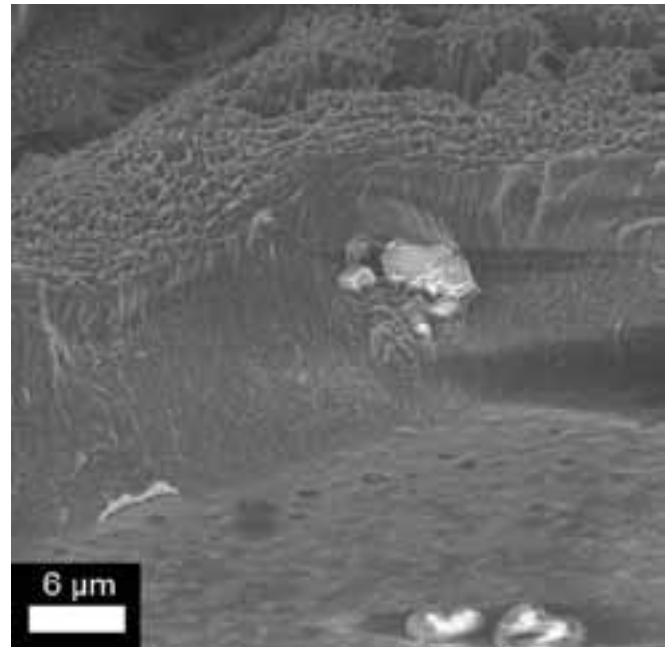


Figure 3: SEM image of Pth coating CNT arrays.

counter electrode, which was immersed in Pth solution, with the reference electrode measuring current. We used cyclic voltammetry to be able to control the amount of Pth coated on the CNTs and ran samples using 5, 10, and 15 cycles.

To evaluate the orientation, thickness, height, and density of the CNTs and Pth coating on CNTs, we used a scanning electron microscope (SEM). A typical fabrication procedure is outlined in Figure 1.

### Results and Conclusions:

After CVD, we found that the Ti/Al/Fe catalyst layer produced the desired CNT arrays, and we used this catalyst layer for further experiments. As shown in Figure 2, the vertically aligned arrays measuring about 10-12 μm tall and a density of about  $2 \times 10^{-7} \text{cm}^2$  was obtained in a typical LPCVD recipe with a three minute growth time.

The CNT arrays were successfully coated with Pth through electrochemical deposition using cyclic voltammetry (Figure 3). However, we were only able to coat a thick layer of Pth on top of the CNTs and further modification of electrochemical process is required to achieve a conformable coating.

### Future Work:

Future research will involve quantifying how much Pth is deposited per cycle during deposition. This will allow us to control coating with the amount of cycles. In addition, we need to determine how to coat the individual CNTs and not just the whole array. Using a photoacoustic technique, we plan

to measure the thermal resistance for our hybrid structures to compare to other TIMs. Additionally, we will run adhesion and electrical/thermal conductivity tests in order to ensure our TIM will adhere to the surfaces as predicted, without affecting the thermal performance. The long-term plan is to develop this material into an effective Thermal Interface Material that can be used in electronics to improve current technology and increase the life-span of electronics.

### Acknowledgements:

I'd like to thank my Principal Investigator, Dr. Baratunde Cola, and my mentor, Dr. Virendra Singh, for their help with my research, and the opportunity to conduct it at Georgia Tech. I'd also like to thank the Georgia Tech IEN coordinators Leslie O'Neill and Nancy Healy. Thank you to the NEST group for their lab facilities and help. Finally, I'd like to thank the National Nanotechnology Infrastructure Network Research Experience for Undergraduates (NNIN REU) Program and the National Science Foundation (NSF) for their help and funding.

### References:

- [1] B. A. Cola, ITEM™, 10 (2010).
- [2] W. Lin, C. Wong, Nano-Bio-Electronic, Photonic and MEMS Packaging, 87 (2009).
- [3] J. Liu, Y. Fu, T. Wang. (IEEE, 2008), pp. 1-7.
- [4] B. A. Cola, P. B. Amama, X. Xu, T. S. Fisher, Journal of Heat Transfer 130, 114503 (2008).

# Understanding Performance Limitations in Organic Transistors

**William Scheideler**

**Biomedical Engineering, Electrical Engineering, Duke University**

*NNIN iREU Site: National Institute for Materials Science (NIMS), Tsukuba, Ibaraki, Japan*

*NNIN iREU Principal Investigator: Dr. Kazuhito Tsukagoshi, International Center for Materials Nanoarchitectonics, National Institute for Materials Science*

*NNIN iREU Mentor: Dr. Yong Xu, International Center for Materials Nanoarchitectonics, NIMS*

*Contact: will.scheideler@duke.edu, tsukagoshi.kazuhito@nims.go.jp, xuyong.hn@gmail.com*

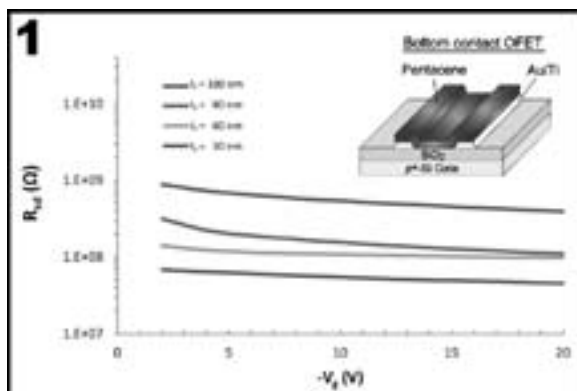


Figure 1: Contact resistance for varying pentacene thickness in TC OFETs (inset).

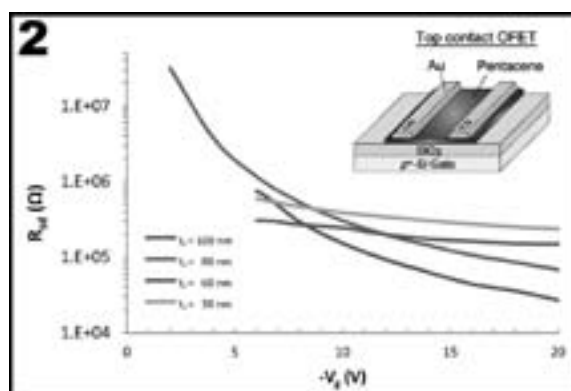


Figure 2: Contact resistance for varying contact thicknesses in BC OFETs (inset).

## Introduction:

Organic field-effect transistors (OFET) are critical components of many prospective organic electronic products [1], but their performance is limited by poor charge injection and weak charge transport, manifesting as high contact resistance and low mobility. The goal of this work was to understand performance limitations in pentacene-based OFETs by varying device architecture and processing to empirically demonstrate optimal design parameters.

## Experimental Methods:

Pentacene OFETs of top/bottom-contact (TC/BC) and bottom-gate (BG) configuration were fabricated (Figures 1 and 2). BC devices suffer from contact effects because molecular self-organization is disrupted, resulting in poor film morphology near the contacts. Small charge injection area ( $\sim$  contact thickness) is also believed to limit performance in BC OFETs. In this study, BC devices with various contact thicknesses were fabricated to explore both issues. Compared to BC OFETs, TC OFETs perform better, demonstrating lower contact resistance and higher mobility. The OSC film is not disturbed by contact deposition and, furthermore, TC OFETs have larger charge injection area as the entire contact surface contributes to injection. However, in TC OFETs, charge carriers must cross the entire OSC film to reach the channel, causing high access resistance. Meanwhile, large numbers of traps limit charge transport. So, TC devices with

different pentacene film thicknesses and diverse dielectric treatments were fabricated to understand contact resistance and trap origins.

Current-voltage (I-V) characterization and low-frequency noise (LFN) measurements were performed in ambient conditions. The contact resistance ( $R_{sd}$ ) was evaluated by the modified transfer length method [3] with devices having different channel lengths. Intrinsic low-field mobility ( $\mu_0$ ) was extracted via the Y-Function method [4]. Normalized power spectral density of drain current fluctuations at  $f = 20$  Hz were plotted against drain current to identify noise mechanisms. The normalized noise spectra were accurately modeled by carrier number fluctuations induced by charge trapping/detrapping and, thus, a surface equivalent trap density ( $N_{ST}$ ) was extracted.

## Results and Discussions:

The  $R_{sd}$  of BC OFETs is depicted in Figure 1 as a function of gate voltage ( $V_G$ ). Surprisingly,  $R_{sd}$  increased with contact thickness, contrary to the expectation that charge injection should be enhanced by greater charge injection area. Our results indicated this enhancement was negligible and the small grain contact region played a dominant role. Thicker contacts produced a steeper edge profile, causing poorer molecular packing. Charge injection was limited by this

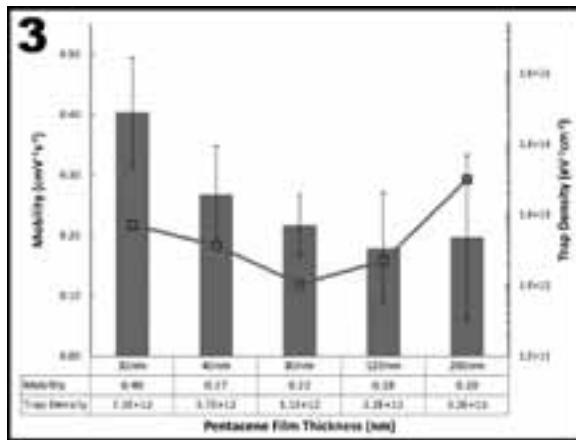


Figure 3: Intrinsic mobility (left axis) and trap density (right axis) for several pentacene thicknesses.

highly resistive zone, yielding high contact resistance and reduced mobility.

Figure 2 illustrates the  $R_{sd}$  in TC OFETs with various pentacene film thicknesses ( $t_{sc}$ ). Simulations showed that  $R_{sd}$  increased drastically with  $t_{sc}$  as VG dependence weakened [2]. The former was due to longer vertical transport required in thicker films, and the latter was from weaker charge concentration modulation by  $V_G$ .

The present results qualitatively match simulations, but the range of magnitudes spanned is much smaller. This non-ideality is likely because of contact metal (Au) diffusion into the pentacene film, which may make the actual  $t_{sc}$  smaller than the nominal thickness. Future experiments will address this by alternative fabrication techniques such as contact lamination.

Besides determining charge injection,  $t_{sc}$  affects charge transport in the channel. In Figure 3, mobility  $\mu_0$  decreased with  $t_{sc}$ . To understand this, the trap density ( $N_{ST}$ ) by LFN was plotted against  $t_{sc}$  in Figure 3, showing an inverse trend to that of mobility. High  $N_{ST}$  in the film might be due to poor film quality and interfacial traps. This agreed with the understanding that thicker grain boundaries will produce more deep traps. Indeed, the nearly proportional dependence of  $N_{ST}$  on  $t_{sc}$  implied uniformly distributed traps within the OSC bulk.

It appears mobility variation was not strictly due to charge trapping. One possible interpretation is limited charge injection in thicker films, as charge must traverse the contact region mainly by hopping. Since the contact provided insufficient charge to the channel, the apparent mobility was limited.

The OSC/dielectric interface is crucial to transport. Figure 4 illustrates the mobility and the surface state density ( $N_{SS}$ , deduced by sub-threshold swing) in TC devices with different treatments of the SiO<sub>2</sub> dielectric. PMMA and PhTS-SAM gave the comparably highest mobility and untreated SiO<sub>2</sub> had lower

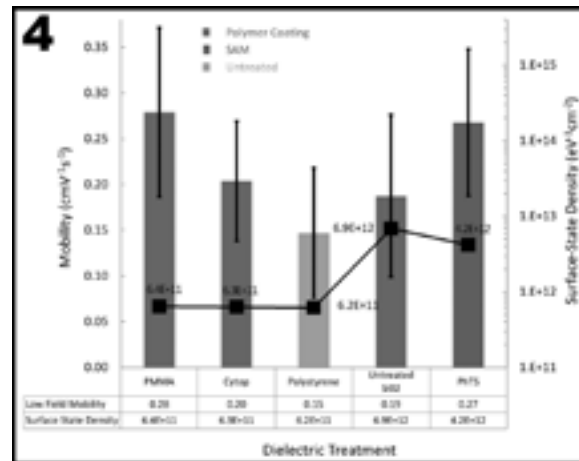


Figure 4: Intrinsic mobility and surface-state density for several dielectric treatments.

mobility, as expected. The small  $N_{SS}$  for polymer treatments (Cytos, PMMA, and polystyrene) showed high interface quality, probably due to the similar material properties between pentacene and polymeric dielectric treatments. Strikingly, a high  $N_{SS}$  was obtained for PhTS-SAM treatment though SAM layers typically improved mobility. Untreated SiO<sub>2</sub> showed the largest  $N_{SS}$ , presumably from charge trapping hydroxyl groups.

The  $N_{ST}$  by LFN indicates pentacene film quality also strongly depends on dielectric, providing additional explanation for the mobility variation. The  $N_{ST}$  in untreated SiO<sub>2</sub> was the largest, followed by PhTS-SAM. Approximately an order of magnitude lower  $N_{ST}$  obtained in PMMA treated devices indicated a higher quality pentacene film.

## Conclusions:

Fabrication and measurement of pentacene-based OFETs with varying device architectures and processing methods enabled deeper understanding of OFET performance limitations. Choosing a proper contact thickness that preserves the film morphology is critical to optimizing charge injection in BC OFETs. For TC OFETs, a thin but a high quality OSC film is key to strong charge injection in the contact and efficient charge transport in the channel. In addition, polymeric dielectrics improved OSC film quality and reduced the interface traps. Future efforts will examine a larger parametric range of device parameters to better understand trends in trap density and contact resistance as well as define changes in the film morphology.

## Acknowledgements:

Dr. Yong Xu, Tsukagoshi-sensei, NNIN iREU, NSF, NIMS.

## References:

- [1] Miyata, Yasuo, et al.; J. Mater Chem, 22, 7715 (2012).
- [2] Xu, Yong, et al.; AFM, (Submitted).
- [3] Xu, Yong, et al.; APL, 97, 6 (2010).
- [4] Xu, Yong, et al.; JAP, 107, 114507 (2010).

# Spin Torque Ferromagnetic Resonance with the Spin Hall Effect

**Oliver Switzer**

**Applied Physics, Bard College**

*NNIN REU Site: Cornell NanoScale Science and Technology Facility (CNF), Cornell University, Ithaca, NY*

*NNIN REU Principal Investigator: Daniel Ralph, CNF/CCMR, Cornell University*

*NNIN REU Mentors: Wan Li and Eugenia Tam, Cornell Center for Materials Research (CCMR), Cornell University*

*Contact: oliverswitzer@gmail.com, ralph@ccmr.cornell.edu, est27@cornell.edu, wl285@cornell.edu*

## Abstract:

The goal of this REU project was to measure the film thickness dependence of spin-torque ferromagnetic resonance (ST-FMR) induced by the spin Hall effect. The spin Hall effect occurs when a current is sent through a conducting, nonmagnetic material, and spin-up and spin-down electrons are separated on either side of the material. This creates what is called a spin current, transverse to the electron current. In this research, the spin Hall effect was used as a source for spin injection in a nonmagnetic, conducting metal to create magnetic precession in an adjacent ferromagnetic film. The purpose of these experiments was to help achieve a better understanding of the spin Hall effect in various materials and the dynamics of spin Hall induced ST-FMR. Photolithography, ion milling and sputter deposition were used to define bilayer structures with contact pads. With these devices, we measured the ferromagnetic resonance signal to quantitatively determine the spin current injection and spin Hall angle.

## Introduction:

Spin transfer by the spin Hall effect has already been demonstrated in research performed by both the Ralph and Buhrman groups at Cornell. Past experiments in the area of spin manipulation have used magnetic materials in order to create spin current and to inject spin angular momentum into ferromagnetic materials. What is unique about this project is that we used the spin Hall effect in a nonmagnetic material to

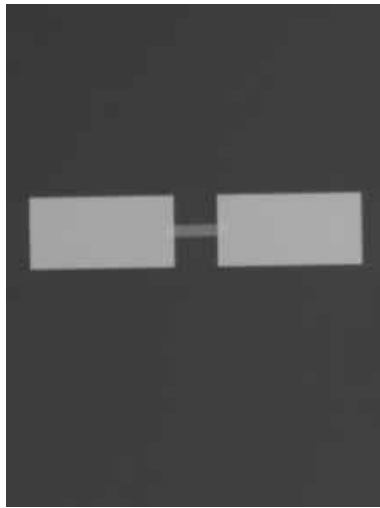


*Figure 1: An image of the bilayer device between to copper contacts.*

create this spin current, which is more energy efficient and a novel way of doing spin manipulation.

## Experimental Procedure:

There were several steps to the fabrication process for the spin torque device. The first step involved sputtering different thicknesses of permalloy (Py) for each device made (varying from about 4 nm to 7 nm for four different devices) and then 3 nm of platinum (Pt). We did our first lithography step to define the basic device structure with ion milling. After this, a second lithography step is done to deposit the contact metals of Ti, Cu and Au onto the surface using e-beam evaporation.

Figure 1 shows an actual device upon which we did our measurements. Figure 2 demonstrates what was happening in the device during the measurement process. The incoming radio frequency current is indicated by  $I_{RF}$ . The colored arrows indicate two different torque vectors that were acting on the magnetic moment of the Py; the blue vector represents the torque associated with the Oersted field of the  $I_{RF}$ , and the red represents the torque associated with the spin transfer from the SHE. The result of these two torques was an oscillation of the magnetic moment of the Py.

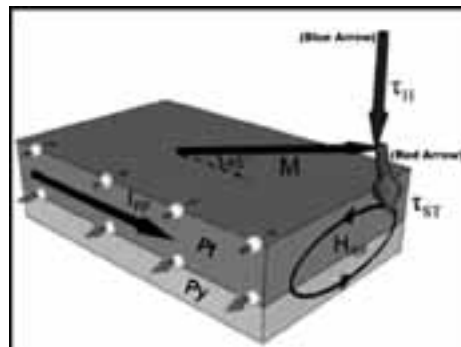


*Figure 2: An illustration of what is happening in the device during the measurement process [1].*

For the ferromagnetic resonance (FMR) measurement set up of our device, a signal generator created a radio frequency voltage across the spin Hall metal. The output was a DC voltage that gave the resonance signal.

We exposed the sample to a scanning magnetic field. A resonance peak was then induced at a certain magnetic field, which was read via the DC voltage signal out, as shown in Figure 3. This process was performed for only three out of four of the different device thicknesses, as the 7 nm sample returned high resistivity readings and very noisy resonance data. This could have been due to any number of errors in the fabrication process, including particulates or resist residue being on the sample before depositing contacts.

The curve was fit to an equation (3) from Liu, et al. [2].

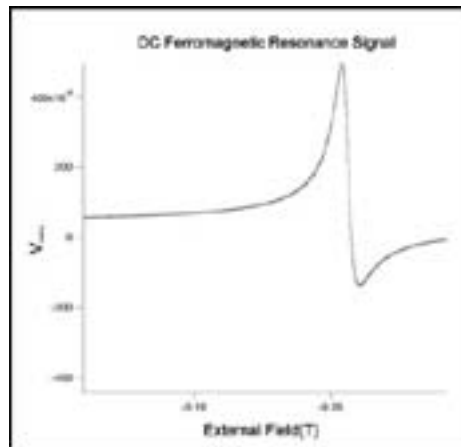


Figure 3: Represents the resonance curve, fit to an equation from Liu, et al. [2].

### Results and Conclusions:

We calculated the spin Hall angle for each device fabricated by decomposing the resonance signal we found from ferromagnetic resonance measurements. Using non-linear graph fitting with the aforementioned equation, we split the resonance signal into its asymmetric component, which represented Spin Transfer, and its anti-symmetric component, which represented the Oersted field from the current. We then took the ratio of these two separate signals to find the spin Hall angle of each device for different thicknesses. Figure 4 represents the correlated data that we found.

Ultimately a positive correlation between spin Hall angle and ferromagnetic layer thickness was found, as shown in Figure 4. There were a couple of issues with the data collected however. The first problem was that the spin Hall angle found for every device was much lower than expected, with the highest value recorded at 0.034, whereas previous spin Hall measurements have shown a spin Hall angle for platinum

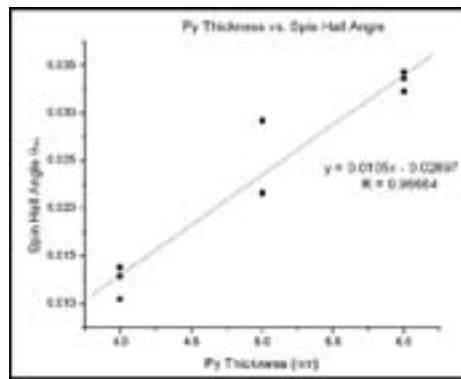


Figure 4: The correlated data after fitting and spin Hall angle calculations.

as large as 0.07 [2]. This was likely due to the fact the demagnetization constant  $M_{eff}$  was not measured for each device.

It is believed that this correction could eliminate the positive correlation in the data and return no change in the spin Hall angle for varying thickness. Further measurements are necessary to determine these values.

### Future Work:

If this positive correlation between ferromagnetic thickness and the spin Hall angle remains correct after parameter corrections, it will likely motivate further investigation into thickness dependence of the spin Hall angle.

### Acknowledgments:

My thanks goes to the National Science Foundation, the National Nanotechnology Infrastructure Network Research Experience for Undergraduates (NNIN REU) Program, the Cornell NanoScale Science and Technology Facility, my PI Dan Ralph, my mentors Wan Li and Eugenia Wan, and my CNF REU Program Coordinator Melanie-Claire Mallison for making this research possible.

### References:

- [1] Luqiao Liu, Chi-Feng Pai, Y. Li, H. W. Tseng, D. C. Ralph, and R. A. Buhrman, Science 336, 555-558 (2012).
- [2] Luqiao Liu, Takahiro Moriyama, D. C. Ralph, and R. A. Buhrman, Phys. Rev. Lett. 106, 036601 (2011).

## Self Assembled Monolayers on Inkjet-Printed ITO

**Ashley Truxal**

**Chemistry, Temple University**

*NNIN REU Site: Lurie Nanofabrication Facility, University of Michigan, Ann Arbor, MI*  
*NNIN REU Principal Investigator: Dr. Rebecca Lorenz Peterson, Electrical Engineering and Computer Science Department (EECS), University of Michigan, Ann Arbor*  
*NNIN REU Mentor: Wenbing Hu, EECS, University of Michigan, Ann Arbor*  
*Contact: ashley.truxal@temple.edu, blpeters@umich.edu, wbhu@umich.edu*

### Abstract and Introduction:

Ink-jet printing allows for cost efficient roll-to-roll manufacture of thin-film transistors (TFTs) over large areas, enabling next-generation transparent displays, touch panels, opto-electronics, and radio frequency identification [1-4].

TFT conductance and cutoff frequency scale inversely with gate length. However sub-micron gate lengths are incompatible with traditional printing techniques, which have  $\sim 20 \mu\text{m}$  resolution [5]. New methods have been investigated to make sub-micron gate length organic TFTs without advanced photolithography [4].

Here, we expanded that approach to treat inkjet-printed indium tin oxide (ITO) electrodes with hydrophobic octadecyltrichlorosilane (OTS) self-assembled monolayers (SAMs) to repel away a second printed ITO electrode, yielding sub-micron electrode gaps. By combining this process with a solution-processed semiconductor, a cost-effective short channel TFT can be made. In this project, we refined inkjet printing of ITO nanoparticle ink to obtain uniform printed ITO patterns, which were annealed to minimize sheet resistance. We used OTS to selectively manipulate the wettability of printed ITO versus various substrates. The effect of SAMs was quantified by contact angle measurements.

Preliminary experiments show that it may be possible to use this process to fabricate narrow gaps between ITO electrodes.

### Experimental Procedure:

A carbon-water ink was used to optimize printing parameters on a DMP-2800 Series Dimatix Inkjet printer (Fujifilm, Santa Clara, CA). An aqueous ITO nanoparticle (NP) dispersion with 18% wt ITO ( $\text{In}_2\text{O}_3$  and  $\text{SnO}_2$ ) and an average particle size of 18 nm (US Research Nanomaterials, Houston, TX) was printed on sodalime glass,  $\text{SiO}_2$ ,  $\text{Si}_3\text{N}_4$ , and Parylene-C substrates. To optimize printed ITO resistance, 2 mm  $\times$  0.1 mm one-layer printed ITO patterns on glass were rapid thermal annealed (RTA) on a JetFirst 150 RTP for four minutes at temperatures of 400-600°C in  $\text{O}_2$ ,  $\text{N}_2$ , or  $\text{N}_2:\text{O}_2$  4:1. Resistance measurements were performed using applied voltages from -5V to 5V.

Selected samples were treated with a 0.2% OTS/toluene solution for 20-25 minutes followed by sequential rinsing in toluene, acetone and isopropanol. Measurements of advancing contact angle were made with a VCA Optima series contact angle instrument (AST Products, Inc., Billerica, MA).

### Results and Discussion:

The printing waveform was optimized to obtain uniform ITO lines with 150 nm thickness per printed layer by tuning

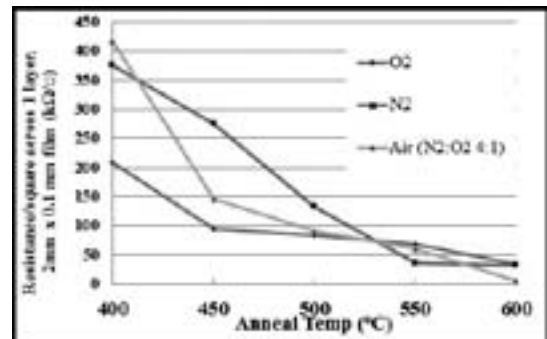


Figure 1: Printed ITO sheet resistance vs. temperature of 4-min RTA in various ambient environments.

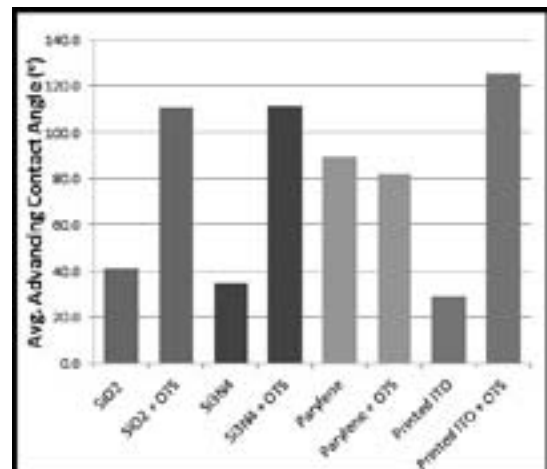


Figure 2: Contact angle of water on ITO and other substrates before and after OTS-SAM treatment.

the following parameters: firing voltages of 16-25V, firing frequency of 1-2 kHz, drop spacing of 18-20  $\mu\text{m}$  and printing height of 0.5-0.75 mm. Post-printing RTA was optimized to minimize ITO resistance: four minutes at 600°C in 4:1  $\text{N}_2:\text{O}_2$  (air) yielded the lowest average sheet resistance of 6.1  $\text{k}\Omega/\square$  for one-layer printed patterns (Figure 1).

Advancing contact angles of water on various substrates with and without OTS treatment were measured (Figure 2). For  $\text{SiO}_2$  and ITO samples, contact angle increased upon OTS treatment due to OTS reaction with surface hydroxyl groups. ITO's change from relatively hydrophilic (52.77°) to notably hydrophobic (106.26°), indicates that OTS forms a SAM on ITO. The contact angle changed least for Parylene-C (88.9° before and 81.73° after OTS treatment), due its lack of a hydroxyl-terminated surface.

Selective wetting was observed between dropcast ITO and parylene after OTS treatment: the parylene could still be wetted, while the ITO film was so hydrophobic that water droplets would not leave a dispensing syringe when in contact with the ITO (Figure 3). In contrast to parylene, OTS-treatment of nitride increased its hydrophobicity, but it still remained more hydrophilic than OTS-treated ITO. Therefore, selective wetting similar to that on parylene was observed on OTS-coated ITO on nitride.

To explore the ability of OTS to define small gaps between ITO electrodes, we printed ITO patterns onto nitride substrates, annealed at 600°C for 4 min in 4:1  $\text{N}_2:\text{O}_2$ , treated with OTS, and dropcast ITO ink. In some areas, dropcast ITO preferred nitride surfaces, however other ITO drops overlapped with OTS-treated printed ITO (Figure 4).

It is likely that the ITO drops were too large in volume to allow for very small-scale hydrophobic interactions to dominate. More investigation is needed to refine the selective wetting process.

## Conclusions:

Inkjet printing and annealing of aqueous ITO NP inks was refined to obtain neatly patterned ITO films of thickness  $\sim 150$  nm/layer, with minimum sheet resistance of 6.1  $\text{k}\Omega/\square$ . Contact angle measurements before and after OTS-SAM treatment show greater increase in hydrophobicity of printed ITO lines compared to substrates such as parylene and silicon nitride. We use this effect to achieve selective de-wetting of secondary ITO ink drops off previously printed ITO lines onto parylene or nitride surfaces. Preliminary results indicate that it may be possible to use such selective wetting processes to achieve sub-micron scale ITO electrode gaps, for high-performance thin film transistors fabricated by inkjet printing.

## Acknowledgements:

This project was supported by the NSF's NNIN REU Program, by NSF BRIGE Award #ECCS1032538, and was done at the University of Michigan's Lurie Nanofabrication

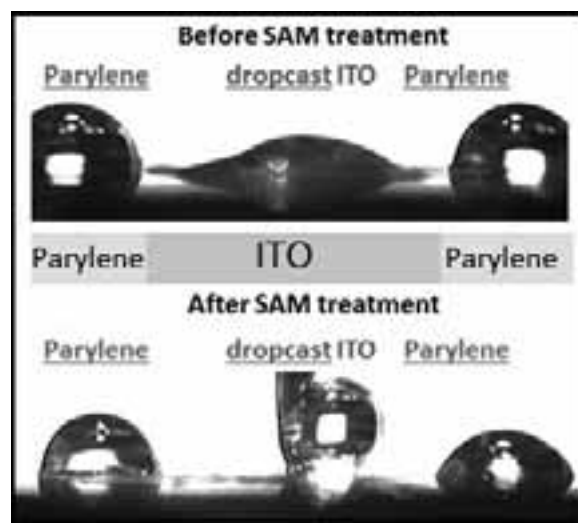


Figure 3: Water wetting on dropcast ITO and parylene before and after OTS-SAM treatment.

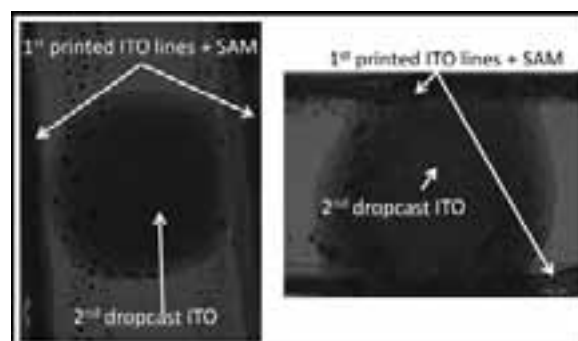


Figure 4: Different samples showing repelling (left) and overlap (right) of ITO dropcast on printed, annealed and OTS-treated ITO patterns.

Facility, an NNIN site. We thank Dr. Xiaogan Liang, Sungjin Wi, Dr. Pilar Herrera-Fierro, and Mykola Kravchenko for their assistance.

## References:

- [1] Kim A., Song, K., Kim, Y., Moon, J.; "All solution-processed, fully transparent resistive memory devices"; ACS Appl. Mat. Interfaces, 3, 4525-4530 (2011).
- [2] Hong, S.J., Kim, J.W., Han, J.I.; "Improvement of electrical properties of printed ITO thin films by heat-treatment conditions"; Current Applied Physics, 11, S202-S205 (2011).
- [3] Noh, Y.Y., Zhao, N., Caironi, M., Sirringhaus, H.; "Downscaling of self-aligned, all-printed polymer thin film transistors"; Nature Nanotechnology, 2, 784-789 (2007).
- [4] Sele, C.W., von Werne, T., Friend, R.H., Sirringhaus, H.; "Lithography-free, self-aligned inkjet printing with sub-hundred nanometer resolution"; Adv. Mater., 17, 997-1001 (2005).
- [5] Zhao, N., Chiesa, M., Sirringhaus, H., Li, Y., Wu, Y., Ong, B.; "Self-aligned inkjet printing of highly conducting gold electrodes with submicron resolution"; J. of Applied Physics, 101, 064513 (2007).

# Fabrication of GaAs-Based Integrated Circuits by Advanced Nanofabrication Techniques

**Daryl Vulis**

**Electrical Engineering, Stony Brook University**

*NNIN iREU Site: National Institute for Materials Science (NIMS), Tsukuba, Ibaraki, Japan*

*NNIN REU Principal Investigator: Dr. Yasuo Koide, National Institute for Materials Science, Tsukuba, Japan*

*NNIN REU Mentors: Dr. Eiichiro Watanabe and Dr. Daiju Tsuya, National Institute for Materials Science, Tsukuba, Japan*

*Contact: daryl.vulis@stonybrook.edu, koide.yasuo@nims.go.jp, watanabe.eiichiro@nims.go.jp, tsuya.daiju@nims.go.jp*

## Abstract:

Gallium arsenide (GaAs), a III-V semiconductor, has recently gained attention due to promising applications in wireless technologies that include power amplifiers and integration of switches for use of different frequency bands. The relatively high electron mobility, lower high frequency noise, and lower parasitic capacitances of GaAs in comparison to silicon make GaAs a suitable choice for high frequency integrated circuits.

This project focused on the creation of three GaAs integrated circuit (GaAs-IC) devices — specifically the: 1) Metal-semiconductor field effect transistor (MESFET), 2) Logic Inverter, and 3) Ring Oscillator — with each subsequent device employing the previous device as a base component. The Schottky barrier intrinsic to the MESFET made it difficult to achieve the necessary positive threshold voltage for creating a functional ring oscillator. Using industrial level design, fabrication, characterization, and analysis techniques, all three devices were ultimately created and the functional ring oscillator achieved an operating frequency of 19.9 MHz — a value comparable to predicted values.

## Approach:

One cycle of the project involved the computer automated design of a new sample (including several devices), followed by fabrication in a cleanroom environment. The devices were then characterized using the manual prober system. Data was analyzed using MATLAB.

## Methods:

**Preparation of GaAs Substrate.** The GaAs substrate used; 1) an n-type GaAs active layer ( $N_D = 3 \times 10^{16}$ ) with an initial thickness of 500 nm on, 2) a semi-insulating GaAs. The GaAs wafer was first cut to the appropriate size. Thinner active layers correspond to higher threshold voltages, so the sample was then etched with  $H_3PO_4 : H_2O_2 : H_2O = 1 : 1 : 50$  to achieve a depth ranging from 100 nm to 500 nm.

**Mesa Fabrication.** The sample was coated with primer (HMDS), then photoresist (AZP4620 : PGMEA = 3 : 1). Samples were exposed to the Mesa pattern using the DL-1000 laser lithography system and hand developed in 2.38%

tetramethylammonium hydroxide (TMAH). A postbake at 140°C prepared the sample for a second etching process that electrically isolated the samples. The photoresist was removed with N-methyl-2-pyrrolidone (NMP).

**Source and Drain Electrode Fabrication.** The sample was coated with primer (HMDS), then two photoresists (PGMI and TSMR8800). Samples were then exposed and developed. Au-Ge/Ni/Au = 1500A/100A/1500A was deposited by the R-DEC e-gun evaporation system. The resist and excess metal was lifted off with NMP. The sample was then annealed at 400°C to prepare the sample for a second etching process that electrically isolated the samples. The photoresist was removed with N-methyl-2-pyrrolidone (NMP).

**Gate Electrode Fabrication.** The sample was coated with primer (HMDS), then two photoresists (LOR5A and AZ5214E). Samples were then exposed and developed. Ti/Au = 2000A/2000A was deposited by the ULVAC jsputter sputtering system. The resist and excess metal was lifted off with NMP.

A completed ring oscillator device is shown in Figure 1.

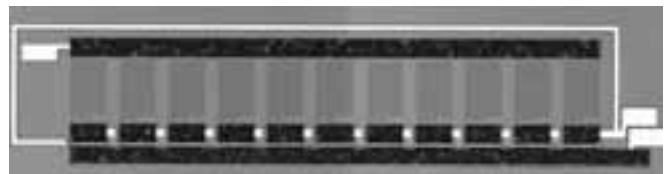


Figure 1: Completed ring oscillator device.

## Results:

**Positive Gate Threshold Voltage Achieved Through T-Gate Design.** An active layer thickness of below 174 nm is needed to achieve a positive threshold voltage. However, functional devices with this thickness are difficult to create due to increased defects at the interface of the active layer and semi-insulating GaAs; effective mobility is determined to drop significantly as active layer thickness is decreased. Initial MESFET fabrication resulted in a maximum threshold

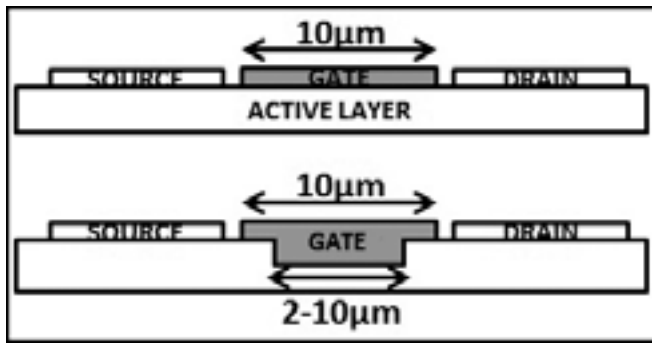


Figure 2: Schematic of T-gate (bottom) with original gate for reference (top).

voltage of  $-0.22\text{V}$  determined from drain current as a function of gate voltage data measured using a manual prober system for each device.

The T-gate design (Figure 2) involved using the gate width of  $10\ \mu\text{m}$  employed in earlier designs while etching a portion of the active layer ranging in width from  $2\ \mu\text{m}$  to  $10\ \mu\text{m}$  centered below the gate metal. By etching the active layer at only this area to  $141.3\ \text{nm}$  and  $172.4\ \text{nm}$ , positive threshold voltages of  $0.15\text{V}$  and  $0.3\text{V}$  were achieved, respectively (Figure 3). The most successful T-gate variation had a  $2\ \mu\text{m}$  base width.

**MESFET and Inverter Performance.** Devices across MESFET and inverter samples were found to be consistent. Strong gate dependences were observed and inverter devices exhibited sensitive input and full-scale output.

**Ring Oscillator Performance.** Functional ring oscillators were fabricated using the T-gate design on the  $174.2\ \text{nm}$  active layer sample. Oscillation frequencies of  $19.9\ \text{MHz}$  were observed for load resistances of  $3.2\ \text{k}\Omega$  and  $1.7\ \text{k}\Omega$  corresponding to applied voltages of  $1.3\text{V}$  and  $0.9\text{V}$ , respectively.

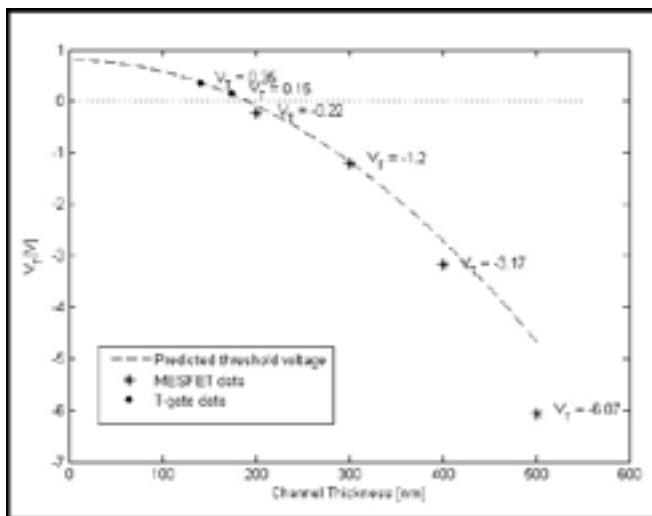


Figure 3: Average threshold voltage as a function of active layer thickness. Values for thicknesses over  $200\ \text{nm}$  correspond to MESFET data while values for thicknesses below  $200\ \text{nm}$  correspond to T-gate data.

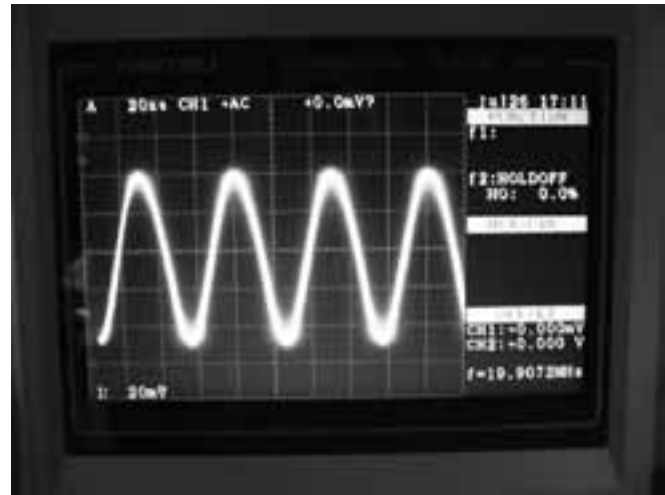


Figure 4: Functional ring oscillator output for  $R = 3.2\ \text{k}\Omega$  and  $V_{DD} = 1.3\text{V}$ .

### Conclusions and Future Work:

The importance of achieving a positive threshold voltage was realized during early iterations. The resulting design and fabrication of the T-gate overcame the decrease in effective mobility for thinner active layers and contributed to the successful fabrication of all three target devices. The ring oscillator output oscillation frequencies of  $19.9\ \text{MHz}$  were comparable to calculated values.

However, the ring oscillator design can be improved in future iterations. A T-gate base width below  $2\ \mu\text{m}$  may increase effective mobility and produce stronger inverting characteristics at lower load resistances, producing higher oscillation frequencies. In addition, it has been observed that full sized  $200\ \mu\text{m}$  by  $200\ \mu\text{m}$  source/drain electrodes have a higher effective mobility and corresponding drain current than the compacted  $100\ \mu\text{m}$  by  $200\ \mu\text{m}$  electrodes used for later samples. Use of full sized versions in future designs may yield similar performance improvements.

### Acknowledgements:

I would like to thank Dr. Yasuo Koide, Dr. Eiichiro Watanabe, Dr. Daiju Tsuya, and the 3D-NanoIntegration Foundry group for hosting me and for offering their guidance over the course of this project. I would also like to thank the National Institute for Materials Science (NIMS) for hosting me and the National Science Foundation (NSF) and National Nanotechnology Infrastructure Network International Research Experience for Undergraduates (NNIN iREU) Program for providing me with this amazing opportunity.

### References:

- [1] Sze, S; "Physics of Semiconductor Devices" (2006).

# Water-in-Ferrofluid Digital Microfluidic System for Single Cell Isolation and Transport

**Elsie V. Bjarnason**

**Chemical and Biomolecular Engineering, North Carolina State University**

*NNIN REU Site: Stanford Nanofabrication Facility, Stanford University, Stanford, CA*

*NNIN REU Principal Investigator: Prof. Roger T. Howe, Electrical Engineering, Stanford University*

*NNIN REU Mentor: José I. Padovani, Electrical Engineering, Stanford University*

*Contact: evbjarna@ncsu.edu, rthowe@stanford.edu, josep@stanford.edu*

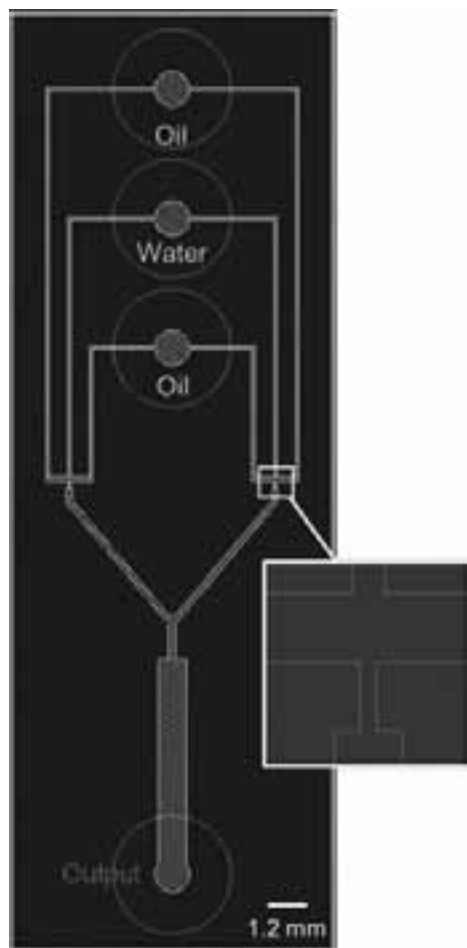


*Figure 1: The layout of our microfluidic chip. The enlarged area is where the two liquids merge and emulsions are generated.*

## Introduction:

The isolation and study of circulating tumor cells (CTCs) is of great interest to researchers and clinicians in the medical field [1]. Current approaches involve labeling the cells, which negatively affects their viability [2]. We envision a label-free microfluidic device capable of isolating and transporting single cells while preserving the viability of the cells. Cells will be encapsulated by aqueous emulsions in an oil-based ferrofluid microfluidic system. A magnetic field will be generated in the system by an electrode array embedded in the device; this will transport the emulsions in a process called negative magnetophoresis.

Our project focused on the design and fabrication of a microfluidic channel to be used in the study, optimization of water-in-ferrofluid emulsions, and the stabilization and characterization of the emulsions generated.

## Design, Fabrication, and Experimental Setup:

A microfluidic system was designed to create and study emulsions of water in oil and of water in ferrofluid. As shown in Figure 1, our system had two emulsion generators with width as a design parameter; ranging from 40, 60, 80, to 100  $\mu\text{m}$ . There were two input ports for oil and one input port for water. The channels symmetrically merged to form two emulsion generators, which then met and rejoined into an outlet channel. Symmetry was used to allow for the study of both emulsion generation and convergence.

A standard multi-step photolithography process was employed to fabricate the chips (see Figure 2). We chose SU-8 50 to form the channel walls and bottom as it is hydrophobic and does not swell in the presence of a hydrocarbon-based oil. The base layer was a quartz wafer, which allowed for imaging from both sides. Good adhesion in bonding the glass cover slip to the top SU-8 layer was difficult with a two-part epoxy. We ultimately used a double-sided cleanroom Kapton<sup>®</sup> tape as the bonding layer and achieved good adhesion (see Figure 3). Ports were attached on top of the cover slip using a standard two-part biocompatible epoxy, and tubing connected the ports to a computer-operated LabSmith pump/valve system.

## Emulsion Generation:

By changing the width of the emulsion generators on our chips, we successfully modulated the size of emulsions. We fabricated chips of generator width 60, 80, and 100  $\mu\text{m}$  and found that the emulsions generated by the 40  $\mu\text{m}$  channels were significantly smaller in diameter than those generated by the 60, 80, and 100  $\mu\text{m}$  channels. This held true regardless of

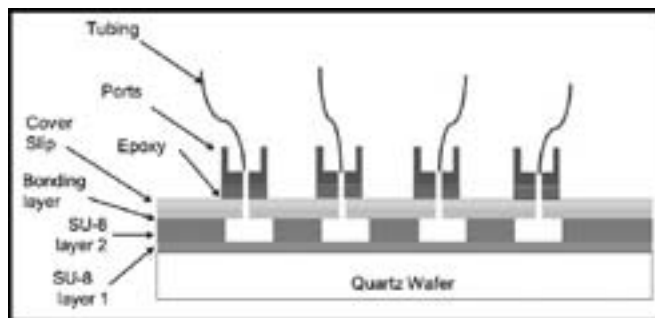


Figure 2: A side view of the multi-step fabrication process. SU-8 and the bonding-layer material were chosen for being hydrophobic and for not swelling in the presence of a hydrocarbon-based oil. Width, a design parameter of SU-8 layer 2, is set to 50, 80, or 100  $\mu\text{m}$ .

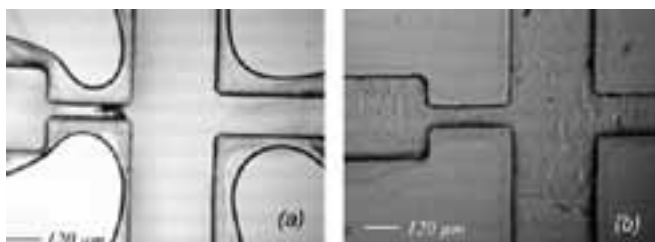


Figure 3: (a) Poor adhesion by epoxy.  
(b) Good adhesion by double-sided Kapton tape.

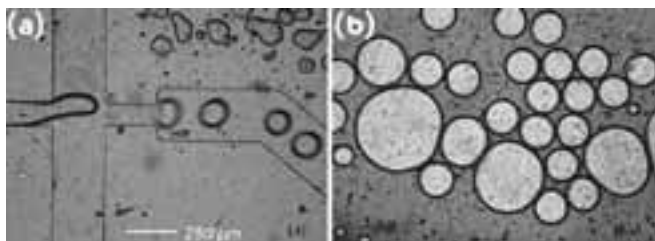


Figure 4: (a) Generation of water-in-mineral oil emulsions, stabilized with a surfactant. (b) Water-in-ferrofluid emulsions coalesce without a surfactant.

the flow rate. We also saw that an increase in the oil flow rate led to a decrease in the emulsion diameter. Figure 4 shows emulsions generated on our chips.

The size and shape of emulsions can be controlled by altering the flow rates of the components [3]. We modulated droplet size by varying the oil flow rate ( $Q_o$ ), the water flow rate ( $Q_w$ ), and the ratio of the water to oil flow rates ( $Q_w/Q_o$ ). We found a non-linear relationship between the emulsion diameter versus the oil flow rate when plotting different  $Q_w/Q_o$  values. We analyzed  $Q_w/A_o$  values of 1/2, 1/4, 1/20, and 1/100 and found all to have a similar non-linear trend. Further data points are needed to fully explain this phenomenon.

We used mineral oil in testing and characterizing the emulsions as it has similar chemical properties to the hydrocarbon-based ferrofluid while being more economical. A surfactant, 1% Span 80, was added to the oil phase to stabilize the emulsions. Without the surfactant, we saw droplets coalesce and Ostwald ripening occur [4].

Water-in-ferrofluid emulsions were generated using our chip. As expected, we found them to be unstable without a surfactant.

## Conclusions and Future Work:

In this work, a microfluidic device was designed and fabricated to study and optimize water-in-oil emulsions. We controlled the size of the emulsions by varying the channel size and input flow rates, and we stabilized the emulsions with a surfactant. We then were able to create water-in-ferrofluid emulsions. The results of these studies will be used in the creation of a label-free microfluidic device capable of isolating and transporting CTCs on a single-cell basis. This second-generation device will be used to further study water-in-ferrofluid emulsions. Cells will be introduced to the system. Magnetic actuation will be used to study the negative magnetophoresis process. Ultimately, a device will be created with the ability to isolate and transfer CTCs.

## Acknowledgements:

This work was accomplished with help from P.I. Professor Roger T. Howe, mentor José I. Padovani, the Howe research group, Stanford University REU program director Dr. Michael Deal, Stanford Nanofabrication Facility (SNF) staff, and fellow Stanford REU students. Funding for this work was graciously provided by the National Science Foundation (NSF), the National Nanotechnology Infrastructure Network Research Experience for Undergraduates (NNIN REU) Program, and the Center for Integrated Systems (CIS) at Stanford University.

## References:

- [1] Roonder, J. Circulating Tumor Cells: The Grand Challenge, *Lab on a Chip* 11, 375 (2011).
- [2] Chen, J. Microfluidic approaches for cancer cell detection, characterization, and separation. *Lab on a Chip*, 12, 1753 (2012).
- [3] Zhihong, N. Emulsification in a microfluidic flow-focusing device: effect of the viscosities of the liquids. *Microfluid Nanofluid* 5, 585-594 (2008).
- [4] Baret, J. Surfactant in droplet-based microfluidics, *Lab on a Chip* 12, 422 (2012).

# Hydrogen Impurities in Tin Dioxide Films Deposited by Pulsed Laser Deposition

**Alex Bryant**

**Materials Science and Engineering, Georgia Institute of Technology**

*NNIN iREU Site: National Institute for Materials Science (NIMS), Tsukuba, Ibaraki, Japan*

*NNIN iREU Principal Investigator: Professor Naoki Ohashi, Optoelectronics Materials Group, NIMS*

*NNIN iREU Mentor: Dr. Ken Watanabe, Optoelectronic Materials Group, National Institute for Materials Science*

*Contact: awbryant@gatech.edu, ohashi.naoki@nims.go.jp, watanabe.ken@nims.go.jp*

## Abstract and Introduction:

Tin dioxide (SnO<sub>2</sub>) is well known for its use as a gas sensor and transparent conducting oxide. It has a rutile-type crystal structure, room temperature band gap of 3.6 eV, and it is a native n-type semiconductor. The source of its n-type conductivity is not well known. Typically, the source is assumed to be oxygen vacancies. As shown in Figure 1, the removal of an oxygen ion causes a charge imbalance, and, to return to charge neutrality, electrons are injected into the material. However, recent density functional theory (DFT) calculations have shown that these oxygen vacancies are actually deep-level donors that are about 1 eV below the conduction band [1]. The electrons contributed by these vacancies are too deep to be activated at room temperature by thermal energy. Therefore, it is unlikely these oxygen vacancies are the source of the native n-type conductivity.

However, DFT calculations also predict that hydrogen acts as a shallow donor in SnO<sub>2</sub> [1, 2]. Hydrogen (H) impurities can inject electrons by nesting H atoms at interstitials in the crystal lattice, directly adding an electron to compensate the addition of a positively charged impurity, or the atoms can replace oxygen atoms within the crystal lattice as hydride ions. The replacement results in electron injection, as seen in Figure 1.

It is clear that understanding the role and effects of H within SnO<sub>2</sub> is very important. As such, the goal of this project was to deposit samples with plasma laser deposition (PLD) and correlate their H concentration with other physical properties. By using PLD, it was possible to ensure the SnO<sub>2</sub> composition and control the thickness, surface morphology, and homogeneity of the resulting films.

## Experimental Procedure:

Initially, fused silica substrates were prepped, loaded into the main PLD chamber, heated to 500°C, and held at that temperature for 40 minutes during which deposition took place. As shown in Figure 1, during deposition a SnO<sub>2</sub> ceramic pellet of purity greater than 99.99% was contained within a chamber with a background oxygen partial pressure of 1.4 × 10<sup>-5</sup> Torr and an oxygen radical gun aimed at the substrate. Then, a laser ablated the surface of the target, creating a plasma that deposited SnO<sub>2</sub> onto the substrate.

After deposition, the sample thickness was measured in a Dektak contact profilometer, the surface morphology was characterized with dynamic force microscopy (DFM), the defect states were determined with photoluminescence (PL), and the crystal structure was checked with x-ray diffraction (XRD) to ensure SnO<sub>2</sub> was deposited. Then, aluminum electrodes were evaporated onto the sample and its Hall effect was measured. Finally, secondary ion mass spectrometry (SIMS) measurements of the samples were taken to observe the concentration of H within the samples.

## Results and Conclusions:

After compiling, plotting, and comparing characterization results, it became clear that samples' H concentrations were very sensitive to changes in deposition conditions. A sample deposited after many runs had an order of magnitude lower H contained than did one deposited right after opening the chamber. Comparing these results to the corresponding Hall

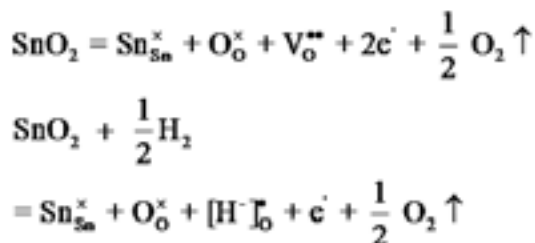


*Figure 1: Chemical equations showing the production of electrons due to either oxygen vacancies (top) or hydrogen impurities (bottom).*

effect data, Figure 2 shows that the carrier concentration cannot be correlated to the H concentration in these samples. As H was expected to be the source of the carriers, this was quite unexpected. Further, from Figure 2 it was clear that large amounts of H were already introduced into the samples during deposition.

These two observations call into question whether or not H is actually acting as a shallow donor. Were the sample to have no defects, the H atoms would be incorporated into the crystal lattice as interstitials — thereby injecting electrons and acting as a shallow donor. However, if there are some defects, such as deep acceptors, the acceptor, which is usually tied to a positive hole, will preferentially bond to any introduced H instead and the electron that would have been injected with this addition of H will be compensated by the hole that was originally tied to the acceptor.

Therefore, all deep acceptors would need to be compensated before H could begin to provide more charge carriers. As it is, PL measurements, represented in Figure 3, indicate three different defect states that luminesce in the visible light range.

Clearly, hydrogen does not seem to affect SnO<sub>2</sub> as expected. Further studies must be done to better understand the role of hydrogen, if there is one.

#### Future Work:

In order to see if additional hydrogen might better illuminate hydrogen's effects on the tin dioxide's physical properties, annealing studies were also performed. These studies are still ongoing at the National Institute for Materials Science (NIMS), and the results obtained for the annealed samples will be published elsewhere by NIMS researchers.

#### Acknowledgements:

This research was conducted under the guidance of Professor N. Ohashi in the Optoelectronic Materials Group at NIMS in Tsukuba, Ibaraki Prefecture, Japan, with funding from the United State's NNIN iREU Program. I could not have taken part in this program without the generous support of NIMS and the NNIN. I would like to acknowledge the help of Dr. I. Sakaguchi, Dr. Y. Adachi, and Dr. T. Ohgaki during my project. I would also like to give special thanks and acknowledgement to Dr. K. Watanabe for his mentorship and help during this project.

#### References:

- [1] Singh, Abhishek Kumar et al., "Sources of Electrical Conductivity in SnO<sub>2</sub>"; Physical Review Letters, 101 055502, Aug. 2008.
- [2] Hlaing Oo, W. M. et al., "Hydrogen donors in SnO<sub>2</sub> studied by infrared spectroscopy and first-principles calculations"; Physical Review, B Volume 82 193201, Nov. 2010.

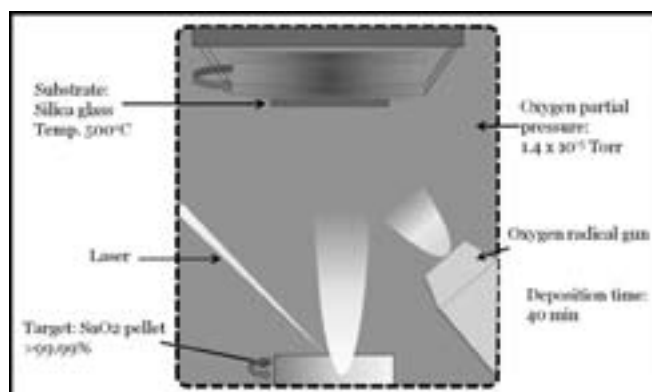


Figure 2: Schematic of how the PLD operates.

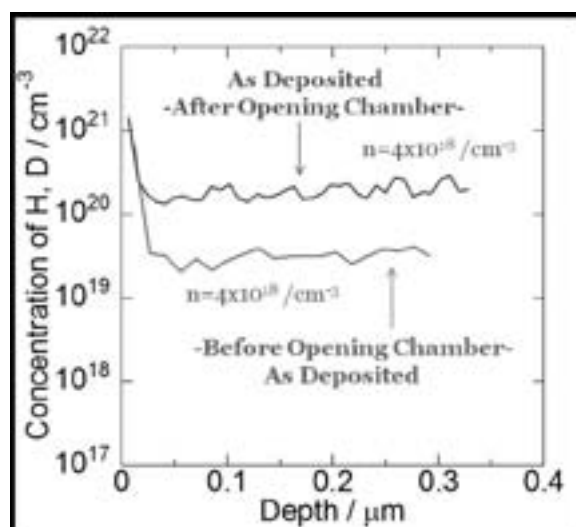


Figure 3: Plot of SIMS data showing, for two different samples, the concentration of hydrogen and deuterium as a function of depth.

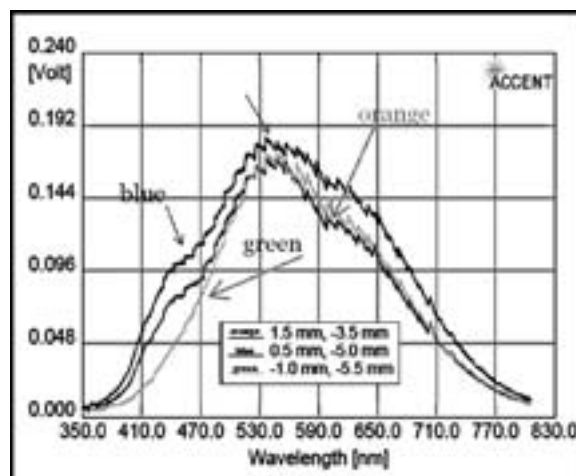


Figure 4: Plot of PL data indicating the presence of defects causing luminescence in the visible light range.

## Correlation between Surface Morphology and Hall Mobility between AlGaAs/GaAs <111> Heterojunctions

Isidro Calderon, Jr.

Mechanical Engineering, Santa Barbara City College

NNIN REU Site: Nanotech, University of California, Santa Barbara, CA

NNIN REU Principal Investigator: Professor Mark Rodwell,  
Electrical and Computer Engineering, University of California, Santa Barbara

NNIN REU Mentors: Dr. Jeremy Law, Dr. Sang-hoon Lee, and Cheng-Ying Huang,  
Electrical and Computer Engineering, University of California, Santa Barbara

Contact: isical91@gmail.com, rodwell@ece.ucsb.edu, jeremylaw@ece.ucsb.edu

### Abstract:

Most of modern electronics are composed of a silicon (Si) metal-oxide semiconductor field-effect-transistor (MOSFET). The rate at which we can improve the Si MOSFET is decreasing due to leakage current and power dissipation from quantum tunneling effects as we make the MOSFET dielectric thinner. Changing the channel material in the MOSFET can provide a resolution to this problem. Indium gallium antimony (InGaSb) grown by molecular beam epitaxy (MBE) serves as a candidate for outperforming Si as a channel material by providing multiple conducting energy states when grown in the <111> orientation. However, crystal defects occur when growing InGaSb on gallium arsenide (GaAs) <111> substrates because of their lattice mismatch. In this work, we studied aluminum gallium arsenide (AlGaAs) and GaAs grown on GaAs <111> substrates, in order to understand future growth of InGaSb materials. Experiments that involved varying V:III beam equivalent pressure (BEP) ratios of GaAs grown on GaAs <111> substrates could assist the process of increasing surface quality in the growth of InGaSb material systems. Experiments that involved varying Si dopant temperatures of AlGaAs on GaAs <111> substrates were also performed to identify similar methods we can incorporate to control the electrical and growth properties of InGaSb.

### Introduction:

This project observed the surface characterization and electrical properties of AlGaAs and GaAs individually grown on GaAs <111> substrates. Successful growth of InGaSb material systems was the ultimate goal, however this could be very difficult. Relative to InGaSb, growth of AlGaAs and GaAs on GaAs substrates were more straight forward and simply easier to utilize. Optimized processes could be achieved that ideally can be applied to future growths of InGaSb.

### Experimental Procedures:

The main characterization techniques used in this project were atomic force microscopy (AFM) and Hall measurement. AFM uses a cantilever that runs across the surface of the sample detecting any changes in surface morphology. The Hall measurement system analyzes the carrier concentration and Hall mobility of the sample. It was desired to know Hall mobility and the surface characterization, so we could attempt to provide a correlation between them. AFM scans of  $20 \times 20 \mu\text{m}^2$ ,  $5 \times 5 \mu\text{m}^2$ , and  $2 \times 2 \mu\text{m}^2$  areas of the samples were taken and analyzed.

The Hall measurements were conducted with a magnetic field generator, four contact probes that would be measuring Hall voltage as well as the power source used to flow current perpendicular to the measured Hall voltage. From the Hall voltage, we calculated the number of charge carriers flowing through the sample.

### Results and Conclusions:

Experiments consisted of varying ratios of elemental components Ga and As which determined the surface quality of GaAs. Initial growths consisted of BEP ratios of 10, 25 and 50. Varying BEP ratios lead to changes in electron mobility as well as electron concentrations. Refer to Figure 1.

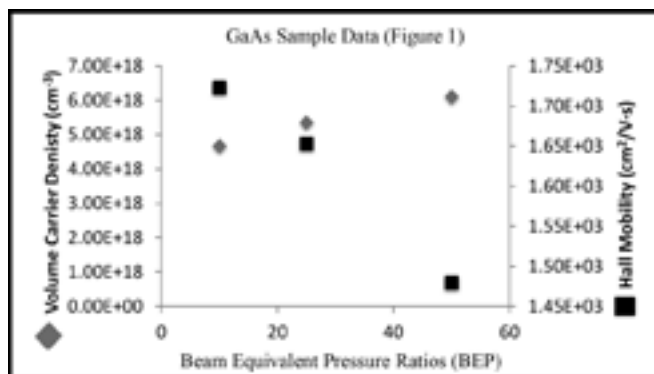


Figure 1: Plot of mobility and carrier concentration as the V:III ratio of GaAs increases, mobility drops and carrier concentration increases.

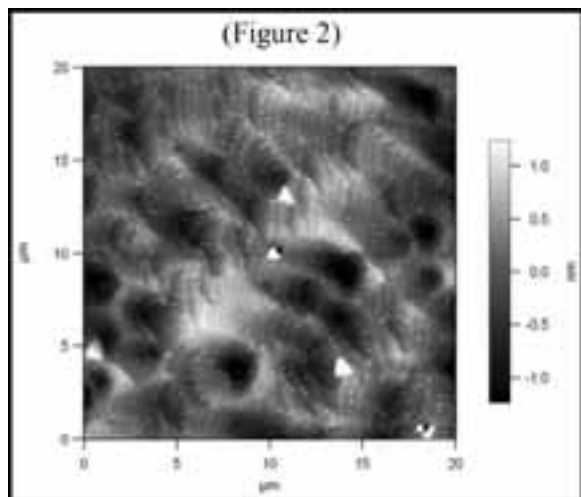


Figure 2: AFM image of GaAs sample with BEP ratio of 10. The surface is smooth relative to higher BEP samples.

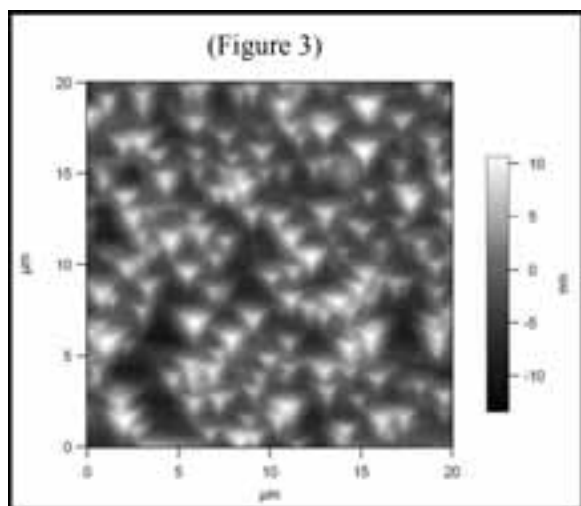


Figure 3: AFM image of GaAs sample with BEP ratio of 50. The surface contains stacking faults or a rougher surface.

Low BEP ratios contributed to smoother surfaces as well as more relatively controlled growth. Refer to Figure 3 for a sample with close-to-ideal surface properties. High BEP ratios led to pyramidal stacking faults and higher carrier concentrations as well as low mobility, which was undesirable. Figure 2 shows this scenario. Results showed no direct correlation between surface morphology and Hall mobility. It was inconclusive to assume whether the Hall mobility became dependent on the actual surface morphology or the amount of transport carriers.

In conclusion, Hall mobility can depend solely on the amount of electrons present for transport, surface morphology or a combination of both.

#### Future Work:

Future work consists of continued experiments of AlGaAs and GaAs with measurements being done at lower temperatures to eliminate the possibility of having the number electrons effect the mobility and isolate the correlation between surface morphology and Hall mobility. Other potential experiments consist of growing InGaSb materials to identify sources of undesired properties. From these results, we hope to determine better processes that can be implemented into the close-to-perfect material growths of InGaSb.

#### Acknowledgements:

Melanie-Claire Mallison, Lynn Rathbun, and the National Nanotechnology Infrastructure Network Research Experience for Undergraduate Program; Samantha Cruz, NNIN UCSB Coordinator; Dr. Jeremy Law, Dr. Sang-Hoon Lee, Cheng-Ying Huang, Mentors; Professor Mark Rodwell, Principal Investigator; National Science Foundation; NNIN REU 2012 Interns.

## Electrical Characterization of Heat-Treated Tin Monosulfide Thin Films

**Annabel Chew**

**Materials Science and Engineering, Columbia University**

*NNIN REU Site: Center for Nanoscale Systems, Harvard University, Cambridge, MA*

*NNIN REU Principal Investigator: Professor Roy G. Gordon, Chemistry and Chemical Biology, Harvard University*

*NNIN REU Mentor: Prasert Sinsermsuksakul, Chemistry and Chemical Biology, Harvard University*

*Contact: arc2148@columbia.edu, gordon@chemistry.harvard.edu, psinerm@fas.harvard.edu*

### Abstract and Introduction:

Tin monosulfide (SnS) thin films have generated much interest in recent years due to their potential application as an absorber layer in thin film photovoltaic cells [1]. Thus, the goal of this project was to improve the quality of SnS films through various methods of heat-treatment by means of grain growth, a reduction in bulk defects, and increased carrier mobility, which can increase the probability of charge collection and thus potentially improve cell efficiency. The effects of the annealing atmosphere (inert nitrogen ( $N_2$ ) versus hydrogen sulfide ( $H_2S$ ) gas), temperature (250-540°C), and annealing time (10 s versus 60 min) on the film's electrical properties were investigated. Scanning electron microscopy (SEM) and Hall measurement results revealed that annealing the films in  $H_2S$  atmosphere produced larger, columnar, and uniform grains with greater mobility as compared to the as-deposited and  $N_2$  annealed SnS. While the heat-treatment of SnS films in  $H_2S$  for 10 s and 60 min both produced films of comparable mobility, the film that underwent the 10 s process had a relatively lower carrier concentration, which is an indicator of the amount of bulk defects present. Therefore, the most desirable SnS films were found to be produced through annealing in a  $H_2S$  atmosphere at 400°C for 10 s.

### Experimental Procedure:

SnS films were deposited using atomic layer deposition (ALD), and annealed at various atmospheres ( $N_2$  or  $H_2S$ ), temperatures (between 250-540°C) and times (10 s or 60 min). These films were heated at an average ramp rate of 0.17°C/s before being held at the annealing temperature for the specified time. The heat-treated films were then studied using the SEM and x-ray diffraction (XRD). Square Hall samples of the heat-treated films 1 cm wide were then prepared through deposition of 200 nm of gold, and removal of excess film using a reactive ion etching (RIE). The various electrical properties of each film were then calculated from the measured Hall voltage of each prepared sample.

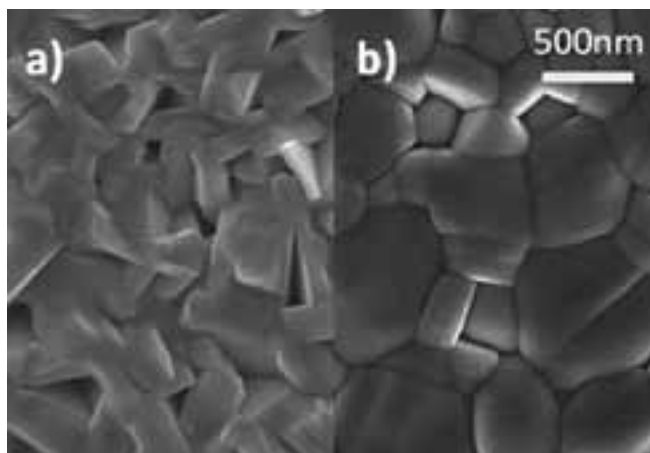


*Figure 1: SEM comparison of SnS grains of (a) as-deposited and (b) heat-treated in  $H_2S$  for 60 min.*

### Results and Conclusions:

Cross-sectional SEM images of the heat-treated films demonstrated that when all other conditions were held constant, larger, more columnar grains were produced by annealing in  $H_2S$  as compared to  $N_2$  and as-deposited films. Increasing the annealing temperature also produced an increased grain size.

Figure 1 demonstrates the significant change in grain size produced by such an annealing process, with the as-deposited film shown on the left in (a) and heat-treated film in  $H_2S$  at 400°C on the right in (b). Such grain growth is beneficial in the development of SnS films for use in photovoltaic devices, since it reduces the probability of charge scattering at the grain boundaries, potentially allowing for more efficient charge collection.

The results of characterization of the electrical properties are shown in Figure 2 and Figure 3 respectively. The as-deposited films are indicated in both graphs by the point at 200°C, which is the deposition temperature.

Figure 2 demonstrates that consistently high mobility can be achieved for films annealed in  $H_2S$  between 250-400°C at annealing times of 10 s and 60 min. However, mobility drops sharply above 250°C when annealed in  $N_2$ . Since annealing in high temperatures is favorable in order to achieve larger grains, annealing in  $H_2S$  is preferred over  $N_2$  because it produces significantly greater mobility at temperatures between 300-400°C. At temperatures above 400°C however, mobility drops significantly, although imaging under the SEM revealed that the grains continue to be significantly larger. Thus the drop in mobility could be a result of increasing amounts of point defects present at higher temperatures.

Carrier concentration is an important parameter because while the film must have sufficient carriers to conduct charge, an excess of carriers could serve as point defects causing unwanted recombination. Two distinct trends in the data shown in Figure 3 can be observed: when annealing was carrying out for 60 min, regardless of the annealing atmosphere, increasing the temperature generally produced an increase in the carrier concentration. For the annealing done for 10 s above 300°C however, increasing the temperature appeared to lower the carrier concentration to a value close to the as-deposited carrier concentration. In particular, a comparison of the two annealing times for  $H_2S$  at 400°C reveals that annealing for 10 s produced a lower carrier concentration, and thus is the more favorable process.

XRD analysis of the heat-treated SnS films, shown in Figure 4, revealed that annealing in  $N_2$  at higher temperatures produced a greater dominance of the <040> peak over the <111> crystal orientation. At 400°C in  $N_2$ , the <040> peak had the greatest intensity, replacing <111> as the dominant crystal orientation. When the film was annealed in  $H_2S$  at 400°C however, no growth of the <040> peak relative to the <111> was observed. This could be due to the fact that annealing in  $N_2$  results in a loss of sulfur from the film, causing the crystallites to rearrange in the most stable <040> orientation in order to accommodate the new sulfur defects formed. On the other hand, since  $H_2S$  is a source of sulfur, annealing in an atmosphere of  $H_2S$  would suppress the loss of sulfur, rendering reorientation unnecessary. Thus, these changes in crystallite orientation could be a further reason for the demonstrated difference in mobility and grain size when annealed in  $N_2$  as compared to  $H_2S$ .

### Acknowledgments:

The National Science Foundation, National Nanotechnology Infrastructure Network Research Experience for Undergraduates (NNIN REU) Program, Harvard University REU Program, Professor Roy Gordon, Prasert Sinsermsuksakul, and Dr Kathryn Hollar.

### References:

- [1] Sinsermsuksakul, P.; Heo, J.; Noh, W.; Hock, A. S.; Gordon, R. G., *Advanced Energy Materials* 2011, 1, (6), 1116-1125.

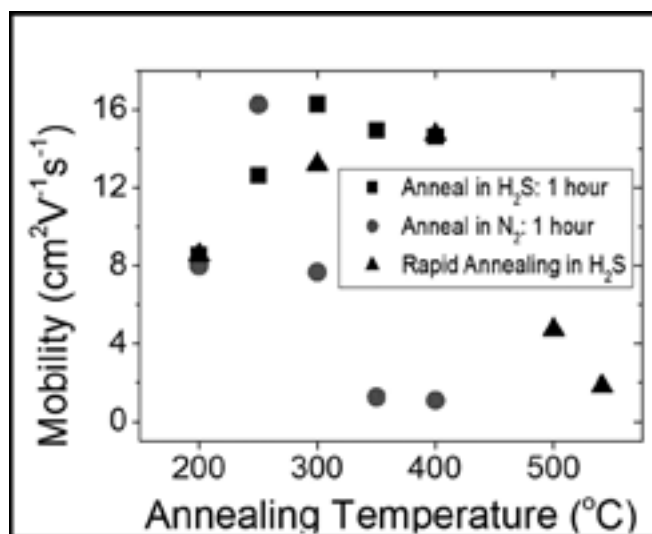


Figure 2: Effect of annealing conditions on carrier mobility in SnS films.

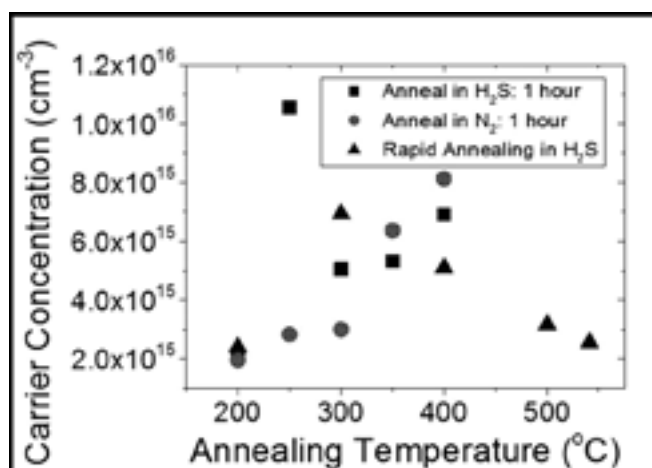


Figure 3: Effect of annealing conditions on carrier concentration.

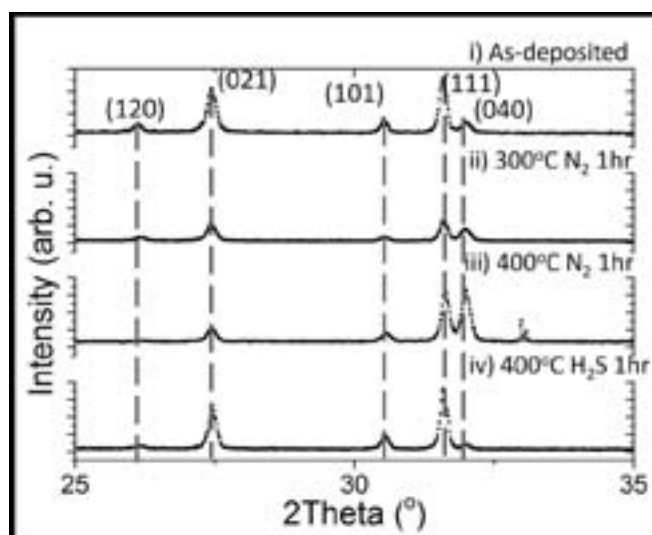


Figure 4: XRD Analysis of crystal orientation shifts due to heat-treatment.

# Ionic Transport Across Atomically Thin Graphene Membranes

**Lauren Cosgriff**

**Bioengineering, University of Pennsylvania**

*NNIN REU Site: Colorado Nanofabrication Laboratory, University of Colorado, Boulder, CO*

*NNIN REU Principal Investigator: Professor Scott Bunch, Mechanical Engineering, University of Colorado*

*NNIN REU Mentor: Lauren Cantley, Mechanical Engineering, University of Colorado  
(2010 NNIN REU at Colorado, 2011 NNIN iREU at TU Delft)*

*Contact: lcos@seas.upenn.edu, jbunch@colorado.edu, lauren.cantley@colorado.edu*

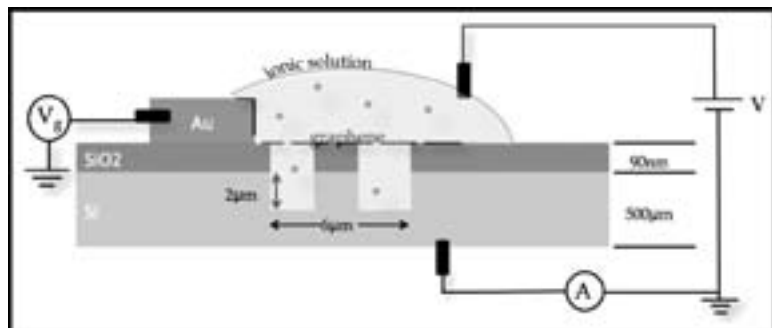


Figure 1: Side view of a completed device schematic.

## Abstract and Introduction:

Membranes for ionic separation in fluids have a promising future in applications ranging from the environment to biotechnology. The mechanical robustness and atomic thinness of graphene make it an ideal candidate for such technology. Graphene, a single atomic layer of sp<sup>2</sup>-bonded carbon atoms, has the potential to achieve high levels of permeability and selectivity at low pressures, therefore making it an inexpensive alternative to current state of the art membranes. The focus of the project was to fabricate and characterize a device allowing for the electrostatic control of ions through pores in a graphene membrane.

## Device Design:

The device consists of a graphene membrane suspended over a well that has been etched into a silicon/silicon dioxide substrate. The graphene is in contact with a gold electrode and supported by a post in the well. A drop of ionic solution is strategically placed so as to simultaneously cover the suspended graphene and contact the electrode (Figure 1). Slight imperfections in the graphene, attributed to induced tears and defects from the transfer process and voids between grain boundaries, should allow the ionic solution to pass through the graphene and fill the well.

A voltage applied to the ionic solution serves as a driving current for ions passing through pores in the graphene membrane [1]. An additional level of control may be introduced by applying a voltage to the electrically contacted graphene. Such a design may allow one to alter the electric field at the membrane interface, and therefore selectively control the flow of ions in solution.

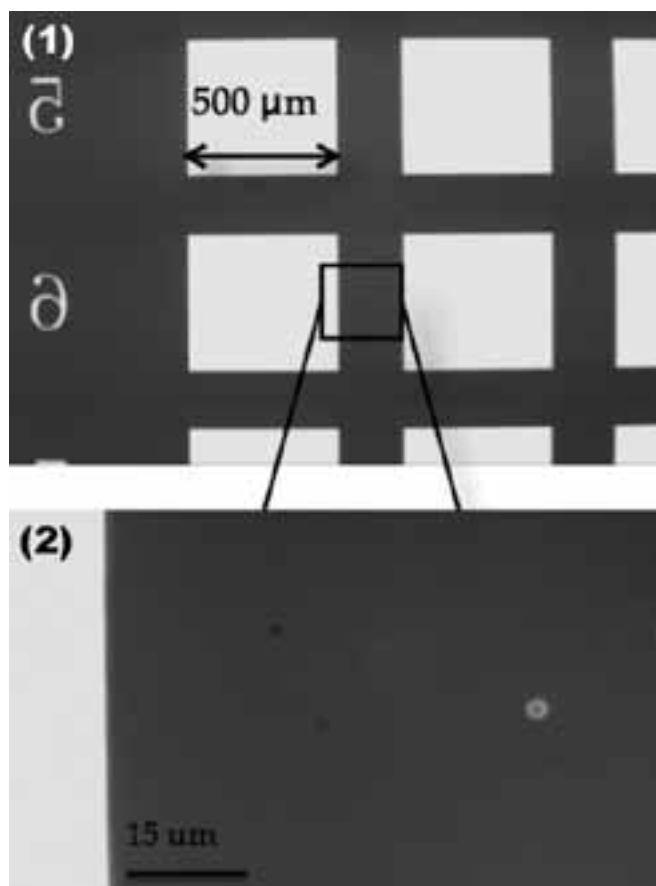
## Fabrication:

The device was fabricated using a bilayer photolithography process. A 500 μm Si wafer with a 90 nm silicon dioxide layer served as the substrate.

Gold electrodes were first patterned onto the wafer using evaporation (10 nm chromium, 50 nm gold) and lift off techniques. Circular wells containing structural post supports were then patterned onto the wafer and etched using standard lithography methods and reactive ion etching. An optical image showing a completed device is shown in Figure 2. The etched annular ring is shown next to the gold electrode (Figure 2, lower). Atomic force microscopy was used to ensure that the wells were etched sufficiently deep into the silicon layer of the wafer. Graphene grown through chemical vapor deposition was then transferred onto the wafer using a dry transfer technique [2], and atomic force microscopy was used to check for suspended graphene.

## Results and Conclusions:

A device without graphene was characterized to ensure that a current was capable of passing through an ionic solution to the silicon back gate. A drop of ionic solution was first placed onto the device using a micropipette. The drop was positioned in a way such that the solution could fill the well and contact the underlying silicon layer. It was also necessary for the drop to contact an adjacent electrode (Figure 3). A two point probe test was used to sweep the voltage applied to the electrode, and the current associated with the silicon back gate was recorded (Figure 4). The voltages applied to



the electrodes varied between -200 mV and 200 mV and the associated currents were in the  $\sim -10$  to 30 nA range. The hysteresis in the graph may be attributed to a capacitance in the solution created by an uneven distribution of ions when the voltage is flipped from negative to positive. The diode like behavior is attributed to the silicon-ionic solution contact. This characterization process will be used in future electrical testing in which a graphene membrane has been incorporated into the device.

#### Future Work:

Future work will include two point probe tests in which a graphene membrane has been suspended over the well. Three point probe testing in which a constant voltage is applied to the ionic solution and a gated voltage is applied to the graphene will also be conducted.

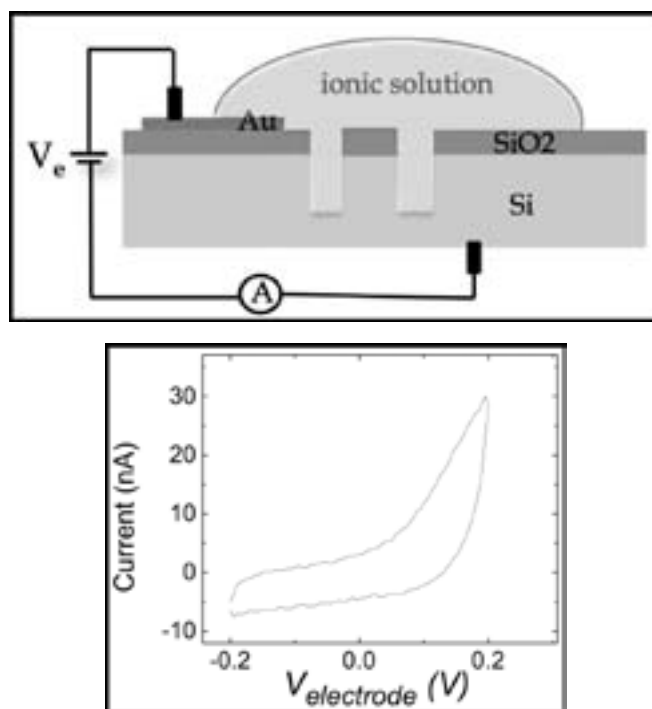


Figure 2, left: Optical image of a device before graphene transfer. (1) Patterned gold electrode. (2) Etched annular ring.

Figure 3, top: Schematic of a two point probe test used to characterize the device before graphene transfer.

Figure 4, bottom: IV curve for a two point probe test characterizing the device before graphene transfer.

#### Acknowledgments:

I would like to thank the National Nanotechnology Infrastructure Network REU Program and the National Science Foundation for funding and sponsoring my research experience. I would especially like to thank Professor Scott Bunch, Lauren Cantley, Xinghui Liu, the Bunch Lab, and the Colorado Nanofabrication Lab for all their support and guidance throughout this project.

#### References:

- [1] Garaj, S.; Hubbard, W.; Reina, A.; Kong, J.; Branton, D.; Golovchenko, J.A.; Graphene as a subnanometre trans-electrode membrane. *Nature Lett.* 2010, 467, 190-193.
- [2] Suk, J., et al. Transfer of CVD-Grown Monolayer Graphene onto Arbitrary Substrates. *ACS Nano*, 2011, 5(9), 6916-6924.

## Synthesis and Characterization of Potassium Sodium Niobate, a Lead-Free Ferroelectric

**Dmitriy Davydovich**

**Physics and Chemistry, University of the Sciences**

*NNIN REU Site: Penn State Nanofabrication Laboratory, The Pennsylvania State University, University Park, PA*

*NNIN REU Principal Investigator: Dr. Susan Trolier-McKinstry,  
Material Science and Engineering, The Pennsylvania State University*

*NNIN REU Mentor: Aaron Welsh, Material Science and Engineering, The Pennsylvania State University*

*Contact: ddavydovich@mail.usciences.edu (or mitay22@yahoo.com), set1@psu.edu, ajwelshpr@gmail.com*

### Abstract:

Many ferroelectrics used in today's devices are lead-based materials, because they exhibit high piezoelectric and dielectric properties. Due to the volatility and toxicity of lead, these materials pose environmental and health concerns. For the past decade, many scientists have begun working towards lead-free alternatives. This allows the material to be integrated on bio-related devices. One of these promising materials is potassium sodium niobate (KNN). This material shows higher piezoelectric and ferroelectric properties than its lead-free competitors. Thus the main goal of this project was to design a solution, which could be laid as a thin-film to be utilized for microelectromechanical devices. We created an array of solutions with different concentration and additives such as chelating agents, stabilizers, and dopants. Currently nine solutions have been deposited via a chemical solution deposition technique. The crystal structure of the films was characterized by x-ray diffraction (XRD). The microstructure of the films was also investigated through the use of a field-emission scanning electron microscope (FESEM). They are now ready for further electrical testing.

### Introduction:

Potassium sodium niobate is a lead-free material known to show high ferroelectric and piezoelectric properties. Its crystal structure develops a spontaneous dipole, which can be reoriented under an applied electric field or mechanical stress. This allows it to transform mechanical energy into electrical energy and vice versa. Its properties allow it to store large amount of charge and release it when needed without having a large charge leak. However, since this is a new material, various ways of improving its properties are still being discovered. Using several different synthesis methods, a set of KNN films was created; each had different additive and its varying concentration.

### Experimental Procedure:

There are several different ways to fabricate KNN. The process chosen involved two alkali precursors: sodium and potassium acetate. The precursors were mixed in 2-methoxy

ethanol, which is a polar organic solvent. The next precursor added was niobium ethoxide. These chemicals were mixed inside a nitrogen glove box and then were set to reflux for four hours at 115°C. Since this solution was very reactive with moisture, the synthesis was conducted in a low humidity environment. After the reflux, the solution was distilled at 130°C until the needed molarity was attained.

For modification of the solution, acetyl acetone was used as a chelating agent. It was introduced to limit the alkali volatility. Varying concentrations of acetic acid were used as a stabilizing agent to prevent moisture reactivity. Finally copper was used as a doping agent to limit the oxygen vacancies and increase ferroelectric properties.

The solution was then deposited on a platinum-coated silicon wafer. The film was spun onto a wafer at 3000 rpm for 30 seconds. After spinning, it was dried at 200°C for five minutes, followed by a pyrolysis at 400°C for five minutes. Then the film was placed into a rapid thermal annealer and was annealed at 550°C for five minutes. This procedure was repeated until there were 7-10 layers of film on the wafer. Then the wafer was annealed for 30 minutes at 700°C in a furnace.

Following the annealing, the solution was first characterized using FESEM in order see the microstructure and the approximate thickness of the film. The film was then subjected to XRD testing to see if all the proper KNN perovskite phases were present. After the XRD testing, the height of the film was verified with contact profilometry. For electrical testing, platinum electrodes were placed on the surface. The film was then etched with KOH all the way to the bottom electrode and was tested for its electric properties.

### Results:

The first solution that was fabricated was 0.2 M. As seen in Figure 1, when deposited, it showed a good microstructure with a uniform grain size. The XRD confirmed the KNN peaks, and subsequent profilometry tests showed that the film was 400 nm thick. Primary electrical tests showed a fairly

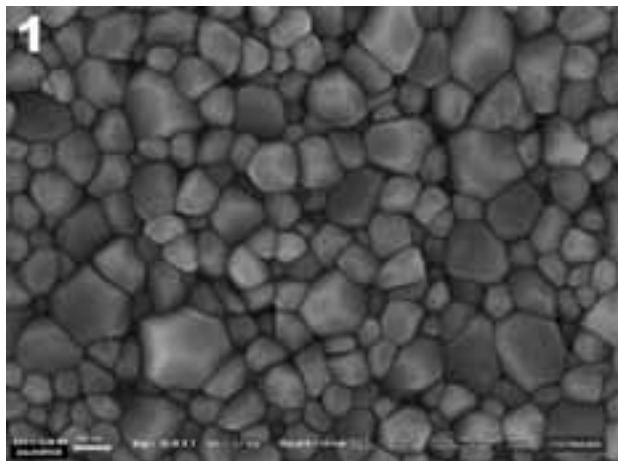


Figure 1: 0.2 M KNN film, 400 nm thickness.

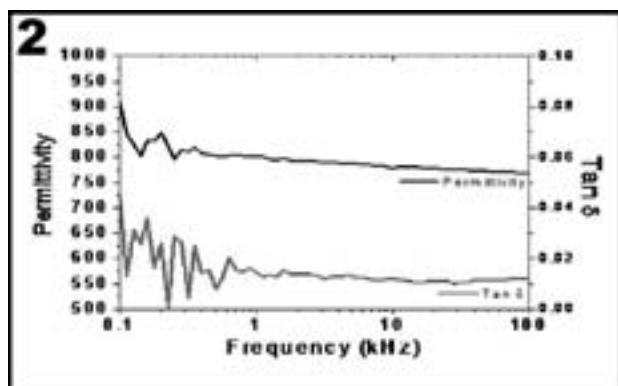


Figure 2: Permittivity and loss tangent of the 0.2 M KNN.

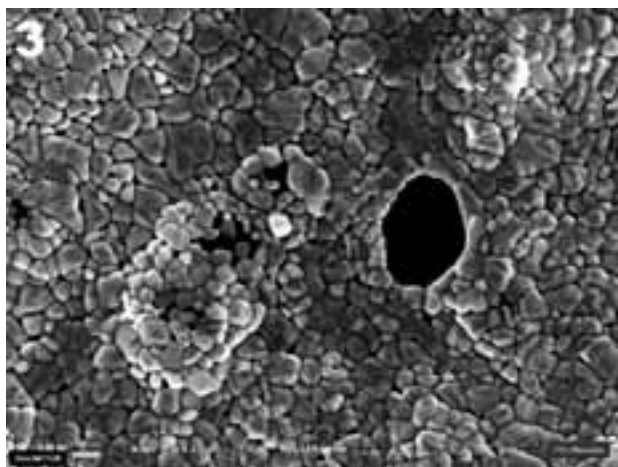


Figure 3: 2:1 KNN:acetylacetone film exhibiting high porosity.

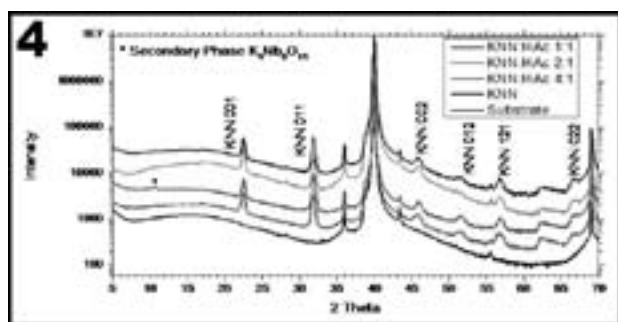


Figure 4: X-ray diffraction plot for films with acetic acid.

high permittivity of 786 at 10 kHz. In addition to that, the loss tangent, at the same frequency, was a low 1.2% as seen in Figure 2. However, when the solution was tested for its ferroelectric properties, the polarization was not able to be switched due to the sample breaking down at low fields. The hysteresis loop was not formed and the solution was deemed dielectric. This was attributed to its small thickness.

The following solutions that were fabricated were 0.4 M. The solution without additives showed an uneven grain size distribution in its microstructure. To counter that acetyl acetone was initially added. However, a low concentration of acetyl acetone did not improve the microstructure. In addition to that, as shown in Figure 3, a higher concentration of acetyl acetone introduced porosity into the films, and thus was deemed unusable. Solutions containing acetic acid showed improved microstructure as the amount of acid increased. The most promising were 33% and 50% by volume. The XRD showed all KNN peaks with an additional peak as seen in Figure 4, which was a potassium deficient secondary phase due to the volatilization of the potassium upon crystallization. The final set of solutions, containing copper acetate, showed that if acetic acid was added, then the combination of the two gave a good microstructure and improved electrical results.

#### Future Work:

In the future, we are trying to eliminate porosity from the microstructure of the film. Most of the focus will be geared towards improving the ferroelectric properties of KNN and making it comparable to its lead-based competitors. The final goal is to integrate this novel material into biomedical devices.

#### Conclusions:

After synthesis and characterization of KNN, it has been found that the solution shows high variability in microstructure based on the different additives. Both films with additives such as acetic acid and acetyl acetone, and films without additives have been fabricated and characterized using FESEM, XRD and profilometry. The last step of characterization is the electric testing, which is still in progress. If the tests show positive results then these films/solutions will be incorporated into an ingestible sensor device.

#### Acknowledgments:

I would like to thank my P.I. Dr. Susan Trolier-McKinstry, the STM group and my mentor Aaron J. Welsh. In addition to that I would like to thank the National Nanotechnology Infrastructure Network Research Experience for Undergraduates Program and the National Science Foundation for funding my research and providing me with this amazing opportunity.

## Phase Transformations in Metal Contacts to $\text{In}_{0.53}\text{Ga}_{0.47}\text{As}$ Nanowires

**Donna Deng**

**Material Science, University of Minnesota – Twin Cities**

*NNIN REU Site: Penn State Nanofabrication Laboratory, The Pennsylvania State University, University Park, PA*

*NNIN REU Principal Investigator: Prof. Suzanne Mohny, Material Science, The Pennsylvania State University*

*NNIN REU Mentor: Joshua Yearsley, Materials Science, The Pennsylvania State University  
(with support from the US Army Research Office)*

*Contact: dengx083@umn.edu, mohny@ems.psu.edu, jdyearsley@gmail.com*

### Abstract:

III-V compound semiconductors such as indium gallium arsenide (InGaAs) are being studied for use in nanoscale transistors as faster, more energy-efficient alternatives to silicon. In order to make use of an InGaAs channel, it must have low-resistance contacts to its source and drain regions. To facilitate the development of appropriate source-drain contacts, phase transformations between InGaAs nanowires and nickel (Ni) and palladium (Pd) metals were studied. Nanowires were etched from an InGaAs film on an indium phosphide substrate, and a metal layer was sputtered onto the sample. Analysis of scanning electron microscopy images and energy dispersive x-ray spectroscopy data collected from annealed samples showed no lateral diffusion of either metal into the nanowires. Pd-sputtered samples showed wire roughening under and close to the pads, suggesting that the presence of the metal catalyzed decomposition of the wires. Furthermore, roughening was more pronounced in samples annealed at lower temperatures, suggesting multiple mechanisms for the decomposition of InGaAs wires in the presence of Pd.

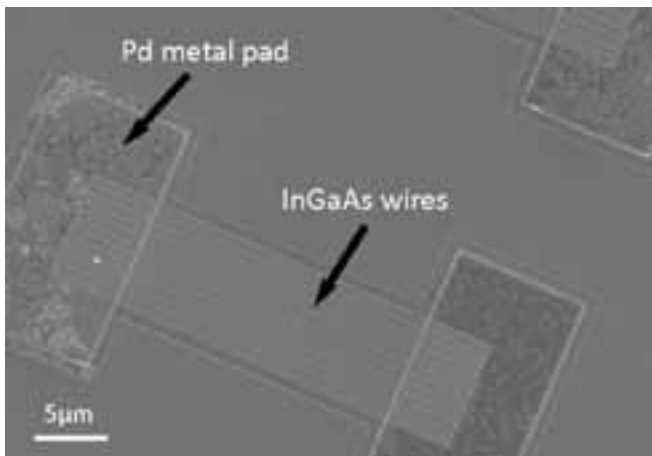


*Figure 1: An SEM of a sample with Pd pads after annealing at 200°C for two minutes. The metal pads are deposited on the ends of the nanowires to facilitate analysis of wires in contact with the pads.*

### Introduction:

Past research in computational electronics has been focused on maximizing the number of silicon transistors able to fit on a substrate. However, as these devices enter the nanoscale and short channel effects become significant, it becomes difficult to increase the density of silicon transistors. Researchers are now looking at increasing the speed and energy-efficiency of transistors. III-V compound semiconductors, such as InGaAs, have higher carrier mobility and faster frequency response than silicon [1]; using these materials as the channel material allows transistors to operate at higher speeds and at lower voltages.

In order to fully utilize such transistors, low-resistance contacts to the source and drain must be realized. Research in thin film InGaAs have shown that both nickel and palladium, when annealed in temperatures at or above 200°C, diffuse into InGaAs to form an intermediate, low-resistance phase [2, 3]. In this project, reactions between nickel and palladium with InGaAs nanowires were studied to better understand phase formations at the nanoscale.

### Experimental Procedure:

Nanowires were fabricated from a film of 50 nm of n-type  $\text{In}_{0.53}\text{Ga}_{0.47}\text{As}$  on an indium phosphide substrate. Nanowires of varying widths (150 to 700 nm) were defined using electron beam lithography, and then wet-etched using a solution of citric acid and hydrogen peroxide. Then, 75 nm of the contact metal was sputtered onto the samples and lifted off to reveal metal pads at the ends of the nanowires, as shown in Figure 1.

The sample sputtered with Ni was annealed at 375°C for two minutes, characterized, and then annealed further for three minutes for a total of five minutes. The samples sputtered with palladium were treated in the same way, but with one sample annealed at 375°C and another at 200°C. A control sample of nanowires without metal pads was also annealed at 200°C for two minutes. All annealing was done in an argon atmosphere.

## Results and Conclusions:

In the control sample, no wire degradation was seen in scanning electron microscopy (SEM), showing the thermal stability of the nanowires. SEM images of Ni-sputtered sample annealed for two minutes showed no sign of phase formation in the nanowires outside the Ni pads. Energy dispersive x-ray spectroscopy (EDS) elemental maps also showed no signal of nickel diffusing laterally into the wires. No significant degradation of nanowires below or outside of the pads could be seen. SEM images and EDS maps taken of the same sample after further annealing showed no differences from data taken after two minutes of annealing.

Figure 3a shows an SEM image of the Pd-sputtered sample annealed at 375°C. Unlike the Ni-sputtered samples, these wires show roughening of edges under the pads, near the ends of the wires. The sample annealed at 200°C shows even more decomposition of the wires. Under the Pd pads, the wires are disintegrating and breaking into pieces, while wires edges are significantly roughening immediately outside of the pads. EDS maps for either samples show no significant Pd signal from outside the contact pads. Again, the data obtained from the samples at annealing times of two minutes and five minutes were the same in terms of wire roughness and EDS signals. The SEM images suggest that the presence of Pd is affecting the nanowires, but no Pd can be detected in them. It is possible that the decomposition of InGaAs in the vapor phase is catalyzed by the presence of Pd.

In summary, neither the Ni-sputtered sample nor the Pd-sputtered sample showed signs of metal diffusing into the InGaAs wires to form intermediate phases. In the case of the Pd-sputtered samples, the wires under and close to the contact pads decomposed. This phenomenon is not seen in the Ni-sputtered sample and suggests that the presence of the palladium is the cause for the wire disintegration. Furthermore, this effect was more prominent in the sample annealed at 200°C than in the sample annealed at 375°C.

## Future Work:

In order to confirm the data obtained, the fabrication, treatment, and analysis of nanowires with palladium pads must be repeated and the SEM and EDS images compared to pre-annealing data. To determine the identity of new phases formed in the palladium case, sample cross sections should be studied in transmission electron microscopy.

## Acknowledgments:

I would like to thank Professor Suzanne Mohny, Joshua Yearsley (supported by the Army Research Office), and the Mohny research group; Kathy Gehoski and the Penn State Nanofabrication Laboratory staff; the National Science Foundation; and the National Nanotechnology Infrastructure Network Research Experience for Undergraduate Program.

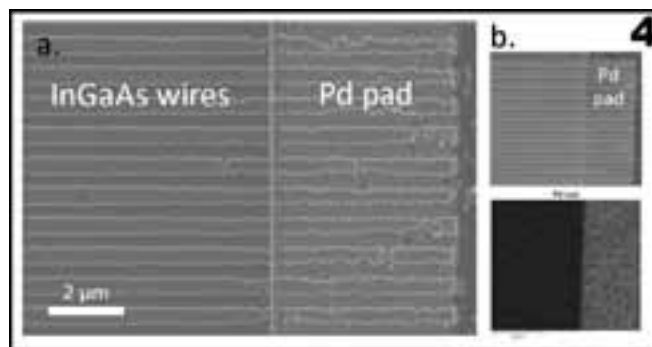
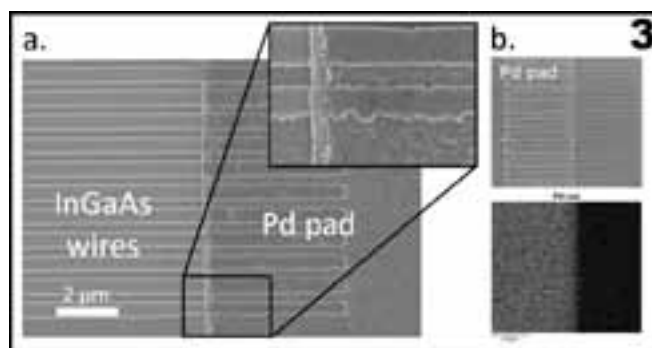
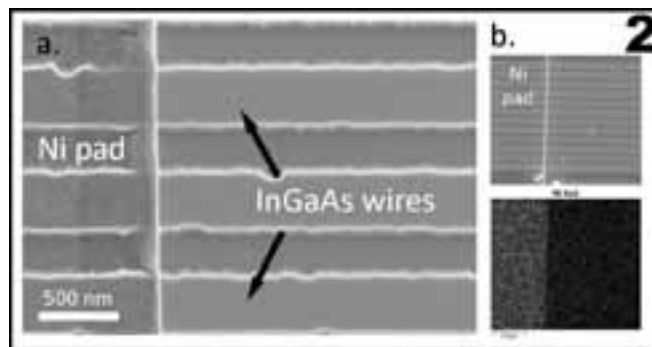


Figure 2, top: InGaAs wires with Ni metal pad after annealing at 375°C for two minutes. a) A close up SEM of the sample. b) The electron image and the corresponding EDS map for Ni signal.

Figure 3, middle: InGaAs wires with Pd metal pad after annealing at 375°C for two minutes. a) An SEM image of the sample. b) The electron image and the corresponding EDS map for Pd signal.

Figure 4, bottom: InGaAs wires with Pd metal pad after annealing at 200°C for two minutes. a) An SEM image of the sample. b) The electron image and the corresponding EDS map for Ni signal.

## References:

- [1] J. A. del Alamo, "Nanometre-scale electronics with III-V compound semiconductors," *Nature*, 479, 317-323 (2011).
- [2] E.Y.-J. Kong, X. Zhang, Ivana, Q. Zhou, and Y.-C. Yeo, "Pd-InGaAs as a New Self-aligned Contact Material on InGaAs," ISDRS (2011).
- [3] X. Zhang, Ivana, H. X. Guo, X. Gong, Q. Zhou, and Y.-C. Yeo, "A Self-Aligned Ni-InGaAs Contact Technology for InGaAs Channel n-MOSFETs," *J. Electrochem. Soc.*, 159 (5), H511-H515 (2012).

## Growth of Boron Nitride Nanowires

**Anderson Hayes**

**Physics, Hampton University**

*NNIN REU Site: Howard Nanoscale Science and Engineering Facility, Howard University, Washington, DC*

*NNIN REU Principal Investigator: Dr. Gary L. Harris, Electrical Engineering, Howard University*

*NNIN REU Mentor: Mr. Crawford Taylor, Electrical Engineering, Howard University*

*Contact: anderson.hayes@my.hamptonu.edu, gharris@msrce.howard.edu, crawford@msrce.howard.edu*

### Abstract:

The objective of this project was to use a horizontal chemical vapor deposition (CVD) reactor to grow boron nitride nanowires on a silicon (Si) substrate using a metal catalyst. Boron nitride is shown to have properties that are compatible with complementary metal oxide semiconductors (CMOS) chips allowing it to be easily incorporated into current and future technologies. Efforts to grow boron nitride nanowires on <111> silicon substrates, <111> silicon with silicon dioxide (SiO<sub>2</sub>) and <100> silicon with a 7 nm metal catalyst of aluminum, cobalt, iron and nickel have not produced nanowires. Boron nanowires however were grown on <100> silicon substrate using a gold catalyst. All experiments were carried out in a CVD system at a pressure of 200 torr, at temperatures of 900-1200°C and flow rates of diborane at 100 standard cubic centimeters per minute (sccm) and ammonia at 250-800 sccm.

### Introduction:

Nanowires, a future technology, hold a lot of promise for use in powerful and versatile circuits. Nanowires are on the order of 100 nm or less, with the electrons being quantum-confined laterally, and thereby occupying energy levels that are different from the traditional continuum of energy levels or bands found in three dimensional materials. We used the vapor liquid solid (VLS) growth method, which is a mechanism for the growth of one-dimensional structures such as nanowires. This method uses chemical vapor deposition (CVD), which is a chemical process used in the semiconductor industry to produce thin film deposition. In CVD, a substrate is exposed to one or more precursors, in our case ammonia (NH<sub>3</sub>) and diborane (B<sub>2</sub>H<sub>6</sub>), which react on the substrate surface to produce the desired material boron nitride (BN).

BN is a wide band gap semiconductor, thus making it applicable in high power and high temperature applications. BN has one of the lowest densities of all the ceramic elements and has excellent machinability, which also makes it ideal for light components for aerospace applications.

### Experimental Procedure:

Si <100>, Si <111> and Si <111> with SiO<sub>2</sub> wafers were cut into one-inch by 0.5-inch pieces, brushed with a soap solution,

rinsed with deionized (DI) water then dried with nitrogen. The samples were then sonicated in trichloroethylene, acetone, and methanol for three minutes before being rinsed in DI water and dried with nitrogen. Each substrate was then coated with either 7 nm of aluminum (Al), cobalt (Co), iron (Fe) or nickel (Ni) by electron beam evaporation or gold (Au) by thermal evaporation.

The substrates were placed on a graphite susceptor on a quartz holder and inside of a quartz inner tube of the CVD reactor. Flow rates of the precursors, NH<sub>3</sub> and B<sub>2</sub>H<sub>6</sub>, were set before being injected into the CVD chamber. Using a radio frequency generator, the substrate was ramped up to the growth temperature and the growth was conducted for a set time. The substrate was then analyzed using a scanning electron microscope (SEM) for nanowire growth, and the energy-dispersive x-ray spectroscopy (EDS) attachment was then used to determine the composition.

### Results and Conclusions:

Growth of BN nanowires proved to be very difficult to accomplish, even after many runs with various changes to growth conditions. Figure 1 is an SEM image of an initial approach with 7 nm of Co on Si <100>, but it did not produce

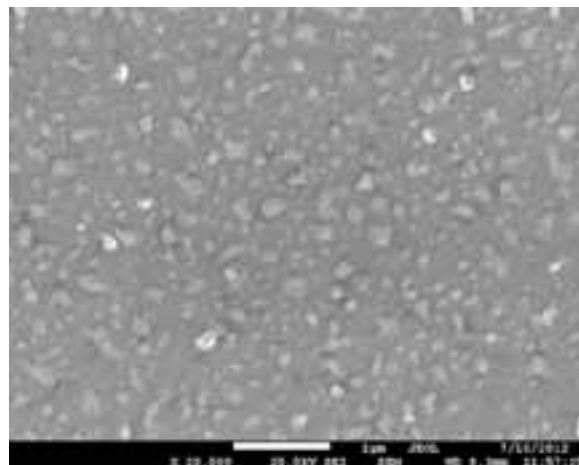


*Figure 1: SEM image of Si <100> with 7 nm Co after initial approach.*

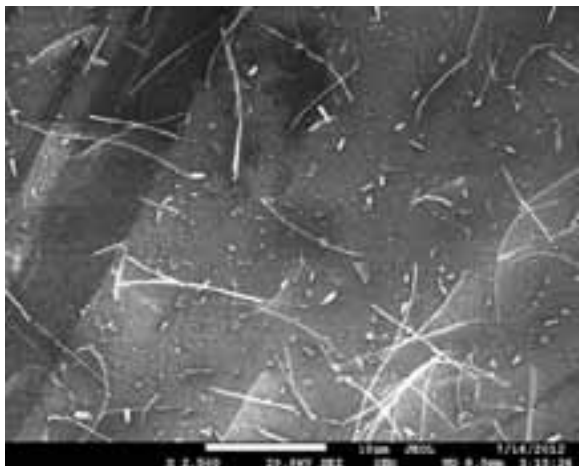


Figure 2: SEM image of Si <100> with 7 nm of Au with Si NW.

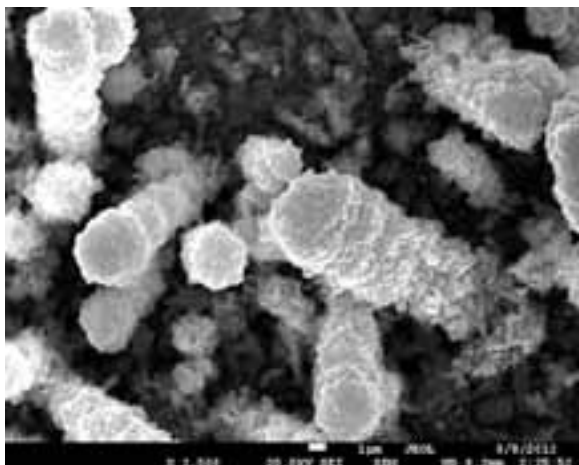


Figure 3: SEM image of Si <100> with 7 nm of Au with BN wire.

any nanowire growth. There were droplet formations on the surface of the substrate, which would suggest that the gases at least reacted with the metal on the surface.

Figure 2 shows an SEM image of nanowire growth on the surface of Si <100> with 7 nm of Au. These nanowires were grown for 60 minutes at a temperature of 900°C, 200 torr pressure, with flow rates of NH<sub>3</sub> at 150 sccm and B<sub>2</sub>H<sub>6</sub> at 100 sccm. Upon doing EDS analysis of this sample, the wire was found to contain 38.38% of boron, 61.62% of silicon, but no nitrogen.

Figure 3 is an SEM image showing BN wire growth on <100> silicon with 7 nm of Au. These BN wires could not be

	Si wires	Si wires doped with B <sub>2</sub> H <sub>6</sub>	BN wires
Temperature (°C)	900	900	1100
Time (min.)	15	15	30
Pressure (torr.)	200	200	200
H <sub>2</sub> (sLm.)	9.5	9.5	9
SiH <sub>4</sub> (sccm.)	50	50	0
B <sub>2</sub> H <sub>6</sub> (sccm.)	0	100	100
NH <sub>3</sub> (sccm.)	0	0	250

Table 1: Growth parameters for BN wire growth.

classified as nanowires since their diameter was not less than 100 nm. Table 1 shows the growth parameters used for this sample. First, Si wires grown with silane (SiH<sub>4</sub>), the Si wires were then doped with B<sub>2</sub>H<sub>6</sub> for 30 minutes, and with both B<sub>2</sub>H<sub>6</sub> and NH<sub>3</sub> for another 30 minutes. After performing EDS on this sample, the tip of the wire showed there was 34.38% of boron, 60.67% of nitrogen and 4.94% of Au.

After weeks of manipulating growth conditions for BN nanowires, the deposition of BN wires was a major accomplishment. Even though BN nanowires were not successfully grown on the silicon substrates with the catalysts used, further efforts to grow BN nanowire and the testing of different thicknesses of Au in dots or films should be attempted.

### Acknowledgments:

I would like to thank my principal investigator Dr. Gary Harris, mentor Mr. Crawford Taylor, Ms. Gurpreet Kaur, and the whole HNF faculty. I would also like to thank the NNIN REU Program and NSF for funding this research.

### References:

- [1] Evaporation (Deposition) Sources from READE. (n.d.). Reade. Retrieved July 10, 2012, from <http://www.reade.com/products/161-evaporation-source-materials/>.
- [2] Manufacturing Processes - Coatings Surface Finishing. (n.d.). Engineer's Handbook. Retrieved July 10, 2012, from <http://www.engineershandbook.com/MfgMethods/cvd.htm>.
- [3] L. Guo and R.N. Singh. "Growth of Boron Nitride Nanowires by Microwave Plasma CVD." Materials Science and Technology Conference (2006).

# Controlling and Understanding the Effects of Reactive Colloids' Packing on Silicon Etching Patterns

**Codey Henderson**

**Chemistry Department, University of South Alabama**

*NNIN REU Site: Penn State Nanofabrication Laboratory, The Pennsylvania State University, University Park, PA*

*NNIN REU Principal Investigator: Dr. Seong Kim, Department of Chemical Engineering, The Pennsylvania State University*

*NNIN REU Mentor: Ala'a Al-Azizi, Department of Chemical Engineering, The Pennsylvania State University*

*Contact: cbh801@jagmail.southalabama.edu, shkim@enr.psu.edu, aaa253@psu.edu*

## Abstract:

Previous research found that amidine-functionalized polystyrene latex (APSL) adsorbed to a silicon substrate and heated produces nanowells whose sizes are dependent on the size of APSL particles. These surface features have applications to mechanical, optical, and electrical devices as well as many procedures in which mask-less fabrication is desirable. This study focused on understanding what effect a highly dense particle packing would have on the etching process and the observable features. A dense monolayer was achieved through spin-coating APSL directly onto the silicon. After heating and toluene cleaning to remove the layer of glassed polystyrene that formed, there was observed an assumed silicon re-deposition covering the nanowells and appearing to coat favorably to particles resting within the nanowells. Preliminary results showed the surface to become more hydrophilic with the presence of the deposited material. Further research aims to confirm the identity of this re-deposition as well as control the formation and removal of the deposited material through an understanding of the formation mechanism. Research will also be conducted examining the effect of the deposited material on the physical properties, such as the hydrophobicity and reflectance, of the sample.

## Introduction:

Nanofabrication of materials is important to the creation of many mechanical, optical, and electrical devices. Traditional fabrication techniques, such as lithography, require expensive, harmful materials and must be carried out in expensive, well-maintained cleanrooms. In contrast, the mask-less fabrication method described by Chaturvedi uses inexpensive, harmless materials and can be performed under desktop conditions [1]. This technique uses an amidine-functionalized polystyrene latex (APSL) adsorbed to the surface of a silicon substrate and heated to 150°C to produce a hydroxide particle, a known etchant of silicon. The hydroxide is produced locally beneath the polystyrene bead, and the etched area is therefore, for silicon <100>, in the shape of an inverted square pyramid the size of the polystyrene bead. Normal fabrication using this technique sets the inter-particle distance based off the

particles' Debye length. This experiment aimed to decrease the inter-particle distance through spin-coating and observe the changes to the etching pattern seen previously.

## Experimental Procedure:

To a plasma-cleaned silicon <100> wafer was spin-coated a solution of 4% wt/v 500 nm APSL at 400 RPM. The sample was then placed in a 23 mL Parr bomb containing 15 mL of DI water. The bomb was then placed in an oven pre-heated to 150°C and cooked for three hours. The sample was allowed to cool inside the bomb, and then placed in toluene for 30 minutes, three times. Imaging of samples was performed with field-emission scanning electron microscopy (FESEM).

## Results and Conclusions:

Though the etching formation process — the creation of an inverted square pyramid — remained the same, the high-density array caused a variation from the expected result. Because of the close proximity of one bead to the next and because the sample was heated above the glass-transition temperature, the polystyrene glassed, forming a hydrophobic layer over the silicon surface. Although the glassed polystyrene did affect and possibly hinder the etching, it did not halt it. Some areas, termed under-etched and shown in Figure 1, had etching formations similar to that of 50 minutes of heating rather than three hours. Other areas, termed over-etched and shown in Figure 2, appeared to have fully etched with the etchings overlapping. In areas where etching was formed fully and correctly, a re-deposition was observed, as seen in Figure 3.

The re-deposition favored, but was not limited to, the etched areas. It appeared similar to the polystyrene bead expected to still be present in the nanowell, giving the appearance that formation was coating the polystyrene. Repeated toluene cleaning did not remove this deposition, shown in Figure 4, and sample surface was found to be more hydrophilic than an un-etched silicon surface. This seemed to suggest that

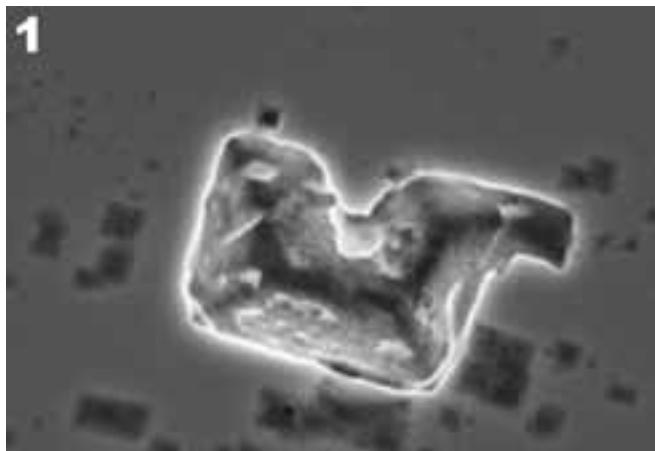


Figure 1: Under-etched 500 nm nanowells.

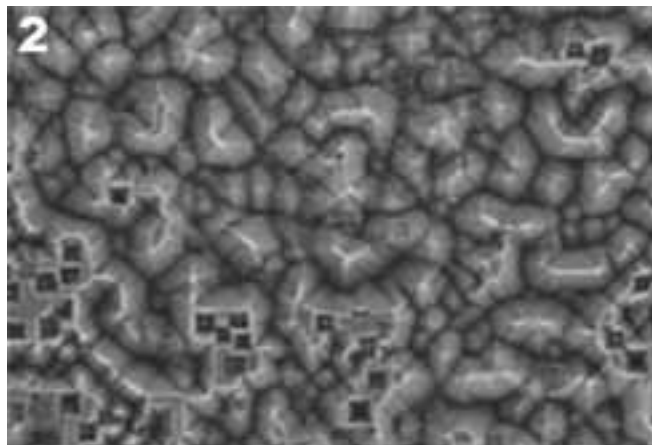


Figure 2: Over-etched 500 nm nanowells.

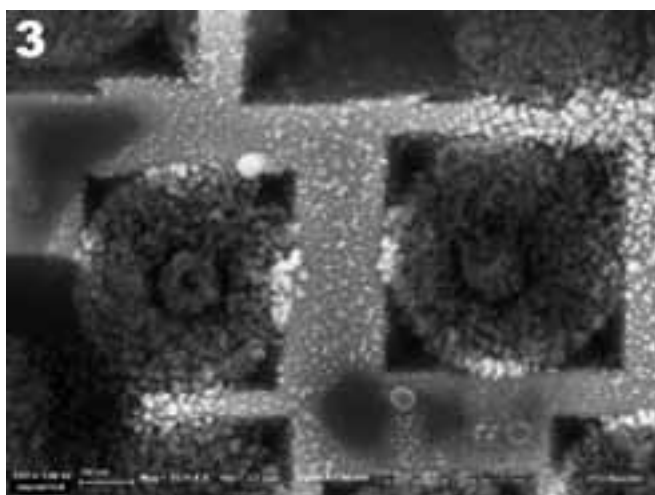


Figure 3: Re-deposited material on top of 500 nm nanowells.

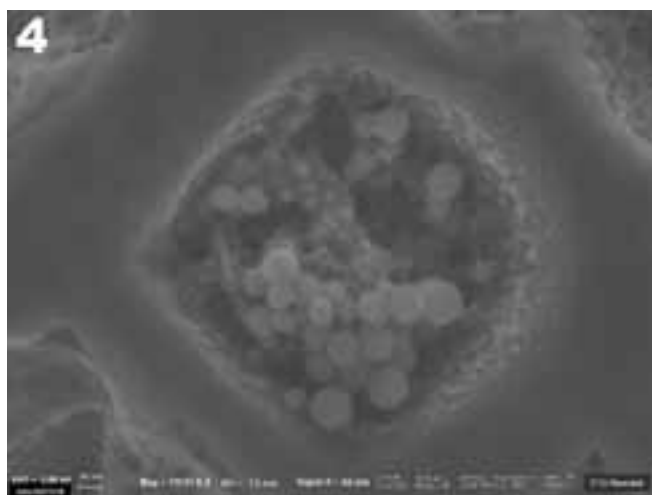


Figure 4: Thrice toluene-cleaned sample with 500 nm nanowells.

the formation was due to a re-deposition of etched silicon. Before the toluene cleaning, most of the deposition appeared to be smaller particles with a small number of larger beads. As the number of toluene cleanings increased, the frequency of the larger beads, seen in Figure 4, increased. This seems to indicate the deposition, while inorganic, was interacting with organic matter. As more of the organic matter was removed through toluene cleaning, the deposited material was left to interact with itself, creating larger beads.

#### Future Work:

It is assumed that the areas of over-etching are due to multi-layering. As such, the spin-coating method needs to be adjusted to ensure the polystyrene layer is indeed a monolayer. The identity of the deposited material needs to be identified, possibly through x-ray diffraction could also help determine the structure of the deposited material before and after toluene cleaning. In addition, FESEM imaging does not reveal clearly whether the deposition is occurring as a coating of the

remaining polystyrene or if the material is a residue within the nanowell that has replaced the particle.

#### Acknowledgments:

I would like to acknowledge my Principal Investigator, Dr. Seong Kim, my mentor, Ala'a Al-Azizi, and Dr. Kim's research group for their support and direction, as well as Dr. Shikuan Yang for his assistance with the spin-coating method. I would also like to thank Penn State's Materials Research Institute staff for their assistance and use of their equipment and the National Nanotechnology Infrastructure Network Research Experience for Undergraduates (NNIN REU) Program for funding.

#### References:

- [1] Chaturvedi, N.; "Maskless Fabrication of Nanowells Using Chemically Reactive Colloids"; *Nano Lett.*, 11 (2), pp 672–676 (2011).

## Assembly of Thermo-Responsive Microcapsules

Ian Holmes

Materials Science and Engineering, Stanford University

NNIN REU Site: Center for Nanoscale Systems, Harvard University, Cambridge, MA

NNIN REU Principal Investigator: Dr. David A. Weitz, Physics, Harvard University

NNIN REU Mentor: Esther Amstad, Physics, Harvard University

Contact: [iholmes@stanford.edu](mailto:iholmes@stanford.edu), [weitz@seas.harvard.edu](mailto:weitz@seas.harvard.edu), [eamstad@seas.harvard.edu](mailto:eamstad@seas.harvard.edu)

### Abstract:

Microcapsules are currently employed for a number of applications ranging from drug delivery vehicles to capsules contained in cosmetic products. In these applications, it is desirable that the microcapsules be able to control the timing of the release of their contents with external stimuli such as temperature changes or light illumination. The focus of this research was to design thermo-responsive microcapsules. Microcapsules were assembled as double emulsions using microfluidic polydimethylsiloxane (PDMS) devices. By varying the flow rates of the inner and middle phases, and by varying the composition of the middle phase that, after it has been polymerized, yielded the capsule shell, it was possible to control the thickness and thermo-response of the capsules.

### Background:

Microcapsules having shells composed of polymers having a lower critical solution temperature (LCST) are well known [1]. Capsules, consisting of a shell that has a LCST, are shriveled at a temperature above the LCST of the polymer and are impermeable to hydrophilic molecules. When the capsules are brought to a temperature below the LCST, they swell, the shells become hydrated, and the capsules become permeable to hydrophilic molecules, thereby releasing their encapsulants.

Conversely, microcapsules having shells composed of polymers having an upper critical solution temperature (UCST) are much less researched. Contrary to polymers that have an LCST, capsules containing a polymer having a UCST would swell and release their encapsulants at temperatures above the UCST. These have numerous possible biomedical, cosmetic, and chemical applications not accessible using capsules with an LCST or no thermo-response.

In this research, we used microfluidic PDMS devices to fabricate double emulsion templates (Figure 1) for microcapsules containing a polymer (poly[2-(methacryloyloxy)ethyl dimethyl-(3-sulfopropyl)ammonium hydroxide]) (PMEDSAH) having a UCST [2]. Additionally, we studied the thermo-response of PMEDSAH in bulk as a function of the amount of triacrylate crosslinker added to the PMEDSAH hydrogel at different temperatures.

### Experimental Procedure:

First, the solutions used for the inner, middle, and outer phases of the drops were prepared. The inner phase was 20% DEXTRAN with a molecular weight of 70 kDa, while the outer phase was HFE 7500 with 1% by weight of a fluorinated surfactant. Three different middle phases containing a solution of 2-(methacryloyloxy)ethyl dimethyl-(3-sulfopropyl)ammonium hydroxide (MEDSAH) and the photo initiator Irgacure 2959 with varied concentrations of cross linker were prepared. One-third parts ethanol was added to increase solubility of the triacrylate crosslinker.

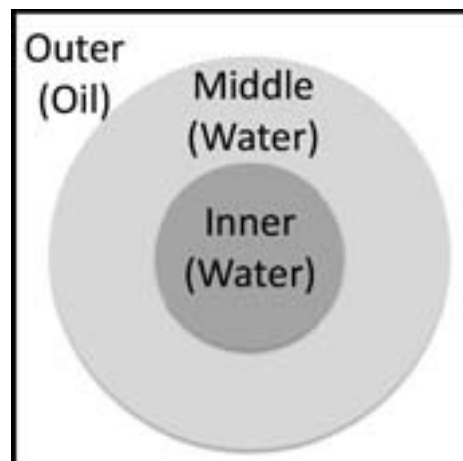


Figure 1: Water/water/oil double emulsion used as template for manufacture of microcapsules.

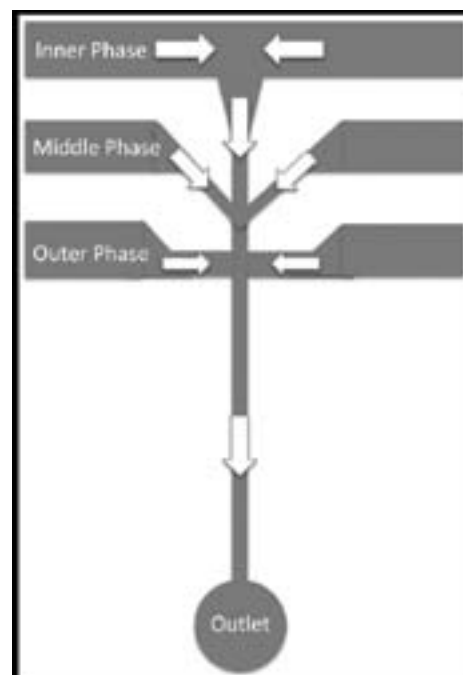


Figure 2: Diagram of microfluidic device used for manufacture of microcapsules.

The three solutions were then injected into a polydimethylsiloxane (PDMS) microfluidic device (Figure 2) with a channel width of 40  $\mu\text{m}$ , using volume flow rate controlled pumps at flow rates varying between 0 and 100  $\mu\text{l/hr}$  for the inner and middle phases, and 1000  $\mu\text{l/hr}$  for the outer phase. The resulting emulsion containing monodisperse microcapsules was collected in vials and placed into a vacuum chamber for 12 hours to remove oxygen. After air bubbles were removed, the samples were irradiated with UV light for 15 minutes to initiate polymerization of the shell (creating pMEDSAH), and heated in an oven at 40°C for 24 hours in order to allow complete polymerization of the shell.

Additionally, samples of the middle phase were synthesized in bulk so as to measure the thermo-response of the PMEDSAH. Cylindrical molds were created by cutting the top off of ½-inch Falcon® tubes and affixing them to Petri® dishes using vacuum grease as an adhesive. Solutions of the middle phase containing no triacrylate crosslinker, 25 mg/mL crosslinker, and 250 mg/mL crosslinker were pipetted into the molds. As above, these samples were placed in a vacuum for a minimum of 30 minutes in order to remove oxygen, and then exposed to ultraviolet radiation to initiate polymerization. The samples were again rested for at least 24 hours in order to ensure that polymerization had completed.

The samples were removed from their molds, their dimensions measured, and placed into individual Petri dishes. Each dish was filled with water and sealed with strips of Parafilm to prevent evaporation. Samples of each crosslinker concentration were placed at 24, 40, and 65°C and their dimensions measured every hour.

### Results and Conclusions:

Microcapsules were successfully assembled using water/water/oil double emulsions as templates. The 100% encapsulation efficiency and high degree of monodispersity make assembly of capsules using microfluidic devices advantageous.

The results of the thermo-response of the bulk samples of the middle phase are shown in Figure 3. One conclusion of this experiment is that crosslinker is necessary to create a thermo-responsive polymer in water, as all samples containing no crosslinker dissolved within two hours of placement in water. However, while some crosslinker is necessary, lower concentrations of crosslinker seem to yield a greater thermo-response. Additionally, the samples stored at 65°C seem to exhibit a greater thermo-response than those stored at lower temperatures. These results matched the expected outcome.

### Future Work:

The microcapsules need to be quantitatively analyzed to determine if varying the rates of infusion for the inner and middle phases during assembly can control the shell thickness. More data needs to be collected for the middle phase in bulk to confirm a correlation between concentrations of cross linker, temperatures, and thermo-response.

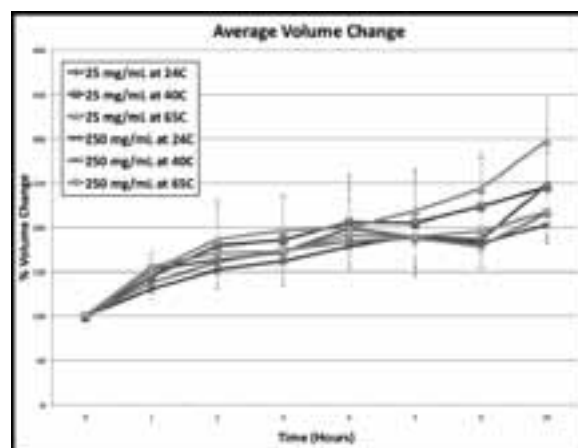


Figure 3: Average volume change of middle phase over time at varying cross linker concentrations and temperature.

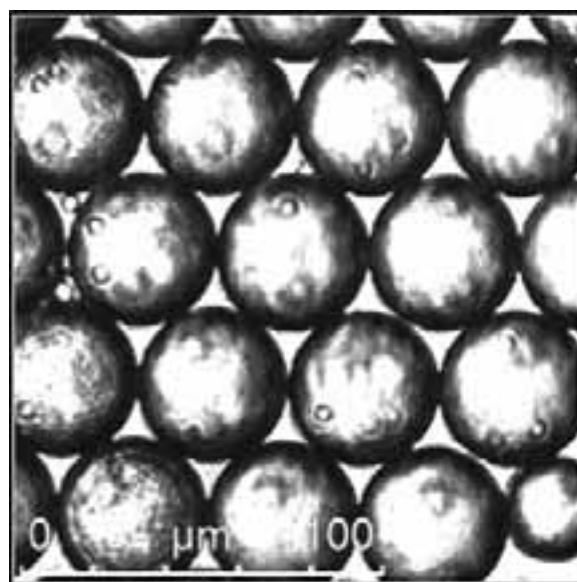


Figure 4: Confocal image of microcapsules assembled at inner and middle flow rates of 50  $\mu\text{l/hr}$ .

### Acknowledgments:

I wish to acknowledge my P.I. David A. Weitz and my mentor Esther Amstad, Kathryn Hollar, Jorge Pozo, Anna Hurlimann, and Tom Kodger for their contributions as well as the National Nanotechnology Infrastructure Network Research Experience for Undergraduates Program and the National Science Foundation for funding.

### References:

- [1] Seiffert, S.; Thiele, J.; Abate, A. R.; Weitz, D. A. J. Am. Chem. Soc. 2010, 132, 6606-6609.
- [2] Xia, Y. N. and Whitesides, G. M. "Soft Lithography." *Angewandte Chemie-International Edition* 1998, 37(5), 551-575.

## Effect of Inert Nanoparticles on Cement Hydration

**Melinda Jue**

**Chemical Engineering, University of Texas at Austin**

*NNIN REU Site: Nanotechnology Research Center, Georgia Institute of Technology, Atlanta, GA*

*NNIN REU Principal Investigator: Kimberly Kurtis, Civil and Environmental Engineering, Georgia Institute of Technology*

*NNIN REU Mentor: Amal Jayapalan, Civil and Environmental Engineering, Georgia Institute of Technology*

*Contact: melindajue@utexas.edu, kimberly.kurtis@ce.gatech.edu, amalrajpi@gatech.edu*

### Abstract:

Inert nanoparticles of titanium dioxide and ultra-fine limestone are used as fillers in Portland cement, because of their potential to reduce the amount of required cement without compromising early age properties. The effect of these fillers on early age hydration of cement was investigated using isothermal calorimetry and specific surface area analysis. Isothermal calorimetry measurements, in the presence of different concentrations of nanoparticles and at different temperatures, were used to determine the apparent activation energy of cement hydration according to the Arrhenius equation. Inert nanoparticles of titanium dioxide and limestone were shown to alter the apparent activation energy and specific surface area of the cement depending on their size and rate of use.

### Introduction:

Cement is one of the most common materials used throughout the world. However, cement production is energy intensive and produces significant amounts of carbon dioxide [1]. The use of fillers in cement is an effective method for reducing cement consumption. The introduction of fillers such as titanium dioxide and limestone could also improve concrete properties including increased workability, strength, or durability. Photocatalytic nanoparticulate titanium dioxide in particular is known to have self-cleaning, pollution reducing, and biocidal capabilities that make it desirable for use as a cement replacement.

The complex series of simultaneous chemical reactions that occur when cement reacts with water is known as cement hydration. Cement hydration results in the formation of calcium silicate hydrate (C-S-H), the main strength-giving phase of hydrated cement, as well as other hydration products. The presence of fine fillers acts as sites for heterogeneous nucleation for hydration that could increase the rate of product formation [2]. The cement hydration reaction follows the Arrhenius equation with the apparent activation energy of cement hydration representing the overall temperature

Filler	Crystal Size (nm)	Agglomerate Size ( $\mu\text{m}$ )	BET Surface Area ( $\text{m}^2/\text{g}$ )
Cement	-	-	0.98
P25	21	0.58	48.02
UFLS	-	0.7	9.47
PC105	15-25	1.2	74.65
PC50	20-30	1.5	42.20

Table 1: Size and specific surface area of raw materials.

dependence of the reactions [3]. The specific surface area can be used as an indication of the progress of hydration, as the addition of fillers could increase the surface area over time due to increased product formation.

### Experimental Procedure:

In order to calculate the apparent activation energy of the cement-filler mixtures, the heat of hydration was measured using an isothermal calorimeter at 15, 25, 35, 45, and 55°C. The water to solids ratio (w/s) was kept constant at 0.5, and the fillers were added at 5 and 10% mass replacement of cement. Samples were run at least in duplicate to measure the effect of the following fillers: PC50, PC105, P25 titanium dioxide, and ultrafine limestone (UFLS). Table 1 lists the crystal and agglomerate size of the fillers compared to cement. Measurements were obtained from 44 to 84 hours depending on the sample temperature. A specific surface area analyzer was used to measure the 1-day and 3-day sample surface areas.

### Results and Conclusions:

From the heat of hydration data, it was observed that the addition of fine fillers increased both the total energy released as well as the rate of heat released compared to the control. P25, the finest filler used in these experiments, exaggerated the effects the most. When comparing the cumulative heat of hydration data, it was observed that the fillers also increased the total heat released. The increase in heat release could be attributed to the fillers acting as heterogeneous nucleation sites and increasing the rate of C-S-H formation.

Heterogeneous nucleation and the increased rate of hydration in the presence of fillers also altered the degree of hydration. The degree of hydration is the fraction of cement that has reacted with the water to form hydration products. Because the cement hydration is temperature sensitive, the degree of hydration could dramatically increase at higher temperatures.

$$\alpha(t) = \alpha_u e^{-\left[\frac{\tau}{t}\right]^\beta}$$

Eq. 1: Three-parameter model for degree of hydration [3].

The degree of hydration curve was modeled according to Equation 1 [4] and the apparent activation energy of each sample was calculated. Table 2 lists the apparent activation energy of each sample mixture up to 50% degree of hydration. All additions of fillers increased the apparent activation energy compared to the control. Yet again, the finest filler P25 had the most prominent effect on the activation energy. The change in apparent activation energy represents the temperature sensitivity of the overall reaction with an increase in activation energy corresponding to a decrease in temperature sensitivity.

The BET surface area and corresponding degree of hydration are listed in Table 3. The specific surface area is a quantitative measure of C-S-H formation and microstructure development. As hydration proceeds, the C-S-H formation continues and the surface area increases. The specific surface area for all filler-cement samples was higher than the control after both one and three days.

This data correlates well with the degree of cement hydration that increased when fillers were added.

In conclusion, it was observed that the different fine filler cement replacements increase all of the measured properties of cement paste. The increase in rate of heat release, total heat of hydration, surface area evolution, and decrease in temperature sensitivity, suggests that inert fine fillers have the potential to replace cement without compromising the early age properties.

**Acknowledgments:**

Thank you to Kimberly Kurtis, Amal Jayapalan, Nancy Healy, Leslie O’Neill, the National Nanotechnology Infrastructure Network Research Experience for Undergraduates (NNIN REU) Program, and the National Science Foundation for making this research possible.

**References:**

- [1] Gregg, J. S.; Andres, R. J.; and Marland, G. Geophys Res Lett. 2008, 35, L08806.
- [2] Jayapalan, A.R., Lee, B.Y., and Kurtis, K.E. Nanotechnology in Construction 3, Proc. 2009. Prague: Springer-Verlag Berlin Heidelberg.
- [3] Poole, J. L.; Riding, K. A.; Juenger, M. C. G.; Folliard, K. J.; and Schindler, A. K. J Mater Civil Eng. 2011, 23, 1654-1661.
- [4] Poole, J. L.; Riding, K. A.; Folliard, K. J.; Juenger, M. C. G.; and Schindler, A. K. ACI Mater J. 2007, 104, 303-311.

Apparent Activation Energy (kJ/mol)							
0%	5% P25	5% UFLS	10% UFLS	5% PC105	10% PC105	5% PC50	10% PC50
36.32	39.12	38.33	37.80	37.58	39.06	36.86	37.80

Table 2. Apparent activation energy at 50% degree of hydration.

	1 Day		3 Day	
	BET Surface Area (m <sup>2</sup> /g)	Degree of Hydration	BET Surface Area (m <sup>2</sup> /g)	Degree of Hydration
Control	14.92	0.46	16.18	0.63
P25	17.33	0.58	22.37	0.70
5% UFLS	5.89	0.49	15.23	0.66
10% UFLS	16.29	0.51	16.68	0.67
5% PC105	16.06	0.50	18.42	0.67
10% PC105	16.10	0.50	19.46	0.66
5% PC50	16.24	0.48	16.72	0.65
10% PC50	16.41	0.48	18.64	0.64

Table 3: Specific surface area for early age samples.

## Influence of Optical Stress on Mixed Oxide Transistors

**Andrew Knight**

**Physics, Norfolk State University**

*NNIN REU Site: ASU NanoFab, Arizona State University, Tempe, AZ*

*NNIN REU Principal Investigator: Dr. Terry L. Alford, Engineering of Matter, Transport and Energy, Arizona State University*

*NNIN REU Mentor: Rajitha Vemuri, School for Engineering of Matter, Transport and Energy, Arizona State University*

*Contact: a.l.knight@spartans.nsu.edu, ta@asu.edu, rvemuri@asu.edu*

### Abstract:

To meet the growing demands of thinner and larger display panels, an improved and reliable semiconducting channel material must be used. Indium-gallium-zinc oxide (IGZO)-based thin-film transistors (TFTs) have presented themselves as a viable option to achieve better carrier mobility, optical transparency and robustness under optical stress conditions. However, the instability of IGZO TFTs remains a problem that must be resolved. In particular, there is deterioration in the threshold voltage ( $V_{th}$ ) during continued operation because of continuous optical stress. In this investigation, we performed illumination stress on TFTs in an attempt to elucidate the root cause of the  $V_{th}$  shift, and several post fabrication anneals to reduce defects due to low temperature fabrication process. The as-fabricated TFTs displayed a  $V_{th}$  shift of -17 V under optical stress, but demonstrated high stability with post-fabrication anneals in different ambients.

### Introduction:

As the ability to scale the dimensions of transistors down to nanometers has improved, the computing powers relative to the sizes of the devices have increased substantially. Thus, consumers have come to expect a level of sophistication and proficiency in everyday electronics that seemed unattainable until a decade ago. From high-resolution smartphones to liquid

crystal and light emitting diode displays, the vast majority of electronic devices all rely on circuitry that is implemented in silicon. Although it is the most effective technology available, single-crystal silicon lacks optical transparency and flexibility. In addition, single-crystal silicon-based fabrication is expensive and unobtainable for large area electronics. Amorphous oxide semiconductors (e.g., IGZO) present a potential solution for applications that require transparency or flexibility.

### Experimental Procedure:

The structure of the IGZO TFT is shown in Figure 1. The gate metal was 150 nm thick molybdenum deposited using DC sputtering. After patterning the gate layer, a stack of silicon oxide ( $\text{SiO}_x$ ), IGZO, and  $\text{SiO}_x$  was deposited through a series of steps. A 200 nm silicon oxide formed the gate dielectric. The 50 nm thick channel material IGZO, with 99.99% pure  $\text{InGaZnO}_4$ , was deposited at an RF power of 100 W and a chamber pressure of 10 mTorr at 80°C, and a 100 nm intermetal dielectric  $\text{SiO}_x$  is deposited at 180°C. The IGZO was patterned and the source-drain metal (Mo) was sputtered to form the source and drain contacts of the TFT. A final step involved deposition of silicon nitride to serve as a passivation layer.

The IGZO TFT samples were annealed in one of four ambients (oxygen, vacuum, forming gas, and air) for 12 hours at 150°C to improve optical and electrical characteristics. Current-voltage characteristics were acquired using a HP 4155B semiconductor parameter analyzer. The TFTs were illumination-stressed for 25,000 seconds in a dark, light-tight setup, and the transfer characteristics were obtained by sweeping the gate voltage, with the drain biased at 10 V and the source grounded. To perform illumination testing, a Dolan Jenner Fiber Lite Illuminator with a light source of intensity 0.5 W/cm<sup>2</sup> and a dual gooseneck optical cable attachment was used. A 410 nm wavelength filter allowed violet light from the source to be used for the illumination tests, and was chosen due to previous reports on illumination stress testing [1] that revealed increasing amounts of photo-induced defects with decreasing wavelengths of light.

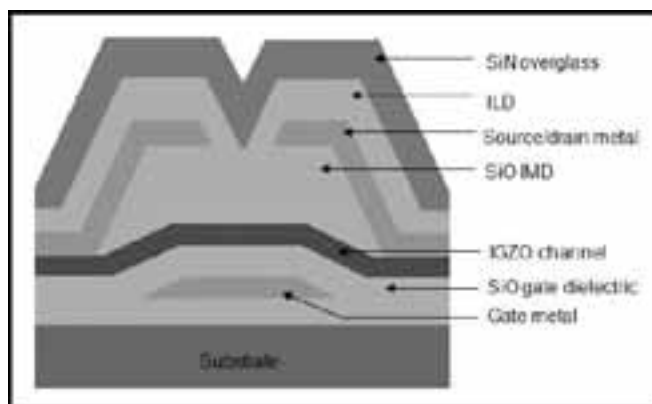


Figure 1: The structure of an IGZO TFT.

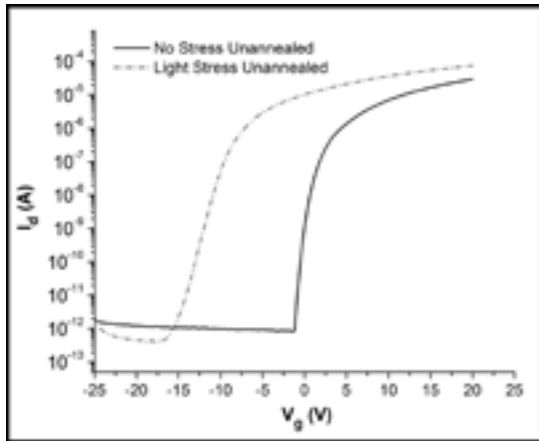


Figure 2: As-fabricated IGZO TFTs unannealed stressed under 410 nm light for seven hours.

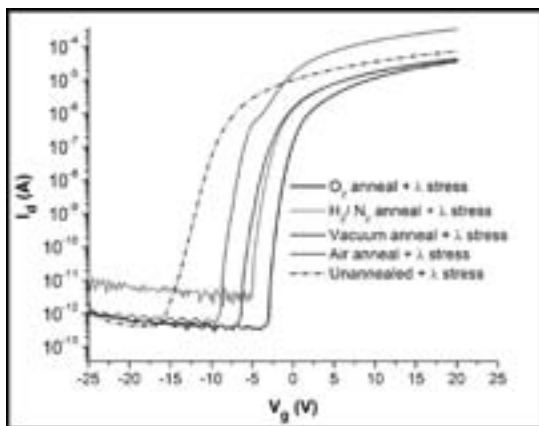


Figure 3: Illumination stress ( $\lambda = 410 \text{ nm}$  for 7H) on post-fabrication annealed IGZO TFTs for 12 h at 150°C.

**Results and Conclusions:**

In Figure 2, during as-fabrication stress testing there was a considerable threshold voltage shift, making the turn-on voltage smaller, and leakage and off currents higher, along with a slight increase in mobility. The  $V_{th}$  change was -17 V during the seven hours of light stressing. In post-fabrication annealed testing, there was great improvement in the transistor performance seen as reduced  $V_{th}$  shift as Figure 3 demonstrates. In Figure 3, the oxygen-annealed sample showed the least deterioration with low off current and steep subthreshold swing. This can be explained by the annihilation of oxygen vacancies by annealing, which otherwise ionize

Air	Vacuum	Oxygen	Forming Gas	Unannealed
-3.6 V	-4.5 V	-1.3 V	-3.3 V	-17 V

Figure 4:  $V_{th}$  shift of unannealed along with air, vacuum, oxygen, and forming gas annealed IGZO TFTs under illumination stress.

to contribute as excess carriers due to photonic stresses [2]. Figure 4 displays the  $V_{th}$  shift of each sample after seven hours of light stress with respect to each device’s own unstressed condition (e.g.,  $\Delta V_{th}$  for oxygen-annealed TFT is calculated by finding the difference between  $V_{th}$  after seven hours and  $V_{th}$  unstressed, but annealed in oxygen).

In conclusion, the results obtained emphasize the importance of post-fabrication annealing of IGZO TFTs whilst the as-fabricated TFT device was driven to near failure under stand-alone illumination stress. Annealing reduces the  $V_{th}$  shift due to annihilation of defects created during low temperature fabrication. The TFTs demonstrate highest stability after annealing in oxygen ambient due to annihilation of oxygen vacancies that contribute most towards excess carriers.

**Future Work:**

Future work will involve investigating the effects of electro-mechanical and mechanical strain on IGZO TFTs fabricated on flexible substrates. In addition, the findings of the current report will be presented at the TMS 2013 Conference.

**Acknowledgements:**

I would like to thank the National Nanotechnology Infrastructure Network Research Experience for Undergraduates Program, the National Science Foundation under Grant No. ECS-0335765, and the ASU NanoFab for providing the opportunity and funding for this experience.

**References:**

- [1] Vemuri, R., Mathews, W., Alford, T.L. “Investigation of Defect Generation and Annihilation in IGZO TFTs during Practical Stress Conditions: Illumination and Electrical Bias.” Submitted to Journal of Physics D: Applied Physics (2012).
- [2] J.H. Kim, U.K. Kim, Y.J. Chung, and C.S. Hwang. “Correlation of the change in transfer characteristics with the interfacial trap densities of amorphous In-Ga-Zn-O thin film transistors under light illumination.” Appl. Phys. Letts. vol. 98, p. 232102 (2011).

## Giant Magnetoresistive Sensors for Biological Applications

**Jonathan Lee**

**Physics, University of Central Florida**

*NNIN REU Site: Nanofabrication Center, University of Minnesota-Twin Cities, Minneapolis, MN*

*NNIN REU Principal Investigator: Prof. Jian-Ping Wang, Electrical and Computer Engineering, University of Minnesota*

*NNIN REU Mentor: Todd Klein, Electrical and Computer Engineering, University of Minnesota*

*Contact: jondlee@knights.ucf.edu, jpwang@umn.edu, klei0349@umn.edu*

### Abstract:

Field-induced domain wall motion through the free magnetic layer of a spin valve nanowire has been observed both electrically and with Bitter Method on a scanning electron microscope. The giant magnetoresistance effect was used to determine the position of the domain wall. Change in depinning field strength due to the presence of magnetic nanoparticles (MNPs) was observed. This work served as preparation to extend to the sensing of biological molecules tagged with MNPs.

### Introduction:

Some diseases increase the concentration of certain proteins in the blood, while others release proteins that would otherwise not be present. Giant magnetoresistive (GMR) sensors have shown the ability to detect target proteins with high sensitivity using MNPs as tags [1]. The device is sensitive to the presence of the MNP stray field, which shields the free layer of the sensor from an externally applied field, requiring more field strength to coerce the free layer magnetization in regions with MNPs present. GMR devices have been observed to detect proteins with a limit of detection in the hundreds of MNPs (< 100 nm diameter), which may miss a very low concentration detection.

To increase detection resolution, investigations were performed in order to manipulate and study the usefulness of magnetic domain walls (DW), which are native to the free layer of sensors with larger detection areas. The advantages of using magnetic DWs in this study were that GMR measurements have shown the location of DWs in the free layer of a GMR nanowire [2], and DWs have been shown to attract MNPs [3]. A smaller, curved sensor area has been studied here and has shown the possibility for increasing resolution to tens of particles.

### Experimental Procedure:

**Fabrication.** The substrate consisted of a silicon <100> wafer with 100 nm of silicon dioxide ( $\text{SiO}_2$ ) coating. The GMR metal stack was placed using a Shamrock RF sputtering device, placing thicknesses

Ta 30Å / IrMn 80Å / CoFe 25Å / Cu 40Å / CoFe 20Å / NiFe 55Å / Ta 50Å.

Sensor areas were designed to have curved shapes in order to easily place magnetic domain walls [4].

Devices were patterned using electron beam lithography with negative resist. The developed resist pattern shielded the sensors from ion-milling employed to remove surrounding metals. Removal of the patterned resist left only the devices on the substrate. Contacts were placed using electron beam lithography followed by an electron beam evaporated metal deposition of 800Å Cu.

**Testing.** A constant current of 10  $\mu\text{A}$  was passed through a device and the voltage across the device measured to calculate device resistance. Data from each device was actively recorded using LabVIEW software reading from a Keithley 2400 SourceMeter during various external magnetic field conditions.

DW depinning strengths were observed multiple times for several nanowires in order to confirm repeatability. Nanowire depinning measurements for the forward and reverse directions were recorded. Domain walls were induced near the center of a device by applying and then removing a magnetic field as shown in Figure 1A. During this step, the free layer aligned to the external field, and, when the field was removed,

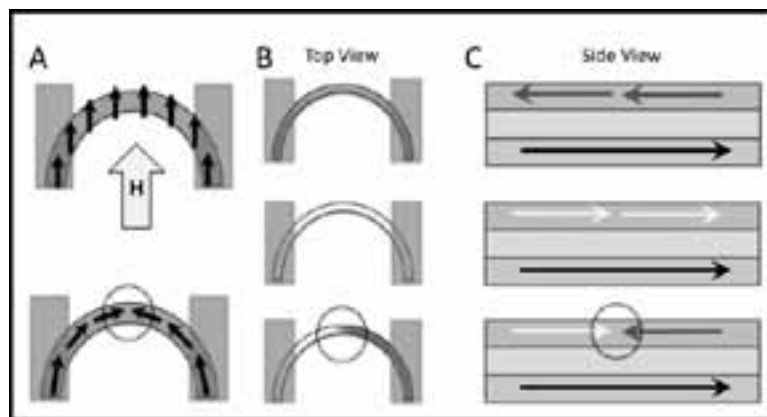


Figure 1: A) Device top view showing domain wall pinning schematic. B) and C) Top and side view of device in three resistance stages. White is parallel, and dark is antiparallel.

the magnetic direction of the free layer relaxed and aligned with the shape-anisotropic direction of the device — leaving a head-to-head domain wall near the middle of the sensing area. The nanowires were then exposed to a diluted solution of 35 nm superparamagnetic iron oxide particles and allowed to incubate for three hours before washing.

### Results and Conclusions:

Resistance measurements before and after DW creation showed an intermediate state, approximately half way between the high and low states. DW depinning field strengths were measured from the central pinning site.

DW depinning field strength was measured by placing a DW near the center of a device using the previously stated method and monitoring resistance as the field was slowly increased from zero in a horizontal direction. DW pinning sites result from fabrication roughness at edges and defects in the wire (contaminant particles, layer unevenness, etc.). Depinning strengths were measured for 200 nm wide nanostripes with and without designed notches of 60 nm. The depinning strengths were  $\sim 50$  Oe, noticeably higher than those with no obvious fabrication roughness  $< 40$  Oe. Also, there were no observable secondary pinning sites for the sensors with notches.

MNP presence was verified using scanning electron microscopy (SEM) before depinning field strength measurements were retaken. By observing the field depinning strength of a device before and after particle application, one could see a shift in the field. A sensor with 8 MNPs on its sensing surface showed a depinning field strength increase of approximately  $8 \pm 2$  Oe, see Figure 4. This is a promising result for progressing the diagnostic capability of GMR biosensors to include detection of target molecules with low concentrations.

### Acknowledgements:

This work was funded by the National Science Foundation, the National Nanotechnology Infrastructure Network REU program, and the University of Minnesota. My sincerest gratitude to Dr. Jian-Ping Wang and his group for their guidance and support, with special thanks to Todd Klein, Angeline Klemm, and the UMN Nanofabrication Center staff.

### References:

- [1] Edelstein, R.L., C.R. Tamanaha, P.E. Sheehan, M.M. Miller, D.R. Baselt, L.J. Whitman, and R.J. Colton. 2000. *Biosensors and Bioelectronics* 14, 805-813.
- [2] Boulle, O., G. Malinowski, and M. Klaui. 2011. *Materials Science and Engineering R* 72, 159-187.
- [3] Vavassori, P. P., Metlushko, V. V., Ilic, B. B., Gobbi, M. M., Donolato, M. M., Cantoni, M. M., and Bertacco, R. R. (2008). *Applied Physics Letters*, vol. 93 (20), 203502.
- [4] Saitoh, Eiji, Hideki Miyajima, Takehiro Yamaoka, and Gen Tatara. 2004. *Nature* 432, 203-206.

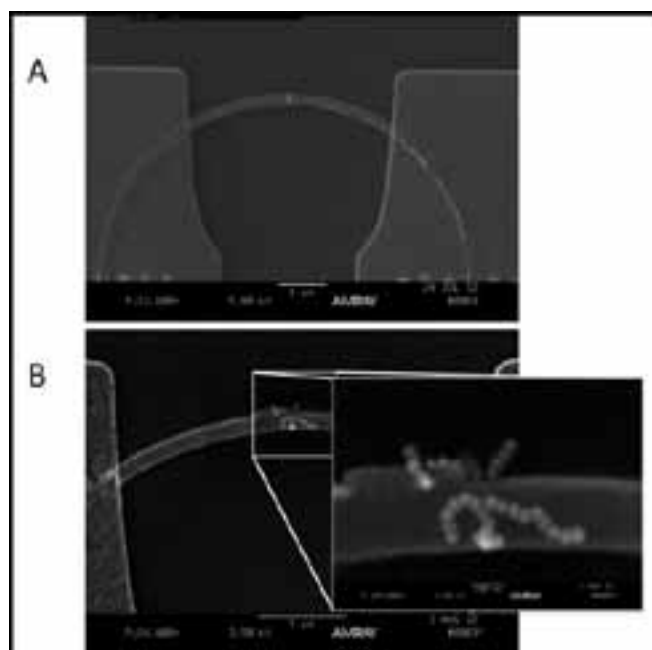


Figure 2: A) SEM image of device without MNPs. B) SEM image of device with MNPs.

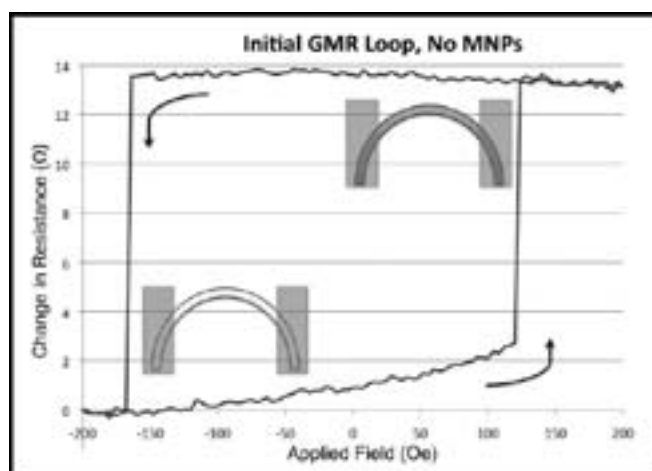


Figure 3: Graph showing the change in resistance by applied field.

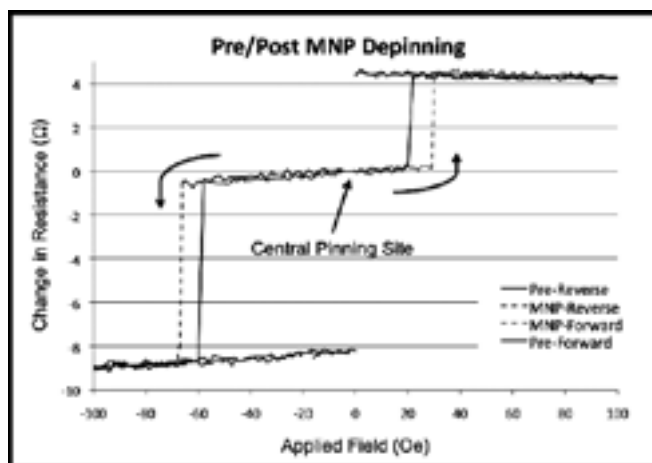


Figure 4: Graph showing the change in resistance from the central pinning site of a device both before (solid) and after (dashed) MNP placement.

## Selective Atomic Layer Deposition

Clay Long

Physics, The Pennsylvania State University

NNIN REU Site: Cornell NanoScale Science and Technology Facility, Cornell University, Ithaca, NY

NNIN REU Principal Investigator: Professor James Engstrom, Chemical Engineering, Cornell University

NNIN REU Mentor: Wenyu Zhang, Chemical Engineering, Cornell University

Contact: [ctl5066@psu.edu](mailto:ctl5066@psu.edu), [jre7@cornell.edu](mailto:jre7@cornell.edu), [wz89@cornell.edu](mailto:wz89@cornell.edu)

### Abstract:

Atomic layer deposition (ALD) of tantalum nitride ( $\text{TaN}_x$ ) has been performed on copper (Cu) and silicon dioxide ( $\text{SiO}_2$ ) substrates with the goal of selective area deposition using self-assembled monolayers (SAMs) as an ALD blocking layer. The films have been analyzed using spectroscopic ellipsometry (SE), contact angle, x-ray photoelectron spectroscopy (XPS), and low energy ion scattering spectroscopy (LEISS). The molecules (heptadecafluoro -1,1,2,2-tetrahydrodecyl) triethoxysilane (HDFTEOS) and 1H,1H,2H,2H-perfluorooctyltrichlorosilane (FOTS) were deposited onto both substrates before ALD. We found that both molecules impeded growth on  $\text{SiO}_2$  for the first 20 ALD cycles, shown with SE as well as XPS. After the initial growth impedance,  $\text{TaN}_x$  appears to grow on itself with a growth rate similar to the surfaces without SAMs.

### Introduction:

Atomic layer deposition (ALD) is a method for depositing thin films characterized by precision thickness control through a series of self-terminating reactions. The technique is similar to chemical vapor deposition (CVD), except that ALD breaks the reaction down into half cycles. In addition to the ability to lay thin films accurately by varying the number of cycles, the gas phase and self-limiting nature of ALD makes it ideal for high aspect ratio depositions. The goal of this project was to study methods for selectively depositing the desired material, tantalum nitride, only onto one substrate and not another.

The ability to deposit material only where it is wanted would be a powerful tool. One place where selective ALD could be beneficial is in the semiconductor industry. Currently copper (Cu) is used as the interconnect metal in devices. However, copper has been shown to diffuse into the dielectric layers creating shorts and heat dissipation problems, limiting the effectiveness of the device [1]. One fix would be to use a thin layer of  $\text{TaN}_x$  between the Cu and dielectric as a diffusion barrier layer [2]. Depositing the film would require a method of selectively depositing  $\text{TaN}_x$  on different areas.

### Experimental Procedure:

Two different substrates were studied: copper and chemical oxide (silicon dioxide, or chem ox). Three different scenarios were examined: 1) plain substrates (no SAMs), 2) with HDFTEOS, or 3) with FOTS. The SAMs were deposited onto both surfaces using a molecular vapor deposition method before the ALD depositions. The large number of fluorine atoms on the SAM molecules could create an unreactive surface that would stop ALD growth. ALD of  $\text{TaN}_x$  at a heater temperature of  $300^\circ\text{C}$  was subsequently performed on the samples. The ALD precursors used for this procedure were pentakis(dimethylamino) tantalum (PDMAT) and ammonia ( $\text{NH}_3$ ).

After depositions, the surfaces were then analyzed using contact angle, spectroscopic ellipsometry, XPS, and LEISS.

### Results:

From contact angle measurements, information was determined about the samples. Figure 1 shows that changes in contact angle occurred after depositing HDFTEOS and after heating the sample to an ALD temperature of  $300^\circ\text{C}$ . This seems to indicate that HDFTEOS was deposited onto the surface, but was not thermally stable on Cu. The change in angle after heating was not observed on chem ox. From spectroscopic ellipsometry, we saw that the long term growth rate of  $\text{TaN}_x$  is  $0.4\text{\AA}$  per cycle with no SAMs and  $0.38\text{\AA}$  per cycle with HDFTEOS. This corroborated theoretical  $\text{TaN}_x$  growth rates as well. Figure 2 is a close up of ultrathin film thickness from spectroscopic ellipsometry. Here we saw that for low ALD cycles, the HDFTEOS made a significant difference in the film thickness. Figure 3 shows XPS areas of the tantalum ( $4d_{5/2}$ ) peak corroborating the difference in tantalum deposition for low  $\text{TaN}_x$  ALD cycles on chem ox. There did not appear to be a difference in the amount of Ta on Cu, as shown in Figure 4. FOTS results were also included in the XPS data, which followed a similar trend as the HDFTEOS surfaces.

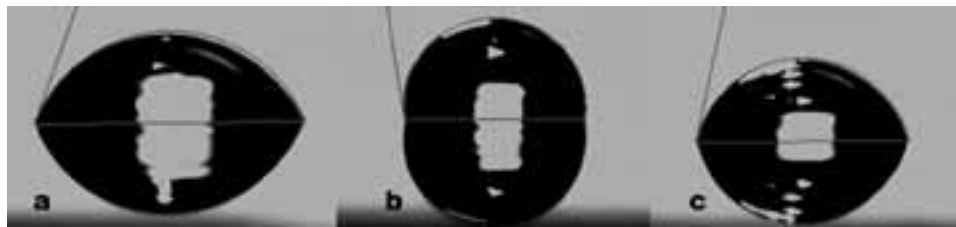
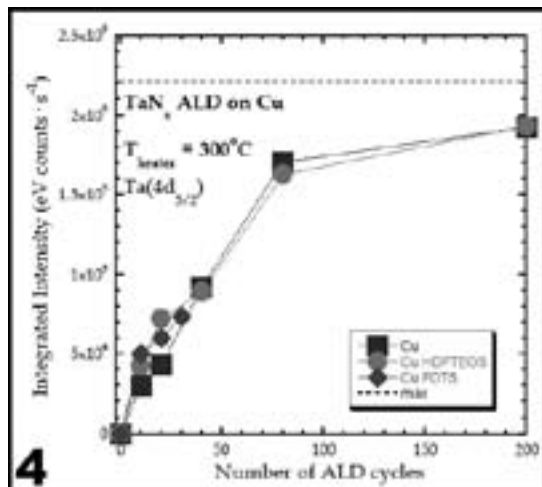
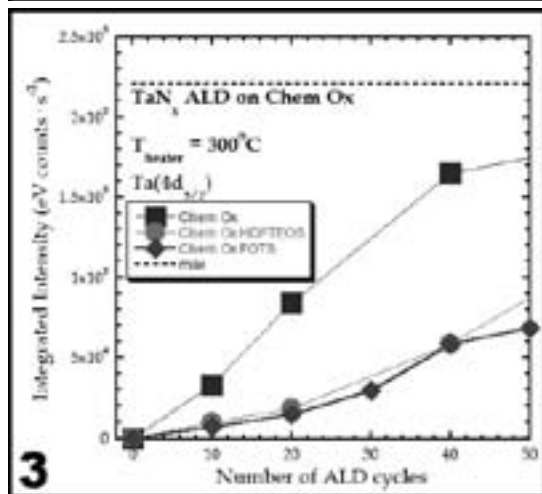
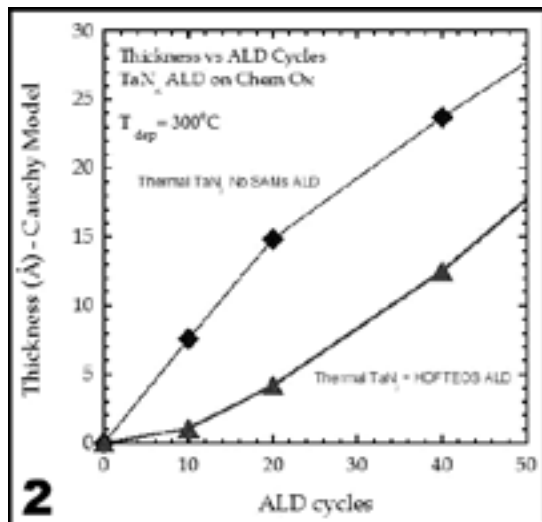


Figure 1: a] No SAMs (69.3°), b] HDFTEOS (98.7°), c] HDFTEOS (77.6°) after 0 ALD cy at 300°C.



LEISS is a surface sensitive technique and is helpful in obtaining information in regards to what is on the topmost layer of our films. Although we predicted that the SAMs formed a uniform monolayer right above the substrate, fluorine was observed with LEISS after as many as 80 TaN<sub>x</sub> ALD cycles on copper with HDFTEOS.

**Conclusions and Future Work:**

The SAMs HDFTEOS and FOTS have been demonstrated to act as a blocking layer for ultrathin films. Both impeded growth on SiO<sub>2</sub>, but on copper, the HDFTEOS was not thermally stable and FOTS did not significantly affect TaN<sub>x</sub> growth. As the number of cycles increased, the blocking layer was less effective because the film began to grow on itself.

The first molecules on the surface likely bound to defects in the SAMs and grew upwards from those points. A more uniform SAM layer could increase the effectiveness of the blocking layer. If tantalum nitride was binding to defects, it would mean that some FOTS or HDFTEOS should still be on the surface until the TaN<sub>x</sub> completely covered it. This hypothesis was supported by the fact that fluorine was observed with LEISS after 80 ALD cycles. Another possible explanation is that fluorine atoms diffused through the film and were being observed on the surface. In the future, we will conduct angle resolved XPS to determine where in the film the fluorine is.

A similar method of applying SAMs to different surfaces and testing the effectiveness as blocking layer could be applied to other films and substrates.

**Acknowledgements:**

I would like to thank the National Nanotechnology Infrastructure Network Research Experience for Undergraduates (NNIN REU) Program and the National Science Foundation for the sponsoring this research. I also appreciate the guidance and support from Wenyu Zhang, James Engstrom, Melanie-Claire Mallison, and the CNF staff.

**References:**

[1] H. Chung, et al. (2006), US Patent 7,049,226.  
 [2] Ma, P. et al Interconnect Technology Conference, 2009. IITC 2009. IEEE International, vol., no., pp.38-40, 1-3 June (2009).

Figure 2: Spectroscopic ellipsometry model dependent film thickness.

Figure 3: XPS Ta (4d<sub>5/2</sub>) peak area as a function of TaN<sub>x</sub> ALD cycles.

Figure 4: XPS Ta (4d<sub>5/2</sub>) peak area as a function of TaN<sub>x</sub> ALD cycles.

# Optimizing the Electrochemical Performance of Cathode Materials for Lithium Ion Rechargeable Batteries

**Peter Luo**

**Chemical Engineering, Princeton University**

*NNIN REU Site: Nano Research Facility, Washington University in St. Louis, St. Louis, MO*

*NNIN REU Principal Investigator: Dr. Richard Axelbaum, Department of Energy, Environmental and Chemical Engineering, Washington University at St. Louis*

*NNIN REU Mentors: Miklos Lengyel and Gal Atlas, Department of Energy, Environmental and Chemical Engineering, Washington University at St. Louis*

*Contact: pluo@princeton.edu, axelbaum@wustl.edu, mlengyel@wustl.edu*

## Introduction:

In recent years, the environmental impact of petroleum-based transportation has led to greater interest in alternatively powered transportation. Electric vehicles (EVs) and plug-in hybrid electric vehicles (PHEVs) are fast becoming a viable alternative, because they are capable of being fueled by electricity from sustainable power sources. In order for EVs to compete with current gas-powered cars, they must provide comparable performance, so their batteries need large capacity and good capacity retention. In our study, we used spray pyrolysis to synthesize cathode materials. The desired product is a layered-layered composite material of the form  $x\text{Li}_2\text{MnO}_3(1-x)\text{Li}(\text{MnNiCo})_{1/3}\text{O}_2$ , where  $x = 0.5$ . We focused on identifying the optimal spray pyrolysis furnace temperatures that yielded the best electrochemical performance.

## Experimental Procedure:

**Precursor Preparation.** In order to obtain the desired powder, a precursor solution was prepared by dissolving specific amounts of metal nitrates to obtain the correct stoichiometry. The product is a layered-layered material of the form  $x\text{Li}_2\text{MnO}_3(1-x)\text{Li}(\text{MnNiCo})_{1/3}\text{O}_2$ , where  $x = 0.5$ , or  $\text{Li}_{1.2}\text{Mn}_{0.53}\text{Ni}_{0.13}\text{Co}_{0.13}\text{O}_2$ .

**Spray Pyrolysis.** Spray pyrolysis is the process by which precursor droplets thermally decompose to create solid particles. The precursor solution, containing the aqueous metal nitrates, was aerosolized with an ultrasonic nebulizer. The aerosolized droplets were then introduced to a carrier gas, saturated with air. The air carried the droplet towards the preheater, which was heated to 200°C. The preheater dried the layer of water surrounding the droplets before they entered the furnace. The furnace temperature was set at 350°C, 450°C,

550°C, 575°C, and 650°C, respectively. The dry precursor droplets thermally decomposed, removing the aqueous portion of the precursor droplet, leaving a dry metal oxide. The powder was collected downstream via vacuum filtration.

**Battery Fabrication and Testing.** The powder obtained from the spray pyrolysis process was annealed at 900°C for two hours in a box furnace, to improve crystalline structure and remove any residual moisture. A slurry was prepared by mixing the annealed powder with a 7% binder solution, and then cast upon an aluminum current collector to create our film. The binder solution consisted of 3.5% carbon black, 3.5% polyvinylidene fluoride (PVDF), and 93% N-Methyl-2-pyrrolidone (NMP). The carbon black assisted in electron transportation from the metal oxides to the aluminum current collector, the PVDF adhered the powder to the aluminum, and the NMP was the solvent.

After the film was made, it was allowed to dry overnight at room temperature and then another night in a vacuum oven to allow the NMP to evaporate. After drying, cathode disks,

13 mm in diameter, were prepared for battery fabrication. The batteries were assembled in an argon-filled glove box. Pure lithium disks were used as the anode to study the performance of the cathode material without side effects arising from the anode. The batteries were subjected to cycle and rate tests on MTI battery testers.

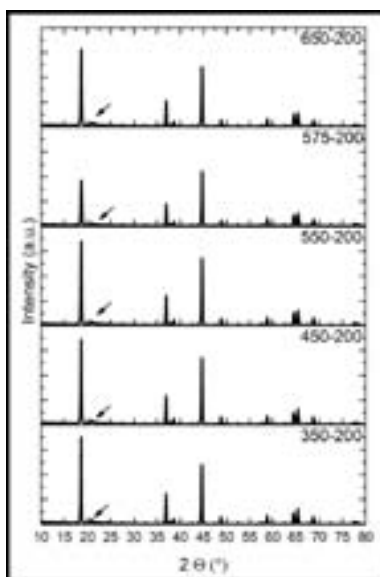


Figure 1: XRD spectra.

## Results and Discussion:

We recorded x-ray diffraction (XRD) spectra of the products synthesized at different temperatures (Figure 1). The exact distances separating the peaks and the ratios of peak intensities indicated a lack of contaminants, and showed the superlattice layered-layered structure

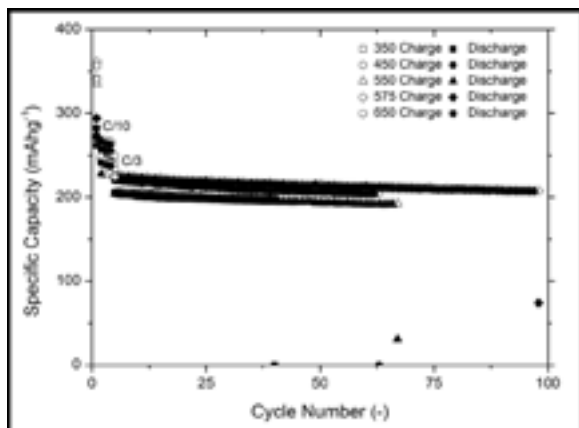


Figure 2: Cycle tests.

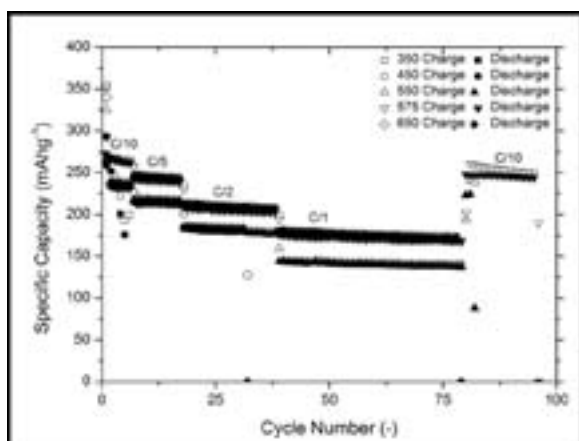


Figure 3: Rate tests.

characteristic of  $x\text{Li}_2\text{MnO}_3(1-x)\text{Li}(\text{MnNiCo})_{1/3}\text{O}_2$ . We produced exclusively our desired product at all temperatures.

The cycle test results (Figure 2) indicated that the battery produced at 575°C yielded the highest reversible charge and discharge capacity. In Figure 2, the x-axis is the cycle number and the y-axis is specific capacity in mAh/g. C/10 and C/3 are the current densities of charge and discharge of each cycle, where C = 200 mA/g. Since the practical capacity of batteries made from layered-layered materials is 200 mAh/g, a battery would be fully charged if charged at a rate of 1C for one hour.

We ran the majority of the cycle test at a rate of C/3 considering that three hours was a reasonable amount of time to recharge a PHEV battery. Each cycle consisted of charging and discharging the battery; and the 575°C battery displayed slightly higher capacity than the other batteries, remaining above 200 mAh/g after 100 cycles.

Rate capability tests (Figure 3) determined how flexibly the material may be discharged at various current rates. The battery began by charging and discharging at a rate of C/10.

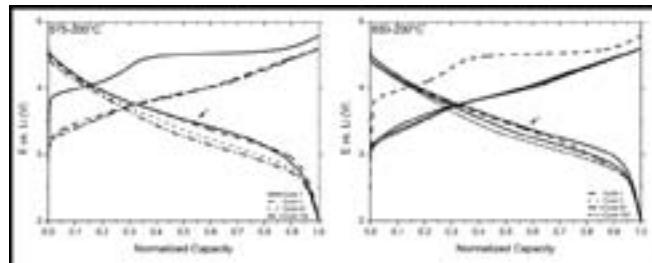


Figure 4: Voltage profile evolutions.

We then began charging and discharging at higher rates, to simulate acceleration and deceleration of EVs. As expected, the capacity of the battery diminished as it was cycled at a higher rate. The 450°C and 575°C batteries had the best performance with capacities above 170 mAh/g at a rate of 1C.

Figure 4 shows voltage profile evolution over time. We observed that with increasing synthesis temperatures, the change in the voltage plateau indicated by the arrows became smaller, showing better voltage profile retention. The x-axis displays specific capacity, while the y-axis displays voltage. The 650°C battery had a much lower voltage drop when compared to the 575°C battery. This is favorable because the voltage output from a certain specific capacity diminishes less over time for the 650°C battery, suggesting higher performance. Not only is it important to have high specific capacity, it is also important to have high output voltages corresponding to those capacities.

### Conclusions and Future Research:

Layered-layered materials deliver very high reversible capacities. The highest capacity was achieved when the reactor temperature was 575°C. Increasing the reactor synthesis temperature improved the voltage profile without compromising the electrochemical performance. The relationship between increased reactor temperature and decreased voltage decay must still be studied. Future work will continue with higher synthesis temperatures as well as doping and variation of lithium concentration. The results will be discussed in an upcoming publication of the group.

### Acknowledgements:

I would like to thank Miklós Lengyel, Gal Atlas, and Dr. Richard Axelbaum for their help with my research. I would also like to thank Dee Stewart, Kate Nelson, and Nathan Reed of the Nano Research Facility, the National Nanotechnology Infrastructure Network Research Experience for Undergraduates (NNIN REU) Program, and the National Science Foundation for this research opportunity.

# Growth and Characterization of GaAs/InAs Quantum Dots By Molecular Beam Epitaxy

**Donnita M. McArthur**

**Optical Engineering, Norfolk State University**

*NNIN REU Site: Howard Nanoscale Science and Engineering Facility, Howard University, Washington, DC*

*NNIN REU Principal Investigator: Dr. Gary Harris, Electrical Engineering, Howard University*

*NNIN REU Mentor: James Griffin, Electrical Engineering, Howard University*

*Contact: d.m.mcarthur@spartans.nsu.edu, gharris@msrce.howard.edu, griffin@msrce.howard.edu*

## Abstract and Introduction:

Quantum dots (QD) are three-dimensional structures that have electronic properties between those of molecules and bulk materials. They can be self-assembled through molecular beam epitaxial growth or fabricated using lithography. In this work, QDs were self-assembled by molecular beam epitaxy (MBE). Growth rates for gallium arsenide (GaAs) and indium arsenide (InAs) were calibrated by reflection high-energy electron diffraction (RHEED). Doping profiles were determined for GaAs using silicon (Si) as the n-type dopant. QD devices were fabricated and compared to quantum well (QW) and quantum free devices.

Quantum dot devices had ideality factors and series resistance values of 1.34 and 61  $\Omega$ , respectively, and had enhanced currents at higher voltages when compared to quantum well and quantum free devices.

## Methodology:

To characterize the MBE tool, growth rates for GaAs and InAs were calibrated, followed by doping profiles for Si. RHEED

oscillations were taken at various Ga furnace temperatures. The oscillations were used to calculate the growth rate in monolayers/sec by dividing the number of oscillations (monolayers) by the elapsed time. A semi logarithmic graph was used to plot growth rates versus furnace temperature.

The doping profiles for Si were acquired by first growing a GaAs buffer layer followed by an Si-doped GaAs layer at a particular silicon furnace temperature. The process was repeated for other samples at different silicon furnace temperatures. Hall measurements were taken to calculate the carrier concentrations of the Si. A semi-logarithmic graph was used to plot carrier concentrations versus furnace temperature.

Three devices were fabricated to examine current changes versus voltage: one with only GaAs, one with a monolayer of InAs (QW device), and one with three monolayers of InAs (QD device, see Figure 1). The samples were grown on  $n^+$  GaAs. The GaAs was grown at 580°C and at 400°C while the InAs was grown at 460°C. The Schottky contacts used in the measurements had an effective diameter of diameter of 237  $\mu\text{m}$ . An I-V curve trace was used to measure the ideality

Au Schottky Contact
MBE n-GaAs cap layer (0.6 $\mu\text{m}$ , $2 \times 10^{16} \text{ cm}^{-3}$ )
MBE n-GaAs confining layer (0.4 $\mu\text{m}$ , $2 \times 10^{16} \text{ cm}^{-3}$ )
InAs QD (3 monolayers)
MBE n-GaAs buffer layer (1 $\mu\text{m}$ , $2 \times 10^{16} \text{ cm}^{-3}$ )
$n^+$ - GaAs substrate
AuGeNi ohmic contact

Figure 1: InAs quantum dot structure.

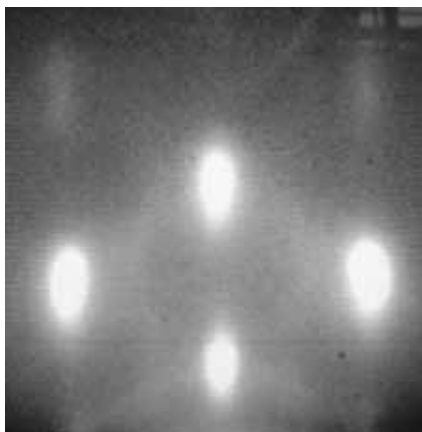


Figure 2: RHEED pattern of three monolayers of InAs on GaAs.

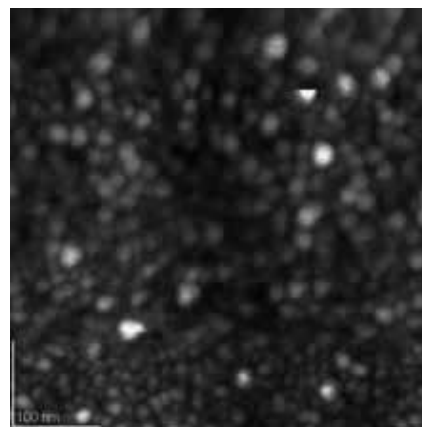


Figure 3: AFM image of InAs quantum dots on GaAs.

factor and the series resistance. A curve trace was also used to acquire current versus voltage data for the three different device structures.

### Results:

RHEED images verified that the InAs structures were not two dimensional and AFM images verified that InAs QD were grown (see Figures 2 and 3, respectively). The ideality factor values for the reference, QW, and QD samples were 1.85, 2.439, and 1.134, respectively. The series resistance values were 77, 145.5, and 61  $\Omega$ , respectively.

Testing revealed that the current in the QD sample was greater than the reference sample (see Figure 4). This result was consistent with what others have found [5]. The current in the QW sample was also less than the QD sample at higher voltages. However at lower voltages the current in the QW device was higher.

### Conclusions:

Growth rates for GaAs and InAs were calibrated up to 1 ML/s and 0.2 ML/s, respectively. Doping profiles for Si in GaAs were obtained up to  $1e18\text{cm}^{-3}$ . Quantum dot and well samples were grown and devices were tested which revealed excess current in the QD sample relative to the QW and reference samples.

### Acknowledgments:

I would like to thank the National National Nanotechnology Infrastructure Network Research Experience for Undergraduates (NNIN REU) Program and the National Science Foundation for funding and sponsoring my research.

### References:

- [1] L.E. Brus, "Chemistry and Physics of Semiconductor Nanocrystals"; [http://www.columbia.edu/cu/chemistry/fac-bios/brus/group/pdf-files/semi\\_nano\\_website\\_2007.pdf](http://www.columbia.edu/cu/chemistry/fac-bios/brus/group/pdf-files/semi_nano_website_2007.pdf). Retrieved 2009-07-07 (2007).
- [2] D.J. Norris, "Measurement and Assignment of the Size-Dependent Optical Spectrum in Cadmium Selenide (CdSe) Quantum Dots"; PhD thesis, MIT. <http://hdl.handle.net/1721.1/11129>. (1995). Retrieved 2009-07-07.
- [3] C.B. Murray, C.R. Kagan, M. G. Bawendi, "Synthesis and Characterization of Monodisperse Nanocrystals and Close-Packed Nanocrystal Assemblies"; *Annual Review of Materials Research* 30 (1): 545–610. Bibcode 2000AnRMS..30..545M. DOI:10.1146/annurev.matsci.30.1.545. (2000).
- [4] Deniz, Derya, "Texture Evolution in Metal Nitride"; <http://www.grin.com/en/doc/266864/texture-evolution-in-metal-nitride-aluminum-nitride-titanium-nitride> (2008).
- [5] Zs. J Horvath, P. Frigeri, S. Franchi, Vo. Van Tuyen, E. Gombria, R. Mosca, L. Dozsa, "Current Instabilities in GaAs/InAs Self-Aggregated Quantum Dot Structures." (2002).

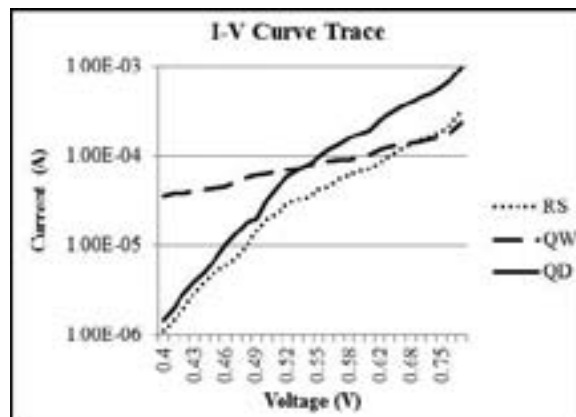


Figure 4: I-V plot of quantum dot, quantum well and reference samples.

## Transport in Near-Surface Two-Dimensional Electron Systems

**Ryan McMorris**

**Chemical Engineering, University of Washington**

*NNIN REU Site: Nanotech, University of California, Santa Barbara, CA*

*NNIN REU Principal Investigator: Christopher Palmstrøm, Departments of Electrical and Computer Engineering and Materials, University of California at Santa Barbara*

*NNIN REU Mentor: Borzoyeh Shojaei, Department of Materials, University of California at Santa Barbara*

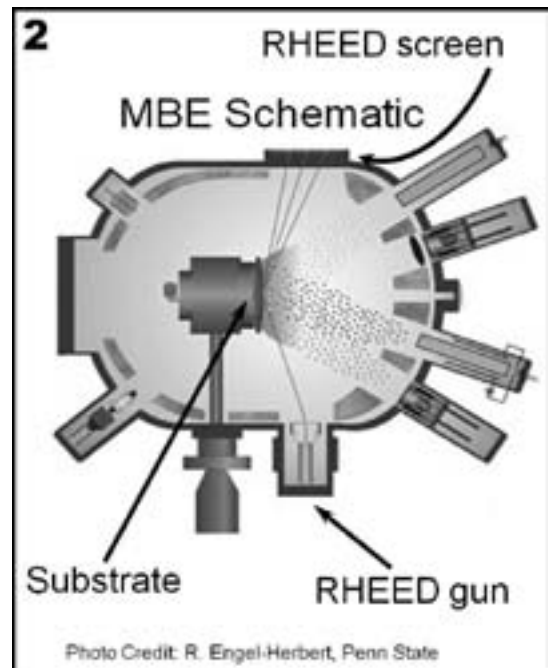
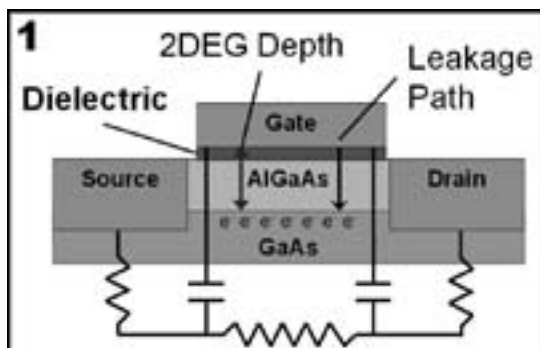
*Contact: rjmc Morr@uw.edu, cpalmstrom@ece.ucsb.edu, borzoyeh@gmail.com*

### Abstract:

Near-surface two-dimensional (2D) electron gases are enabling platforms for controlling single electrons in quantum dots and using electron spin as a quantum bit in quantum computation. The requirements for the material system that forms the 2D electron gas are low levels of disorder to reduce scattering, the 2D electron gas be as close to the surface as possible to lead to abrupt confinement potentials created by depletion top gates, and spacer layers between the 2D electron gas and surface have low leakage currents under an applied gate bias. The design of a sub-50 nm deep modulation doped AlGaAs/GaAs heterostructure that forms a 2D electron gas at the AlGaAs/GaAs interface is presented. Magneto-transport measurements in a sub-50 nm deep 2D electron gas formed at the interface of a modulation doped AlGaAs/GaAs heterostructure grown by molecular beam epitaxy are presented. The addition of a high- $\kappa$  dielectric layer was implemented with the purpose of decreasing gate leakage. Characterization of the dielectric and processing techniques are presented and discussed.

### Background:

Our project had two primary goals and we approached these independently. First we wanted to grow and characterize a sub-50 nm deep two-dimensional electron gas or 2DEG. Second we wanted to explore deposition techniques for high- $\kappa$  dielectrics on top of III-V heterostructures. Motivation for this project included a previously successful qubit, created via a double quantum dot design in the same material system. This design by Weperen, et al., was at a depth of 110 nm. This deeper 2DEG functioned well, but needed to be shallower in order to improve scalability.



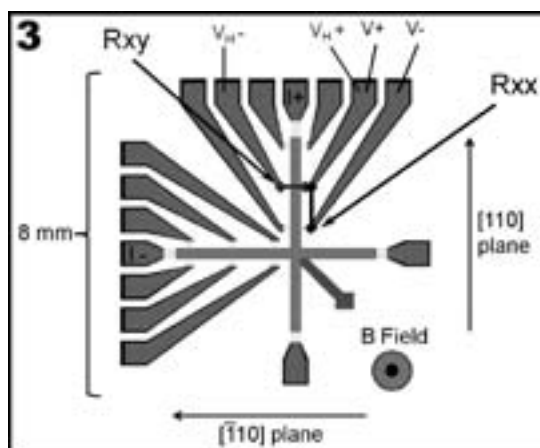
### Experimental Procedures:

Samples were grown by molecular beam epitaxy. This process uses high purity elemental sources under ultrahigh vacuum to grow precise monolayers of material on a substrate. Reactive high energy electron diffraction or RHEED was used to calibrate the growth rate for each layer as RHEED can identify specific surface interaction effects which exist for the various surface states. This process works by real time analysis of the surface of the substrate as growth occurs.

Photolithography was then used to pattern the surface of the samples with our Hall bar design. This technique was effective as it is relatively easy to etch through the 40 nm of material above the 2DEG, thus controlling the conduction pathways in the sample. This type of experiment was useful as it told us how effectively and efficiently our 2DEG was functioning.

### Transport Measurements on 40 nm Deep 2DEG:

We primarily measured 40 nm deep 2DEG's and used a Hall bar setup in order to perform measurements. Measurements included basic transport such as sheet resistance and mobility



as well as an analysis of Shubnikov de Haas oscillations and Hall plateaus. The schematic above shows how the Hall bar design was used to take basic voltage measurements which can be used to calculate sheet resistance, carrier density, and mobility.

Before taking these measurements however, we used theoretical modeling with the purpose of improving the 2DEG's design, and recognizing likely problems within the system. We used a 1D self consistent Schrodinger-Poisson solver developed by Greg Snider. Results of this modeling indicated that a parallel conduction pathway might form in the delta-doping layer, hindering performance. However, further analysis showed that an applied gate voltage would quickly eliminate the problem.

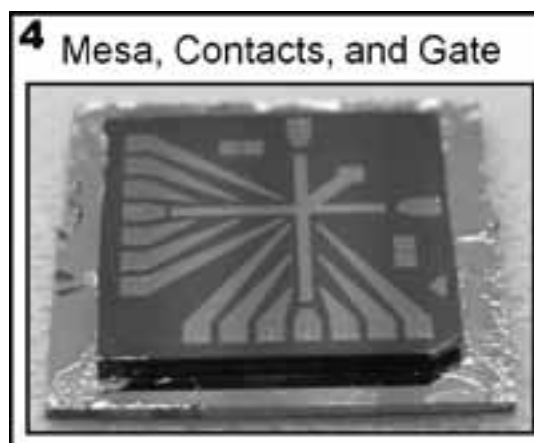
Our first set of measurements was a sheet resistance vs. temperature analysis. This measurement showed that the 2DEG had truly metallic character, with resistance falling close to 0 at low temperature (lowest of  $\sim 3\text{K}$ ) as was expected in a functioning 2DEG. Further data analysis showed that low temperature carrier density and mobility were both in the ranges expected at  $3.4 \times 10^{11} \text{ (cm}^{-2}\text{)}$  and  $239,000 \text{ (cm}^2\text{/Vs)}$  respectively. These results matched with the previously mentioned theoretical modeling quite well and indicated a high quality 2DEG.

Lastly, an analysis of the measured voltages under a varying magnetic field from 0 up to 7 Tesla was performed at 1.8 K. As expected, our 2DEG showed Shubnikov de Haas oscillations and Hall plateaus.

Results such as these further confirm the high quality of the system and its design.

### Characterizing High-k Dielectric Deposition:

For the second part of the project, we needed to deposit a thin layer ( $\sim 10 \text{ nm}$ ) layer of our chosen dielectric. We used aluminum oxide and deposited by atomic layer deposition. This technique was used due to its high precision in depth and high quality thin films. Using the trimethylaluminum precursor and  $\text{H}_2\text{O}$  purge gas, we deposited our 10 nm layer. Characterization of this surface was done by ellipsometry and



x-ray photoelectron spectroscopy (XPS). The ellipsometer showed that we had successfully deposited 10.5 nm. Additionally XPS analysis showed that our surface was 64% oxygen and 36% aluminum. Obviously this was not the 3 to 2 ratio that we would expect, so further work is necessary in this area.

### Summary:

In conclusion, we successfully grew a 40 nm deep 2DEG and characterized the transport properties. Additionally we developed and studied dielectric depositions over near surface 2DEG's in III-V heterostructures.

Short term future work will include exploring an anneal step as a solution to the oxygen rich dielectric layer, taking low temperature gated magneto-transport measurements, and comparing hafnium oxide over aluminum oxide in place of the aluminum oxide alone.

Long term efforts will include measuring leakage and noise using a quantum point contact and measuring the level of screening caused by the dielectric using a quantum point contact in proximity to a quantum dot.

### Acknowledgements:

I would like to acknowledge my principal investigator Christopher Palmstrøm, my mentor Borzoyeh Shojaei, the entire Palmstrøm group, as well as these organizations: National Nanotechnology Infrastructure Network Research Experience for Undergraduates (NNIN REU) Program, National Science Foundation, University of California Santa Barbara, Intelligence Advanced Research Projects Activity, Materials Research Laboratory, and California NanoSystems Institute.

### References:

- [1] van Weperen, B. D. Armstrong, E. A. Laird, J. Medford, C. M. Marcus, M. P. Hanson, and A. C. Gossard, Phys. Rev. Lett. 107, 030506 (2011).

# Controlling the Composition and Morphology of $\text{Si}_{1-x}\text{Ge}_x$ Nanowires

Ryan Murphy

Chemistry, Clemson University

NNIN REU Site: Nanotechnology Research Center, Georgia Institute of Technology, Atlanta, GA

NNIN REU Principal Investigator: Dr. Michael Filler, Chemical and Biomolecular Engineering, Georgia Institute of Technology

NNIN REU Mentor: Ildar Musin, Chemical and Biomolecular Engineering, Georgia Institute of Technology

Contact: rjmurphymail@gmail.com, michael.filler@chbe.gatech.edu, ildarm@gatech.edu

## Abstract:

Silicon (Si) and germanium (Ge) semiconductor nanowires can be utilized in next generation electronic, photonic, and energy conversion devices. Si, Ge, and  $\text{Si}_{1-x}\text{Ge}_x$  materials are also well studied and currently used in industry. Optoelectronic properties, such as the band gap, can be tuned by modulating the alloy composition, thus allowing for a wider range of uses. The focus of this project was to create arrays of  $\text{Si}_{1-x}\text{Ge}_x$  alloy nanowires with varying, but simultaneously uniform, compositions. This goal has been difficult to achieve to date. Nanowires were grown with the gold catalyzed, bottom-up, vapor-liquid-solid mechanism throughout the compositional range. Using scanning electron microscopy (SEM), energy-dispersive x-ray spectroscopy (EDX), and Raman spectroscopy, we demonstrated control of  $\text{Si}_{1-x}\text{Ge}_x$  alloy composition, but struggled to achieve highly aligned arrays. Nanowires frequently kinked to the  $\langle 112 \rangle$  directions and underwent conformal deposition, which resulted in tapered structures. Therefore, we employed a sidewall species, methylgermane, in an attempt to overcome this.

## Introduction:

Semiconductor nanowires have many promising applications in next generation electronic, photonic, and energy conversion devices. Silicon (Si) and germanium (Ge) are superb choices for these semiconductor devices because there is already an

extensive knowledge base of Si and Ge materials. By growing different concentrations of  $\text{Si}_{1-x}\text{Ge}_x$  nanowires, it was possible to tune optoelectronic properties such as the band gap [1]. While alloy nanowire growth has been achieved, growing highly uniform arrays of  $\text{Si}_{1-x}\text{Ge}_x$  nanowires with varying, but simultaneously uniform compositions has been difficult to date [2, 3].

## Experimental Procedure:

$\text{Si}_{1-x}\text{Ge}_x$  nanowires were grown using the gold catalyzed, bottom-up, vapor-liquid-solid growth method as seen in Figure 1. Fifty nanometer (nm) gold nanoparticles were deposited on a Si  $\langle 111 \rangle$  wafer. The sample was heated in a cold-wall vapor deposition furnace to  $375^\circ\text{C}$  and  $\text{GeH}_4$  partial pressure was raised to 0.44 Torr to grow short Ge stubs. Finally,  $\text{GeH}_4$  partial pressure was dropped to 0.025 Torr and  $\text{SiH}_4$  partial pressure was raised to 0.050-1.000 Torr. By varying the partial pressure of  $\text{SiH}_4$ , the concentration of the wires could be varied.

To determine the growth conditions, we used the Arrhenius equation, which allowed us to calculate the theoretical Ge concentration of the nanowires from the ratio of  $\text{GeH}_4$  partial pressure to  $\text{SiH}_4$  [4]. The nanowires were characterized using an SEM, leading to discovery of issues in the nanowire arrays such as kinking or tapering of wires.

Uncontrollably kinking and compositional gradients caused by tapering limits the usability of nanowire arrays in device applications. In order to increase the uniformity of the arrays,  $\text{GeH}_3\text{CH}_3$  was used in place of  $\text{GeH}_4$  during the growth step in order to introduce a methyl group as a sidewall species. As a result, the temperature of the growth step had to be raised to  $475^\circ\text{C}$  to prevent kinking caused by  $\text{GeH}_3\text{CH}_3$  [5]. The concentrations of the wires were measured using EDX. Because the Si substrate would affect the EDX measurement, the nanowires were transferred to carbon tape.

## Results and Conclusions:

Raman spectroscopy was used to confirm the nanowires were alloys and not another type of superstructure. As seen in Figure 2, the Raman spectrum of the nanowires showed a

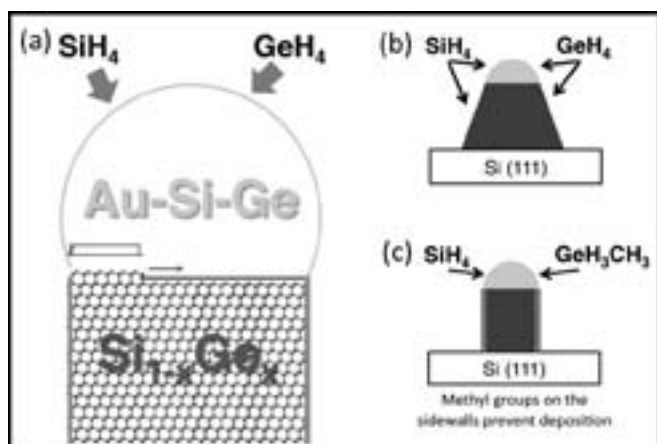


Figure 1: (a) Schematic of the VLS growth method and schematic of wire growth (b) with and (c) without  $\text{GeH}_3\text{CH}_3$ .

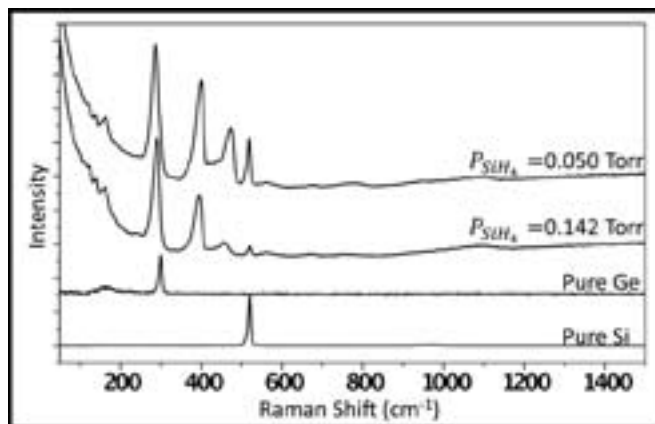


Figure 2: Raman spectrum of  $\text{Si}_{1-x}\text{Ge}_x$  nanowires and pure Ge and Si wafers. Intensity scale is adjusted.

distinct shift in the Si-Si peak and the Ge-Ge peak as well as a strong intensity Si-Ge peak, which confirmed the existence of  $\text{Si}_{1-x}\text{Ge}_x$  alloys [6]. EDX was used to determine the concentration of the nanowires. As the fraction of  $\text{GeH}_3\text{CH}_3$  increased, the Ge concentration in the nanowires also increased, as seen in Figure 3. By comparing SEM images of nanowires grown with and without  $\text{GeH}_3\text{CH}_3$  (Figure 4), it can be seen that  $\text{GeH}_3\text{CH}_3$  eliminated tapering at high Ge concentrations; however, kinking remains an issue at lower Ge, higher Si concentrations.

### Future Work:

By tuning process conditions, it will be possible to grow nanowires over a wider range of Ge concentrations. Further research into surface chemistry will result in better control of nanowire sidewalls and increase the uniformity of nanowire

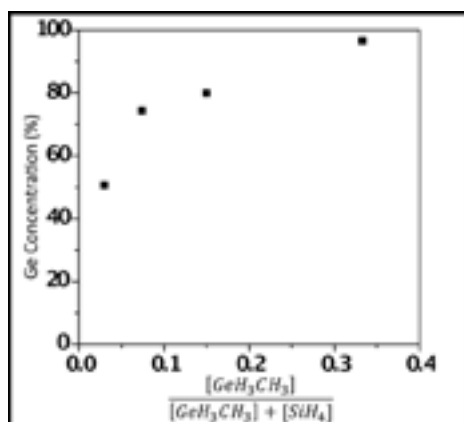


Figure 3: Percent Ge concentration as determined by EDX vs. the fraction of the  $\text{GeH}_3\text{CH}_3$  partial pressure.

arrays. Finally, once uniform arrays of  $\text{Si}_{1-x}\text{Ge}_x$  nanowires are perfected, they can be used in many next generation electronic, photonic, and energy conversion devices.

### Acknowledgments:

I would like to thank Dr. Michael Filler, Ildar Musin, and the entire Filler research group for their leadership and guidance throughout my internship. I would also like to thank Leslie O'Neill, Joyce Palmer, and Nancy Healy for their commitment to the NNIN REU program at Georgia Tech. Furthermore, I would like to thank Georgia Tech and its cleanroom staff, especially John Pham for his dedication to minimizing downtime of equipment. Finally, I would like to thank the National Nanotechnology Infrastructure Network Research Experience for Undergraduates Program and the National Science Foundation for their support and funding.

### References:

- [1] Yang, J.; et. al.; "Band-gap modulation in single-crystalline  $\text{Si}_{1-x}\text{Ge}_x$  nanowires"; Nano Letters, 6, 2679-2684 (2006).
- [2] Givan, U.; Patolsky, F.; "Pressure-Modulated Alloy Composition in  $\text{Si}_{1-x}\text{Ge}_x$  Nanowires"; Nano Letters, 9, 1775-1779 (2009).
- [3] Potie, A.; et. al.; "Controlled growth of SiGe nanowires by additions of HCl in the gas phase"; Journal of Applied Physics, 110, 8 (2011).
- [4] Lew, K.; et. al.; "Effect of growth conditions on the composition and structure of  $\text{Si}_{1-x}\text{Ge}_x$  nanowires grown by vapor-liquid-solid growth"; Journal of Materials Research, 21, 2876-2881 (2006).
- [5] Musin, I.; Filler, M.; "Chemical Control of Semiconductor Nanowire Kinking and Superstructure"; Nano Letters, 12, 3363-3368 (2012).
- [6] Yang, B.; et. al.; "Low-temperature epitaxial growth of Ge-rich Ge-Si-C alloys: Microstructure, Raman studies, and optical properties"; Journal of Applied Physics, 84, 2001-2017 (1998).

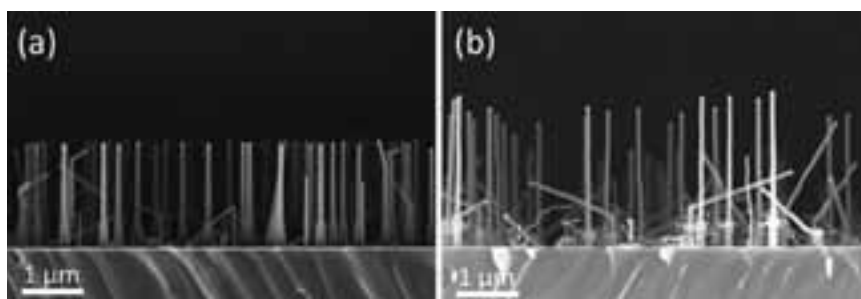


Figure 4: SEM images of  $\text{Si}_{1-x}\text{Ge}_x$  nanowires.

(a) Wires grown with  $\text{GeH}_4$  (375°C,  $P_{\text{SiH}_4} = 0.214$  Torr,  $P_{\text{GeH}_4} = 0.105$  Torr).

(b) Wires grown with  $\text{GeH}_3\text{CH}_3$  (475°C,  $P_{\text{SiH}_4} = 0.025$  Torr,  $P_{\text{GeH}_3\text{CH}_3} = 0.050$  Torr).

# Indium Arsenide Quantum Dot Lasers

**Justin Norman**

**Chemical Engineering and Physics, University of Arkansas, Fayetteville**

*NNIN REU Site: Nanotech, University of California, Santa Barbara, CA*

*NNIN REU Principal Investigator: Dr. Arthur Gossard, Materials, University of California, Santa Barbara*

*NNIN REU Mentor: Alan Liu, Materials, University of California, Santa Barbara*

*Contact: jcnorman@uark.edu, gossard@engineering.ucsb.edu, ayliu01@engineering.ucsb.edu*

## Introduction:

Electron leakage and heat generation due to the increasingly small scale and dense packing of device components are major limitations to further downscaling modern electronics. Optoelectronics, devices that utilize a combination of optical and electronic components, represent a potential solution to these problems by taking advantage of the fact that optical signals do not suffer from the issues of tunneling or Joule heating while also being more energy efficient and faster than electronic signals. In pursuit of these ideal characteristics, the goal of this project was to produce a suitable light source for optoelectronic applications.

Specifically, our goal was to produce a laser using indium arsenide (InAs) quantum dots (QDs) as the active region. InAs QDs are excellent candidates for data transfer applications due to their three-dimensional confinement, which leads to discrete energy levels dependent on the quantum dot size. This means not only that the emission wavelength of the laser can be tuned by changing the dot size, but also that the necessary threshold current densities are lower than those of quantum wells and bulk material because fewer carriers are needed for population inversion. Additionally, the large gap between energy levels gives quantum dot lasers (QDLs) essentially temperature invariant operation.

## Material Design and Growth:

Molecular beam epitaxy (MBE) was used as the method of growing the laser materials. MBE is a technique that uses ultrahigh vacuum and careful control of material flux during deposition to ensure that materials form epitaxially on the surface. Due to the extreme vacuum, MBE is able to grow materials with remarkably low contamination levels. Meanwhile, the slow, epitaxial deposition means that the thickness of a deposited layer can be controlled with monolayer precision while—through controlling the flux of multiple materials at a time—the composition of a single layer can also be controlled with extreme precision.

The structure of our QDL is shown in Figure 1, while the band diagram for the material is shown in Figure 2. From the band structure, it can be seen that under an applied voltage conduction electrons will travel down the conduction band and be confined in the potential wells of the quantum dots,

while holes will travel up the valence band and do the same. The result of this process was a large number of holes and electrons confined in the low bandgap region, where they could easily recombine producing photons, which in turn stimulate further radiative recombination.

## Material Characterization:

Before actual laser devices were grown, the MBE growth conditions had to be calibrated. For this purpose, special calibration samples were grown that were similar to the actual laser structure, but with greatly thinned waveguiding

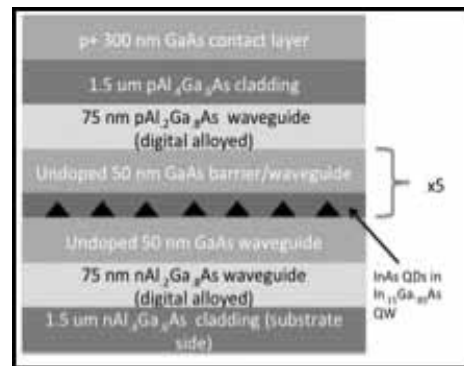


Figure 1: A schematic of the laser material.

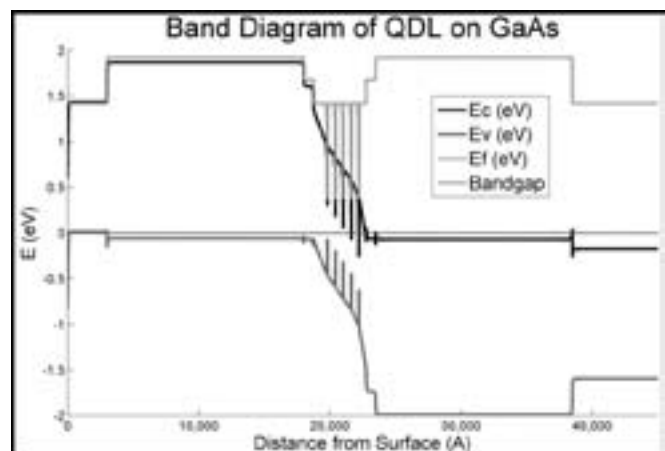


Figure 2: The band diagram of the laser material.

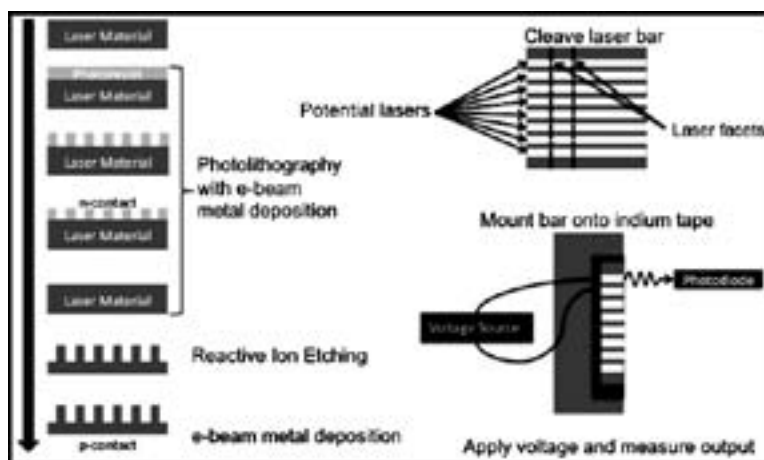


Figure 3: Laser processing procedure.

regions and an additional layer of QDs grown on the top surface at identical growth conditions to the centrally located QDs. These samples were characterized using atomic force microscopy (AFM) and photoluminescence (PL) to determine the morphological and optical properties of the quantum dots.

Atomic force microscopy was used to obtain an image of the quantum dots on the top surface of the material. These images were used to assess the uniformity and density of quantum dots on the surface, which were assumed to be similar to those that would be found in the identically grown active region. Calibration samples corresponding to the growth conditions of successful laser devices had estimated dot densities of  $3.2 \times 10^{10} \text{ cm}^{-2}$ . Higher dot densities were considered better because it meant there were more recombination centers to generate photons.

Photoluminescence was used to characterize the optical properties of the calibration sample. This technique uses a laser to optically excite the quantum dots and then measures the light produced upon relaxation. PL measurements indicated that optical emissions occurred at a wavelength of 1220 nm in the central region of the sample, which corresponds to the region used in device production. The full width at half maximum was found to be very uniform across the sample surface with a value of 40 nm.

### Device Processing:

Once the laser material was grown, a series of processing steps had to be performed to create a functioning laser. The process is summarized in Figure 3. A combination of photolithography and electron beam (e-beam) metal deposition was used to deposit the top electrode for the device in a series of bars. Reactive ion etching was then used to turn the bulk laser material into a series of laser bars by etching through the

laser active region. Next, e-beam metal deposition was used to deposit the bottom electrode. To complete the process, a section of the sample was cleaved from the rest with the cleaved edges, becoming the laser facets.

### Results:

InAs QDLs were successfully fabricated and found to lase at threshold current densities as low as  $260 \text{ A/cm}^2$ . The photoluminescence measurements suggest that this lasing occurs at a wavelength of 1220 nm, but the actual spectral profile of the light output has not yet been measured.

### Future Work:

Future work is planned to refine the laser growth and processing procedures to achieve lower threshold currents. Once satisfactory devices are being produced, attempts will be made to grow the laser material on a silicon substrate—a necessary step to be able to integrate the lasers in current technology.

### Acknowledgements:

I would like to thank the NNIN REU Program for this wonderful opportunity, as well as the NSF for funding. I would also like to thank UCSB and Samantha Cruz for hosting and coordinating the program. I would like to give special thanks to Alan Liu for guiding and teaching me throughout the program, as well as Dr. Arthur Gossard for providing guidance and allowing me to work on this project. I would also like to thank Chong Zhang for his assistance and teaching during the laser processing.

# Work Function Tuning in Amorphous TaWSiC Metal Gates for Integrated Circuits

**Jordan Occeña**

**Engineering Physics, University of Tulsa**

*NNIN REU Site: Stanford Nanofabrication Facility, Stanford University, Stanford, CA*

*NNIN REU Principal Investigator: Prof. Yoshio Nishi, Electrical Engineering, Stanford University*

*NNIN REU Mentor: Jiaomin Ouyang, Materials Science and Engineering, Stanford University  
(2008 NNIN REU at Stanford)*

*Contact: jordan-occeña@utulsa.edu, nishiy@stanford.edu, jouyang@stanford.edu*

## Abstract:

Use of amorphous tantalum tungsten silicon carbide (TaWSiC) metal gates has the potential to reduce gate work function variation, but for application in integrated circuits, their work function should also be tunable. In this work, the ratio of W/Ta in TaWSiC gates was varied in order to tune the work function. While the results indicate a partial trend of increasing work function as the ratio of W/Ta is increased, data inconsistencies suggest that oxygen contamination during processing may have caused unreliable work function measurements.

## Introduction:

As transistors continue to scale down in size to allow faster, denser, and more efficient integrated circuits, polycrystalline silicon, traditionally used as the transistor gate material, has been replaced by polycrystalline metal. For optimal circuit and device performance, the work function of this gate material should exhibit minimal variation and be tunable to specific values for different applications. However, the work function of polycrystalline metal has been shown to vary with grain orientation [1]. As gates are scaled down to sizes comparable to those of individual grains, the gate work function can vary significantly between devices, as illustrated in Figure 1 [2]. An amorphous metal, in contrast, avoids this work function variation because it lacks grains (Figure 1).

Tantalum tungsten silicon carbide (TaWSiC) is an amorphous alloy that is thermally stable, making it potentially compatible with integrated circuit processing [3]. However, additional work is needed to determine whether the work function of amorphous TaWSiC gates can be tuned to desired values for integrated circuit applications. The work function of an alloy depends on the work functions of the constituent metals. Thus, it is expected that varying the ratio of W/Ta in TaWSiC would allow tuning of its work function. A previous (unpublished) investigation by Ouyang suggested a trend of increasing work function with increasing tungsten percentage. Here, we report on a reinvestigation and extension of that previous study of work function tuning in TaWSiC.

## Experimental Procedure:

Metal-oxide-semiconductor capacitors were fabricated to determine the work function of amorphous TaWSiC gates with various W/Ta ratios. Silicon oxide was thermally grown on n-doped silicon wafers and wet-etched to form a terrace of oxide with thicknesses ranging from 2 nm to 10 nm, followed by a 2 nm deposition of hafnium oxide using atomic layer deposition. TaWSiC gates 30 nm thick were deposited by co-sputtering with tantalum, tungsten and silicon carbide targets, and the ratio of W/Ta was varied by varying the power to the tungsten and tantalum targets. Capacitors 200  $\mu\text{m}$  in diameter were patterned using photolithography and annealed in forming gas for 30 minutes at 300°C.

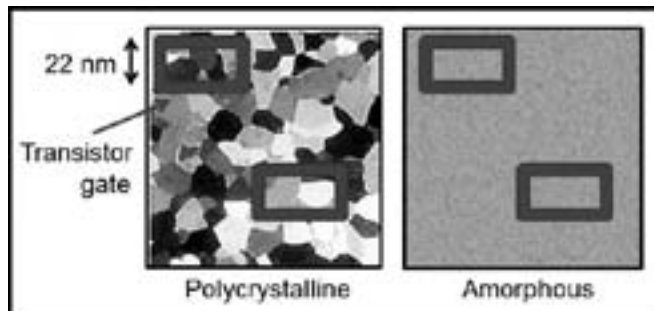


Figure 1: Illustration of gates on polycrystalline vs. amorphous metal. Different shades represent different grain orientations.

$$V_{FB} = \Phi_{ms} - \frac{Q}{\epsilon} EOT$$

The effective work functions of the different gate compositions were extracted using the simplified equation in Figure 2, where  $V_{FB}$  is the flatband voltage,  $\Phi_{ms}$  is the difference between the work functions of the metal gate and silicon,  $Q$  is the fixed charge in the oxide,  $\epsilon$  is the permittivity of the oxide, and  $EOT$  is the effective oxide thickness. In order to model a linear relationship between  $V_{FB}$  and  $EOT$ , charges in the oxide were

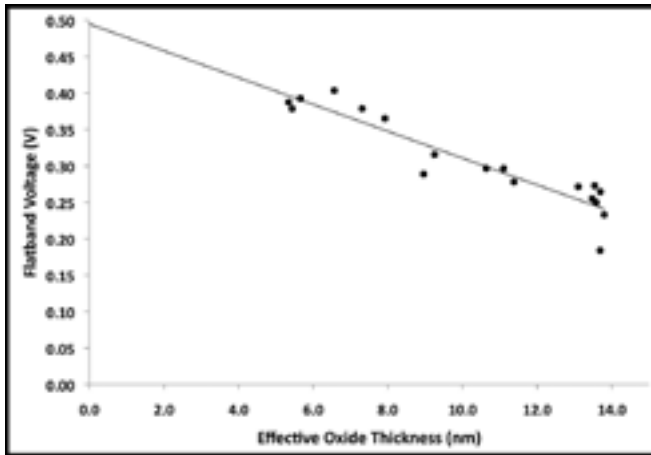


Figure 3: Example plot of  $V_{FB}$  vs.  $EOT$ ; the y-intercept is  $\Phi_{ms}$ .

Previous Work			Present Work		
	x	WF		x	WF
	0	4.58		0	4.392
	20	4.68		50	4.453
	40	4.82		60	4.514
	60	4.9		70	4.584
	80	4.57		80	4.657

Figure 4: Work functions for various compositions of TaWSiC in this work compared with work function values found in the previous investigation by Ouyang.

assumed to be constant and evenly distributed. The flatband voltages for capacitors of various effective oxide thicknesses were determined from capacitance-voltage measurements.

A graph of  $V_{FB}$  vs.  $EOT$  was plotted for each composition, and a linear fit was used to extract  $\Phi_{ms}$  from the y-intercept for each graph (Figure 3). The gate work function was then calculated from  $\Phi_{ms}$  and the work function of the silicon wafer.

**Results and Discussion:**

Figure 4 displays the work functions for various compositions of TaWSiC in this work as well as a comparison with the previous investigation by Ouyang. We note that data was unable to be obtained for some of the compositions in this work due to time constraints.

Both data sets exhibited a partial trend of increasing work function as the ratio of W/Ta increased, but this trend was

inconclusive due to inconsistencies in the data. Both data sets contained points that deviated from the trend. Additionally, the work function values of this work were shifted down from those found in the previous investigation for the same compositions. An examination of the calculations behind this data suggests that oxygen contamination in the metal gate may have contributed to these inconsistencies. Because  $Q$  and  $\epsilon$  from the equation in Figure 2 were held to be constant, we expected the slopes of the  $V_{FB}$  vs.  $EOT$  graphs to be similar for all samples, but instead observed significant variation. Work by Grubbs has shown that oxygen contamination in tungsten gates shifts both the slope of the  $V_{FB}$  vs.  $EOT$  graph and the work function value, suggesting that oxygen contamination may explain similar shifts in this work [4].

**Future Work:**

Future work will focus on the development of simpler amorphous gate metals. Amorphous metal gates with fewer component elements would potentially be less susceptible to the inconsistent work function measurements discussed above and more compatible with other integrated circuit processing techniques, facilitating eventual implementation of amorphous metal gates to reduce work function variation in integrated circuits.

**Acknowledgements:**

Thank you to the following for their guidance and support: Prof. Yoshio Nishi, Prof. Bruce Clemens, Dr. Michael Deal, Jiaomin Ouyang, Ranida Wongpiya, Stanford Nanofabrication Facility staff, National Nanotechnology Infrastructure Network REU Program, National Science Foundation, and the Center for Integrated Systems at Stanford University.

**References:**

- [1] Fall, C. J., et al. Physical Review B, 65(4), 045401-1 2001.
- [2] Zhang, X., et al. IEDM, 2009.
- [3] Grubbs, M. E., et al. Appl. Phys. Lett. 97, 223505, 2010.
- [4] Grubbs, M. E., et al. Electron Device Letters, 30(9), p. 925, 2009.

## Formation of Quantum Dots by Aerosol Reactor

**Adam Roberge**

**Chemical Engineering, Waynesburg University**

*NNIN REU Site: Nano Research Facility, Washington University in St. Louis, St. Louis, MO*

*NNIN REU Principal Investigator: Dr. Da-Ren Chen, Department of Energy, Environmental, and Chemical Engineering, Washington University of St. Louis*

*NNIN REU Mentor: He Jing, Department of Energy, Environmental, and Chemical Engineering, Washington University of St. Louis*

*Contact: rob0746@student.waynesburg.edu, chen@seas.wustl.edu, jingh04@gmail.com*

### Abstract:

Nanometer sized semiconductors, or quantum dots (QDs) are sought after for their size-dependent photoluminescent properties. The synthesis of QDs in the past has been by the hot solvent injection approach. An alternative to hot solvent injection is aerosol route formation, which has the potential to be a continuous and large scale QD production method. This study focused on: (a) the aerosol route formation of QDs, and (b) examination of the effects of the ratio between the cadmium (Cd) and selenium (Se) precursors. The first part of the study was primarily to create QDs of various sizes with emission wavelengths ranging from blue (465 nm) to red (608 nm) using an aerosol-based synthesis. The second part of the study explored the effects of the molar ratio of cadmium acetate to Se on particle growing rate and the photoluminescent properties. Various molar ratios were tested, 1:5, 1:2, 1:1, 2:1, and 5:1, of cadmium acetate to selenium.

### Introduction:

Quantum dots (QDs) are desired for their photoluminescent properties. By tuning the size of the QDs, the band gap can be altered. The specific size of the band gap contributes to a certain wavelength of emission. Researches have been able to use the very specific emission wavelengths in devices such a light emitting diodes as well as in bio-imaging. QDs have been attached to certain proteins that attach to tumors and then fluoresce under ultra-violet light, which makes the tumors visible.

The most common method used to produce QDs is hot-solvent injection method. This method injects hot solvent into a heated precursor and the amount of time the solvents are left in the reaction mixture determines the size of the QD. This method is difficult to operate on a large scale. Another method for producing QDs is aerosol furnace formation. In this method, the precursors are combined into an atomizer and sprayed into a tube furnace, which cooks the QDs at a specific temperature. The QDs are then collected in a bubbler. This method allows for continuous QD production as well as scaled-up production. The purpose of this study is to further explore the aerosol furnace formation of QDs as well as the effect of the molar ratio of Cd to Se.

### Experimental Procedure:

Our procedure was modified from Didenko, et al. [1]. All reagents were used as received from Sigma Aldrich. We weighed 0.104 grams cadmium acetate dihydrate ( $\text{Cd}(\text{Ac})_2$ ) reagent grade 98% assay and placed it into 1.92 ml oleic acid technical grade 90% assay. Then we heated the solution with a heater set to 140°C until the  $\text{Cd}(\text{Ac})_2$  totally dissolved. A 10 mL toluene chromasolv reagent 99.9% assay was added into the solution, which was then cooled to 40°C with the heater set to 30°C. In another container, we weighed 0.192 g Se 100 mesh 99.5+% into 1.6 ml trioctylphosphine (TOP) technical grade 90% assay. The solution was mixed until the Se totally dissolved.

Once the oleic acid and  $\text{Cd}(\text{Ac})_2$  solution was cooled, the second solution containing Se and TOP was added. The solution was shaken well to mix and was added to the atomizer, which had a spray with a mean diameter size of  $\approx 0.33 \mu\text{m}$ . Finally, 15 ml toluene was placed into each bubbler. The temperature of the Lindberg/Blue tube furnace was set (see Figure 1). Once the furnace reached the desired temperature, the nitrogen gas tank was turned on. The pressure before the atomizer was set to 40 psi. The vacuum was turned on, and the valve was adjusted on the Magnahelic laminar flow meter so the flow rate was 0.75 lpm. The reaction was allowed to take place for two hours. The vacuum was turned off and then the nitrogen gas tank was turned off also. The sample was then collected from the bubblers.

For the second part of the study, the same procedure was followed, but the molar ratio of the precursors was altered. Four different molar ratios of  $\text{Cd}(\text{Ac})$  to Se were tested: 1:2, 1:1, 2:1, and 5:1.

### Results and Conclusions:

From our testing, various-sized QDs were produced by aerosol reactor; see Figure 2 (note the full color version on the cover). The emission wavelengths of these dots ranged from 450-608 nm (see Figure 3). QDs with the Cd-to-Se ratio of 1:1 had minimum reduction in emission intensity and wavelength as compared to those with the ratio of 1:5 (see Figure 4).

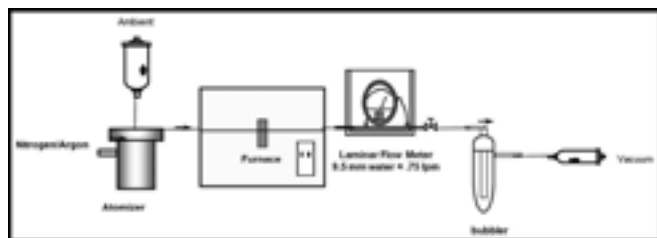


Figure 1: Experimental set-up as modified from Didenko [1].

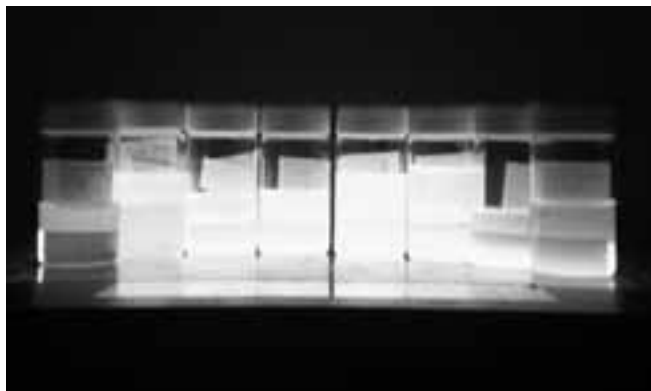


Figure 2: Samples ranging in temperature from 220-350 under UV light (note the full color version on the cover).

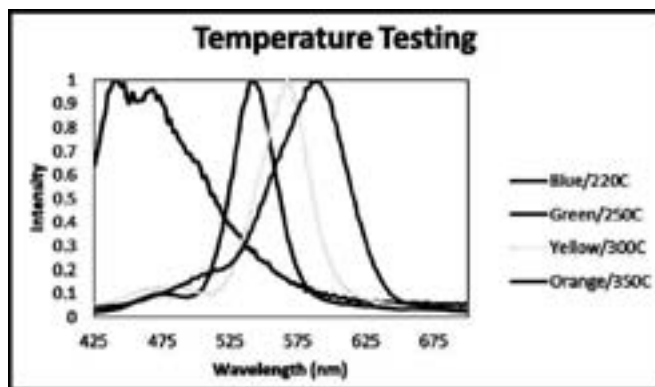


Figure 3: Normalized emission spectra of temperature testing.

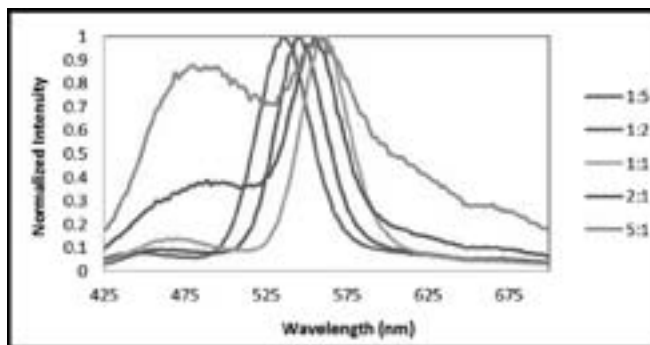


Figure 4: Normalized emission spectra of molar ratio testing.

The 1:1 ratio may prove to be a viable option for future synthesis. The reduced amount of precursor could eliminate the need for “washing” of product, which would reduce waste.

### Future Work:

More development is needed to test and improve the QD collection efficiency of the system. Further testing is also needed to find environmental-friendly solvent(s) for the synthesis. At last, testing is necessary to improve the purification process to remove excess un-reacted precursors.

### Acknowledgments:

The author would like to thank the National Science Foundation, the National Nanotechnology Infrastructure Network Research Experience for Undergraduates (NNIN REU) Program, and the staff of the Washington University

in St. Louis Nano Research Facility (NRF). In addition, the author would like to thank Principal Investigator Dr. Da-Ren Chen and mentor He Jing.

### References:

- [1] Didenko, Yuri T., and Kenneth S. Suslick. “Chemical Aerosol Flow Synthesis of Semiconductor Nanoparticles.” *Journal of the American Chemical Society* 127.35 (2005): 12196-12197
- [2] Su, Huaipeng, John D. Dixon, Andrew Y. Wang, Jeremy Low, Jian Xu, and Jinggang Wang. “Study on Growth Kinetics of CdSe Nanocrystals with a New Model.” *NanoScale Research Letter* 5 (2010): 823-28. Springer, 25 Mar. 2010.
- [3] Rosenthal, Sandra, James McBride, Stephen Pennycook, and Leonard Feldman. “Synthesis, Surface Studies, Composition and Structural Characterization of CdSe, Core/shell and Biologically Active Nanocrystals.” *Surface Science Reports* 62.4 (2007): 111-57.

## Etch Study of Zirconium Oxide Nanoparticle Photoresist

**Andrew Sanville**

**Engineering Physics and Mathematics, University of Wisconsin-Madison**

*NNIN REU Site: Cornell NanoScale Science and Technology Facility, Cornell University, Ithaca, NY*

*NNIN REU Principal Investigator: Christopher K. Ober, Department of Materials Science and Engineering, Cornell University*

*NNIN REU Mentor: Christine Ouyang, Department of Materials Science and Engineering, Cornell University*

*Contact: asanville@wisc.edu, cko3@cornell.edu, cyo3@cornell.edu*

### Abstract:

As feature sizes continue to decrease, the need for high etch-resistance photoresist becomes more apparent. Using thin films creates lower aspect ratio patterns and effectively prevents pattern collapse. However, due to poor etch-resistance, achieving deep trenches on thin films can be difficult, as one will often etch through the photoresist before etching the substrate as desired. A promising potential solution lies in inorganic resists. This study looked at one such resist, a zirconium oxide ( $ZrO_2$ ) nanoparticle-based resist. These zirconium oxide nanoparticles are surrounded by methacrylic acid ligands, where the inorganic core has high etch-resistance and the photochemical reactions can occur at the organic ligands. This project looked at the effects of different lengths of oxygen plasma cleaning before etching to see its effects on etch-resistance of the nanoparticles in tetrafluoromethane ( $CF_4$ ) and sulfur hexafluoride ( $SF_6$ ) gases. The oxygen clean appears to have little effect on the etch-resistance of the film.

### Introduction:

Many processes today implement photolithography to create features. This process involves exposing a photo-active coating to light in order to create a pattern [1]. The coating acts as a protective layer, allowing for etching of the pattern into the substrate. These photo-active compounds are the source of much research as they can continue to be improved.

One such material is an inorganic complex consisting of zirconium-based nanoparticles. These nanoparticles have high etch-resistance, a desirable trait when making small features. High etch-resistance allows for one to use thinner films, as one needs less photoresist (the photoactive compound) during the etch phase [2]. Thinner films prevent the patterns from failing by avoiding tall and narrow structures that would be prone to defects.

This study examined the properties of this complex process. In particular, it sought to optimize the etch step of the resist by looking at the effects of various oxygen plasma clean times on the etch properties of thin films of the particles in  $CF_4$  or  $SF_6$  plasma etches.

### Procedure:

The nanoparticles were synthesized and processed according to literature [2]. The wafer was exposed to light using the ABM contact aligner at the Cornell NanoScale Science and Technology Facility (CNF). The wafer was exposed under 254 nm light using contact lithography.

The wafer was then cut into fragments and exposed to either  $CF_4$  or  $SF_6$  plasmas in the Oxford 81 and PlasmaTherm PT72 respectively (also at the CNF). The samples were exposed for thirty second intervals, up to two and a half minutes. The thickness of the remaining films was then measured using spectroscopic ellipsometry.

### Results and Conclusions:

Figure 1 shows the change in thickness due to the oxygen clean. The thickness decreased at an exponential rate. The decrease in etch time could represent the oxygen consuming all of the organic compounds on the surface of the film and then its inability to etch into the zirconium oxide. Further study should be done to confirm this theory, looking at the composition of the film before and after the etch.

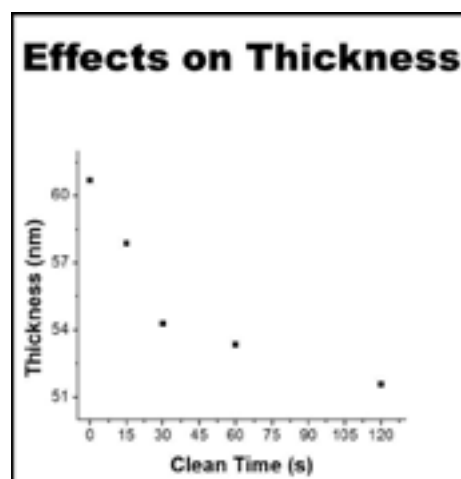


Figure 1: The change in thickness as a result of the oxygen clean.

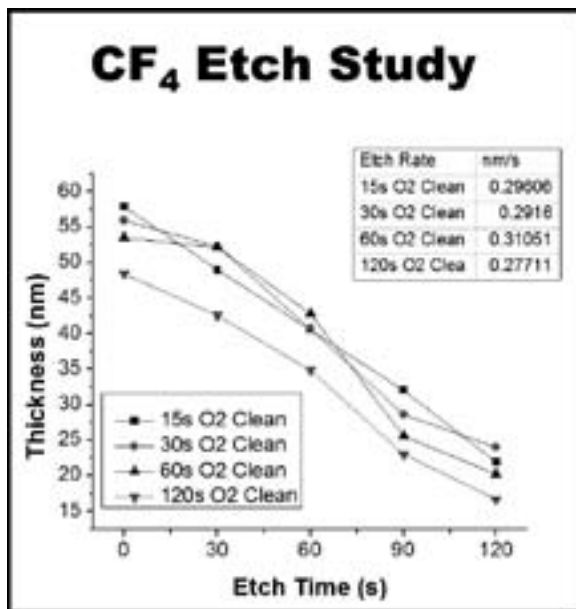


Figure 2: The results of etch study performed in  $CF_4$  gas with various  $O_2$  clean times.

Figure 2 shows the effects on the film in a  $CF_4$  plasma etch. Overall, other than a thickness decrease, not much change was seen in the etch resistance of the film. Figure 3 shows the effects on the film in a  $SF_6$  plasma etch. Although, the 30s etch appeared to have a much faster etch rate, this could just be due to artifacts in the data. It does not appear that the oxygen clean step had a significant effect on the etch rate. In the end, further study should be done to confirm these results and help further optimize etching.

Overall, the research proved that the photoresist is for the most part unaffected by the oxygen clean in these processes. In neither process was a noticeable difference apparent in the etch step. The photoresist held up well in both plasma etches, giving fairly consistent etch rates. These positive results lend evidence to the durability and strength of the resist.

#### Acknowledgements:

I would like to thank my mentor, Christine Ouyang, as well as Dr. Markos Trikeriotis and Marie Krysak, and my

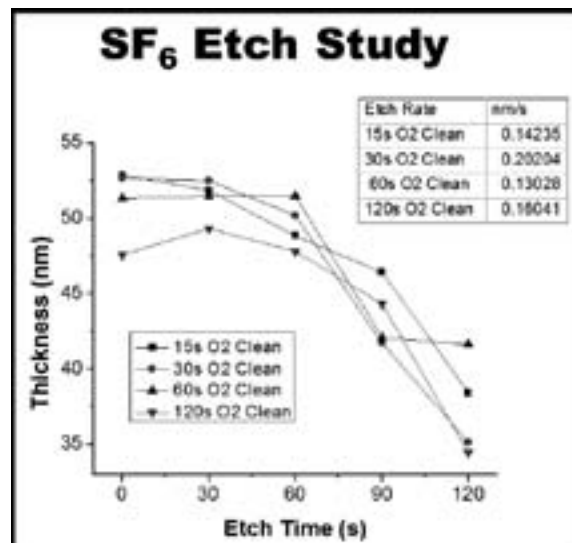


Figure 3: The results of etch study performed in  $SF_6$  gas with various  $O_2$  clean times.

principal investigator, Prof. Christopher K. Ober, for hosting me and assisting me with this project. In addition I would like to thank the CNF staff, in particular Melanie-Claire Mallison and Rob Ilic, for all their support. Finally, I would like to thank the National Science Foundation, the National Nanotechnology Infrastructure Network Research Experience for Undergraduates (NNIN REU) Program, and Sematech for funding this research.

#### References:

- [1] Ito, H.; "Chemical Amplification Resists for Microlithography"; *Advanced Polymer Science*, 172, 41-53 (2005).
- [2] Trikeriotis, M, Krysak, M, Chung, Y. S., et. al.; "A new inorganic EUV resist with high-etch resistance"; *SPIE*, 8322, 1-6 (2012).

# Investigation of TiO<sub>2</sub> Films Deposited by Low-Temperature ALD Process for Future CMOS

**Karl Schliep**

**Chemistry and Mathematics, University of Minnesota Morris**

*NNIN iREU Site: National Institute for Materials Science (NIMS), Tsukuba, Ibaraki, Japan*

*NNIN iREU Principal Investigator: Toyohiro Chikyo, International Center for Materials Nanoarchitectonics (MANA), National Institute for Materials Science*

*NNIN iREU Mentor: Toshihide Nabatame, MANA Foundry, National Institute for Materials Science*

*Contact: schli115@morris.umn.edu, chikyo.toyohiro@nims.go.jp, nabatame.toshihide@nims.go.jp*

**Abstract:**

Anatase-type titanium dioxide (TiO<sub>2</sub>) thin films were investigated for their application in three dimensional (3D) integrated circuit (IC) designs. The TiO<sub>2</sub> films were deposited using atomic layer deposition (ALD) over other types of deposition because it offers both angstrom-order thickness resolution and the unique conformal deposition required for 3D fabrication. TiO<sub>2</sub> was deposited with four differing cycles resulting in four different thicknesses ranging from 3-7 nm. These samples were separately annealed at 300, 400, and 500°C. Electrical characterization revealed that only the 500°C fabrication process produced TiO<sub>2</sub> usable for effective 3D integrated circuits.

**Introduction:**

The nominal feature size of components in integrated circuit (IC) technology has decreased drastically over the last several decades producing electronics that are increasingly more advanced. However, scientists have come to realize that this nominal feature size of the components is quickly approaching both physical and quantum mechanical limits. The quantum mechanical limits arise from electrons tunneling through the thin silicon dioxide (SiO<sub>2</sub>) insulator layer resulting in low current. The physical limits arise because the technology is approaching thin films that are a single molecule thick. To circumvent these limitations, scientists have begun researching both materials with a higher dielectric constant than SiO<sub>2</sub> to limit quantum tunneling, and new IC designs involving 3D fabrication of the IC components.

One promising 3D fabrication technique is the Gate-Last process which, as the name indicates, deposits the gate on the IC component last. This process requires that the fabrication temperature be less than 500°C and have an insulating layer with dielectric constant,  $\kappa$ , greater than 30. One material that has been investigated by many researchers

for applications in future IC technology is TiO<sub>2</sub>, because in its rutile phase its dielectric constant is over 20 times larger than SiO<sub>2</sub>. However rutile-type TiO<sub>2</sub> only forms at temperatures higher than 600°C [1]. The other major polymorph of TiO<sub>2</sub> is the anatase structure, which forms at lower temperatures and has a dielectric constant of approximately 30 — making it an ideal material for the insulating layer of the Gate-Last process. We investigated anatase-type TiO<sub>2</sub> as a possible high- $\kappa$  insulator for the Gate-Last process by determining its dielectric constant at three fabrication temperatures; 300, 400, and 500°C. The 500°C case was carried out previously by M. Kimura, but the results will be shown here.

We prepared TiO<sub>2</sub> films on SiO<sub>2</sub>/Si samples by ALD, using tetrakis(dimethylamino)titanium (TDMAT) and water gas. These films were used to construct capacitors with structure TaC/TiO<sub>2</sub>/SiO<sub>2</sub>/Si with fabrication temperatures of 300, 400, and 500°C. Using these capacitors, we studied the relationship between TiO<sub>2</sub> thickness and fabrication temperature to determine how the fabrication temperature affected the dielectric constant of TiO<sub>2</sub>.

**Experimental:**

TiO<sub>2</sub> thin films were deposited onto a SiO<sub>2</sub>/Si substrate using ALD. The ALD process consisted of 50, 66, 83, and 100 cycles, where one cycle consisted of inflow of TDMAT, then argon (Ar) gas, then H<sub>2</sub>O, and again Ar gas to purge the

Sample	Cycles	Annealing Temperature	SiO <sub>2</sub> Thickness ± Error	Before Annealing TiO <sub>2</sub> Thickness ± Error	After Annealing TiO <sub>2</sub> Thickness ± Error
1	100	400	4.754±0.00586	5.287±0.00491	5.317±0.00506
2	100	300	4.758±0.00603	5.205±0.00501	5.449±0.00495
3	50	400	4.734±0.00623	2.666±0.00544	2.840±0.00537
4	50	300	4.746±0.00621	2.698±0.00439	2.837±0.00581
5	83	400	4.793±0.00618	4.229±0.00503	4.355±0.00573
6	83	300	4.795±0.00635	4.214±0.00485	4.438±0.00571
7	66	400	4.821±0.00620	3.343±0.00503	3.482±0.00517
8	66	300	4.781±0.00623	3.348±0.00520	3.547±0.00520

Figure 1: Fabrication specifications and thickness results.

system before the next cycle. The substrate temperature was 200°C and the TDMAT precursor was kept at 100°C for the deposition. Post deposition annealing was done under O<sub>2</sub> atmosphere with flow rate of 50 sccm. The temperature was ramped at 10°C up to 300, or 400°C and held there for 30 s. The top TaC electrode of the capacitor was deposited by sputtering to a thickness of 150 nm. The samples were then annealed in a 3%H<sub>2</sub>/N<sub>2</sub> gas to rectify any oxide ion charge.

The film thicknesses were determined by ellipsometry, and the results are shown in Figure 1. The electrical properties of the TaC/TiO<sub>2</sub>/SiO<sub>2</sub>/Si capacitors were investigated using high-frequency capacitance-voltage (C-V) and leakage current-voltage (I-V) measurements. High-frequency C-V measurements were executed at 500 kHz and the oscillation amplitude was 30 mV. I-V measurements were performed using a step voltage sweep with a voltage step of 0.05 V. The structure of the TiO<sub>2</sub> films was determined previously using XRD, by M. Kimura, and is shown in Figure 2.

### Results and Discussion:

The XRD data shows how that only the anatase-type TiO<sub>2</sub> was deposited for all three fabrication temperature. The C-V data in Figure 3 shows that with a 500°C fabrication temperature, the dielectric constant was 34.8, at 400°C the dielectric constant was 22.8, and at 300°C the data was too inconsistent for a dielectric constant to be determined. Thus, only the 500°C fabrication process produced a TiO<sub>2</sub> thin film suitable for the 3D Gate-Last process.

We believe that the 300°C and 400°C fabrication temperatures were not high enough to reduce the film defects. Further research is needed to confirm this hypothesis by characterizing the film quality. We also attribute the inconsistent electrical properties of the 300°C fabrication process to poor TiO<sub>2</sub> film quality.

### Conclusions:

TiO<sub>2</sub> thin films deposited at 500°C show promise as effective insulators for 3D fabrications, whereas the films deposited at 400°C and 300°C need to be investigated further, because of their low dielectric constant and inconsistent electrical properties. Further research is also needed to both characterize the films boundary conditions and to determine the film quality before any concrete conclusions can be made.

### Acknowledgements:

I'd like to thank my Principal Investigator Toyohiro Chikyo, my mentor Toshihide Nabatame, my lab mates M. Kimura and H. Yamada, the MANA Foundry Staff, Lynn Rathbun, Akemi Iwasawa, National Institute for Material Science, the National Nanotechnology Infrastructure Network International Research Experience for Undergraduates Program, and the National Science Foundation for making this possible.

### References:

- [1] Kadoshima, M. et al, Thin Solid Films 424 (2003) 224-228.

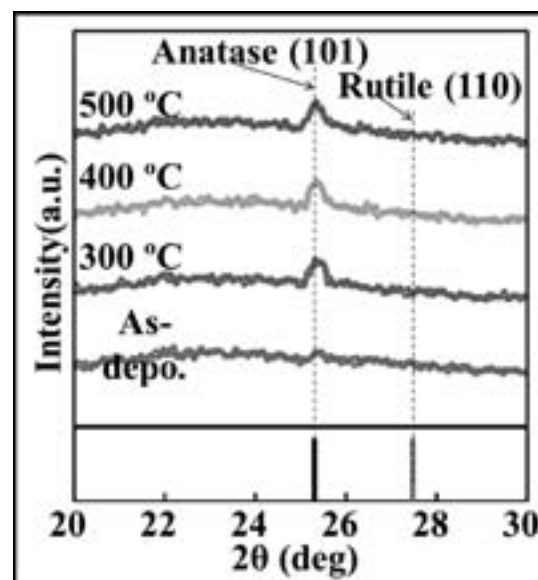


Figure 2: XRD patterns of TiO<sub>2</sub> films annealed at different temperatures.

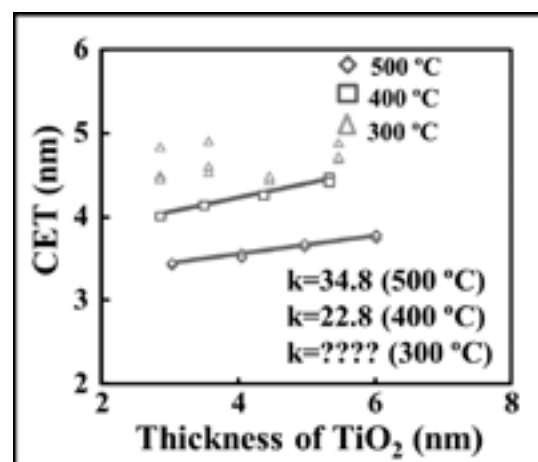


Figure 3: Capacitance Equivalent Thickness vs. Physical Thickness of TiO<sub>2</sub>.

## Engineering Carbon Nanotube Microdrops Using Microfluidic Devices

**YooSun Shim**

**Chemical and Biomolecular Engineering, Johns Hopkins University**

*NNIN REU Site: Center for Nanoscale Systems, Harvard University, Cambridge, MA*

*NNIN REU Principal Investigator: Dr. David Weitz, Engineering and Applied Science, Department of Physics, Harvard University*

*NNIN REU Mentor: Dr. Michael De Volder, School of Engineering and Applied Science, Harvard University*

*Contact: yshim5@jhu.edu, weitz@seas.harvard.edu, mdevolder@seas.harvard.edu*

### Abstract:

Since the discovery of carbon nanotubes (CNTs) by Sumio Iijima in 1991 [1], they have been of great interest to the nanotechnology community. In this work, we explored microfluidic drop generators to fabricate CNT microdrops with a controlled geometry and fast throughput. On the one hand, CNT microdrops were assembled using CNTs water suspensions in oil. On the other hand, we explored the fabrication of CNT shells according to the Pickering emulsion principle. These CNT microdrops were first validated using shear mixing in vials and then transferred to microfluidic drop generators.

### Introduction:

Graphene is a planar sheet of sp<sup>2</sup>-hybridized carbon atoms in a honeycomb structure; and CNTs are essentially graphene sheets rolled into cylindrical structures. There are two types of CNTs. First, single sheet of graphene rolled in to a cylinder is referred to as single-walled carbon nanotubes (SWNT), and multiple layers of graphene rolled are known as multi-walled carbon nanotubes (MWNT). The diameter of CNTs can range from less than 1 nm to more than 100 nm depending on the size and number of graphene shells; and the length of the nanotubes varies from tens of nanometers up to several centimeters, hereby truly bridging nanometer and macroscopic length scales [2].

CNTs attract interest in the nanotechnology community due to their unique characteristics. For instance, their mechanical properties include high tensile strength (~ 37 GPa), and Young's modulus (1 TPa). The electrical conductivity can be as high as 10<sup>9</sup> A/cm<sup>2</sup>, and the measured room temperature thermal conductivity for an individual MWNT is around 3000 W/m•K, which is greater than that of natural diamond [3].

In this work, we looked into new shaping methods of these nanomaterials.

### Experimental Procedure:

**Materials.** CNTs used in this work were MWNTs with the diameter of nine nanometers and length of approximately 0.5 to 3  $\mu\text{m}$ . These were acquired from NanoCyl, product type NC7000. Carboxyl functionalized CNT were fabricated by hot nitric acid treatment while refluxing at 60°C. CNT-water suspensions were made by sonication and subsequent centrifugation of carboxylic CNTs as well as CNT-surfactant. Typically, suspensions of a few weight percent Span 80, SDBS, SDS, Tween, and F127, and ABIL were sonicated for a few hours at low energy, followed by a one hour centrifugation at 5000 g. Also for the continuous phase, various fluids were tested including water, mineral oils, and kerosene.

**Droplet Formation by Shear Mixing.** CNT suspension was inserted to a vial containing an oil phase and the vial was shaken to generate CNT microdrops. Calibrated microscopes, as well as scanning electron microscopy (SEM) was used to characterize the droplets.

**Droplet Formation by Microfluidic Devices.** Glass capillary microfluidic devices were fabricated as follows. First, two round capillaries were tapered by a micropipette puller. The capillary surfaces were treated with *n*-octadecyltrimethoxyl silane, making them hydrophobic, thereby preventing the water-based drops to collapse to the glass. Then as shown in Figure 1, the tapered capillaries are aligned co-axially and

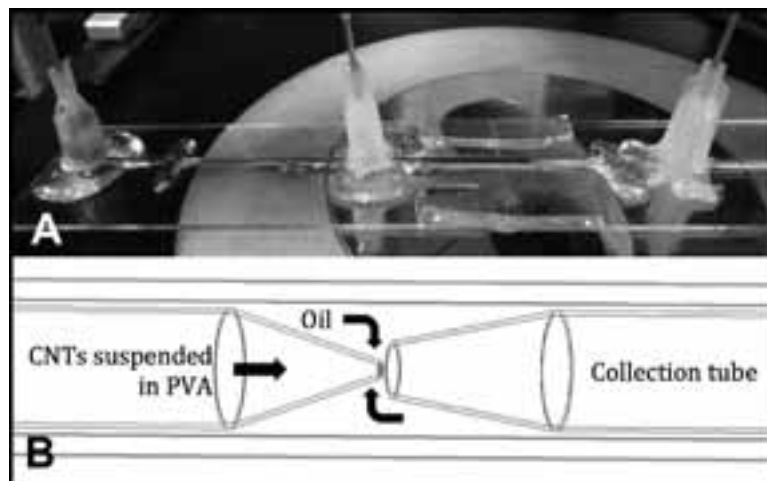


Figure 1: A) Microfluidic glass capillary device.  
B) Close up schematic diagram of the device.

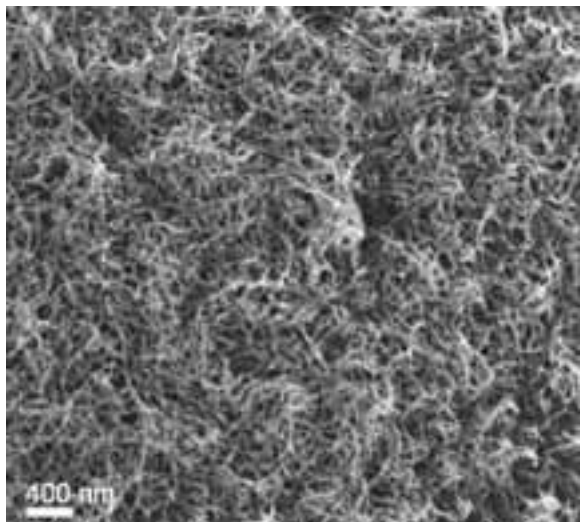


Figure 2: Close up SEM image of the CNT microdrop surface revealing the CNTs.

inserted into a square capillary. Epoxy was used to glue them together.

Next, plastic syringes containing CNT suspension and the continuous oil phase were connected to syringe pumps. The pump flowed liquids to the microfluidic device at a constant flow rate and therefore, the device made monodispersed CNT microdrops. The device was also connected to a hydrophobic collection vial for further research. SEM was used to take images.

**Pickering Emulsions.** CNT shells were fabricated based on the Pickering emulsion principle. This principle relies on particles that sit astride the oil-water interface, to reduce the total surface energy. The particle refers to a solid object or a small liquid droplet with a size ranging anywhere from two nanometers to a few millimeters. In this work, we formed hollow particles using carboxyl functionalized CNTs adsorbed in a water-cyclohexane interface. This process was in accordance with prior work found in literature. Chen, et al., prepared CNT microcapsules by using plasma treated CNTs and cyclohexane [4].

### Results and Conclusions:

As shown in Figure 3, stable CNT microdrops were generated using both the shaking and the microfluidic device. Using image analysis, the diameter of the drops was determined. The diameter distribution of solid CNT microdrops from the microfluidic device was concentrated around 100  $\mu\text{m}$ . However, the diameter distribution from the shaking method ranged from 10  $\mu\text{m}$  to 120  $\mu\text{m}$ . Also, changing the flow rates, the diameter of the drops made by the microfluidic device can be controlled.

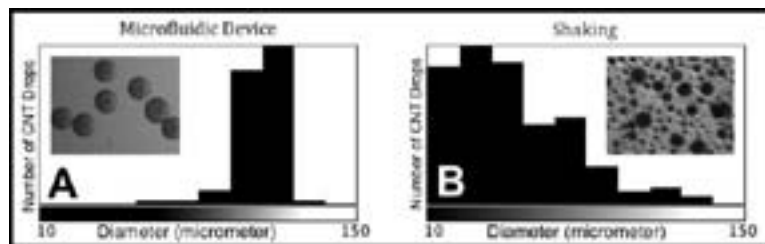


Figure 3: A) Microdrops generated by the microfluidic device and diameter distribution. B) Microdrops generated by shaking a vial and diameter distribution.

### Future Work:

Coalescence was a problem throughout the project. Especially the fact that the Pickering emulsion CNT microdrops coalesced inside the plastic tubing while traveling to the collection vial. Also, the other CNT microdrops coalesced, particularly when their diameter exceeded 100  $\mu\text{m}$ . Some approaches to the problem this summer were the following; to provide more time for stabilization, longer plastic tubing was used in the microfluidic device, and also, the tubing was sonicated for Pickering emulsions, in accordance to a procedure found in literature. Further work is needed in order to stabilize these drops.

### Acknowledgments:

I would like to thank my mentor, Dr. Michael De Volder, and my PI, Dr. David Weitz, for their support and guidance throughout the summer. Funding was provided the National Nanotechnology Infrastructure Network Research Experience for Undergraduates (NNIN REU) Program and the National Science Foundation.

### References:

- [1] Iijima S; "Helical Microtubules of Graphitic Carbon"; Nature, 354, 56 (1991).
- [2] Wang X; "Fabrication of Ultralong and Electrically Uniform Single-Walled Carbon Nanotubes on Clean Substrates"; Nano Letters, 9, 3137 (2009).
- [3] Baughman R; "Carbon Nanotubes – the Route Toward Applications"; Science, 297, 787 (2002).
- [4] Chen, W; "Novel Synthesis of Self-assembled CNT Microcapsules by O/W Pickering Emulsions"; Materials Letters, 64, 2589 (2010).

## Heteroepitaxial Growth of Diamond on SiC Substrates

**Andrew Tam**

**Electrical Engineering, Rice University**

*NNIN REU Site: Howard Nanoscale Science and Engineering Facility, Howard University, Washington, DC*

*NNIN REU Principal Investigator and Mentor: Dr. Gary Harris, Electrical Engineering, Howard University*

*Contact: atamsplitter@gmail.com, gharris@msrce.howard.edu*

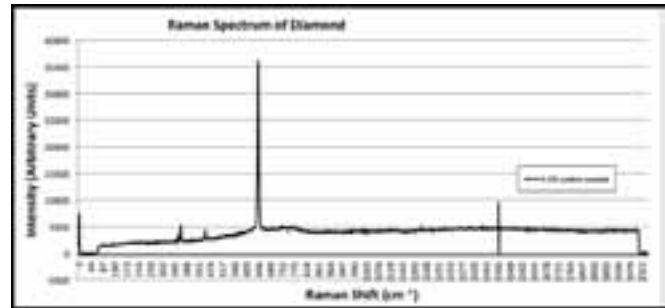
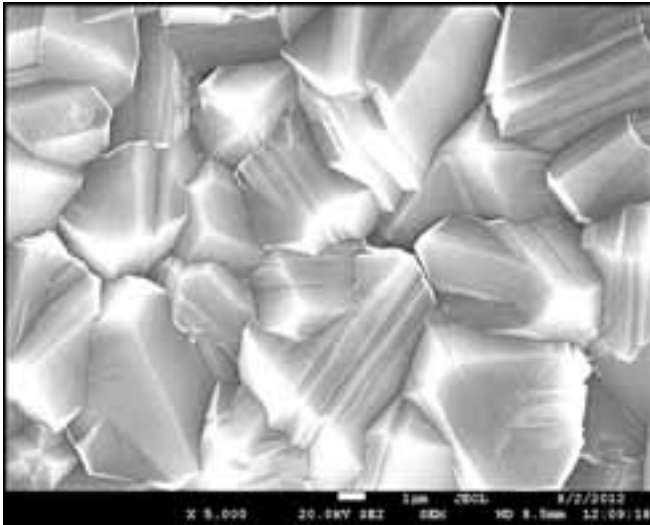


*Figure 1, left: Surface of best sample.*

*Figure 2, above: Raman spectrum of best sample.*

### Abstract:

Diamond's high carrier mobility, thermal conductivity, and breakdown voltage allow for faster and higher power electronic devices than those made of silicon. Growth of thin, high quality diamond films has been consistently achievable since the 1980's by chemical vapor deposition (CVD) and works best on diamond substrates. However, as diamond substrates are expensive and cannot be commercially grown large enough for mass production, this project explores silicon carbide as an alternative growth substrate. Diamond films were grown using hot filament chemical vapor deposition (HFCVD) under two filament configurations, with differing growth times and carbon-to-hydrogen ratios to determine optimal growth conditions. Quality of the diamond films was characterized by Raman spectroscopy, scanning electron microscopy (SEM), and energy-dispersive x-ray spectroscopy (EDS). Hall measurements were performed on selected samples to determine the electrical properties of the films. Fabrication of Schottky diodes was attempted, but samples were too conductive for electronic device applications.

### Introduction:

Diamond's superior carrier mobility, high thermal conductivity and high breakdown voltage make it ideal for high-speed power transistors. Silicon carbide (SiC) makes a good growth substrate for diamond because it also has a high thermal conductivity and breakdown voltage, making it suitable for use under the same high-power conditions. Additionally, SiC wafers can be grown large enough for mass production, while diamond substrates cannot [1]. Our project focused on growing unintentionally doped layers of diamond on semi-insulating SiC.

### Experimental Procedure:

To prepare clean substrates, SiC wafers were brushed with soap and deionized water, and rinsed with acetone and methanol. The samples were then seeded for diamond growth by immersion in an equal volume mixture of 5 nm-size diamond particle slurry and methanol, and placed in an ultrasonic bath for ten minutes. The sonication process scratched up the SiC surface and deposited the nano-size diamond particles on the surface; both the scratches and particles acted as nucleation sites during growth. Six samples of SiC were prepared this way, five of the hexagonal 6H polytype and one of the cubic 3C polytype.

Growth of diamond was achieved in a hot filament chemical vapor deposition (HFCVD) reaction chamber. Diatomic hydrogen ( $H_2$ ) and methane ( $CH_4$ ) were passed over an electrically heated tungsten filament, causing them to react and deposit carbon on the surface of the SiC. One 6H sample was grown under a configuration of three straight filaments, while the remaining four 6H samples and the 3C sample were grown under a single, coiled filament configuration. Before growth, carburization was performed; a larger concentration of methane-to-hydrogen was passed through the chamber at a sub-growth temperature to bond carbon atoms to the outside of the tungsten filament and thereby prevent contamination of the substrate and diamond layer. The carbon ratio was then reduced and the filament current increased to achieve the desired growth temperature. The coiled filament setup had a shutter to protect the substrate from unintentional deposition of carbon during the carburization process.

The straight filament sample was grown for eight hours at a temperature of  $2200^\circ C$  and a pressure of 30 torr, with a 1.5% concentration of methane-to-hydrogen. The samples in the coiled filament setup were all grown at a temperature of  $2600^\circ C$  and pressure of 20 torr. Of the 6H samples, we grew in a 2% concentration of methane-to-hydrogen for 18 hours, a 1.5% concentration of methane-to-hydrogen for 21 hours, and a 1% concentration of methane-to-hydrogen for 20.5 hours. Subsequently, a 6H sample and 3C sample were both grown at  $2600^\circ C$  and 20 torr in a 1.5% carbon concentration for a short run of 2.25 hours.

### Results and Conclusions:

Scanning electron microscope (SEM) images revealed well-faceted, polycrystalline diamond on all samples. All samples exhibited microcrystals of diamond except the 6H and 3C grown for 2.25 hours, which exhibited nanocrystals of diamond. The 6H 1.5% sample grown under the coil filament experienced the highest deposition rate ( $0.86 \mu m/hr$ ) and the highest purity Raman spectrum; no graphite peak was visible. The 6H 2% and 1% samples both experienced film stress. The 2% sample had almost as high a deposition rate, but with a significant graphite peak; the 1% sample had a small graphite

peak but a low deposition rate. A concentration of 1.5% carbon under the coil filament was determined to be the best sample.

Hall measurements were performed on the 1.5% 6H sample under the straight filament, and the 1.5% and 1% 6H samples under the coil filament. Mobility of the straight filament sample was  $112 \text{ cm}^2/V\text{-s}$ , while the coil filament 1.5% and 1% mobilities were 9.28 and  $32.34 \text{ cm}^2/V\text{-s}$ , respectively. Carrier concentration for the straight filament sample was on the order of  $10^{18} \text{ cm}^{-3}$ , while for the coil filament samples, it was on the order of  $10^{15} \text{ cm}^{-3}$ . Schottky diodes were unsuccessful, as all metal-diamond contacts were ohmic even without annealing.

### Future Work:

The high carrier concentrations indicate unintentional dopants; energy dispersive x-ray spectroscopy (EDS) on the back of free-standing diamond from the 2% sample revealed 9% tungsten from the filament. Improving the carburization process to reduce the contamination of the substrate will decrease the conductivity. Annealing may also reduce bulk defects and decrease carrier concentration [2].

### Acknowledgements:

I would like to thank Dr. Gary Harris, James Griffin, Crawford Taylor, and the Howard Nanoscale Facility, along with R.D. Vispute and Blue Wave Semiconductor. I also wish to thank the National Nanotechnology Infrastructure Network Research Experience for Undergraduates Program and the National Science Foundation.

### References:

- [1] Ueda, K., et al.; "Diamond FET Using High-Quality Polycrystalline Diamond with  $f_T$  of 45 GHz and  $f_{max}$  of 120 GHz"; IEEE Electron Device Letters, Vol. 27, No. 7 (July 2006).
- [2] Foord, J., et al.; "High Carrier Mobility in Polycrystalline Thin Film Diamond"; Applied Physics Letters, Vol. 72, 353 (1998).

## Carbon Doping of $\langle 10\text{-}11 \rangle$ GaN by Plasma-Assisted Molecular Beam Epitaxy

Caroline Yu

Electrical Engineering, The Cooper Union for the Advancement of Science and Art

NNIN REU Site: Nanotech, University of California, Santa Barbara, CA

NNIN REU Principal Investigator: James S. Speck, Materials Department, University of California, Santa Barbara

NNIN REU Mentor: Brian McSkimming, Materials Department, University of California, Santa Barbara  
(2007 NNIN REU, UCSB; 2008 NNIN iREU, Japan)

Contact: [yu8@cooper.edu](mailto:yu8@cooper.edu), [speck@mrl.ucsb.edu](mailto:speck@mrl.ucsb.edu), [mcskimming@engineering.ucsb.edu](mailto:mcskimming@engineering.ucsb.edu)

### Abstract:

Magnesium (Mg) is the most commonly used acceptor dopant in gallium nitride (GaN) devices. Acting as a deep acceptor with an activation energy of  $\sim 200$  meV, Mg can introduce electrical and optical complications. Carbon has been demonstrated to be a possible alternative acceptor dopant atom with a lower activation energy [1]. Carbon-doped GaN (GaN:C) samples were homoepitaxially grown on  $\langle 10\text{-}11 \rangle$  and  $\langle 10\text{-}1\text{-}1 \rangle$  planes using plasma-assisted molecular beam epitaxy (PAMBE). A root mean square (RMS) surface roughness of 0.248 nm was achieved as verified by atomic force microscopy (AFM). There was no apparent crystal degradation from carbon doping as demonstrated by full-width half-max calculations of x-ray diffraction (XRD) rocking curves. Hall Effect and current-voltage measurements were used to electrically characterize the samples.

### Introduction:

GaN is a wide band-gap III/V semiconductor material that is used in many short-wavelength emitting devices. Through its alloys, GaN devices are able to function over the entire visible spectrum. GaN has a wurtzite crystal structure lacking inversion symmetry; therefore, polar, non-polar, and semi-polar planes are available for growth. Much research has dealt with growth on the polar  $\langle 0001 \rangle$  plane. This project examined growth on the semi-polar  $\langle 10\text{-}11 \rangle$  plane.

To obtain electrically-conducting, extrinsic semiconductor material, impurities are placed into the semiconductor. When an acceptor atom takes an electron from a valence band shell, holes are produced. When holes are the majority carrier, the material is said to be p-type. Magnesium is commonly used as the acceptor dopant in GaN material. Because magnesium is a deep acceptor with a relatively high activation energy of  $\sim 200$  meV, only  $\sim 1\%$  of the impurities are ionized. An increase in doping is necessary to obtain desirable hole concentrations; this increase leads to additional imperfections. Carbon has been predicted to be an alternative to magnesium [2]. Green, et al. [3], showed that, while being the primary dopant, carbon will incorporate and self-compensate on the  $\langle 0001 \rangle$  plane [3]. It was also demonstrated that  $\text{CBr}_4$  is an effective carbon

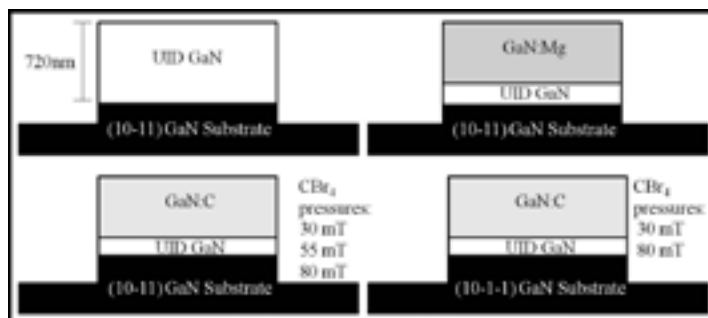


Figure 1: Growth layer(s) on semi-polar GaN substrates. Not to scale.

source that has no significant impact on growth rate and crystal quality of GaN material grown by RF-plasma-assisted MBE.

Hikosaka, et al. [1], demonstrated p-type conduction in GaN:C grown on the  $\langle 1\text{-}101 \rangle$  plane by metal-organic vapor phase epitaxy. The hole density within the GaN was controllable by varying the carbon precursor flow rates. To further investigate the physical and electrical properties of carbon-doped material, GaN:C was grown on the  $\langle 10\text{-}11 \rangle$  plane using PAMBE in this study.

### Experimental Procedure:

PAMBE was used to grow UID GaN, GaN:Mg, and GaN:C with  $\text{CBr}_4$  foreline pressures of 30, 55, and 80 mT on bulk semi-polar  $\langle 10\text{-}11 \rangle$  GaN as well as GaN:C with  $\text{CBr}_4$  foreline pressures of 30 and 80 mT on bulk  $\langle 10\text{-}1\text{-}1 \rangle$  GaN. Sample schematics are shown in Figure 1.

All GaN samples were grown using a Varian GenII system with a substrate temperature of  $710^\circ\text{C}$ . “Active” nitrogen was provided by a Veeco Uni-bulb nitrogen plasma source using RF-plasma power of 300 W and a nitrogen flow rate of 0.4 sccm. Elemental gallium was introduced via a standard SUMO effusion cell. These conditions correspond to a growth rate of  $\sim 8$  nm/min.

AFM images were taken using a Veeco Dimension 3000/3100 scanning probe microscope to measure surface morphology and roughness. XRD measurements were taken using a PANalytical X'Pert PRO MRD high-resolution x-ray diffractometer to observe crystal quality. Hall effect measurements were taken on mesa-isolated photolithographically-defined metal contacts on a Van der Pauw pattern as shown in Figure 2. Al/Au contacts were deposited on UID GaN samples while Pd/Au contacts were deposited on all other samples.

### Results and Conclusions:

Visible step-edges in the AFM images of all samples indicate good step-flow growth, as seen in Figure 3. As  $\text{CBr}_4$  foreline pressure increased, surface roughness decreased. The average RMS surface roughness of GaN:C samples was calculated to be 0.248 nm, indicating atomically smooth surfaces. Samples grown on  $\langle 10\text{-}1\text{-}1 \rangle$  were 47% smoother than those grown on  $\langle 10\text{-}11 \rangle$ . Full-width half-max (FWHM) calculations of the XRD rocking curves were all within one standard deviation of the average FWHM except one, suggesting no significant crystal degradation due to carbon incorporation, as shown in Figure 4.

The single outlier was the sample grown on  $\langle 10\text{-}1\text{-}1 \rangle$  with the highest  $\text{CBr}_4$  foreline pressure of 80 mT with a FWHM of more than one standard deviation smaller than the average. This result suggests that with increasing  $\text{CBr}_4$ , there is improvement of crystal quality on  $\langle 10\text{-}1\text{-}1 \rangle$ .

Hall effect measurements were inconclusive due to Schottky behavior of the metal contacts; however, current-voltage measurements taken from contacts on top of the mesa to the substrate at the base of the mesa suggest rectifying p-n diode type behavior. As the substrate is n-type material, the growth layer is subsequently suggested to have p-type behavior.

### Future Work:

The growth layer should be better isolated from the substrate to avoid carrier leakage and help generate conclusive Hall effect measurements. Better electrical characterization will confirm that the  $\langle 10\text{-}11 \rangle$  and  $\langle 10\text{-}1\text{-}1 \rangle$  planes generates higher carrier ionization via carbon doping.

### Acknowledgements:

Many thanks to my mentor, Brian McSkimming; PI, James Speck; REU coordinator, Samantha Cruz; and family and friends. I am indebted to the NNIN REU Program and NSF for funding.

### References:

- [1] Hikosaka, et al., Phys. Stat. Sol.(c) 3, No. 6, 1425 (2006).
- [2] Seager, et al., J. Appl. Phys. 92, No. 11, 6553 (2002).
- [3] Green, et al., J. Appl. Phys. 95, No. 12, 8456 (2004).



Figure 2: Four Hall probes on Van der Pauw patterned mesa-isolated photolithographically-defined contacts.

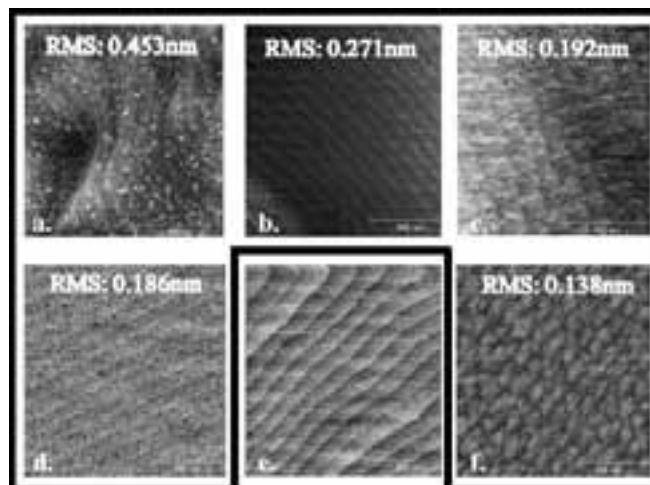


Figure 3: Approximately one micron AFM images. a,b,c.  $\langle 10\text{-}11 \rangle$  GaN:C. d,f.  $\langle 10\text{-}1\text{-}1 \rangle$  GaN:C. e. Evident step-flow growth of GaN:Mg. a, d / b / c, f.  $\text{CBr}_4$  foreline pressure of 30, 55, 80 mT, respectively.

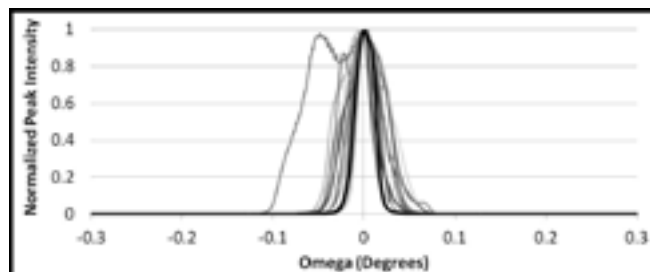


Figure 4: Normalized Omega-2 Theta x-ray diffraction rocking curves. Pre-grown  $\langle 10\text{-}11 \rangle$  GaN represented in bold. Second peak seen in  $\langle 10\text{-}11 \rangle$  GaN:C 80 mT samples.

## Characterization of XeF<sub>2</sub> Etching for Release of Piezoelectric Micro-Robots

**Ramon Alonso**

**Mechanical Engineering, San Joaquin Delta College**

*NNIN REU Site: Lurie Nanofabrication Facility, University of Michigan, Ann Arbor, MI*

*NNIN REU Principal Investigator: Prof. Kenn Oldham, Mechanical Engineering, University of Michigan, Ann Arbor*

*NNIN REU Mentor: Jongsoo Choi, Mechanical Engineering, University of Michigan, Ann Arbor*

*Contact: ralonso766@students.deltacollege.edu, oldham@umich.edu, jongs@umich.edu*

### Abstract and Introduction:

Thin-film piezoelectric micro-robots could potentially help save human lives with their ability to do reconnaissance in hazardous places, or help avoid costly demolition processes during infrastructure maintenance by utilizing images provided from inconvenient and/or unreachable locations. In order to achieve these goals, there should be an optimized fabrication process for these micro-robots using microelectromechanical systems (MEMS) technology.

A critical fabrication step in MEMS technology is the safe release of these micro-robots using xenon difluoride (XeF<sub>2</sub>) etching, which etches only silicon in an isotropic manner. Due to the nature of isotropic etching, the etching results depend on the amount and location of the silicon's open surface area. Micro-robots can also be designed with trenches such that XeF<sub>2</sub> gas flows through the trenches and undercuts piezoelectric actuators, allowing free movement. Thus, the geometry and location of the trenches is important to successfully release micro-robots.

In this work, XeF<sub>2</sub> etching of several piezoelectric micro-robot designs have been characterized, which can be used to modify the design of the micro-robots for a faster and safer release. Additionally, the etching of C<sub>4</sub>F<sub>8</sub> polymer, which was deposited on the side wall of the trenches in deep reactive ion etching (DRIE), was characterized after the polymer was observed to protect silicon from being etched.

### Experimental Procedure:

**Characterization of Fluorocarbon Polymer.** Polymer etching was tested using modules containing dummy micro-robotic devices fabricated from silicon oxide and gold. Images

were taken of each module using the scanning electron microscope (SEM). Then, tape was placed on the module to prevent the fluorocarbon polymer from being deposited at certain locations. Next, a fluorocarbon polymer was deposited on the module. Afterward, the tape was removed confirming the polymers presence. Subsequently images were taken using the SEM to further verify the presence of the fluorocarbon polymer. The SEM also provided the thickness of the polymer where the tap was. Later the fluorocarbon polymer was removed using an oxygen based recipe. This recipe was then confirmed to remove the fluorocarbon polymer after SEM images showed no fluorocarbon polymer on the module.

**Releasing Micro-Robotic Devices.** XeF<sub>2</sub> etching was completed on silicon wafer modules containing between one and fifteen micro-robotic devices of various shapes. First, the module was mounted with the backside exposed on a six-inch silicon wafer with crystal bond. Then the sample was etched with reactive ion etching (RIE), removing the oxide layer. Next the module was etched using deep reactive ion etching (DRIE) process to etch away the silicon until there was visible etching on the module. Subsequently the module was removed from the silicon wafer and the photoresist (PR) material was removed from the module. The cleaned module was mounted with the topside exposed on a silicon wafer and then placed in the STS Pegasus to remove the residual Teflon<sup>®</sup> using the oxygen-based cleaning recipe. Later, the module was detached from the silicon wafer and cleaned. Thereafter the module was mounted with the backside exposed on a silicon wafer and the DRIE process was continued until the oxide layer was visible.

The wafer was then placed in hot water until the module released from the wafer. To prepare for  $\text{XeF}_2$  etching, the module was placed on a glass slide and taped along the edges to prevent  $\text{XeF}_2$  from etching the sidewalls of the module. The module was etched with  $\text{XeF}_2$  until the sample was released from the wafer as it was designed to do. Finally the top side's protective oxide layer was removed from the module.

### **Results:**

Two patterns were observed after completing the  $\text{XeF}_2$  etching process on the modules. The first pattern was that micro-robotic devices designed with the same geometry would have similar etch rates and releasing times. This pattern emerged regardless of where the micro-robotic devices were located on the module. Some samples observed were located as far as 1000 microns from each other.

The second pattern demonstrated how the amount of time needed to release the micro-robotic devices was heavily dependent upon the geometry of the backside etching area. It was found that a greater etching area on the backside led to a significantly faster release of the micro-robot.

### **Conclusion and Future Works:**

Through the releasing of different micro-robots, we were able to determine that the etch rate is dependent upon the number

of micro-robotic devices on a module and the geometry of those devices. However, the most significant factor is the geometry of the backside etching area. Therefore, if a module has devices with different geometry and/or backside etching areas, they will be released at different times. This results in over-etching of the faster-releasing devices, making them unusable. Accordingly, we suggested alterations for the area of the backside etching on devices that have more geometric features, in order to reduce the etching time and release all of the micro-robotic devices at the same time. With these changes in place it would be possible to increase the yield of adequately released micro-robots.

In the future, the group would be able to test this theory with more fabricated micro-robotic devices using these design changes. Also the group would be able to characterize the micro-robotic devices to find the optimum design and integrate them in the final micro-robot.

### **Acknowledgments:**

I would like to thank Professor Oldham for supporting me through this intensive internship. I would also like to thank Jongsoo Choi for training me and helping me through all the roadblocks that this research presented. I would finally like to thank the NNIN REU Program, NSF and LNF lab for providing funding and the opportunity to experience this wonderful internship.

## Two-Dimensional Buckled Nanoscale Nanomembrane as Tunable Grating

**Adel Azghadi**

**Mechanical Engineering, Los Angeles Pierce College**

*NNIN REU Site: ASU NanoFab, Arizona State University, Tempe, AZ*

*NNIN REU Principal Investigator: Dr. Hanqing Jiang, Associate Professor of Mechanical Engineering, School for Engineering of Matter, Transport and Energy, Arizona State University*

*NNIN REU Mentor: Teng Ma, Research Associate in Mechanical Engineering, School for Engineering of Matter, Transport and Energy, Arizona State University*

*Contact: adelazghadi@aol.com, hanqing.jiang@asu.edu, tengma@asu.edu*

### Abstract:

We have developed a tunable, optical two dimensional (2D) grating which can be used for measuring thermal-induced strain based on buckled thin film with periodic sinusoidal patterns on elastomeric substrates. One dimensional (1D) sinusoidal gratings and 2D herringbone gratings with a submicron scale have been fabricated with nanometer-thick gold (Au) film coated on uniaxial and biaxial pre-tensioned polydimethylsiloxane (PDMS) substrates, respectively. Due to the competition between the soft elastomeric substrates and relatively stiff Au films, uniform periodic wavy profiles are created upon releasing the pre-tension. The level of pre-strain, the mechanical properties of the PDMS and Au, and the thicknesses of Au films determine the amplitudes and wavelengths of wavy structures. The buckling profiles can be tuned mechanically by changing the level of pre-strain applied on the elastomeric substrate. Moreover, characteristics of the buckles vary based on the thickness of the stiff Au nanomembrane. Different methods of producing a stiff film on top of an elastomeric substrate have been established so far, while for this project, we focused on deposition of Au on PDMS by plasma sputter coating to create 2D herringbone buckles, which has the advantage of being low cost and extremely time efficient.

### Introduction:

During the past few years the reliability of electronics packaging has received increasing attention, due to the soaring sales of iPhone and iPad. There are various electronic packaging failure modes like cracking, delamination and fatigue. Among them, the most well-known and often investigated mechanics issue for electronic packages is interface reliability. There is a great need for characterizing the deformations and strains in interfaces to the thermo-mechanical loadings caused by coefficient of thermal expansion (CTE) mismatches. Strain sensor using optical grating is a relatively new experimental mechanics method for measuring deformation and strain. Our method of making a buckled thin film on PDMS as a grating provides the capability of making uniform patterns at micro and submicron lever spontaneously without conventional photolithography techniques. More importantly, the wavelengths of buckling structure can be easily controlled by the

thickness of Au film deposition at nanometer level which enables great tunability for optical grating.

### Experimental Procedure:

The first part of our project was producing 1D ripples in Au nanomembrane stiff films. First, a thin slide of polydimethylsiloxane (PDMS) was prepared by mixing silicone elastomeric base and curing agent at the ratio of 10:1 by weight. After curing the PDMS at 80°C for three hours, we applied a desirable pre-strain on our substrate by mechanical stretcher only in one direction (x-direction). A thin layer of Au was coated on top of the pre-tensioned substrate by argon plasma-assisted sputter coating. Finally, releasing the pre-strain in the PDMS led to a compressive force in the Au film as the PDMS relaxed to zero strain, leading to periodic buckling.

In the second part of our research, we focused on 2D herringbone nanomembrane buckling. 2D samples were prepared with almost the same procedure as 1D, except that in the second step, we stretched our substrates in both X and Y directions sequentially (first in X and then in Y direction). Also, after coating the pre-stretched substrate with Au, the sample had to be released sequentially in both directions, but in reverse order (first in Y, then in X direction). This time, by releasing the sample 2D zigzag shape, buckling appeared in the nanomembrane.

### Results:

Four 1D sample wavelengths and amplitudes of nanomembrane ripples were studied throughout the project. Figure 1 shows us the possible relationships [1] for amplitude and wavelength of the buckles based on thickness of the Au layer and level of pre-strain. The buckling period, amplitude, pre-strain and thickness of the Au film are characterized by " $\lambda$ ", "A", " $\epsilon_{pre}$ " and " $h_f$ " respectively. Coating time determined the thickness of the Au nanomembrane linearly, and every thirty seconds corresponded to 5 nm.

Based on graphs in Figure 2, by increasing the coating times, both wavelength and amplitude of buckles became larger.

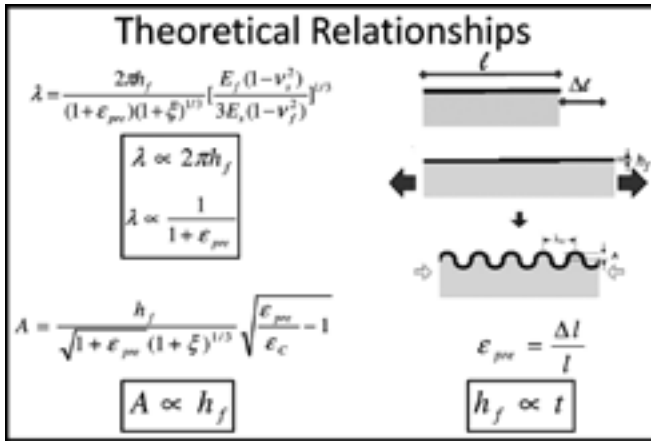


Figure 1: Theoretical relationships.

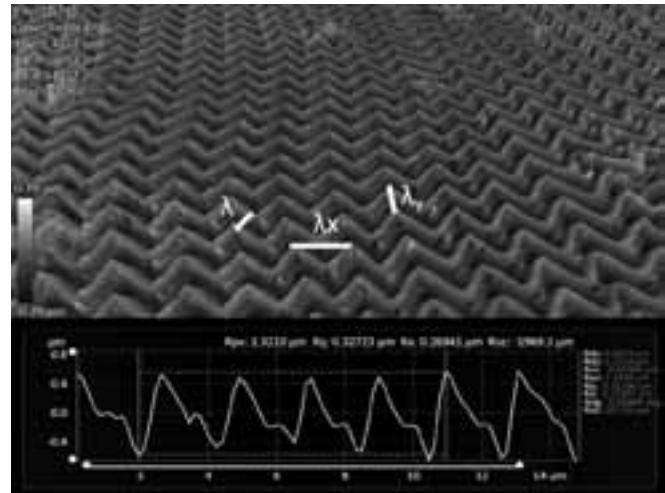


Figure 3: Optical profilometer image, 2D buckling, deposition time is 2.5 min, pre-strain of 15%.

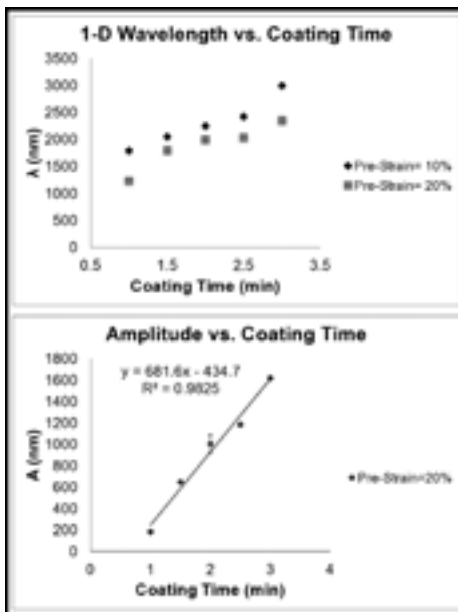


Figure 2: a) 1D wavelength vs. coating time graph, b) amplitude vs. coating time graph.

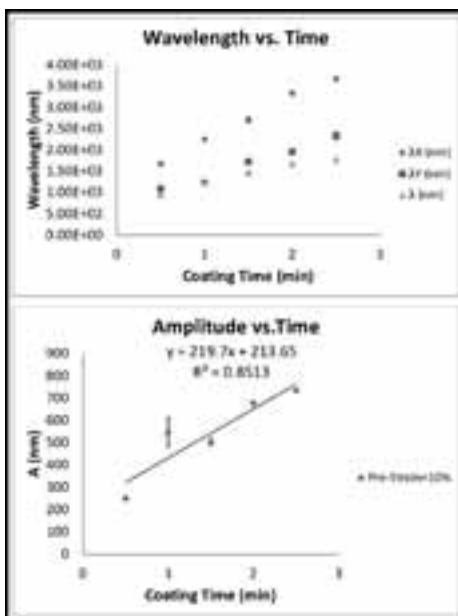


Figure 4, left: 2D wavelengths vs. coating time graph, b) amplitude vs. coating time graph.

Also as pre-strain became larger the wavelength of the ripples decreased. These results supported our theoretical relationships.

Figure 3 is the 3D image of 2D buckles using optical profilometer. For each 2D buckle, three different wavelengths were measured,  $\lambda_x$ ,  $\lambda_y$  and  $\lambda_z$ , in X, Y and normal to buckle direction, respectively. Figure 4 shows that all three types of wavelengths are in direct relationship to the coating time. Also amplitude of the wrinkling profile increases when coating time increases. These results also are a proof to our theoretical relationships.

**Future Work:**

In 2D buckles by increasing the pre-strain to even a greater level (25%-50%), the smallest wavelength ( $\lambda$ ) was inversely proportional to the pre-strain, which means that as we stretched our samples to a greater extend, the wavelength of the buckles became smaller. Also if we can find a way to coat a thinner layer of gold, we might be able to produce gratings with wavelength closer to the wavelength of the natural light by even a smaller pre-strain. Moreover, we found out that creating a 2D herringbone structure in relatively stiff nanomembrane gold film on top of PDMS by argon plasma sputter coating is a low cost and time-efficient method.

**Acknowledgements:**

At this point I would like to thank my principal investigator Dr. Hanqing Jiang and my mentor Teng Ma for the time that they have spent with me this summer and all they have taught me. Also I would like to say thank you to Dr. Trevor Thornton, our site coordinator at Arizona State University, and the Center for Solid State Electronic Research (CSSER). Finally I would like to thank the NNIN REU Program and the National Science Foundation for funding this program.

**References:**

- [1] Cunjiang, Y; "Forming wrinkled stiff films on polymeric substrates at room temperature for stretchable interconnects applications"; Thin Solid Films, 519, 819 (2010).

## Nanoparticle Sorting in Microfluidic Channels

**Rachel Baarda**

**Physics, University of Utah**

*NNIN REU Site: Nanotech, University of California, Santa Barbara, CA*

*NNIN REU Principal Investigator: Professor Andrew Cleland, Physics, University of California, Santa Barbara*

*NNIN REU Mentor: Dr. Sukumar Rajauria, Physics, University of California, Santa Barbara*

*Contact: rabaarda@gmail.com, anc@physics.ucsb.edu, sukumar.rajauria@gmail.com*

### Abstract:

A device capable of detecting, characterizing and sorting nanoparticles and important biological targets would be an invaluable tool both for public health monitoring and for biomedical research. We describe the development of a microfluidic device that should permit the high-throughput sorting of nanoparticles, potentially able to sort hundreds to thousands of particles per second.

### Introduction:

The ability to manipulate biologically relevant nanoparticles such as viruses, proteins, and synthetic nanoparticles would be a boon for medical research. Examples of the utility of such a device include aggregating rare particle types or efficiently imaging representative particles in a diverse mixture. Current methods of sorting particles are impractical for use in processing polydisperse samples. We describe the development of a microfluidic device that should permit high-throughput nanoparticle sorting. The device consists of a microchannel, an optical sensor, and a fluid actuator. Sorting is accomplished by driving fluid on-demand using a piezoelectric transducer (PT), actuated by an optical sensor sensitive to particles passing through the microchannels. We have performed a systematic study of PT actuation using a laser vibrometer, and have explored various means of coupling the PT and the microfluidic device. Through this study, we have developed an improved method for mounting the PTs to the microfluidic device that we expect will demonstrate more effective fluid actuation.

### Experimental Procedure:

**Device Fabrication.** The device's microchannels were cast in the transparent elastic polymer polydimethylsiloxane (PDMS). The mold used to cast the PDMS consists of patterned SU-8 photoresist. PDMS was spun onto the mold, then cured on a hotplate for 10-15 minutes at 140°C. We coupled the PTs to

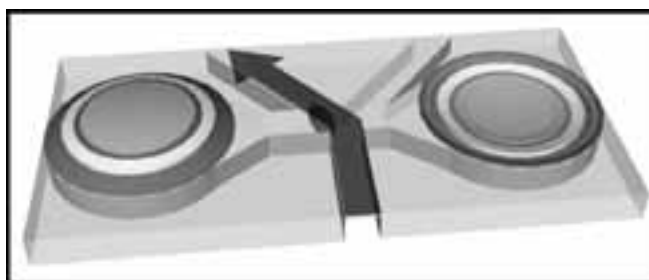


*Figure 1: Particle actuation.*

the microchannels by embedding them in a second layer of PDMS, which was cured for 20-40 minutes at 140°C. Each of the two PTs was placed over a reservoir which directed fluid perpendicular to the direction of particle flow (see Figure 1). Once the PDMS had hardened, we peeled it from the mold and cored ports for fluid injection using a biopsy punch. We prepared the PDMS for bonding by exposing it to UV ozone, and then we bonded it to a glass substrate and cured it for 3-5 hours at 140°C. Fluid and fluorescent polystyrene nanoparticles were injected into the microchannels from pressurized reservoirs connected to flexible tubing inserted into the ports. Both PTs were connected to a function generator. Particles were forced through a fluid restriction and detected by an optical sensor, which signaled the function generator to actuate the PTs to direct the particle as desired.

**Device Characterization.** Piezoelectric materials deform mechanically in response to applied voltage. We induced sinusoidal vibration in the PTs using a function generator with frequencies in the kilohertz range. We characterized these PTs and the PDMS that formed our device's channels using a laser vibrometer. This tool measures the vibration of a reflective surface by measuring the phase shift difference between the reflected laser beam and a reference beam.

## Results and Conclusions:

We performed a variety of vibrometry experiments to determine the behavior of the device as driving voltage, frequency, and measurement location were varied.

We measured the resonance characteristics of the PTs by applying a fixed voltage to the PTs while modulating the driving frequency from 1-50 kHz. At each frequency, we found the peak-to-peak displacement of the PT as measured by the vibrometer. The resulting curve showed that the PTs act as harmonic oscillators with resonance frequencies close to 7 kHz, in accordance with the manufacturer's specifications. We performed these experiments on several PTs in three distinct environments: 1. The PT was glued onto a hollow metal cylinder. This showed the clearest resonant peak and two harmonics; 2. The PT was embedded in PDMS; and 3. The PT was embedded in PDMS and bonded to glass. In addition, the microchannels were filled with DI water. The results are summarized in Figure 2.

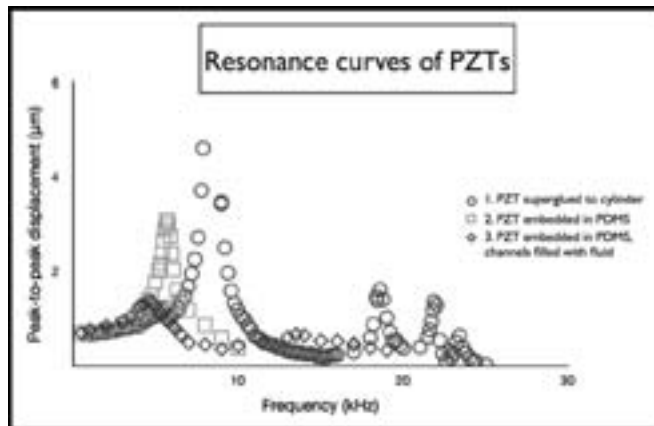


Figure 2: Resonance curves of PTs.

Because PDMS is an elastomer, we examined the possibility of vibrations propagating through it. We tested this by determining that the PTs were coupled together by PDMS vibrations: that is, we found that each PT could drive the respective other. When one PT was driven by the function generator, we found that the other PT showed a resonance curve similar to (though smaller than) that of the driving PT.

We examined the PDMS vibration further by measuring the PDMS itself. We applied a layer of silver paint to a sample to make it reflective and measured the peak-to-peak displacement of the PDMS as we moved the vibrometer beam away from the edge of the driving PT. The results, summarized in Figure 3, showed a standing wave in the PDMS whose amplitude was reduced when the sample was made of stiffer PDMS.

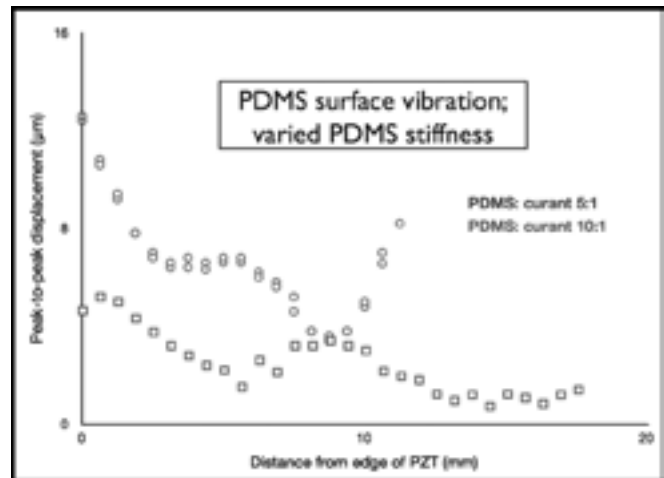


Figure 3: Standing waves in PDMS.

In light of these data, we desired a way to isolate the PT vibration from the PDMS so that fluid actuation would be discrete and well-controlled. This was accomplished by machining brass funnels on which the PTs could be mounted, the stems of which could be inserted into ports in the PDMS. Vibrometry measurements showed that this modification successfully isolated the PT vibrations from the PDMS: we repeated both experiments testing for PDMS vibration without finding a signal in any case.

## Future Work:

Future direction for this project includes further calibrating the device to allow for well-controlled particle actuation. Once the device works predictably with the polystyrene nanoparticles, biological samples could begin to be processed.

## Acknowledgments:

I would like to thank Sukumar Rajauria and Andrew Cleland for their exceptional guidance, Jorge Carvalho for his expertise in chemistry and Matlab, and Samantha Cruz for her advice and resourcefulness as program coordinator. I would like to acknowledge Chris Axline for beginning and developing this project. Finally, I would like to acknowledge and thank the National Nanotechnology Infrastructure Network Research Experience for Undergraduates Program and the National Science Foundation for funding this project.

## Carbon Nanotube Microfluidic Channels for Cell Manipulation

**Michael Bellavia**

**Bioengineering, SUNY Binghamton**

*NNIN REU Site: Lurie Nanofabrication Facility, University of Michigan, Ann Arbor, MI*

*NNIN REU Principal Investigator: Anastasios John Hart, Mechanical Engineering, University of Michigan, Ann Arbor*

*NNIN REU Mentor: Kendall Teichert, Mechanical Engineering, University of Michigan, Ann Arbor*

*Contact: mbellav1@binghamton.edu, ajohnh@umich.edu, kbt@umich.edu*

### Abstract and Introduction:

Due to their remarkable porosity (~99%), electrical and mechanical robustness, and ability to be chemically functionalized, vertically aligned carbon nanotubes ("CNT forests") are a promising material for use in lab-on-a-chip devices. Utilizing these in bio-MEMS (e.g. for bioparticle detection) provides several prospective advantages over conventional solid materials (polydimethylsiloxane or PDMS, silicon or Si). These include the capability for flow both around and through the nanoporous structures to increase particle-surface interaction and greater selectivity for small (e.g. 10 nm) particles [1].

Current literature has illustrated the prospects of CNT structures placed within the fluid flow. Alternatively, this project aimed to demonstrate the capability of CNT forests as microfluidic channel walls. Ultimately, flow through various geometries could be exploited for potential biomedical applications.

Via photolithography, patterns for flow channels were transferred onto a Si wafer. A base layer of alumina was deposited, overlaid with a layer of iron catalyst. The wafer was diced into individual devices then placed in a tube furnace and forest growth achieved by thermal chemical vapor deposition (CVD) using a mixture of helium, hydrogen, and ethylene, at 775°C.

Testing was accomplished with a benchtop fluidic system consisting of a syringe pump, acrylic/PDMS chip dock, and a camera-equipped stereoscope for visualization. Flow through the CNT channels was verified, and experiments using polystyrene beads and human monocytes suspended in the fluid flow were observed.

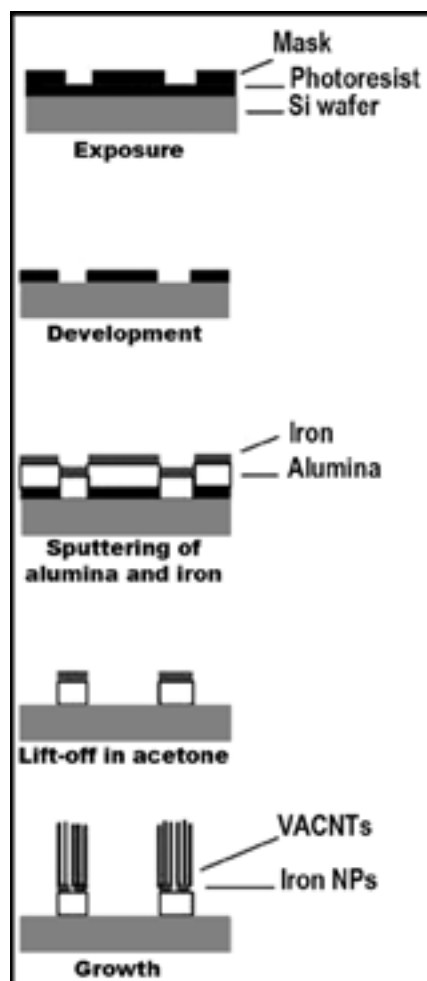


*Figure 1: Step by step fabrication of microfluidic devices.*

### Methods:

Photolithography and sputtering (10 nm alumina and 1 nm iron) were implemented to define the catalyst regions for forest growth on a Si wafer. Afterwards, the wafer was diced into individual devices. CNT growth was performed in a tube furnace.

First the substrate was annealed in 100 sccm  $H_2$  and 400 sccm helium (He) at 775°C for 10 minutes. Next, the substrate was removed from the furnace and allowed to cool in stagnant annealing gases (He,  $H_2$ ). It was then re-inserted for growth in 400 sccm He, 100 sccm  $H_2$ , and 100 sccm  $C_2H_4$  at 775°C for various durations. (See Figure 1.)

Difficulties in fluid transfer motivated particular mount designs. The initial concept was a short ( $\approx 1$  cm) PDMS cylinder with a cavity extending upwards from the bottom to house the chip and forest. Holes were punched above the chip reservoirs and aligned to another punched from the side. A dispensing needle was placed in the side hole and connected via silicone tubing to a syringe pump. Fabricating the cavity properly proved challenging.

Once the PDMS covers contacted the forest, further adjustment would damage the forest. Further, leakage over the forest was noted. To circumvent

this, an acrylic/PDMS chip docking system was developed (Figure 2a) and placed under a stereoscope. An adjustable stage, its vertical movement controlled by a micrometer, was positioned below an acrylic piece machined with vertical channels. These channels were aligned with the reservoirs of a bare silicon chip. A layer of PDMS with holes aligned to both those of the chip and the acrylic was placed on top of the chip. The stage was moved upward with the micrometer until the PDMS on the chip applied sealing pressure to the acrylic

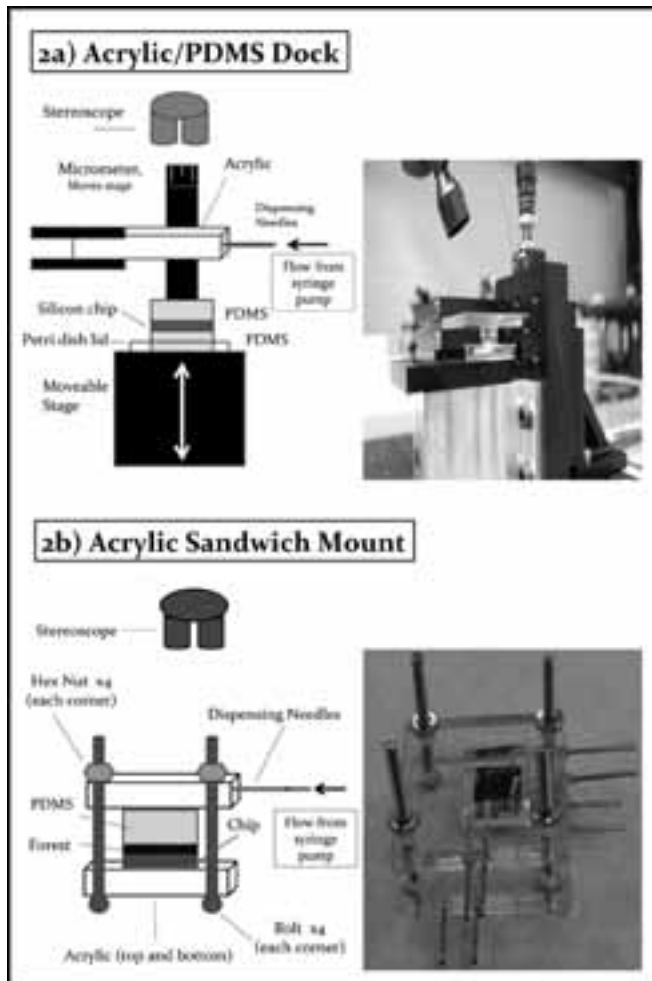


Figure 2: Schematics.

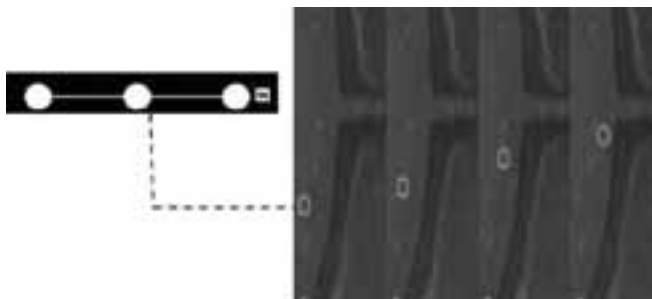


Figure 3: A monocyte (within the circle) moves from a reservoir into a channel. The frames (labeled 1-4) are each separated by a fourth of a second.

plate. An assortment of materials with different elasticity, such as rubber, foam, and PDMS were used as backing for the chip as a means of improving sealing to the acrylic. Flow tests were conducted at infusion rates between  $30 \mu\text{L/hr}$  and  $10 \mu\text{L/min}$  using  $3$ ,  $10$ , and  $15 \mu\text{m}$  polystyrene beads. Sandwiching the chip between  $\approx 5 \text{ mm}$  layers of PDMS was found to be adequate, as it most reliably prevented leakage.

A portable mount (Figure 2b) was constructed; a PDMS layer between two acrylic squares machined with vertical channels

spaced to fit whatever device. With this, several flows of monocytes, a variety of white blood cell, were undertaken (Figure 3).

To simulate the pressure drops to be experienced in the flow, flow through certain designs was analyzed with COMSOL Multiphysics, a finite element software package. Pressures and velocities from select geometry were compared to pressure results found from a flow equation assuming rectangular channels cited in the *Microfluidics and Nanofluidics Handbook* by Mitra and Chakraborty [1]. These flows will be related to experimental results in future work.

### Results:

Preliminary flows of polystyrene beads and monocytes through CNT forests were performed successfully. Monocytes flowed rapidly even after the pump was stopped, but after a time, backflow occurred. This may be due to inadequate sealing. Imaging with the stereoscope camera did not provide satisfactory resolution. Further analyses might be conducted with fluorescence microscopy.

Close agreement was evident between the average velocities at the inlets for the COMSOL™ model and those of the fluidics equation. This asserts that COMSOL can be sensibly extrapolated to modeling other devices or new geometries.

### Future Work:

The fluidic delivery system shall be improved and testing systematized for the procedure to be efficient and easily repeatable. The forests are fragile, necessitating more precise alignment strategies for the PDMS overlay such that sealing is obtained with less risk of harm to the forest. This would greatly expedite testing. A redesign of the flow geometries could contribute to this, and will be undertaken.

Optimization of the CNT growth conditions is required to fabricate CNT devices with consistent and repeatable fluidic properties. Further, the wealth of properties innate in CNTs such as photoluminescence as well as outstanding tensile strength and electrical conductance, make them attractive candidates for further integration in innovative microfluidic devices.

### Acknowledgements:

I'd like to express my earnest gratitude for the guidance of Kendall Teichert. I am indebted to Professor John Hart and the Mechanosynthesis Group. Lastly, I'd like to thank the National Science Foundation and NNIN REU Program for this opportunity.

### References:

- [1] Fachin, F., et al., *Journal of MEM Systems* (2011): 1428-1438.

## Fabrication of MEMS Using Cheap Substrates

**Ryan Gaudreau**

**Engineering Science, Stony Brook University**

*NNIN REU Site: Howard Nanoscale Science and Engineering Facility, Howard University, Washington, DC*

*NNIN REU Principal Investigator: Dr. Gary L. Harris, Electrical Engineering, Howard University*

*NNIN REU Mentor: Dr. William L. Rose, Electrical Engineering, Howard University*

*Contact: ryan.gaudreau@yahoo.com, gharries@msrce.howard.edu, wbullrose@gmail.com*

### Abstract:

The objective of this project was to create microelectromechanical systems (MEMS) using paper as the substrate and piezoresistive carbon ink to create a device that was sensitive to force. The idea behind this approach was to minimize cost and maximize ease of production. To achieve our objective, we used a paper cantilever design to correlate the relationship between force and change in resistance of the device, and subsequently the relationship between current and applied force. Our results showed a linear relationship. The next part of the project required us to apply this relationship to create a useful device. We opted on creating a microphone made from paper and the piezoresistive material. This was based on the fact that the relationship between force and resistance would facilitate the modulation of current in much the same way as the moving coil in a magnetic field in a conventional microphone. We were able to successfully accomplish our goals after several designs were tested and optimized.

### Introduction:

Microelectromechanical systems (MEMS) are becoming increasingly popular. MEMS are used today in many fields, from biotechnology, medicine, communications, to inertial sensing [1]. In an attempt to decrease cost and time of production, paper-based MEMS are now being researched as a cheap alternative [2]. A paper MEMS device does not require a clean room, takes less than an hour to make, and cost only cents to produce. These attributes make them very attractive.

Our project sought to use a piezoresistive material on a paper substrate in order to create a practical device. Our project was divided into two parts. The first part sought to examine the relationship between force and change of resistance/current on the piezoresistive material, and then in the second part, apply this in a practical way. We decided we could use the properties of the device to build a paper microphone.

### Fabrication and Experimental Procedure:

The first part of our experimental procedure required us to design paper MEMS to test and correlate the relationship

between force and resistance of the piezoresistive material. To do this we used the drawing software Corel Draw X5 to design cantilever systems. We then used an Epilog Helix Laser to cut the devices out. Carbon-based piezoresistive paint was applied to the device and allowed to dry, followed by a silver based conductive paint. A Wheatstone bridge was constructed on a breadboard to precisely measure the resistance of our device.

The MEMS was fixed onto a mounting device that slowly lowered the cantilever of the MEMS onto a precision balance, applying a measurable force. Applying force to the cantilever put force on the piezoresistor, therefore changing its resistance and causing current to flow through the ammeter. The adjustable resistor was then manipulated until the current read zero. The resistance of the adjustable resistor could then be read using a multi meter. Using the equation for a Wheatstone bridge, the resistance for the MEMS could be found and thus correlated to force.

We tested several single cantilevers and double cantilever designs applying the force and varied distance from the piezoresistive material (Figure 1). We were thus able to establish a relationship between the force and resistance, and consequently, current.

For the second phase of our procedure, we used the same fabrication process as above to design and cut out our piezoresistive paper microphone. We tested several designs to first create a working microphone and then to optimize it. A basic microphone circuit was made using a capacitor, resistor, the paper microphone, a signal wire to connect to a speaker, and a ground wire. The setup consisted of fastening the samples to a rigid cardboard frame. Once attached, the samples were tapped and spoken into to test their effectiveness.

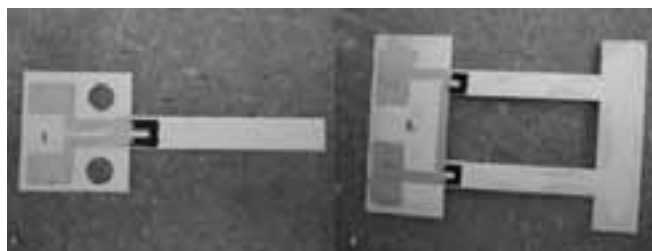


Figure 1: Single and double arm cantilever design.

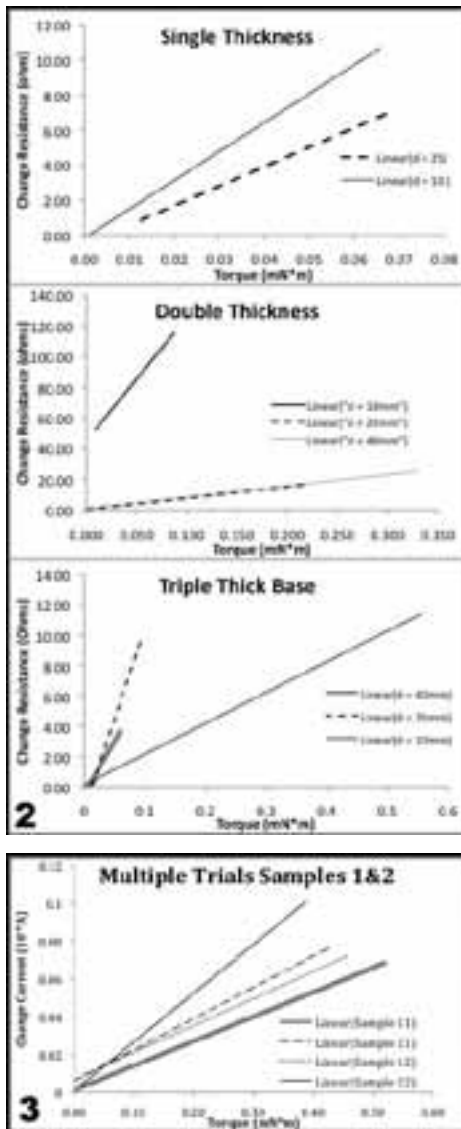


Figure 2, top: Graphs of torque vs. resistance for single arm cantilever for different thicknesses of the cantilever.

Figure 3, bottom: Double arm cantilever trials testing two samples' change of current vs. torque.

## Results and Conclusions:

The results from tests done on the single cantilever system showed a linear relationship between force and resistance within our testing range. We found that making contact with the cantilever closer to the base gave the most linear reading, greatest range, and highest resolution. It was found that increasing the base stiffness increased the resolution and gave a more linear reading, but not by a significant amount. When we doubled the thickness of the entire MEMS, there was significant improvement in force range, and linear readings were observed at all tested distances (Figure 2). Upon testing the double arm cantilever, we found that a double thickness design of this model also provided the greatest range and sensitivity. This model was using force as a function of both current and resistance, and linear results were found for both. Figure 3 shows the results for the change of current vs. force test.

We were able to design and construct a paper piezoresistive microphone. Many designs were tested in order to optimize the device and produce the desired results. At first, only taps could be faintly heard through a speaker. We optimized our design even further and then connected to an amplifier. We were then able to clearly distinguish words, proving that the principle works. Upon further design modifications, the microphone was able to transmit music clearly (Figure 4). Further areas of research on this idea would be to condense the sound, diminish background noise, and decrease the size.

## Acknowledgements:

I would like to thank Dr. Gary L. Harris and Dr. William L. Rose, as well as the rest of the research group at Howard University. I am also thankful to the National Nanotechnology Infrastructure Network Research Experience for Undergraduates (NNIN REU) Program, and the National Science Foundation.

## References:

- [1] [www.memsnets.org](http://www.memsnets.org)
- [2] Xinyu, L., et al., "Paper-based Piezoresistive MEMS sensors"; Lab/Chip, 2011, p2189-2196.
- [3] [www.sensorland.com](http://www.sensorland.com)

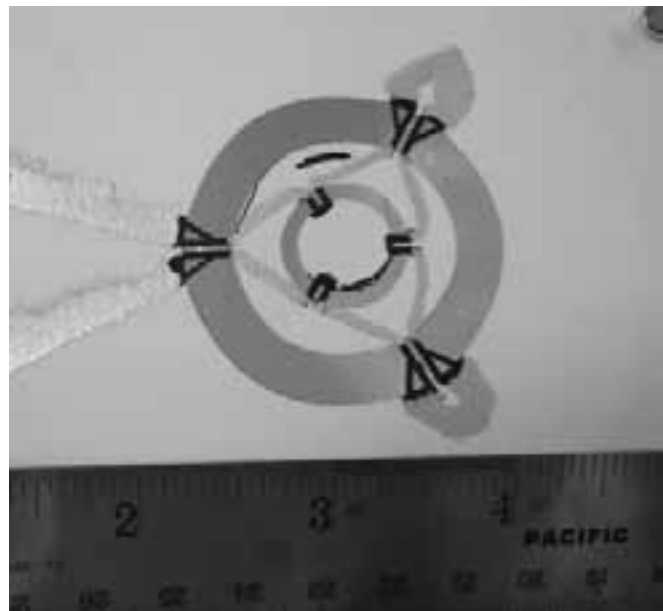


Figure 4: Final working model of the paper microphone.

## Fabrication and Characterization of a Micromachined In-Plane Directional Piezoelectronic Microphone

**Jia Gloria Lee**

**Physics, University of California Berkeley**

*NNIN REU Site: Microelectronics Research Center, The University of Texas at Austin, Austin, TX*

*NNIN REU Principal Investigator: Dr. Neal A. Hall, Electrical and Computer Engineering, University of Texas at Austin*

*NNIN REU Mentor: Michael Kuntzman, Electrical and Computer Engineering, University of Texas at Austin*

*Contact: gloria\_lee@berkeley.edu, nahall@mail.utexas.edu, mlkuntzman@gmail.com*

### Abstract:

The fabrication of a microelectromechanical system (MEMS) microphone, which consists of a beam that responds to a pressure gradient across its longer axis and employs piezoelectronic readout, is described. The advantages of this design included its small form factor, directionality, potentially low self-noise, and the ability to apply active feedback to the system for feedback-altered dynamics. The beam was 2.5 mm  $\times$  1.54 mm  $\times$  20  $\mu$ m and fabricated out of silicon (Si). The piezoelectric material used was lead zirconate titanate (PZT). The device's directional response is presented, along with modifications for optimizing the fabrication process.

### Introduction:

The purpose of this project was to develop and demonstrate a fabrication process for an in-plane directional microphone that would improve noise performance and source localization in hearing aid and advanced cell phone applications [1]. The microphone was based on a previous design inspired by the parasitoid fly *Ormia ochracea* [2], but replaced the complex optical readout with more elegant piezoelectric readout and modified the pivot mechanism to increase the sensitivity of the microphone.

The microphone consisted of a beam suspended from compliant springs. The beam exhibited high bending stiffness and low rotational stiffness, allowing it to respond to sound traveling along its longer axis (x-axis) by rotating about its shorter axis (y-axis), while preventing it from responding to sound coming in from the top (z-axis) or y-axis by bending. The rocking motion deformed the springs and strained the

piezoelectronic material deposited on them, producing a voltage which could be read out (see Figure 1).

### Experimental Procedure:

The device was fabricated on a silicon-with-imbedded-oxide-layer (SOI) wafer. One micrometer ( $\mu$ m) of low-temperature silicon oxide ( $\text{SiO}_x$ ) was deposited on the top as an adhesion layer and 4  $\mu$ m on the bottom as an etch mask. Titanium (Ti) was evaporated on top using electron-beam evaporation and oxidized in a 700°C furnace to form a 180 nm titanium oxide ( $\text{TiO}_2$ ) diffusion barrier against the PZT.

Top and bottom electrodes for the PZT and electrode bondpads were created by using photolithography to mask the wafer, sputtering 40 nm of Ti for adhesion and 160 nm of platinum (Pt), then lifting off the excess. An 800 nm layer of commercially prepared PZT were deposited using the sol-gel method, patterned with photoresist, and wet-etched in a 200:20:2 mL solution of deionized water : hydrochloric acid : hydrofluoric acid ( $\text{H}_2\text{O}:\text{HCl}:\text{HF}$ ).

The beams and springs were formed by patterning with photoresist and dry-etching through the  $\text{TiO}_2$ ,  $\text{SiO}_x$ , and epitaxial Si of the SOI wafer with sulfur hexafluoride ( $\text{SF}_6$ ), fluoroform ( $\text{CHF}_3$ ), and  $\text{SF}_6$  plasmas respectively. The hinges were formed by depositing 1  $\mu$ m of sacrificial oxide via plasma-enhanced chemical vapor deposition (PECVD), patterning with photoresist, and dry-etching with  $\text{CHF}_3$ , then depositing 2  $\mu$ m of amorphous silicon (a-Si) via PECVD, patterning with photoresist, and dry-etching with  $\text{SF}_6$ .

A deep silicon etch (DSE) was performed on the backside of the SOI wafer to remove the Si handle layer underneath the beam and springs. A cross-section of the finished device is shown in Figure 2.

### Results and Future Work:

Figure 3 shows a scanning electron microscope (SEM) image of the finished device. Some problems with the fabrication process for the top electrode bondpads and hinges were discovered.

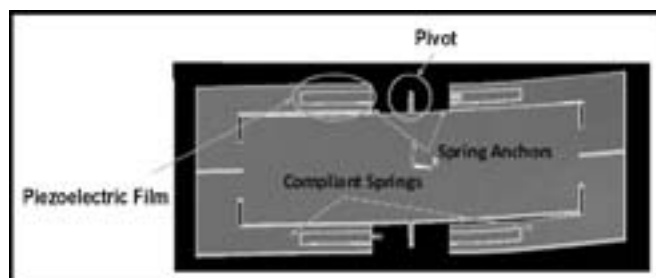


Figure 1: Operational schematic of in-plane directional microphone.

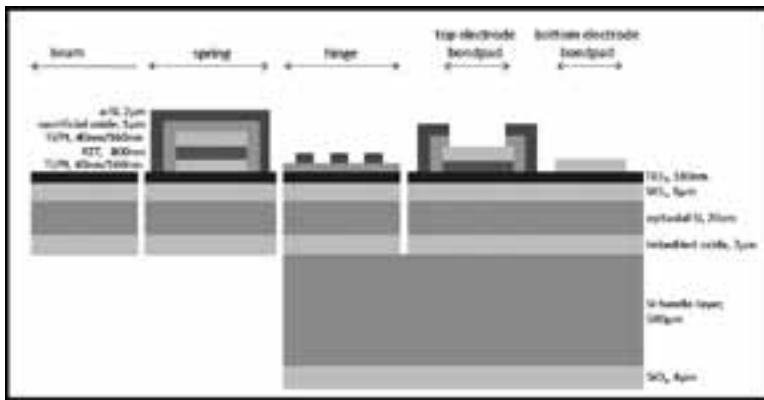


Figure 2: Cross-sectional diagram of finished device.

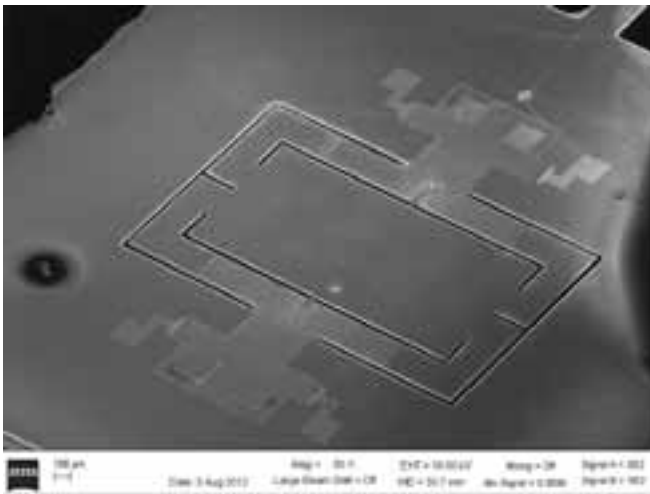


Figure 3: SEM image of finished device.

The a-Si adhered poorly to the top bondpads and peeled off, especially around the corners. In the subsequent plasma etches, the bondpads were etched through. We attribute the missing top electrode bondpads to two factors: 1) stress from depositing two different materials on top of each other, which caused the silicon to peel off most of the bondpads, leaving them exposed during the  $\text{SF}_6$  etch, and 2) insufficient selectivity between the silicon/oxide layers and platinum during dry-etching.

To improve adhesion, we propose depositing a thinner, lower-stress Si layer and/or using circular bondpads instead of square ones to prevent the peeling that occurred around the corners, where the stress was highest. Additionally, depositing a thick layer of chrome over the platinum should reduce selectivity requirements and prevent etching through the bondpads.

The hinges designed to allow the beam to rotate freely did not turn out because the deposited a-Si had bad step coverage. This created discontinuous hinges that would not hold the pins in place if the oxide was etched from underneath. In the future, a silicon deposition method with better step coverage, such as low pressure chemical vapor deposition (LPCVD) poly-silicon, should be used to form the hinge.

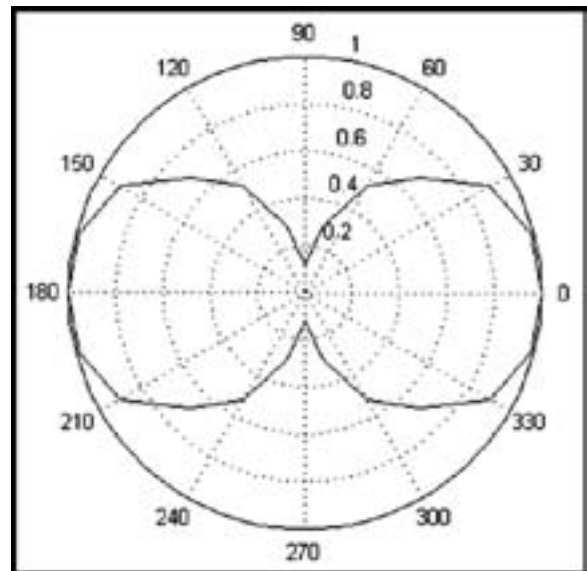


Figure 4: Directivity measurement showing the normalized sensitivity versus angle of incident sound.

In skipping the hinge release step, the hinge became a torsional pivot, allowing the beam to twist about its shorter axis, but preventing it from rotating freely.

Acoustic measurements were performed to determine the directivity of a microphone with a torsional pivot. The microphone was isolated with its x-axis facing a speaker placed 2.5' away ( $0^\circ$  position). The microphone was rotated in  $15^\circ$  increments from  $0^\circ$  to  $90^\circ$  and its sensitivity to acoustic actuation was recorded. The directivity at 11.9 kHz is displayed in Figure 4. The microphone exhibited maximum sensitivity of 14.8 mV/Pa at  $0^\circ$ , and minimum sensitivity of 1.70 mV/Pa at  $90^\circ$ , showing the expected bidirectional polar pattern with 18.8dB difference in sensitivity between the  $0^\circ$  and  $90^\circ$  positions.

### Acknowledgements:

I would like to thank my mentor Michael Kuntzman, professor Dr. Neal Hall, the Hall research group, Dr. Marylene Palard, Jeannie Toll, Christine Wood, and the rest of the Microelectronics Research Center staff at UT Austin for their support, guidance, patience, and infinite kindness. I would also like to thank the NNIN REU Program, National Science Foundation, Melanie-Claire Mallison, and Lynn Rathbun for providing this research opportunity.

### References:

- [1] Amlani, A; "Speech-Clarity Judgments of Hearing-Aid-Processed Speech in Noise: Differing Polar Patterns and Acoustic Environments"; International Journal of Audiology, 45, 319-330 (2006).
- [2] Miles, R; "A Low Noise Differential Microphone Inspired by the Ears of the Parasitoid Fly *Ormia Orchracea*"; Journal of the Acoustical Society of America, 125, 2013-2026 (2009).

## Optimizing the Delivery of Toxins and Glycans to Photonic Biosensor Surfaces

**Abubakar Abid**

**Computer Science with Molecular Biology, Massachusetts Institute of Technology**

*NNIN REU Site: Nanotechnology Research Center, Georgia Institute of Technology, Atlanta, GA*

*NNIN REU Principal Investigator: Dr. Ali Adibi, School of Electrical and Computer Engineering, Georgia Tech*

*NNIN REU Mentors: Dr. Ali Eftekhari and Farshid Ghasemi, School of Electrical and Computer Engineering, Georgia Tech*

*Contact: aabid93@mit.edu, ali.adibi@ece.gatech.edu, eftekhari@ece.gatech.edu, farshid.ghasemi@gatech.edu*

### Abstract and Introduction:

Photonic biosensors allow for precise, real-time, and label-free detection of biomolecules by using micro-ring resonators, which are ring-shaped waveguides that permit different frequencies of light to resonate, as a function of the concentration of target molecules near the biosensor surface [1, 2]. The localization of target molecules to the surface occurs through a biochemical bond; in this case, that bond was between target toxin proteins and carbohydrate glycans, which were attached to the surface using a glutaraldehyde-based surface treatment [3].

The focus of this project was to optimize the delivery of glycans and toxins to the surface of the biosensor with high resolution and high throughput, while fabricating the biosensor to be reusable and have the ability to multiplex, or detect multiple toxins at the same time. In order to fabricate a multiplexing biosensor, different glycans needed to be dispensed on the various micro-ring resonators on the biosensor surface. Therefore, a system of microfluidic channels was printed, allowing users to dispense solutions with high throughput. In order to increase resolution and reduce droplet size, an intermediate layer of 15-micron parylene was deposited above the microfluidic channels for delivering reagents, in a process known as “print-and-peel” [4]. It was shown that a system of channels to deliver glycans could be patterned on top of this parylene, and could be peeled off mechanically along with the parylene, making the biosensors reusable.

Finally, contact angle measurement revealed the need for a pumping mechanism, so a cladding layer of polydimethylsiloxane (PDMS) was activated with ultraviolet ozone treatment, bonded to the microfluidic channels, and tested for leaks. Successful demonstrations of these surface components have paved the way for the fabrication of a complete biosensor that can be effectively used to detect toxins.

### Experimental Procedure:

In order to create a system of microfluidic channels, 15-micron series 2000 SU-8 photoresist was spin-coated onto a test silicon wafer. The photoresist was then exposed at a dosage of 140 mJ/cm<sup>2</sup>. While this was sufficient to create channels

in photoresist, in order to test the print-and-peel method, a 15-micron layer of parylene was deposited, using the Specialty Coating Systems Parylene Labcoater, on top of the photoresist. In some samples, a release agent (2% micro-clean) was first lightly swabbed to facilitate the eventual parylene peeling.

The parylene was then coated with another layer of the same SU-8, which, however, needed to be exposed at 210 mJ/cm<sup>2</sup>. This created successive layers of SU-8, separated by parylene, which could be mechanically peeled off, allowing reusability and even higher resolution (see Figure 1).

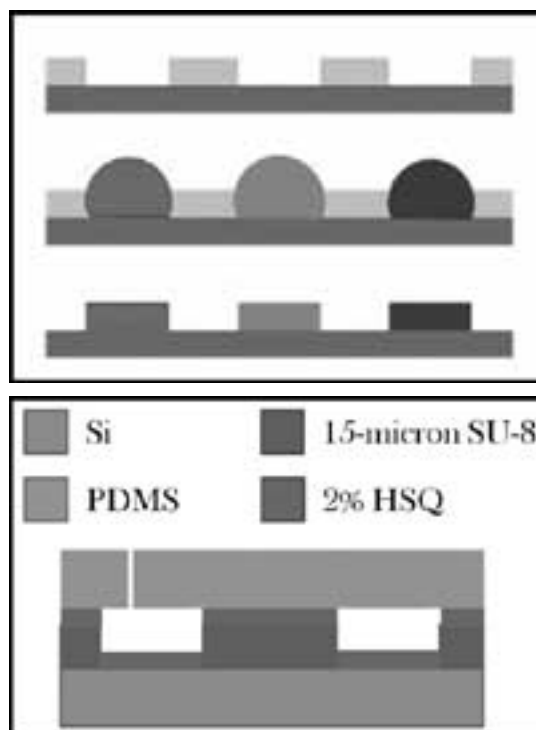


*Figure 1, top: In the print-and-peel method, parylene (patterned) is etched, solutions (hemispheres) are dispensed, and parylene is then peeled.*

*Figure 2, bottom: Schematic of the final surface layers on the biosensor.*



*Figure 3, above: Parylene, sandwiched between two layers of SU-8, is successfully peeled off.*

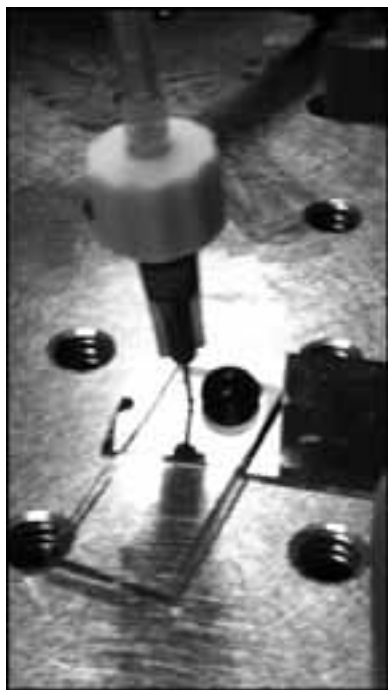


*Figure 4, left: As solution is pumped through the microfluidic channels, some leakage occurs.*

In addition, after the wafer was treated with glutaraldehyde (in order to bind glycans to the surface), the surface wettability was characterized using a contact angle goniometer. The need for a pumping mechanism was realized, and, in order to pump into the SU-8 channel, a layer of 2% hydrogen silsesquioxane (HSQ) was spin-coated on the parylene.

Then, on some samples, the HSQ surface and the layer of PDMS were activated with an ultraviolet ozone treatment for two minutes, and then, the two surfaces were mechanically bonded. The PDMS served as a cladding layer through which solutions could be pumped into the microfluidic channels (see Figure 2).

### Results and Conclusions:

After the system of SU-8 microfluidic channels had been created and coated with parylene, which was itself coated

with SU-8, the peeling-off of parylene was attempted. In order to facilitate this peeling-off, some SU-8-coated samples had been swabbed with 2% micro-clean. It was found that 100% of the samples swabbed with the micro-clean peeled off (see Figure 3), while only 50% of the non-swabbed samples peeled off, and in the latter case, the peeling often resulted in lower-quality channels in the lower layer of SU-8.

At the same time, it was found that the glutaraldehyde-based protocol for binding glycans increased the contact angle of water on the wafer from 52.0° to 68.1°. This increase in hydrophobicity suggested that treated microfluidic channels would be unable to carry solutions on their own; thus, a pumping mechanism was created by cladding the channels with PDMS (with a thin layer of HSQ in between to facilitate bonding), permitting a syringe to pump solutions through the microfluidic channels. Because this resulted in significant leakage, in some samples, the HSQ-coated channels and PDMS were both activated. It was empirically found that a two-minute ozone activation resulted in the strongest bond and the least leakage (see Figure 4).

Several aspects of reagent delivery have been demonstrated and optimized over the course of this project. As these components are perfected, the fabrication of a toxin-detecting photonic biosensor becomes more possible, allowing for efficient detection of glycan-binding toxins, such as ricin and the cholera toxin B, which endanger many human populations.

### Acknowledgments:

I would like to express my utmost gratitude to my mentors, Farshid Ghasemi and Dr. Ali Eftekhari, and my principal investigator, Dr. Ali Adibi, for their continued guidance. I would also like to thank the National Nanotechnology Infrastructure Network (NNIN) staff, particularly the Georgia Tech site coordinators, as well as the NNIN Research Experience for Undergraduates Program and the National Science Foundation for making this program possible.

### References:

- [1] Lee S, Eom SC, et al. "Label-free optical biosensing using a horizontal air-slot  $\text{SiN}_x$  microdisk resonator." *Optics Express*. 2010; 18[20]: 20638-20644
- [2] Xudong F, White IM, et al. "Sensitive optical biosensors for unlabeled targets: A review." *Analytica Chimica Acta*. 2008; 620: 8-26.
- [3] Varki A, Cummings RD, Esko JD, et al., editors. "Essentials of Glycobiology." 2nd edition. Cold Spring Harbor (NY): Cold Spring Harbor Laboratory Press; 2009. Chapter 27.
- [4] Tan CP, Cipriany BR, et al. "Nanoscale resolution, multicomponent biomolecular arrays generated by aligned printing with parylene peel-off." *Nano Letters*. 2010; 10[2]: 719-25.

## Silicon Heterojunction Photovoltaic Cells

**Hans Banerjee**

**Electrical and Computer Engineering,  
University of Illinois at Urbana-Champaign**

*NNIN REU Site: Microelectronics Research Center, The University of Texas at Austin, Austin, TX*

*NNIN REU Principal Investigator: Prof. Sanjay Banerjee, Electrical and Computer Engineering, University of Texas at Austin*

*NNIN REU Mentors: Emmanuel Onyegam and Sayan Saha, Electrical and Computer Engineering, University of Texas at Austin*

*Contact: banerje8@illinois.edu, banerjee@ece.utexas.edu, onyegam@utexas.edu, sayan.saha@utexas.edu*

### Abstract and Introduction:

A key advantage of silicon heterojunction photovoltaic cells over conventional cells is that they have potentially higher efficiencies [1]. They can be made using remote plasma chemical vapor deposition (RPCVD), a low temperature process that prevents carrier lifetime degradation and thus improves open-circuit voltage ( $V_{oc}$ ) [2]. Both single (SHJ) and dual (DHJ) heterojunction cells were fabricated by depositing a-Si:H onto n-type silicon wafers using RPCVD. SHJ cells were fabricated with and without intrinsic silicon “i-layers,” and with different thicknesses of p-doped a-Si:H at the front.

According to I-V testing, the SHJ cells with an i-layer produced a higher  $V_{oc}$  than those without one, suggesting the i-layer aids in passivation. Thicker p-doped layers resulted in lower short-circuit current density ( $J_{sc}$ ), due to absorption in the p-doped layer reducing quantum efficiency at short wavelengths. DHJ cells were fabricated with varying back surface field (BSF) layer thicknesses. A 30 nm BSF layer produced a similar  $V_{oc}$  and  $J_{sc}$  to one of 20 nm, indicating that thicker BSF layers do not significantly reduce back surface recombination. The SHJ and DHJ cells showed similar efficiencies (~15%). This may be due to non-optimized doping of the BSF layer in the DHJ cells, or their lack of an i-layer leading to lower quantum efficiency.

### Experimental Procedure:

Three SHJ and two DHJ cells were fabricated using RPCVD. Schematic diagrams of these cells are given in Figure 1. The SHJ cells were constructed with and without intrinsic a-Si:H i-layers, and with different thicknesses of p-doped a-Si:H at the front. The DHJ cells were fabricated with varying back surface field (BSF) n+doped a-Si:H layer thicknesses. The doping concentration of the p-doped and n-doped a-Si:H layers was held constant for all cells through constancy of the

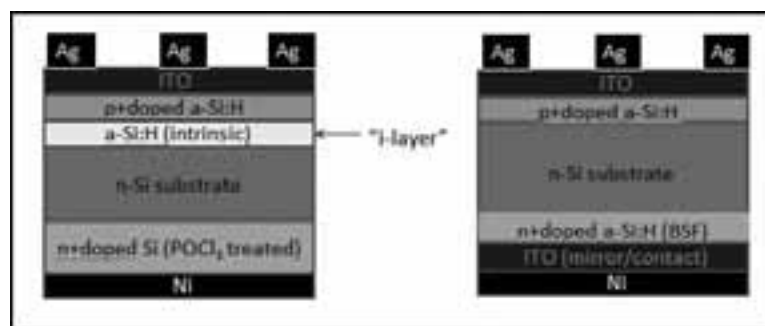


Figure 1: Schematic diagram for SHJ (left) and DHJ (right) cells.

Single HJ						
Cell	i-layer	Front p+	$V_{oc}$	$J_{sc}$	Fill Factor	Eff.
No I	0 nm	18.6 nm	632 mV	30.9 mA/cm <sup>2</sup>	77.0%	15.1%
718-2	6 nm	11 nm	637 mV	32.0 mA/cm <sup>2</sup>	77.5%	15.8%
719-2	7 nm	17 nm	637 mV	30.3 mA/cm <sup>2</sup>	78.8%	15.2%
Dual HJ						
Cell	Back n+	Front p+	$V_{oc}$	$J_{sc}$	Fill Factor	Eff.
716-2	20 nm	18.6 nm	616 mV	31.6 mA/cm <sup>2</sup>	77.3%	15.0%
716-3	30 nm	18.6 nm	619 mV	31.9 mA/cm <sup>2</sup>	77.9%	15.4%

Figure 2: Physical and electrical measurements of fabricated cells.

relevant RPCVD parameters. I-layers were not incorporated into the DHJ cells due to time constraints; the effect of the i-layer on PV cell characteristics was studied solely through the SHJ cells. Physical characteristics of the five cells are shown in Figure 2. All cells were metalized with nickel at the back and screen printed with silver paste at the front to improve electrical contact.

## Results and Discussion:

I-V and effective quantum efficiency testing was conducted on the cells. The I-V data for all the cells is shown in Figure 2. The effective quantum efficiency (EQE) between the wavelengths of 300 and 1200 nm is plotted in Figure 3 for SHJ cells and Figure 4 for DHJ. One notable result of this data is that both DHJ cells performed similarly in the EQE tests. The  $V_{oc}$  and  $J_{sc}$  of both cells were comparable as well (Figure 2). It can thus be concluded that having a thicker BSF than 20 nm does not significantly reduce back surface recombination in DHJ cells.

In SHJ cells, the  $V_{oc}$  of the cells with an i-layer was slightly higher ( $\sim 5$  mV) than that of the cell without it. This shows that the presence of an i-layer aids in the prevention of front surface recombination. However, the  $V_{oc}$  of the sample with the 7 nm i-layer had the same  $V_{oc}$  as the one with the 6 nm i-layer, possibly indicating that 6 nm of a-Si:H provides sufficient passivation.

In terms of current, the cell with the thinnest front p+doped layer clearly displayed the best  $J_{sc}$ . The explanation for this becomes clearer upon viewing Figure 3 and comparing the EQE curves for 718-2 and 719-2. The cell with the thinner front p-layer (718-2) exhibits significantly higher quantum efficiency at the lower wavelengths ( $< 700$  nm). Thus, it seems that the thicker front p-layer of 719-2 was absorbing more light at short wavelengths, which leads to lower generation of effective charge carriers. It can be concluded that an overly thick a-Si:H layer at the front junction leads to reduced EQE at short wavelengths, and therefore adversely affects current.

## Future Work:

When comparing SHJ and DHJ cells, the efficiency for both types is around 15%, depending on the various parameters. At first glance, it does not seem like the DHJ cells perform any better than the SHJ. However, it is worth noting that the DHJ cells were done without i-layers, which could have increased  $V_{oc}$  and efficiency like they did for the SHJ cells. Also, the doping concentration of the BSF layer in the DHJ cells may not be optimal. Future experiments with DHJ cells will be conducted with the i-layer thickness and BSF layer doping concentration as variables. Finally, texturing the surface of PV cells helps efficiency by reducing surface reflections and trapping light inside the cells for longer, leading to more generated carriers and higher current [3]. Texturing was omitted for the sake of time in this brief study, but can be performed to achieve higher efficiencies on future cells.

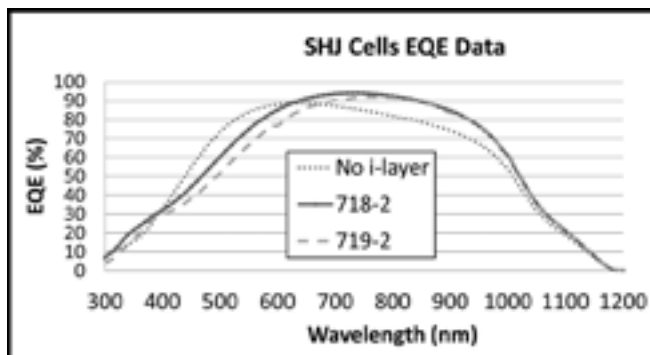


Figure 3: Quantum efficiency graph of SHJ cells.

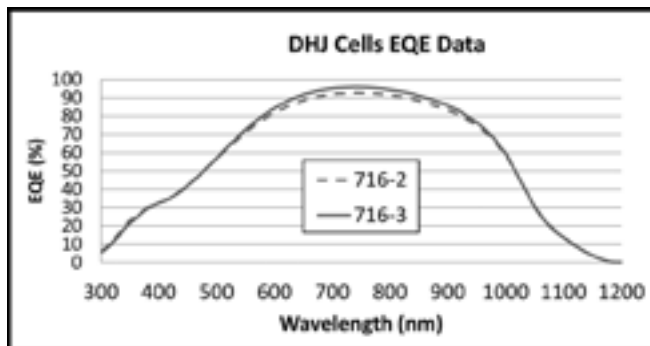


Figure 4: Quantum efficiency graph of DHJ cells.

## Acknowledgements:

I would like to acknowledge the National Nanotechnology Infrastructure Network Research Experience for Undergraduates Program and the National Science Foundation for selecting me and funding me for this prestigious research opportunity. I would also like to thank my mentors Emmanuel Onyegam and Sayan Saha, my P.I. Dr. Sanjay Banerjee, and everyone at the Microelectronics Research Center for all of their help.

## References:

- [1] Y. Tsunomura, et al; "Twenty two percent efficiency HIT solar cell"; *Solar Energy Materials and Solar Cells* 93 (2009) 670-673.
- [2] D. Sarkar, et al.; "Remote Plasma Chemical Vapor Deposition for High Efficiency Ultra-thin  $\sim 25$  Microns Crystalline Si Solar Cells," 38th IEEE PVSC, June 3-8, 2012.
- [3] M. Edwards, et al; "Effect of texturing and surface preparation on lifetime and cell performance in heterojunction silicon solar cells"; *Solar Energy Materials and Solar Cells* 92 (2008) 1373-1377.

## Anti-Reflective Coatings for Room Temperature Terahertz Quantum Cascade Laser Sources

Alexander Buck

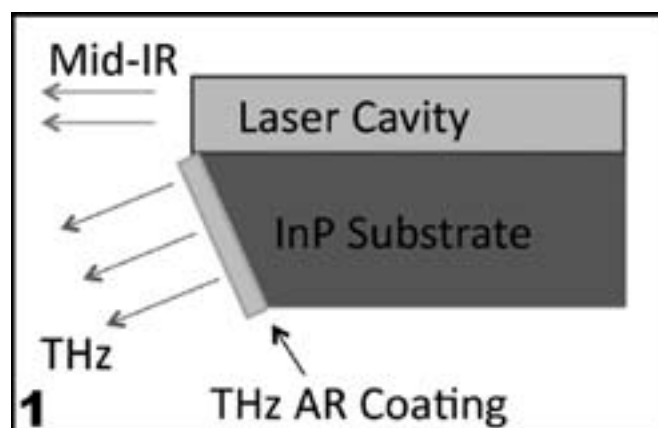
Applied Physics, Rensselaer Polytechnic Institute

NNIN REU Site: Microelectronics Research Center, The University of Texas at Austin, Austin, TX

NNIN REU Principal Investigator: Professor Mikhail Belkin, Electrical and Computer Engineering, University of Texas at Austin

NNIN REU Mentor: Karun Vijayraghavan, Electrical and Computer Engineering, University of Texas at Austin

Contact: bucka2@rpi.edu, mbelkin@ece.utexas.edu, karun@utexas.edu



### Abstract and Introduction:

There are currently no electrically-pumped semiconductor lasers that can operate in the 1-5 terahertz (THz) spectral range at room temperature. An alternative method of producing room temperature THz light is based on intra-cavity difference frequency generation (DFG) in dual wavelength mid-infrared quantum cascade lasers. Our THz DFG sources can provide tunable output of over 20 microwatts in the 1-5 THz range at room temperature. However, for these devices an estimated 30% of the THz radiation is reflected back into the laser from the emission surface. A schematic is shown in Figure 1. Single-layer anti-reflective (AR) coatings were investigated as a method for improving the power output by reducing these reflection losses.

### Experimental Procedure:

Mathematica was used to simulate the transmission of several different AR coatings using Equation 1 [1]. For a single coating, the appropriate layer thickness is given as

$$T = 4 * \left[ \frac{n^2}{n_s} + \frac{n_s}{n^2} + 2 + \left( \frac{1}{n_s} + n_s - \frac{n^2}{n_s} - \frac{n_s}{n^2} \right) \cos^2 \left( 2 * \pi * n * \frac{d}{\lambda} \right) \right]^{-1}$$

Equation 1:

$n$  = refractive index of AR coating  
 $n_s$  = refractive index of substrate

$d$  = coating thickness  
 $T$  = transmitted intensity

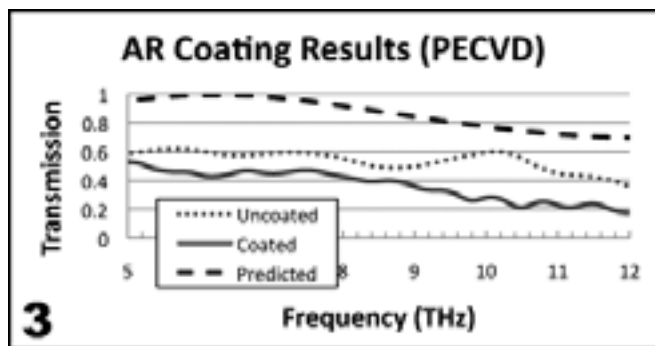
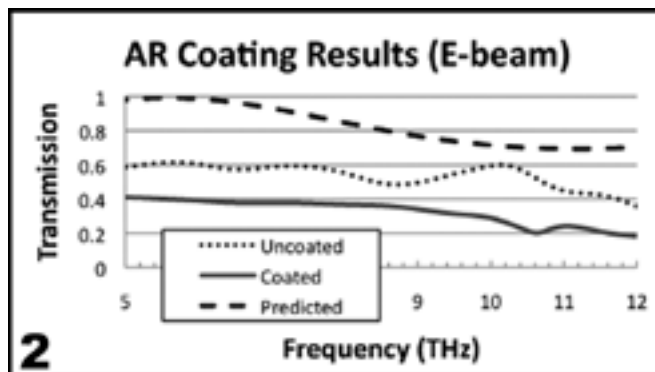
$d = \lambda_{\text{THz}} / 4n_{\text{AR}}$ , where  $n_{\text{AR}}$  is the refractive index of the AR coating materials and is also the geometric mean of the substrate and air refractive indices.

For our devices, the THz emission was traveling from an indium phosphide (InP) substrate ( $n \approx 3.6$ ) into air ( $n \approx 1$ ), yielding an ideal refractive index of 1.91 for an AR coating in the 1-5 THz range. Silicon dioxide ( $\text{SiO}_2$ ) was used for AR coatings because of its near-ideal refractive index ( $n_{\text{SiO}_2} = 2.00$ ) and low absorption losses in the THz [2]. Parylene and Pyrex® were also considered, but discarded due to equipment constraints.

To test the coating,  $\text{SiO}_2$  was applied to bare high-resistivity InP (HR-InP) and high-resistivity silicon (HR-Si) wafers. High-resistivity wafers were chosen to reduce the THz transmission loss due to free carrier absorption. Silicon wafers were used because of their availability and ideal dielectric properties (low absorption loss and a refractive index close to that of InP,  $n_{\text{Si}} = 3.50$ .)

Two methods were used to deposit  $\text{SiO}_2$ . The primary deposition method used was electron beam (e-beam) evaporation. The e-beam system allowed for precise layer thickness control. A  $6.9 \mu\text{m}$  layer of  $\text{SiO}_2$  was deposited at  $70^\circ\text{C}$  and a maximum rate of  $6 \text{ \AA/s}$  onto both HR-Si and HR-InP wafers. The layer thickness was monitored during deposition with a crystal quartz oscillator and confirmed using a Veeco Dektak 150 profilometer.  $\text{SiO}_2$  began flaking off of the InP sample immediately after deposition, making accurate measurement impossible. A Bruker Vertex 70 Fourier transform infrared spectrometer (FTIR) was used to measure the transmission spectrum of the samples before and after the application of AR coatings. The results for HR-Si samples are shown in Figure 2.

Plasma-enhanced chemical vapor deposition (PECVD) was another technique used to deposit  $\text{SiO}_2$ . PECVD can achieve very high growth rates ( $\sim 1 \mu\text{m/hr}$ ) at the expense of lower thickness uniformity. A  $5.9 \mu\text{m}$  layer of  $\text{SiO}_2$  was deposited at  $200^\circ\text{C}$  onto both HR-InP and HR-Si wafers. Post-deposition profilometry was used to measure the film thickness.



As in the case with e-beam deposition, the  $\text{SiO}_2$  film did not adhere well to the InP sample and flaked off easily. A substantial amount ( $\sim 500$  nm) of bowing was also observed in the coated HR-Si wafers. FTIR spectrometry was used to compare the transmission spectra of the Si wafer before and after deposition. The results are compared to the simulated transmission in Figure 3.

### Results and Conclusions:

For both PECVD and e-beam evaporation, the actual transmission of THz light was significantly less than theory predicted. In each case, the addition of an  $\text{SiO}_2$  AR coating did not increase the transmission of THz light for any of the measured frequencies. The absorption losses of the e-beam deposition were consistently 5% higher than those of the PECVD samples. We suspect that the high absorption of the AR coating overcompensated for any improvement in the transmission. The trend in the post-coating transmission spectrum for both cases suggests that the AR coating improved transmission for some frequencies relative to others. However, without knowing exactly the absorption characteristics of

$\text{SiO}_2$  in these frequencies, we cannot conclude that the AR coating truly decreased the amount of light reflected.

For both deposition methods, the poor adhesion of  $\text{SiO}_2$  to the InP samples and the observed bowing on the Si samples could be due to the difference in the thermal expansion between the  $\text{SiO}_2$  and InP. A large difference would cause a buildup of stress in the  $\text{SiO}_2$  film and cracks could form if the stress goes beyond a critical threshold. To account for the discrepancy between the two methods, we suspect several factors.

First, the higher temperature deposition via PECVD likely produced a more uniform layer than the lower temperature e-beam deposition. Second, the e-beam deposition took place over several sessions, which might have created several distinct layers, leading to losses between each layer. It is also possible that contaminants from the deposition chamber or other samples might have been in the  $\text{SiO}_2$  target used for E-beam deposition.

We also suspect that the literature values of the real and imaginary parts of the refractive index for  $\text{SiO}_2$  were significantly different from those in our materials. The dielectric properties of  $\text{SiO}_2$  depend heavily on the deposition methods used; it is likely that the literature values for amorphous material were not accurate for E-beam and PECVD deposited material. This error would likely have shifted the predicted peak in transmission, possibly even beyond the measurement range of our FTIR spectrometer.

### Future Work:

For future progress, Parylene-C will be investigated as an alternative to  $\text{SiO}_2$ . Parylene has a well-developed deposition process and would eliminate much of the variability present in working with  $\text{SiO}_2$ . An ion source assisted e-beam deposition might also give a lower-absorption AR coating.

### Acknowledgements:

Professor Mikhail Belkin; Karun Vijayraghavan; Yifan Jiang; The National Nanotechnology Infrastructure Network Research Experience for Undergraduates Program; The National Science Foundation.

### References:

- [1] Jihua Xu, Applied Physics Letters 91, 121104 (2007); doi: 10.1063/1.2786587.
- [2] Palik, E; "Handbook of Optical Constants of Solids", Volume II, 1997.

## Fabrication of Metallic and Dielectric Nanowires for Realizing Optical Filters

**Amanda Ellison**

**Biochemistry, Missouri University of Science and Technology**

*NNIN REU Site: Nano Research Facility, Washington University in St. Louis, St. Louis, MO*

*NNIN REU Principal Investigator: Dr. Viktor Gruev, Computer Science and Engineering, Washington University in St. Louis*

*NNIN REU Mentor: Shengkui Gao, Department of Computer Science and Engineering, Washington University in St. Louis*

*Contact: alexb2@mst.edu vgruev@wustl.edu gaoshengkui@go.wustl.edu*

### Introduction:

Light has three main components—intensity, wavelength, and polarization. Intensity and wavelength can be detected by the human eye; however, polarization cannot. This is because polarization is the orientation at which the wave travels forwards in space. Polarization can be manipulated using optical filters, such as using aluminum nanowires (Al NWs) oriented in 45° angles to each other. When polarized light is shown on these filters, areas of the filters appear dark and others appear bright. This is because the angle of polarization at the dark areas is perpendicular to the angle of the array;

therefore, the light is blocked. The array in the light areas is parallel to the angle of the light's polarization.

Our lab this summer was fabricating arrays of micron squares using contact photolithography in order to further study the crosstalk effect between pixels. Contact photolithography is achieved by printing an image on a substrate by the use of a photomask and ultraviolet light. After the array is complete, photos are taken using an optical microscope. The samples are then subjected to a reactive ion etch using various gases to etch through the photoresist, silicon dioxide, aluminum oxide layers and partially through an aluminum layer. More pictures are taken to verify the shape.

We attained squares from  $3 \times 3 \mu\text{m}$  to  $7 \times 7 \mu\text{m}$ . These arrays will further be used to measure the crosstalk effect between a pixel and the neighboring pixels.

### Experimental Procedure:

The process used was contact photolithography, which required many different steps. The objective was to optimize each photoresist's recipe to produce the most replicable and accurate square results. First, the sample was coated with a photoresist—a UV light sensitive material [1]. Next the sample followed the processes listed in Table 1, depending on the type of photoresist being used.

### Results and Conclusions:

The photoresists used during contact photolithography each gave a significantly different result even after trying to optimize exposure, baking, and development times.

Photoresist AZ 5214	Photoresist SU-8 2 with OmniCoat Under-Layer
<b>Coating:</b>	<b>OmniCoat®</b>
Step 1: 500 rpm at 100 rpm/s for 10 sec	Step 1: 500 rpm at 100 rpm/s for 5 sec
Step 2: 3000 rpm at 300 rpm/s for 30 sec	Step 2: 3000 rpm at 300 rpm/s for 30 sec
Step 3: 0 rpm at 300 rpm/s down for 1 sec	<b>Bake:</b>
<b>Pre-Bake:</b>	200°C for 1 min
110°C for 1 min	<b>Cool to room temperature.</b>
<b>Expose:</b>	<b>SU-8 2</b>
10.7 sec	<b>Coating:</b>
<b>Reversal Bake:</b>	Step 1: 500 rpm at 100 rpm/s for 5 sec
110°C for 2 min	Step 2: 3000 rpm at 300 rpm/s for 30 sec
<b>Flood Exposure:</b>	Step 3: 0 rpm at 300 rpm/s down for 1 sec
30 sec	<b>Pre-Bake:</b>
<b>Develop:</b>	65°C for 7 min
AZ 327 for 40 sec with slight agitation	95°C for 10 min
Rinse with deionized water and dry with N <sub>2</sub>	120°C for 8 min
<b>Photoresist S1805</b>	<b>Expose:</b>
<b>Coating:</b>	30 sec
Step 1: 6000 rpm at 300 rpm/s for 30 sec	<b>Post Bake:</b>
Step 2: 0 rpm at 300 rpm/s down for 1 sec	65°C for 10 min
<b>Pre-Bake:</b>	95°C for 10 min
115°C for 1.5 min	120°C for 5 min
<b>Expose:</b>	<b>Develop:</b>
12 sec	SU-8 developer for 10 min with slight agitation
<b>Reversal Bake:</b>	<b>Rinse with isopropyl alcohol and deionized water.</b>
115°C for 1.5 min	<b>Dry with N<sub>2</sub></b>
<b>Develop:</b>	
MF-319 for 1 min with slight agitation	
Rinse with deionized water and dry with N <sub>2</sub>	

Table: Photoresist recipes using contact photolithography to produce squares.

The AZ 5214, as a negative photoresist, produced the least effective results. In Figure 1, it is evident that the  $7 \times 7 \mu\text{m}$  square is a four-pointed star. We speculate that perhaps the photoresist was over-developed because a small square is seen within the center of the star with the points radiating from the sides of the square figure.

The next photoresist was SU-8 2, which produced diamond figures for all squares ranging from  $3 \times 3$  to  $7 \times 7 \mu\text{m}$ , as seen in Figure 2. This photoresist was optimized up to a 50 minute pre- and post-bake time combined. This, however, did not improve the efficiency as projected. We assume that this photoresist cannot achieve such features on a micron or nano scale.

The photoresist that was the most successful was the positive S1805. This still fabricated a failed result of octagons as seen in Figure 3. Changing the bake time, as in the past two photoresists, did not affect the outcome we achieved, leading us to conclude that this photoresist cannot perfectly attain the squares we require.

Electron beam lithography obtained the most successful squares as seen in Figure 4. This process had the greatest success and precision, but it increased the cost of the mask produced.

Our lab concluded that the photoresists may be causing the shape formation; however, after more study we deduced that the samples we were creating contained a thicker layer of photoresist around the edges; edge beads. This phenomenon caused problems in the subsequent steps and was probably the reason our shapes were not squares.

#### Future Work:

The next process for the experiment is to attach the pixel mask array to a photodiode. This will allow the team to block a pixel and measure the overall crosstalk effect by quantifying how many photons have left neighboring pixels to enter the blocked pixel. When the crosstalk effect is fully understood, the lab will be able to correct for this shift in photons when using the polarization camera. This camera will then be used further in the imaging of cancerous cells which emit a polarized light versus normal non-cancerous cells that emit no polarization characteristics.

#### Acknowledgements:

Thank you to the NNIN REU Program and the NSF. Thank you to my PI, Dr. Viktor Gruev, and my mentor, Shengkui Gao; as well as the staff at Washington University in St. Louis.

#### References:

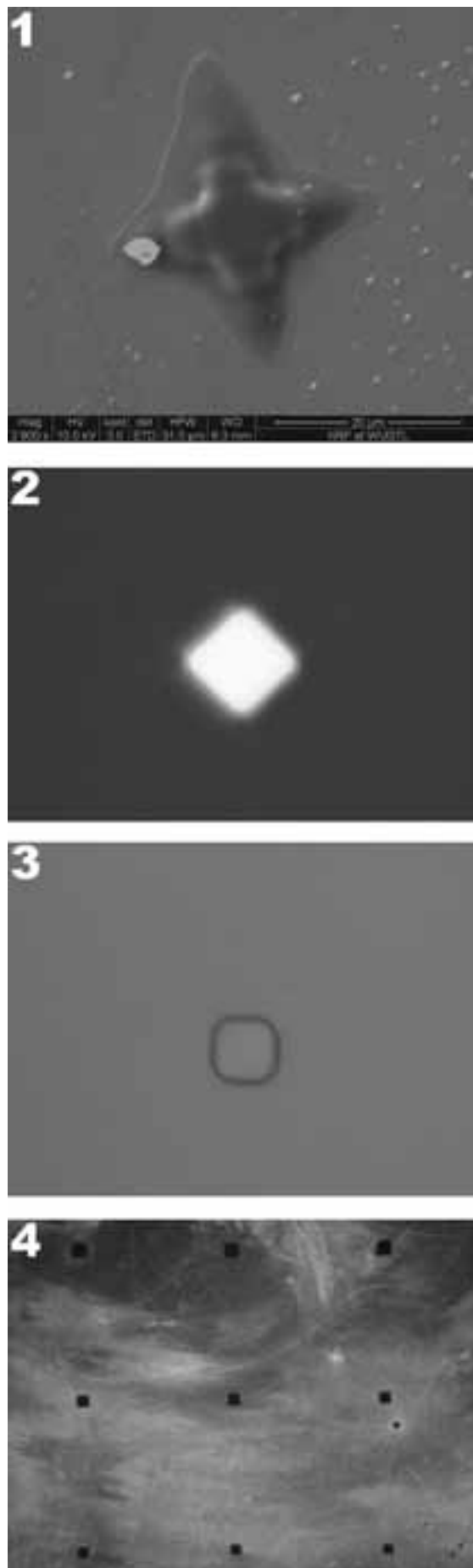
- [1] S. Campbell. The Science and Engineering of Microelectronic Fabrication. 2001.

*Figure 1: AZ 5214, a negative photoresist, produced a four-pointed star.*

*Figure 2: SU-8 2 produced diamond figures for all squares ranging from  $3 \times 3$  to  $7 \times 7 \mu\text{m}$ .*

*Figure 3: Positive S1805 photoresist was the most successful, but still fabricated a failed result of octagons.*

*Figure 4: Electron beam lithography obtained the most successful squares with the greatest success and precision.*



## Integration of Embedded CMOS Chips for On-Chip Optical Communication

**Kyle Guess**

**Polymer Science, The University of Southern Mississippi**

*NNIN REU Site: Nanotech, University of California, Santa Barbara, CA*

*NNIN REU Principal Investigator: Professor Luke Theogarajan,  
Electrical and Computer Engineering, University of California, Santa Barbara*

*NNIN REU Mentor: Avantika Sodhi, Electrical and Computer Engineering, University of California, Santa Barbara*

*Contact: kyle.guess@eagles.usm.edu, ltheogar@ece.ucsb.edu, avantikasodhi@uemail.ucsb.edu*

### Abstract and Introduction:

The rapid development of telecommunications infrastructure in developing nations, the advent of high-speed cellular data networks and the recent popularization of cloud computing continue to drive demand for more robust and energy efficient data networks. The dominant source of power utilization in these networks is the electrical interconnect due to the high energy cost of moving data between the computing and communication blocks. Losses inherent in electrical interconnections between computing and telecommunications infrastructure may be mitigated by utilizing optical interconnects instead.

In recent decades, many electronic-photonic integration techniques have been explored, however, a process that is truly compatible with complementary metal-oxide-semiconductor (CMOS) technology has yet to be developed.

In this work, a novel integration technique that circumvents most of the difficulties faced by existing methods is presented. It allows for the integration of CMOS dies into silicon photonic substrates. The process is based on the creation of a chip-specific imprinted hard mask utilizing localized polymerization of a heat-curable poly(dimethylsiloxane) (PDMS) elastomer, which allows for the embedment of multiple dies into a single mask. Localized polymerization around individual dies is performed by the independent temperature control of the arm and stage of a flip-chip bonder. The masked substrate is then subjected to a series of reactive ion etching steps in order to create chip-specific cavities with length and width dimensional tolerances of less than  $10\ \mu\text{m}$ , enabling close integration of the CMOS die and photonics substrate.

### Experimental Procedure:

In order to examine potential changes in the electrical characteristics of integrated dies, dies patterned with series and parallel RLC oscillator circuit designs were created via traditional contact photolithography, metallization, lift-off, and dicing techniques. Each die measured 1.5 mm long by 1.5 mm wide.

The procedure for the integration technique executed was as follows:

A passive silicon photonics substrate (optical substrate) containing silicon waveguides cladded by layers of silicon dioxide ( $\text{SiO}_2$ ) was bonded to a Si carrier substrate using photoresist as an adhesive. Dow Corning Sylgard® 184 PDMS elastomer was mixed in a 6:1 base-to-curing agent weight ratio and spin-coated onto the optical substrate. The optical substrate was then placed onto the stage of a flip-chip bonder, which was kept cool to prevent polymerization of the entire surface coating. A die was picked up by the arm and tip of the flip-chip bonder, properly positioned over the optical substrate, and pressed into the prepolymer. Heating of the die by the arm initiated polymerization in the area immediately surrounding the die. Following the heating period, the arm was allowed to cool. Prior to liftoff of the arm, air was discharged through the tip for  $800\ \mu\text{s}$  to aid in the release of the die. Detailed flip-chip bonder temperature and applied force parameters are shown in Figure 1.

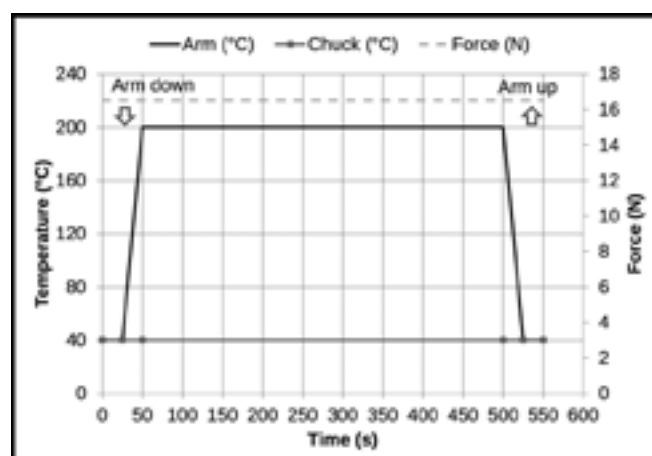


Figure 1: Flip-chip bonder temperature and applied force profile.



Figure 2: Vacant through-substrate cavity (left) and integrated RLC circuit die (right).

Following die embedment, the optical substrate was baked at 110°C for 10 minutes to cure the entirety of the elastomer mix atop the substrate. Afterwards, the die was removed from the mask, and residual PDMS that remained underneath it was removed via reactive ion etching (RIE). Inductively coupled plasma (ICP) RIE was used to remove the waveguide cladding layers. Bosch process deep RIE was employed to etch through the silicon waveguide core and the optical substrate base. The bulk of the remaining PDMS hard mask was removed manually, and the optical substrate was freed from the carrier. Residual PDMS was removed via reaction with tetra-n-butylammonium fluoride in a solution prepared as described by Balakrisnan, et al. [1].

The optical substrate was bonded upside down to a carrier substrate, and the die was fitted into the etched cavity. Backside planarization and filling of the gaps between the integrated die and the cavity walls was accomplished by spin-coating Filmtronics Incorporated 500F spin-on glass (SOG) onto the backside of the optical substrate. The SOG was soft-baked sequentially at 95°C, 175°C, and 200°C for two minutes per temperature. A total of three layers of SOG were applied in this manner.

### Results and Conclusions:

Two optical substrates are shown in Figure 2. For a sense of scale, the die measures approximately 1550  $\mu\text{m}$  by 1550  $\mu\text{m}$ . The largest die-to-wall gap is approximately 15  $\mu\text{m}$  wide, significantly larger than the smallest gap achieved in other samples created via the employed integration technique and similar methods [2]. This discrepancy is likely the result of distortion of the mask upon removal of the die prior to the etching procedure, and can be easily minimized with increased caution during die removal.

### Future Work:

Planarization of the upper surface of the optical substrate could not be carried out due to time constraints. However, this can be achieved by plasma-enhanced chemical vapor deposition of a layer of  $\text{SiO}_2$ , which can then be polished flat via chemical mechanical polishing. Traditional photolithographic and ICP RIE processes can then be employed to pattern and etch through the upper  $\text{SiO}_2$  layer to uncover metal contacts atop integrated dies and the optical substrate. Standard metallization and lift-off techniques can then be used to deposit a top metallization layer to establish electrical connections between integrated CMOS dies and optoelectronic devices, thus enabling the creation of electronic-photonic integrated circuits.

### Acknowledgements:

I would like to thank Professor Luke Theogarajan, Avantika Sodhi, and all of the Biomimetic Circuits and Nanosystems Research Group for their guidance, support, and immense assistance. I would also like to thank Samantha Cruz, NNIN REU Site Coordinator, and the entire Nanotech staff. Of course, this research experience would not have been possible without the generous sponsorship from the NNIN REU Program; the NSF; the University of California, Santa Barbara; the Intelligence Advance Research Projects Activity, and Aurion Incorporated.

### References:

- [1] Balakrisnan, B., et al. *Journal of Micromechanics and Microengineering*; Vol. 19, No. 4;047002-047008 (2009).
- [2] Uddin, A., et al. *IEEE Transactions on Components, Packaging, and Manufacturing Technology*; Vol. 1, No. 12; 1996-2004 (2011).

## Microring Resonators in Silicon Photonic Circuits

**Daniel Klemme**

**Physics and Mathematics, Bethel University**

*NNIN REU Site: Colorado Nanofabrication Laboratory, University of Colorado, Boulder, CO*

*NNIN REU Principal Investigator: Dr. Miloš Popović, Electrical, Computer, and Energy Eng., University of Colorado, Boulder*

*NNIN REU Mentor: Dr. Jeffrey Shainline, Electrical, Computer, and Energy Engineering, University of Colorado, Boulder*

*Contact: djk43877@bethel.edu, milos.popovic@colorado.edu, jeffrey.shainline@colorado.edu*

### Abstract:

Microring resonators in silicon photonic circuits have, for the first time, been fabricated using equipment at the University of Colorado, Boulder. The fabricated rings have a free spectral range of 2.8 THz, and a quality ( $Q$ ) factor of up to 31,000 has been observed.

### Introduction:

Silicon (Si) photonics is an emerging technology that promises to allow for control of light on a compact chip analogously to how silicon microelectronics manipulates electricity. Si photonics may save the continued Moore's Law scaling of microelectronics by providing a solution to the energy efficiency problem faced by today's microelectronics. It will also potentially allow many table-top optical systems to be condensed onto a single chip. Microring resonators are ring-shaped, closed-loop optical waveguides with a radius on the order of a micron, which are capable of selecting a narrow frequency band of light from a spectrum. They work by being placed near a waveguide and coupling to the evanescent field. The light travels around the ring, and if an integer multiple of the wavelength is the same as the circumference of the ring, constructive interference occurs, while other wavelengths destructively interfere. The narrow resonant band is either transferred to another waveguide or lost to absorption and scattering while the remaining spectrum continues on the original path. This selectivity property causes microring resonators to be of interest to the telecom industry, where resonant microrings can be used as filters in wavelength-division multiplexed (WDM) communication systems. The project focus was to fabricate devices that incorporate microring resonators via electron beam lithography, and to characterize their optical frequency response, including bandwidth, quality factor ( $Q$ ) and free spectral range (FSR).

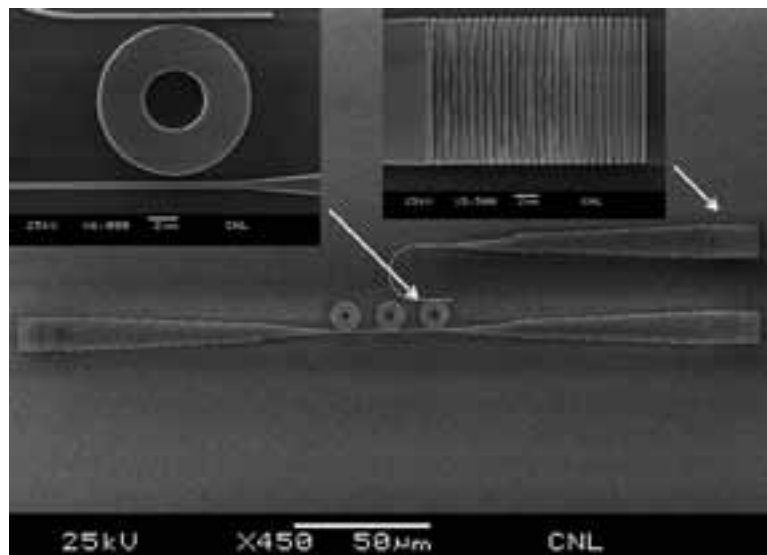


*Figure 1: Scanning electron microscope image of the devices that were fabricated and tested. Light enters through the grating on the left side and comes out through one of the two gratings on the right side. From left to right, the three rings have coupling distances of 200, 350, and 500 nm. The rings have an outer radius of 5  $\mu\text{m}$  and an inner radius of 2  $\mu\text{m}$ .*

### Experimental Procedure:

The fabrication process of the devices began by spinning an  $\sim 150$  nm thick layer of the polymer poly(methyl methacrylate) (PMMA) onto a silicon-on-oxide chip. The chip was placed inside a scanning electron microscope (SEM) that interfaces with the pattern layout program DesignCAD to cause the beam of electrons to write any desired shape using any dose of charge per area.

PMMA is normally used as a positive electron beam resist in the 100s of  $\mu\text{C}/\text{cm}^2$  regime, but when the dose is increased to 10,000 or more  $\mu\text{C}/\text{cm}^2$ , the polymer cross-links where the pattern is written, causing the resist to become negative, which was desirable for the relatively long and narrow structures we were interested in fabricating (see Figure 1).

We then developed the sample in acetone for 40 seconds and used a reactive ion etching (RIE) process to etch all the way through the 220 nm thick Si layer to the oxide layer below.

### Results and Conclusions:

A fiber laser was coupled into the left grating and out from the bottom right grating. The light coupled back into the laser was measured against the total power output of the laser to provide a measurement of the power extinction. The laser was swept from 1500 to 1620 nm in increments of 5 pm to obtain the plot shown in Figure 2. Each downward spike happened at a resonance where the rings removed light from the original waveguide and either transmitted it to another waveguide or lost it to radiation or absorption. The spectrum was fairly complicated by virtue of having three rings of differing coupling distances and also due to the fact that the rings were 3  $\mu\text{m}$  wide and therefore capable of supporting multiple modes. There appeared to be two separate sets of resonances that each had a free spectral range of 2.8 THz.

A close-up view (Figure 3) revealed an additional structure present in the resonances. Namely, it was apparent that there were secondary and tertiary resonances that occurred in the vicinity of the central spike and that the central spike seemed to be made up of two closely-spaced resonances. It was likely that the secondary and tertiary resonances were higher-radial-order modes allowed by the large width of the rings.

The two closely spaced resonances are called doublets and are due to the breaking of degeneracy of clockwise and counter-clockwise propagating modes caused by imperfections in the rings, which break the rotational symmetry. However, there was not sufficient time for complete characterization of all modes in the spectrum. We did however measure the width of the central peak at the 3 dB point to be 50 pm and since it was centered at 1571.9 nm, it had a  $Q$  factor of 31,000, which was not much larger than the  $Q$  factor found in the other resonances.

In summary, fabrication of silicon photonic devices is now possible at the University of Colorado Boulder, and these devices have demonstrated a  $Q$  factor of 31,000.

### Acknowledgements:

I would like to thank my entire lab group and especially my PI Dr. Miloš Popović and mentor Dr. Jeffrey Shainline for their tireless support and advice throughout the project. I would also like to thank the NSF for funding this research opportunity as well as the NNIN for offering and organizing the undergraduate research program.

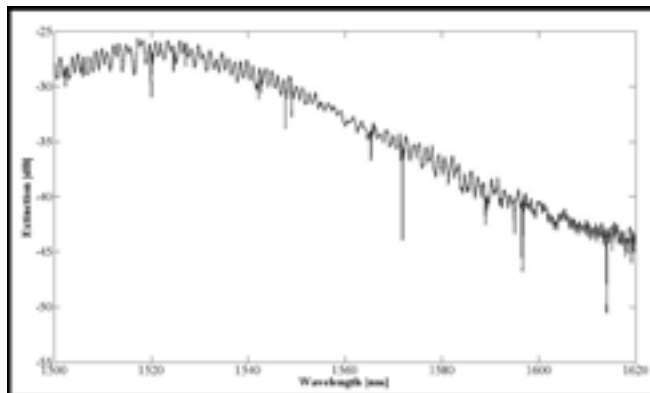


Figure 2: Spectrum sweep from 1500 to 1620 nm showing the resonance spikes due to the rings. Note that the y-axis is a dB scale.

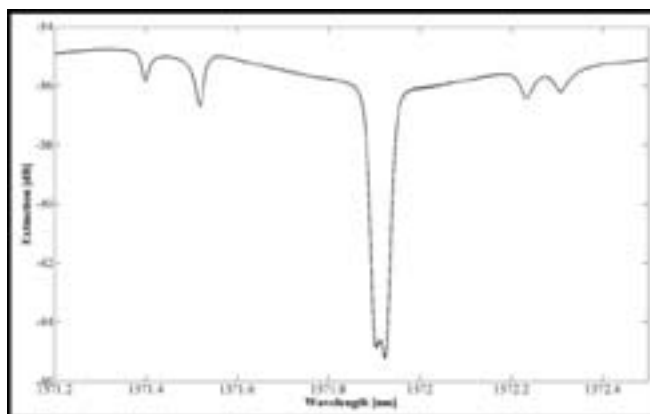


Figure 3: Zoomed in view of the resonance centered near 1572 nm. Secondary and tertiary resonances can be seen on either side of the central spike, which itself seems to be made up of two closely-spaced resonances.

## Microheaters for Thermo-Optic Tuning of Silicon Photonic Devices

Juan Pablo Llinás

Electrical Engineering, University of Illinois at Urbana Champaign

NNIN REU Site: Colorado Nanofabrication Laboratory, University of Colorado, Boulder, CO

NNIN REU Principal Investigator: Miloš Popović, Department of Electrical, Computer, and Energy Engineering, University of Colorado Boulder

NNIN REU Mentor: Jeffrey Shainline, Department of Electrical, Computer, and Energy Engineering, University of Colorado Boulder

Contact: llinas2@illinois.edu, milos.popovic@colorado.edu, jeffrey.shainline@colorado.edu

### Abstract:

Silicon photonic devices have a broad range of uses, from chemical sensors to filters and modulators integrated with complementary metal oxide semiconductor (CMOS) microelectronics. As a result, these devices have applications that include future microprocessors, signal processing, biomedical devices, telecommunications, and more. A major drawback of silicon (Si) photonics is the sensitivity to device dimensions. Changing the width of a ring resonator by as little as a single atomic lattice will shift the resonant frequency by several gigahertz (GHz). This level of dimensional control is impossible in fabrication, so it is necessary to actively tune devices for operation. Because Si has a high thermo-optic coefficient, microheaters can be used to efficiently tune Si photonic devices and change their behavior. In this work, chromium microheaters were fabricated on top of a 1  $\mu\text{m}$ -thick oxide cladding layer above microring resonators using photolithography and lift-off. Using a proportional-integral-derivative (PID) controller, the heaters were programmed to dissipate constant power over the rings and change their resonant frequencies. Robust heaters were demonstrated with a tuning ability of a full free spectral range and up to 60 GHz/mW.

### Introduction:

Microring resonators are Si photonic devices that act as filters. These devices drop light of a certain frequency, the resonant frequency of the ring, from a waveguide. The resonant frequency of the rings depends on the geometry of the rings as well as the index of refraction of Si. Because silicon's index of refraction depends on temperature, microheaters can actively change the resonant frequency of microring resonators. It is of interest to produce power-efficient tuning, i.e. produce as large a wavelength tuning as possible with a given amount of

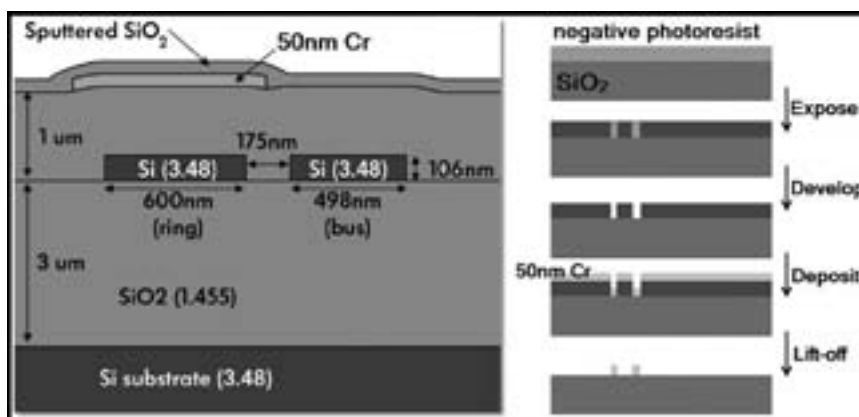
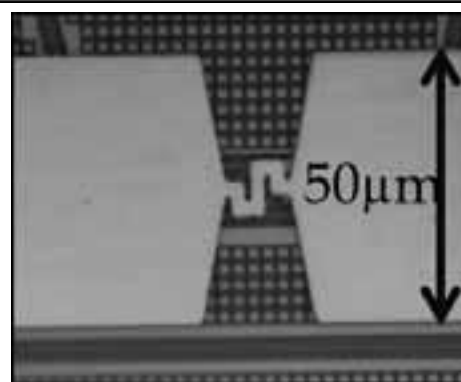


Figure 1, above: Cross section of the fabricated chip (left) and fabrication process (right).

Figure 2, right: Chromium microheater on top of a microring resonator.



dissipated power, which is possible in Si photonics because of the large thermo-optic coefficient of Si, and the micron-scale size of the devices that need to be heated to a high temperature.

The goal of this project was to fabricate microheaters and demonstrate thermal tuning of microring resonators.

### Methods:

A metal had to be chosen before the dimensions of the heaters were determined. The candidates were titanium and chromium because they are affordable metals with high resistivity.

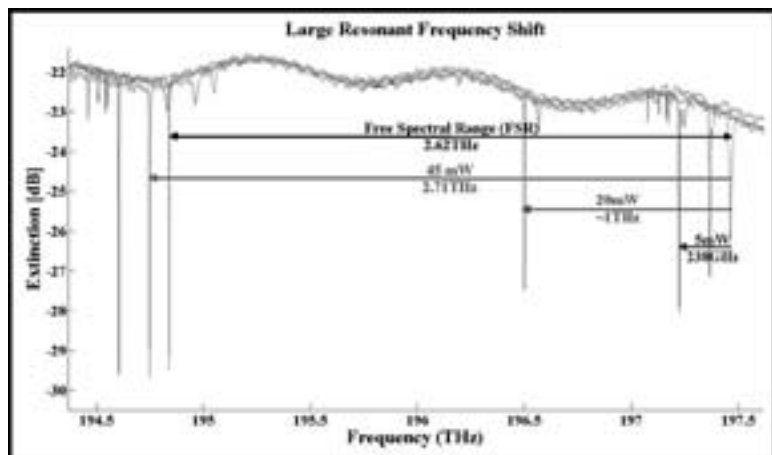


Figure 3, above: Tuning past a full FSR of a microring. The resonant frequency at ~ 197.5 THz is the resonant frequency of the ring at room temperature.

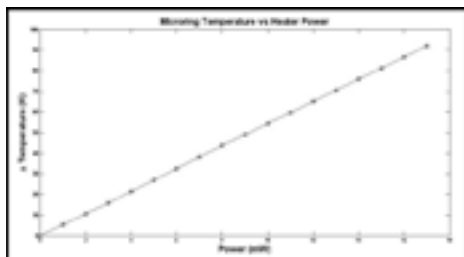


Figure 4: Change of temperature at the ring as a function of the power dissipated by the heater. Power was incremented by 1 mW from 0-17 mW.

Out of both metals, titanium has the highest resistivity ( $4.2 \times 10^{-7} \Omega\text{m}$  at  $20^\circ\text{C}$ ), but it also oxidizes quickly. Thus, we chose chromium because it would yield more robust heaters. Figure 1 shows the cross section of the fabricated chip as well as the fabrication process of the heaters.

We started with chips that had the rings, waveguides, and the  $1 \mu\text{m}$   $\text{SiO}_2$  cladding, which protected the waveguides from metal contamination [2]. Optical photolithography and lift-off were then used to fabricate the heaters on top of the  $\text{SiO}_2$  cladding. The desirable resistance of the heaters was  $500 \Omega$  to  $10 \text{ k}\Omega$ . Devices with a wire thickness of  $50 \text{ nm}$  and widths from  $1.5 \mu\text{m}$  to  $3 \mu\text{m}$  were fabricated in order to get heaters with desirable resistance that covered the area of the rings. Figure 2 shows one of the fabricated devices.

To test the heaters, a probe station and a PID controller, written in LabVIEW, were used. The PID controller measured the current going through the heater and the voltage drop. With this feedback, the PID controller changed the voltage across the heater so that it reached the desired steady state. Light was then coupled into the chip and a sweep of  $1500 \text{ nm}$  to  $1590 \text{ nm}$  wavelength was taken to determine the resonance of the ring.

A sweep was taken while dissipating constant power over the heater and the shift in resonance was measured.

## Results and Conclusions:

First, an optical transmission wavelength sweep was taken while dissipating power from zero milliwatts (mW) to  $17 \text{ mW}$  across the heater with a step size of  $1 \text{ mW}$ . Since the resonant frequency of this ring changed by  $\sim 10.7663 \text{ GHz/K}$  and the thermo-optic coefficient of silicon was nearly constant over this range ( $23^\circ\text{C}$ - $123^\circ\text{C}$ ), the temperature of the ring could be determined as a function of power dissipated [1].

Furthermore, a linear relationship between the change in temperature of the ring and the power dissipated by the heater is shown in Figure 4. This was expected because of the near-constant thermo-optic coefficient with temperature, and the fact that thermal diffusion itself was a linear process (like an RC electrical circuit), the heater covers the whole top area of the ring. Thus, the temperature should drop linearly across the  $1 \mu\text{m}$   $\text{SiO}_2$  cladding.

It was important for the heaters to be efficient and be able to tune the rings over a large range of frequencies. Figure 3 shows the tuning of a ring past its free spectral range, FSR, the difference between adjacent resonant frequencies. This was all the tuning necessary for this ring since tuning past the FSR was not necessary — one could simply use the adjacent resonance's passband beyond a one-FSR detuning. Also, a  $50 \text{ GHz/mW}$  to  $60 \text{ GHz/mW}$  tuning efficiency was measured.

Considering the desired resonant frequency of a microring can be off by a few hundred gigahertz after it is fabricated, the microring can be tuned to its desired response with a few milliwatts dissipated by the heater. Furthermore, complex multiple-ring devices, like higher order filters, typically have slight (a few gigahertz) mismatches between ring frequencies. These can be compensated with sub-milliwatt power in the microheaters.

## Acknowledgements:

I would like to thank the National Nanotechnology Infrastructure Network Research Experience for Undergraduates (NNIN REU) Program, the National Science Foundation, Professor Popović and his research group, and the Colorado Nanofabrication Laboratory for making this project possible.

## References:

- [1] M. Popović, "Theory and Design of High-Index-Contrast Microphotonic Circuits," Ph.D. Thesis, MIT (Cambridge, MA), Sep. 15, 2007.
- [2] T. Barwicz, M. A. Popovic, F. Gan, M. S. Dahlem, C. W. Holzwarth, P. T. Rakich, E. P. Ippen, F. X. Kartner, and H. I. Smith, "Reconfigurable silicon photonic circuits for telecommunication applications", Proc. SPIE 6872, 68720Z-1-12 (2008).

# Metasurface Dichroic Mirrors and Applications to Solar Energy via Spectral Splitting

**Adam J. McMullen**

**Mechanical Engineering, Rice University**

*NNIN REU Site: Microelectronics Research Center, The University of Texas at Austin, Austin, TX*

*NNIN REU Principal Investigator: Dr. Edward T. Yu, Electrical and Computer Engineering, University of Texas at Austin*

*NNIN REU Mentor: Ping-Chun Li, Electrical and Computer Engineering, University of Texas at Austin*

*Contact: adamj.mcmullen@gmail.com, ety@ece.utexas.edu, pcutexas@gmail.com*

## Abstract:

Multi-junction solar cells are the current leaders in efficiency since they reduce thermal losses by employing series-connected sub-cells with different bandgap energies. However, they are costly to produce and limited by current matching, because each solar cell is connected in series with one another. One alternative is to simply split light into ideal bandwidths and tailor separate photovoltaic modules to each bandwidth. Conventional dichroic mirrors can selectively split light by reflecting certain bandwidths while transmitting others. However, these mirrors do not operate well under different angles of incidence, which is critical for concentrated photovoltaics. Simulations show that metasurface structures can achieve similar characteristics to those of conventional dichroic mirrors while remaining resilient to the angle of incidence (AoI). Two such structures were created using electron beam lithography and were subject to transmittance testing. We proposed a low-loss, AoI-resilient single-layer metasurface dichroic mirror that could split light into ideal bandwidths for such a solar module. Simulation and experimental data show promising results, however, a multi-layer structure may be more ideal.

## Introduction:

Multi-junction solar cells are highly efficient (max around 43.5%), but they are quite costly and limited by current matching since each sub-cell is connected in series. Alternatively, dichroic mirrors could be used to split light into different bandwidths and separate photovoltaic modules could collect energy specific to each bandwidth. Figure 1 shows a sample apparatus that could be used to split incoming light into separate bandwidths for concentrated solar energy collection.

Conventional dichroic mirrors can split light into separate bandwidths. However, these mirrors do not operate well under non-normal incident angles. When using concentrated photovoltaics, the AoI of light constantly varies due to the high concentration. Simulations show that metasurface dichroic mirrors have characteristics similar to those of conventional dichroic mirrors while remaining resistant to the AoI.

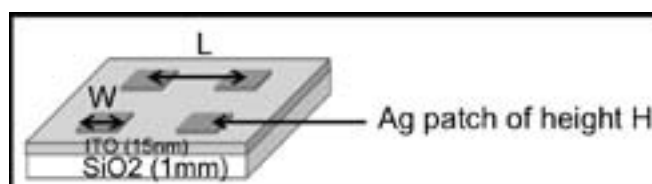
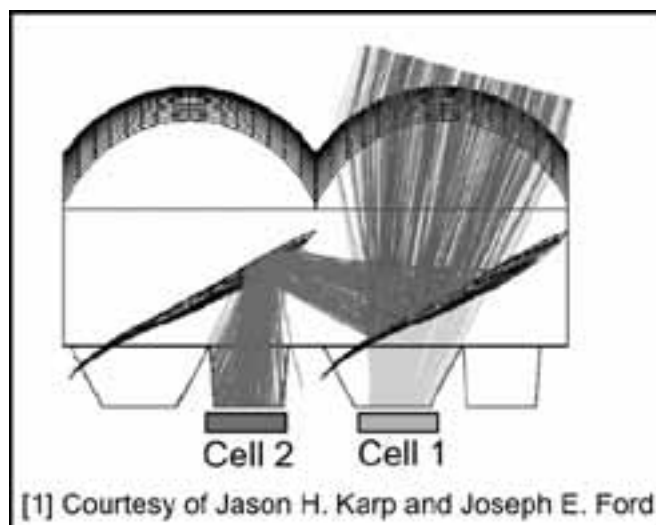


Figure 2: Idealized periodic section of the metasurfaces that were simulated and constructed.



[1] Courtesy of Jason H. Karp and Joseph E. Ford

Figure 1: Possible solar concentrator apparatus that depicts both the concentration and splitting of light.

## Experimental Procedure:

After extensive simulations of a single-layer structure using RSoft DiffractMOD, as depicted in Figure 2, we decided to create two structures. Structure 1 was defined by  $W = 100$  nanometers (nm),  $L = 200$  nm, and  $H = 40$  nm. Structure 2 by  $W = 200$  nm,  $L = 400$  nm, and  $H = 40$  nm. The structures were created in four steps: (1) Coating the substrate (1 mm  $\text{SiO}_2$  with 15 nm ITO on top) with positive resist, (2) Using electron beam lithography to design the patterns and developing the sample, (3) Using electron beam evaporation to deposit 2 nm of Ge (adhesion layer) and then 40 nm of Ag on the sample, and (4) Lift-off of the excess deposition.

The structures were then tested using a device that consisted of a light source, a diffraction grating, a monochromator to select a specific wavelength of light, and a detector. The light was first shone (under TM polarization) through an empty hole to the detector. This calibration data was recorded, and then the sample was placed on the sample holder such that light could shine through it. By comparing the initial light that passed through empty space to that which passed through the sample, we calculated the transmittance of our samples. Additionally, the sample holder could rotate, allowing for calculations at different AoI.

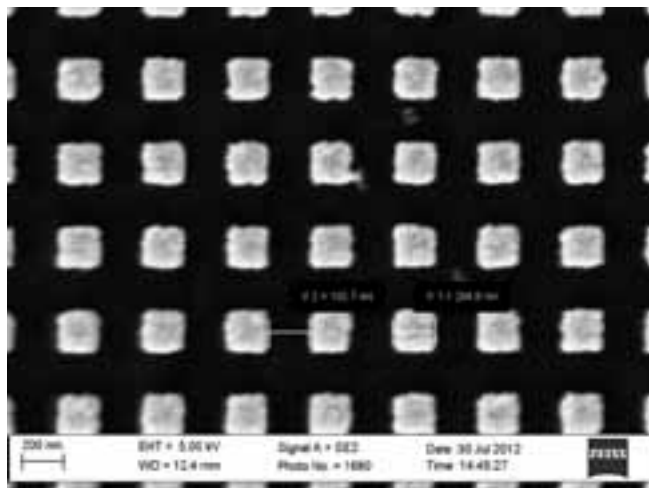


Figure 3: SEM image of the 200 nm structure.

### Results and Conclusions:

Both samples were successfully fabricated. Figure 3 shows a close up of the 200 nm structure, with measurement bars. However, after thorough testing, the samples became damaged, and the subsequent data collection began to deteriorate in accuracy. Regardless, useful data was collected.

Figure 4 depicts the transmittance graphs for the experiments using the 100 nm structure. All data was collected under TM polarization. Dichroic mirrors were relatively sensitive to the AoI. Their transmittance dip (or reflectance peak) significantly shifted as the AoI increased. The simulations and experiments with the 100 nm structure showed a transmittance dip that was resilient to the AoI. However, the actual trend did redshift a bit more than predicted, and the dip was not as strong as predicted. This was probably due to sample damage, as this sample tended to somewhat rub off while testing. Regardless, the structure remained more resilient to the AoI than conventional dichroic mirrors.

### Future Work:

Multi-layer structures may be more ideal for such a spectral splitting apparatus. In [2], the double-layer structure studied has a transmittance dip with a wider bandwidth dip, which is more similar to the conventional dichroic mirror. Furthermore, this structure was resistant to the AoI up to about 40°. By using metasurface dichroic mirrors, according to [3], a concentrated solar module with four mirrors and five photovoltaic collectors may have an estimated efficiency around 43%.

### Acknowledgments:

I would like to thank Dr. Edward T. Yu for working with me on this project throughout the summer. His input was invaluable, and he was a pleasure to work with. Additionally, Ping-Chun Li deserves the highest of praise for dealing with a recent college freshman graduate. I am thankful for his experience, courtesy, and time devoted to my understanding of this project. Furthermore, thanks to Jean L. Toll, Ms. Christine P. Wood, and Dr. Marylene Palard for organizing the internship and keeping me on track. Additionally, I would like to thank the National Science Foundation and the National Nanotechnology Infrastructure Network Research Experience for Undergraduates Program for funding.

### References:

- [1] J. H. Karp and J. E. Ford; "Multiband Solar Concentrator Using Transmissive Dichroic Beamsplitting," Proc. SPIE 7043, 70430F1-8 (2008).
- [2] Li, Ping-Chun, and Edward T. Yu. "Wide-Angle Wavelength-Selective Multilayer Optical Metasurfaces Robust to Interlayer Misalignment." Unpublished Data (2012).
- [3] Green, M. A. and Ho-Baillie, A. (2010), "Forty three per cent composite split-spectrum concentrator solar cell efficiency." Prog. Photovolt: Res. Appl., 18: 42-47. doi: 10.1002/pip.924.

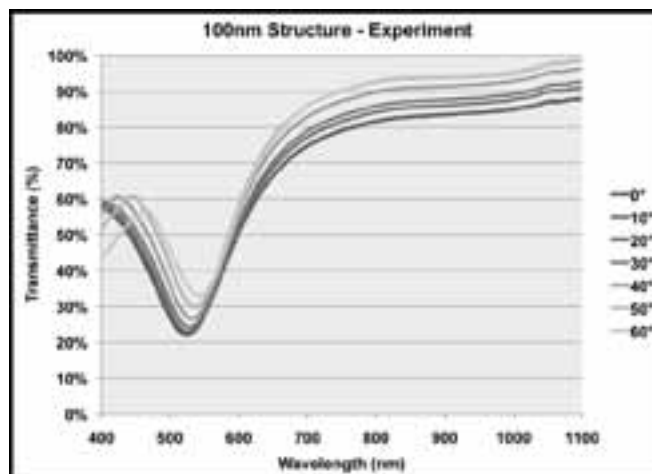


Figure 4: Graph of the 100 nm experiment structure depicting the resilience of the transmittance dip to the AoI.

# Strain Color Coding Using Localized Surface Plasmon Resonance of Gold Nanoparticles

**Jared Newton**

**Biomedical Engineering, Texas A&M University**

*NNIN REU Site: Nano Research Facility, Washington University in St. Louis, St. Louis, MO*

*NNIN REU Principal Investigator: Dr. Parag Banerjee, Department of Mechanical Engineering and Materials Science, Washington University in St. Louis*

*NNIN REU Mentor: Sriya Banerjee, Department of Mechanical Engineering and Materials Science, Washington University in St. Louis*

*Contact: jarednewton33@tamu.edu, parag.banerjee@gmail.com, banerjees@seas.wustl.edu*

## Abstract:

Current methods for measuring and quantifying strain are generally only applicable at the macro and upper micro scale. Consequently many disciplines that require small scale strain measurements rely on simulation-based data. A previous study of localized surface plasmon resonance (LSPR) of gold nanoparticles (AuNP) led to the development of a plasmon ruler equation that relates plasmon peak shift with interparticle separation and particle diameter.

The current project optimizes this methodology to develop a novel technique involving AuNP that could potentially be used for lower micro and nano scale strain measurements. AuNP were deposited onto polydimethylsiloxane (PDMS) using thermal evaporation. Strain was systematically applied to the coated PDMS and the plasmon shift was measured using ultraviolet-visible (UV-Vis) spectroscopy. Six different AuNP depositions were investigated to determine the effect of AuNP size and distribution on the sensitivity of strain measurements: 2, 5, 9, 12, 17, and 20 nm. The 9 nm deposition sample allowed for sensitive measurements between 0.2 and 16.5 percent strain. If this method was applied to a smaller scale,

it would allow for sensitive nano scale strain measurements. This novel approach could lead to the development of a new style of strain gauge that could quantify deformation over extremely small distances.

## Introduction:

Strain is a unit-less quantification of localized deformation as a material is stretched or compressed. Current devices used to measure strain are extremely useful and accurate for measuring macro and upper micro level strain. However, size constraints, temperature dependence, single directional capabilities, and adhesion interference makes it difficult to apply these methods for use at the micro and nano scale.

LSPR is a phenomenon that occurs as the electrons of metal nanoparticles resonate with respect to one another resulting in the absorption of the light with a frequency equal to that of the respective plasmonic resonance [1]. Jain, et al., modeled this interaction with the development of the plasmon ruler equation which allows for the calculation of interparticle separation based on plasmonic shift as modeled in Figure 1 [2]. The current project optimized this interaction in order to show that LSPR could be used in order to quantify micro and nano strain.

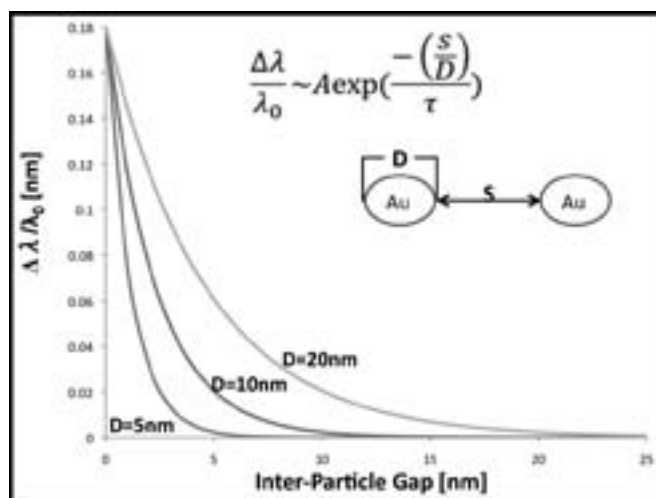


Figure 1: Plasmon ruler equation modeling for different particle diameters.

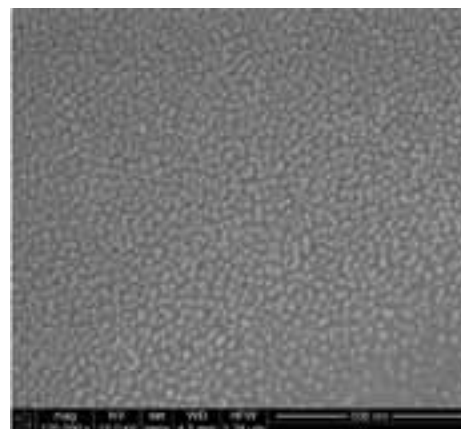


Figure 2: SEM image of thermally evaporated AuNP on glass.

### Experimental Procedure:

PDMS was prepared using a Slygard 184 Elastomer kit in a 9:1 ratio of elastomer to hardener. The PDMS mixture was first placed in vacuum below and brought back to atmospheric pressure multiple times to ensure that all bubbles were voided, and then allowed to cure at 100°C for 35 minutes until thoroughly hardened.

Each cured PDMS sheet was cut into dog-bone structures typically used for strain testing. Next, AuNP were deposited on the samples using thermal evaporation. Figure 2 shows two scanning electron microscope (SEM) images of thermally evaporated AuNP on glass, demonstrating the uniformity of distribution achieved. Six samples, each with increasing depositions, were produced; 2, 5, 9, 12, 17, 20 nm. The samples were mounted onto a designed strain holder and multiple strains were systematically applied. The absorbance spectrum during each stretch was observed and recorded using UV-Vis. A stationary camera was used to record an angle of rotation of the cylindrical piece of the holder during each stretch. The angle was then measured using ImageJ photo software and used to calculate the applied strain as is demonstrated in Figure 3. Four samples of each deposition, each placed in slightly different orientations within the thermal evaporator, were produced in order to determine reproducibility and sensitivity.

### Results and Conclusions:

Each sample was analyzed through observation of the changing plasmon peak with respect to the applied strain allowing for the following conclusions. A comparison of the unstretched samples showed increasing absorbance as well as a red-shift of the plasmon peak for each increasing deposition. Figure 4 shows the plasmonic shift data of one of the 5, 9, and 12 nm samples, which show conclusive evidence that the method was successful in measuring strain with blue-shifts of the plasmon peak for each increasing strain. The 17 and 20 nm samples yielded no apparent trends. It was first

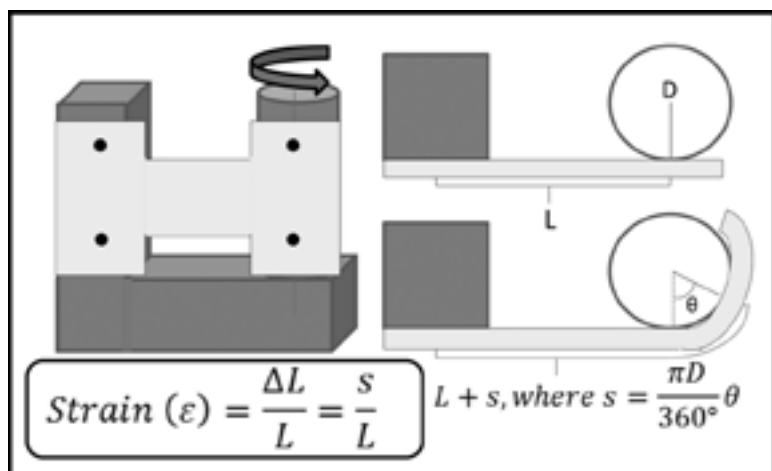


Figure 3: Strain holder setup and demonstration of strain calculation.

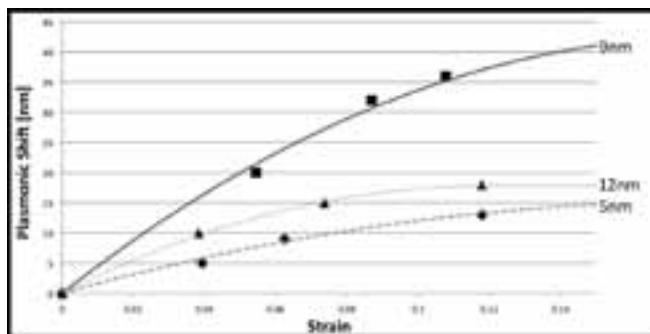


Figure 4: One of the 5, 9, and 12 nm AuNP deposition samples showing plasmon peak shift vs. strain applied.

concluded that there is an optimal range of deposition of AuNP for strain testing purposes. Second, the sample B of the 9 nm deposition was determined to be the most sensitive, allowing for deformation quantification between 0.2 and 16.5 percent strain. In our particular setup, this allowed for strain measurements between 200  $\mu\text{m}$  and 1 mm, however, if applied to a smaller scale, this method could allow for sensitive nano scale strain measurements.

### Future Work:

Further characterization of the procedure is necessary to determine the effects of deposition on sensitivity and repeatability. Continued experimentation needs to be conducted with attempts to control particle size and separation. This would theoretically allow for narrower plasmon peaks and thus more accurate readings of plasmon peak shifts. Last, using polarized light to perform absorption testing would allow for plasmon measurement along a single direction.

### Acknowledgements:

The author would like to thank the NNIN REU Program as well as the NSF for the opportunity and funding to perform research this summer. The author would also like to thank Dr. Banerjee and the members of the L.E.A.N laboratory as well as the Nano Research Facility and faculty at Washington University in St. Louis for their support and help.

### References:

- [1] Barnes, W.L., Dereux, A., Ebbesen, T.W., "Surface Plasmon Subwavelength Optics", *Nature*, vol. 424, pp. 824-830, 2003. DOI: 10.1038/nature01937.
- [2] Jain, P.K., Wenyu, Huang, Mostafa E.A., "On the Universal Scaling Behavior of the Distance Decay of Plasmon Coupling in Metal Nanoparticle Pairs: A Plasmon Ruler Equation", *Nano Letters*, vol. 7, pp.2080-2088, 2007. DOI: 10.1021/nl071008a.

## Sub-Wavelength Gratings for Multi-Spectral Infrared Detection and Imaging

Katherine Nygren

Physics and Mathematics, Saint Olaf College

NNIN REU Site: Lurie Nanofabrication Facility, University of Michigan, Ann Arbor, MI

NNIN REU Principal Investigator: Prof. Jamie Phillips, Department of Electrical Engineering and Computer Science, University of Michigan, Ann Arbor

NNIN REU Mentor: Justin Foley, Applied Physics Program, University of Michigan, Ann Arbor (2008 NNIN REU at the University of Minnesota)

Contact: [nygrenk@stolaf.edu](mailto:nygrenk@stolaf.edu), [jphilli@umich.edu](mailto:jphilli@umich.edu), [foleyjm@umich.edu](mailto:foleyjm@umich.edu)

### Abstract:

Infrared spectral filtering based on Fabry-Perot etalons requires high reflectance, low loss mirrors to enable next generation infrared imaging and spectroscopy. A silicon on air (Si/air) diffraction grating was investigated as a broadband mirror in the long wavelength infrared (8-12  $\mu\text{m}$ ) based on the concept of high refractive index contrast sub-wavelength grating (HCG). Conventional and Bosch process reactive ion etches (RIE) were optimized and optical responses compared. The sidewall profiles obtained from the conventional RIE were non-vertical while those from the Bosch process were vertical but scalloped. Fourier transform infrared (FTIR) spectroscopy was used to characterize the gratings and the results compared to the COMSOL Multiphysics simulations. The grating reflectance was found to be insensitive to etch method differences and the suspended structure shows agreement with simulations despite bowing caused by design and fabrication processes.

### Introduction:

Thermal and long wavelength infrared (8-12  $\mu\text{m}$ ) imaging is used for surveillance and targeting when visibility is limited. Current imaging systems are restricted due to their intensity-based imaging method. Better object distinguishability of future systems requires spectral filtering capabilities of the long wavelength infrared (LWIR), which has further applications in spectroscopy. Fabry-Perot (FP) etalons use two low-loss high reflectance mirrors separated by a multiple of a half wavelength of the desired frequency to filter light, as seen in Figure 1a. The resonant wavelength transmits, while the other wavelengths destructively interfere. Higher mirror reflectance yields a narrower transmittance band and correspondingly a more selective filter. Distributed Bragg reflectors (DBRs) are conventionally used as low loss mirrors for lasers and spectral filters, however, fabrication of layer thicknesses required for the LWIR is difficult to reliably achieve due to wafer uniformity and curvature issues.

High refractive index contrast sub-wavelength gratings (HCGs) can be used as alternative broadband low loss mirrors in FP etalons requiring only two dielectric layers. HCGs consist of a high refractive index grating on top of a low refractive index layer. The grating dimensions are smaller than the wavelengths of the LWIR spectrum. HCGs are attractive candidates for broadband high reflectance mirrors required for effective FP etalon filtering.

### Experimental Procedure:

Figure 1b depicts the silicon on air (Si/air) HCG investigated. These materials have minimal loss in the LWIR and have a high index contrast (3.4/1.0). The gratings were fabricated on a silicon on insulator (SOI) wafer using standard photolithography, two methods of reactive ion etches (RIEs), a hydrofluoric (HF) etch, and critical point drying. The conventional RIE used a hydrogen bromide (HBr) plasma etch and an oxygen plasma clean to remove the photoresist. The second RIE used the Bosch process based on sulfur

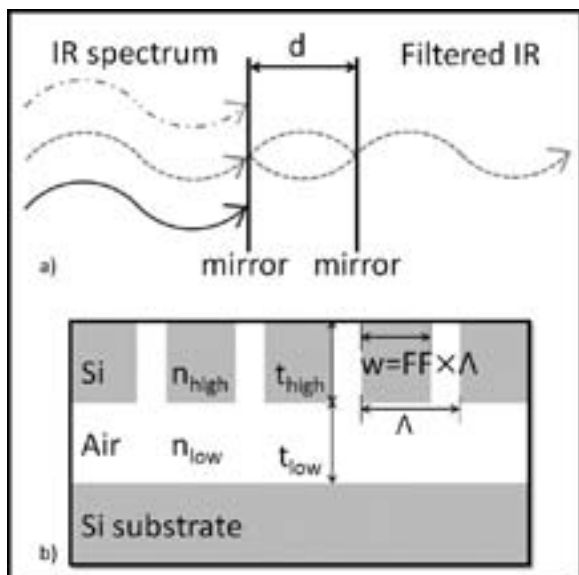


Figure 1: a) Diagram of a Fabry-Perot etalon. b) A two layer system consisting of high refractive index grating ( $n_{\text{high}}$ ) on top of a low refractive index material ( $n_{\text{low}}$ ). By changing the heights ( $t_{\text{high}}$  and  $t_{\text{low}}$ ), period ( $\Lambda$ ) and width ( $w$ ) of the grating, the response can be tuned.

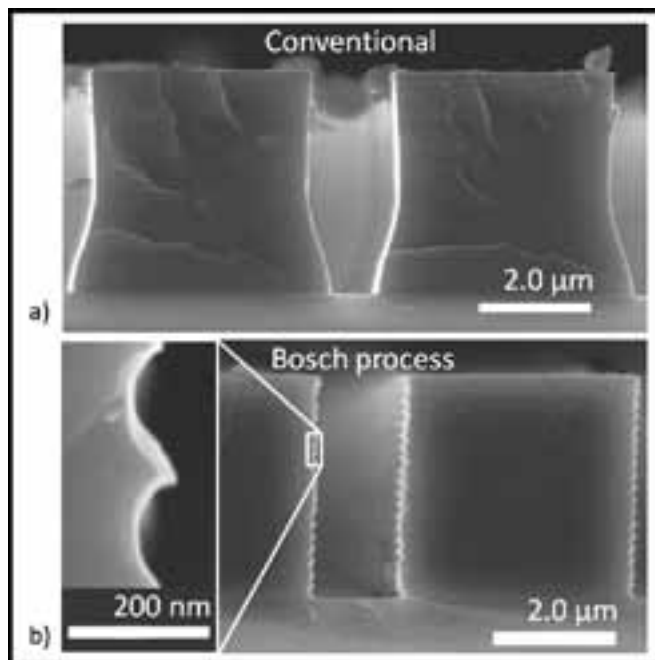


Figure 2: Cross-sectional SEM images showing; a) smooth but beveled conventional RIE sidewall profiles, and b) straight but scalloped Bosch process RIE sidewall profiles.

hexafluoride ( $\text{SF}_6$ ) as the etch gas, octafluorocyclobutane ( $\text{C}_4\text{F}_8$ ) as the passivation gas, and an oxygen plasma clean.

The HF etch was used to remove the sacrificial silicon dioxide ( $\text{SiO}_2$ ) from the SOI providing the suspended structure. A critical point dryer was subsequently used to minimize adhesion affects between the grating and the substrate.

Using a scanning electron microscope (SEM), cross-sectional images allowed for sidewall profile comparisons for etch optimization. The reflectance and transmittance of each grating were measured using Fourier transform infrared (FTIR) spectroscopy before and after the HF etch. Measurements were taken from three different locations on each sample.

### Results:

The SEM images show smooth, but beveled, sidewall profiles for the conventional RIE, whereas scalloped, but vertical, sidewalls for the Bosch process, as seen in Figure 2. The optical responses of the two gratings showed little difference before the sacrificial layer was removed. After the HF etch, the gratings bowed and touched the substrate 150  $\mu\text{m}$  from the edge of the grating due to gravity and adhesion. By reducing the suspension length, this problem can likely be mitigated. Figure 3 shows the similar optical responses of the two etch processes with the Bosch process response red shifted, possibly as a result of different heights of the air gap. The reflectance measurements at the edges gave good agreement with COMSOL Multiphysics simulated responses, as seen in Figure 4.

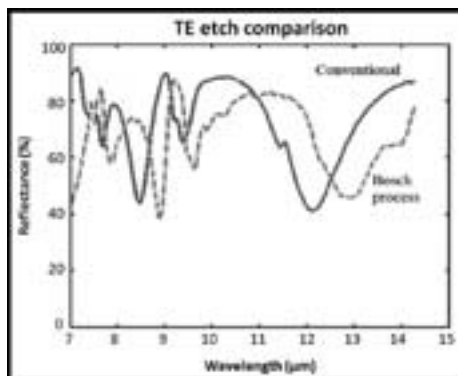


Figure 3: Optical responses of gratings produced by conventional and Bosch process RIEs are similar with the response from the Bosch process red shifted.

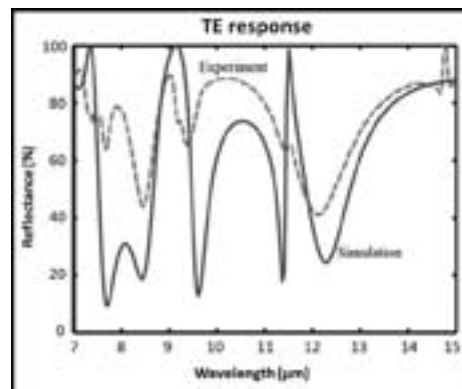


Figure 4: Experimental and simulated structure responses with peak agreement.

### Conclusions:

Si/Air HCGs were fabricated using conventional and Bosch process RIEs. The measured IR response seems insensitive to etch process differences and shows agreement with the simulated response. By further optimizing the suspended length, it is likely the bowing that was witnessed will be resolved.

### Acknowledgments:

I would like to thank my mentor, Justin Foley, and my principal investigator, Prof. Jamie Phillips, for their patience and willingness to teach. I would also like to thank the Lurie Nanofabrication Facility staff for assistance, especially Russ Clifford and Matt Oonk. I would like to acknowledge the NNIN REU Program and its staff Brandon Lucas and Trasa Burkhardt, as well as the NSF and the University of Michigan College of Engineering for supporting this effort.

### References:

- [1] Mateus, C. F. R.; "Ultrabroadband Mirror Using Low-Index Cladded Subwavelength Grating"; IEEE Photon. Technol. Lett. 16, 518 (2004).
- [2] Foley, J.; "Broadband long-wavelength infrared Si/SiO<sub>2</sub> subwavelength grating reflector"; Optics Lett. 37, 1 (2012).

## Top-Gated Graphene-Based Ultrafast Electro-Optic Modulators

Jacob M. Rothenberg

Physics, University of Rochester

NNIN REU Site: Colorado Nanofabrication Laboratory, University of Colorado, Boulder, CO

NNIN REU Principal Investigator: Thomas R. Schibli, Physics, University of Colorado

NNIN REU Mentor: Chien-Chung Lee, Physics, University of Colorado

Contact: jrothenb@u.rochester.edu, trs@colorado.edu, chienchunglee@gmail.com

### Abstract:

Graphene's universal linear optical absorption, extraordinary carrier mobility, and zero-gap band structure motivate its use as an electro-optic modulator. The optical absorption of graphene can be altered via electrostatic doping. This electrostatic doping is achieved by applying a gate voltage between graphene and a gate electrode in a thin film structure. Improving on a previously achieved back-gated model, a top-gated geometry was investigated due to its ability to accommodate applications requiring both transmissive and reflective modulators, including utilization in low-loss Bragg reflectors and monolithic fiber lasers. In return for this enhanced versatility, the top-gated device required direct deposition of the dielectric material on graphene, which can lead to destruction of the graphene. Dielectric media that can be deposited on graphene with minimal damage were explored, including alumina and silicon monoxide. In this work, a top-gated modulator using alumina as a gate dielectric was successfully fabricated. Alumina was effective in preserving graphene while also exhibiting strong dielectric properties.

### Introduction:

Electro-optic modulators are a fundamental component of most modern opto-electronic systems, ranging from telecommunications to solid-state lasers. The operating principle

of these modulators is the electro-optic effect, which is a change of a material's optical properties under the presence of an electric field. While many materials exhibit this effect, graphene is of particular interest due to its electrical properties, including extraordinary electron mobility. These properties mean that the electro-optic effect occurs at very high speeds in graphene, resulting in ultra-fast modulation. These extraordinary modulation speeds, coupled with the absence of phase distortion due to graphene's two-dimensional structure are in essence the motivation for graphene's use in electro-optic modulators.

### Experimental Procedure:

The fabrication process is outlined in Figure 1. Monolayer graphene grown by chemical vapor deposition (CVD) was transferred onto glass microscope slides by a wet transfer process. Metal electrodes were then deposited by thermal evaporation (20 nm Ti and 80 nm Al), and patterned using a positive photoresist and lift-off method. Titanium (Ti) was used to assist the adhesion of the aluminum (Al) layer on graphene and to reduce the contact resistance of the electrode on graphene. The graphene outside the ring-electrodes was removed by reactive-ion etching to minimize the device capacitance. A 220 nm thick aluminum oxide ( $\text{Al}_2\text{O}_3$ ) dielectric layer was deposited onto the graphene by electron-beam evaporation. A 200 nm silver layer was then grown by thermal evaporation, giving the device a reflective geometry. The silver film acted as both

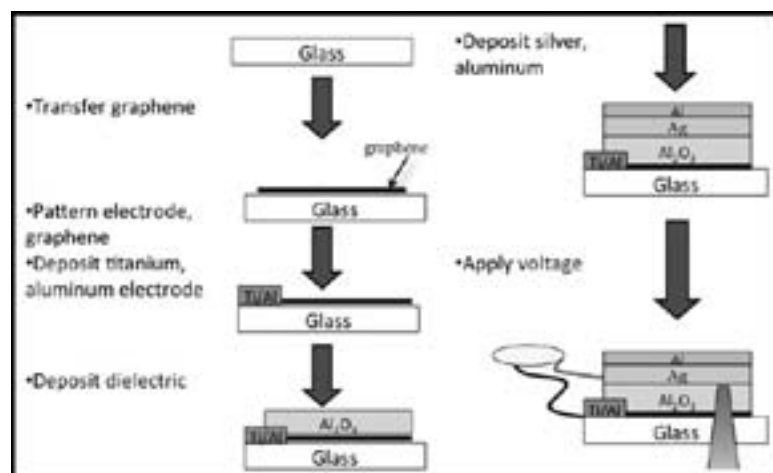


Figure 1: Major fabrication steps.

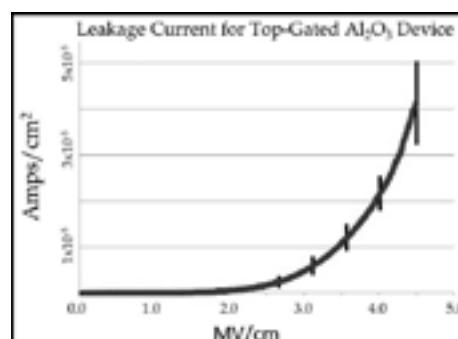


Figure 2: Typical behavior for the dependence of leakage current density on applied electric field for top-gated  $\text{Al}_2\text{O}_3$  devices.

a mirror and top-gate electrode. An additional Al layer was deposited to serve as a protective layer.

### Results:

The breakdown voltage of the devices was characterized by a two-point probe setup. Figure 2 shows the results from a fabricated device, which was durable under fields up to 4.5 MV/cm. Combined with the measured dielectric constant of  $\epsilon \approx 10.9$  of our  $\text{Al}_2\text{O}_3$  films, which was in agreement with earlier studies [1], this high breakdown field strength enabled substantial electrostatic doping, and hence, strong optical modulation. Devices fabricated using silicon monoxide (SiO) as a dielectric layer showed breakdown under fields of 0.5 MV/cm and a measured dielectric constant of  $\epsilon \approx 5.5$ . The superior dielectric properties of  $\text{Al}_2\text{O}_3$  over SiO made it clear that  $\text{Al}_2\text{O}_3$  was a more favorable dielectric for this device.

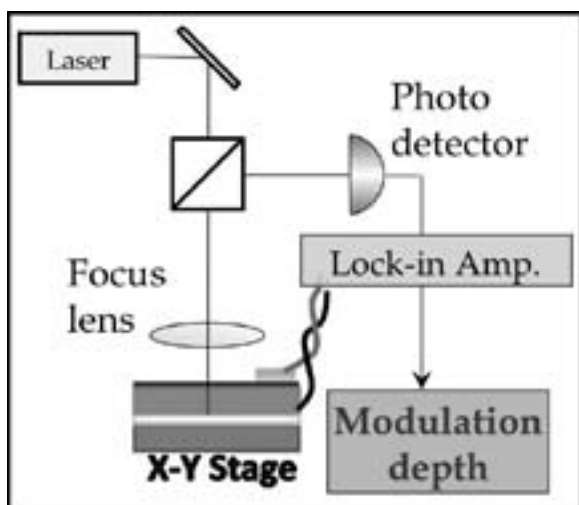


Figure 3: Setup used to measure modulation depth.

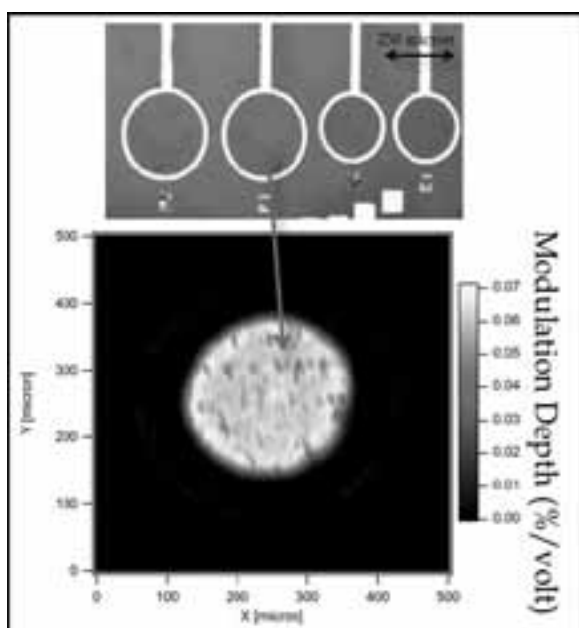


Figure 4: Top: SEM of several modulators on a chip. Bottom: 2D scan of modulation depth across one ring electrode.

The setup used to characterize the modulation depth is shown in Figure 3: A continuous-wave laser at 1.55  $\mu\text{m}$  wavelength was reflected off the sample, which was placed on a translational XY-stage. For each location on the sample the reflectivity change versus applied AC voltage was recorded. A resulting 2D modulation map is shown in Figure 4.

We observed uniform modulation across the active area, besides small processing defects that likely originated from the transfer of the graphene to the substrate. These defects were small enough so that they did not have a significant impact on the performance of the device. The consistent modulation depth across the graphene verified that the fabrication process did not substantially alter the electronic and optical properties of the graphene layer.

### Conclusions:

We have fabricated a top-gated graphene-based modulator. We found that  $\text{Al}_2\text{O}_3$  was a suitable dielectric due to its transmissivity, benign interaction with graphene during deposition, and strong dielectric properties. Most notably of these dielectric properties was the high breakdown voltage, which allowed for a considerable shift of graphene's Fermi level and large achievable modulation depths. We also saw uniform modulation across the active area, which confirmed that graphene remained intact during the fabrication process.

### Future Work:

More characterization, including a measurement of the modulation speed, is needed to further understand the effectiveness of this device. In addition, more work needs to be done to allow this device to be transmissive. This could be achieved by replacing the silver mirror with another layer of graphene, for example. A transmissive geometry has exciting applications including use in low-loss Bragg reflectors and monolithic fiber lasers.

### Acknowledgments:

I would like to thank the National Nanotechnology Infrastructure Network Research Experience for Undergraduates Program and the University of Colorado at Boulder for funding this project. Special thanks go to Chien-Chung Lee and Thomas Schibli for the invaluable guidance. I would also like to thank Bart Van Zeghbroeck, Jan Van Zeghbroeck, Tomoko Borsa, Bounkheana Chhun, Ian Haygood, Tzu-Min Ou, and Zefram Marks.

### References:

- [1] M.Y. Seo, et al., "Characterization of  $\text{Al}_2\text{O}_3$  films grown by electron beam evaporator on Si substrates"; Nanoelectronics Conference Publications 3rd International (3-8 Jan. 2010): 238-239.

## Volume Nano-Structured Optics for 3D Superresolution Imaging

**Aubrey Shapero**

**Electrical Engineering, Stanford University**

*NNIN REU Site: Colorado Nanofabrication Laboratory, University of Colorado, Boulder, CO*

*NNIN REU Principal Investigator: Dr. Rafael Piestun, Electrical, Computer, and Energy Eng., University of Colorado Boulder*

*NNIN REU Mentor: Anurag Agrawal, Electrical, Computer, and Energy Engineering, University of Colorado Boulder*

*Contact: ashapero@stanford.edu, rafael.piestun@colorado.edu, anurag.agrawal@colorado.edu*

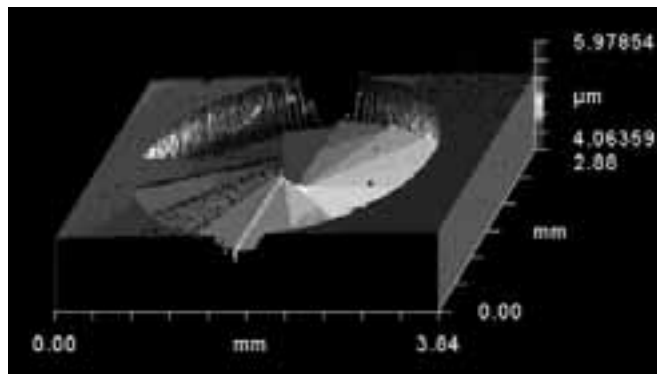


*Figure 1: 2D optical profilometry of a phase mask fabricated at the CNL. This is a computer generated model of the mask based off height map measurements. (See cover for full color version.)*

### Abstract and Introduction:

Superresolution microscopy is an imaging technique capable of resolution beyond the diffraction limit [1]. One way to overcome the diffraction limit is by imaging a sparse group of fluorescent molecules so that none or only a few of the neighboring molecules emit photons simultaneously. By repeating this process, an image can then be generated by precisely localizing all the molecules seen up to a given instant [2-4].

Superresolution is now limited by the ability to localize a single molecule. In this paper, we present a phase mask that can be inserted in the Fourier plane of a microscope between the object and the camera. The phase mask modifies the transfer function of the imaging system in such a way that information about a molecule's position can be extracted more effectively than with a clear aperture. The phase mask was etched into quartz using four binary masks to achieve sixteen distinct heights. An accelerated image template-matching algorithm is described to retrieve the molecules' location from the captured images.

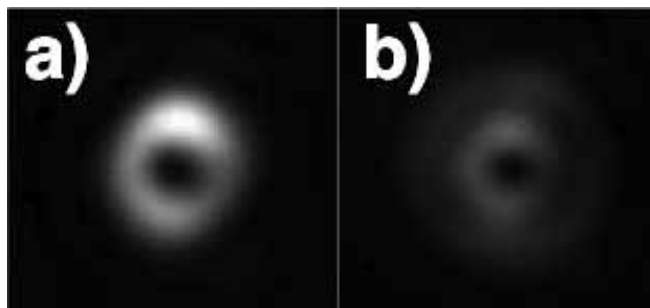


*Figure 2: PSF of the phase mask a) in focus, and b) out of focus.*

### Fabrication:

The choice material for the phase mask was quartz because it is transparent and sturdy. We started by cleaning a 1" × 1" quartz slide in nanostrip bath. Then a 40 nm thick layer of chrome was thermo-evaporated onto one side of the slide. Circular apertures were inserted into the chrome using photolithography and chemical etching. The chrome side was now considered the bottom for the following reactive ion etching (RIE) steps, to physically separate the two different processes.

The optical path length, and therefore the phase of light, is changed depending on the thickness of the quartz slide at any particular point. We selected certain depths with a technique known as binary masks: using  $N$  masks, we could select a location on our phase mask to a certain depth with  $N$  bits of precision. Each mask patterned an area in the phase mask to be depressed by a certain depth by photolithography. The following RIE step extruded vertically downward any exposed quartz. Thus  $N$  masks yield up to  $2^N$  distinct heights, but requires  $N-1$  precise alignments, a nontrivial task.

Increasing the number of distinct heights increases the diffraction efficiency. For example, 16 levels via four phase masks can potentially achieve 99% diffraction efficiency [5]. Figure 1 shows a 16-level phase mask fabricated at the Colorado Nanofabrication Laboratory (CNL) causing a phase shift from 0 to  $2\pi$ .

### Algorithm:

An accelerated image template-matching algorithm is described to retrieve a molecule's location from the captured images. The parameters for 3D superresolution imaging are  $X$ ,  $Y$ , and  $Z$ , where  $X$  and  $Y$  are the transverse coordinates of the captured image, and  $Z$  is depth along the optical axis. The centroids of the sparse blurs in the captured image set the  $X$  and  $Y$  coordinates. The  $Z$  coordinate is quickly found after normalizing for image size and intensity, in the following way. Rather than searching for the maximally matching template, the algorithm finds the highest matching weighted average of all the templates. If the  $Z$ -resolution of the templates is high enough, the algorithm should report a weighting vector with nonzero entries for only two neighboring templates. This is implemented by solving the following optimization problem:

$$\begin{aligned} \text{minimize} \quad & \|V_{imp}(Vw - v_0)\| \\ \text{subject to} \quad & \mathbf{1}^T w = 1 \\ & w \geq 0, \end{aligned}$$

where  $V$  is a library matrix in which every column is one of the template images reshaped into a vector,  $w$  is the free variable representing the weights of the templates,  $v_0$  is the measured image reshaped into a vector, and  $V_{imp}$  is a diagonal matrix allowing the pixels located nearer the center to be considered more important to match.

The best choice of objective function is not yet determined; both the  $l_1$  and the  $l_2$  norms seem promising in preliminary simulations but other convex functions may work too. The nonzero entries in the vector  $w$  correspond to certain distances with different weights. To solve the problem, we used CVX, a package for specifying and solving convex programs [6].

Another advantage this approach has over brute force template-matching is that sub template  $Z$ -resolution can be achieved.

### Results and Conclusions:

The phase mask was successfully fabricated and characterized by optical analysis and white light profilometry, showing that the measured 2D profile was close to the intended shape. In a photon-limited environment, such as molecular imaging, it is critical that the phase mask have high power transmission efficiency. The measured power transmission efficiency of the fabricated phase mask at the designed frequency was  $92.0 \pm 0.5\%$ . The point spread function (PSF) was confirmed to have a ring shape, as the various phase shifts should all destructively interfere at the center, shown in Figure 2. We have confirmed that our algorithm can match a template with simulated noise successfully.

### Future Work:

As future work, the optimization algorithm could be finalized, such as determining the objective function and the  $V_{imp}$  term. An antireflection coating could enhance the power transmission efficiency even further, increasing the signal-to-noise ratio. In addition, superresolution experiments could be performed, and the data could be processed.

### Acknowledgments:

I would like to thank Dr. Rafael Piestun, my mentor Anurag Agrawal, and Ginni Grover for their support and guidance. Funding and support were provided by the NSF, the NNIN REU Program, and the CNL.

### References:

- [1] Chan, W.-S., et al., "Super-resolution reconstruction in a computational compound eye imaging system," *Multidimensional Systems and Signal Processing*, 2007.
- [2] Betzig, E., et al., *Science* 313, 1642-1645 (2006).
- [3] Rust, M. J., et al., *Nat Meth* 3, 793-795 (2006).
- [4] Hess, S. T., et al., *Biophys J* 91, 4258-4272 (2006).
- [5] Dammann, H. "Spectral characteristic of stepped-phase gratings"; *Optik* 53, 409.
- [6] CVX Research, Inc. CVX: Matlab software for disciplined convex programming, version 2.0. <http://cvxr.com/cvx>, April 2011.

## CIS Nanocrystals with Inorganic Ligands for Photovoltaics Devices

**Cherrelle Thomas**

**Chemical Engineering, Howard University**

*NNIN REU Site: Microelectronics Research Center, The University of Texas at Austin, Austin, TX*

*NNIN REU Principal Investigator: Dr. Brian Korgel, Chemical Engineering, University of Texas at Austin*

*NNIN REU Mentor: Jackson Stolle, Chemical Engineering, University of Texas at Austin*

*Contact: cherrelle.thomas@yahoo.com, korgel@che.utexas.edu, cjstolle@utexas.edu*

### Abstract:

Films of copper indium diselenide ( $\text{CuInSe}_2$  or CIS) nanocrystals capped with inorganic ligands were studied for use in photovoltaic devices (PVs). CIS nanocrystals were synthesized by colloidal arrested precipitation with oleylamine capping ligands. Oleylamine was exchanged for inorganic metal chalcogenide complex (MCC) ligands. These nanocrystals were dispersed in dimethyl sulfoxide, enabling the formulation of a "solar ink" that was spray-coated onto molybdenum (Mo)-coated glass substrates. The nanocrystal films were thermally annealed under argon and limited sintering was observed. Typically, grain growth of CIS films requires high temperature ( $> 500^\circ\text{C}$ ) and Se-rich atmosphere.

### Introduction:

As energy demand continues to increase, technologies that can harness and convert sunlight to electricity efficiently and economically are becoming more and more needed. Photovoltaic (PV) devices convert light directly into electricity. Silicon solar cells currently dominate the PV market, but silicon-based PVs are still too expensive. New PV technology is needed to make PV solar energy cost-competitive with fossil fuels. Copper indium selenide (CIS) is one promising thin film semiconductor material for lower-cost PVs. One approach to CIS deposition with potentially very low cost is to generate solar inks of nanocrystals that can be deposited from solution under ambient conditions. Using this approach, CIS nanocrystal-based PVs have achieved power conversion efficiencies up to 3% without high temperature processing of the absorber layer [1, 2].

The relatively low device efficiencies have been due to organic ligands on the nanocrystals, which prevent agglomeration and allows solution processing but create an electrically insulating barrier between nanocrystals. Organic ligands can be replaced with inorganic metal chalcogenide complexes (MCCs) to improve electrical conductivity of nanocrystal films. Recently, PV devices have been made with inorganic ligand-capped nanocrystals, but with low efficiency [3].

One additional limitation was the need to process with hydrazine, which is environmentally unfriendly. We have been able to develop inorganic ligand-capped CIS nanocrystals that disperse in dimethyl sulfoxide (DMSO), a polar organic

solvent that is environmentally friendly and easier to handle than hydrazine, in the nanocrystal film processing and have used MCC ligands to cause grain growth in CIS nanocrystals without selenization.

We also examined the films after a high temperature heat treatment. One approach to obtaining higher efficiencies from nanocrystal absorber layers is to sinter them into crystalline films. Usually sintering requires Se vapor in addition to high temperature. Annealing the nanocrystal films at high temperature under Ar did lead to a small amount of crystal grain growth, presumably enabled by the inorganic Se-containing capping ligands.

### Methodology:

Colloidal oleylamine-capped CIS nanocrystals were synthesized by arrested precipitation as previously described [3, 4]. Ligand exchange was performed in a nitrogen-filled glove box by adding the nanocrystals to 0.5 ml of 0.25 M  $\text{In}_2\text{Se}_4$ -MCC ligand, and 3 ml of hydrazine. After stirring for two days, the nanocrystals were transferred from the toluene to the hydrazine phase and the toluene was decanted. The nanocrystals were precipitated by adding 8 ml acetonitrile, followed by centrifugation. The particles were redispersed in 1.5 ml of dimethyl sulfoxide (DMSO).

CIS nanocrystals dispersed in DMSO were spray-cast onto Mo-coated glass substrates heated to  $150^\circ\text{C}$ . The nanocrystal films were annealed in an argon atmosphere at  $500^\circ\text{C}$ - $600^\circ\text{C}$  for 20 minutes. PV devices were then fabricated and tested as described in the literature [2]. Nanocrystal films were also characterized by scanning electron microscopy (SEM) and x-ray diffraction (XRD).

### Results and Discussion:

**CIS Nanocrystals Before Sintering.** Figures 1 and 2 show transmission electron microscopy (TEM) images of oleylamine-capped CIS nanocrystals before and after exchanging with inorganic ligands. The nanocrystals are approximately 15 nm in diameter and do not change size after ligand exchange, but do appear to be slightly more prone to aggregation.

CIS nanocrystal films were deposited onto Mo-coated glass substrates and were annealed under Ar at temperatures between 500°C-600°C. Figure 3 shows an SEM image of the annealed nanocrystal film at 575°C and Figure 4 shows XRD data for nanocrystal films annealed at various temperatures. There was a small, yet noticeable, amount of sintering and crystal grain growth. The  $\langle 112 \rangle$  peak in the XRD patterns in Figure 4 became slightly sharper as well after annealing, consistent with grain growth. PV devices fabricated from these films showed only a small PV response with a very low device efficiency of only 0.2%. More device tests are required to determine whether these materials will be suitable for PVs.

### Conclusions:

CIS nanocrystal films capped with inorganic  $\text{In}_2\text{Se}_4$ -MCC ligands and dispersed in DMSO, which is not toxic like hydrazine, can be deposited safely under ambient conditions. These inorganic-capped CIS nanocrystals appear to exhibit sintering and crystal grain growth with high temperature annealing without Se vapor. The preliminary device tests using these nanocrystal films gave low efficiencies, but the materials require further study.

### Acknowledgements:

I would like to thank the following organization and people for making this experience come about: The National Nanotechnology Infrastructure Network Research Experience for Undergraduates (NNIN REU) Program, National Science Foundation (grant # IIP-1134849), IUCRC, The University of Texas at Austin, Korgel group, Dr. Marylene Palard, Christine Wood, Jeannie Toll, and Melanie-Claire Mallison.

### References:

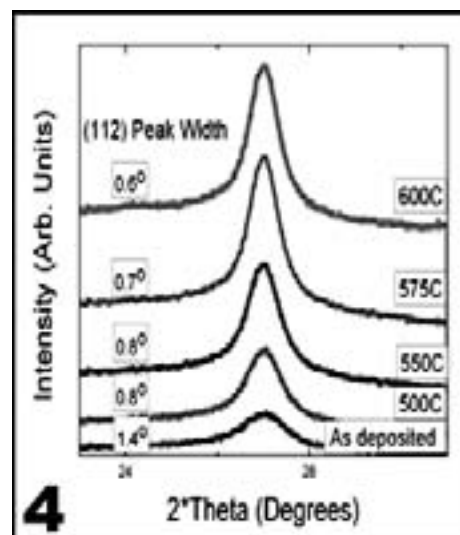
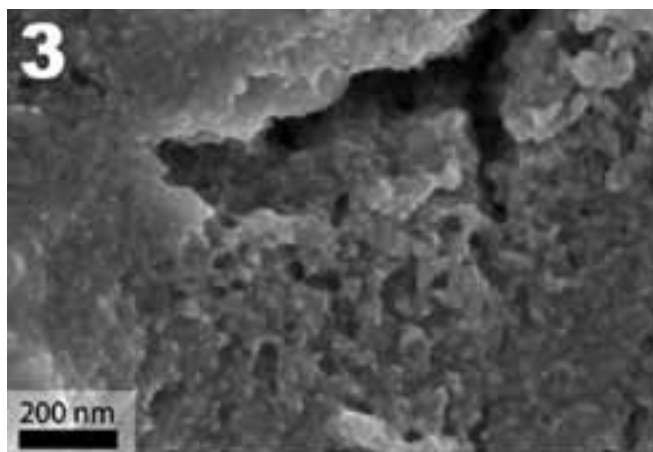
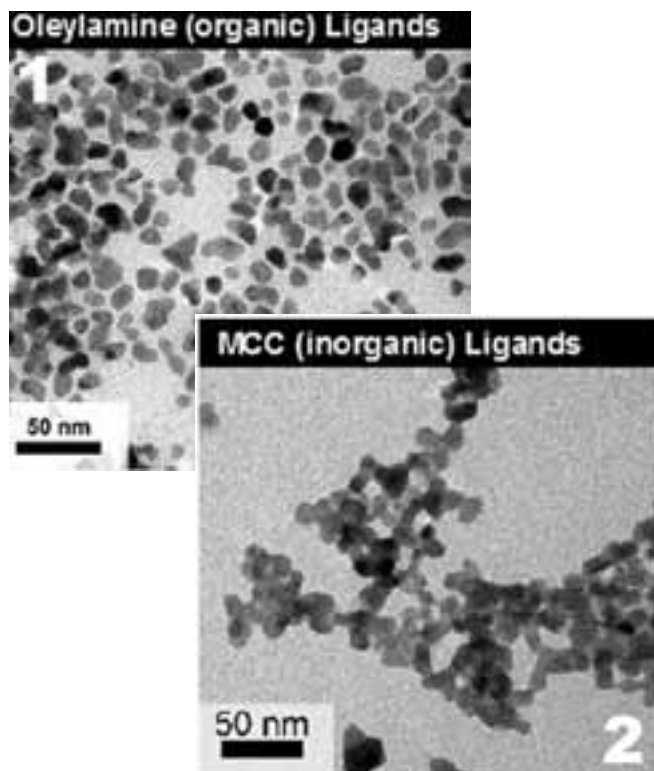
- [1] Panthani, M. G.; Akhavan, V.; Goodfellow, B.; Schmidtke, J. P.; Dunn, L.; Dodabalapur, A.; Barbara, P. F.; Korgel, B. A. *J. Am. Chem. Soc.* 2008, 130, 16770-16777.
- [2] Akhavan, V. A.; Goodfellow, B. W.; Panthani, M. G.; Reid, D. K.; Hellebusch, D. J.; Adachi, T.; Korgel, B. A. *Energy Environ. Sci.* 2010, 3, 1600-1606.
- [3] Stolle, J. C.; Panthani, M. G.; Harvey, T. B.; Akhavan, V. A.; Korgel, B. A. *ACS Appl. Mater. Interfaces*, 2012, 4, 2757-2761.
- [4] Jiang, Chengyang; Lee, Jong-Soo; Talapin, Dmitri V. *J. Am. Chem. Soc.* 2012, 134, 5010-5013.

Figure 1, top left: A TEM of oleylamine-capped CIS NCs.

Figure 2, top right: After exchange, aggregated MCC-capped CIS NCs.

Figure 3, middle: SEM of MCC-capped CIS NCs annealed at 575°C.

Figure 4, bottom: FWHM of the 112 peak of MCC-capped CIS NCs annealed from 500°C-600°C.



## Development of AirSpaced VIPA's for Use in Optical Coherence Tomography

**Timothy Welsh**

**Electrical Engineering/Physics, University of San Diego**

*NNIN REU Site: Stanford Nanofabrication Facility,  
Stanford University, Stanford, CA*

*NNIN REU Principal Investigator: Audrey Ellerbee,  
Electrical Engineering, Stanford University*

*NNIN REU Mentors: Tahereh Marvdashti and Heeyoon Lee,  
Electrical Engineering, Stanford University*

*Contact: twelsh-13@sandiego.edu, audrey@ee.stanford.edu,  
tahereh@stanford.edu, lhy2090@stanford.edu*

### Abstract:

Optical coherence tomography (OCT) is a high resolution, non-invasive technique for imaging scattering media (e.g., biological tissue). Similar to ultrasound, OCT nominally produces one-dimensional cross-sectional images called A-scans. The number of data points acquirable in an A-scan, and consequently imaging depth, is related to the spectral resolution of the detector being used. To increase the spectral resolution, we fabricated a low-cost cross-dispersing spectrometer based on an air-spaced virtually imaged phased array (VIPA). A VIPA is a slightly tilted etalon that allows for high angular dispersion of broadband incident light. The performance of a VIPA depends heavily on surface reflectivity, as well as cavity dimensions and the index of refractive of the cavity medium. VIPAs of various reflectivities were constructed via metal deposition on glass slides and optical flats; the reflectivities were measured via the Hitachi 4001 Spectrophotometer. Their finesse, FSR, and spectral dispersion characteristics were measured via photodetector. We show that sufficiently capable VIPAs can be constructed far more cheaply than commercial varieties, and will enable the development of high performance, affordable OCT systems.

### Introduction:

OCT is essentially a white light interferometer: in a Michelson configuration, polychromatic light travels different paths to a reference reflector (mirror) and multi-layered sample after passing through a beamsplitter. Reflected light from both paths interfere constructively at the detector for spatial frequencies corresponding to the position of layers in the sample. The resulting interferogram may be sampled in k-space either by using a spectrometer to collect wavelength information directly (spectral domain OCT), or as a function of time using a photodiode and swept-source laser (swept-source OCT). Similar to ultrasound, OCT nominally produces one-dimensional cross-sectional images called A-scans; 2D (B-scans) and 3D (C-Scans) images can be generated by raster scanning the OCT beam. The primary signal that OCT measures is the intensity of light that is back-scattered from various layers in the sample. Modern OCT systems offer resolutions of 1-10  $\mu\text{m}$  and 5-15  $\mu\text{m}$  in the axial and lateral dimensions, respectively.

In SDOCT, a range of wavelengths can encode depth information in your sample. Your imaging depth is dependent on the number of data points (pixels) that you can detect in the A-scan using a spectrometer. After the

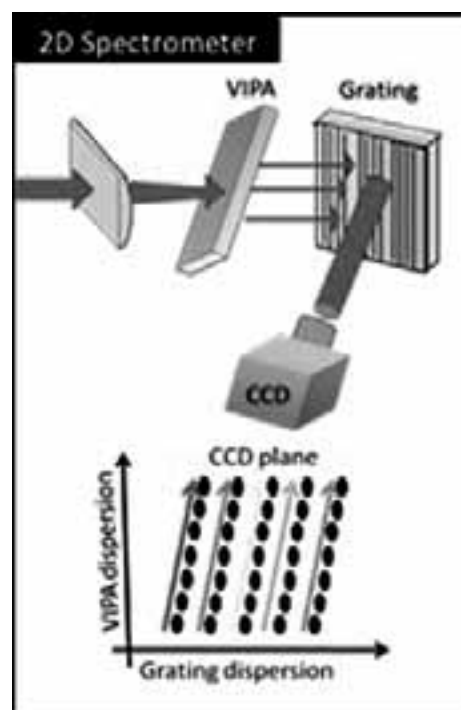


Figure 1: Schematic of VIPA operation in an SDOCT setup.

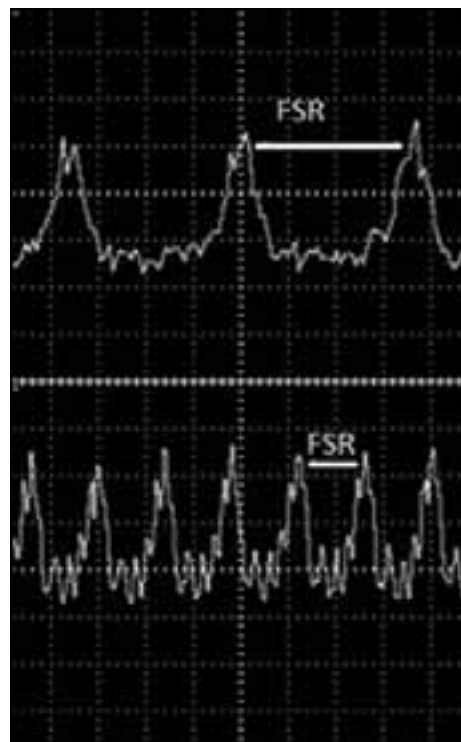


Figure 2: VIPA transmission peaks of 1.1 MHz (top) and 2 MHz (bottom).

beam passes through the VIPA it impinges on an ordinary diffraction grating. The product of this is a 2D dispersion pattern as seen in Figure 1; this allows more pixels on a detector to be utilized and thus increases the imaging depth of the OCT system.

A VIPA is a slightly tilted etalon that allows for high angular dispersion of light by wavelength. When a ray of light enters the VIPA, it undergoes multiple internal reflections between the partially reflecting plates. Each time a ray is reflected, it is partially transmitted, and the remaining reflected light undergoes a phase change. This leads to an important property of the VIPA, due to constructive and destructive interference: there is only a single angle at which a certain wavelength may propagate. Furthermore different wavelengths may overlap on the same position if the FSR of the cavity is sufficient.

### Procedure:

We hoped to reduce the cost of obtaining a VIPA by cheaply fabricating one from readily available equipment. In order to control the reflectivity of each side of the VIPA and thus control the finesse of the VIPA, silver was deposited on glass slides and optical flats via metal sputtering. An Innotech metal deposition system was used. The thickness of the deposited metal film could be precisely controlled by modifying the beam power and exposure time. In total we produced four different thicknesses: 50 nm, 15 nm, 10 nm, and 8 nm. These should have corresponded to reflectivities of 92%, 82%, 70%, and 50%, respectively; however of the slides we measured, we found this was not the case. We tested the 50 nm and 15 nm slides on the Hitachi 4001 spectrophotometer and found they corresponded to reflectivities of 75% and 50%, respectively.

We built a holder for the VIPA in order to test it. A Santec broadband swept source laser centered at 1300 nm was line-focused by a cylindrical lens; the beam then passed through

the VIPA into a normal focusing lens, which focused the VIPA output into the fiber-coupled photodetector. Since we used a swept-source laser, the photodetector read out was a series of peaks from which we gathered the finesse and FSR data.

### Results:

The VIPA we tested had a finesse of 4.5, which exceeded the goal of 4. As well, we found we could tune the finesse of the VIPA with an acceptable degree of accuracy. Figure 2 shows the observed transmission data for an FSR of 1.1 MHz and 2 MHz, respectively. This shows we were successful in meeting our design goals, having constructed a sufficiently capable VIPA for approximately \$300, a significant improvement over the original \$6000 price tag.

Additionally we have shown fabrication is low-cost and simple, and the drawbacks due to the air-spaced nature of the VIPA can be overcome and turned into an advantage with proper construction of a holding apparatus.

### Acknowledgments:

Michael Deal and the NNIN REU Program, along with the NSF for funding the project. Heeyoon Lee, Tahereh Marvdashti, and Audrey Ellerbee for guiding me and assisting me in this project. J. Provine for contributing his time and expertise at ungodly hours to make fabrication possible.

### References:

- [1] Lipson, S.G.; Lipson, H.; Tannhauser, D.S. (1995). *Optical Physics* (3rd ed.). London: Cambridge U.P. pp. 248.
- [2] Hernandez, G. (1986). *Fabry-Pérot Interferometers*. Cambridge: Cambridge University Press.
- [3] Xiao, S.; Weiner, A.M.; Lin, C.; 2004. *IEEE Journal of Quantum Electronics*(Vol. 40 No. 4).

# Enhancing the Luminescence Efficiency of GaSb-Based Dilute-Nitrides by Rapid Thermal Annealing

**Nathaniel Wendt**

**Computer Engineering, Gonzaga University**

*NNIN REU Site: Microelectronics Research Center, The University of Texas at Austin, Austin, TX*

*NNIN REU Principal Investigator: Seth Bank, Electrical and Computer Engineering, The University of Texas at Austin*

*NNIN REU Mentor: Hari Nair, Electrical and Computer Engineering, The University of Texas at Austin*

*Contact: nwendt@zagmail.gonzaga.edu, sbank@ece.utexas.edu, hnair@austin.utexas.edu*

## Abstract:

It has been shown that gallium antimonide (GaSb)-based dilute-nitrides display improved photoluminescence (PL) with *in situ* annealing in the molecular beam epitaxy (MBE) growth chamber under a Sb ambient. This improvement in luminescence efficiency translates into improved performance of optoelectronic devices, such as lasers, where this will lead to a reduction in threshold current densities. However, similar improvement in luminescence efficiency was not observed during *ex situ* annealing in a rapid thermal annealing (RTA) furnace. The ability to recreate similar annealing performance in the RTA would allow for increasingly efficient annealing. Upon further study, we determined that the degradation in PL resulted from over-annealing of the sample. Attributing this issue to the silicon (Si) carrier wafer, which has a higher band gap than the GaSb sample, infrared radiation was heating the sample more than indicated by the carrier wafer pyrometer measurement.

We mitigated this issue by integrating a low bandgap indium arsenide (InAs) layer into the carrier wafer and were able to ensure that our sample was below the temperature indicated by the pyrometer. This optimization allowed us to pinpoint the optimal annealing temperature more accurately and achieve PL performance similar to that of *in situ* annealing.

## Introduction:

Semiconductor lasers operating in the mid-infrared are highly sought after for their applications with infrared countermeasures, gas sensing, and free space optical communication. GaSb-based dilute-nitrides are an attractive solution for these applications, but require optical quality enhancement. Similar materials, namely gallium arsenide (GaAs)-based dilute-nitrides, have shown significant improvement

in optical quality by annealing [1]. Furthermore, it has been shown that *in situ* annealing in the molecular beam epitaxy (MBE) growth chamber has improved optical quality of GaSb-based dilute-nitrides materials. While this method has proved effective, the process is time intensive. This project aimed to dramatically improve the time efficiency of annealing by employing a rapid thermal annealing (RTA) furnace.

Since the pyrometer in the RTA measures the temperature of the carrier wafer, the material of this carrier wafer significantly affects the annealing process. Also, the lamps in the RTA emit photons over a wide energy spectrum. Si, with a bandgap of 1.12 eV at 300 K, is less responsive to temperature than the GaSb-based sample at approximately 0.73 eV at 300 K. Photon energies between these two bandgaps (0.73 eV to 1.12 eV) are absorbed by the sample and not the carrier, leading to overannealing. Overannealing has been shown to considerably degrade the optical quality of GaAs-based dilute-nitrides [2]. This underscores the need for a carrier wafer of equal or lower bandgap than the sample so that the carrier wafer is at the same temperature as the sample.

## Experimental Procedure:

Figure 1 shows the sample structure that was used for the annealing studies. Annealing was carried out at varying temperatures for one minute in a AW 610 RTA furnace under a nitrogen ambient. We used two different carrier wafers for the annealing studies: InAs (bandgap 0.354 eV) and Si (bandgap 1.12 eV). A Si proximity cap was utilized to prevent Sb loss from the sample surface. Optical quality was characterized by use of the photoluminescence (PL) lab with a diode pumped solid-state laser (DPSS) operating at 532 nm. The PL spectrum was obtained using a grating monochromator and an InSb



Figure 1: Sample structure used for annealing studies.

photodetector cooled to 77 K. All PL scans were scaled to a standard sample for comparison.

### Results and Conclusions:

Figure 2 shows the increased responsiveness of the InAs carrier wafer from constant lamp intensity in the RTA than GaSb and Si. This indicates that when annealing with a Si carrier wafer, the sample temperature may be significantly higher than the temperature indicated by the RTA pyrometer leading to overannealing.

We were able to reproduce optical quality enhancement within 17% of *in situ* annealing with the InAs carrier wafer. Figure 3 illustrates this considerable improvement over the Si carrier wafer that was within 33% of *in situ* annealing. We believe that this improvement was due to the lower bandgap of the InAs carrier wafer. By ensuring that the sample temperature was equal to or lower than the carrier wafer, we were able to achieve better temperature feedback, and thus, avoid overannealing.

### Future Work:

These studies should be continued by more precisely optimizing the annealing temperatures to more closely replicate or improve upon *in situ* annealing. Additional study would investigate various sample structure variations and their effects on annealing effectiveness.

### Acknowledgements:

I would like to extend special thanks to Seth Bank and Hari Nair for their continual and extensive support throughout this project. I would also like to thank the other members of the LASE group for their advice, along with the National Science Foundation and the National Nanotechnology Infrastructure Network Research Experience for Undergraduates (NNIN REU) program.

### References:

- [1] H.P. Xin, K.L. Kavanagh, M. Kondow, and C.W. Tu; "Effects of rapid thermal annealing on GaInNAs/GaAs multiple quantum wells"; Journal of Crystal Growth, 201/202, 419-422 (1999).
- [2] Seth R. Bank, Homan B. Yuen, Hopil Bae, Mark A. Wistey, and James S. Harris, Jr; "Overannealing effects in GaInNAs(Sb) alloys and their importance to laser applications"; Applied Physics Letters, 88, 221115 (2006).

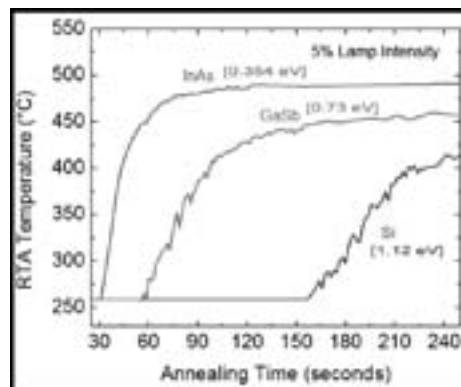


Figure 2: Various carrier wafer responses to constant RTA lamp intensity. With decreasing bandgap the response of the carrier wafer improves.

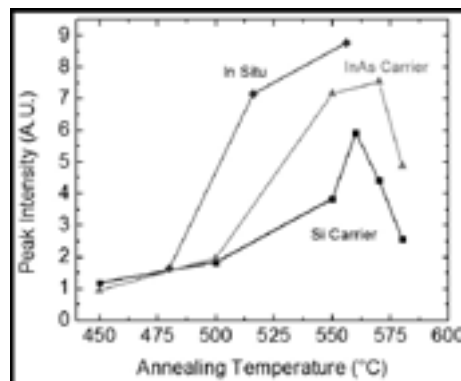


Figure 3: Si and InAs carrier wafer annealing as compared to *in situ*.

## Electrically and Optically Obtaining $Q$ of High Stress SiN Devices

**Patrick Yu**

**Engineering, University of North Texas**

*NNIN REU Site: Cornell NanoScale Science and Technology Facility, Cornell University, Ithaca, NY*

*NNIN REU Principal Investigator: Prof. Jeevak Parpia, Department of Physics, Cornell University*

*NNIN REU Mentors: Vivekananda Adiga, Department of Applied and Engineering Physics, Cornell University;*

*Roberto De Alba, Department of Physics, Cornell University; Rob Ilic, Cornell NanoScale Facility, Cornell University*

*Contact: pa.yu@hotmail.com, jmp9@cornell.edu, vpa8@cornell.edu, rd366@cornell.edu, rob@cnf.cornell.edu*

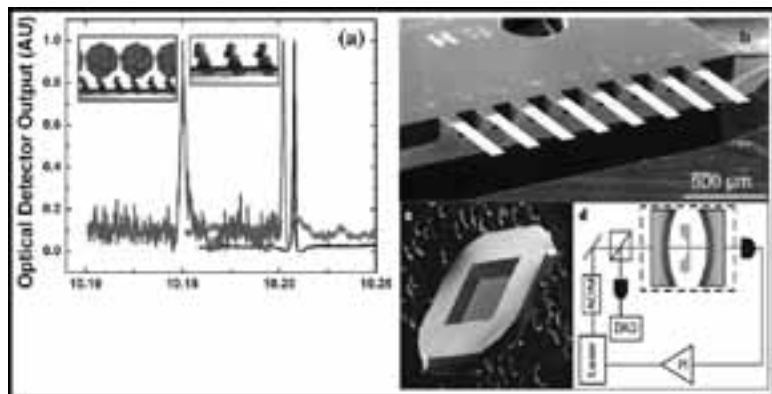


*Figure 1: (a) Virus detection method [1]. (b) Chemical sensor [2]. (c) Device used in (d) an optomechanical experiment [3].*

### Abstract:

High-stress silicon nitride (SiN) membranes show extremely high mechanical quality factors ( $Q$  of up to 4 million) and are useful for applications in resonant sensors, oscillators and optomechanical experiments. Here we fabricated high  $Q$  stoichiometric SiN membranes by depositing SiN using a low pressure chemical vapor deposition (LPCVD) process followed by back etching of a pre-patterned Si wafer. Monolayer graphene and thin gold pads were deposited onto this suspended membrane so as to create a conductive region that would enable the capacitive readout of the resonant motion. Amplitude of motion in resonance is usually detected using interferometric means in a custom built laser setup. The optical readout is to be compared to the electrical readout where the amplitude of resonant motion is detected by passing a source-drain current through the graphene via wire-bonded gold pads. The resonant motion should modulate the resistance of the graphene. The readouts display  $Q$  factors of the composite resonator as high as 100,000. We concluded that electrically active SiN resonators maintained the ultra-high  $Q$  and therefore are useful for the above-mentioned applications.

### Introduction:

Microelectromechanical (MEMS) devices are well-suited for many applications. Because of high resonance frequencies, high quality factors ( $Q$ ), and low masses, MEMS resonators can be used to probe the limits of quantum mechanics that larger resonators cannot. In addition, MEMS devices are more effective in terms of miniaturization, power conservation, and force sensitivity [1]. Future applications of these devices include usage as signal processors, oscillators, and improved sensors in pressure, temperature, charge, spin, and mass [2].

It has been previously reported that the  $Q$  of high stress SiN devices has reached up to 4 million, making them ideal for the aforementioned applications [4, 5]. High stress SiN devices are often studied in optomechanical experiments due to their high  $Q$  factors. However, we wanted to also perform electrical experiments on the high stress SiN devices so as to read them out electrically rather than optically.

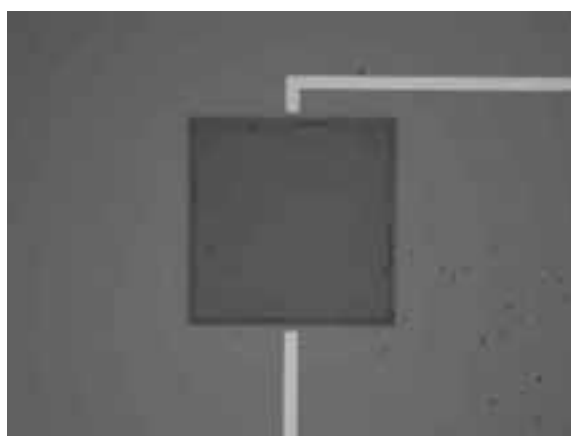


*Figure 2: An optical image of a  $300\ \mu\text{m} \times 300\ \mu\text{m}$  membrane device on a  $60\ \text{nm}$  thick nitride layer covered with  $0.3\ \text{nm}$  of monolayer graphene with  $30\ \text{nm}$  of gold.*

### Fabrication Process and Methodology:

The first step in our fabrication process was to use a thermal oxidation process to grow 1  $\mu\text{m}$  of silicon oxide ( $\text{SiO}_2$ ) followed by a deposition of 60 nm stoichiometric nitride ( $\text{Si}_3\text{N}_4$ ), using a LPCVD process. We created our suspended membranes using plasma and KOH etches of the back side of the wafer. Then, graphene was transferred and patterned on these suspended membranes. Electrical contacts to the graphene were achieved by gold deposition, followed by lift off. The buffered oxide etch was used to remove the oxide layer to create the high stress nitride membrane.

We used an electrical drive to actuate the resonant motion of the membrane, and detected that resonance electrically and optically. The electrostatic drive was produced using a combination of DC and AC voltages. The piezo-controlled mirror was charged with both DC and AC voltage while the membrane was grounded. In the optical setup, the amplitude of this reflectance change at resonance depended directly on the physical motion of the membrane and the position of the membrane with respect to the mirror. In the electrical setup, a DC voltage source was used to cause a source-drain current to detect the resonant motion of the membrane.

### Results:

The resonant frequency decreased as the gate voltage was swept from 0 V to 30 V (or 0 V to -30 V) due to capacitive softening. In capacitive softening, as the voltage increased, the membrane was attracted to the fixed electrode encountering a larger field gradient. The field gradient resulted in a force that opposed the device's mechanical restoring force, leading to a decrease in resonant frequency. Motion of the piezo-controlled mirror towards the device also caused the electric field gradient to increase, which decreased the resonant frequency.

Oscillations in both resonant frequency and amplitude of the resonant motion are due to the absorption of the light by graphene membrane.  $Q$  factors of up to 100,000 were detected with our devices.

### Conclusions:

We are certain that our optical and electrical experimental setups are fully operational. Now that we can optically detect resonant motion using an electrical drive, we will work on electrically detecting  $Q$  by passing current through gold contact pads that will act as the source and drain of the current. After successfully fabricating high-stress SiN devices using  $\text{SiO}_2$  as a protective layer, we were able to perform optomechanical experiments with our current optical setup. In these optical mechanical experiments, we have not only been able to obtain  $Q$  factors of up to 100,000, but we have also seen interesting phenomena such as capacitive softening and the photothermal effect in action.

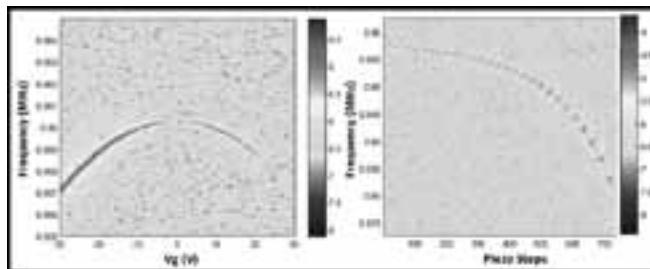


Figure 3: Both graphs depict capacitive softening, but the image on the right illustrates the photothermal effect due to optical back action.

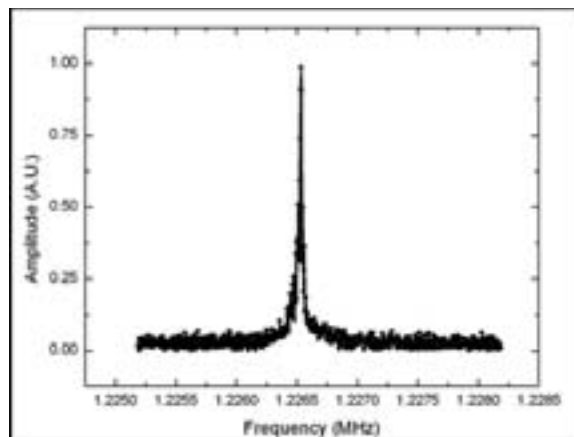


Figure 4: The Lorentzian curve of the resonant frequency is used to determine the  $Q$  factor which, in this case, is 90,000.

### Future Work:

Long-term goals are to conduct  $Q$  measurements at near absolute zero temperatures (30-50 mK) so as to optimize  $Q$  for any sort of devices and to study other dissipation mechanisms caused by other factors such as clamping.

### Acknowledgements:

I would like to thank the National Science Foundation for grants DMR-0908634, ECCS-1001742, and DMR 1120296. I would also like to thank the National Nanotechnology Infrastructure Network Research Experience for Undergraduates (NNIN REU) Program and the Cornell NanoScale Facility for making this research possible.

### References:

- [1] Ilic, et al., Appl. Phys. Lett., V. 85(13), 27 (2004).
- [2] M. K. Baller, et al., Ultramicroscopy 82 (2000), 1-9.
- [3] Thomson, et al., Nature, Vol 452, 72-76, 2008.
- [4] Adiga, et al., Appl. Phys. Lett., 99, 2513103 (2011).
- [5] Adiga, et al., Accepted for publication in J. App. Phys. (2012).

## Characterization of Si-Nanowires for Biosensor Applications

**Andrew Acevedo**

**Biomedical Engineering, Washington University in St. Louis**

*NNIN iREU Site: Institut Für Bio- Und Nanosysteme (IBN), Forschungszentrum, Jülich, Germany*

*NNIN iREU Principal Investigator: Dr. Svetlana Vitusevich, Peter Grünberg Institute 8, Forschungszentrum Jülich*

*NNIN iREU Mentor: Sergii Pud, Peter Grünberg Institute 8, Forschungszentrum Jülich*

*Contact: andrew.acevedo@wustl.edu, s.vitusevich@fz-juelich.de, s.pud@fz-juelich.de*

### Abstract and Introduction:

Silicon nanowire field effect transistors (Si NW FETs) are promising structures for the development of new biosensors due to their ability to directly translate interactions with target molecules into readable signals [1]. They are highly sensitive and selective and capable of real-time response and label-free detection. However there are challenges with stability and reproducibility in the development of such sensors due to the property changes over time of the thin gate dielectric when exposed to an electrolyte, low signal to noise ratio due to the small size of the NWs, and an increased role of surface effects.

In order to develop and to find the optimal dielectric passivation for Si NW sensors this project is focused on the investigation of the influence of an electrolyte liquid gate on the physical and electrical properties of the NW FETs covered with a thin silicon dioxide ( $\text{SiO}_2$ ) passivation layer. Noise spectroscopy was employed to characterize the performance of the devices in the electrolyte and without it. This technique provides a number of advantages. Noise measurements allow for the determination of various kinetic parameters from experimental data gathered without time-varying external excitation.

In addition, data extracted from noise spectra contains information about structure performance, and quality of the samples, making noise spectroscopy a powerful tool for monitoring device state. Noise spectra were measured and analyzed for Si NW FETs of 500 nm width and a variety of lengths (2-16  $\mu\text{m}$ ) with a thin  $\text{SiO}_2$  passivation layer (10 nm thickness) in air and phosphate buffered saline (PBS) at different

liquid gate and back-gate voltages. Parameters of interest include the effects on threshold voltage and charging time of the device gate dielectric.

### Methods:

Drain voltage spectral density was measured for samples of varying nanowire length (2-16  $\mu\text{m}$ ) over a range of different applied back-gate voltages; first in air, then in PBS. A constant source-drain voltage of 100 mV was applied to the samples to ensure linear regime of operation. The noise spectra of the device were registered using a HP Spectra Analyzer after the output signal from the sample was passed through a low-noise

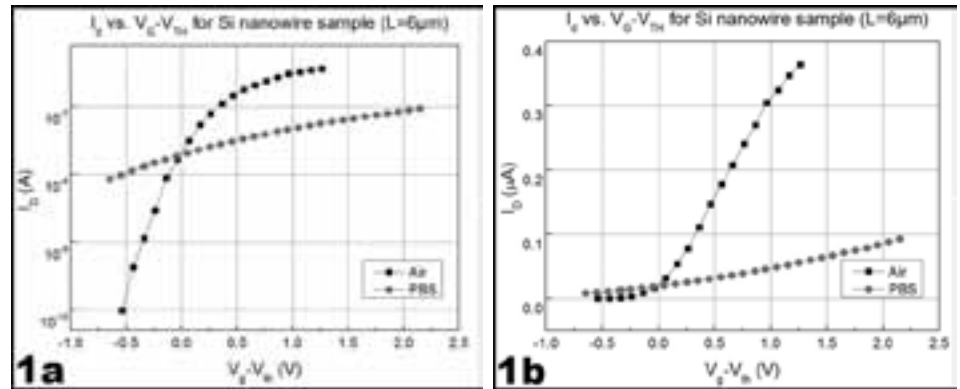


Figure 1: Drain Current vs.  $V_{GATE} - V_{THRESHOLD}$  for a 6  $\mu\text{m}$  sample shown in (A) semi-log and (B) linear scale.

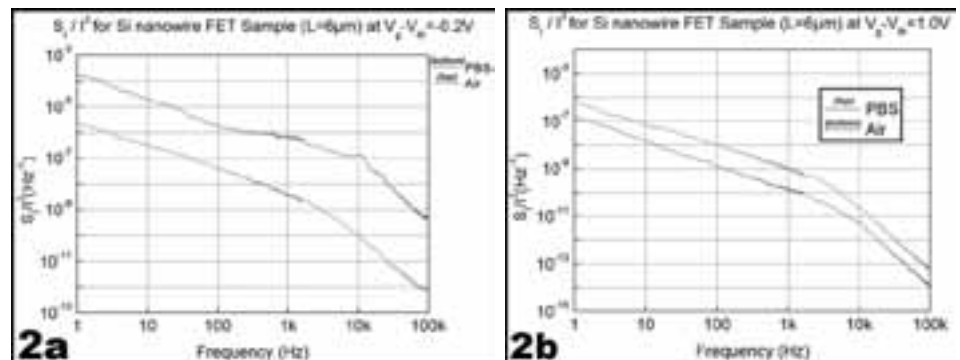


Figure 2: Normalized Current Noise Spectral Density measured for a 6  $\mu\text{m}$  sample in (A) the sub-threshold region and (B) above threshold voltage region.

homemade amplifier with gain 100 dB. A custom program was designed to measure the drain current and spectra data. This data was then analyzed using OriginLab software to determine the effects of PBS on threshold voltage and the noise spectra. The current spectral density,  $S_I$ , was calculated using the measured voltage spectral density and the equivalent resistance of the measurement scheme.

### Results and Discussion:

The first parameter of interest of our device was the effects that PBS had on the samples' threshold voltages. Drain current in the samples was measured over a range of backgate voltages, and the transfer characteristics of the FETs were then plotted. Threshold voltage was calculated by applying a best fit approximation to the linear region of the curves. Figure 1 shows typical transfer characteristics measured for a sample of length  $6\ \mu\text{m}$  in (A) semi-log and (B) linear scales. From Figure 1A, it can be seen that the addition of PBS affects the sub-threshold current of the sample, and thus facilitates exchange between interface traps of the top dielectric with the channel of the Si NW FET in the sub-threshold region. Therefore, the interaction of the electrolyte with the nanowire FET structures results in changes of the state of the interface traps. Also, an increase in threshold voltage is registered when the sample is exposed to PBS, indicating a change in surface charge of the NW transistor.

Figure 2 shows normalized current spectral density,  $S_I / I^2$ , at (A) sub-threshold backgate voltage,  $V_{\text{bg}} - V_{\text{TH}} = -0.2\text{V}$  and (B) above threshold voltage,  $V_{\text{bg}} - V_{\text{TH}} = 1.0\text{V}$ , measured in air and PBS. In the sub-threshold region, the normalized current spectral density of fluctuations in the device decreased when PBS was introduced to the sample. This decrease can be explained by the changing of the surface charge due to PBS and thus the charge state of traps in the sample's top dielectric and partly by increases in the sub-threshold current without a corresponding increase of the noise (Figure 1A).

Above the threshold voltage, submerging the sample in PBS appears to increase the amount of fluctuations in the sample. The lower value of the current at  $V_{\text{bg}} - V_{\text{TH}} = 1.0\text{V}$  in PBS (see

Figure 1B) only partially explains this behavior. If change in the number of charge carriers was the only cause, then the ratio of currents in air to PBS and the ratio of  $S_I / I^2$  in PBS to air would be similar.

Figure 1B shows that the current in air is three times higher than the current in PBS at this voltage. However,  $S_I / I^2$  at 100 Hz, is ten times greater in PBS than in air. Thus, the change in number of carriers is not the only factor influencing the change in noise level. We suggest that another component of this variation is a change in the mobility of the charge carriers due to a change in the behavior of the traps at the interface between the semiconductor and the top dielectric caused by the PBS.

### Conclusions and Future Directions:

It was shown that the exposing the nanowire samples to PBS not only affects the number of charge carriers, but also most likely results in a change in mobility of charge carriers. Further experiments need to be done to determine what other factors affect the stability and reliability of the samples working with the liquid gate. The next step will be to compare the properties of the Si NW FET samples passivated with different thin film dielectric layers in air and in PBS. Measurements will also be performed after exposing the samples to cell media for the development of neuron-nanowire FET hybrid structures.

### Acknowledgements:

I would like to thank Dr. Svetlana Vitusevich, Sergii Pud, and the rest of the Vitusevich lab for hosting me. Also, thank you to the NNIN iREU Program and the National Science Foundation for funding this experience.

### References:

- [1] "Silicon nanowire field-effect transistor-based biosensors for biomedical diagnosis and cellular recording investigation"; Chen, K; Li, B; Chen, Y; Nanotoday (2011) 6, 131-154.

## Production of Solid State Spin Qubits

**Dashiell R. Bodington**

**Physics, Rensselaer Polytechnic Institute**

*NNIN REU Site: Nanotech, University of California, Santa Barbara, CA*

*NNIN REU Principal Investigator: Professor David D. Awschalom, Physics, The University of California, Santa Barbara*

*NNIN REU Mentor: Steven J. Brown, Materials, The University of California, Santa Barbara*

*(2009 NNIN REU at University of Colorado, Boulder)*

*Contact: bodind2@rpi.edu, awsch@physics.ucsb.edu, sbrown@physics.ucsb.edu*

### Introduction:

The focus of this project was to design and create an electron irradiation setup at The University of California, Santa Barbara (UCSB) to produce solid state spin quantum bits (qubits) in diamond and silicon carbide. Unlike the conventional bit, which is either 0 or 1, a qubit can be 0, 1, or any superposition of the two states. Quantum computing takes advantage of this property to perform some tasks, such as factoring and searching, much faster than conventional computers can. The setup designed during this project will allow efficient qubit engineering under precisely controlled conditions.

### The Qubits:

Solid state spin qubits have several advantages over current qubit technologies: they have long coherence times ( $\sim 2$  ms) at room temperature, are optically readable, are scalable as a system, and certain polytypes of silicon carbide can be integrated easily into silicon devices.

A solid state spin qubit consists of a crystal vacancy complex containing a localized electron density. The spin state of this density can be manipulated with microwave frequency magnetic field and the state is read out optically. In diamond, the qubit structure consists of an atomic vacancy adjacent to a substitutional nitrogen atom. In silicon carbide there are six

qubit structures. Four of them are known to be divacancies in varying orientations. Figure 1 shows each qubit structure.

The preferred method for creating these atomic vacancies is electron irradiation. Electron irradiation gives even distribution of qubits and a relatively low level of unwanted crystal damage, but creation is inefficient. Only 0.1% of the nitrogen atoms in diamond samples become part of viable qubits, and every extra nitrogen atom interferes with qubit coherence. Currently, samples must be sent to third parties for processing where we have minimal control over irradiation conditions. By creating a facility to manufacture qubits ourselves, we hope to improve creation efficiency and engineer samples with controlled qubit densities, and higher qubit densities than have been made before.

### The Project:

To create these qubits, an irradiation setup was designed to interface with the UCSB free electron laser (FEL). The FEL's 5 MeV electron beam is diverted through the sample irradiation setup and into a beam dump. To protect the electron accelerator and eliminate scattering, the entire path of the beam must be under ultra-high vacuum conditions (UHV =  $10^{-9}$  Torr). Because many materials outgas under

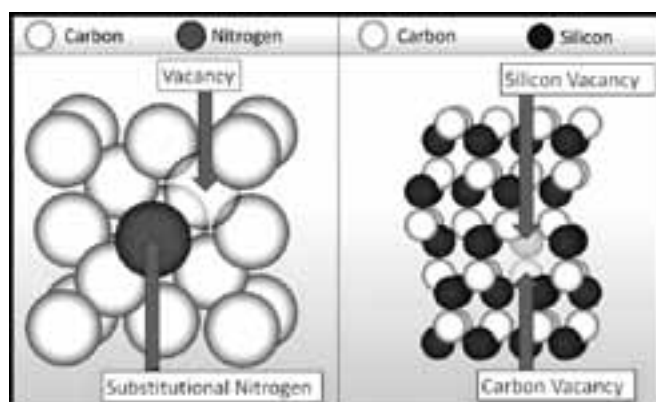


Figure 1: Nitrogen vacancy center in diamond (left) and silicon carbide divacancy (right).

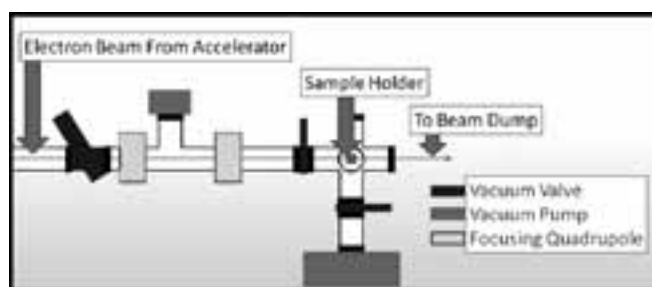


Figure 2: The irradiation addition layout.

UHV conditions, all parts in the vacuum, including sealing gaskets, must be metal. An estimated 9 W will be absorbed by the sample during irradiation so all parts of the system must withstand or dissipate this heat.

### The Design:

The final design met all of the challenges of the high energy beam, UHV environment, and more. For the safety of the electron accelerator, the irradiation addition was automatically isolated from the rest of the beamline in the event of a leak, and could be manually isolated in multiple sections for access and pumping. For efficiency, the addition used standard vacuum parts with the exception of the sample holder, and a small volume to pump down. Figure 2 shows the irradiation addition to the FEL facility. The sample holder was a  $20 \times 16 \times 75$  mm block of copper with five insets for samples on the front face. The holder was threaded onto a high-power  $\frac{3}{4}$ " copper feedthrough that was attached to a linear-shift bellows mechanism to offer a 50 mm movement range.

The sample holder and beam were aligned using a 6 mm diameter calibration hole at the bottom of the holder while maximizing the current at the beam dump. When the system was aligned, the 7 mm spacing between samples allowed us to move between all five samples without breaking the vacuum. The calibration process also provided an electron flux measurement that could be used to calculate irradiation dose when the sample was in the beam. For heat conduction out of both faces of the samples, each was secured in its inset by a 4 mm thick copper faceplate and two bolts. Heat was drawn from the sample holder via the feedthrough which was water cooled outside the chamber for vacuum safety.

To reduce unnecessary heating there was a free path for the beam through the center of each faceplate and through the holder behind each inset. The first sample holder accommodated two  $2.3 \times 2.3$  mm samples and three  $3 \times 3$  mm samples, but the threaded attachment made installing other sample holders for future experiments simple.

Figure 3 shows the elements of the irradiation assembly and Figure 4 shows the finished sample holder.

### Conclusion and Future Work:

At this point the irradiation addition to the FEL is under construction. Several components required for the protection of the accelerator are being ordered. When completed, the setup will be used to study how different irradiation conditions affect resulting qubit quality.

### Acknowledgements:

This project would not have been possible without input and support from many individuals. The Awschalom Group provided tremendous feedback and assistance throughout the project. Engineer David Enyeart and Research Scientist Gerald Ramian, of the UCSB FEL staff, provided regular consultation on construction, acquiring parts, and interfacing to the beam. Professor Christopher Palmstrom provided input on the construction of UHV systems and considerations for the optimal design. And the NSF, NNIN REU Program, UCSB, DARPA, and the Air Force provided funding and facilities.

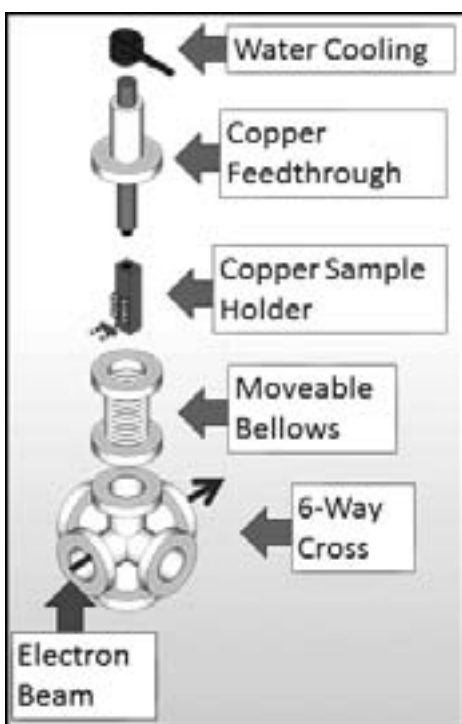


Figure 3: The irradiation assembly.

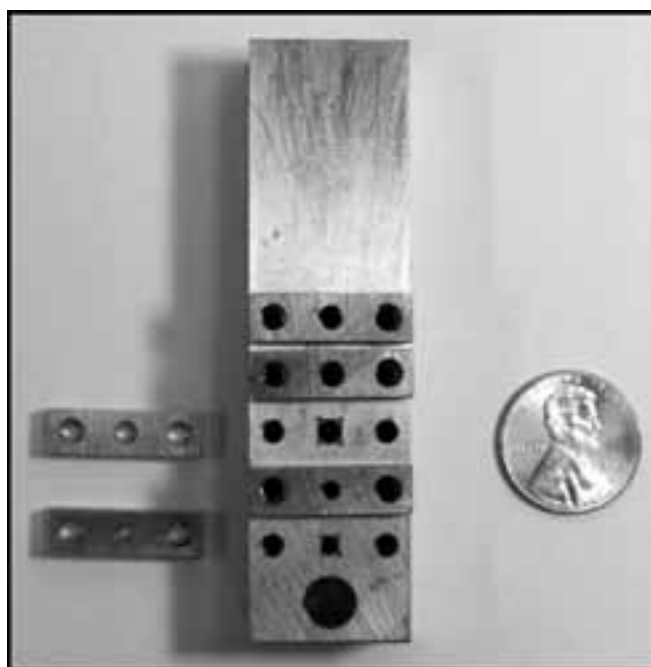


Figure 4: The completed sample holder.

## Fractal Electrodes

**Patrick Butera**

**Chemical Engineering, University of Connecticut**

*NNIN REU Site: ASU NanoFab, Arizona State University, Tempe, AZ*

*NNIN REU Principal Investigator: Dr. Michael Kozicki, School of Electrical, Computer, and Energy Eng., Arizona State University*

*NNIN REU Mentor: Ankitha Chandran, School of Electrical, Computer, and Energy Engineering, Arizona State University*

*Contact: patrick.butera@uconn.edu, michael.kozicki@asu.edu, achand27@asu.edu*



*Figure 1: A sample cathode. Dendrites are growing to the left as more silver ions reach the cathode. There are multiple layers of dendrites visible.*

### Abstract:

Fractal electrodes (dendrites) provide an opportunity to improve many electrical and optical areas including solar cells, sensors, and in the future, retinal replacements. They offer a unique ability to carry either information or charge with minimal resistance, while only covering a small fraction of surface area. These electrodes can be easily made by applying an electric field between an anode and cathode which causes the dendritic metal electrodeposit to form. One key characteristic of the fractal electrodes is the fractal dimension, which is used to describe non-Euclidean geometries. The purpose of this project was to determine the level of control that can be obtained through use of constant current and constant voltage during electrodeposit growth. Thin films of silver were deposited on slides via thermal evaporation. The mask used provided channels between the silver electrodes in which the dendrites could grow. The dendrites, as seen in Figure 1, were then imaged and processed to determine their fractal dimension. It was found that the fractal dimension decreases with an increase in field, in both constant current and voltage trials. The data confirms that a stronger field leads to more one dimensional growth.

### Experimental Procedure:

Silver (Ag) deposition was carried out using thermal vapor deposition. The chamber of the Cressington was vacuumed down to  $3 \times 10^{-6}$  mbar. Between 47 and 50 nm of Ag was deposited on the glass slide. Channels to carry out the electrodeposition were created with a mask of Mylar tape. Each channel was probed using an Agilent 4155C semiconductor parameter analyzer. Either constant voltage or constant current were applied across the channel for various amounts of time to produce the dendrites. Once the dendrites were grown, an Axiophot microscope was used to produce the images. Three images were taken for each dendrite. The fractal dimension was calculated in MatLab using a box counting approximation. Results were then averaged for the three images to calculate the fractal dimension for the trial. Experiments at 2 volts and  $25 \mu\text{A}$  were tested from two minutes to ten minutes every minute. For 5 volts,  $35 \mu\text{A}$ , and  $50 \mu\text{A}$  trials, the times tested went from 90 seconds to 240 seconds every 30 seconds. And the higher field trials, 10 volts and  $75 \mu\text{A}$ , were tested from 30 seconds to 60 seconds in ten second intervals.

### Results and Conclusions:

As seen in Figure 2, the higher the voltage, the lower the fractal dimension tended to be. Similarly, when the current was held constant, higher currents lead to lower fractal dimensions. For the constant voltage trials, Figure 2, the data was not scattered, with the exception of one outlier. The constant current data was much more varied, as seen in Figure 3.

There are many possible areas of error, especially during the probing. One example is how far the probes were from the channel. This varied from sample to sample. Another potential reason could be the contact of the probe to the deposited silver. If the probe was pressing too hard, it could scrape off the silver, which would increase the resistance. On the other hand, if the probe was not pressed hard enough, then the probe would not be making good contact with the silver. For more exact data, these problems would need to be addressed, but a strong negative trend was found.

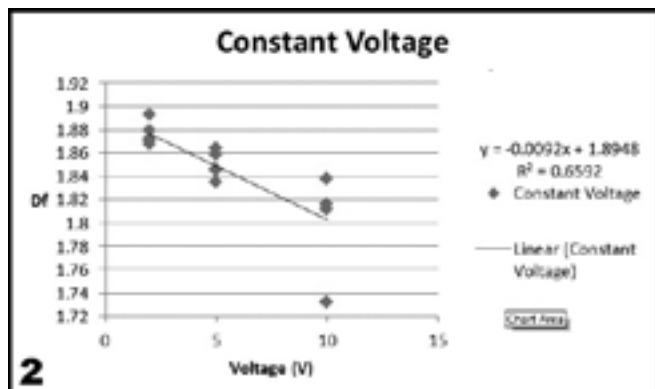


Figure 2: Fractal dimension for each constant voltage trial. The plot points to a strong downward trend.

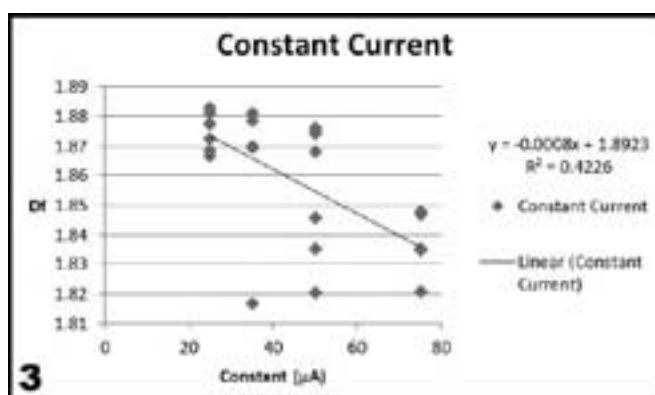


Figure 3: Fractal dimension for each constant current trial. While data is more scattered than the constant voltage trials, the same trend is prominent.

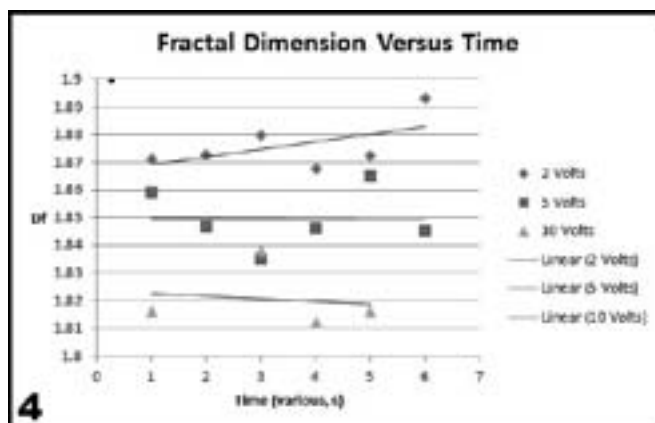


Figure 4: Fractal dimension versus time. The time scales vary depending on the voltage. For 2 volts, the times tested were every minute, for 5 volts every 30 seconds, and 10 volts was every 10 sec.

For each voltage and current tested, the fractal dimension to time relationship was tested. Figure 4 shows this relationship for the constant voltage trials only. It was obvious that no clear trend existed with respect to time. The dendrites were not growing far enough to cause any difference compared to the randomness of the sampling. If more exact methods were used, it would make sense for the fractal dimension to have a slight decrease with respect to time.

**Future Work:**

The data gotten from the above experimental procedure is useful for silver electrodeposits grown in de-ionized water at room temperature. However, if any of these constraints change, more testing will need to be done. The effect of temperature on dendrite growth would also seem to be a more sensitive way of controlling the formation.

**Acknowledgments:**

I would like acknowledge my principal investigator, Dr. Michael Kozicki, and my mentor, Ankitha Chandran, for their time and for everything they taught me. Thanks also to my site director, Dr. Trevor Thornton. Finally, thank you to the National Nanotechnology Infrastructure Network Research Experience for Undergraduates Program, the National Science Foundation, and the Center for Solid State Electronics Research at Arizona State University for providing the opportunity and funding for this amazing experience.

## Improving Superconducting Resonators for use in Quantum Computing

**Marcos Echeverria**

**Applied Physics, California State University San Marcos**

*NNIN REU Site: Nanotech, University of California, Santa Barbara, CA*

*NNIN REU Principal Investigator: Dr. Andrew Cleland, Department of Physics, University of California Santa Barbara*

*NNIN REU Mentor: Anthony Megrant, Department of Physics, University of California Santa Barbara*

*Contact: echev004@csusm.edu, anc@physics.ucsb.edu, aem02@umail.ucsb.edu*

### Abstract:

Superconducting coplanar waveguides (CPWs) are essential elements in building quantum computers [1] and in single photon detectors for astrophysics [2]. Reducing energy loss in these waveguides is critical to improving their performance. One source of energy loss in coplanar waveguides arises from parasitic coupling to unwanted electromagnetic modes that occur where there are asymmetries or discontinuities in the circuit layout. The effect of these asymmetries and discontinuities can be minimized by adding additional wiring (“crossovers”) to the waveguide geometry. However, the dielectric materials that serve as structural supports for the crossovers add additional loss through different mechanisms. We will discuss a method of fabricating crossover wiring in the form of freestanding air bridges, which will still suppress unwanted modes, but will not use a lossy dielectric for structural support.

### Background:

Quantum computation relies on bits of information being stored as excitations in a quantum mechanical object. Unfortunately, these excitations decay as the object loses energy to its environment. This may be represented as a classical “bit” of information spontaneously changing from a “1” to a “0”. The loss of energy/information is one of the biggest obstacles facing all of the proposed quantum computation architectures. Thus, reducing sources of energy loss is vital to building a quantum computer.

Energy loss occurs when moving and storing information in a superconducting circuit. A coplanar waveguide is a type of microwave transmission line that is used to move information in a quantum circuit, similar to how wires move information in an integrated circuit. A waveguide with boundary conditions such as electrical opens or shorts on both of its ends will resonate at a fundamental frequency that is defined by the length of the CPW. These resonators are used to store information for later retrieval as well as to aid in both the communication and isolation of qubits.

The CPW consists of a conducting plane lying on a dielectric substrate. The conducting plane is divided into three sections consisting of a center conductor surrounded on either side

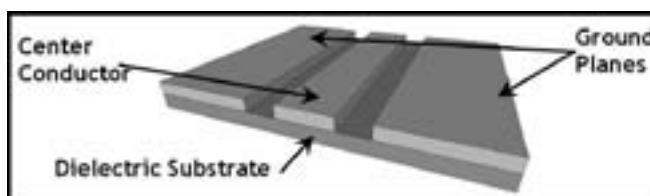


Figure 1: Coplanar Waveguide (CPW).

by ground planes (Figure 1). This geometry supports several electromagnetic modes, two of which are the desired even mode and the parasitic odd mode. The odd mode is a source of energy loss for the even mode, but it can be suppressed using a superconducting strip to force the ground planes to the same electrical potential. Currently the superconducting strip is supported by a dielectric, hydrogen terminated amorphous silicon. While this crossover method suppresses the odd mode, the supporting dielectric introduces a different source of loss not described here.

### Methods:

A research group in the Netherlands has developed freestanding air bridges (Figure 2). First, they spin a  $3\ \mu\text{m}$  layer of positive photoresist over a CPW. A lithography step leaves behind a rectangular bar of resist covering the CPW.

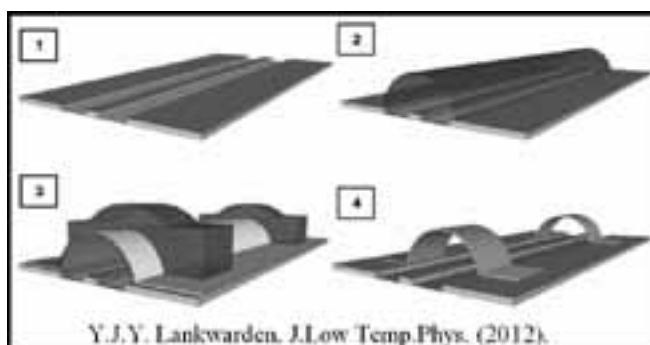


Figure 2: Air bridge fabrication process.

Heating the bar of resist above its glass transition temperature results in an arched shape, which serves as scaffolding for the air bridges. A thin layer of aluminum is deposited, followed by another layer of resist. A second lithography step covers the aluminum at the bridge locations. An etching step removes excess aluminum, and all of the remaining scaffolding resist is removed leaving behind freestanding air bridges.

This method could prove less lossy than the current crossover method, because it does not require a dielectric for support. The air bridge method also reduces the number of fabrication steps, which should improve device performance. Since the qubits used in these circuits are temperature sensitive devices, it is imperative that the resist have a low reflow temperature, and can be spun on at  $\sim 3 \mu\text{m}$  to set the height of the air bridges. SPR220-3.0 photoresist can be spun on at  $3 \mu\text{m}$ , but its reflow temperatures are not known, so separate samples of SPR220-3.0 were baked at temperatures in the range  $115^\circ\text{C}$ - $155^\circ\text{C}$  for three minutes each. The reflowed resist was analyzed using profilometry and atomic force microscopy (AFM).

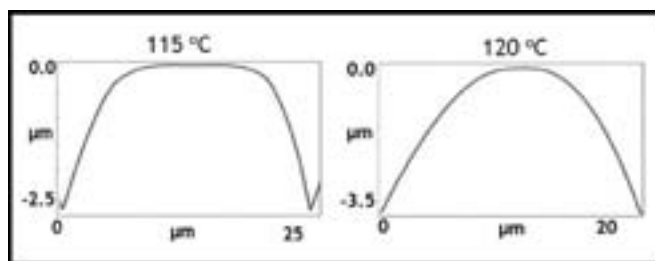


Figure 3: SPR220-3.0 photoresist baked at the indicated temperature for three minutes.

### Results and Conclusions:

The results show edge rounding at all temperatures (Figure 3), however at  $120^\circ\text{C}$ , a clear semi cylindrical shape appeared.

Temperature data was taken up to  $155^\circ\text{C}$ , but after  $120^\circ\text{C}$ , there was no significant change in the shape of the photoresist. Since the profilometer has a relatively large  $12 \mu\text{m}$  tip radius, we verified the above results using AFM images (not shown) of before and after reflow.

We have discussed a method of suppressing the odd CPW mode that does not rely on a lossy dielectric for support. The reflow characteristics of SPR220-3.0 photoresist were characterized, and the reflow temperature of SPR220-3.0 was determined to be  $120^\circ\text{C}$ . This low reflow temperature should save our sensitive devices from thermal degradation.

After fabricating the air bridges, resonators will be used to compare the losses between air bridges and crossovers. This will improve the quality of our CPW circuit and add robustness to the architecture of superconducting quantum computers.

### Acknowledgements:

I would like to thank my mentor Anthony Megrant for all his help and insight. I would also like to thank my P.I. Dr. Andrew Cleland, Samantha Cruz, the entire Martinis Group, and the whole NNIN REU staff for letting me be a part of this program.

### References:

- [1] Lucero, E., Computing prime factors with a Josephson phase qubit quantum processor, arXiv:1202.5707v1, 2011.
- [2] Lankwarden, Y. J. Y., Bruijn, M. P. Development of NbTiN-Al Direct Antenna Coupled Kinetic Inductance Detectors, Journal of Low Temperature Physics, 167(3-4), 367-372, 2012.
- [3] Mariani, M., Photon shell game in three-resonator, Nature Physics, Vol 7, 1-18, 2011.

# The Effects of Surface Passivation on Trap Levels in Silicon Nanocrystals

**William Andres Gaviria Rojas**

**Electrical Engineering, Massachusetts Institute of Technology**

*NNIN REU Site: Nanofabrication Center, University of Minnesota-Twin Cities, Minneapolis, MN*

*NNIN REU Principal Investigator: Prof. Stephen Campbell, Electrical and Computer Eng., University of Minnesota-Twin Cities*

*NNIN REU Mentor: Dr. Richard Liptak, Electrical and Computer Engineering Department, University of Minnesota-Twin Cities*

*Contact: williamg@mit.edu, campb001@umn.edu, lipt0010@umn.edu*

## Introduction:

Silicon nanocrystals (Si-NC) systems have a wide variety of applications due to their optical properties, and their growth can be easily incorporated into Si fabrication methods already established in industry, making Si-NCs an attractive alternative to bulk Si. Recent developments have allowed for the synthesis of Si-NCs that are resistant to oxidation through surface passivation [1]. However, the effects of surface passivation on the electronic properties of Si-NCs remain unknown. With this in mind, our research focused on the investigation of trap levels in Si-NCs and the effects of passivation on these traps.

## Experimental Details:

The Si-NCs were created using non-thermal plasma synthesis with both  $\text{SiH}_4$  and  $\text{SF}_6$  gas in order to produce H and F terminated Si-NCs. Details on Si-NCs and passivated Si-NCs growth are described by Pi, et al. [2], and Liptak, et al. [1], respectively. Metal-oxide-semiconductor (MOS) capacitors were fabricated by annealing RTA cleaned n-type Si <100> in a  $\text{O}_2$  ambient in order to create a thin  $\text{SiO}_2$  interface, followed by the deposition of Si-NCs on the  $\text{SiO}_2$  layer.

In order to optimize our measurements, we then utilized atomic layer deposition (ALD) to deposit a high- $\kappa$  dielectric ( $\text{HfO}_2$ ) layer on top of the Si-NCs, and finished by evaporating aluminum back and gate contacts. We fabricated devices with no Si-NCs (for control), a 30-second deposition Si-NCs layer, and a one-minute deposition Si-NCs layer for both bare Si-NCs and surface passivated Si-NCs samples. A topological overview of the device structure can be seen in Figure 1.

The trap centers of our fabricated MOS structures were then investigated using capacitance-voltage (C-V) profiling and deep level transient

spectroscopy (DLTS) in order to confirm the presence of traps as well as to characterize the energy level and trap cross-section of these trap centers. The C-V profiles were acquired at different frequencies of 200, 50, and 10 kHz and the DLTS data was acquired using a temperature range of 35K-420K and a rate window of approximately  $16 \text{ s}^{-1}$ .

## Results:

The C-V profiles of the samples (not shown), suggest the presence of trap levels in a number of ways: (1) The decrease in accumulation in both the bare and passivated Si-NCs samples indicated the presence of majority traps; (2) Stretchout indicated a greater number of trap levels in the bare and passivated Si-NCs samples; (3) The decrease in depletion in both the bare and passivated Si-NCs samples suggested a higher concentration of interface and majority trap levels; and (4) A greater change in the depletion capacitance was observed for the bare and passivated Si-NCs samples than for the control sample, indicating an increase in interface state density. It is also worth noting that the change in depletion capacitance was greater in the passivated samples.

The C-V measurements also demonstrated hysteresis in all samples for all profiling frequencies, as can be seen in Figure 2. The negative shift of approximately 0.5 V in the down trace of all the measurements is consistent with previously observed values by Kwon, et al., and this memory effect confirms the presence of Si-NCs in the samples [3].

The DLTS measurements are shown in Figure 3 and the trap levels found are summarized in Table 1. These results show that the trap levels found in

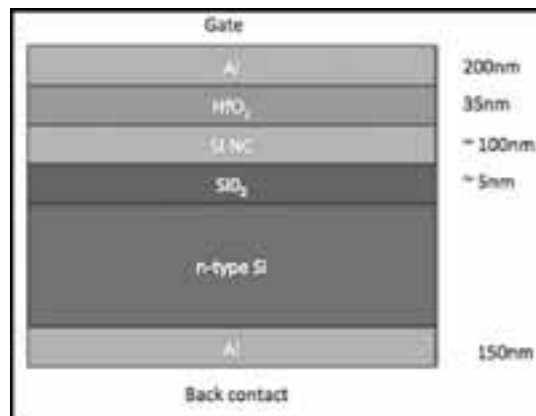


*Figure 1: Cross-sectional side view of the fabricated MOS-capacitors with embedded Si-NCs. The approximate thickness of each layer is shown at the right of the corresponding layer.*

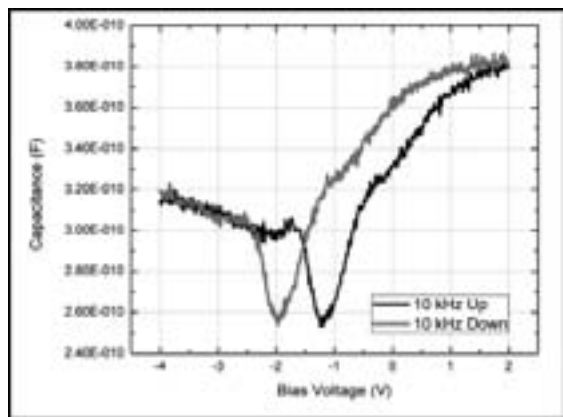


Figure 2, above left: C-V profile shows the hysteresis profile for a 10 kHz scan of the passivated sample.

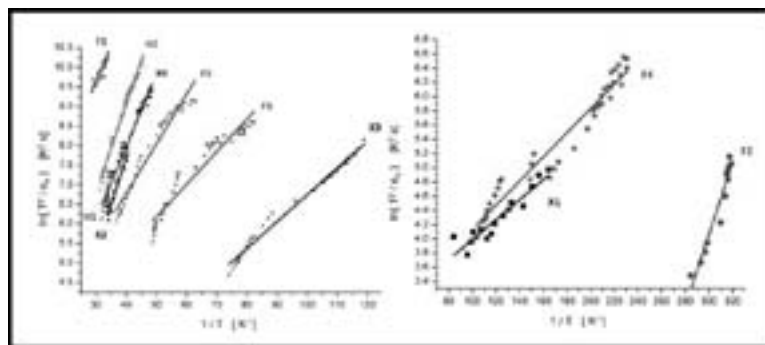


Figure 3, above right: Arrhenius plots of our DLTS measurements show the presence of multiple traps levels. Each trap is labeled and more information can be found in Table 1.

Table 1, at right: List of the corresponding activation energy, capture cross-sections and temperature peaks for the trap levels found.

Control				Passivated Si-NCs			
Trap	E (ev)	$\sigma$ (cm <sup>2</sup> )	Peak (K)	Trap	E (ev)	$\sigma$ (cm <sup>2</sup> )	Peak (K)
X1	0.01	4.1x10 <sup>-21</sup>	60	F1	-0.16	4.0x10 <sup>-20</sup>	350
X2	0.39	7.4x10 <sup>-16</sup>	270	F2	0.05	2.1x10 <sup>-17</sup>	40
X3	0.07	3.5x10 <sup>-22</sup>	100	F3	0.13	1.6x10 <sup>-11</sup>	230
X4	0.19	4.5x10 <sup>-22</sup>	270	F4	0.02	3.5x10 <sup>-12</sup>	60
Bare Si-NCs				F5	-0.08	2.3x10 <sup>-13</sup>	170
Trap	E (ev)	$\sigma$ (cm <sup>2</sup> )	Peak (K)				
H1	-0.53	1.7x10 <sup>-17</sup>	270				
H2	0.22	4.4x10 <sup>-17</sup>	290				

our bare Si-NCs samples are not consistent with previously reported values by Souifi, et al. [4] and Kwon, et al. [3], which can be attributed to different Si-NCs growing methods. The traps found also have capture cross-section orders of magnitude smaller than expected, which has been previously observed and attributed to charge tunneling into the Si-NCs and a lower density of states at the Si-NCs by Antonova, et al. [5].

Overall, surface passivation appears to remove deep level traps in Si-NCs while creating shallow level traps for both majority and minority carriers. Considering that an F-terminated Si surface oxidizes much faster than an H-terminated Si surface [6], the removal of deep level traps in Si-NCs by surface passivation supports proposed theories that deep level traps in Si-NCs are caused by hydrogen dangling bonds [7]. However, not enough data has been collected to make any serious assessment and further research is needed to: (1) confirm the validity of the observed trap levels, and (2) correlate growth parameters with observed trap levels.

**Acknowledgements:**

A special thanks to Prof. Stephen Campbell and Dr. Richard Liptak for their continued mentorship and support. This

research opportunity would have also been impossible without funding from the NSF and National Nanotechnology Infrastructure Network Research Experience for Undergraduates (NNIN REU) Program, the help of Prof. Douglas Ernie, and the facilities of the Electrical and Computer Engineering Department, University of Minnesota.

**References:**

- [1] R.W. Liptak, B. Devetter, J.H. Thomas, III, U. Kortshagen, S.A. Campbell. Nanotechnology. 20 035603 (2009).
- [2] X.D. Pi, R.W. Liptak, S.A. Campbell, U. Kortshagen. Appl. Phys. Lett. 91, 083112 (2007).
- [3] Y.H. Kwon, C.J. Park, W.C. Lee, D.J. Fu, Y. Shon, et al. Appl. Phys. Lett. 80, 2502 (2002).
- [4] A. Souifi, P. Brounkov, S. Bernardini, C. Busseret, L. Militaru, G. Guillot, T. Baron. Materials Science and Engineering: B 102 99-107 (2003).
- [5] I. Antonova, E. Neustroev, S. Smagulova, J. Jedrzejewski. Phys. Status Solidi C. 6, No. 12, 2704–2706 (2009).
- [6] R.A. Haring, M. Liehr. J. Vac. Sci. Technol. A 10, 802 (1992).
- [7] K. Lips, P. Kanschhat, W. Fuhs. Sol. Energy Mater. Sol. Cells 78, 513 (2003).

## Self-Organized Nanostructural Pattern Formation under Ion Beam Irradiation

**Michael Hovish**

**Nanoscale Science, College of Nanoscale Science and Engineering, SUNY Albany**

*NNIN REU Site: Center for Nanoscale Systems, Harvard University, Cambridge, MA*

*NNIN REU Principal Investigator: Prof. Michael J. Aziz, School of Engineering and Applied Sciences, Harvard University*

*NNIN REU Mentor: Joy C. Perkinson, School of Engineering and Applied Sciences, Harvard University*

*Contact: mhovish@albany.edu, aziz@seas.harvard.edu, joyc@seas.harvard.edu*

### Abstract:

Ion bombardment is a diverse laboratory technique with many applications including reactive ion etching, focused ion beam milling, ion implantation, sputter deposition, and ion beam characterization techniques such as Rutherford backscattering spectrometry (RBS). Of particular interest are the nano-topologies that form under the presence of ion irradiation. Periodic nanoscale ripples, dots, and high-aspect ratio structures can self-organize under ion bombardment. However, the relative importance of various mechanisms that underlie the self-organization process are poorly understood.

This project aimed to investigate the importance of ion beam-injected stress as a mechanism influencing the dynamics of nanoscale ripples. It has previously been observed that ripples will propagate along the surface of certain materials during ion bombardment, and a recently-developed theory attributes this phenomenon to beam-injected stress. Our study aimed to test this theory by quantitatively measuring ripple propagation velocity at a variety of incidence angles for comparison with the functional form of velocity vs. angle predicted by theory. A 30 keV Ga<sup>+</sup> focused ion beam was used to irradiate Si <001>. *In situ* scanning electron microscopy (SEM) was used to directly record the ripple dynamics.

Additionally, a methodology for measuring the propagation of ripples with respect to fluence (ions•cm<sup>-2</sup>) was developed and preliminary measurements were taken.

### Introduction:

There has been much attention granted to self-organized nanostructures that propagate under the presence of ion bombardment [1]. Nanoscale features at and below 100 nm have been shown to form under both focused and unfocused ion beams, a process known as “sputter patterning.” In a recent study, a regular array of nanodots with diameters as small as 7 nm were fabricated [2]. However, there is little understanding on how to control the ion induced self-organization process. A cohesive theory by which we can understand the governing mechanisms of ion induced self-organization could lead

to a high level of control and manipulation of nano-pattern formation.

In this work, we investigated the propagation velocity at which nano-ripples propagated along the surface of Si <001> under the raster of a focused ion beam. Parallel mode ripples were observed to propagate in a direction anti-parallel to the incoming gallium ions.

Note, the term “propagation velocity” used in this report does not refer to the traditional concept of velocity. Rather, “propagation velocity” was measured in  $\frac{nm}{fluence}$ , i.e. how far a ripple would propagate under a given amount of ion impingement.

### Experimental Procedure:

A 30 keV beam of focused Ga<sup>+</sup> ions was produced using an NVision 40 Dual Beam focused ion beam (FIB) outfitted for *in situ* SEM. FIB and SEM guns were fixed at an angle  $\Theta = 54^\circ$  from each other, while the specimen stage had the freedom to tilt. The angle between the specimen stage and the FIB gun is denoted  $\Theta_{FIB}$  and was held constant at  $30^\circ$ . Although we were ultimately interested in varying the angles of incidence,  $\Theta_{FIB}$  was held constant while beam current, dwell time and other tool specific parameters were optimized. Beam currents of 80 pA and 150 pA were utilized to expose a  $100 \mu\text{m}^2$  area of p-type Si <001>. We minimized dwell time, set pixel overlap to 53%, and passed the ion beam over the exposed area many times, thereby approximating uniform radiation. This was done to ensure ripples were not directly written by the FIB.

Real-time Fast Fourier Transform was used to observe the evolution of periodicity while post-mortem Fast Fourier Transform was used to ascertain final periodicity of the ripples. In order to measure propagation velocity, measurements were made on how long it took for the Raith FIB software to execute one exposure loop. Using this metric, we correlated the amount of ions impinging on the surface between SEM frames.

## Results and Conclusions:

Figure 1 exhibits the relevance of dwell time. At sub-microsecond dwell times (1a), nanoscale ripples were apparent. As we increased dwell time, the ion beam was able to mill deeper into the surface, thereby directly writing nano-topologies. Dwell time should therefore be minimized in order to ensure that features are not directly written onto the surface.

*In situ* SEM was employed to record the evolution of ripples shown in Figure 2. We incrementally increased the total fluence, measuring the time to deliver the total fluence. Using this trend, we correlated the amount of ions impinging the surface between video frames and obtained a preliminary propagation velocity of  $35.8 \text{ nm}/10^{17} \text{ ions}\cdot\text{cm}^{-2}$  anti-parallel to the beam direction. This falls within an order of magnitude reported by [3] earlier this year.

It has been observed that there are inconsistencies in the functioning of the Raith software, and so further characterization of the ion flux is required to ensure repeatability of the metric.

## Future Work:

Obtaining the measure for propagation velocity requires further characterization. Once fully characterized, measurements will be used in comparison to what theory predicts. With the aid of a verified theory, we hope to research more complex material systems and nanostructures.

## Acknowledgements:

Prof. Michael J. Aziz, Joy C. Perkinson, Nicholas Antoniou, National Nanotechnology Infrastructure Network Research Experience for Undergraduates (NNIN REU) Program, National Science Foundation.

## References:

- [1] P. Sigmund and M.-fysiske Meddelelser, "Ion Beam Science: Solved and Unsolved Problems," pp. 1-5, 2006.
- [2] Q. Wei, J. Lian, S. Zhu, W. Li, K. Sun, and L. Wang, "Ordered nanocrystals on argon ion sputtered polymer film," *Chemical Physics Letters*, vol. 452, no. 1-3, pp. 124-128, Feb. 2008.
- [3] H. Gnaser, B. Reuscher, and A. Zeuner, "Propagation of nanoscale ripples on ion-irradiated surfaces," *Nuclear Instruments and Methods in Physics Research Section B: Beam Interactions with Materials and Atoms*, vol. 285, pp. 142-147, Aug. 2012.

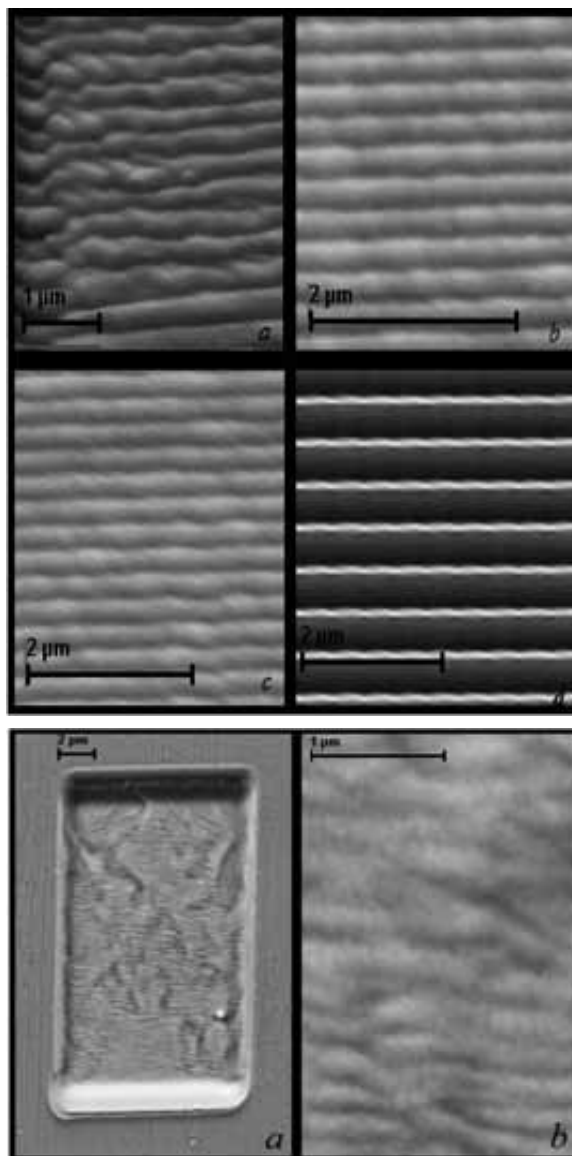


Figure 1, top: Dwell Time varied:  $0.1 \mu\text{s}$  (a),  $6.4 \mu\text{s}$  (b),  $12.8 \mu\text{s}$  (c),  $25.6 \mu\text{s}$  (d). Scale bar index:  $1 \mu\text{m}$  (a),  $2 \mu\text{m}$  (b),  $2 \mu\text{m}$  (c),  $2 \mu\text{m}$  (d).

Figure 2, bottom: Post-ion bombardment: a.  $11.12 \mu\text{m} \times 19.49 \mu\text{m}$  milled area, magnification  $2.03 \text{ kx}$ . b. High magnification ( $15.05 \text{ kx}$ ) of nanoscale ripples. Scale bar index:  $2 \mu\text{m}$  (a),  $1 \mu\text{m}$  (b).

## Cryoelectronic Characterization of Organic Molecules

**Matthew Kiok**

**Chemistry, Tulane University**

*NNIN iREU Site: Institut Für Bio- Und Nanosysteme (IBN), Forschungszentrum, Jülich, Germany*

*NNIN iREU Principal Investigator: Professor Doctor Roger Würdenweber, Peter Grünberg Institut 8*

*NNIN iREU Mentor: Tino Ehlig, Peter Grünberg Institut 8*

*Contact: mkiok@tulane.edu, r.woerdenweber@fz-juelich.de, t.ehlig@fz-juelich.de*

### Abstract:

The temperature dependence of electronic properties of conducting and semi-conducting materials is a well-studied phenomenon, with many interesting effects in low temperature ranges. This project sought to develop a method by which the temperature dependence of capacitance of gold on glass or sapphire inter-digitated capacitors could be characterized, in addition to their inherent frequency dependence. The purpose of this was to establish a reference capacitance for each substrate, such that the capacitance of subsequently deposited or grown organic monolayers could be calculated independently of inherent capacitance via subtraction of the coated samples' values from the reference values. This is especially pertinent in the lower temperature ranges (sub 100K) as unusual effects have been observed previously, especially with ferroelectric materials. The capacitors were first fabricated via photolithography, gold deposition, and liftoff processes in the cleanroom. Afterwards, their capacitance was measured across a wide range of temperature and frequency, from 50K to 300K and 20 Hz to 2 MHz respectively.

With referencing complete, the samples underwent oxygen plasma cleaning, followed by silinization in an inert atmosphere with octyltrichlorosilane under various pressures and concentrations of the reagent to yield organic monolayers on the substrate surface. The presence of monolayers was verified via contact angle measurements. Finally, the capacitances of the newly coated substrates were measured in the same fashion as the references and their results compared. For octyltrichlorosilane, no noticeable difference in capacitance was measured.

### Experimental Procedure:

Interdigitated capacitors of three orientations made of gold were initially fabricated in the cleanroom. The capacitors were patterned onto glass and sapphire substrates and exposed by contact lithography for 4.7 seconds. The metal was then sputtered onto the samples under reduced pressure. The purpose of the three orientations was to determine the best position for perpendicular deposition. Liftoff was performed outside the

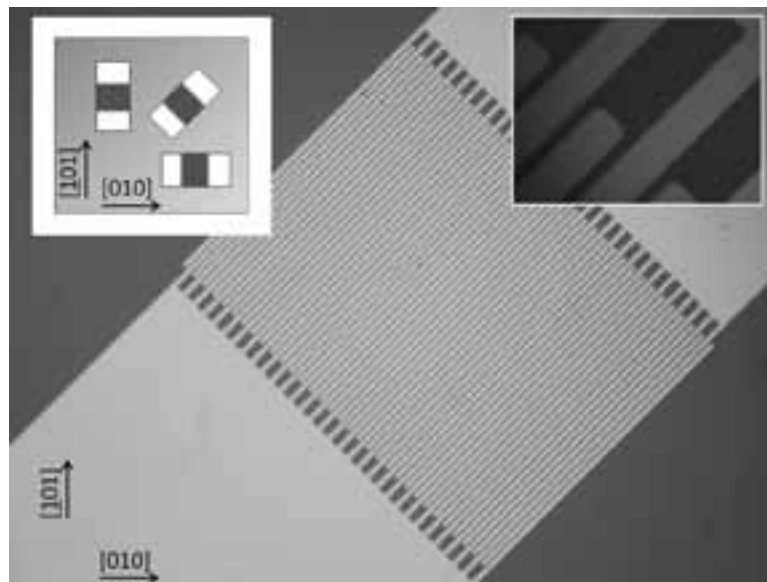


Figure 1: Structure of the interdigitated capacitors and the three orientations.

cleanroom in acetone under sonication. Each “finger” of the capacitor was approximately 10  $\mu\text{m}$  wide and separated by 5  $\mu\text{m}$ . Afterwards, one orientation of the capacitor was bonded to a probe and the capacitance was measured under varying temperature and frequency; 50K-300K and 20 Hz to 2 MHz. This was repeated for the other two orientations.

After a reference capacitance had been established for the capacitors, they underwent oxygen plasma cleaning in order to provide a clean surface for subsequent silinization. The silinization process entailed leaving the substrate in an enclosed system with liquid octyltrichlorosilane under reduced pressure for one hour. Contact angle measurements were performed before and after silinization to verify deposition on the substrate surface. Measured values before silinization were approximately 0 to 5°, and post silinization values ranged from 90 to 110°, suggesting deposition of mono and bi layers. The capacitance for the newly silinized samples was measured in the same manner as the reference samples.

The results were compared and no noticeable difference was observed between the silinized and reference sample.

### **Results and Discussion:**

As stated previously, this project sought to develop a process by which the electrical properties, the dielectric constant specifically, of various organic molecules could be measured and calculated. Several issues had to be addressed in order to optimize the process, namely fabrication defects, short circuits, and adhesion problems. Despite the relatively large scale of the structures, the samples demonstrated extraordinary sensitivity to fabrication parameters such as exposure and development times. Even the best samples were still prone to developing defects during the liftoff stage, where a small amount of residual gold could result in a short circuit in the capacitor. Finally, bonding certain samples to the probe was problematic due to the poor adhesion between the bonding wire and the metal. This issue was resolved through creative

positioning of the bonding wire and the use of conducting paint as a glue to assist bonding. The final remaining issue is whether or not this process is sensitive enough to detect differences between reference and silinized samples. Due to time limitations, only octyltrichlorosilane was measured, and more alkylated silane derivatives need to be tested before a conclusive result can be obtained.

### **Acknowledgements:**

The author would like to thank Professor Roger Wördenweber, Tino Ehlig, Thomas Grellmann, Eugen Hollmann, and Kirill Greben for their assistance and kindness both in and out of lab. Additionally, this project would not have been possible without the National Nanotechnology Infrastructure Network International Research Experience for Undergraduates (NNIN iREU) Program and the generosity of the National Science Foundation.

## Construction of a Modulated Potential Superlattice

**Phillip Meyerhofer**

**Department of Physics, Saint Vincent College**

*NNIN REU Site: Penn State Nanofabrication Laboratory, The Pennsylvania State University, University Park, PA*

*NNIN REU Principal Investigator: Jun Zhu, Department of Physics, The Pennsylvania State University*

*NNIN REU Mentors: Jing Li and Ke Zou, Department of Physics, The Pennsylvania State University*

*Contact: phillip.meyerhofer@email.stvincent.edu, jzhu82@gmail.com, jingli.psu@gmail.com, sky22124@gmail.com*

### Abstract:

A superlattice is a periodic structure composed of at least two different materials and may be used to change the band structure of a semiconductor. We studied the construction of a periodically modulated potential superlattice (with a 60-200 nm period) that we predicted would allow microscale manipulation of electron transport properties in graphene. Using electron beam lithography and reactive ion etching followed by metal deposition, we constructed complete 200 nm and 140 nm period superlattices. We also pushed the size limitations of our process to lay ground work for 100 nm and 60 nm period superlattices.

### Introduction:

The study of graphene's electrical properties has been and continues to be a popular field of research. Our particular interest was in the prediction that by applying the correct periodic potential, electrons could be made to move freely in graphene without scattering. We investigated the parameters necessary to produce such a potential.

Because the mean free path of electrons in graphene is on the order of tens to hundreds of nanometers, the periodicity of the potential must be around a few tens of nanometers to affect the movement of electrons. The way we chose to attempt to create this potential was by constructing a superlattice (see Figure 1). This superlattice alternated gold with silicon

oxide. Applying a voltage to the gold created a potential and the spaces of insulating silicon oxide limited the size of the potential. We chose to pursue this process by using a top down approach.

### Methods:

We began with a typical silicon wafer covered in 290 nm of thermally grown silicon oxide. We needed to etch the surface to create a space that would be filled with gold. The patterning of the surface prior to etching was done using electron beam lithography. We chose the resist Zep 520a because of its resistance to etching and its resolution.

One-hundred to about fifty nanometer trenches alternating with same-sized spaces were easily achieved using a Vistec 5200 and a standard develop procedure of 180 seconds in n-amyl acetate, followed by thirty seconds in 8:1 MIBK to IPA, and another thirty seconds in straight IPA to stop the develop process. However, as we approached the 30 nm mark out, the electron beam dose went straight from under-exposed to over-exposed (see Figures 2 and 3). This appeared to be because of proximity effect damage on the adjacent resist walls.

When the electrons were shot at the resist during exposure they broke the polymer chains and at the same time excited secondary electrons. Most of these secondary electrons were much less energetic and, especially at high accelerating voltages (we used 100kV), did not travel far laterally — only a few nanometers. These secondary electrons thus contributed mostly to exposing the pattern in the resist. There were, however, some fast secondary electrons (possibly caused by backscattering) that traveled much further and caused infidelity in the pattern.

This collateral damage became increasingly important as the patterns being written became smaller and closer together. Because of this, as our structures got closer and closer together, the damage to the thin walls of the trenches became catastrophic to the point where our somewhat harsh develop procedure removed not only the parts that we wanted to expose, but also large parts of the adjacent resist that had been damaged by stray electrons.

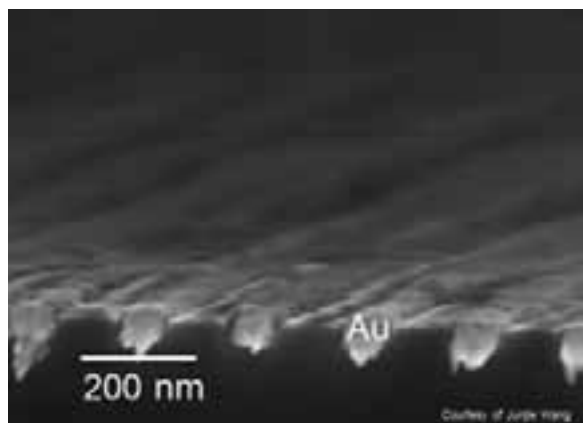


Figure 1: Superlattice.

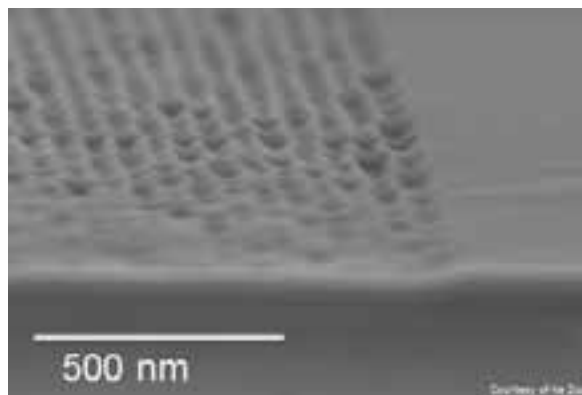


Figure 2: Underexposed line space pattern.

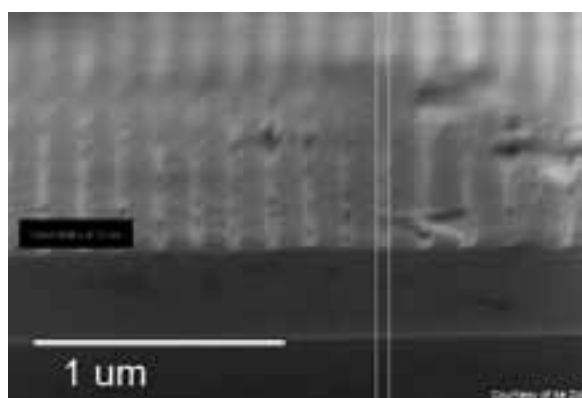


Figure 3: Overexposed line space pattern.

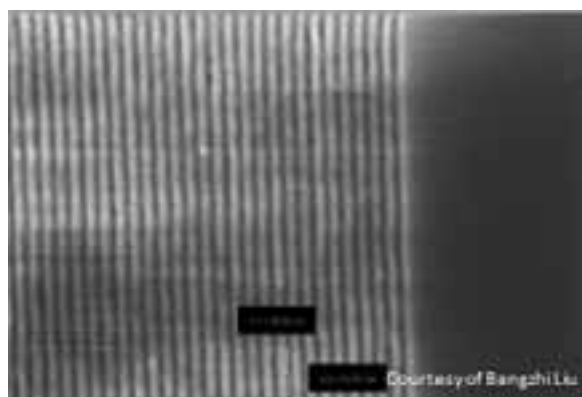


Figure 4: Cold develop lines.

In order to make this process work, we needed a develop process that was gentle enough to leave the damaged resist, while still removing the exposed resist. A shorter develop time (thirty seconds to a minute and a half) was attempted, but without success. The shorter develop time had to be combined with a colder develop temperature. Because of the kinetics of the removal process, it was possible to make the developer cool enough (down to  $\sim 4^{\circ}\text{C}$ ) that it removed the normally exposed resist while leaving intact the damaged/partially exposed sides (see Figure 4). In order to make this work, it was necessary to increase the dose to a much higher level.

Success using a similar technique was achieved by Mr. Frazier Mork, as reported at the 2012 NNIN REU Convocation [1]. Using a cold develop and a 30 nm thick resist, as well as dose correction, his group achieved  $\sim 20$  nm line spacing.

### Conclusions:

Using our process, we believe that it would be difficult to decrease the resist thickness any more than our 140 nm — which we achieved using 1:1 ratio anisole to zep — because the pattern must then survive etching. We etched with a combination of  $\text{CF}_4$  and  $\text{CHF}_3$ . Metal deposition may be done with regular electron beam evaporation, and finally for lift off, we used warm remover PG with sonication. (Acetone would also work though it is less aggressive.) We achieved a successful superlattice (see Figure 1) that was too large for experimentation, although it did demonstrate the method. Using the cold develop method, we demonstrated the technique's viability for use in smaller structures.

### Acknowledgements:

Thanks to Professor Jun Zhu for letting me work in her lab as well as Ke Zou and Jing Li for working with me. I would also like to thank Junjie Wang for his help and advice, and the Nanofab staff at Penn State for entertaining my numerous questions. Finally, thanks to the NNIN REU Program and the NSF for funding and making this research possible.

### References:

- [1] "Substrate Conformal Imprint Lithography"; F. Mork, 2012 NNIN REU Research Accomplishments, pgs. 216-217.

## Optical Characterization and Solar Cell Application of GaAs/Al<sub>0.8</sub>Ga<sub>0.2</sub>As Quantum Wells

Lauren M. Otto

Physics and Mathematics, Bethel University

Electrical Engineering, University of Minnesota-Twin Cities

NNIN iREU Site: National Institute for Materials Science (NIMS), Tsukuba, Ibaraki, Japan

NNIN iREU Principal Investigators and Mentors: Prof. Hiroyuki Sakaki, President of

Toyota Technological Institute, NIMS Fellow; Dr. Takeshi Noda, Photovoltaic Materials, NIMS

Contact: lauren-otto@bethel.edu, h-sakaki@toyota-ti.ac.jp, noda.takeshi@nims.go.jp

### Abstract:

The theoretical efficiency limit of current single p-n junction solar cells is  $\sim 33\%$ . Intermediate energy states in the solar cell's band gap allow low energy photons to induce carrier excitations, increasing efficiency [1]. Quantum well solar cells contain such states, but carriers excited in the barrier often relax into the wells where they become trapped and recombine, reducing efficiency. Because of a large momentum difference, the use of an indirect material may suppress carrier trapping and recombination, resulting in greater solar cell efficiency. Using GaAs/Al<sub>0.8</sub>Ga<sub>0.2</sub>As quantum well structures, we find that carriers trapped in our quantum wells cannot easily escape, and current measurements show no significant recombination among carriers generated in the indirect barrier region. Our data suggest that the trapping of these carriers may indeed be suppressed, but further investigation is necessary.

### Introduction:

Solar cells (SCs) convert solar energy to electricity. Current SCs only utilize part of the solar spectrum, so room for improvement remains. Intermediate band (IB) SCs are a possible solution because they allow low energy photons ( $<$  SC's band gap) to excite carriers from the valence band (VB) to the conduction band (CB) [1]. Quantum well (QW) IB SCs are easy-to-fabricate layers of different band gap materials, leading to finite potential wells in the VB and CB, each having discrete hole and electron states [2]. Unfortunately, barrier-excited carriers often relax into the well, become trapped, and recombine. The SC's efficiency is reduced because these carriers do not contribute to the current.

Indirect barrier QW structures are expected to suppress the trapping of barrier-excited carriers. Unlike a direct barrier, the  $\Gamma$ -state of indirect Al<sub>x</sub>Ga<sub>1-x</sub>As ( $x > 0.45$ ) has the greatest energy, and the X-state has the least. Indirect barrier-excited carriers were expected to thermally relax to the X-state. Then, conservation of momentum and narrow QW width would increase probability of carrier contribution to the current. Since the lattice constant is not dependent on Al composition, GaAs/Al<sub>0.8</sub>Ga<sub>0.2</sub>As QWs were grown to study the possible application of indirect barrier QWs as SCs and were

characterized using photoluminescence (PL), photocurrent (PC), and voltage dependent current (I vs. V) experiments.

### Fabrication:

Two sets of samples were fabricated.

First, two undoped,  $\sim 3$  nm wide, 10-QW structures were grown with molecular beam epitaxy (MBE) for PL measurements. A low Al content  $x = 0.3$  sample served as a traditional, direct barrier reference sample for a high Al content  $x = 0.80$  sample. Second, two high Al content ( $x = 0.80$ ), doped SCs were grown using MBE. A 0-QW sample served as a reference for a  $\sim 3$  nm wide, 10-QW sample. Photolithography and sputtering were used to create devices for PC and I vs. V measurements.

### Results and Discussion:

PL occurs when excited carriers recombine and emit a photon [3]. After excitation with a 532 nm laser, the spectrum emitted is observed with a charge-coupled device detector. For the reference sample, temperature increase showed a red shift in peak energy and a decrease in intensity [4]. Quantitative analysis showed that direct sample carriers "see" the lowest energy  $\Gamma$ -state as barrier. Indirect barrier PL stabilized at 125 K as seen in Figure 1. Carrier recombination still occurred, and qualitative analysis predicted high AE. Indirect sample carriers likely "see" the highest energy  $\Gamma$ -state as barrier. Since carriers were not likely to escape to the X-state, they were less likely to relax into the well from the X-state.

PC collected across the visible light spectrum showed carrier excitation energies, including below the band gap. This information was used to determine the exact Al composition and well thickness as labeled in Figure 2 [5].

I vs. V measured from reverse to forward bias with photons above and below the Al<sub>0.8</sub>Ga<sub>0.2</sub>As  $\Gamma$ -state band gap of 2.56 eV show carrier trapping and recombination effects. At low voltage, a steep band profile contributed to easy well-

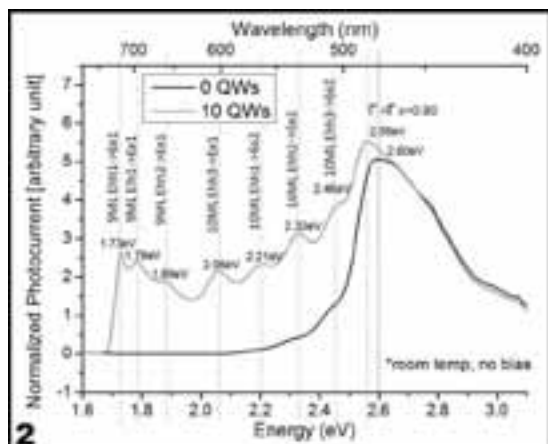
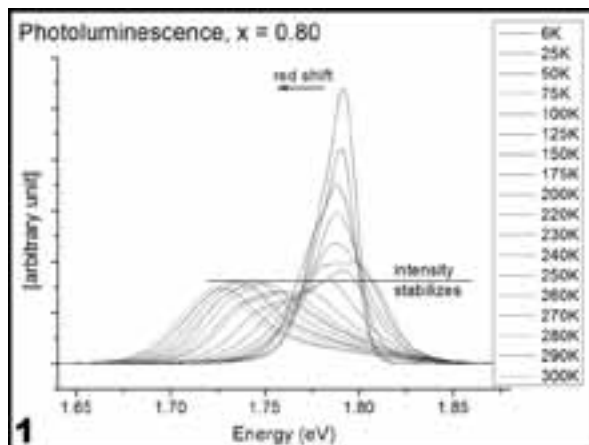


Figure 1, top: Temp. dependent photoluminescence.

Figure 2, bottom: Photocurrent spectra.

generated carrier escape, and current was high as seen in Figure 3. A higher voltage yielded a flatter band profile, so carriers could not escape and contribute to the current. This voltage dependence agreed with high AE. Figure 4 shows that barrier-excited carriers were not likely to relax into the wells, and contribution to the current regardless of voltage was expected. No voltage dependence was observed, which is consistent with expectations, but further study is required to prove that carrier trapping is suppressed.

### Summary:

PL showed high confinement and AE in high Al content, 10-QW sample.  $I$  vs.  $V$  confirmed this high confinement for well-excited carriers and suggested that the trapping of barrier-excited carriers may be suppressed. Further investigation includes measuring PC at different voltage biases and  $I$  vs.  $V$  at low temperature. A 1-QW sample will also be to more purely study carrier trapping and escape.

### Acknowledgements:

Special thanks to Dr. Takeshi Noda, Prof. Hiroyuki Sakaki, Martin Elborg, Dr. Masafumi Jo, Dr. Takaaki Mano,

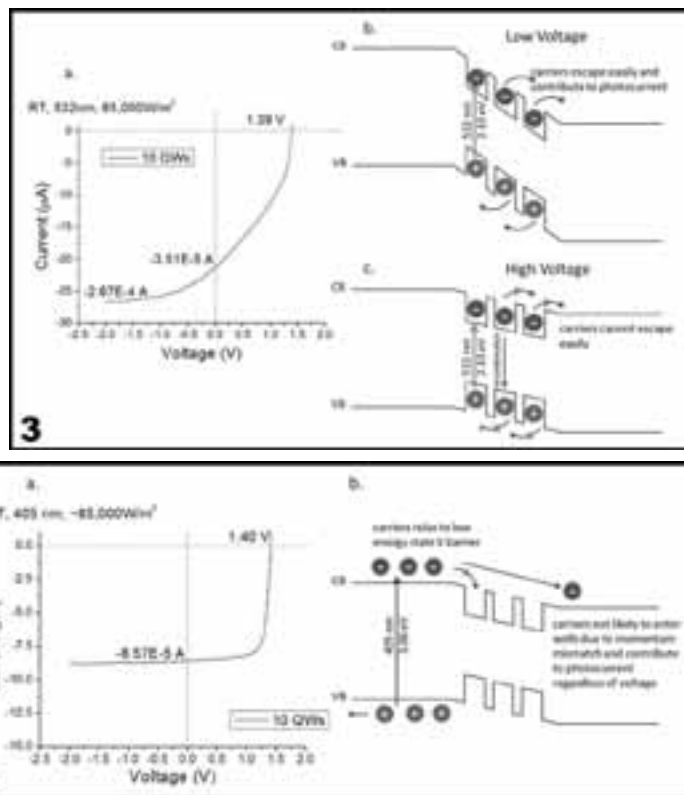


Figure 3, top:  $I$  vs.  $V$  with well-excited carriers.

Figure 4, bottom:  $I$  vs.  $V$  with barrier-excited carriers. No significant voltage dependence was observed.

Dr. Takuya Kawazu, Kumiko Higuchi, the National Institute for Materials Science, the National Nanotechnology Infrastructure Network International Research Experience for Undergraduates (NNIN iREU) Program, and the National Science Foundation.

### References:

- [1] Luque, A. and Marti, A. (1997). Increasing the Efficiency of Ideal Solar Cells by Photon Induced Transitions at Intermediate Levels. *Physical Review Letters*, 78(26), 5014-5017.
- [2] Davies, J. H. (2006). *The Physics of Low-Dimensional Semiconductors* (6th printing). Cambridge, England: Cambridge University Press.
- [3] Fox, M. (2006). *Optical Properties of Solids* (5th printing). Oxford, England: Oxford University Press.
- [4] Jiang, D. S. et al. (1988) Temperature Dependence of Photoluminescence from GaAs Single and Multiple Quantum-well Heterostructures Grown by MBE. *Journal of Applied Physics*, 64(3), 1371-1377.
- [5] Barnes, J. et al. (1996). Characterization of GaAs/InGaAs Quantum Wells Using Photocurrent Spectroscopy. *Journal of Applied Physics*, 79(10), 7775-7779.

## Oxidation of CVD Grown Carbon Nanotubes for Applying Magnetic Complexes for Spin Transport Measurements

Francisco Pelaez, III

Chemical Engineering, University of Texas at Austin

NNIN iREU Site: Institut Für Bio- Und Nanosysteme (IBN), Forschungszentrum, Jülich, Germany

NNIN iREU Principal Investigator: Dr. Carola Meyer, PGI-6, Forschungszentrum Jülich

NNIN iREU Mentor: Robert Frielinghaus, PGI-6, Forschungszentrum Jülich

Contact: francisco.pelaez.iii@gmail.com, c.meyer@fz-juelich.de, r.frielinghaus@fz-juelich.de

### Abstract and Introduction:

Due to their high aspect ratio and few nuclear spins, carbon nanotubes (CNTs) can be used as one-dimensional models to observe fundamental spin transport. Polarizing electron spins have been done on CNTs by attaching individual magnetic complexes. Different magnetic complexes and attachment mechanisms have been used [1], but the one of interest here are tetramanganese (II) complexes with manganese as the metal [2, 3]. Regardless of the complex however, functional groups need to be introduced to the CNTs in order to chemically attach the complexes.

For this aim, the CNT networks were oxidized at 420°C in air, pure O<sub>2</sub>, and an ~ 50/50 mix of N<sub>2</sub>/O<sub>2</sub> to control the oxidation rate. To measure the degree of oxidation, Raman spectroscopy and resistance measurements across CNT networks were done. An increase in oxidation was expected to show a decrease in resistance and an increase in defects in the CNT network. At 420°C, the results showed that there were no significant effects on the tubes. Although at 450°C, results from previous experiments showed an increase in defects from the Raman spectroscopy [4].

### Methods:

CNTs were grown in a tube furnace at 860°C on a one-cm<sup>2</sup> quartz substrate using a Fe/Mo catalyst. Using this procedure, networks of CNTs were grown on the substrate and then Ti/Pt (3/70 nm) contacts were deposited on the pristine networks. Figure 1 shows how these square contacts were distributed on the quartz substrate along with an atomic force microscope (AFM) image of the networks. The tubes were oxidized in air, pure O<sub>2</sub>, and an O<sub>2</sub>/N<sub>2</sub> mixture. In air, the tubes were oxidized in a muffle oven. Pure O<sub>2</sub> and O<sub>2</sub>/N<sub>2</sub> oxidations were performed in a tube furnace. The gasses bubbled through water before going into the oven because COOH groups are needed for a latter functionalization [2].

The CNTs were characterized by a Bruker RAMII spectrometer with Fourier-transformed Raman measurements at an excitation wavelength of 1064 nm. Figure 2 displays an example of a Raman spectrum data with the D and G peak labeled. The ratio of the area underneath the D and G

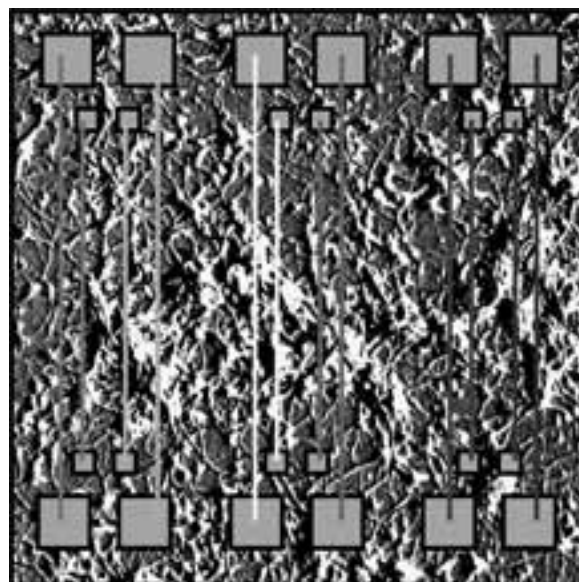


Figure 1: The contacts were arranged on the substrate with the contacts represented by the grey squares. A “large vertical” configuration is shown with the large lines being current and the short lines are voltage measurement. The sets of colors show that we can perform six measurements across the sample. The 10-micron by 10-micron AFM image underneath shows the networks on the substrate (not to scale compared to the substrate).

peak was sensitive to the number of defects created and was obtained by using a numerical approach. The peaks were subtracted from a linear background and then a trapezoidal rule was performed to get the areas and ratios.

The resistance across the CNT network was also measured using two probe and four probe measurements. Using the contacts, a current was swept through the network and the voltage drop was measured at each oxidation step to obtain the resistance. Since the samples were not homogenous, different combination of contacts were tried across the sample. Figure 1 represents how a four probe measurement “large vertical” configuration was done.

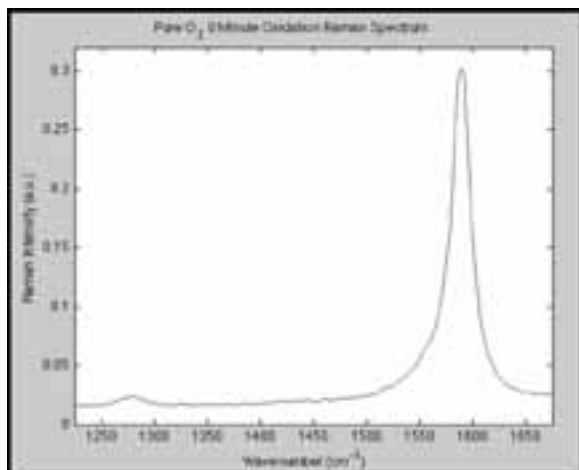


Figure 2: Pure  $O_2$  zero minute Raman spectrum to show the D and G peak shown as the left and right peak, respectively.

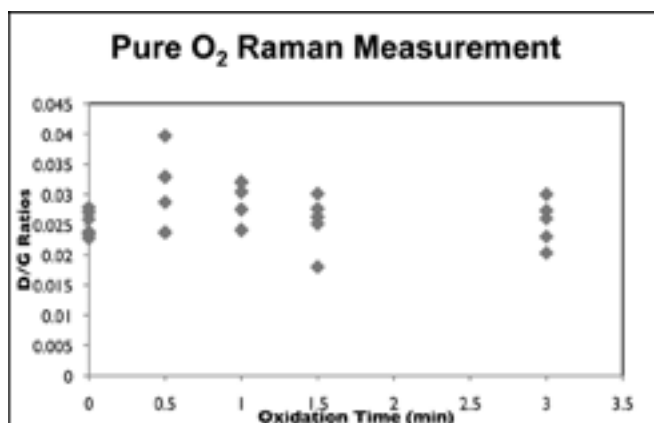


Figure 3: D/G Ratios from pure  $O_2$  measurements. As shown the ratios stay constant within the error of the measurements.

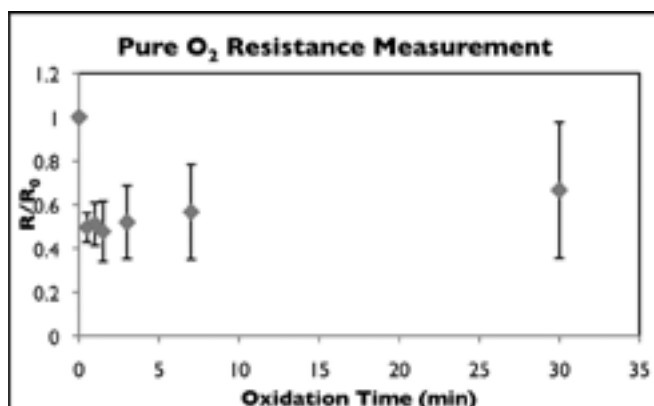


Figure 4: Resistance measurement of the pure  $O_2$  sample from the large vertical configuration shown in Figure 1.

## Results and Discussion:

The ratio between the area under the D peak and the area under the G peak stayed constant throughout the oxidation, as shown by Figure 3. The resistance across the channels for all three conditions went down sharply after an initial oxidation of thirty seconds to a minute and then stayed constant within the errors of the measurements until oxidation was stopped after 30 minutes. Figure 4 displays the results of the resistance measurements of pure  $O_2$  with the “large vertical” configuration.

The D/G plots didn't seem to show strong evidence for defect formation on the CNTs. This was likely due to the fact that  $420^\circ\text{C}$  was not hot enough for significant amount of defect formation. With the resistance, the initial drastic drop can be attributed to the CNTs crosslinking, which would create stronger paths for the current to flow through. Afterwards, the resistance stays constant within the errors of the measurements. This agrees with the little to no defects formed on the CNTs. At  $450^\circ\text{C}$ , on the contrary, oxidation definitely takes place; the D/G ratio saturates to twice of its original value and resistance decreases until 12 min [4].

## Conclusions:

CNTs were grown in a tube furnace in a network on top of a quartz substrate. The CNTs were oxidized in three different manners, pure  $O_2$ ,  $N_2/O_2$  mix, and air, all at  $420^\circ\text{C}$ . These tubes were analyzed using Raman spectroscopy and resistance measurements. The Raman measurements did not show any change in the D/G ratio, but the resistance decreased. The constant D/G ratio was most likely due to the fact that  $420^\circ\text{C}$  was not hot enough to create defects on the tubes. The sharp drop in resistance after initial oxidation can be explained by CNTs crosslinking.

## References:

- [1] L. Bogani and W. Wernsdorfer. Molecular Spintronics Using Single-Molecule Magnets. *Nature Materials*. 7, 179-186 (2008).
- [2] C. Meyer, C. Besson, R. Frielinghaus, et al. Covalent Functionalization of Carbon Nanotubes with Tetramanganese Complexes. *physica status solidi (b)*. (to be published).
- [3] E. Kampert, F. Janssen, D. Boukhvalov, et al. Ligand-Controlled Magnetic Interactions in Mn4 Clusters. *Inorg. Chem.* 48, 11903-11908 (2009).
- [4] M. Slot. Raman spectroscopy and electronic transport measurements on carbon nanotube networks: influence of oxidation and functionalization with {Mn4} complexes. Bachelor thesis, RWTH Aachen University, Germany (2012).

## Monolayer Molybdenum Diselenide

**Elisa M. Russo**

**Chemistry, Biology, Gannon University**

*NNIN REU Site: Cornell NanoScale Science and Technology Facility, Cornell University, Ithaca, NY*

*NNIN REU Principal Investigator: Paul L. McEuen, Laboratory of Atomic and Solid State Physics, Cornell University, Kavli Institute at Cornell*

*NNIN REU Mentor: Kathryn L. McGill, Laboratory of Atomic and Solid State Physics, Cornell University, Kavli Institute at Cornell*

*Contact: emr244@cornell.edu, mceuen@ccmr.cornell.edu, klm274@cornell.edu*

### Abstract:

We fabricated a device based on few-layer molybdenum diselenide ( $\text{MoSe}_2$ ), a unique two-dimensional (2D) semiconducting material in the family of transition metal dichalcogenides. Unlike its sister material, molybdenum disulfide ( $\text{MoS}_2$ ), monolayer  $\text{MoSe}_2$  is largely unexplored [1]. Here, we employed the same exfoliation technique developed by the winners of the 2010 Nobel Prize in Physics for their work with graphene [2]. In this method, scotch tape is used to exfoliate  $\text{MoSe}_2$  crystals. These crystals are then deposited on the surface of a silicon dioxide/silicon chip. Using an optical microscope, few-layer  $\text{MoSe}_2$  pieces are identified. A precise measurement of the thickness of each  $\text{MoSe}_2$  piece is determined using atomic force microscopy. By combining these methods with electron-beam lithography to create a transistor, we can ultimately examine the unexplored optical and electronic properties of monolayer  $\text{MoSe}_2$ .

### Introduction:

In recent years 2D semiconducting materials have been produced that exhibit interesting electrical and optical properties. In monolayer materials, electrons behave differently than in bulk materials. As electrons move through monolayer materials, they are confined to two dimensions, thus resulting in different properties. Graphene is a 2D material that has been greatly explored. One interesting property of graphene is that it has a very high electron mobility of  $200,000 \text{ cm}^2 \text{ V}^{-1}\text{s}^{-1}$  [3]. However, graphene does not have a

naturally existing band gap and its on/off current ratio of five is very low [4]. Due to this lack of a naturally existing band gap, graphene is not an ideal material for making transistors. For the fabrication of 2D transistors, it is essential to find new 2D semiconducting materials. Recently, a family of compounds known as the transition metal dichalcogenides has been of interest in monolayer form. One transition metal dichalcogenide, molybdenum disulfide ( $\text{MoS}_2$ ), has been studied widely in monolayer form. This material has a band gap of 1.8 eV, an on/off current ratio of  $10^8$ , and an electron mobility of  $380 \text{ cm}^2 \text{ V}^{-1}\text{s}^{-1}$  [5].

We explored another transition metal dichalcogenide, molybdenum diselenide ( $\text{MoSe}_2$ ), with the hopes of finding a material with similarly high on/off ratio, but with a lower band gap, and a higher electron mobility.

$\text{MoSe}_2$ , shown in Figure 1, is an inorganic compound that has been used in bulk form for many years as a dry lubricant. The predicted band gap of a monolayer based on the band structure of a bulk crystal is 1.6 eV. The approximate height of a single layer of  $\text{MoSe}_2$  is 0.65 nm, as determined from a bulk crystal. Once these layers are exfoliated and isolated, then electrical and optical properties of this unexplored monolayer material may be investigated.

### Experimental Procedure:

First, we deposited  $\text{MoSe}_2$  crystals on Scotch™ tape and then ripped the tape apart several times until the crystals were very fine. Due to van der Waals interactions, this material's layers could be easily ripped apart. Second, the tape containing the exfoliated  $\text{MoSe}_2$  crystals was placed on top of a silicon chip with 285 nm of thermally grown  $\text{SiO}_2$ . Then we rubbed the tape against the chip to transfer the exfoliated crystals from the tape onto the chip. Next, an optical microscope was used to scan the chip for possible monolayer, bilayer, and trilayer pieces of  $\text{MoSe}_2$ . This process took advantage of the way that  $\text{MoSe}_2$  absorbs light to determine if a piece could possibly be one to a few layers thick. Typically, a monolayer to bilayer of  $\text{MoSe}_2$  appears pink to light purple in color.

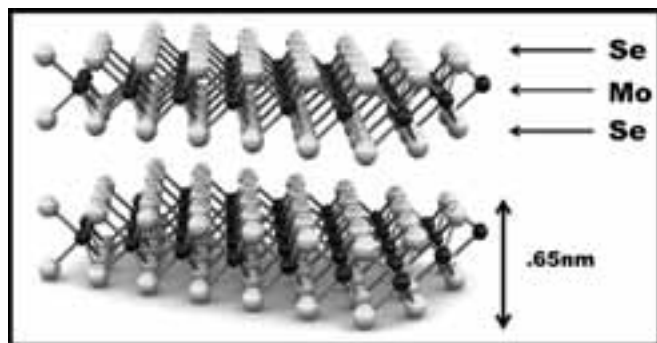


Figure 1: Structure of  $\text{MoSe}_2$ , after [1].

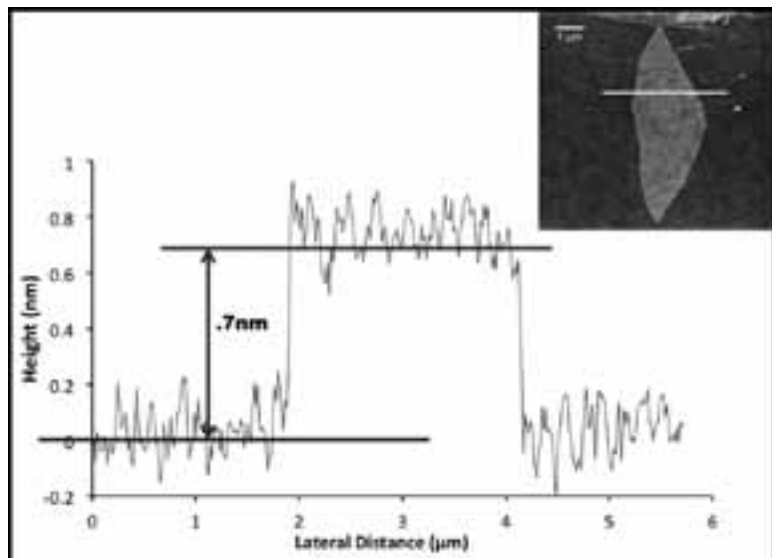


Figure 2: Cross-sectional plot of a monolayer of  $\text{MoSe}_2$ . The AFM image is in the upper-right corner; the cross-section is indicated by the white line.

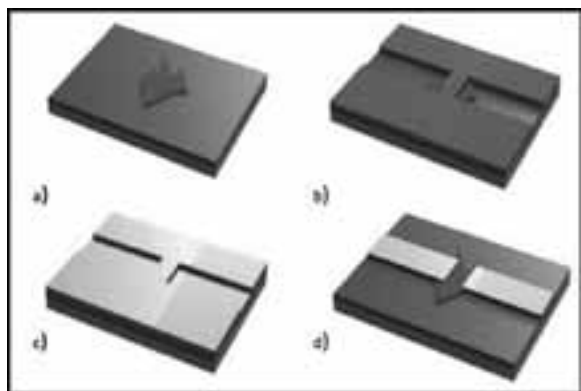


Figure 3: Device fabrication process.

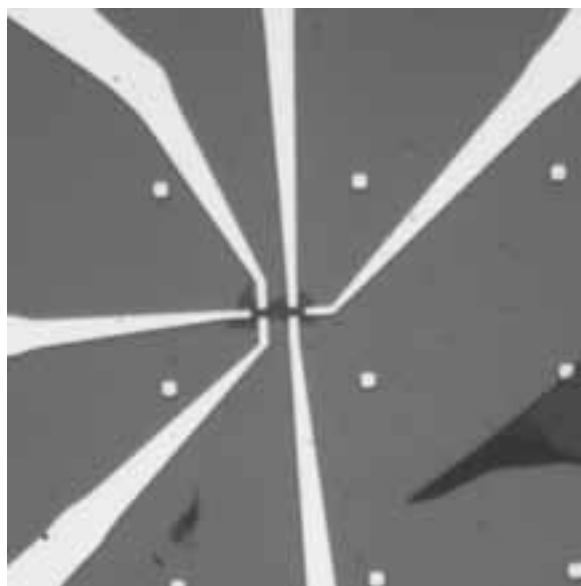


Figure 4: Completed device made from a trilayer piece of  $\text{MoSe}_2$ .

Then an atomic force microscope (AFM) was used to confirm the height of interesting  $\text{MoSe}_2$  pieces. By looking at a cross-sectional plot of the  $\text{MoSe}_2$  sample, shown in Figure 2, we were able to measure the height of each piece. Keeping in mind that a single layer of  $\text{MoSe}_2$  as measured from a bulk crystal is 0.65 nm thick, we used the AFM cross-sections to determine if a given piece was a monolayer, bilayer, or trilayer. Our device fabrication process is illustrated in Figure 3.

Fabrication started with a thin piece of exfoliated  $\text{MoSe}_2$  on the silicon chip (Figure 3a). Next, the chip was spun with resist. Exposure to the chip via electron-beam lithography and development followed (Figure 3b). Finally, 50 nm of Au were evaporated for electrodes (Figure 3c). The transistor device was completed upon lift-off of the Au (Figure 3d).

Figure 4 shows the fine features one of the several devices that were successfully fabricated.

### Summary and Future Work:

We successfully exfoliated and isolated few-layer  $\text{MoSe}_2$ . Sixty thin samples of  $\text{MoSe}_2$  were exfoliated and measured using AFM, and several few-layer  $\text{MoSe}_2$  devices were successfully fabricated. We are currently working towards measuring the electrical and optical properties of  $\text{MoSe}_2$ . The devices we fabricated will be used specifically to look at the band gap, on/off current ratio, and mobility of monolayer  $\text{MoSe}_2$ .

### Acknowledgements:

We extend our thanks to the National Nanotechnology Infrastructure Network Research Experience for Undergraduates (NNIN REU) Program, National Science Foundation, Cornell NanoScale Science and Technology Facility, Rob Ilic, Melanie-Claire Mallison, and to all the CNF Staff.

### References:

- [1] B. Radisavljevic, A. Radenovic, J. Brivio, V. Giacometti, and A. Kis, *Nature Nanotechnology* 6, 147-150 (2011).
- [2] K. S. Novoselov, A. K. Geim, S. V. Morozov, D. Jiang, Y. Zhang, S. V. Dubonos, I. V. Grigorieva, and A. A. Firsov, *Science* 306, 666-669 (2004).
- [3] K.I. Bolotin, K.J. Sikes, Z. Jiang, M. Klima, G. Fudenberg, J. Hone, P. Kim, H.L. Stormer, *Solid State Communications* 146, 351-355 (2008).
- [4] F. Xia, F. Xia, D. B. Farmer, Y-M. Lin, and Ph. Avouris, *Nano Letters* 10, 715-718 (2010).
- [5] H. Wang, L. Yu, Y-H. Lee, Y. Shi, A. Hsu, M. Chin, L-J. Li, M. Dubey, J. Kong, T. Palacios, *Nano Letters*, doi: 10.1021/nl302015v.

## Oxidation Effect in Single Dot Quantum Junctions

Reyu Sakakibara

Chemical Biology: Electrical Engineering and Computer Science,  
University of California, Berkeley: Massachusetts Institute of Technology

NNIN iREU Site: Delft University of Technology (TU Delft), Netherlands

NNIN iREU Principal Investigator: Prof. dr. ir. Herre van der Zant, Quantum Nanoscience, Technische Universiteit Delft

NNIN iREU Mentor: MSc. Michele Buscema, Quantum Nanoscience, Technische Universiteit Delft

Contact: reyu@mit.edu, h.s.j.vanderzant@tudelft.nl, m.buscema@tudelft.nl

### Abstract:

Three-terminal devices with a monolayer of quantum dots (QD) between nanometer-spaced gold electrodes allows for the study of single electron quantum transport. Indeed, IV measurements for a 50 nm device show characteristic Coulomb staircase under dark condition and with 543 nm and 670 nm light. However, lead selenide (PbSe) devices of various sizes exhibited current fluctuations on the order of nanoAmperes (nA) over time, both under dark condition and with light. Also, a slow relaxation after shining light was observed. With increasing oxidation, the devices stabilized and the relaxation time decreased, which suggests the surface state of the QD governs transport through the device.

### Device Fabrication:

The devices had high aspect ratios: while the width of the devices varied from 10  $\mu\text{m}$  to 20 nm, the gap between the electrodes was kept at about 6 nm to fit the QD monolayer. In order to achieve this, a layer of chromium (Cr) was evaporated on top of titanium (Ti) adhesion and first gold (Au) electrode layers. The growth of  $\text{Cr}_x\text{O}_y$  led to an overhang over the edges of the first layer. The overhang served as a mask for the second Au electrode layer, producing 6 nm gaps when the Cr and oxide were etched away [1]. A monolayer of PbSe colloidal QD was deposited via the dipcoating method [2]. Ligand substitution, which increases coupling to the electrodes, was performed with 1,2-ethanedithiol (EDT).

### Theory:

Device behavior was modeled on single electron resonant transport, which assumed weak coupling (though coupling may be much stronger because EDT is short). The QD can be considered to have discrete quantum levels (Figure 1).

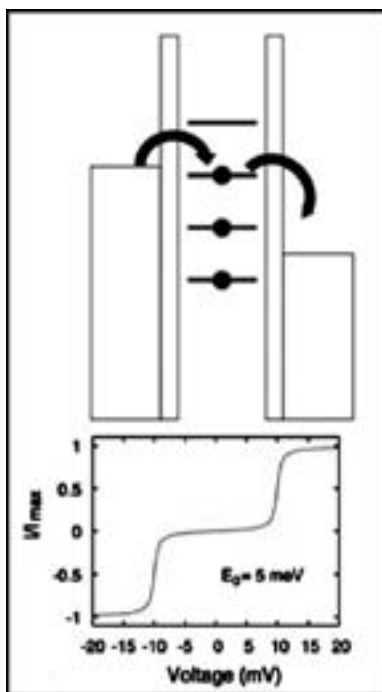


Figure 1: Schematic of chemical potentials of QD and electrodes; Coulomb staircase.

Tunnel barriers separated the QD from the electrodes on each side, wherein the electrons obeyed the Fermi-Dirac distribution. To observe quantum behavior, low temperature was required to ensure that the energy difference between quantum levels in the QD ( $\sim 1 \text{ meV}$ ) and the charging energy of the device ( $e^2/2C$ ), where  $C$  is the capacitance of the device,  $\sim 25 \text{ meV}$ ) were greater than the thermal energy of the charge carriers.

In these devices, current was driven by the chemical potential difference between the charged states in the QD and the electrodes. For resonant transport, the chemical potential of the QD charged transition state must lie within the bias window, which is the energy range between the chemical potentials of the electrodes. Electrons with energy resonant with the QD level tunneled from occupied states in the source to the QD, then ended up in empty states in the drain. A sharp increase in current was observed as a step when the bias window enclosed a resonance.

At low bias, current was suppressed as there were no transitions that were within the bias window. For the QD to undergo a charge transition (by adding or removing an electron to or from the QD), a charging energy penalty was required. This region of high differential resistance is known as a Coulomb blockade and is observed as a flat region in the IV curves.

Photoconductance depended on the formation of excitons and extraction of charge carriers to the electrodes. Formation of excitons depended on the absorption rate, which depended on laser power. Photoconductance varied monotonically with the laser power density; therefore, increased current should be observed with increased laser power.

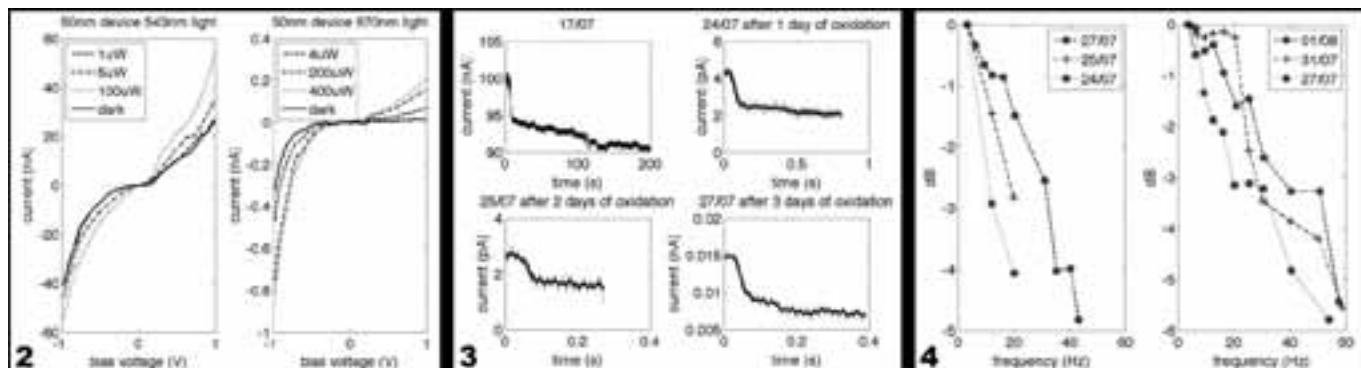


Figure 2, left: Coulomb staircase in 50 nm device at 10K.

Figure 3, middle: Continuous-wave measurement of current decay at room temperature.

Figure 4, right: Time-resolved measurement with modulated light intensity at room temperature.

## Results:

IV measurements were performed from -1V to 1V in vacuum and at cryogenic temperatures. Figure 2 shows a 50 nm device that exhibited step behavior characteristic of single or few QDs. Photoconductance was observed for both 543 nm and 670 nm. The Coulomb blockade region became smaller with increased laser power as well. For the larger devices with more QDs, the IV curves were smoother, indicating that the presence of many QDs smoothed out the staircase behavior of a single QD. However, the reference dark IVs changed by a few nA over days, with no apparent trend for the change in Coulomb blockade region size or magnitude of current. Measurements of current over hours at 0.5V showed fluctuations of order nA as well.

The devices were exposed to air in room temperature one day at a time. After each day of oxidation, continuous-wave and time-resolved measurements were performed. For the continuous-wave measurement, after shining 670 nm 100  $\mu$ W light, the devices were then covered and the decay of the current was observed over time. For the other measurements, the intensity of the light was modulated at increasing frequencies in order to observe when the device stopped exhibiting photoresponse. The value of 3dB was a metric for the cutoff of photoresponse.

Figure 3 clearly shows the relaxation time decreased with increased oxidation, especially dramatically after one day. Figure 4 shows that with the frequency for the cutoff of photoresponse increased with increased oxidation. These both indicate that the device showed clearer photoresponse with increased oxidation.

## Future Work:

Oxidation reduces the time dependence of current and the relaxation time in these three-terminal devices. However, the measurements performed were only preliminary measurements and oxidation was not performed in a completely controlled fashion. Future work includes oxidation of different systems in a more controlled manner, with variation of QD type (CdSe, for example) and device width.

## Acknowledgments:

This work was supported by the National Science Foundation under Grant No. ECS-0335765. This work was performed at Technische Universiteit Delft in the Netherlands. Special thanks to Professors Herre van der Zant and Hans Mooij, mentor Michele Buscema, Lynn Rathbun, the Molecular Electronics and Devices group, and the National Nanotechnology Infrastructure Network International Research Experience for Undergraduates (NNIN iREU) Program.

## References:

- [1] Prins, F., et al., Photonic gating in nanoscale quantum-dot photo-detectors. Submitted.
- [2] Fursina, A., et al., Nanogaps with very large aspect ratios for electrical measurements. *App. Phys. Lett.* 2008, 92, 113102.
- [3] Thijssen, J.M., et al., Charge transport and single-electron effects in nanoscale systems. *Phys. Stat. Sol. (b)*. 2008, 245, 1455-1470.

## A 3D Circuit QED Architecture with Separate Readout and Coupling Cavities

**Kevin Tien**

**Electrical Engineering, The Cooper Union  
for the Advancement of Science and Art**

*NNIN iREU Site: Delft University of Technology (TU Delft), Netherlands*

*NNIN iREU Principal Investigator and Mentor: Dr. Leonardo DiCarlo, Dept. of Quantum Nanoscience  
in the Faculty of Applied Sciences, Delft University of Technology*

*Contact: kvn.tien@gmail.com, l.dicarlo@tudelft.nl*

### Abstract:

This work presents the development of a three dimensional circuit quantum electrodynamics (3D cQED) architecture with separate cavities for inter-quantum bit (qubit) coupling and for qubit readout. Such a separation allowed for optimization of the cavities for their separate tasks, as opposed to the compromise necessary in single-cavity architectures. The device designed was a 3D analogue of a working multi-resonator, multi-transmon qubit device in standard, planar circuit QED. By switching from coplanar waveguide (CPW) resonators to 3D cavity resonators, we expected to attain significantly higher qubit and resonator coherence times (tens of microseconds), allowing realization of complex quantum computing algorithms, while retaining the virtue of physical scalability. The architecture pursued also included local flux tuning of qubit transition frequencies, necessary for control

of qubit-qubit interactions on nanosecond timescales. We present here the design, simulation and initial characterization of the first prototype.

### Introduction:

The emergence of cQED as a leading paradigm for the solid-state realization of quantum information processing has inspired a slew of refinements on the basic topology, which uses CPW resonator(s) to couple to one or more qubits. One such refinement replaces the CPW resonator(s) with 3D superconducting cavity resonator(s), a change that improves coherence times. Another refinement introduces separate cavities for readout and for memory/coupling. A multi-cavity scheme allows for specialized tuning of qubit-cavity coupling strength,  $g$ . A high  $g$  is desired between the qubit and the dispersively coupled readout cavity in order to increase the distinction between the measurements corresponding to the two qubit states, translating to an increase in readout fidelity. However, such strong coupling between the qubit and the inter-qubit coupling cavity creates residual cross-coupling between qubits. If resonant gates are used, then this coupling can be decreased to mitigate these negative inter-qubit effects while still matching the gate times achieved with dispersive gates.

It was thus straightforward to combine the above two ideas and to conceive of a multi-resonator, multi-qubit 3D cQED architecture. It should be noted that any such architecture should ideally also include the flux bias lines needed to tune the qubit transition frequencies on nanosecond timescales, needed to realize multi-qubit gates. In this work, we made use of a transmon qubit consisting of two superconducting aluminium islands connected by two Josephson junctions, all on a sapphire substrate.

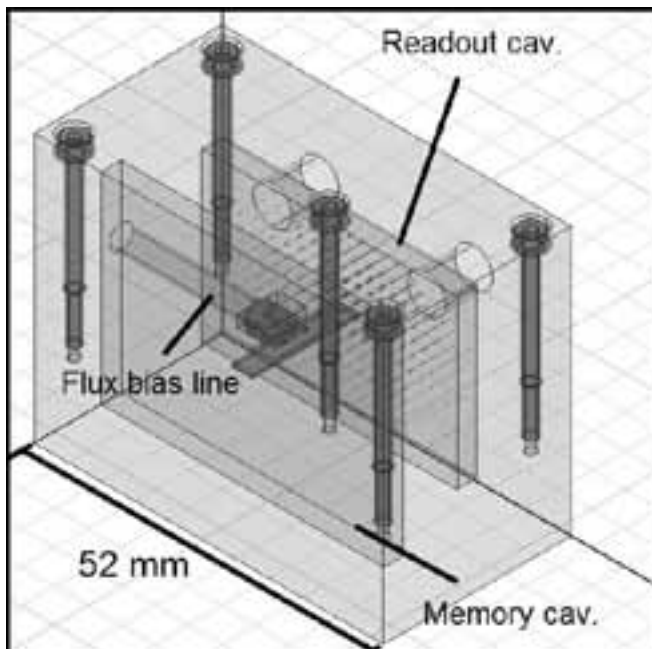


*Figure 1: HFSS model of device geometry. The qubit substrate straddles the two cavities. The fundamental mode of the readout cavity is displayed as a vector plot.*

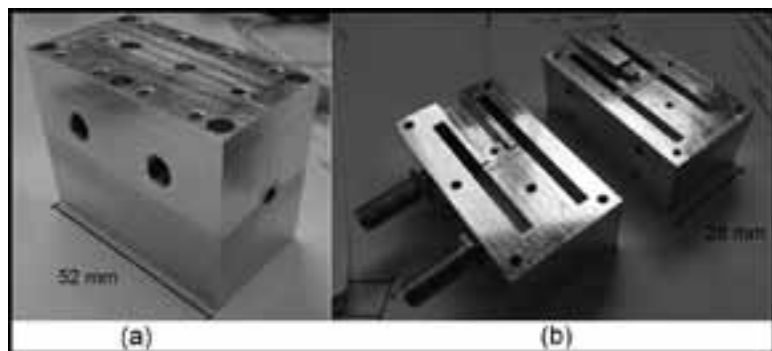


Figure 2: (a) Fabricated device, fully assembled.  
(b) Fabricated device in two halves with connector/substrate visible.

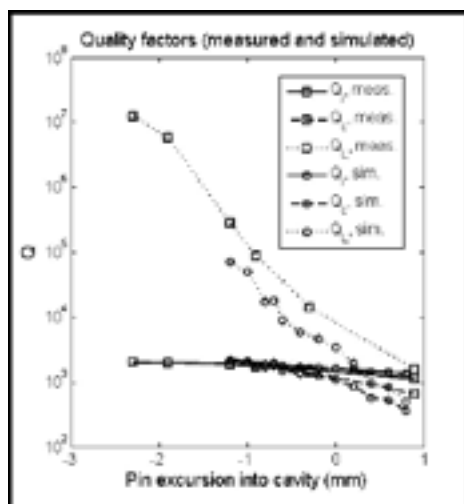


Figure 3: Loaded, intrinsic, and external quality factors as simulated and as measured. In simulation, zero dielectric loss is assumed, and the cavity is defined with bulk conductivity  $3.8 \times 10^7$  S/m.

## Design:

The cavity design was carried out primarily using ANSYS high frequency structure simulator (HFSS), a full wave simulator that allowed modeling of high-frequency electromagnetic behavior in arbitrary geometries. With HFSS, we could determine the geometries that provided the desired resonant frequencies and make predictions concerning the coupling and intrinsic quality factors of the individual cavities. Figure 1 displays the HFSS model for reference.

The qubit design was carried out using ANSYS Maxwell, a simulator geared towards electro- and magneto-static simulations. We employed it to calculate the inter-island capacitance of the qubit structure, a parameter that determines the charging energy of the qubit. Due to the device geometry, however, the physical size of the qubit was nearly a fifth of a wavelength at the highest operating frequency of interest. This implied that the super-conducting islands acted as distributed elements, rather than as lumped elements, casting some uncertainty on the simulation results.

Flux bias was controlled by applying a voltage between a shorted trace and ground, generating a current through the

trace that in turn gave rise to a magnetic flux normal to the plane of the trace. The use of very small profile connectors was necessary due to the relatively high (7 GHz) frequencies of operation of the device. We employed a standard miniature subminiature push-on (SMPM) edge launch connector to realize the connection of a coaxial cable to the trace on the substrate.

## Fabricated Device:

The finalized design was sent to a professional rapid CNC prototyping company for manufacture in aluminium 6082-T651. Figure 2 depicts the fabricated device. In actual operation, the qubit and flux bias geometry will be fabricated on the displayed substrate, and the connector will be wirebonded to the flux bias geometry.

## Experimental Results:

At this time, only room temperature measurements of transmission through the readout cavity have been made, varying coupling strength by using coupling pins of different lengths. Good qualitative agreement is seen between HFSS and measured results. Ten resonant modes of the readout cavity were observed and differed from those predicted by simulation by, at most, 150 MHz. The average deviation was 45 MHz, and the median deviation was 20 MHz. The desired resonant frequency for the fundamental mode of the readout cavity was 7 GHz; the observed value was 7.03 GHz. Figure 3 depicts measured and simulated quality factors for the readout cavity.

## Conclusions:

A preliminary two-cavity one-qubit device has been fabricated, and initial characterization does not deviate significantly from predicted behavior. The next step is to characterize the device under superconducting conditions (i.e., low temperatures) and finalize/fabricate a qubit for this device. At this time, a scaled-up three-cavity two-qubit device has been fabricated, and future work will include realization of quantum algorithms with the benefits of this architecture.

## Acknowledgements:

We would like to thank Dr. Leo DiCarlo for his role as principal investigator, Diego Ristè and Vishal Ranjan for helpful discussion, and Remco Roeleveld for final machining. We thank the entire QT team for their overall support, especially Hans Mooij for his role as our formal contact here. Finally, we thank the NNIN iREU Program and the NSF for their financial support.

## Production and Characterization of Topological Insulators

**Adam Blonsky**

**Physics, University of Wisconsin - Madison**

*NNIN REU Site: NanoTech User Facility, University of Washington, Seattle, WA*

*NNIN REU Principal Investigator: Dr. Xiaodong Xu, Physics, University Of Washington*

*NNIN REU Mentor: Bo Zhao, Physics, University of Washington*

*Contact: azblonsky@gmail.com, xuxd@uw.edu, peterzh@uw.edu*

### Abstract:

Topological insulators (TIs) represent a novel category of material whose bulk insulates, but whose surface conducts. The ability to produce topological insulators would be of great interest, because electron states can cross the insulating band gap, as well as surface conduction and spin-locking properties [1]. Bismuth selenide ( $\text{Bi}_2\text{Se}_3$ ) is one of the best candidates for three dimensional (3D) TIs. Our project focuses on developing a method to produce undoped and doped  $\text{Bi}_2\text{Se}_3$  via vapor-liquid-solid (VLS) deposition. Upon examination with a scanning electron microscope (SEM), energy dispersive x-ray spectroscopy (EDS) and x-ray diffraction (XRD), we found that both nanoribbons and nanowires about  $5 \mu\text{m}$  in length formed; the doped sample with 61.4% selenium, 33.30% bismuth, 5.66% antimony by atomic percentage, and the undoped sample with 61.62% selenium and 38.38% bismuth. Being able to produce these doped and undoped topological insulators opens up exciting new avenues of research into their properties and possible applications.

### Introduction:

In the last few years a new electronic crystal state was discovered, the topological insulator (TI). It is a unique state in which normal insulating states exist in conjunction with spin-

momentum locked electronic states. These extra electronic states are the source of much interest due to the fact that they cross the electronic band gap, as shown in Figure 1; leading to various interesting properties [1]. However, these states are difficult to examine due to the fact that they only exist on the crystal's surface, and therefore could be masked by bulk conduction from unintentional doping. To eliminate this effect, nanostructures, such as wires and ribbons that have large surface-to-volume ratio, are the ideal structure to find these topologically insulating states.

In order to create the best TIs, we must choose the correct material. The material we chose in this case was bismuth selenide ( $\text{Bi}_2\text{Se}_3$ ), due to the fact that it can exist as a nanostructured crystal, has a very simple band structure, is easily obtained, and can be doped with antimony [2].

Doping is the process where atoms in a crystal are substituted with similar atoms. In this case antimony substituted the bismuth atoms, which opened a band gap in the topological insulating states [3].

Our objective was to produce and characterize both antimony doped and undoped  $\text{Bi}_2\text{Se}_3$  nanostructures in order to test TI properties.

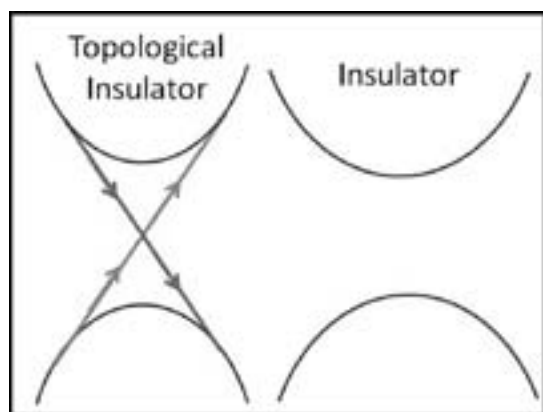


*Figure 1, above: Band diagram of an insulator and a TI. The arrows represent spin-momentum locking.*

*Figure 2, right: Our tube furnace setup where the growth took place, the crucible with  $\text{Bi}_2\text{Se}_3$  at the center of the glass tube.*



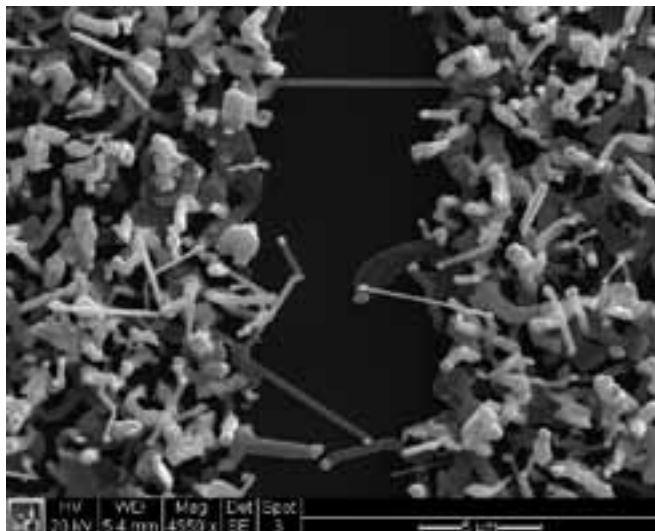


Figure 3: SEM image of Bi<sub>2</sub>Se<sub>3</sub> wires 5-10  $\mu$ m in length on a silicon substrate.

### Methodology:

We went about producing the Bi<sub>2</sub>Se<sub>3</sub> nanostructures via vapor-liquid-solid growth (VLS). In this process, the Bi<sub>2</sub>Se<sub>3</sub> source material was heated up and then carried to the substrate by an inert carrier gas. The substrate itself was coated with a 20 nm gold film prior to growth, and also heated so that the film melted and beaded up. These gold droplets catalyzed crystal formation as the vapor Bi<sub>2</sub>Se<sub>3</sub> deposited on the silicon substrate [4]. Our specific growth process used a tube furnace and argon as a carrier gas, as shown in Figure 2. The Bi<sub>2</sub>Se<sub>3</sub> source was placed at the center of the furnace, while the substrate was placed 9-11 inches away (380°C ~ 450°C). The furnace was pumped down to 500 mtorr and heated to 490°C for 2.5 hours. The argon source was at a pressure of 12 psi.

### Results:

Our growth resulted in many nanowires and some nano-ribbons forming that were 5-10  $\mu$ m in length, as shown in Figure 3. The characterization with XRD showed that the crystal structure matched up with Bi<sub>2</sub>Se<sub>3</sub> rather than other compounds containing bismuth and selenium. SEM and EDS verified that our bismuth selenium ratio was at 37.09% of bismuth and 62.91% of selenium, which was close to the expected 2:3 stoichiometry. Samples with antimony doping were characterized by EDS with atomic percentages of 33.30% bismuth, 61.04% selenium and 5.66% antimony, as shown in Figure 4, which agrees with direct substitution of bismuth with antimony.

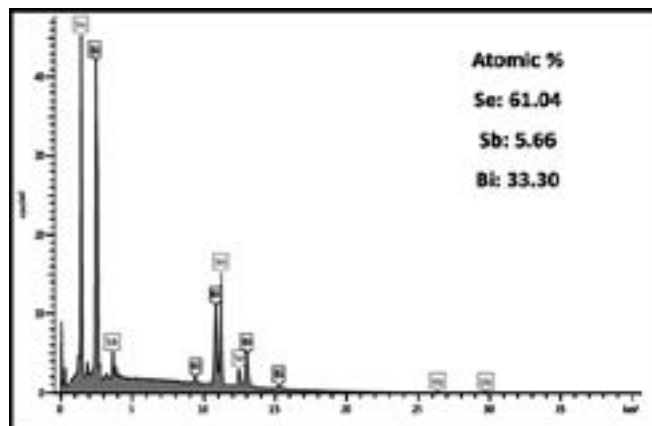


Figure 4: EDS graph on the atomic percentages of bismuth, selenium and antimony in a doped sample of Bi<sub>2</sub>Se<sub>3</sub>.

### Discussion and Future Work:

The production of these topological insulators was successful and matched our expectations. Now what is left to be done in this project is to perfect the drop casting method where the nanostructures are transferred from the silicon substrate to an insulating substrate in order to create electronic devices for testing.

### Acknowledgements:

I would like to acknowledge the National Nanotechnology Infrastructure Network Research Experience for Undergraduates Program and the National Science Foundation for allowing me this opportunity. I would also like to thank my principal investigator, Xiaodong Xu, my mentor Bo Zhao, and another member of the lab group, Jason Ross, for their help and guidance during this experience. I also wish to thank the Nanotech User Facility for their use of the equipment, and Paul Wallace for his aid in working with my material.

### References:

- [1] M. Hasan, et al., Topological Insulators, Rev. Modern Phys. 82 (2010).
- [2] Y. Cui, et al. Opportunities in chemistry and materials science for topological insulators and their nanostructures, Nature Materials 9, 225-229 (2010).
- [3] Y.L. Chen, et al. Massive Dirac Fermion on the Surface of a magnetically doped Topological Insulator, Science 329 (2010).
- [4] E.I. Givargizov, Fundamental Aspects of VLS Growth, Journal of Crystal Growth 31 (1975) 20-30.

## AFM-Assisted Etching and Electrical Characterization of Graphene

**Camille L.M. Everhart**

**Department of Mechanical Engineering, Massachusetts Institute of Technology**

*NNIN REU Site: Cornell NanoScale Science and Technology Facility, Cornell University, Ithaca, NY*

*NNIN REU Principal Investigator: Prof. Amit Lal, School of Electrical and Computer Engineering, Cornell University*

*NNIN REU Mentors: Kwame Amponsah, School of Electrical and Computer Engineering, Cornell University;*

*Hadi Hosseinzadegan, School of Electrical and Computer Engineering, Cornell University*

*Contact: everhart@mit.edu, amit.lal@cornell.edu, eka8@cornell.edu*

### Abstract:

A pressure sensor, consisting of graphene transferred onto a chromium/ gold (Cr/Au) electrode and a silicon nitride ( $\text{Si}_3\text{N}_4$ ) membrane, exhibits ultra high sensitivity. The device's high piezoresistivity was explored, and further measurements on the fabricated devices were taken for optimal design. Where typical, medical-grade pressure transducers have a sensitivity of 10 mV/V/mmHg, our device more than quadrupled this with as much as 50 mV/V/mmHg [1]. The transferred graphene was analyzed, employing scanning transmission electron microscopy (STEM), and both Raman and electron energy loss spectroscopy (EELS).

### Introduction:

In the current era of electronics, the rate of increase in device density has decreased. Graphene, exhibiting exceedingly high electron mobility, has become a promising supplemental material to carry electrons for device operation, and its piezoresistivity has made it a candidate for high sensitivity strain transduction. Perfectly structured, low-area regions of mono-layered graphene have been produced through exfoliation, but larger areas are required for manufacturing. The process widely used for large-area synthesis involves chemical vapor deposition (CVD) on a copper substrate, and transferal via polymer. This commonly introduces impurities and defects within the graphene. Quality-assurance in the films can be verified through Raman spectroscopy and EELS, which respectively assure the number of layers and the composition of the film. STEM allows direct imaging of the film to verify the hexagonal crystal lattice.

### Device Fabrication:

The device fabrication started with a double-sided polished (DSP),  $\langle 100 \rangle$ , p-type silicon wafer, with 500 nm of low stress, low pressure CVD (LPCVD) silicon-nitride. After removing photoresist with an oxygen dry etch, an anisotropic KOH wet etch terminated on the nitride layer, forming the membrane. Electron-beam evaporated electrodes, consisting of 140 nm of gold on top of a 10 nm chromium adhesion layer, were patterned through optical lithography and lift-off in warm acetone. Copper (99.8%) foil was cleaned in chrome etchant, dried, and placed in a nanotube furnace, optimized to grow graphene through low pressure chemical vapor

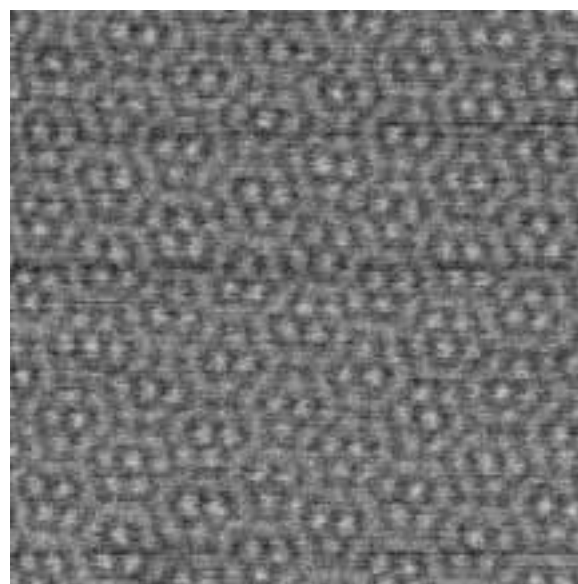
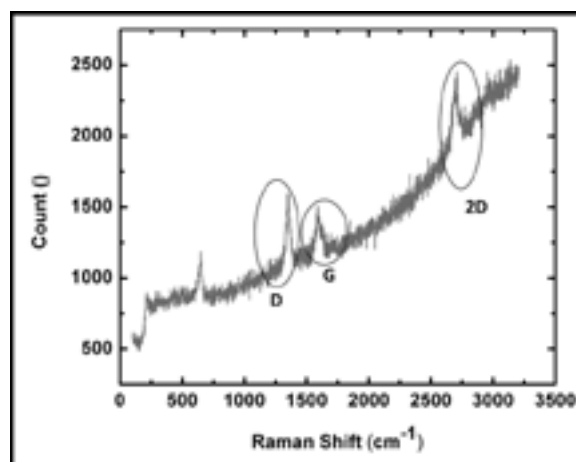


*Figure 1, top: Raman spectroscopy of graphene on copper substrate, where the D, G, and 2D peaks characteristic of graphene are shown. The D peak, which shows defects within the lattice, is very high in this particular sample. The G peak verifies the  $sp^2$ -bonds of graphene. The 2D peak can be used for identifying the number of layers. In this case, it is likely mono or bilayer graphene.*

*Figure 2, bottom: Nion STEM image of multi-layer graphene. Honeycomb atomic structure visible.*

deposition (LPCVD). Poly(methyl methacrylate) (PMMA) was spun onto each sample at 4000 rpm for one minute, and the copper was removed with iron (III) chloride etchant. After transferal through five baths of deionized water, each sample was placed onto the device membrane and left to dry. Lastly, the PMMA was ashed in a 325°C air ambient for three hours.

### Graphene Quality Measurements:

High-quality graphene consists of planar,  $sp^2$ -bound carbon atoms in a crystalline, honeycomb lattice. Raman spectroscopy was used to characterize the thickness of the carbon films. For our pressure sensor, multilayered graphene was suitable. Figure 1 shows a Raman spectrogram of graphene on Cu-foil. The background noise is due to the copper, but the D (defect), G (graphitic), and 2D peaks of graphene are clearly visible. STEM imaging of suspended graphene sheets is shown in Figure 2: an image of the atomic structure of a multi-layered film. The large defect peak of the sample shown is not necessarily representative of the graphene on our devices, as the growth process was improved. However, machinery issues hindered the acquisition of a better plot.

An unexpected finding of our film characterization was iron residue from the Cu-etching process. EELS confirmed a considerable amount of iron was found on our sample, but the existence of this iron has not shown to interfere with the efficacy of the device (Figure 3).

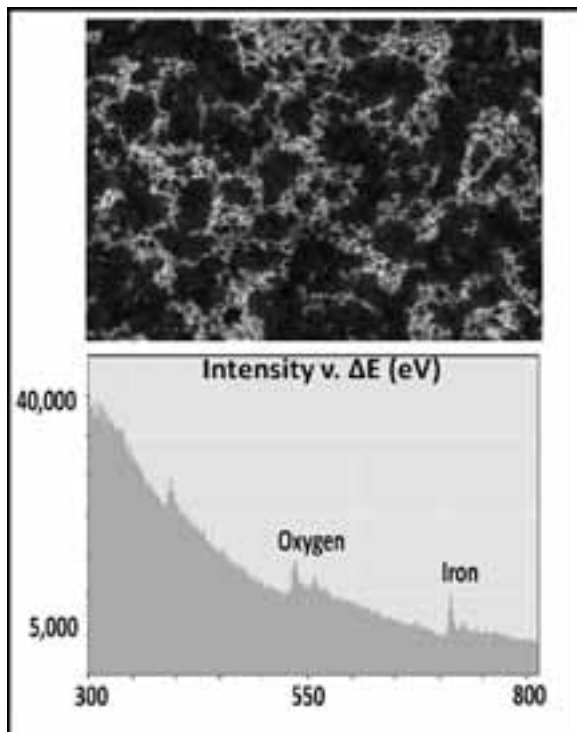


Figure 3: Nion STEM image of graphene on 50 nm silicon nitride nitride (top). The amorphous, high-contrast material confirmed to be iron through EELS, coming from the copper etchant used in the graphene transfer protocol (bottom).

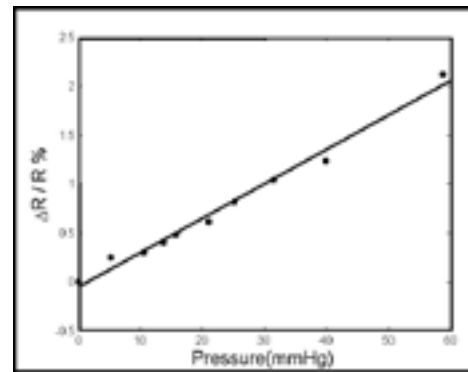


Figure 4: Fractional change in resistance vs. the applied pressure (mmHg). The current device, exhibiting 25% change at 5 mmHg, may be more sensitive for small pressures than its predecessor, which reached 15% at 6 mmHg. More measurements must be done for verification.

### Pressure Sensitivity Measurements:

The set of four electrodes on each device were used for four-point probe measurements, using an applied pressure drop and measuring the corresponding change in resistance (Figure 4). The applied pressure causes strain in the graphene film, changing its resistance. As stated in the original paper for this device, the pressure sensor should be highly non-linear [2]. However, the thicker membrane used in this study did not rupture and reached significantly higher pressures than expected from the first study. It is therefore possible that the results displayed here are all within a relatively linear regime. Further measurements were not able to be taken to confirm this hypothesis.

### Conclusions:

The current device is a viable microelectromechanical systems (MEMS) sensor, suitable for high sensitivity applications without requiring linearity. Further measurements will have to be taken. Hall effect measurements through the Van der Pauw method will have to be done to obtain the electron mobility of our graphene samples. Ascertaining piezoresistive non-linearity in the sensor via applied pressure, and actuating the membrane at resonance and using optical interferometry to determine strain, will be the likely next steps.

### References:

- [1] Carr, J. J., and Brown, J. M. (Apr 2, 2010 ). Introduction to biomedical equipment technology, third edition. Prentice Hall. Retrieved from <http://zone.ni.com/devzone/cda/ph/p/id/227>.
- [2] Hosseinzadegan, H., Pandey, M., and Lal, A. (2012). "Ultra High Sensitivity Graphene Piezoresistive Pressure Sensor"; 2012 IEEE 25th International Conference.
- [3] Hodkiewicz, Joe. "Characterizing Graphene with Raman Spectroscopy"; Thermo Fischer Scientific, n.d. Web. 07 Aug. 2012.
- [4] Meyer, J. C., et. al., "On the Roughness of Single- and Bi-layer Graphene Membranes"; Cornell Library, arxiv.org/, n.d. Web. 07 Aug. 2012.

## Engineering the Charge Occupancy of Nitrogen Vacancies in Diamond

**William Gilpin**

**Physics, Princeton University**

*NNIN REU Site: Center for Nanoscale Systems, Harvard University, Cambridge, MA*

*NNIN REU Principal Investigator: Professor Marko Lončar, Department of Electrical Engineering, Harvard University*

*NNIN REU Mentor: Dr. Khadijeh Bayat, Department of Electrical Engineering, Harvard University*

*Contact: wgilpin@princeton.edu, loncar@seas.harvard.edu, kbayat@seas.harvard.edu*

### Introduction:

Nitrogen vacancy (NV) centers are point defects in a diamond lattice that occur when a carbon atom is substituted with a nitrogen atom while a neighboring carbon atom is removed entirely. The resulting gap in the lattice has many desirable properties, such as paramagnetism and optical energy level transitions, that make it an ideal candidate for single-photon optics and quantum computing applications [1]. But the NV center tends to lose one of its surrounding electrons due to recombination with wandering positive charges in the crystal, providing a damaging barrier to the development of large-scale, multipartite quantum networks.

This project sought to deter this process by depositing transparent metal oxides and films on the surface of diamond nanowires, with a goal of inducing charge discontinuities at the surface that would stabilize the electronic configuration of the lattice by inducing a negative charge excess in the region around the defect. Additionally, metal oxide semiconductor field effect transistor (MOSFET) devices were designed that used a voltage gate on the surface of bulk diamond to accomplish the same effect, albeit with more control of the dopant level in the region due to modulation of surface voltage [2]. Designs and fabrication processes for both devices were created and ensemble measurements of devices using confocal microscopy have begun.

### Procedure:

**Nanowire Fabrication.** High-temperature, high-pressure Type Ib diamonds were obtained (HPHT, Element Six) and polished, and surface contaminants were removed with a boiling bath of equal parts perchloric, sulfuric, and nitric acid. 1%XR was spin-coated onto the diamond surface, followed by equal parts FOx-16 and methyl isobutyl ketone resists. Arrays of disks ranging from 200 nm to 250 nm in diameter were then patterned with varying dosages using an electron beam lithography system (Elionix ELS-F125). Tetra-methyl ammonium hydroxide was used to

develop the resist, and reactive ion etching was used to carve away diamond from around the disk patterns, creating pillars roughly 1.5 microns in height. Excess resist was removed using boiling Piranha etch (80% sulfuric acid, 20% hydrogen peroxide). Surface oxides were then deposited using atomic layer deposition (50 nm SiO<sub>2</sub> and 16 nm Al<sub>2</sub>O<sub>3</sub>), and the nanowires subsequently underwent rapid thermal annealing (three hours in O<sub>2</sub>).

**MOSFET Fabrication.** Diamonds were obtained and cleaned in the same manner as the nanowire samples. Using plasma-enhanced chemical vapor deposition, the polished surface was coated with 400 nm of silicon dioxide, onto which HDMS primer and SH1813 photoresist were spin-coated consecutively. Exposure was performed using direct write photolithography on a Heidelberg uPG501 with typical doses in the range of 100mJ. The patterned sample was then developed and placed in buffered oxide etch for two minutes. After cleaning and optical inspection, the sample was coated with 300 nm lift-off resist LOR 3 3A followed by 500 nm SH1805. A second mask was then aligned to the visible oxide pattern and exposed with the same dosage. The SH1805 was developed, and the sample was then covered with 150 nm of gold using electron beam evaporation. The assembly was left overnight in Remover-PG at 80°C for gold lift-off. After the gold contacts were inspected and the sample was cleaned, 500 nm indium tin oxide was deposited on the sample using sputtering (AJA Orion 3) and then topped with HDMS/SH1813 photoresists in the same manner as the first

layer. A final mask was aligned and exposed, and the ITO layer was then chemically etched using a mixture of equal parts concentrated hydrochloric acid and water.

### Results and Future Work:

Based on numerical models, devices were designed and fabricated that locally doped the diamond surface by donating free electrons into the diamond conduction band. Nanowires [3] were chosen to receive passivation coatings because they had a high

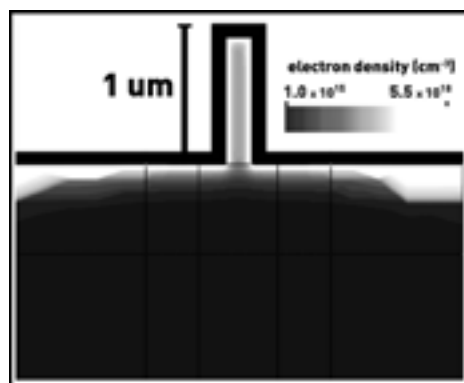


*Figure 1: A finite element simulation of doping in a diamond nanowire due to a surface coating of silicon dioxide.*

ratio of surface area to volume, allowing maximal theoretical carrier concentration around the vacancy center (Figure 1).

After recipe optimization, wires were successfully created on the surface of bulk diamond that exhibited satisfactory deposition uniformity for two different oxides (Figure 2), suggesting that the method successfully can be adapted for a variety of different oxides and thicknesses.

MOSFET devices were designed that adhered to material parameters determined by numerical simulations while allowing experimental flexibility. A three-mask photolithography process, including a gold lift-off step, was designed and optimized to yield high fidelity to the original digital design (Figure 3). While the process was originally developed on a silicon substrate for convenience, some difficulty was encountered in adapting the method for a smaller (2.5 mm square) diamond substrate, in part due to difficulty focusing and aligning on a smaller sample. These problems are purely technical in nature, and are expected to be resolved by the use of a specialized sample holder for the diamond during the lithography process.

Anti-correlation was successfully measured in photons emitted from the devices, and the nanowires yielded a clear fluorescence signal under laser excitation (Figure 4). Repeated measurements of ensembles of each type of device, however, are necessary to determine whether there is a significant increase in fluorescence from diamonds with devices, which would signal successful charge state stabilization of NV centers.

### Acknowledgments:

This project would not have been possible without the constant advice of my mentor, Dr. Khadijeh Bayat, who first ideated the project and who developed models illustrating how the effect could be attained. Our principal investigator, Professor Marko Lončar, supported the research and advised on our approach. Jennifer Choy, Birgit Hausmann, I-Chun Huang, and Dr. Madhi Baroughi — all provided recipes and methods and assisted with process optimization and troubleshooting. Additional appreciation goes to Dr. Kathryn Hollar, Jim Reynolds, Jorge Pozo, Melanie-Claire Mallison, and Dr. Lynn Rathbun. This research was supported by the NNIN REU Program and the National Science Foundation.

### References:

- [1] Mizouchi, N., et al.; “Electrically driven single-photon source at room temperature in diamond”; *Nature Photonics*, 6, 299-303 (2012).
- [2] Grotz, B., et al.; “Charge state manipulation of qubits in diamond”; *Nature Communications*, 1-6 (2012).
- [3] Babinec, T.M., et al.; “A diamond nanowire single-photon source”; *Nature Nanotechnology*, 5, 195-199 (2010).

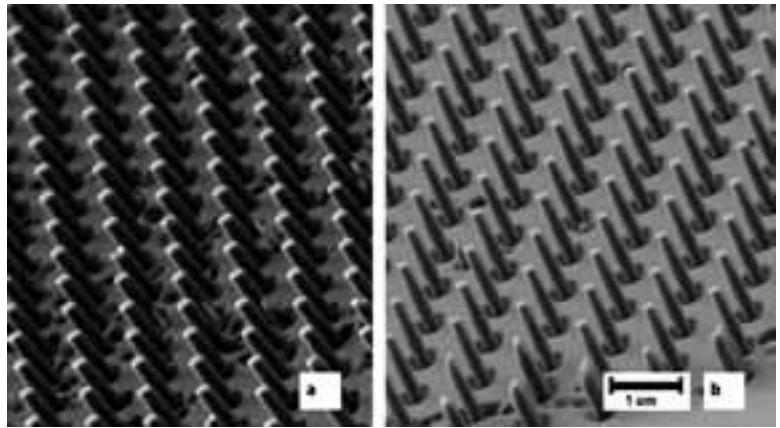


Figure 2: Diamond nanowires that have been coated with (a) 50 nm silicon dioxide, and (b) 22 nm aluminum oxide.

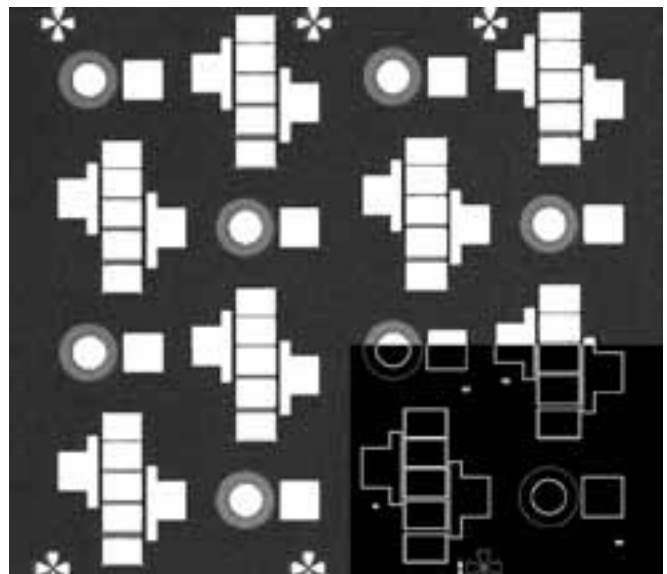


Figure 3: MOSFET structures on silicon. The smaller disks are 60 μm in diameter, and the original CAD design is inset.

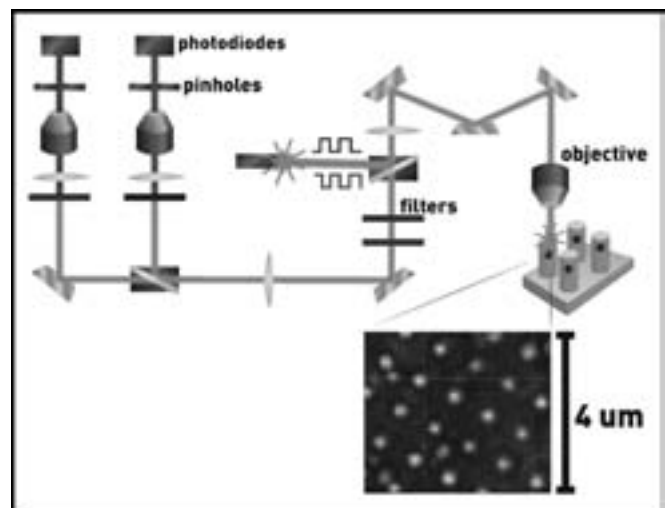


Figure 4: The confocal microscopy measurement setup, with a sample image of NV centers in nanowires.

## Sacrificial Polymers and Their use in Patternable Air-Gap Fabrication

**David Goldfeld**

**Chemistry and Physics, University of Chicago**

*NNIN REU Site: Nanotechnology Research Center, Georgia Institute of Technology, Atlanta, GA*

*NNIN REU Principal Investigator: Paul A. Kohl, Chemical and Biomolecular Engineering, Georgia Institute of Technology*

*NNIN REU Mentor: Erdal Uzunlar, Chemical and Biomolecular Engineering, Georgia Institute of Technology*

*Contact: dgold@uchicago.edu, paul.kohl@chbe.gatech.edu, eruzunlar@gatech.edu*

### Abstract:

Patternable air-gaps are added to electrical and mechanical structures in semiconductor and MEMS devices as a means to decrease the dielectric constant, add mechanical compliance, and facilitate microfluidics. In this study, sacrificial polymers and standard photolithographic techniques were used as a way to create air gaps. A photodefinable sacrificial polymer was created by adding photoacid generator (PAG) to the sacrificial polymer mixture. Air gaps were made by patterning the sacrificial polymer into the desired structure, covering it with an overcoat polymer, and decomposing the remaining sacrificial material. There are three problems associated with this fabrication technique: (i) the patterning resolution was coarse, (ii) residue was produced during the decomposition of the polymer, and (iii) wide structures tended to collapse. These problems were investigated through process optimization, quartz crystal microbalance (QCM), and overcoat modification, respectively. In addition, a new sacrificial polymer, PDM-1088, was investigated. PDM-1088 increased the resolution of the pattern, QCM measurements indicated the amount of remaining residue, and hardening the overcoat allowed the fabrication of structures several hundred micrometers wide. Micrometer scale air gaps were successfully fabricated through common photolithographic techniques, permitting the integration of these structures into semiconductor processing.

### Introduction:

Air-gaps have yet to be created using standard electronics processing techniques. They are desirable for use in semiconductor and MEMS devices as a means to decrease dielectric constant, add mechanical compliance, and facilitate microfluidics. In this study, photopatternable air-gaps were successfully fabricated by improving each of the three major problems associated with sacrificial polymers: i) difficulty patterning the sacrificial polymer, ii) residue after decomposition, and iii) wide structure collapse.

### Experimental Procedure:

Sacrificial polymers were used to create patternable air gaps. First, a new polymer, PDM-1088, was mixed with a photoacid generator (PAG) so that it could be patterned. The

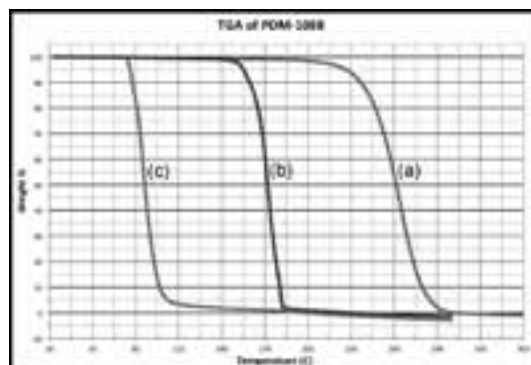


*Figure 1: Thermogravimetric analysis graph of PDM-1088; (a) without additives, (b) loaded with PAG, and (c) loaded with PAG and exposed to 248 nm UV light.*

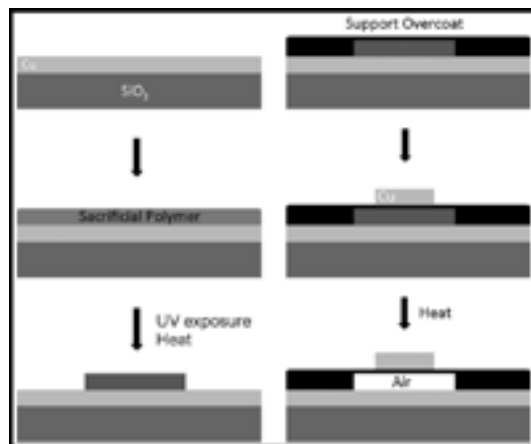


*Figure 2: Schematic of air gap fabrication method.*

PAG released a proton upon heating or by exposure to 248 nm UV light. The acid significantly decreased the decomposition temperature of the sacrificial polymer.

As shown in Figure 1, PDM-1088 mixed with PAG has a lower decomposition temperature (170°C) than the next polymer (260°C) and the exposed polymer/PAG mix has an even lower decomposition temperature (85°C).

Through standard photolithography, as explained in Figure 2, PDM-1088 was spin-coated onto a copper (Cu)-sputtered

silicon wafer and a pattern was exposed. Upon heating to 120°C, the exposed portions decomposed. An overcoat material was then spin-coated onto the sample. Two different overcoat polymers were used in this study; polyimide and Avatrel 8000 (polynorbornene). The overcoat was then exposed to 365 nm UV light to activate the polymer cross-linkers and was cured at 150°C for one hour. Finally, the sample was exposed a second time at 248 nm, activating all remaining PAG, followed by a six hour cure at 150°C to decompose the remaining PDM-1088.

### Results:

There are three major issues associated with this processing technique: i) patterns are coarse due to polymer reflow and proton diffusion, ii) the polymer leaves behind a notable residue after decomposition, and iii) wide structures tend to collapse in the center due to surface tension. These problems were solved systematically by modifying the processing approach in three ways.

PDM-1088 has a glass transition temperature of 90°C, which is higher than previous sacrificial polymers. Decreasing the processing temperature increased control of the polymer reflow resulting in the fabrication of clean patterns.

Quartz crystal microbalance (QCM) was used to measure the mass left behind after polymer decomposition. This quantification of the residue allowed modification of the processing techniques, polymer choice, and PAG loading to achieve minimal residue. Polymer samples were spin-coated onto quartz crystals. The crystal was allowed to equilibrate to its resonant frequency in the QCM, and then the residue was washed off without removing the sample from the instrument. Finally, the solvents were evaporated at room temperature and the crystal equilibrated again to its resonant frequency. The change in frequency allowed us to use the Sauerbrey equation [1] to calculate the mass of the residue left on the crystal. Figure 3 shows the linear relationship between polymer thickness and residue, meaning the residue is dependent on the composition of the formulation.

Wide air-gap structures were successfully fabricated by modifying the overcoat material. Avatrel 8000 was not strong enough to hold up air-gaps wider than 100  $\mu\text{m}$  as the surface tension pulled the overcoat onto the substrate. To strengthen the Avatrel, extra trimethylolpropane triglycidyl ether (TMPTGE) was added to the polymer. TMPTGE is a trifunctional polymer crosslinker used with Avatrel 8000, and the addition significantly increased the hardness, as seen in Table 1. By increasing the hardness, the resulting polymer was able to withstand surface tension pull, even at a thickness of 7  $\mu\text{m}$ . Adding TMPTGE worked significantly better than several other attempted methods, including the addition of surfactant (Triton X-100) and the addition of a second, glass-like polymer (epoxycyclohexyl polyhedral oligomeric silsesquioxane, or POSS).

### Conclusions:

By modifying processing methods and incorporating the use of PDM-1088, we successfully fabricated air gaps several hundred micrometers wide and only 5  $\mu\text{m}$  tall. For the first time, such structures were achieved with an overcoat thickness less than 10  $\mu\text{m}$ .

### Future Work:

The fabrication method we developed can now be used in direct applications including electronic interconnects, MEMS, and microfluidics. More work needs to be completed to increase resolution, reduce residue, and create wide structures for certain applications.

### Acknowledgments:

Thank you to the Kohl Group, support staff at Georgia Institute of Technology, and Monica Hochstein, an RET who contributed to this work. This research was part of the National Nanotechnology Infrastructure Network REU Program and is supported by the National Science Foundation. Thank you to Promerus<sup>®</sup>, LLC for their polymer contributions.

### References:

- [1] [http://en.wikipedia.org/wiki/Sauerbrey\\_equation](http://en.wikipedia.org/wiki/Sauerbrey_equation)

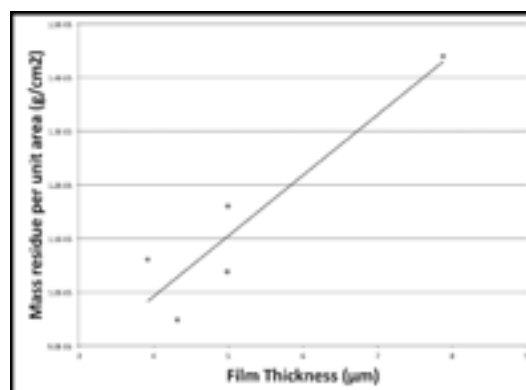


Figure 3: QCM results of mass residue vs. polymer thickness (PDM-1088 with PAG).

Overcoat	Elastic Modulus (GPa)	Hardness (GPa)
Avatrel	2.44	0.155
Avatrel + TMPTGE	3.19	0.199
Avatrel + POSS	1.49	0.169
Air Gap	0.71	0.121

Table 1: Hardness and elastic modulus values of modified Avatrel 8000 overcoats.

## Biomaterialized Nanopore Membranes on Silicon for Nanoparticle Translocation

Melissa Gosse

Chemical and Biomolecular Engineering, Johns Hopkins University

NNIN REU Site: ASU NanoFab, Arizona State University, Tempe, AZ

NNIN REU Principal Investigator: Dr. Michael Goryll, Electrical Engineering, Arizona State University

NNIN REU Mentor: Xiaofeng Wang, Electrical Engineering, Arizona State University

Contact: mgosse1@jhu.edu, michael.goryll@asu.edu, xiaofeng.wang.2@asu.edu

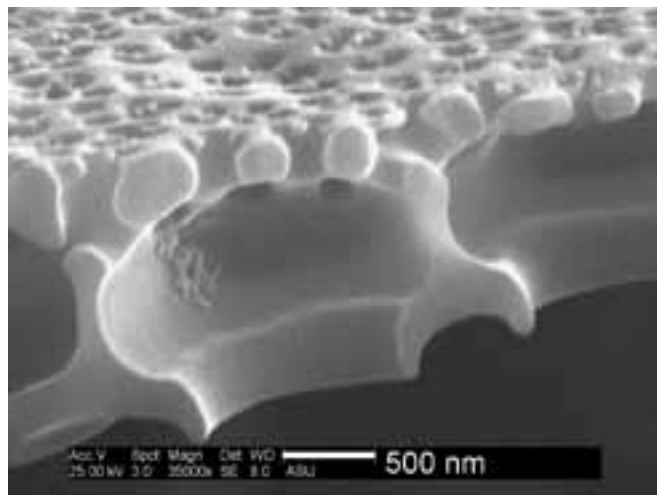


Figure 1: Scanning electron micrograph of the cross section of a diatom showing the different pore sizes.

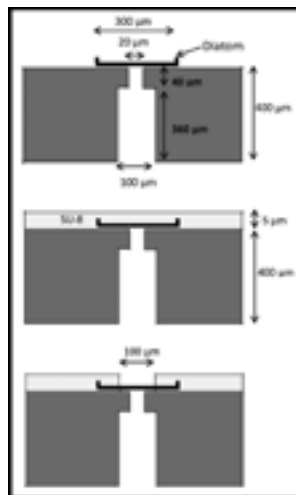


Figure 2: Schematic diagram of fabrication process.

Two photoresists were tested, SU-8 and NOA-60. SU-8 is a negative UV-curable photoresist that is well established in contact lithography. NOA-60 is polyurethane-based resin that adheres to glass. Therefore, it requires an anti-adhesion layer to enable release from the glass mask and the sample. Polydimethylsiloxane (PDMS) was used as the anti-adhesion layer as suggested in [1].

However, our experiments proved that the PDMS layer was ineffective in enabling separation of photomask and substrate after UV exposure.

SU-8 proved to be successful in meeting the criteria in combination with a sulfuric-peroxide mixture (SPM) treatment.

### Abstract and Introduction:

Nanopores have many biological applications. They can be used as single molecule detectors, deoxyribonucleic acid (DNA) sequencing, and potentially be functionalized to simulate lipid bilayers or nuclear pore complexes. However, these nanopores are expensive and time consuming to make using conventional microfabrication techniques. An alternative to these top-down processed nanopores is diatoms. Diatoms are a major group of algae that synthesize a three-tier network of silica pores for their cell wall, which can be seen in Figure 1. They can grow up to 300  $\mu\text{m}$  in diameter, yet the smallest pores are approximately 40 nm wide. In order to have access to these nanopores, the diatoms need to be positioned and immobilized over 20  $\mu\text{m}$  pores etched through silicon wafers.

Currently, the diatoms are manually placed over the pores and a UV curable epoxy, Norland optical adhesive-60 (NOA-60), is manually dispensed around the diatom. In order to create a more efficient process with a higher yield, standard contact lithography was explored to immobilize the diatoms over the micropore. The criteria used to determine the effectiveness of the process was to check for absence of leakages, breaking of the diatom or clogging of the nanopores.

### Fabrication Process:

Oxidized silicon wafers with through-wafer pores were used as substrates. The pore diameter on the back side of the wafer was 100  $\mu\text{m}$  and the pore diameter on the front side was 20  $\mu\text{m}$ . Details on the fabrication process of the silicon micropores can be found in [2].

Diatoms were deposited on the wafer from a 1:1 water:ethanol solution and positioned over the silicon the micropore using a micromanipulator. Subsequently, positively charged poly-L-lysine was used to form a temporary bond between the negatively charged diatom and the oxidized silicon wafer. After poly-L-lysine was deposited on the chip, SU-8 3005 was spun on at 3,000 rpm for 30 seconds. Once the post-exposure bake was completed, the mask consisting of a 100  $\mu\text{m}$  dot was aligned over the 20  $\mu\text{m}$  through-wafer pore. Exposure was completed on an EVG-620 with a dose of 350 mJ.

After the post-exposure bake, the chip was developed in SU-8 developer for two minutes and rinsed with isopropyl alcohol. A schematic of the process can be seen in Figure 2. The SPM treatment was completed using a 3:1 ratio of sulfuric acid to

peroxide. The diatom chip was placed in the mixture for two minutes.

### Results and Discussion:

Indication of open pores was found by testing for nanoparticle translocations using the setup in Figure 3. The diatom chip was placed between two chambers containing a nanoparticle solution of 100 nm polystyrene beads. Silver chloride-coated silver (Ag/AgCl) electrodes were inserted in each chamber and a constant voltage of 400 mV was applied. When a particle passed through a diatom nanopore, it changed the electrical resistance. Using the equation  $V = IR$ , a resistance increase lead to a decrease in current at a constant voltage. Therefore, a nanoparticle passing event resulted in a quick dip in ionic current.

Figure 3 shows the graph of multiple 100 nm polystyrene bead translocation events through diatom pores. The negative value of the current is due to an offset caused by the Ag/AgCl electrodes that have to pass the current. This also leads to the drift in baseline current.

One of the major concerns of using SU-8 was the possible stress it could put on the diatom during the baking process, which could cause cracking and breaking of the diatom. It can be seen in Figure 4 that SU-8 does not exert any excessive stress on the diatom. The SU-8 layer also formed a clean, complete seal around the diatom.

### Conclusions:

The process described proved to be successful in immobilizing the diatoms without any leaks, breaking, and clogging the diatom's nanopores. It was found that NOA-60 was problematic to use via contact lithography, because its strong adhesion to glass, and even PDMS, prevented clean separation of the substrate from the photomask. The SPM treatment was effective in removing residual SU-8. However it is still unclear how much the cleaning step affects the pore size of the nanopores, because the size of the pores varies with each diatom.

### Future Work:

Future work includes testing to determine the effect of the SPM treatment on the diatom membrane as well as a process for positioning and securing multiple diatoms over the micropores without using a micromanipulator.

### Acknowledgements:

I would like to thank my PI, Dr. Michael Goryll, and my mentor, Xiaofeng Wang, for their guidance and time, and the staff at the Center for Solid State Electronics Research at Arizona State University. I would also like to thank the National Nanotechnology Infrastructure Network Research Experience for Undergraduates Program and the National Science Foundation for funding this great experience.

### References:

- [1] E. Sollier, C. Murray, P. Maoddi and D. Di Carlo, Lab Chip, 11, 3752-3765 (2011).
- [2] S.J. Wilk, L. Petrossian, M. Goryll, T.J. Thornton, S.M. Goodnick J.M. Tang and R.S. Eisenberg, Biosensors and Bioelectronics 23, 183-190 (2007).

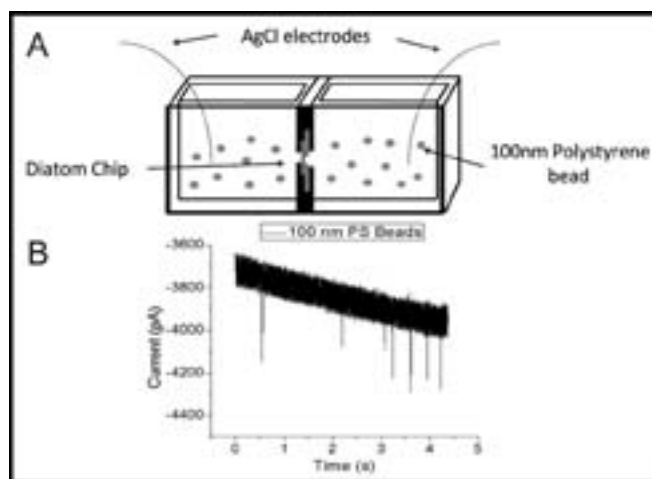


Figure 3: (a) Nanoparticle translocation setup. (b) Graph of multiple 100 nm polystyrene bead translocation events through open pores.

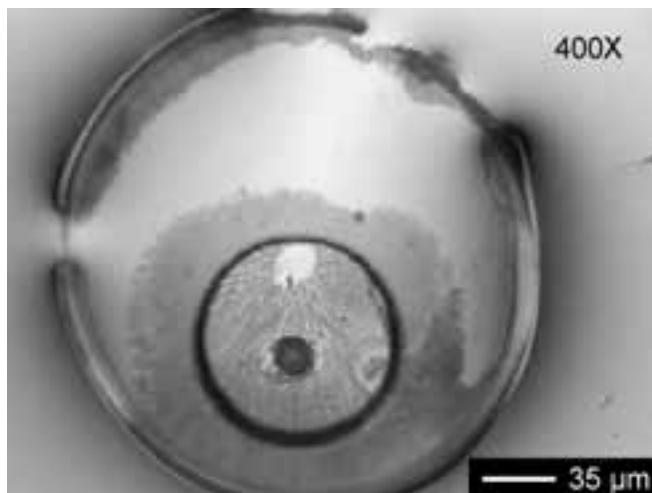


Figure 4: Optical micrograph of diatom after SU-8 coating and exposure.

## Fabrication of Graphene Field Effect Transistors

**Lee Hamstra**

**Materials Science and Engineering, Cornell University**

*NNIN REU Site: Colorado Nanofabrication Laboratory, University of Colorado, Boulder, CO*

*NNIN REU Principal Investigator: Tomoko Borsa, Electrical, Computer, and Energy Eng., University of Colorado at Boulder*

*NNIN REU Mentor: Tzu-Min Ou, Electrical, Computer, and Energy Engineering, University of Colorado at Boulder*

*Contact: lbh45@cornell.edu, tomoko.borsa@colorado.edu, tzumin.ou@colorado.edu*

### Abstract:

Graphene is an exciting new material because of its two-dimensional nature and interesting mechanical and electrical properties. There is still much room for development in methods for growing graphene, such as chemical vapor deposition (CVD) on copper. Making field effect transistors (FETs) with graphene is a practical way to assess the characteristics of a given sample of graphene and determine if a method for creating graphene is effective. The focus of this project was to fabricate graphene FETs to assess the quality of graphene grown through CVD on copper. This process was broken down into three main steps: (1) the electrochemical transfer of graphene from copper to silicon (Si) wafers, (2) the patterning of electrodes onto the graphene covered wafers, and (3) the electrical testing of resulting devices through four-point-probe and transistor measurements. Graphene was transferred through the application and removal of poly(methyl methacrylate) (PMMA) on copper (Cu). The electrodes were patterned using photolithography and evaporative metal deposition. Four-point-probe and transistor measurements were attempted as a means to assess the sheet resistance, carrier mobility, and carrier density of the graphene.

### Introduction:

In the future, graphene may be used in a wide variety of devices, but if these devices are ever going to be produced commercially, there needs to be much improvement in methods for growing high quality graphene. The purpose of this project was to fabricate graphene field effect transistors (FETs) to assess the quality of graphene grown through CVD on Cu and examine problems in the fabrication process.

### Experimental Procedure:

The experimental procedure broke down into five main steps: (1) the preparation of the substrate, (2) the transfer of graphene from copper onto the substrate, (3) the patterning of electrodes onto the graphene, (4) the deposition of the back-gate metal, and (5) the characterization of the graphene.

A heavily doped Si wafer (n-type, <100>, 0.01-0.02  $\Omega$ -cm) was used as the substrate for the graphene FETs. The wafer had to be oxidized to have an oxide thickness of 90 nm so that the graphene would be visible on top of the oxide [1].

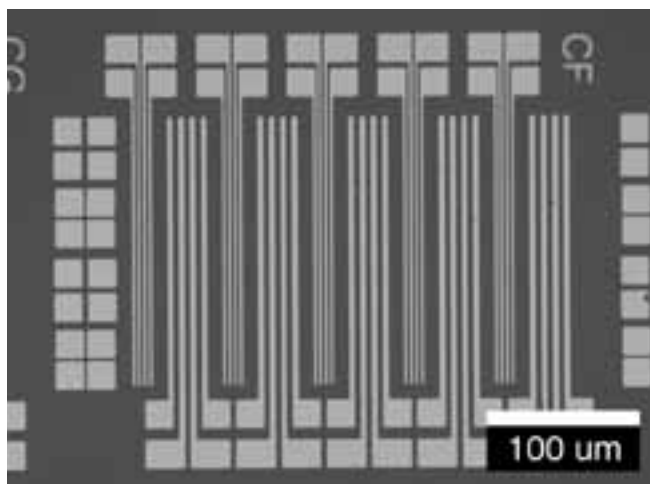


*Figure 1: Electrode pattern; small fingers are 2  $\mu$ m wide and large fingers are 4  $\mu$ m wide.*

Graphene was transferred from copper to the substrate through an electrochemical reaction. Poly(methyl methacrylate) (PMMA) was spun onto the copper sheet before hooking up the copper sheet to function as a cathode in a potassium hydroxide (KOH) bath with a steel electrode serving as the anode. Hydrogen gas forming on the surface of the copper lifted off the PMMA, with the graphene attached to its underside. This sheet of PMMA was then cleaned and scooped up with the substrate.

After removing the PMMA with remover PG and annealing the sample to clean the graphene, electrodes were patterned onto the surface of the graphene in a pattern that can be seen in Figure 1 through photolithography and evaporative metal deposition.

The final fabrication step was the deposition of the back-gate metal. The back-gate metal was deposited after stripping away the backside oxide with buffered oxide etch (BOE).

Characterization was done through use of a probe station and parameter analyzer. The goal was to use four-point-probe and transistor measurements, though in the end, only four-point-probe measurements were conducted.

## Results and Conclusions:

Three main problems were encountered during fabrication: (1) the oxide had to have a specific thickness, (2) the transfer process caused the graphene to fold up on itself, as shown in Figures 2 and 3, and (3) the nickel electrodes adhered poorly to the graphene, as shown in Figure 4.

The first problem was addressed through using dry oxidation to make the oxide slightly thicker than desired and then using BOE to fine-tune the thickness of the oxide. The second problem was caused by remover PG attacking photoresist residue under the graphene during the PMMA removal step. This problem was addressed by changing the order of fabrication steps to allow for nanostrip cleaning directly before transfer to ensure that the surface of the substrate was clean. Given the limited amount of time for the research project, the third problem was not addressed although possible solutions have been formulated.

Due to the problems with fabrication, data was only successfully collected from a single device as the electrodes proved difficult to probe. The four-point-probe measurement suggested a sheet resistance of  $7700 \Omega/\text{sq}$  with very high probe contact resistances of  $200 \Omega$  per contact, and a nickel-graphene contact resistance of  $5.38 \times 10^{-4} \Omega\text{-cm}^2$ . The measured sheet resistance was 20 times higher than expected, likely because of uneven contact between the nickel and graphene and discontinuities within the graphene sheet.

Three main ideas have been put forward to address the nickel-graphene adhesion problem in the future. First, the mask should be redesigned to have larger probe pads to make probing the devices easier. Second, new metals, such as platinum, should be experimented with as possible nickel substitutes. Finally, a reactive ion etching step might be done to etch the graphene into strips before patterning electrodes onto the surface so that contact pads can remain on the oxide with only fingers on the graphene. After this problem is addressed, more characterization needs to be done.

## Acknowledgements:

I would like to thank the National Nanotechnology Infrastructure Network Research Experience for Undergraduates (NNIN REU) Program for giving me the opportunity to do this research, the National Science Foundation for providing the funding, and the University of Colorado at Boulder and the Colorado Nanofabrication Lab for providing an excellent setting to conduct research. I would also like to thank my research group, Bart Van Zeghbroeck, Zefram Marks, Ian Haygood, Tomoko Borsa, and especially Tzu-Min Ou, for all of the assistance they gave me.

## References:

- [1] P. Blake, et al., "Making Graphene Visible," Applied Physics Letters, 91, 063124, 2007.

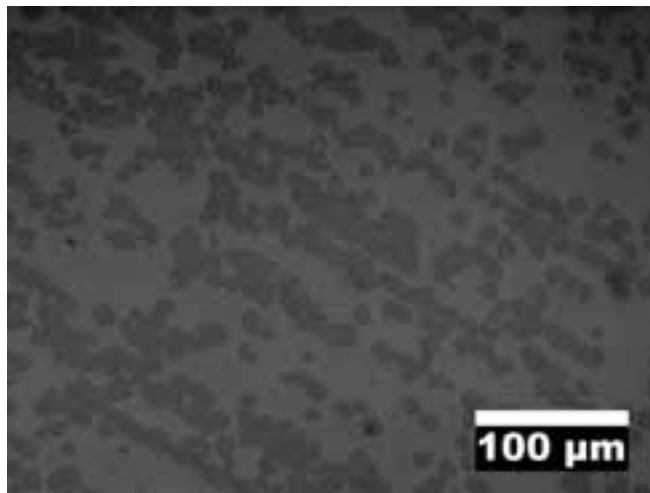


Figure 2: Graphene prior to PMMA removal.

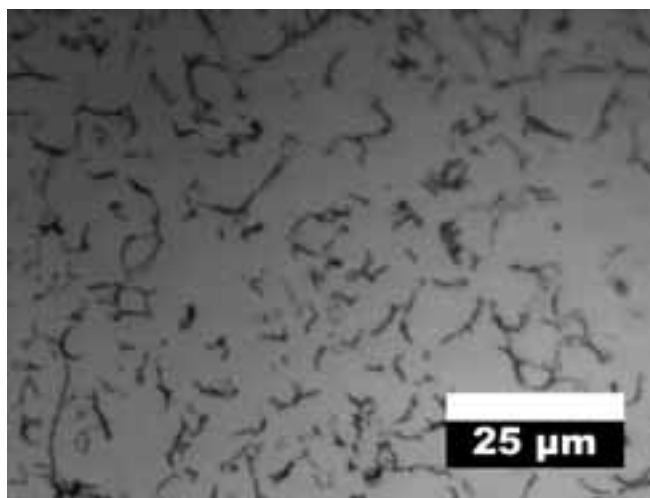


Figure 3: Graphene after PMMA removal.

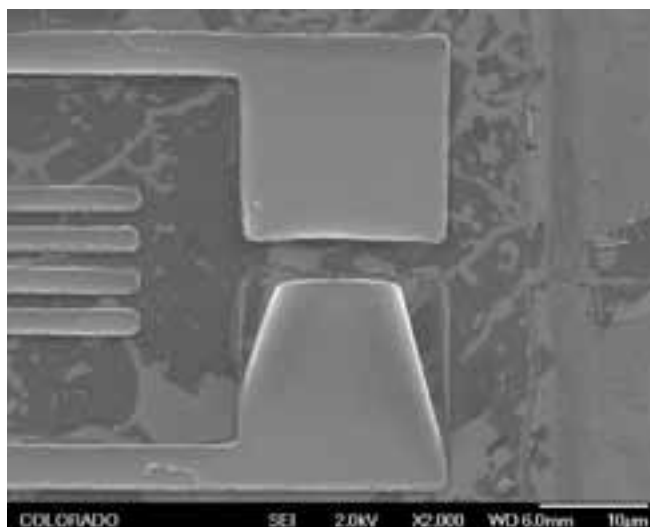


Figure 4: Nickel electrodes over graphene.

## Testing the Properties and Characteristics of Chitin Thin Films

**Kamil Makhneja**

**Biomedical Engineering, Boston University**

*NNIN REU Site: NanoTech User Facility, University of Washington, Seattle, WA*

*NNIN REU Principal Investigator: Professor Marco Rolandi, Material Science and Engineering, University of Washington*

*NNIN REU Mentor: Dr. Jungho Jin, Material Science and Engineering, University of Washington*

*Contact: kamilmak@bu.edu, rolandi@uw.edu, jinuine@uw.edu*

### Abstract and Introduction:

Chitin, the second-most abundant polysaccharide found in nature, has increased biocompatibility and biodegradability compared to cellulose, the most abundant polysaccharide. Found in crustaceans, cephalopods and mushrooms, chitin can be used to create new polymeric devices and to reinforce pre-existing technologies for various applications [1]. In this project, chitin nanofiber thin films were fabricated and characterized to determine their material properties. The fabrication process used the highly-volatile solvent 1,1,1,3,3,3-hexafluoro-2-propanol (HFIP) [2]. As the HFIP slowly evaporated, chitin nanofibers self-assembled through hydrogen bonding to form a thin film sheet. The thin films were tested and measured for material properties: Instron 4505 (upgraded to 5500R) and dynamic mechanical analyzer (DMA) for mechanical properties, x-ray diffraction (XRD) for composition, thermomechanical analysis (TMA) for thermal properties, and a Porosimeter for physical characteristics. These fabricated thin films provide an avenue to create potential applications in wound healing, tissue scaffolds, and polymer reinforcement.

### Experimental Procedure:

Chitin thin films were prepared from 0.5% (w/v) chitin/HFIP solutions. The solution was drop-casted and promptly covered to slow the evaporation of HFIP. A few holes were made in the cover to insure the complete evaporation of HFIP. The solution was placed in a fume hood and allowed to evaporate for 8-10 days. When the thin film was set, the characterization process began. First, TMA was performed to determine the coefficient of thermal expansion (CTE). The change in length was measured as temperatures were cycled from 25°C to 180°C and back down to 25°C three times.

To test mechanical properties, an Instron and DMA were employed. Both tests involved a simple tensile test on the sample, closely following ASTM D882-10 [3]. Kapton HN 100 sheets from DuPont were used as a control for both experiments. The Instron applied a maximum force of 20 N with an extension rate of 0.1 mm/min. Using the DMA, we performed a "Static Stress Test."

After calibration, the DMA applied a load that went from 110 mN to 5000 mN at 100 mN/min.

An XRD helped us determine the formation of our chitin. The test was performed on the samples by scanning from  $2\theta$  at 3° to 55° with a 0.02 step-size following all necessary precautions while dealing with radiation equipment.

Lastly, a Porosimetry test was completed to determine the presence and characteristics of pores in the thin films. Multiple thin films, weighing a total of 0.0455 g, were loaded into the testing apparatus and mercury was intruded through the samples to determine the existence and size of the pores.

### Results and Conclusions:

As previously noted, chitin self-assembles into nanofibers due to HFIP evaporation. This fabrication process helped yield 3 nm nanofibers in a thin film that ranges from 10 to 200  $\mu\text{m}$  in thickness [2].

The CTE values from the TMA test ranged from about 38 to 186 ppm/K, but literature states that the values should be closer to 9.8 ppm/K [1]. This discrepancy can be attributed to nanofiber alignment in a two-dimensional plane while experimentation was performed in the third dimension.

The Instron and DMA tests provided results for Young's Modulus (stiffness) that did not entirely match literature results. Our control Kapton® and chitin film were specified to have a stiffness of 2.5 GPa [1, 4], but our Instron results gave an average stiffness of 1.187 GPa. Nonetheless, chitin thin films were tested on the Instron and the chitin showed an average stiffness of 1.09 GPa with a large standard deviation of 815 MPa as seen in Figure 1. To double-check, DMA tests were carried out in hopes for more accurate and precise results. DMA tests showed Kapton and chitin stiffness at about 732 MPa and 307 MPa, respectively. These disagreements in values can be a result of the testing methods, testing equipment, and inconsistent samples. Interestingly enough, if outliers of the Instron tests were taken into account, the two experiments showed that Kapton was about twice as stiff as chitin.

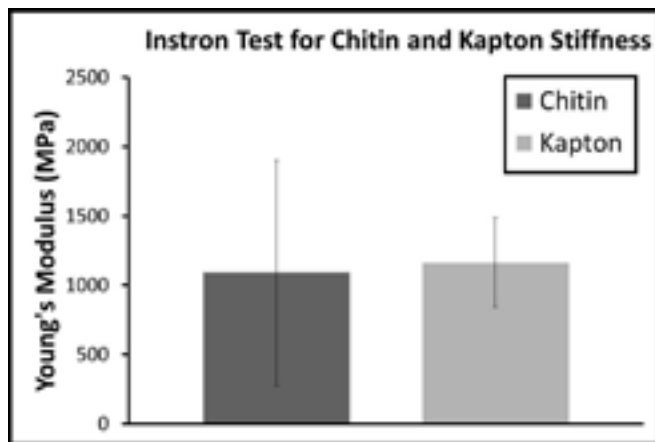


Figure 1: Kapton = 1.187 GPa with 325 MPa standard deviation. Chitin = 1.09 GPa with 815 MPa standard deviation.

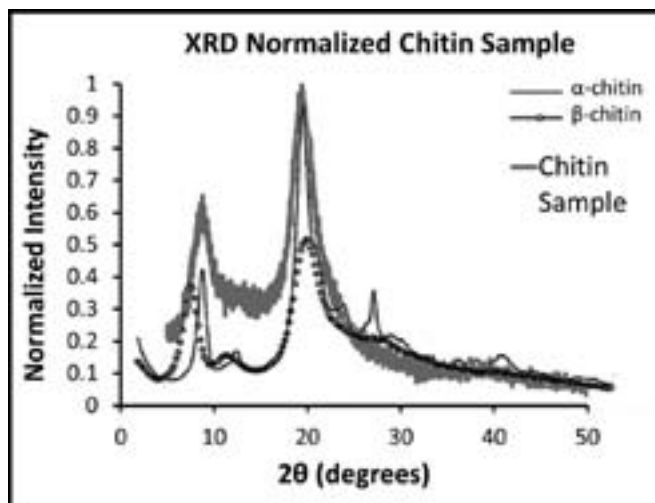


Figure 2: XRD of chitin thin film compared to  $\alpha$ - and  $\beta$ -chitin.

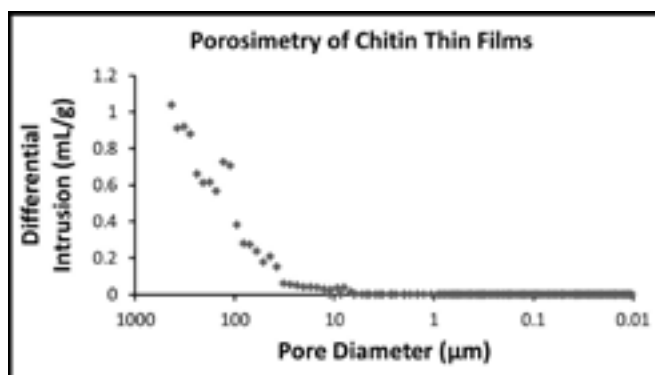


Figure 3: Porosimetry results of chitin thin film test.

XRD results, in Figure 2, were fairly conclusive in showing that our chitin thin films exhibited  $\alpha$ -chitin (nanofibers are aligned parallel and antiparallel [5]). This orientation caused the nanofibers to pack closer together due to hydrogen bonding. This transformation of  $\beta$ -chitin in the chitin powder to  $\alpha$ -chitin in the thin film was a result of the HFIP evaporation process.

The graph of the Porosimetry results, represented in Figure 3, shows spikes that occur at a higher pore diameter, a result of mercury filling the voids in between the different thin film samples. But with smaller pore diameters, the mercury could not penetrate through the thin films, meaning that if pores are present, they are smaller than 10 nm.

### Future Work:

In the future, we will try to test our chitin thin films on equipment specifically designed for thin films testing. Hopefully, this will reveal better results for our stiffness values. Another aspect we would like to test is how the concentration of chitin/HFIP solution affects chitin thin film properties. Lastly, we will try to formulate sample preparation methods that yield consistent thin films.

### Acknowledgements:

I acknowledge Professor Marco Rolandi, Dr. Jungho Jin, and the entire Rolandi Research Group for giving me an opportunity to help conduct this research and teaching me scientific research skills. I would also like to thank MSE User Facility and Nanotechnology User Facility personnel for their help and advice. Lastly, I wish to thank the National Nanotechnology Infrastructure Network Research Experience for Undergraduates (NNIN REU) Program and National Science Foundation for allowing me to participate in such an intellectual program.

### References:

- [1] Ifuku, S., Green Chemistry, 13, 1708, (2011).
- [2] Zhong, C., Soft Matter, 6, 5298, (2010).
- [3] ASTM Standard D882-10, ASTM International, West Conshohocken, PA, (2010), [www.astm.org](http://www.astm.org).
- [4] DuPont, [kapton.dupont.com](http://kapton.dupont.com).
- [5] Lavall, R. L., Bioresource Technology, 98, 2465, (2007).

## Temperature Dependent Electrical Resistivity of $\text{La}_x\text{Lu}_{1-x}\text{As}$

**Maria Michael**

**Mechanical Engineering, University of Virginia**

*NNIN REU Site: Microelectronics Research Center, The University of Texas at Austin, Austin, TX*

*NNIN REU Principal Investigator: Dr. Deji Akinwande, Electrical and Computer Engineering, University of Texas at Austin*

*NNIN REU Mentors: Somayyeh Rahimi and Milo Holt, Electrical and Computer Engineering, University of Texas at Austin*

*Contact: mem8as@virginia.edu, deji@ece.utexas.edu, nrahimi@gmail.com, miloholt@utexas.edu*

### Abstract:

We report the temperature-dependent resistivity of lanthanum lutetium arsenide ( $\text{La}_x\text{Lu}_{1-x}\text{As}$ ) thin films grown by molecular beam epitaxy. Thicknesses of measured films were 30, 100 and 500 nm. Studies on the resistivity of  $\text{La}_x\text{Lu}_{1-x}\text{As}$  films suggest semimetallic behavior for temperatures ranging 78 to 295 K. Resistivity was measured using a cross sheet resistor van der Pauw (VDP) structure fabricated onto samples employing planar fabrication techniques. The linear fit of resistivity vs. temperature likely indicates electron-phonon scattering as the dominant mechanism, for temperatures from 78 to 295 K [1]. The increase in resistivity by increasing thickness was likely due to increasing interface roughness from imperfect growth at large thickness scales.

### Introduction:

The discovery of graphene, a stable two-dimensional structure of carbon, has opened the door to the study of other thin films. Materials such as III/V and rare earth arsenides are suggested as “beyond graphene” materials. Investigation of electrical

transport properties of rare-earth arsenides can lead towards a comprehensive understanding of carrier transport properties of these compounds and the development of novel electronic devices. To begin exploration of this, electrical properties of  $\text{La}_x\text{Lu}_{1-x}\text{As}$  ( $x = 47$  and 48%) alloys were characterized as a function of thickness and temperature.

One of the most accurate methods for measuring sheet resistance of thin films is achievable by employing van der Pauw structures (Figure 1). The method is advantageous because it allows measurements to be taken of arbitrary lamellae by strategic placement of electrodes at the perimeter.

### Experimental Procedure:

The sample stack was grown by molecular beam epitaxy (MBE). To account for impurities in the wafer left after heat treatment, 200 nm of gallium arsenide (GaAs) were grown onto a commercially available GaAs wafer. Ten monolayers (ML) of an LuAs spacer layer were grown next, followed by  $\text{La}_x\text{Lu}_{1-x}\text{As}$  and another 10 ML LuAs. The stack was capped

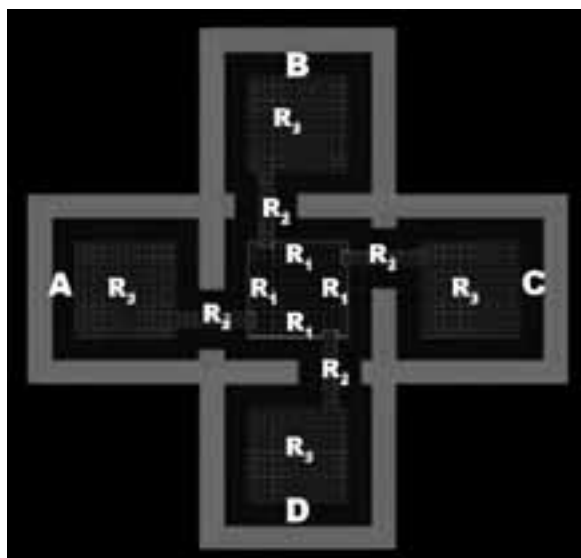


*Figure 1: A van der Pauw structure where  $R_1$  indicates resistance in the region of interest,  $R_2$  the arm resistance, and  $R_3$  the surface shunt resistance of the contact pad. Image courtesy S. Rahimi.*

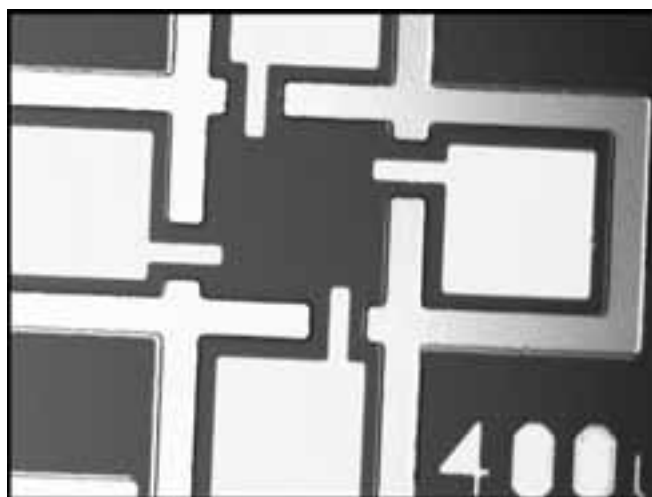


*Figure 2: A fabricated VDP device.*

by 15 nm GaAs to prevent oxidation of the alloy. Spacer layers separated LaLuAs from GaAs on both sides to prevent it from diffusing.

Fabrication of van der Pauw devices began by spin-coating cleaned samples with negative photoresist, AZ-5214. A Karl Süss MJB4 was used for lithography. Electrodes were deposited using electron beam evaporation (CHA SR-10 metal deposition tool), with a nickel adhesive layer and 41.1 nm gold. A lift-off process was required to form electrodes.

Following the second layer mask's lithography, devices were isolated by mesa-etching in a 1:1:20 solution of  $H_3PO_4:H_2O_2:H_2O$ . A fabricated device can be seen in Figure 2.

Low temperature measurements were taken using a Lakeshore cryogenic four probe system. The van der Pauw method was used [2, 3], requiring measurements be taken in two positions (see Figure 1). In the  $0^\circ$  degree position, current was run from pad A to B, and the voltage drop was measured between C and D. In the  $90^\circ$  position, current was run between pads D and A, and the voltage drop was measured between B and C. For both positions, measurements were first taken with a forward current (+I) and then with the reverse (-I). Using these four values,  $R_{00}'$  was calculated, according to the equation below. Similarly,  $R_{90}'$  was calculated.

$$R_{00}' = \frac{V_{CD}(+I) - V_{CD}(-I)}{I_{AB} - I_{BA}}$$

From the average of the two, sheet resistance was found from the VDP formula, below.

$$R_S = \frac{\pi}{\ln 2} R_{AVE} * f$$

A correctional factor,  $f$ , was used to correct for asymmetry in the structure. For this data, the correctional factor was 1.00, indicating high symmetry of devices.

Resistivity was calculated by multiplying the sheet resistance by thickness.

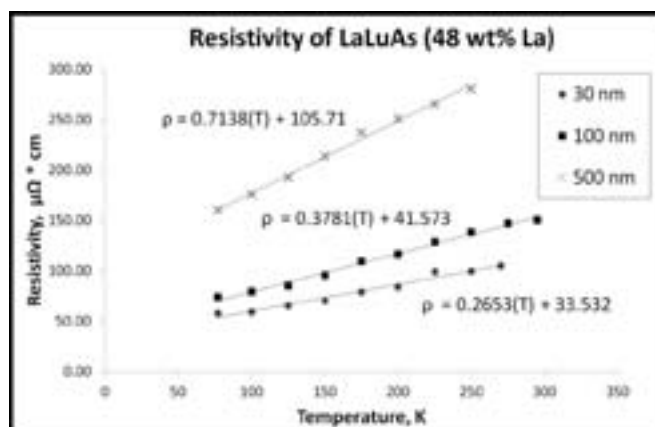


Figure 3: An analysis of data reveals increasing thickness corresponding with increasing resistivity.

The alloys exhibited semi-metallic behavior, increasing in resistivity with increasing temperature (Figure 3). The plots of resistivity vs. temperature and sheet resistance vs. temperature were linear. For this temperature range, 78 to 295 K, the linear fit likely indicates electron-phonon scattering as the dominant scattering mechanism [1]. The difference in resistivity between 30 and 500 nm samples averaged 193% and between 30 and 100 averaged 26%, with the 30 nm sample showing lower resistivity in both cases.

### Conclusions:

The increase in resistivity with thickness was independent of temperature, suggesting impurities as an underlying cause. The trend likely also results from differing surface roughness. As thicker layers are grown by the MBE method, surface roughness between interfaces tends to increase [4].

### Future Work:

Based on these results, as well as data showing temperature dependent resistivity of 3 nm  $La_xLu_{1-x}As$ , a paper will be drafted describing electrical transition properties of rare earth arsenides. This paper, "Temperature dependent electrical resistivity and resistivity tuning of LuAs thin films by Lanthanum" (coauthors S. Rahimi, E.M. Krivoy, J. Lee, M.E. Michael, S.R. Bank, D. Akinwande), will be submitted to Applied Physics Letters.

### Acknowledgements:

The researcher thanks the National Nanotechnology Infrastructure Network Research Experience for Undergraduates Program and the National Science Foundation for their funding; Dr. Bank and Erica Krivoy for their collaboration and MBE sample growth; Michael Ramon, Ricardo Garcia, and William Osler for their assistance with fabrication and measurement equipment.

### References:

- [1] Heremans, J., Issi, J., Rashid, A., and Saunders, G., "Electrical and thermal transport properties of arsenic", Journal of Physics of the Solid State, 10(22), 4511-4522, (1977).
- [2] Buehler, M. G., and Thurber, W. R., "An experimental study of various cross sheet resistor test structures", Solid State Science and Technology, 125(4), 645-650, (1978).
- [3] van der Pauw, L. J., A method of measuring the resistivity and Hall coefficient on lamellae of arbitrary shape. Phillips Technical Review, 20(8), 220-224, (1958).
- [4] Sakaki, H., Noda, T., Hirakawa, K., Tanaka, M., and Matsusue, T., "Interface roughness scattering in GaAs/AlAs quantum wells", Applied Physics Letters, 51(23),1934-1936, (1987).

## Photovoltaic Devices Fabricated with CIGS Nanocrystal Inks

Isao Mori

Electronic Engineering, The University of Tokyo

NNIN iREG Site: Microelectronics Research Center, The University of Texas at Austin, Austin, TX

NNIN iREG Principal Investigator: Prof. Brian A. Korgel, Department of Chemical Engineering, The University of Texas at Austin

NNIN iREG Mentor: Taylor Harvey, Department of Chemical Engineering, The University of Texas at Austin

Contact: i-mori@if.t.u-tokyo.ac.jp, korgel@che.utexas.edu, tharvey@che.utexas.edu

### Introduction:

Photovoltaic devices (PVs), which convert sunlight into electricity directly, are a promising energy source because they are renewable and clean. To be widely used, they need high power conversion efficiency (PCE) and low cost. Spray-deposited [1] thin-film  $\text{CuIn}_{1-x}\text{Ga}_x\text{Se}_2$  (CIGS) PVs have the potential to achieve this goal.

In this approach, a CIGS layer was deposited as an ink and then thermally annealed under selenium atmosphere—a process called selenization—to achieve high efficiency. The quality of the annealed CIGS nanocrystal film was highly dependent on the selenization conditions. We investigated various parameters related to selenization to improve power conversion efficiency (PCE).

### Fabrication Process:

Solar cells were fabricated on soda-lime glass with a layered molybdenum (Mo) / CIGS / cadmium sulfide (CdS) / zinc oxide (ZnO) / indium tin oxide (ITO) structure. One micrometer ( $\mu\text{m}$ ) of Mo was sputter deposited on soda-lime glass (Delta Technologies), followed by spray deposition of approximately  $1 \mu\text{m}$  of CIGS nanocrystals. The nanocrystal film was annealed in argon (Ar) for one hour between  $475^\circ\text{C}$  and  $525^\circ\text{C}$ . The substrate was then inserted into a graphite box and annealed under selenium atmosphere at  $500^\circ\text{C}$  for ten minutes. CdS was then deposited by chemical bath. A window layer of 50 nm of ZnO and 600 nm of ITO were sputtered to complete the device.

### Experiments:

Various pre-selenization treatments of the CIGS nanocrystal films were studied. Devices were annealed in Ar before CIGS deposition (Mo bake), after CIGS deposition (pre-selenization anneal), or soaked in a sodium chloride (NaCl) bath [2]. The Mo bake consisted of annealing a back contact in an argon atmosphere at  $475^\circ\text{C}$  for one hour just after Mo deposition. The pre-selenization anneal was carried out at  $475^\circ\text{C}$  in Ar for one hour immediately after depositing the CIGS layer.

Sel #	Pre-Se. Anneal	Mo Bake	NaCl Bath	PCE [%]	$V_{oc}$ [V]	$J_{sc}$ [ $\text{mA}/\text{cm}^2$ ]	FF
359	No	No	No	0.071	0.221	-1.163	0.276
360	No	No	Yes	0.096	0.163	-2.287	0.257
361	No	Yes	No	0.230	0.395	-2.088	0.279
362	No	Yes	Yes	0.243	0.334	-2.607	0.279
363	Yes	No	No	1.485	0.477	-10.460	0.298
364	Yes	No	Yes	1.006	0.478	-7.746	0.272
365	Yes	Yes	No	2.760	0.474	-20.075	0.290
366	Yes	Yes	Yes	1.832	0.410	-11.839	0.378

Figure 1: Measurement results of Mo baked, pre-selenization annealed, or NaCl bath soaked samples.

It is known that sodium plays a role in CIGS crystallization [2] and during these anneals sodium diffuses from the soda-lime to the Mo/CIGS interface. Sodium was also added directly to the CIGS film by soaking the CIGS-coated substrate in a 1 g/L aqueous NaCl bath of for 15 minutes before selenization.

Figure 1 shows the measurement results of samples with these pre-selenization treatments. All photovoltaic device measurements were performed under Air Mass 1.5 illumination.  $V_{oc}$  is open circuit voltage and  $J_{sc}$  is short circuit current density. FF is a fill factor—the ratio of the product of voltage and current at maximum power and the product of  $V_{oc}$  and  $J_{sc}$ . The Mo bake and pre-selenization anneal both exhibited a positive effect on improving PCE.

The effect of the temperature ramp rate during selenization was also studied. Films were selenized for ten minutes after ramping the temperature at 20, 50, 80 and  $110^\circ\text{C}/\text{min}$  to  $500^\circ\text{C}$ . The nanocrystal films were treated prior to selenization by annealing at  $475^\circ\text{C}$  and soaking the films in a NaCl bath.

Device PCEs were 0.008% for  $20^\circ\text{C}/\text{min}$ , 0.034% for  $50^\circ\text{C}/\text{min}$ , 0.230% for  $80^\circ\text{C}/\text{min}$  and 0.251% for  $110^\circ\text{C}/\text{min}$ . Higher ramp rates produced higher PCE. Scanning electron

microscope (SEM) images (Figures 2 and 3) show that the crystalline domains in the selenized CIGS films were larger when ramped at 110°C/min compared to 20°C/min. Films with larger crystalline grains are expected to have decreased recombination of electrons and holes for improved PCE. In addition, the thickness of the molybdenum selenide ( $\text{MoSe}_2$ ) layer, generated by converting Mo to  $\text{MoSe}_2$  during selenization, of 20°C/min was 664 nm, while that of 110°C/min was 373 nm. A thin  $\text{MoSe}_2$  layer was better, as thicker  $\text{MoSe}_2$  layers increased the series resistance in the device and degraded PCE.

Next, we investigated different CIGS layer deposition processes. Two processes were used where Process 1 was the conventional method and Process 2 was a new proprietary one. Pre-selenization and NaCl bath were performed in both of Process 1 and 2.

Figure 4 shows the I-V curve of the device fabricated with Process 2. The PCE of Process 2 was 6.564%, while that of Process 1 was 0.191%. Process 2 also improved  $FF$ — $FF$  of Process 2 was 50.6%, while that of Process 1 was 30.1%. These results were supposed to be caused by the high quality of the CIGS layer fabricated with Process 2.

### Conclusions:

Spray-deposited CIGS nanocrystal films were selenized to increase PV device efficiency. Various processing parameters were studied. Pre-selenization anneal, molybdenum bake, higher heating ramp rate and new CIGS layer deposition process yielded substantial improvements in device efficiency.

### Acknowledgments:

This is an achievement of the National Nanotechnology Infrastructure Network International Research Experience for Graduates Program funded by the National Science Foundation. My principal investigator was Dr. Brian A. Korgel and my mentor was Mr. Taylor Harvey, both of whom belong to the Department of Chemical Engineering, the University of Texas at Austin. Ms. Marylene Palard, Ms. Jean L. Toll, and Ms. Christine P. Wood helped me a lot during this program. My attendance at this program was also supported by the National Institute for Materials Science (NIMS) in Japan. Dr. Keijiro Hirahara and Ms. Noriko Ito, who belong to NIMS, also helped me a lot. I am from Shibata Mita Laboratory, Department of Electrical Engineering and Information Systems, Graduate School of Engineering, the University of Tokyo. I thank all of these organizations and people.

### References:

- [1] Panthani, M. G. et al.; Journal of the American Chemistry Society, vol. 130, no. 49, pp. 16770–16777 (2008).
- [2] Guo, Q. et al.; Progress in Photovoltaics: Research and Apps (2012).

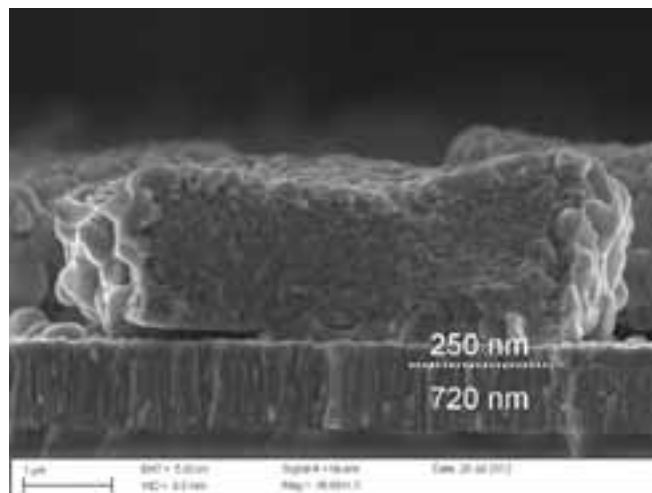


Figure 2: Cross section SEM image of 20°C/min ramp rate sample.

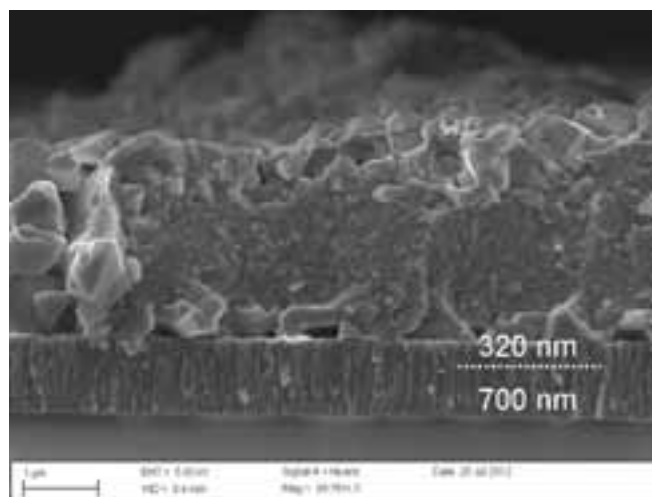


Figure 3: Cross section SEM image of 110°C/min ramp rate sample.

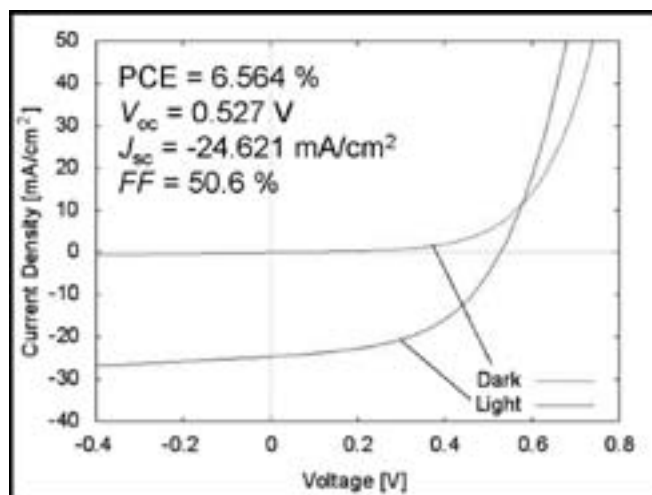


Figure 4: I-V curve of sample fabricated with new proprietary process.

## Substrate Conformal Imprint Lithography

**Frazier Mork**

**Physics, Carleton College**

*NNIN REU Site: Cornell NanoScale Science and Technology Facility (CNF), Cornell University, Ithaca, NY*

*NNIN REU Principal Investigator: Donald Tennant, Cornell NanoScale Science and Technology Facility, Cornell University*

*NNIN REU Mentors: Melina Blees, Physics, Cornell University; Noah Clay, CNF, Cornell University*

*Contact: morkf@carleton.edu, tennant@cnf.cornell.edu, clay@cnf.cornell.edu, bleesm@gmail.com*

### Abstract:

Substrate conformal imprint lithography (SCIL) is capable of high resolution and is less sensitive to defects inherent in traditional nanoimprints. This makes SCIL promising for both research and industrial applications. We report here progress toward imprinting dense features at 15 nm critical dimensions (CDs). The study includes an improved process employing ZEP resist to minimize line edge roughness (LER) on the master wafer mold down to 2-3 nm. Imprinted features on initial trials were found to exhibit a negative linewidth change on the order of tens of nanometers. The SCIL process employs a wave generation process making localized and global distortions possible from stretching the flexible PDMS-on-glass stamp. To characterize this, we created a second SCIL mask and printed wafers for pattern placement accuracy tests over the entire area of imprinted wafers.

### Introduction:

Moore's law predicted that the number of transistors on a chip should double roughly every two years, due, in part, to ever smaller dimensions. However, photolithography, the technique most commonly used today, is nearing the resolution limit imposed by the wavelength of light. One common method for patterning features smaller than photolithography can achieve is electron beam lithography, but this is prohibitively expensive and unfit for use in manufacturing because of the time required. Patterns made using electron beam lithography can, however, be replicated using NanoImprint lithography (NIL), at a fraction of the cost. NIL is a stamping process used to transfer features from a previously patterned master wafer into imprint resist on daughter wafers, which can then be cured. However, NIL faces its own challenges—the high pressures used and repeated exposure to resist can wear down features on the master wafer over time. Additionally, because the stamps used are inflexible, any particulates on them can result in unpatterned regions and can damage the master.

Substrate conformal imprint lithography (SCIL) [1] is a new variant of nanoimprint lithography using a flexible polydimethylsiloxane (PDMS) replica of the master wafer,

making it possible to pattern over particulates. Also, because the master wafer is only used as a mold, it is better protected, which reduces the cost of repeatedly patterning new masters. However, because the stamp is flexible, it may induce distortion either of the printed features or in their placement on the wafer. We wanted to characterize that distortion and test SCIL's resolution limits to see whether it would be a good candidate for manufacturing at the nanoscale.

### Methods:

In the SCIL process, PDMS stamps are molded from features etched into silicon master wafers. These stamps are then imprinted into a resist on daughter wafers, which are then UV cured. When the stamp is peeled away, the features are left behind in the resist on the daughter wafers.

To create the master templates, we used photolithography or electron beam lithography to pattern wafers which we etched using a reactive ion etcher. After removing any remaining resist, we added a monolayer of perfluorooctyltrichlorosilane (FOTS), a highly fluorinated molecule, as an anti-stick coating. We applied a layer of custom PDMS to the thin glass stamp and cured it to use as a SCIL mask. We imprinted these into wafers coated with Amonil (AMO, GmbH) resist using a modified Suss MA6 contact aligner. This tool allowed us to precisely control the imprint force and separation between the stamp and the imprint resist.

The first stamps we tested were made using an ASML 5500/300C deep ultraviolet stepper to pattern the master. This stamp was used to confirm that SCIL was capable of reproducing fine features over a large area as well as to troubleshoot any initial problems.

Tests of SCIL's resolution limit, however, required a master wafer with extremely small features. Towards this end, we created a dense pattern of 15 nm lines using electron beam lithography using ZEP520 (Zeon Chemical) as a resist. To achieve these challenging results, we used a combination of feature size biasing, dose biasing, and shot pitch modulation.

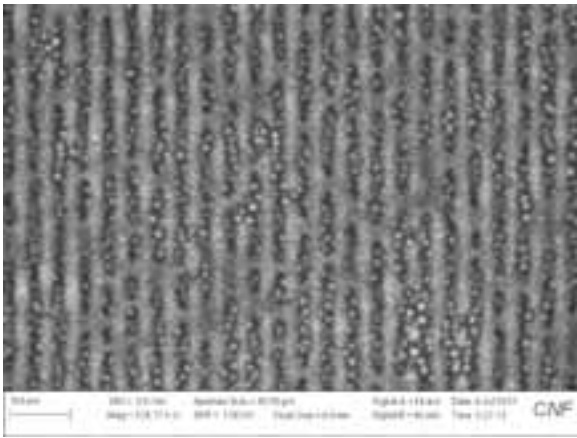


Figure 1: Early attempt to fabricate 20 nm trenches in ZEP520 resist before feature size biasing or cold development temperatures were used.

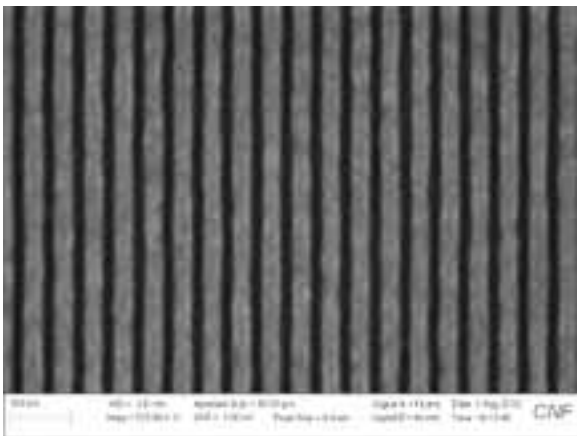


Figure 2: 15 nm trenches in 30 nm thick ZEP520 resist for patterning the master wafer needed for the SCIL resolution tests.

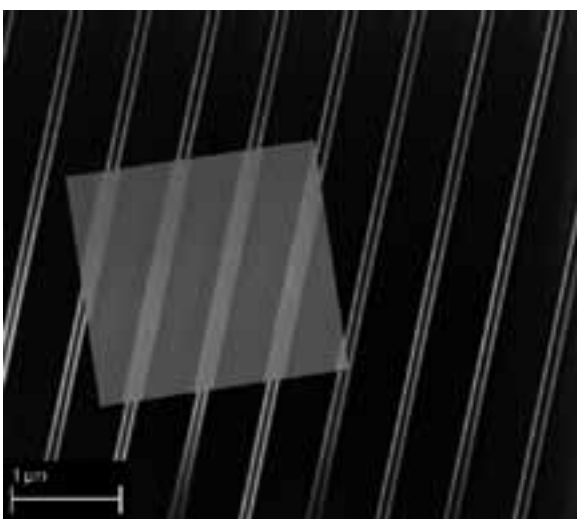


Figure 3: SCIL imprint and master wafer (inset) illustrating size changes in SCIL.

We also tested different development chemicals, temperatures, and times to optimize feature size and minimize LER. We also employed proximity error correction to compensate for the effect of backscattered electrons on the dosage [2].

The result was a silicon master wafer ideally suited to these resolution tests (Figures 1 and 2).

Finally, in order to characterize distortion in the pattern across the entirety of the wafer, we imprinted a stamp with an array of large crosses, 60  $\mu\text{m}$  tall, onto a 6-inch wafer. Use of this stamp will indicate how accurately the stamp places these crosses across the wafer by comparing cross positions with the original master. The measurement will be made using the metrology capability of the JBX6300FS electron beam lithography system, which uses a laser interferometer to calibrate its stage position.

### Results and Conclusions:

Using the stamp made with deep UV lithography, we initially confirmed that SCIL is capable of patterning submicron features over a broad area. We fabricated a stamp with crosses for the pattern placement accuracy tests, which we successfully imprinted. This awaits metrology measurements. To evaluate the resolution limits of SCIL, we optimized the process used to produce the master wafer. This process used cold xylenes as a developer and incorporated CAD corrections including proximity error correction and feature size biasing to improve resolution and LER. A master wafer with dense patterns of lines down to 15 nm was fabricated. Preliminary imprints with a similar mask demonstrate an overall decrease in linewidth of 80 nm from 170 nm lines as they were measured on the original master wafer (Figure 3). The source of this “shrinkage” has yet to be investigated.

Data from these pattern placement accuracy tests and resolution tests will make it possible to further improve the SCIL process in the future and to determine suitable applications for it as a manufacturing method.

### References:

- [1] Ji, Ran, et al., “UV Enhanced Substrate Conformal Imprint Lithography (UV-SCIL) Technique for Photonic Crystals Patterning in LED Manufacturing.” *Microelectronic Engineering* 87.5-8 (2010): 963-67.
- [2] Pavkovich, J., “Proximity Error Correction Calculations by the Integral Equation Approximate Solution Method.” *Journal of Vacuum Science and Technology* 4.1 (1985): 159-63.

## Engineered Metallic Structures and Nanofabrication Techniques for Plasmonic Biosensors

**Stephen Olson**

**Physics, Bethel University**

*NNIN REU Site: Nanofabrication Center, University of Minnesota-Twin Cities, Minneapolis, MN*

*NNIN REU Principal Investigator: Prof. Sang-Hyun Oh, Electrical and Computer Eng., University of Minnesota-Twin Cities*

*NNIN REU Mentor: Prof. Nathan C. Lindquist, Physics, Bethel University*

*Contact: olso5576@umn.edu, sang@umn.edu, n-lindquist@bethel.edu*

### Abstract:

Optical energy can be harnessed on the nanoscale by exploiting plasmonic resonances in metallic nanostructures. These resonances are the result of the unique optical properties of metals and their abundance of conduction electrons. Utilizing these properties, it is possible to engineer metallic nano-devices that operate with large electric field intensities confined in and around the structure. Due to these large fields, optical, chemical and spectroscopic properties can be probed with high sensitivity. This project covers the various fabrication methods unique to the precise fabrication of metallic nano-structures as well as some applications as nano-optical sensors.

### Introduction:

Plasmons are collective oscillations in the electron cloud density of a conductor, usually metal. At the surface of a material, they are called surface plasmons. These oscillations can be induced by electromagnetic radiation at specific frequencies. If certain conditions are met, a photon can couple with a plasmon forming a surface plasmon polariton (SPP). This is a propagating electromagnetic wave on the surface of the metal at the interface of a dielectric and the conductor. The SPP is transverse-magnetic, meaning that an evanescent electric field extends into both the metal and dielectric, normal to the interface. This electric field extends no more than a few hundred nanometers (nm) into the dielectric and is strongest near the surface. We are able to use this electric field to probe the near-field region [1]. If a plasmon is induced on a small metal particle, i.e. with size dimensions on the order of or less than the wavelength of incident light, a propagating electromagnetic wave is not formed. Instead, electrons oscillate with the changing electric field, forming areas of high electric field, or “hot-spots” [1]. This is known as localized surface plasmon resonance (LSPR). These hot-spots can be employed to trap particles and perform surface enhanced Raman spectroscopy (SERS) [2].

We can engineer structures on the nanoscale that exhibit these plasmonic properties. However, because plasmons can be excited by deformities on the surface, it is critically important that our devices have smooth surfaces to ensure optimal performance.

### Fabrication Procedures:

Because smooth surfaces were so important for our devices, we platformed the entire fabrication process around the technique of template-stripping. This process required a silicon mold, which was then deposited over with metal. The metal was then epoxied to a glass slide, cured, and finally removed from the mold; this resulted in the inverse of the mold patterned in the metal, possessing ultrasmooth surfaces. Template stripping also allowed the mold to be reused, enabling high-throughput fabrication of devices [2]. We used two different methods to fabricate the molds.

For high resolution patterning, we employed electron beam lithography. After patterning a spin-coat layer of photoresist, we used etch processes to carve the mold. Depending on the etch depth needed, sometimes a hardmask layer was utilized. For lower resolution patterning, we used focused ion beam lithography. This method did not require photoresist, however it could not match the resolution capabilities of electron beam lithography. This method did enable the direct fabrication of molds.

In some cases, we determined that we did not need to template-strip our structures. In these situations, we used electron beam or photolithography to pattern a stencil mask. We then deposited metal over the mask and performed a chemical liftoff. All open areas of the stencil were filled in with metal, resulting in surfaced patterned structures.

**Devices:**

Using the methods described above, we fabricated an assortment of devices, some of which are not contained within this report. The following figures show several devices in various stages of production.

**Bowtie Array (Figure 1).** These bowties were fabricated by depositing gold over a stencil mask and performing liftoff. They facilitated the formation of LSPRs, with hot-spots focused in the gap at the center of the bowtie. They have been used to trap particles in this hot spot and to aid in performing SERS.

**Sharptips Prior to Template Stripping (Figure 2).** Using electron beam lithography, dry etching, atomic layer deposition, and thermal metal evaporation, an array of sharp-tipped lines were fabricated. When template stripped, they focused to a narrow point. These devices displayed interesting plasmonic effects and concentrated hot spots at the tips of the structures. (*Image courtesy of Timothy W. Johnson.*)

**Nanochannels, HSQ on Silicon (Figure 3).** Using electron beam lithography, it was possible to achieve high resolutions, as exemplified here. These were 20 nm lines of HSQ on silicon. After development, HSQ becomes chemically similar to  $\text{SiO}_2$  and can be used as a hardmask for etching. This image was taken prior to etching.

**Future Work:**

The main thrust of this research was designing and building plasmonic biosensors.

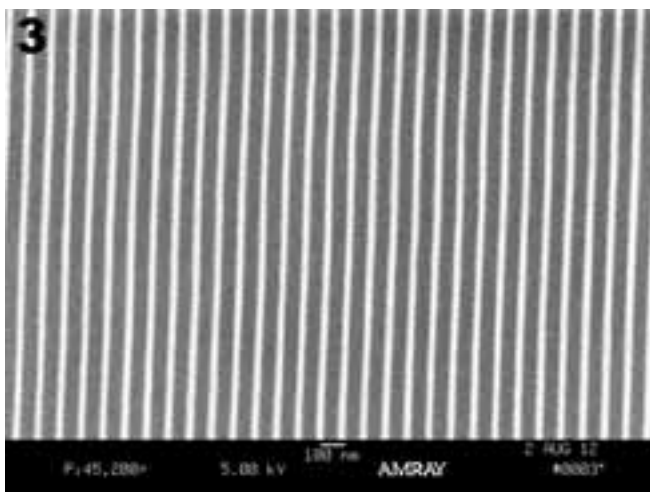
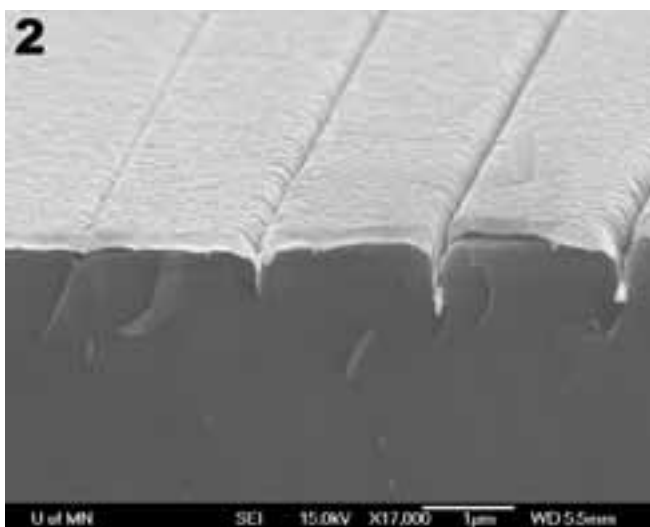
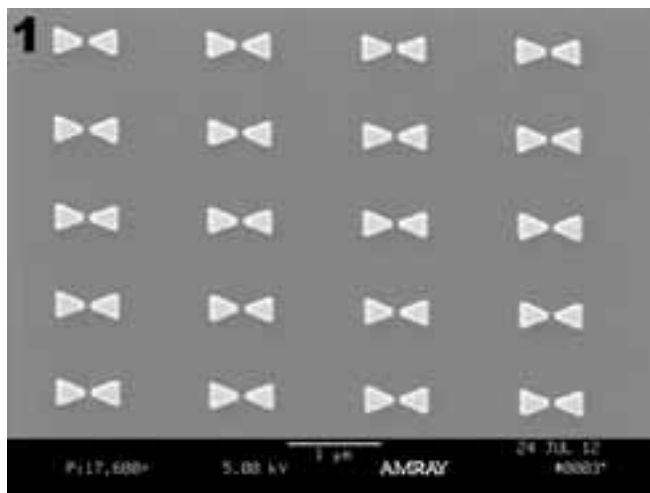
As demonstrated, devices are in various stages of completion. The obvious next steps include finishing fabrication and testing the devices. Based on test results, the devices can be optimized and results published.

**Acknowledgments:**

Timothy W. Johnson, Sudhir Cherukulappurath, Xiaoshu Chen, Luke R. Jordan, Jincy Jose, NFC Staff, University of Minnesota, National Nanotechnology Infrastructure Network Research Experience for Undergraduates (NNIN REU) Program, and National Science Foundation (NSF).

**References:**

- [1] Lindquist, N.C. Engineering metallic nanostructures for surface plasmon resonance sensing (Dissertation). U. of Minnesota. (2011).
- [2] Lindquist, N.C., Nagpal, P., McPeak, K. M., Norris, D. J., Oh, S-H. Engineering metallic nanostructures for plasmonics and nanophotonics. *Rep. Prog. Phys.* 75 (2012).



## Atomic Layer Deposition Process Optimization and Characterization of Amorphous Metal-Oxide Films

**Emily Ross**

**Engineering, Harvey Mudd College**

*NNIN REU Site: Stanford Nanofabrication Facility, Stanford University, Stanford, CA*

*NNIN REU Principal Investigators: Prof. Roger T. Howe and Prof. Philip H.S. Wong, Electrical Engineering, Stanford University*

*NNIN REU Mentors: Dr. J. Provine and Max Shulaker, Electrical Engineering, Stanford University*

*Contact: emross@hmc.edu, rhowe@stanford.edu, hspwong@stanford.edu, jprovine@stanford.edu, maxms@stanford.edu*

### Abstract:

Atomic layer deposition (ALD) is used to create conformal thin films that have many applications due to the wide range of available materials and precisely-controlled thicknesses. Amorphous metal-oxide thin films are good candidate materials for dielectric gates, diffusion barriers and biocompatible coatings, among many other applications. ALD processes that have not been fully optimized and characterized result in wasted precursor, longer fabrication times and incomplete understandings of the films themselves. In this work, the processes for hafnium dioxide ( $\text{HfO}_2$ ) and zirconium dioxide ( $\text{ZrO}_2$ ) films were optimized for uniformity by varying precursor pulse and carrier gas purge times to create the most uniform films. The temperature dependence of film characteristics and differences between thermal and plasma-enhanced processes was explored for titanium dioxide ( $\text{TiO}_2$ ) films. Uniformity was determined by comparing thicknesses measured by an ellipsometer at different positions in the reaction chamber. This project yielded ALD metal-oxide processes optimized for uniformity and a better understanding of film characteristics. All data is available on the Stanford Nanofabrication Facility's website.

### Introduction:

ALD is a nanofabrication process consisting of a cyclic self-limiting chemical reaction with vapor-phase precursors, but only surface-phase reactions. A cycle of ALD consists of four steps; 1) surface saturation by precursor A, 2) purge of excess precursor A from the reaction chamber, 3) surface saturation by precursor B, and 4) purge of excess precursor B. For metal-oxide films, precursor A is the base metal with ligands attached and precursor B is water (for thermal processes) or oxygen plasma (for plasma processes). Steps 1 and 3 are quantified by the "pulse time," which is how long the valve on the cylinder containing the precursor stays open and is thus related to the amount of precursor in the reaction chamber. Steps 2 and 4 are quantified by the "purge time," which is how long the background carrier gas ( $\text{Ar}$  or  $\text{N}_2$ ) flows through the reaction chamber without carrying any new precursor.

We sought to maximize film uniformity, minimize precursor waste, and minimize process runtime by varying only Steps 1 and 2. Thus, "pulse time" and "purge time" specifically refer to the precursor A pulse time and the purge time immediately after that, respectively. Other parameters varied were temperature, background carrier gas flow rate, type of deposition tool and water or oxygen plasma as precursor B. We also determined deposition rates.

### Experimental Procedure:

Depositions were performed on two simultaneously-run 4-inch silicon wafers (placed side-by-side in the reaction chamber) after a standard RCA clean. The film thickness was measured at nine points per wafer, resulting in 18 thicknesses per deposition. These were used to compute the average thickness and non-uniformity, which was the standard deviation divided by the average thickness. We ran 100 cycles of ALD for all depositions (except those used to determine the deposition rate) on one of two Cambridge Nanotech ALD systems: Fiji or Savannah.

### Results and Conclusions:

The  $\text{ZrO}_2$  processes on both the Savannah and Fiji systems were wasting precursor A. We were able to determine the threshold for surface saturation by decreasing the pulse time for the Savannah process. A lack of surface saturation was indicated by a significant decrease in average thickness (Figure 1) as well as high non-uniformity. The standard recipe was adjusted from having a pulse time of 0.40s to 0.15s, saving a significant amount of precursor A. Increasing the purge time decreased the non-uniformity of the film (Figure 2), indicating that vapor-phase reactions took place at shorter purge times. This was also why the Fiji process had a non-uniformity of over 10% until the purge time was increased from 20s to 50s.

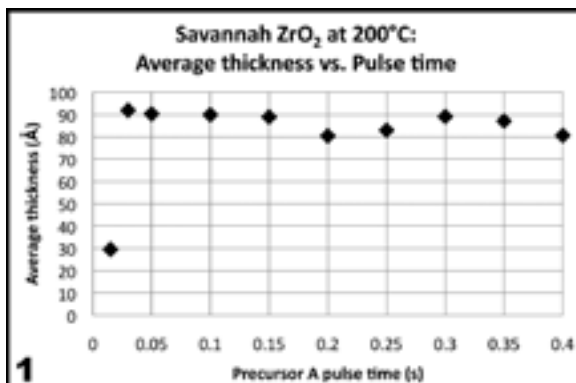


Figure 1: The thickness dropped off at a pulse time of 0.015s. The pulse time must be at least 0.03s to reach surface saturation.

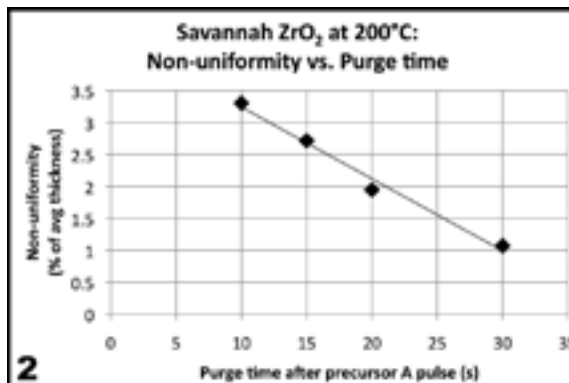


Figure 2: The non-uniformity of the film decreased as the purge time increased, indicating vapor-phase reactions occurred at shorter purge times.

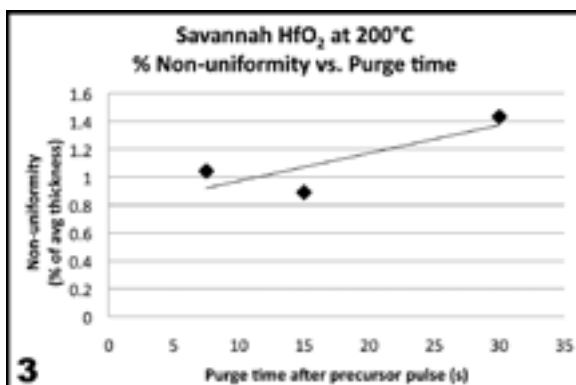


Figure 3: The non-uniformity of the film increased as the purge time increased, indicating desorption occurred at longer purge times.

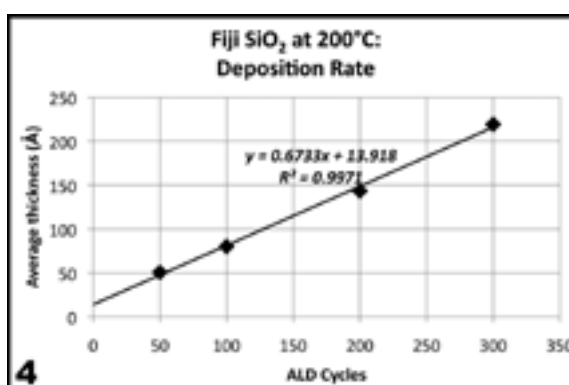


Figure 4: The Fiji  $\text{SiO}_2$  deposition rate is  $0.7\text{Å}/\text{cycle}$ .

The Savannah  $\text{HfO}_2$  process was verified to be at optimal performance. Pulse time, purge time and background flow were varied to confirm that the standard recipe had the highest uniformity. However, it was found that desorption of precursor A occurred at longer purge times (Figure 3) due to excessive volatility. Despite this trend, the initial purge time of 15s had the lowest uniformity, indicating that it was a good balance between desorption and potential vapor-phase reactions.

The deposition rate of Fiji  $\text{SiO}_2$  was  $0.7\text{Å}/\text{cycle}$  with 14Å of native oxide (Figure 4), which is due to oxygen diffusing into the substrate at room temperature before deposition. The deposition rate of Savannah  $\text{ZrO}_2$  was  $0.8\text{Å}/\text{cycle}$  with 11Å of native oxide.

Thermal and plasma Fiji  $\text{TiO}_2$  films were deposited at 100–300°C. The plasma films showed little change in average thickness over the temperature range. The thermal films were thicker at lower temperatures due to precursor condensation.

#### Future Work:

The Fiji  $\text{ZrO}_2$  process should be further optimized to increase uniformity and reduce precursor waste. More process opti-

mization should be done on the plasma Fiji  $\text{TiO}_2$  process because most films had twice the non-uniformity of those from the thermal process for the explored temperature range. The Fiji  $\text{TiO}_2$  deposition rate should also be determined. Capacitors can be made with the films to determine the electrical properties such as breakdown voltage and capacitance with respect to both high and low sweeping voltages. These properties could then be compared for films deposited at different temperatures, by different tools or through different processes (thermal vs. plasma).

#### Acknowledgments:

I would like to thank Professor Roger T. Howe, Professor Philip H.S. Wong, Dr. J. Provine, Max Shulaker, Dr. Michelle Rincon, Andrei Iancu, the Howe research group, staff at the Stanford Nanofabrication Facility, the National Science Foundation, the National Nanotechnology Infrastructure Network Research Experience for Undergraduates Program, and Stanford University's Center for Integrated Systems.

## A Study of Integrating Societal and Ethical Issues into NNIN REU

**Merrill Brady**

**Politics and Pre-Medical Studies, Bates College**

*NNIN REU Site: Cornell NanoScale Science and Technology Facility, Cornell University, Ithaca, NY*

*NNIN REU Principal Investigator: Dr. Katherine McComas, Department of Communications, Cornell University*

*NNIN REU Mentor: Gina Eosco, Ph.D. Student, Department of Communications, Cornell University*

*Contact: mbrady3@bates.edu, kam19@cornell.edu, gme7@cornell.edu*

### Abstract:

Societal and Ethical Issues (SEI) in nanotechnology have gathered recent attention and importance given its federal focus under the 21st Century Nanotechnology Act [1] (2003). Perceptions of how effective SEI training is, as well as to what extent ethical conceptions penetrate into undergraduate work and beyond, is of particular interest in order to better the Research Experience for Undergraduates (REU) Program of the National Nanotechnology Infrastructure Network (NNIN). Interviews of both current education coordinators at NNIN REU sites and former REUs from the Cornell NanoScale Facility (CNF) are used to accumulate and compare SEI training practices. The review and interview results are used to formulate a summary report of findings and best practices for NNIN sites to use as a program guide.

Program	REU Program Goals	Skills Learned
UPenn SUNFEST VaNTH BIO REU Workshop 2010	Professional presentation	Communicate effectively and professionally, develop appropriate communication for certain audiences
Penn State	Think insightfully, problem solve	Personally reflect on ethical topics, develop a moral imagination
Carnegie Mellon University	Think insightfully, problem solve	Understand the ethics of care, recognize environmental applications of engineering
University of Washington	Study natural disasters	Recognize societal issues; human and economic consequences

Figure 1: Goals and projected skill sets common among evaluated programs.

### Introduction:

The 21st Century Nanotechnology Act [1] (2003) emphasized the need to address societal and ethical issues of nanotechnology. This study set out to contribute to that initiative by first conducting a literature review on Research Experience for Undergraduates (REU) programs. The review compiled educational experiences from the REU programs and other non-REU undergraduate programs that teach societal and ethical issues to students within a science or technology domain. A total of ten institutions or programs were analyzed to contribute to part I of the summary report. As seen in Figure 1, certain program goals and skills targeting undergraduates to think critically about ethical and societal considerations resonate throughout the literature. The specific practiced and evaluated types of activities include PowerPoint presentations, lunch discussions, news articles or legislative documents to read, case studies and role-playing to perform, small panel discussions, societal and ethical issues (SEI) lunches, field trips to industries, or weekly classes on ethics in science.

NNIN Coordinator Interviews	Former CNF REU Interviews
1. Size of REU program	1. Relationship with PI
2. Amount of SEI education already in place before you started	2. Relationship with mentor
3. PI/staff interest and support for SEI	3. Relationship with fellow REU's
4. Current program; practices used	4. Amount of talk about nanotechnology in casual conversation
5. Personal opinion on adequacy of SEI program	5. Amount of SEI in casual conversation versus in training discussion
6. Personal opinion on challenges to presenting effective SEI education	6. Source of SEI discussion
7. Amount of information and idea sharing among NNIN coordinators	7. Motivation for SEI consideration during REU summer
8. Personal opinion on the best practices for SEI education	8. Current opinions; your values regarding SEI
	9. Suggestions for SEI education

Figure 2: Categories encompassing interview questions of each subject group.

To explore the usefulness of these ideas, interviews with the education coordinators in the NNIN were conducted to gather a comprehensive look at how education coordinators are implementing SEI activities in their respective REU programs. In addition, interviews with previous REUs were conducted to assess what they think about society and ethics, and if they believe their REU experience at all influenced their thinking.

### Results and Discussion:

The NNIN Education Coordinators (EC) participated in phone interviews lasting between 10-20 minutes. Figure 2 provides the categories of questions. Similar to the literature review findings, the ECs also found that lectures and informal discussions were the easiest type of event to organize and most liked by the undergraduate participants. The literature review found that there was an emphasis on training mentors to communicate the ethics of their project to their undergraduates. The ECs commented that although that was a great idea, there was limited time to train the mentors in addition to training the REU participants.

As a suggestion, ECs could work with SEI coordinators to increase the mentors' comfort for such topics, as this could foster a friendlier and more informative relationship between mentors and their respective undergraduate student.

There are three main findings from both the EC interviews and the previous REU student phone interviews. To better the communication of ethics and increase societal awareness, mentors and ECs should focus on the connections, conversations, and critical thinking skills of the undergraduates REU participants. The *connections* break down into the student's work environment, which is a critical for motivating and engaging SEI discussion. Students need to feel that their mentors and principal investigators (PIs) are approachable and friendly to spark the second finding, *conversations*. *Conversations* refer to the length and frequency of societal

and ethical discussions between an undergraduate and their mentor or PI on their respective project. The friendliness and amount of socialization during the internship between undergraduate and mentor, PI, or other facility users, and the nature of such casual narrative with those involved in the research project influence how the student thinks about SEI.

Both the connections and conversations maintain the third domain for better SEI education, which is the level of *critical thinking* for undergraduates to develop. Raising awareness about their research projects' ethics and societal implications during the summer builds a framework of thought for their future careers. The challenge of communicating the paramount topics of SEI is a process that is continually built upon tried practices and current successes.

To further study the motivation and degree of ethical considerations by REU interns, a short survey was conducted of the 2012 REU participants. The survey tested such factors as motivation and its relationship to one's personal sense of moral responsibility.

### Acknowledgments:

I would like to thank my mentor, Gina Eosco, and principal investigator Katherine McComas, for their abiding guidance and insight. Thank you to all of the NNIN Coordinators and former REU students who donated their time and energy to participating in the interviews so that my work proved worthwhile. Funding was provided by the National Nanotechnology Infrastructure Network Research Experience for Undergraduates (NNIN REU) Program and the National Science Foundation.

### References:

- [1] 21st Century Nanotechnology Research and Development Act, 108<sup>th</sup> Congress Public Law 153 (2003).

## Nanotechnology Companies in the U.S.A: A Web-Based Analysis of Companies and Poverty Alleviation

**Duy Do**

**Electrical Engineering, San Antonio College**

*NNIN REU Site: Nanotechnology Research Center, Georgia Institute of Technology, Atlanta, GA*

*NNIN REU Principal Investigator: Dr. Susan Cozzens, School of Public Policy, Georgia Institute of Technology*

*NNIN REU Mentor: Mr. Thomas Woodson, School of Public Policy, Georgia Institute of Technology*

*Contact: duy\_dot@yahoo.com, scozzens@gatech.edu, tswoodson@gatech.edu*

### Abstract:

In the United States, many firms are expanding their research and development on nanotechnology products. But what products are being developed and who will benefit from them? This study answers these questions by analyzing the goals, nanotechnology experience, corporate social responsibility and products from companies' websites. Based on patent data from the Center for Nanotechnology and Society-Thematic Research Cluster One, we obtained a list of fifty-five firms that are leaders in nanotechnology in water, energy and agri-food. We chose these areas because we think they will have a big impact on the poor and on inequality. Out of the fifty-five companies, twenty-seven mention nanotechnology. Moreover thirty-one firms are developing products that will benefit both the rich and poor, while only seven firms, such as computer and textile industries, focus only on rich consumers. In general, agri-food companies do not discuss nanotechnology on their websites. Most of the companies produced intermediate materials used by other companies; very few of the companies sell nano-products directly to consumers. Overall, we conclude that nineteen out of fifty-five companies are developing nanotechnology products, like low cost water filters or solar cells that could help the poor and reduce inequality.

### Introduction:

Governments spend a large amount of money on research and development for a variety of problems. Three important areas that have received attention are water, agri-food and energy technologies. For example, we are at an extremely critical stage in our energy use portfolio. The world bases much of its energy use on non-renewable fossil fuels and nuclear power, and another potential technology that can ameliorate our dependence on fossil fuels faces a lot of public controversy.

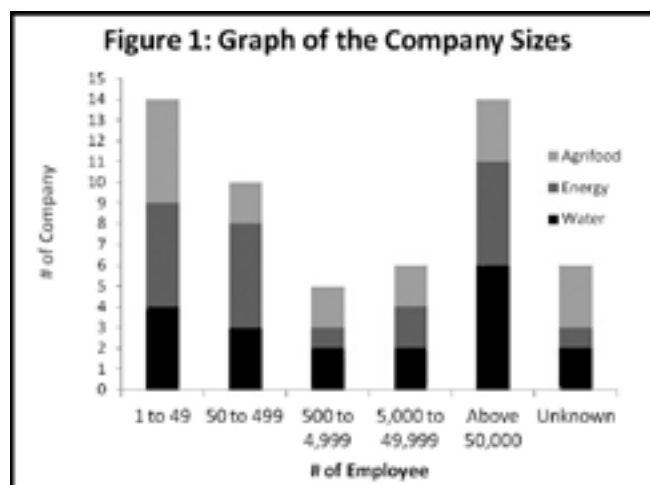
However, there are many solutions to these problems and we think research and development in nanotechnology can address some of these issues. Therefore, the purpose of this research was to perform a web-based analysis of nanotechnology companies in United States: What nano-products are being developed? Who benefits from these products? Does nanotechnology alleviate poverty?

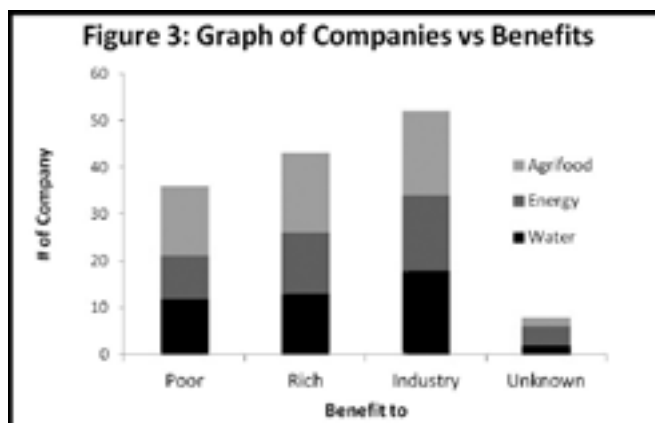
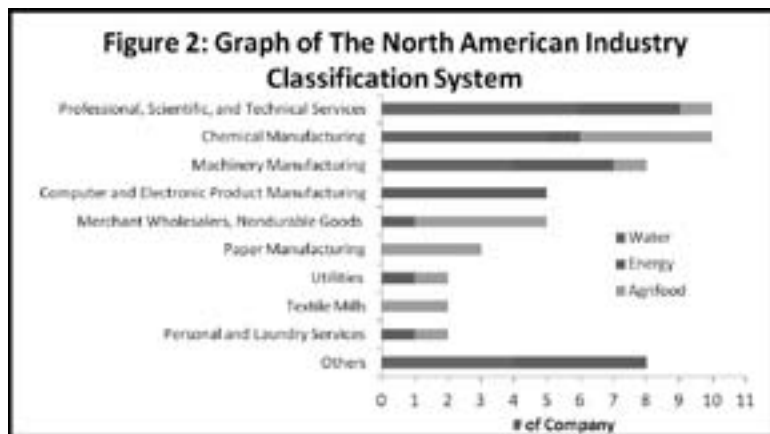
### Methodology:

The Center for Nanotechnology and Society-Thematic Research Cluster One provided patent data from 2005 to 2009 of the top companies with nanotechnology patents in United States. We focused on three areas; water, energy and agri-food. We chose these areas because we think they will have a big impact on poverty and related inequalities. In each of the categories, we selected the top twenty nano-patenting companies — however there were only fifty-five companies total in the sample because some companies were repeated in two different categories. For example, General Electric was a top producer of nanotechnology patents in both energy and water nanotechnology patents.

After compiling a list of companies, we went to each company's website and collect information about their history, research, products and size. In addition to basic company information, we used their search tool to find out what the companies said about poverty and nanotechnology.

A second major source was Nexus Lexus Academic. We used that site to search for the North American Industry Classification System (NAICS) of the companies. Finally we analyzed the information we found.





**Results and Conclusions:**

The companies were a variety of sizes; fourteen companies had under fifty employees; while another fourteen had more than 50,000 employees (Figure 1). For example, in 2011, International Business Machines Corporation had 433,362 employees, but at the same time Konarka Technologies Incorporation had only twenty-five employees. Small firms were energies nanotechnology companies usually established late in the twentieth century.

In Figure 2, we used NAICS, “the standard used by Federal statistical agencies in classifying business establishments for the purpose of collecting, analyzing, and publishing statistical data related to the U.S. business economy.” [1]. Many companies span a variety of different fields. Once we had the list of companies, we examined the types of products they made and who would benefit from those products. We then classified the companies as either helping the poor, rich, or industry (Figure 3).

More than thirty firms develop products that will benefit the poor. For example, Koch Membrane is “helping millions of people live healthier lives by developing better ways to purify the world’s water sources, improve food processing, and

more.” [2]. Nanosolar says, “By printing CIGS-inks on low-cost aluminum foil, Nanosolar is utilizing its proprietary high-throughput roll-to-roll printable semiconductor technology to enable the world’s lowest-cost thin-film solar panels.” [3].

We found few companies benefit only the rich. Companies that sell products that only help the rich are developing products like expensive apparels or furniture that has anti-static, and spill technology.

We found that twenty-seven companies discuss nanotechnology on their websites. However, none of the agri-food companies mentioned nanotechnology. We suspect these companies are hesitant to talk about nanotechnology because nanotechnology is not well-known by the public, therefore the public might have negative reactions of having nanotechnology in their food.

Most of the products produced by these twenty-seven companies were intermediate materials, like chemicals, used by other companies. Very few companies sold the nano-products directly to consumers.

Only twenty-seven of the fifty-five companies mention poverty. For example, one company said that, “Our membrane filtration elements are in use worldwide, producing enough clean water daily to sustain healthy living for four hundred million people” [4]. However, when we examined the products of the companies, only nineteen out of fifty-five companies were developing nanotechnology products, like low cost water filters or solar cells, that could help the poor and reduce inequality.

**Acknowledgements:**

I would like to acknowledge the National Nanotechnology Infrastructure Network Research Experience for Undergraduates (NNIN REU) Program and the National Science Foundation for funding. I also thank my mentor, Thomas Woodson, Principal Investigator, Dr. Susan Cozzens, site coordinators, Dr. Healy Nancy and Leslie O’Neil, NNIN staff and everyone who helped me on this summer research project.

**References:**

- [1] Census Bureau <<http://www.census.gov/eos/www/naics/>>
- [2] Koch Membrane System <<http://www.kochmembrane.com/About-Us.aspx>>
- [3] Nanosolar Communication. Nanosolar Raises \$70-Million in New Capital. (2012) <<http://www.nanosolar.com/company/blog>>
- [4] Hydranautics <<http://www.membranes.com>>



## INDEX of 2012 NNIN REU, iREG, and iREU Sites

<b>Arizona State University</b> .....	<b>58, 64, 98, 130, 176, 206</b>
<b>Cornell University</b> .....	<b>4, 18, 70, 102, 118, 170, 192, 200, 216, 222</b>
<b>Georgia Institute of Technology</b> .....	<b>6, 16, 66, 96, 110, 140, 204, 224</b>
<b>Harvard University</b> .....	<b>82, 94, 122, 182, 202</b>
<b>Howard University</b> .....	<b>46, 90, 106, 124, 136</b>
<b>The Pennsylvania State University</b> .....	<b>8, 86, 88, 92, 186</b>
<b>Stanford University</b> .....	<b>22, 44, 76, 114, 166, 220</b>
<b>University of California, Santa Barbara</b> .....	<b>28, 80, 108, 112, 126, 132, 148, 174, 178</b>
<b>University of Colorado at Boulder</b> .....	<b>36, 56, 84, 150, 152, 160, 162, 208</b>
<b>The University of Michigan, Ann Arbor</b> .....	<b>2, 62, 72, 128, 134, 158</b>
<b>University of Minnesota-Twin Cities</b> .....	<b>12, 40, 100, 180, 218</b>
<b>The University of Texas at Austin</b> .....	<b>138, 142, 144, 154, 164, 168, 212, 214</b>
<b>University of Washington</b> .....	<b>32, 38, 42, 48, 198, 210</b>
<b>Washington University in St. Louis</b> .....	<b>24, 34, 50, 54, 104, 116, 146, 156</b>
<b>Ecole Nationale Supérieure des Mines de Saint Etienne, France</b> .....	<b>10, 14</b>
<b>IBN, Forschungszentrum, Jülich, Germany</b> .....	<b>60, 172, 184, 190</b>
<b>NIMS, Tsukuba, Ibaraki, Japan</b> .....	<b>20, 30, 52, 68, 74, 78, 120, 188</b>
<b>TU Delft, Netherlands</b> .....	<b>26, 194, 196</b>

## INDEX of 2012 NNIN REU Interns, Mentors, and Principal Investigators

### A

<b>Abdallah, Ali</b> .....	<b>2</b>
<b>Abid, Abubakar</b> .....	<b>140</b>
<b>Acevedo, Andrew</b> .....	<b>172</b>
<b>Achilefu, Samuel</b> .....	<b>24</b>
<b>Adibi, Ali</b> .....	<b>140</b>
<b>Adiga, Vivekananda</b> .....	<b>170</b>
<b>Agrawal, Anurag</b> .....	<b>162</b>
<b>Akinwande, Deji</b> .....	<b>212</b>
<b>Al-Azizi, Ala'a</b> .....	<b>92</b>
<b>Alford, Patrick</b> .....	<b>40</b>
<b>Alford, Terry</b> .....	<b>98</b>
<b>Alonso, Ramon</b> .....	<b>128</b>
<b>Amponsah, Kwame</b> .....	<b>200</b>
<b>Amstad, Esther</b> .....	<b>94</b>
<b>Anwar, Sharlin</b> .....	<b>4</b>
<b>Atlas, Gal</b> .....	<b>104</b>
<b>Awschalom, David</b> .....	<b>174</b>
<b>Axelbaum, Richard</b> .....	<b>104</b>
<b>Azghadi, Adel</b> .....	<b>130</b>
<b>Aziz, Michael</b> .....	<b>182</b>

### B

<b>Baarda, Rachel</b> .....	<b>132</b>
<b>Banerjee, Hans</b> .....	<b>142</b>
<b>Banerjee, Parag</b> .....	<b>156</b>
<b>Banerjee, Sanjay</b> .....	<b>142</b>
<b>Banerjee, Sriya</b> .....	<b>156</b>
<b>Bank, Seth</b> .....	<b>168</b>
<b>Bao, Zhenan</b> .....	<b>44</b>
<b>Bayat, Khadijeh</b> .....	<b>202</b>
<b>Bazile, Quachel</b> .....	<b>6</b>
<b>Beach, Samuel</b> .....	<b>28</b>
<b>Belkin, Mikhail</b> .....	<b>144</b>
<b>Bellamkonda, Ravi</b> .....	<b>16</b>
<b>Bellavia, Michael</b> .....	<b>134</b>
<b>Benton, Rachel</b> .....	<b>42</b>
<b>Bhattacharjee, Nirveek</b> .....	<b>32</b>
<b>Biniek, Krysta</b> .....	<b>22</b>
<b>Biswas, Pratim</b> .....	<b>34</b>
<b>Bjarnason, Elsie</b> .....	<b>76</b>
<b>Blees, Melina</b> .....	<b>216</b>
<b>Blonsky, Adam</b> .....	<b>198</b>

<b>Bodine, Martha</b> .....	<b>36</b>
<b>Bodington, Dashiell</b> .....	<b>174</b>
<b>Borsa, Tomoko</b> .....	<b>208</b>
<b>Brady, Merrill</b> .....	<b>222</b>
<b>Brower-Thomas, Tina</b> .....	<b>46</b>
<b>Brown, Steven</b> .....	<b>174</b>
<b>Bryant, Alex</b> .....	<b>78</b>
<b>Buck, Alexander</b> .....	<b>144</b>
<b>Bunch, Scott</b> .....	<b>84</b>
<b>Burns-Heffner, Colin</b> .....	<b>8</b>
<b>Buscema, Michele</b> .....	<b>194</b>
<b>Butera, Patrick</b> .....	<b>176</b>

**C**

- Calderon, Jr., Isidro** ... .. 80  
 Campbell, Ian ... .. 56  
 Campbell, Stephen ... .. 180  
 Cantley, Lauren ... .. 84  
 Chadha, Tandeep ... .. 34  
 Chandran, Ankitha ... .. 176  
 Chandra, Nishant ... .. 64  
 Chechetka, Svetlana ... .. 30  
 Chen, Da-Ren ... .. 116  
**Chew, Annabel** .. .. 82  
 Chikyo, Toyohiro ... .. 120  
 Choi, Jongsoo ... .. 128  
 Clay, Noah ... .. 216  
 Cleland, Andrew ... .. 132, 178  
 Cola, Baratunde ... .. 66  
 Corredor, Charles ... .. 42  
**Cosgriff, Lauren** ... .. 84  
 Cozzens, Susan ... .. 224

**D**

- Dang, Audrey** ... .. 10  
 Dauskardt, Reinhold ... .. 22  
 Davidson, Patricia ... .. 18  
**Davydovich, Dmitriy** ... .. 86  
 De Alba, Roberto ... .. 170  
**Dean, Leon** ... .. 12  
 Dekker, Nynke ... .. 26  
**Deng, Donna** ... .. 88  
 De Volder, Michael ... .. 122  
 DiCarlo, Leonardo ... .. 196  
**Do, Duy** .. .. 224  
 Dorfman, Kevin ... .. 12

**E**

- Echeverria, Marcos** ... .. 178  
 Eftekhar, Ali ... .. 140  
 Ehlig, Tino ... .. 184  
 Ellerbee, Audrey ... .. 166  
**Ellison, Amanda** ... .. 146  
 Engstrom, James ... .. 102  
 Eosco, Gina ... .. 222  
**Everhart, Camille** ... .. 200

**F**

- Fiedler, Callie ... .. 36  
 Filler, Michael ... .. 110  
 Fleischer, Candace ... .. 6  
 Foley, Justin ... .. 158  
 Fortner, John ... .. 50  
 Frielinghaus, Robert ... .. 190

**G**

- Gao, Shengkui ... .. 146  
**Gaudreau, Ryan** ... .. 136  
**Gaviria Rojas, William Andres** . 180  
 Ghasemi, Farshid ... .. 140  
**Gilbertson, Jennifer** ... .. 14  
**Gilpin, William** .. .. 202  
**Goldfeld, David** ... .. 204  
 Goodnick, Stephen ... .. 64  
 Gordon, Roy ... .. 82  
 Goryll, Michael ... .. 206  
 Gossard, Arthur ... .. 112  
**Gosse, Melissa** ... .. 206  
 Griffin, James ... .. 106  
 Gruev, Viktor ... .. 146  
**Guess, Kyle** ... .. 148  
**Gupta, Sonali** ... .. 16

**H**

- Hald, Eric ... .. 40  
 Hall, Neal ... .. 138  
**Hamstra, Lee** .. .. 208  
 Hanagata, Nobutaka ... .. 30  
 Harouaka, Ramdane ... .. 8  
 Harris, Gary ... .. 90, 106, 124, 136  
 Hart, Anastasios John ... .. 134  
 Harvey, Taylor ... .. 214  
**Hayes, Anderson** ... .. 90  
**Henderson, Codey** ... .. 92  
 Herrera-Fierro, Pilar ... .. 2  
**Hirokawa, Soichi** ... .. 56  
**Hirotsu, Kelsey** ... .. 44  
**Holmes, Ian** ... .. 94  
 Holt, Milo ... .. 212  
**Hood, Keevin** ... .. 58  
 Hosseinzadegan, Hadi ... .. 200  
**Hovish, Michael** ... .. 182  
 Howe, Roger ... .. 76, 220  
 Huang, Cheng-Ying ... .. 80  
**Huang, Kevin** ... .. 60  
**Hummel, Gwendolyn** ... .. 62  
 Hu, Wenbing ... .. 72

**I**

- Ilic, Rob ... .. 170

**J**

- James, Briana** ... .. 46  
 Jayant, Krishna ... .. 4  
 Jayapalan, Amal ... .. 96  
 Jiang, Hanqing ... .. 130  
 Jin, Jungho ... .. 210  
 Jing, He ... .. 116  
**Johnson, Camryn** ... .. 18  
**Jue, Melinda** .. .. 96  
 Jun, Young-Shin ... .. 54

**K**

- Kan, Edwin ... .. 4  
 Kim, Deok-Ho ... .. 32  
 Kim, Seong ... .. 92  
**Kiok, Matthew** ... .. 184  
 Kirk, James ... .. 38  
 Klein, Todd ... .. 100  
**Klemme, Daniel** ... .. 150  
**Knight, Andrew** ... .. 98  
 Kohl, Paul ... .. 204  
 Koide, Yasuo ... .. 74  
 Korgel, Brian ... .. 164, 214  
 Kozicki, Michael ... .. 176  
 Kuntzman, Michael ... .. 138  
 Kurtis, Kimberly ... .. 96

**L**

Lal, Amit ... 200  
**Lambdin, Olivia** ... 20  
 Lammerding, Jan ... 18  
**Lampe, Corinne** ... 22  
 Law, Jeremy ... 80  
**Lee, Alexander** ... 48  
 Lee, Chien-Chung ... 160  
 Lee, Heeyoon ... 166  
**Lee, Jia Gloria** ... 138  
**Lee, Jonathan** ... 100  
 Lee, Mina ... 26  
 Lee, Sang-hoon ... 80  
 Leleux, Pierre ... 14  
 Lengyel, Miklos ... 104  
 Li, Jing ... 186  
 Li, Ping-Chun ... 154  
 Li, Wan ... 70  
 Lindquist, Nathan ... 218  
 Liptak, Richard ... 180  
 Litz, Jonathan ... 48  
 Liu, Alan ... 112  
**Llinás, Juan Pablo** ... 152  
 Lončar, Marko ... 202  
**Long, Clay** ... 102  
**Luo, Peter** ... 104

**M**

**MacKenzie, Ian** ... 50  
**Makhnejia, Kamil** ... 210  
 Malliaras, George ... 10, 14  
**Margita, Kaleigh** ... 24  
 Marvdashti, Tahereh ... 166  
 Masiello, David ... 48  
 Ma, Teng ... 130  
**McArthur, Donnita** ... 106  
 McComas, Katherine ... 222  
 McEuen, Paul ... 192  
 McGill, Kathryn ... 192  
**McGuinness, Morgan** ... 26  
 McLeod, Robert ... 36  
**McMorris, Ryan** ... 108  
**McMullen, Adam** ... 154  
 McSkimming, Brian ... 126  
 Megrant, Anthony ... 178  
 Meyer, Carola ... 190  
**Meyerhofer, Phillip** ... 186  
 Meyofer, Edgar ... 2  
**Michael, Maria** ... 212  
 Mikulics, Martin ... 60  
 Mohney, Suzanne ... 88  
**Mori, Isao** ... 214  
**Mork, Frazier** ... 216  
**Murphy, Ryan** ... 110  
 Musin, Ildar ... 110

**N**

Nabatame, Toshihide ... 120  
 Nagasaki, Yukio ... 20  
 Nair, Hari ... 168  
**Nakamoto, Christopher** ... 28  
 Nakanishi, Jun ... 20  
**Newton, Jared** ... 156  
 Nishi, Yoshio ... 114  
 Noda, Takeshi ... 188  
**Norman, Justin** ... 112  
**Nygren, Katherine** ... 158

**O**

Ober, Christopher ... 118  
**Occeña, Jordan** ... 114  
 Oh, Sang-Hyun ... 218  
 Ohashi, Naoki ... 78  
 Oldham, Kenn ... 128  
**Olson, Stephen** ... 218  
 Onyegam, Emmanuel ... 142  
**Otto, Lauren** ... 188  
 Ou, Tzu-Min ... 208  
 Ouyang, Christine ... 118  
 Ouyang, Jiaomin ... 114  
**Overvig, Adam** ... 64

**P**

Padovani, José ... 76  
 Pai, S. Balakrishna ... 16  
 Palmstrøm, Christopher ... 108  
 Parpia, Jeevak ... 170  
**Parry, Ryan** ... 66  
 Payne, Christine ... 6  
**Pelaez, III, Francisco** ... 190  
 Perkinson, Joy ... 182  
 Peterson, Rebecca Lorenz ... 72  
 Phillips, Jamie ... 158  
 Piestun, Rafael ... 162  
**Pletcher, Kendall** ... 30  
 Popović, Miloš ... 150, 152  
 Posner, Jonathan ... 42  
 Provine, J. ... 220  
 Pud, Sergii ... 172

**R**

Rahimi, Somayyeh ... 212  
 Rais-Zadeh, Mina ... 62  
 Rajauria, Sukumar ... 132  
 Ralph, Daniel ... 70  
 Ratner, Daniel ... 38  
 Ray, Jessica ... 54  
**Reit, Radu** ... 32  
**Roberge, Adam** ... 116  
 Rodwell, Mark ... 80  
 Rolandi, Marco ... 210  
 Rose, William ... 136  
**Ross, Emily** ... 220  
**Rothenberg, Jacob** ... 160  
 Russo, Elisa ... 192

**S**

- Saha, Sayan ... 142  
**Sakakibara, Reyū** ... **194**  
 Sakaki, Hiroyuki ... 188  
 Sanaur, Sébastien ... 10  
**Sanville, Andrew** ... **118**  
**Scheideler, William** ... **68**  
 Schibli, Thomas ... 160  
**Schliep, Karl** .. **120**  
**Schoening, Jonathan** . ... **34**  
 Schroder, Dieter ... 58  
 Shainline, Jeffrey .. 150, 152  
**Shapero, Aubrey** ... **162**  
 Sheats, Julian ... 12  
 Shim, Yonghyun ... 62  
**Shim, YooSun** ... **122**  
 Shojaei, Borzoyeh ... 108  
 Shulaker, Max ... 220  
 Singh, Virendra . ... 66  
 Sinsersuksakul, Prasert .. 82  
 Sodhi, Avantika . ... 148  
 Speck, James ... 126  
 Stolle, Jackson .. 164  
 Stoykovich, Mark . ... 56  
**Suralik, Kelly** .. **52**  
**Swartz, Stephanie** .. **36**  
**Switzer, Oliver** ... **70**

**T**

- Tam, Andrew** . ... **124**  
 Tam, Eugenia ... 70  
 Tang, Rui .. 24  
 Tashiro, Kentaro ... 52  
 Taylor, Crawford .. 90  
 Teichert, Kendall .. 134  
 Tennant, Donald ... 216  
 Theogarajan, Luke ... 28, 148  
**Thielen, Brianna** ... **38**  
**Thomas, Cherrelle** . ... **164**  
**Tien, Kevin** . ... **196**  
 Tracy, Clarence . ... 64  
 Trolrier-McKinstry, Susan . ... 86  
**Truxal, Ashley** ... **72**  
 Tsukagoshi, Kazuhito ... 68  
 Tsuya, Daiju .. 74

**U**

- Uzunlar, Erdal ... 204

**V**

- van der Zant, Herre ... 194  
 Vemuri, Rajitha . ... 98  
 Vijayraghavan, Karun ... 144  
 Vitusevich, Svetlana . ... 172  
**Vrla, Geoffrey** ... **40**  
**Vulis, Daryl** ... **74**

**W**

- Wang, Evan ... 44  
 Wang, Jian-Ping ... 100  
 Wang, Xiaofeng ... 206  
 Watanabe, Eiichiro ... 74  
 Watanabe, Ken ... 78  
 Weitz, David . ... 122  
 Weitz, David . ... 94  
 Welsh, Aaron ... 86  
**Welsh, Timothy** . ... **166**  
**Wendt, Nathaniel** .. **168**  
 Wong, Philip . ... 220  
**Wong, Whitney** . ... **54**  
 Woodson, Thomas ... 224  
 Wördenweber, Roger ... 184

**X**

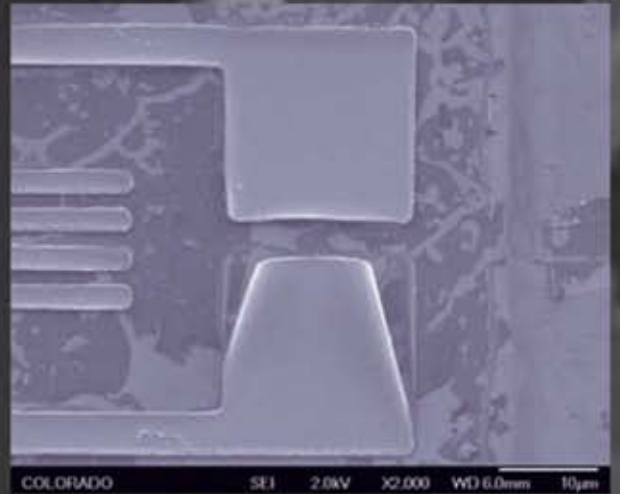
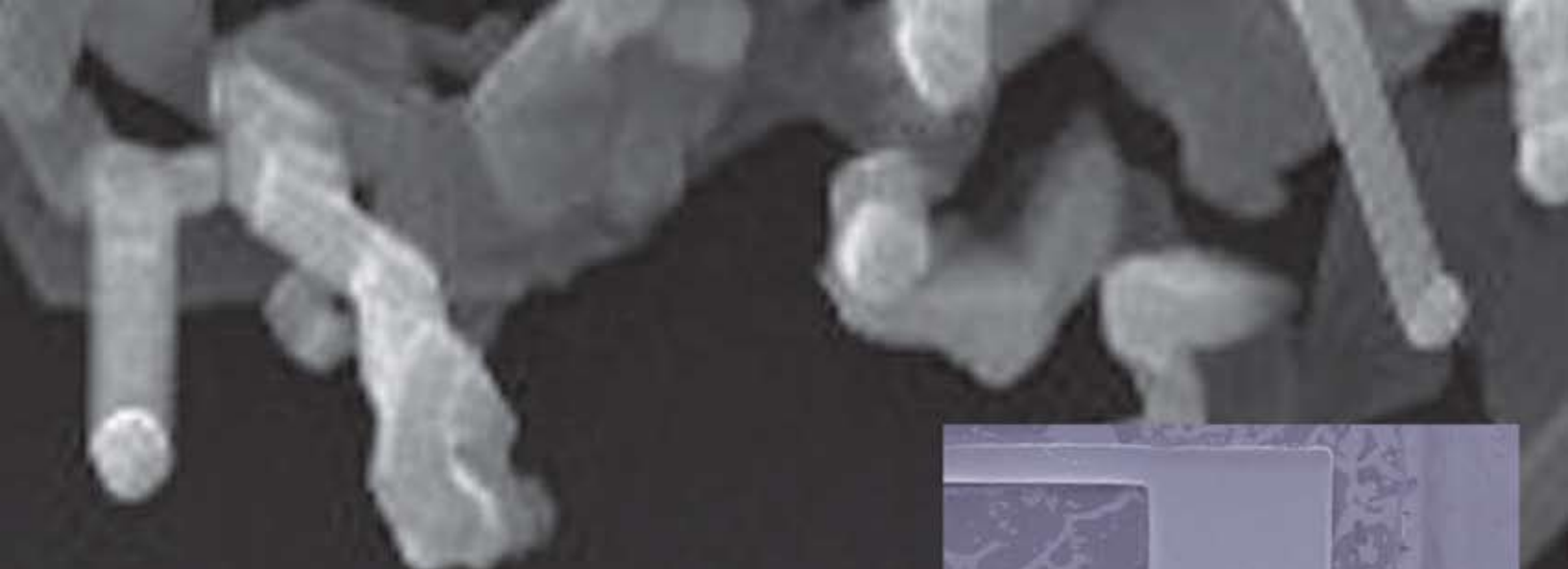
- Xu, Xiaodong ... 198  
 Xu, Yong ... 68

**Y**

- Yang, Xuan ... 58  
 Yearsley, Joshua ... 88  
 Yeh, Yin-Ting ... 8  
**Yu, Caroline** ... **126**  
 Yu, Edward ... 154  
**Yu, Patrick** . ... **170**

**Z**

- Zhang, Wenyu ... 102  
 Zhao, Bo ... 198  
 Zheng, Siyang ... 8  
 Zhu, Jun ... 186  
 Zou, Ke ... 186

The logo for the National Nanotechnology Infrastructure Network (NNIN). It features the letters "NNIN" in a large, blue, stylized font. Below the logo, the website address "www.nnin.org" and the tagline "Serving Nanoscale Science, Engineering & Technology" are displayed in a smaller blue font. The background is a grayscale SEM image of a nanowire network.

**NNIN**  
www.nnin.org  
Serving Nanoscale Science,  
Engineering & Technology

